HAL open science

Comparative study of particle-based methods SPH and LBM for the simulation of multiphase slug flows in pipes

Thomas Douillet-Grellier

▶ To cite this version:

Thomas Douillet-Grellier. Comparative study of particle-based methods SPH and LBM for the simulation of multiphase slug flows in pipes. Fluids mechanics [physics.class-ph]. Ecole Normale Supérieure Paris-Saclay, 2019. English. NNT : . tel-02310293v1

HAL Id: tel-02310293

https://theses.hal.science/tel-02310293v1

Submitted on 10 Oct 2019 (v1), last revised 15 Oct 2019 (v2)

HAL is a multi-disciplinary open access archive for the deposit and dissemination of scientific research documents, whether they are published or not. The documents may come from teaching and research institutions in France or abroad, or from public or private research centers.

L'archive ouverte pluridisciplinaire **HAL**, est destinée au dépôt et à la diffusion de documents scientifiques de niveau recherche, publiés ou non, émanant des établissements d'enseignement et de recherche français ou étrangers, des laboratoires publics ou privés.

université PARIS-SACLAY

école normale supérieure paris–saclay

NNT : 2019SACLN030

Étude comparative des méthodes d'origine particulaire SPH et LBM pour la simulation d'écoulements polyphasiques intermittents dans des conduites

Thèse de doctorat de l'Université Paris-Saclay
préparée à l'École Normale Supérieure Paris-Saclay

Ecole doctorale n°574 Mathématiques Hadamard (EDMH)
Spécialité de doctorat : Mathématiques Appliquées

Thèse présentée et soutenue à Cachan, le 7 octobre 2019, par

THOMAS DOUILLET-GRELLIER

Composition du Jury :

Damien Violeau EDF R&D & LHSV	Rapporteur
Ulrich Rüde FAU Erlangen-Nürnberg	Rapporteur
David Le Touzé École Centrale de Nantes	Président du jury
Laure Quivy École Normale Supérieure Paris-Saclay	Examinatrice
Sébastien Leclaire École Polytechnique de Montréal	Examinateur
Florian De Vuyst Université Technologique de Compiègne	Directeur de thèse
François Bertrand École Polytechnique de Montréal	Co-encadrant
Henri Calandra Total E&P	Co-encadrant
Philippe Ricoux Massachusetts Institute of Technology	Invité

Thèse de doctorat

Remerciements

Évidemment, je tiens à remercier en premier lieu mon directeur de thèse Florian De Vuyst pour son accueil, son accompagnement et sa bienveillance tout au long de ces 3 ans. Du côté de Total, je remercie Philippe Ricoux et Henri Calandra qui m'ont permis, en m'aidant à obtenir un financement CIFRE, de mener cette thèse dans d'excellentes conditions et qui m'ont suivi dans mes travaux de recherche depuis plus de 4 ans. Je remercie également François Bertrand, David Vidal et Sébastien Leclaire pour leur accueil durant mon séjour à Polytechnique Montréal qui a donné un bon coup d'accélérateur à ma fin de thèse.

Je remercie les membres du jury d'avoir bien voulu prendre le temps de relire mon manuscrit et d'assister à ma soutenance.

J'ai une pensée toute particulière pour les membres de l'équipe de recherche à laquelle j'appartenais durant mes deux années au MIT : John Williams, Bruce Jones, Kai Pan, Ranjan Pramanik et Sam Raymond. C'est eux les premiers qui m'ont poussé à me lancer dans un doctorat et qui m'ont fait découvrir le monde de la recherche.

Sur un plan plus personnel, je voudrais dire merci aux copains du CMLA pour les rigolades, les débats, les manifs, pour avoir supporté mon côté râleur et pour tous les apéros ! Je pense en particulier à Pierre, Ludo, Mounir, Batiste, Marie, Cédric, Charles et Christophe et j'en oublie. Je remercie aussi le personnel du labo, notamment Virginie, Alina et Véronique pour leur bonne humeur.
Je n'oublie pas mes amis parisiens : Maurice, Stan, Fayçal et Pierre-Yves bien sûr mais aussi Vincent, Virgile et Nari Yanne. Cela n'aurait pas été la même sans vous.

Merci à ma petite sœur, mes parents et mes grand-parents pour leur soutien inoxydable.

Merci à Elena pour les respirations bavaroises et pour m'avoir rejoint à Paris. L'avenir est à nous.

Enfin, je voudrais terminer en remerciant parmi d'autres : Elie Yaffa, Basil Poledouris, Prince Rogers Nelson, Michael West, Ophlin Russell, Jean Tenenbaum, Andre Young & Calvin Broadus, Valentin Le Du, Ennio Morricone, Mory Samaké & Stéphane Joachim ainsi que Owen Moncrieffe.

Between the time when the oceans drank Atlantis and the rise of the sons of Aryas,
There was an age undreamed of, and onto this, Conan,
Destined to wear the jeweled crown of Aquilonia upon a troubled brow.
It is I, his chronicler, who alone can tell thee of his saga.
Let me tell you of the days of high adventure !

— Subötai, Hyrkanian archer, c. 1982

Contents

Résumé **1**

Introduction **11**

1 An overview of particle methods **21**
1.1 Meshless particle methods . . . 22
1.2 Other particle methods . . . 34
1.3 Classification of particle methods . . . 36

2 Smoothed particle hydrodynamics **39**
2.1 Derivation of the SPH interpolation . . . 40
2.2 SPH approximation of Euler equations . . . 54
2.3 Key features . . . 60
2.4 Stabilization procedures . . . 61
2.5 Boundary conditions . . . 66
2.6 Time integration . . . 69
2.7 Multiphase SPH . . . 69

3 Lattice Boltzmann method **77**
3.1 Probability distribution functions . . . 78
3.2 Equilibrium . . . 82
3.3 Boltzmann Equation . . . 84
3.4 Chapman-Enskog expansion . . . 86
3.5 $\mathcal{H}$-Theorem . . . 91
3.6 Discretization . . . 91
3.7 Units . . . 101
3.8 Key features . . . 102
3.9 Alternative collision operators . . . 104
3.10 Boundary conditions . . . 105
3.11 LBM Variants . . . 109
3.12 Multiphase LBM . . . 110

4 Comparison of multiphase formulations of SPH and LBM **121**
4.1 Multiphase LBM model . . . 122
4.2 Multiphase SPH model . . . 126
4.3 Validation test cases . . . 131
4.4 Intermittent two-phase flows in pipes . . . 148
4.5 Conclusion . . . 159

5 Multiphase SPH for the simulation of intermittent flows in pipes **161**
5.1 Flow regimes . . . 162
5.2 Flow transitions . . . 169
5.3 Applied cases with high density and viscosity ratios . . . 174
5.4 Influence of the spurious interface fragmentation correction . . . 176

5.5 Comparison with experimental data . . . 186
5.6 Conclusion . . . 194

Conclusions and perspectives **195**

A *D2Q9* **MRT matrixes** **201**

B Technical details in the Chapman-Enskog expansion **203**
B.1 Isotropic tensors of order 2 and 4 . . . 203
B.2 Calculation of f_1 . . . 204
B.3 Calculation of σ_1 . . . 205
B.4 Calculation of $\mathbf{q}_1$ . . . 206
B.5 Gaussian-type integrals in D dimensions . . . 207

C Entropic considerations on the LBGK model for advection-diffusion **209**
C.1 LB method for the 1D advection-diffusion equation . . . 210
C.2 Equilibrium distributions . . . 211
C.3 Discrete H-Theorem . . . 212
C.4 Numerical experiments . . . 214
C.5 Other entropy functionals . . . 216
C.6 Conclusion . . . 217

Bibliography **219**

Nomenclature **237**

Résumé

Contexte

Ce travail de thèse s'inscrit dans le domaine de la mécanique des fluides numérique et a été réalisé dans le cadre du dispositif CIFRE (Convention Industrielle de Formation par la REcherche) de l'ANRT (Association Nationale de la Recherche et de la Technologie) sponsorisé par l'entreprise pétrolière et gazière Total. L'objectif initial était d'étudier les apports et les limitations des méthodes dites "particulaires" pour l'étude des écoulements polyphasiques. Devant l'ampleur de la tâche, il a été très rapidement décidé de se concentrer exclusivement sur la comparaison de deux méthodes d'origine particulaire de nature très différente mais ayant un fort potentiel dans la modélisation des problèmes polyphasiques [Huang 2015, Wang 2016, Li 2016] : la méthode *Smoothed Particle Hydrodynamics* (SPH) et la méthode de Boltzmann sur réseau (*Lattice Boltzmann Method* - LBM). Ces deux méthodes numériques sont principalement utilisées pour résoudre, par des moyens complètement distincts, les équations de Navier-Stokes. Ces équations, dans le cas monophasique d'un fluide faiblement compressible avec une viscosité constante, sont rappelées ci-dessous dans leur formulation eulérienne et accompagnées d'une équation d'état pour obtenir un système fermé :

$$\begin{cases} \frac{\partial \rho}{\partial t} + \rho \nabla \cdot \boldsymbol{u} & = 0, \\ \rho \frac{\partial \boldsymbol{u}}{\partial t} + \rho \nabla \cdot (\boldsymbol{u} \otimes \boldsymbol{u}) & = -\nabla p + \mu \nabla^2 \boldsymbol{u} + \rho \boldsymbol{g}, \\ p & = f(\rho), \end{cases}$$

où ρ est la densité, μ est la viscosité, $\boldsymbol{u}$ est le vecteur vitesse, p est le tenseur de pression, $\boldsymbol{g}$ est le terme de gravité et f est une équation d'état reliant la pression à la densité. La première équation est l'équation de continuité alors que la seconde est celle de bilan de quantité de mouvement.

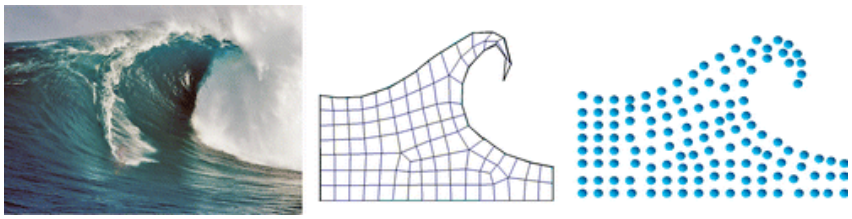

Figure 1: Discrétisation d'une vague avec et sans maillage.

Outre leurs potentialités intrinsèques pour modéliser les problèmes polyphasiques, nous avons décidé de restreindre notre champ d'étude à ces deux méthodes pour plusieurs raisons. Concernant SPH, nous voulions capitaliser sur l'expérience acquise avec cette méthode durant les deux années précédant le début de ce doctorat [Douillet-Grellier 2016c, Douillet-Grellier 2016b, Douillet-Grellier 2016a, Pramanik 2016, Das 2016, Pan 2018]. Pour LBM, il s'agit d'une demande de Total qui était déjà intéressé par cette méthode pour l'étude des écoulements en milieux poreux et qui souhaitait continuer d'explorer les possibilités offertes par LBM.

SPH est une méthode sans maillage lagrangienne introduite à la fin des années 1970 pour des applications en astrophysique [Lucy 1977, Gingold 1977] puis étendue à la mécanique des fluides standard. SPH peut être vue de deux façons : d'abord, il s'agit d'une technique de discrétisation d'équations aux dérivées partielles comme celles de Navier-Stokes, mais c'est aussi un système Hamiltonien discret composé de points matériels de masse constante dont l'évolution est suivie dans le temps. L'aspect

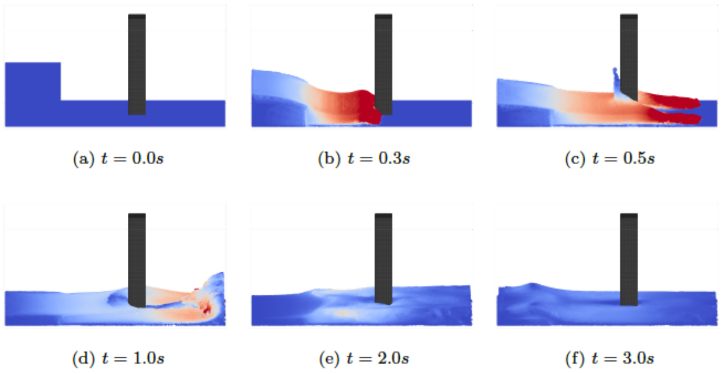

Figure 2: Une simulation SPH 3D de rupture de digue avec obstacle (extrait de [Pan 2015]).

purement sans maillage de SPH permet de se libérer de certaines contraintes liées à l'utilisation d'un maillage. Cependant, cela a aussi un coût. En effet, puisqu'il n'y a pas de connectivité prédéfinie entre les particules, une recherche des plus proches voisins doit être effectuée à chaque pas de temps ce qui est un frein à l'efficacité numérique du code. Parmi les nombreuses applications de la méthode SPH, on peut citer l'astrophysique [Springel 2010], l'hydrodynamique [Violeau 2016], la géophysique [Libersky 1991, Bui 2008, Douillet-Grellier 2016c, Douillet-Grellier 2016a] et l'infographie [Ihmsen 2014]. Des revues très complètes ont été publiées sur le sujet [Monaghan 2012, Price 2012, Shadloo 2016].

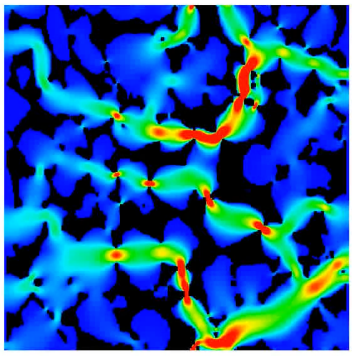

Figure 3: Une simulation LBM 2D d'écoulement monophasique à travers un milieu poreux (faite avec Palabos - `www.palabos.org`).

LBM, quant à elle, provient de deux origines distinctes : la théorie cinétique des gaz avec vitesses discrètes et la méthode des gaz sur réseau avec des automates cellulaires (*Lattice Gas Cellular Automata* i.e. LGCA ou LGA [Frisch 1986a]). A la fin des années 1980, les fonctions de densités de probabilités ont été introduites dans LGCA donnant ainsi naissance à la LBM. Cette méthode consiste à résoudre l'équation de Boltzmann dans un espace de vitesses discrètes ce qui est équivalent à résoudre les équations de Navier-Stokes pour des nombres de Mach et de Knudsen assez faibles (c'est ce qu'on appelle l'expansion multi-échelle de Chapman-Enskog [Viggen 2009]). En pratique, LBM se distingue des autres méthodes pour différentes raisons. D'abord, elle opère sur un réseau uniforme (réseau carré ou hexagonal principalement). Ensuite, elle se base sur un algorithme local, composé d'opérations arithmétiques simples sans termes différentiels, ce qui rend le code court, rapide et bien adapté à l'exécution parallèle [Harting 2005]. Enfin, les méthodes traditionnelles de mécanique des fluides numérique nécessitent le calcul de variables macroscopiques (vitesse, pression, densité)

alors que LBM suit l'évolution de fonctions de densité de probabilité de présence de particules à une position, une vistesse et un instant donnés [Benzi 1992]. LBM est utilisée depuis plus de 15 ans pour la simulation d'écoulement dans des géométries complexes, dans les milieux poreux en particulier [Cancelliere 1990, Ferreol 1995, Ahrenholz 2006, Guo 2002a].

Outre les cas de validations classiques, il a fallu choisir un cas d'application cible qui soit à la fois pertinent dans le cadre des activités de Total et simulable avec les deux méthodes. Dans un premier temps, nous avions pensé aux écoulements dans les milieux poreux mais la littérature étant déjà abondante sur le sujet, SPH apparaissait peu compétitive sur cette problématique (au delà de la simple faisabilité) par rapport à LBM. Finalement, nous avons préféré nous concentrer sur le problème des écoulements dits à bouchons (*slug flows* en anglais) dans des conduites. Ce régime d'écoulement se caractérise par l'émergence de bulles, qui occupent la majeure partie ou l'entièreté de la conduite, séparées entre elles par des phases pures ou quasi-pures de liquide comme montré sur la Fig. 4. Ces bulles peuvent mesurer jusqu'à plusieurs dizaines de mètres. C'est un régime qui est donc naturellement intermittent. Les écoulements à bouchons se retrouvent dans de nombreuses applications scientifiques et industrielles [Hewitt 2010] telles que les installations de transferts thermiques ou les équipements d'extraction de solvants mais aussi en météorologie. Dans le cadre de l'industrie pétrolière, on peut les retrouver dans les pipelines qui acheminent le pétrole et le gaz jusqu'aux raffineries où ces écoulements intermittents sont hautement indésirables [Sausen 2012]. Ce type d'écoulement est connu pour endommager les installations (phénomènes du marteau d'eau, étouffement de compresseurs, débordement dans les séparateurs) et pour réduire l'efficacité du transport des fluides.

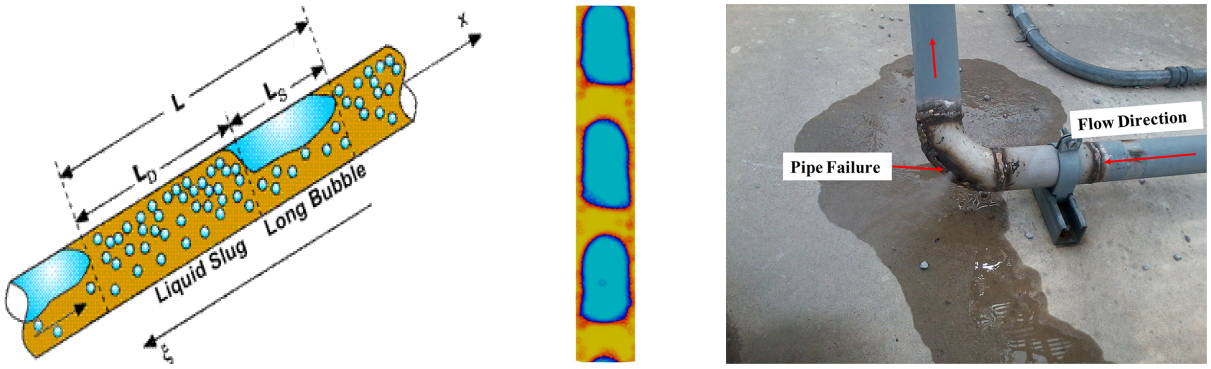

(a) (b) (c)

Figure 4: Exemples d'écoulements à bouchons. (a) Schéma d'un écoulement à bouchons dans une conduite oblique. (b) Simulation SPH 2D d'un écoulement à bouchons dans une conduite verticale. (c) Exemple d'une conduite endommagée à cause d'un écoulement à bouchons.

Les mécanismes qui génèrent ces écoulements intermittents sont bien connus. Dans le cas d'une conduite horizontale, les bouchons dits "hydrodynamiques" (*hydrodynamic slugging*) sont induits par l'instabilité de Kelvin-Helmholtz. Dans certaines conditions de vitesses superficielles et de géométrie, des vagues de liquide apparaissent causant ainsi une augmentation locale de la vitesse du gaz et une diminution locale de la pression. Dès lors, une force de succion engendre une augmentation du niveau de liquide jusqu'à atteindre le haut de la conduite créant ainsi un bouchon. Une méthode classique pour éviter l'apparition d'un bouchon hydrodynamique est l'utilisation de cartes de régimes d'écoulement, comme par exemple sur la Fig. 5 qui permettent d'opérer dans des conditions où les bouchons ont très peu de chances de se former.

Dans le cas d'une conduite non-horizontale, des écoulements intermittents à bouchons peuvent

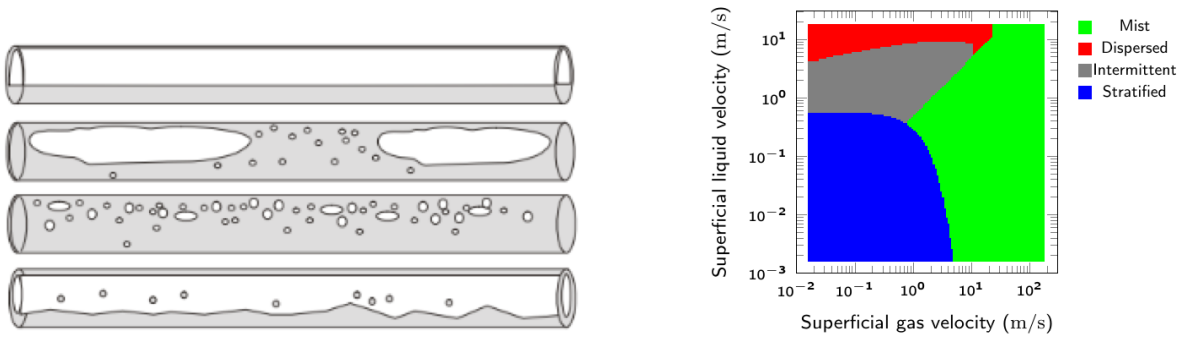

(a) (b)

Figure 5: (a) De haut en bas : écoulement stratifié (*stratified*), intermittent (*intermittent*), dispersé (*dispersed*) et brumeux (*mist*) (b) Exemple de carte de régimes d'écoulement adaptée de [Taitel 1976].

être engendrés par les effets combinés de la gravité et de la géométrie du terrain sur lequel la conduite repose [Sánchez-Silva 2013]. Certaines géométries de conduites, comme les coudes, peuvent piéger le liquide qui s'accumulera jusqu'à atteindre la partie supérieure de la conduite créant ainsi un bouchon qui sera emporté par l'écoulement de manière périodique (*terrain slugging*). En outre, des bouchons peuvent aussi se former dans les tubes prolongateurs (*risers*) qui relient le fond de la mer avec une plateforme pétrolière. Brièvement, un bouchon de liquide peut se former à la base du tube prolongateur bloquant ainsi le gaz qui arrive. A cause de la pression qui va en augmentant, le liquide commence à remplir le tube formant ainsi un bouchon qui engorge le séparateur placé à la sortie du tube. Enfin, des bouchons peuvent aussi être générés par des changements de débit ou à cause d'un piston racleur (*pigging*).

La question principale lorsqu'on étudie les écoulements à bouchons dans le cadre décrit ci-dessus est de savoir si, oui ou non, ces bouchons se forment et de chercher un ou plusieurs critères qui contrôlent leur apparition [Zhang 2017]. Le cas échéant les quantités d'intérêt sont la taille, le temps de transit et la fréquence de ces bouchons. La compréhension de la formation des écoulements intermittents est un domaine de recherche actif depuis des années. Dans ce contexte, les approches de type CFD (*Computational Fluid Dynamics*) [Lu 2015, Pedersen 2017] sont un outil précieux pour prédire ces phénomènes dans l'industrie pétrolière.

Au niveau industriel, les premières simulations [Taitel 1980, Viggiani 1988, Sarica 1991] ont été menées dans le milieu des années 1980. De nos jours, dans l'industrie du pétrole, deux logiciels commerciaux sont en compétition pour la simulation des écoulements intermittents : OLGA développé par le groupe SPT [Bendiksen 1991] et LedaFlow proposé par Kongsberg [Kongsberg 2014]. Une comparaison détaillée de ces deux programmes [Belt 2011] conclut que ces deux codes sont également performants pour des cas simples mais qu'ils ont des soucis pour simuler les cas complexes avec une phase gazeuse dominante. D'un point de vue académique, différents modèles et méthodes ont déjà été considérés pour simuler les problèmes d'écoulements à bouchons. Parmi ceux-ci, on peut citer la méthode du volume de fluide (*volume-of-fluid*) [Taha 2004, Al-Hashimy 2016], la méthode des lignes de niveaux (*level-set*) [Fukagata 2007, Lizarraga-García 2016], LBM [Yu 2007], SPH [Minier 2016] ou l'approche des champs de phase (*phase field*) [He 2008, Xie 2017]. Cependant, ces techniques ont été appliquées en général à des problèmes de micro-fluidique. Il apparaissait donc intéressant dans le cadre de cette thèse d'explorer les apports et les limitations de SPH et LBM dans le cadre de la simulation d'écoulements à bouchons pour l'industrie pétrolière.

Objectifs

Le cadre général étant ainsi posé, on peut synthétiser les objectifs de la thèse autour de 3 axes.

1. Rappeler les fondements mathématiques des méthodes SPH et LBM en les replaçant dans le paysage des méthodes dites "particulaires".

2. Comparer les formulations polyphasiques de SPH et LBM sur des cas de références ainsi que sur des cas simples d'écoulements à bouchons.

3. Choisir la méthode la plus adaptée et compléter l'étude par la simulation de cas appliqués et expérimentaux.

Plan du manuscrit

Ce manuscrit de thèse va s'articuler autour de cinq chapitres :

Le **chapitre 1** sera l'occasion de faire un récapitulatif sur les méthodes particulaires. En effet, l'appellation "particulaire" pouvant recouvrir un grand nombre de cas (lagrangien, eulérien, avec/sans maillage, discret/continu, général/spécifique), il est nécessaire d'y apporter une définition claire. On rappellera donc les grand principes des méthodes particulaires sans maillage ainsi que ceux des méthodes particulaires plus atypiques. Enfin, on proposera une classification des ces méthodes où l'on pourra retrouver SPH et LBM.

Le **chapitre 2** sera exclusivement consacré à l'état de l'art de la méthode SPH. On présentera en détail la dérivation de l'interpolation SPH ainsi que la discrétisation des équations classiques de la mécanique des fluides. On s'arrêtera sur les procédures de stabilisation inhérentes à SPH mais aussi sur les conditions aux limites et l'intégration temporelle. Enfin, le chapitre se conclura sur une revue des formulations polyphasiques disponibles pour SPH avec un accent particulier sur l'approche CSF (*Continuum Surface Force*) proposée par [Hu 2006] qu'on utilisera dans le reste du manuscrit.

Le **chapitre 3** présentera l'état de l'art de la méthode LBM. On s'intéressera en particulier à l'expansion de Chapman-Enskog ce qui nous amènera à expliquer la dérivation complète des équations de LBM en partant de l'équation de Boltzmann. On passera également en revue, les principales conditions aux limites disponibles et quelques variantes de LBM. On terminera, comme pour la chapitre précédent, sur une revue comparative des principales formulations polyphasiques en détaillant plus précisément l'approche des gradients de couleur [Reis 2007], qui sera la méthode utilisée dans la suite de ce document.

Le **chapitre 4** entrera dans le cœur du sujet, en proposant une comparaison de deux formulations polyphasiques choisies pour SPH et LBM : la méthode du gradient de couleur en LBM et la méthode CSF pour SPH. On mènera donc une étude comparative des deux approches, dans un premier temps sur une collection de cas tests variés : cavité entrainée, montée par capillarité, bulles statiques et instabilités de Rayleigh-Taylor. Puis, on poursuivra la comparaison sur des cas d'écoulements à bouchons périodiques ainsi qu'avec des conditions au limites entrée/sortie.

Le **chapitre 5** ne concernera que SPH et permettra d'explorer plus profondément le potentiel de SPH

pour simuler différents types de régimes d'écoulements et les transitions entre ces régimes, mais aussi des cas d'écoulements intermittents, avec des ratios de densité et de viscosité et une géométrie plus proche de la réalité du terrain. On poursuivra avec une étude paramétrique de l'impact d'un terme correctif d'interface sur les simulations précédentes. Enfin, on présentera pour finir une comparaison avec des données expérimentales.

Contributions

On peut résumer les contributions propres à la thèse en quelques points détaillés ci-dessous. On rappelle qu'il s'agit d'une thèse industrielle, les contributions sont donc davantage pratiques et appliquées que théoriques.

1. Construction d'un code SPH/LBM polyphasique Pour les besoins de cette thèse, il a donc fallu écrire deux codes, un pour SPH et un pour LBM. Il a été choisi de travailler avec le langage Fortran, accéléré en utilisant OpenMP. Les codes sont hébergés sur la plateforme de développement de Total à Houston (git, bitbucket, JIRA) et sont donc formatés et bâtis selon les standards en vigueur au sein des équipes de développement de Total. Ils utilisent quelques fonctions utilitaires provenant de la bibliothèque d'imagerie sismique de Total. Le pré-processeur est le même pour les deux codes, il s'agit du programme en accès libre *pyck* (`https://github.com/brucedjones/pyck`). Il a été écrit par moi-même et un ancien collègue en Python/C++ (via *swig*) dans le cadre d'un précédent projet sponsorisé par Total. Le post-traitement est effectué avec Paraview pour la partie visualisation et MATLAB pour la génération de graphes en tout genre. Les fichiers d'entrée/sortie sont au format VTK (ASCII et binaire sont supportés). Les deux codes partagent la même structure de données : deux types dérivés (*derived types*) contenant respectivement tous les tableaux requis pour les calculs (densité, vitesse, ...) et tous les paramètres nécessaires à la simulation. D'abord, ces deux types dérivés sont initialisés, alloués puis remplis avec les valeurs lues dans les fichiers d'entrée. Ensuite, une boucle en temps va appliquer l'algorithme SPH ou LBM (calcul des variables macroscopiques, calcul des dérivés temporelles, application des conditions aux limites et intégration en temps) en opérant sur les types dérivés. Cette boucle en temps produit, à intervalles réguliers, un fichier de sortie VTK qui est utilisé pour le post-traitement. Il y a cependant quelques différences notables entre les deux codes. D'abord, SPH repose sur une décomposition de domaine pour effectuer la recherche des plus proches voisins nécessaire à chaque itération. Cette méthode permet de chercher les particules voisines d'une particule donnée seulement dans les cellules adjacentes à celle qui contient la particule courante et pas dans tout le domaine. De plus, toujours dans une optique d'optimisation, le code SPH procède à un tri régulier des particules dans les tableaux afin de limiter les accès mémoires distants. Le code LBM ayant par nature un algorithme local, on a fait usage autant que possible de la vectorisation des opérations pour accélérer les calculs. On a limité l'écriture de boucles sur les composantes d'un tableau au maximum (exceptées celles accélérées par OpenMP) pour travailler directement sur la globalité du réseau quand c'était possible. Concernant l'efficacité respective des deux codes, LBM reste une méthode bien plus rapide que SPH et cela malgré les progrès importants réalisés sur le sujet dans la communauté SPH. En effet, on rappelle que LBM est basé sur un réseau et donc la connectivité entre les nœuds est connue, a priori, alors que SPH est une méthode purement lagrangienne. On doit donc effectuer une recherche des plus proches voisins à chaque pas de temps pour chaque particule. Pour information, le code LBM est environ 4 fois plus rapide que le code SPH ($1.03.10^{-6}$s/nœud pour LBM contre $3.85.10^{-6}$s/particule pour SPH) sur un ordinateur portable équipé d'un processeur Intel Core i7 de 2.9 GHz à 4 coeurs et de 16 Gb de RAM. Ces chiffres sont à prendre avec précaution puisque les codes ne sont pas optimisés et ne sont donc pas réprésentatifs du potentiel HPC de LBM et SPH.

2. Conditions aux limites d'entrée/sortie polyphasiques Lors de nos investigations, nous avons rapidement réalisé que nous allions avoir besoin d'implémenter des conditions aux limites d'entrée/sortie. En effet, les conditions aux limites périodiques ne suffisent pas à simuler tous les cas possibles car elles sont difficiles à mettre en œuvre d'un point de vue expérimental. Il est beaucoup plus naturel de travailler avec des conditions aux limites d'entrée/sortie. Dans notre cas, l'objectif est de pouvoir injecter en entrée deux phases simultanément avec des vitesses superficielles différentes et d'avoir une condition de pression en sortie. Ajoutons que si en entrée, on connait le profile de l'écoulement a priori, en sortie cela n'est pas le cas du tout, on peut avoir des bulles plus ou moins grosses ou des phases pures. Pour SPH, après avoir épluché la littérature sur le sujet, nous avons décidé de partir des idées proposées par [Tafuni 2018, Alvarado-Rodríguez 2017] pour le cas monophasique et de les étendre au polyphasique. L'apport étant le traitement des variables à l'interface, voir Sect. 4.2 pour les détails. Cette approche est basée sur l'utilisation de zones tampons contenant des particules à l'entrée et à la sortie du domaine. Pour LBM, nous avons choisi d'étendre les conditions d'entrée/sortie de Zou-He [Zou 1997] avec un traitement spécifique pour le champ de couleur, voir Sect. 4.1 pour plus de précisions. L'idée consiste à travailler avec les fonctions de distributions totales du modèle des gradients de couleur et de leur appliquer l'algorithme classique proposé par Zou-He. Ensuite, il faut redistribuer ces quantités en prenant en compte la valeur du champ de couleur. Il faut ajouter qu'ayant utilisé une fonction d'équilibre particulière, il a fallu re-dériver la méthode de Zou-He avec cette fonction ce qui ajoute un terme correctif supplémentaire. Tout comme pour SPH, on verra que ces conditions aux limites ne sont pas parfaites mais ont le mérite d'être stables (surtout en sortie) pour une assez large plage de nombres de Reynolds et de ratios de densité et de viscosité. En outre, elles sont plutôt simples à implémenter.

3. Validation et comparaison des formulations Une fois les codes écrits, il a fallu les valider sur une collection de cas tests classiques monophasiques et polyphasiques : bulle statique, instabilité de Rayleigh-Taylor, cavité entraînée et montée par capillarité. Nous avons choisi de mener cette campagne de validation en parallèle pour SPH et LBM afin de pouvoir comparer les résultats des deux méthodes. Nous avons ensuite poussé la comparaison sur des cas d'écoulements à bouchons périodiques, comme montré par exemple sur la Fig. 6, ainsi qu'avec des conditions aux limites de type entrée/sortie. A notre connaissance, une telle étude comparative, présentée dans le Chap. 4, n'avait pas été faite par le passé. Nous insistons sur le fait que les formulations adoptées pourraient probablement être améliorées en implémentant des techniques plus avancées, disponibles dans la littérature. La principale conclusion de ce travail est que, d'après nos résultats, LBM est plus précise et possède un meilleur ordre de convergence que SPH mais est très limitée par sa zone de stabilité. Plus clairement, quand les conditions de stabilité de LBM sont remplies, celle-ci est plus performante que SPH mais ces conditions réduisent fortement le champ d'applications de la méthode, que ce soit en terme de nombre de Reynolds ou de ratios de densités et/ou de viscosités. Étant donné que nous voulions poursuivre notre étude des écoulements dans les conduites sur des cas plus réalistes sortant a priori de la zone de stabilité de LBM, nous avons décidé de ne poursuivre ce travail qu'avec SPH.

4. Étude de l'applicabilité de SPH à des cas plus réalistes Dans le Chap. 5, nous avons choisi de ne conserver que SPH et de prolonger notre étude à des cas plus réalistes. Nous entendons par "plus réalistes" des cas avec des vitesses plus importantes, des géométries plus proches du terrain et des ratios de densités et de viscosités de type gaz/pétrole. Dans un premier temps, on s'est donc attaché à explorer plus largement la carte d'écoulement de la Fig. 5, en s'intéressant aux autres régimes d'écoulement (stratifié, dispersé, brumeux) et aux transitions de l'un à l'autre, comme montré sur la Fig. 7. Dans un second temps, on s'est intéressé à des cas d'écoulements à bouchons de type hydrodynamique et de

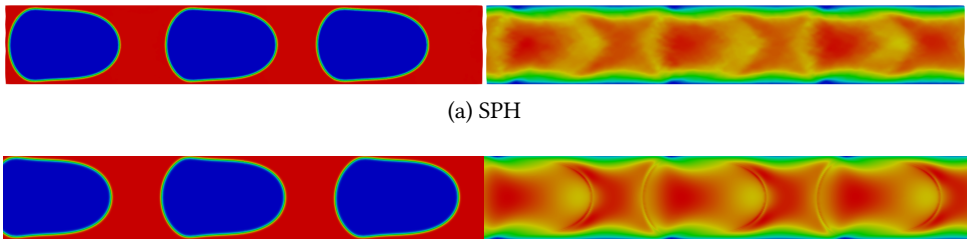

(a) SPH

(b) LBM

Figure 6: Distribution des phases (gauche) et champs de vitesse normalisés (droite) à l'état stationnaire périodique pour $Re = 50$.

terrain pour montrer le potentiel de la méthode sur ce créneau. Enfin, nous terminons avec des simulations de cas réels pour lesquels nous avons des résultats expérimentaux et auxquels nous pouvons nous comparer directement. Une fois, de plus, à notre connaissance, un tel travail n'était pas disponible dans la littérature existante.

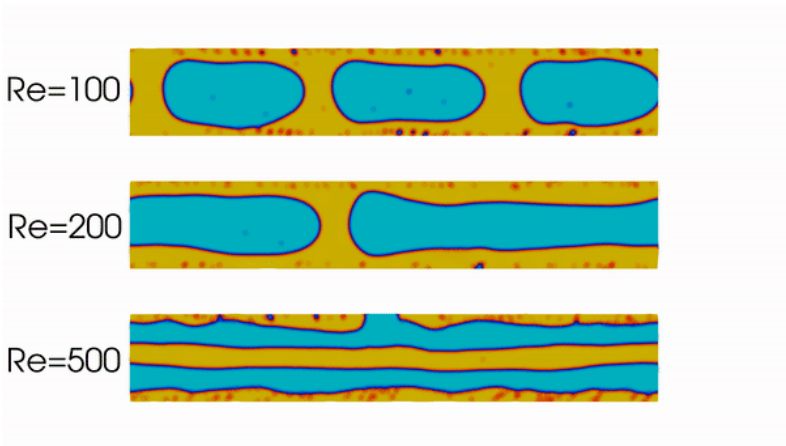

Figure 7: Distribution des phases pour différents types de régimes d'écoulements simulés avec SPH avec des ratios de densités et de viscosité de type air/eau.

5. Étude paramétrique de l'influence d'un terme correctif SPH En utilisant la formulation SPH polyphasique proposée par [Hu 2006], nous avons vite été contraints, comme suggéré dans la littérature, d'ajouter un terme correctif du type, $\boldsymbol{F}_a^{corr} = \varepsilon \sum_{b \in \Lambda_a, b \notin \Omega_a} \left(\frac{1}{\Theta_a^2} + \frac{1}{\Theta_b^2} \right) \nabla_a w_{ab}$, pour éviter une fragmentation non-physique de l'interface. Ce terme est contrôlé par un paramètre libre ε. Le lien entre ce paramètre et des valeurs physiques n'est pas clair [Szewc 2016]. Dans la Sect. 5.4, nous avons donc regardé l'impact de cette force corrective sur les simulations SPH précédentes, pour différentes valeurs de ε. Nous avons notamment remarqué que cette force peut influer sur le caractère intermittent de l'écoulement et qu'il doit donc être utilisé avec précaution.

6. Exploration de considérations entropiques en LBM Enfin, au cours de la thèse, nous nous sommes également intéressés à la LBM pour les équations d'advection-diffusion 1D avec l'opérateur BGK. Il s'agit ici seulement d'une amorce de travail qui est présentée dans l'Appendice C. On arrive

notamment à obtenir un théorème $\mathcal{H}$ à partir de considérations entropiques. Cela nous permet d'obtenir une évaluation fine de la dissipation d'entropie, que l'on vérifie via des expériences numériques, mais aussi de réinterpréter l'opérateur de collision BGK comme le gradient d'une fonctionnelle lagrangienne associée à un problème de minimisation. Il conviendrait de pousser l'analyse plus loin, notamment en 2D, nous n'avons, malheureusement, pas eu le temps d'aller jusque là.

Limitations

Aspect HPC La comparaison des vitesses d'exécution des deux méthodes ne sera pas abordée. En effet, nous avons implémenté les méthodes pour qu'elles s'exécutent le plus rapidement possible mais nous n'avons pas eu le temps de prendre en compte les avancées algorithmiques les plus récentes sur ce sujet, ni d'ajouter une couche MPI (*Message Passing Interface*), pour l'accélération multi-machine, ni de porter le code sur GPU (*Graphics Processing Unit*). Cela ne nous permet pas d'émettre un avis valable sur cette thématique.

Simulations 2D Pour des raisons pratiques (temps de calcul, simplicité), toutes nos simulations sont réalisées en 2D. Le passage en 3D ne pose pas a priori d'obstacles majeurs, cela requiert juste une implémentation plus lourde, une attention particulière pour certains problèmes géométriques et une nouvelle campagne de validation. Nous n'avons pas eu le temps d'aller jusque là.

Turbulence On ne prendra pas en compte les phénomènes turbulents. Il existe des moyens d'implémenter des modèles de turbulences dans les méthodes SPH et LBM et il serait intéressant de pousser l'analyse plus loin en intégrant ces modèles, en particulier pour les quelques cas à haut Reynolds présentés ci-après. Nous pensons que la viscosité turbulente pourrait avoir un effet stabilisant sur les champ de pression.

Publications

Ce travail de recherche a donné lieu à 4 publications (2 journaux, 2 conférences) :

- **Douillet-Grellier, T.**, De Vuyst, F., Calandra, H., & Ricoux, P. (2018). Simulations of intermittent two-phase flows in pipes using smoothed particle hydrodynamics. Computers & Fluids.
- **Douillet-Grellier, T.**, De Vuyst, F., Calandra, H., & Ricoux, P. (2018). Influence of the spurious interface fragmentation correction on the simulation of flow regimes. In Proceedings of the International 13th SPHERIC Workshop, June 26-28, Galway, Ireland.
- De Vuyst, F. & **Douillet-Grellier, T.** (2018). Entropic considerations on the LBGK model for advection-diffusion. In Proceedings of 39th Ibero-Latin American Congress on Computational Methods in Engineering (CILAMCE), November 11-14, Paris, France.
- **Douillet-Grellier, T.**, Leclaire, S., Vidal, S., Bertrand F. & De Vuyst, F. (2019). Comparison of multiphase SPH and LBM approaches for the simulation of intermittent flows. Computational Particle Mechanics.

En outre, 2 publications (2 conférences) sur des thématiques SPH débutées avant le doctorat ont aussi eu lieu pendant la thèse :

- Pramanik, R., Pan, K., Jones, B. D., Albaiz, A., Williams, J. R., **Douillet-Grellier, T.**, & Pourpak, H. (2017). Numerical Simulation of Fracture Propagation in Layered Rock. In Proceedings of 51st US Rock Mechanics/Geomechanics Symposium, June 25-28, San Francisco, California, USA.
- Raymond, S. J., Jones, B. D., Pramanik, R., Pan, K., **Douillet-Grellier, T.** & Williams, J. R. (2017). On the efficacy of augmenting SPH simulations of mixed-mode failure with the Material Point

Method. In Proceedings of the SPHERIC Beijing International Workshop, October 17-20, Beijing, China.

Introduction

Context

This doctoral thesis comes within the scope of computational fluid dynamics and has been undertaken thanks to the CIFRE (*Convention Industrielle de Formation par la REcherche*) funding provided by the ANRT (*Association Nationale de la Recherche et de la Technologie*) and sponsored by the french oil and gas company Total. The initial goal was to study the contributions and limitations of "particle" methods for the simulation of multiphase flows. In order to reduce the scope of investigations, it has been quickly decided to focus exclusively on the comparison of two particle-based methods from very different origins but with a strong potential to model multiphase flow problems [Huang 2015, Wang 2016, Li 2016] : the Smoothed Particle Hydrodynamics (SPH) method and the Lattice Boltzmann Method (LBM). These methods are mainly used to solve, by different means, the Navier-Stokes equations. These equations, for a single phase weakly compressible fluid with a constant viscosity, are recalled hereafter in their Eulerian formulation alongside an equation of state to close the system :

$$\begin{cases} \frac{\partial \rho}{\partial t} + \rho \nabla \cdot \boldsymbol{u} & = 0, \\ \rho \frac{\partial \boldsymbol{u}}{\partial t} + \rho \nabla \cdot (\boldsymbol{u} \otimes \boldsymbol{u}) & = -\nabla p + \mu \nabla^2 \boldsymbol{u} + \rho \boldsymbol{g}, \\ p & = f(\rho), \end{cases}$$

where ρ is the density, μ is the viscosity, $\boldsymbol{u}$ is the velocity, p is the pressure, $\boldsymbol{g}$ is the gravity term et f is an equation of state linking density and pressure. The first and second equations are respectively the continuity and the momentum equations.

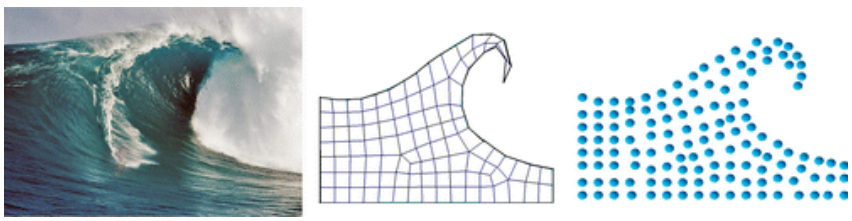

Figure 8: Meshbased and meshless discretization of a wave.

Beyond their intrinsic abilities to model multiphase problems, we have decided to restrain our scope of research to two methods for several reasons. For SPH, we wanted to take advantage of the experience acquired with this method during two years before the beginning of this doctoral work [Douillet-Grellier 2016c, Douillet-Grellier 2016b, Douillet-Grellier 2016a, Pramanik 2016, Das 2016, Pan 2018]. Concerning LBM, it was a Total request who was already interested by this method for porous media flows applications and wanted to keep exploring the potential of LBM.

SPH is a Lagrangian meshfree method introduced in the late 70's for astrophysics applications [Lucy 1977, Gingold 1977] and later expanded to standard fluid mechanics. SPH can be seen from two different perspectives. On one hand, it is a way to discretize partial differential equations such as the Navier-Stokes equations. On the other hand, it is a discrete Hamiltonian system composed of material points of constant mass that are tracked in time. Its pure meshless nature allows to get rid of many issues associated with meshing. However, it comes at some expenses too. Since there is no connectivity between particles, a neighbor searching procedure has to be carried for every particle at every time step, which

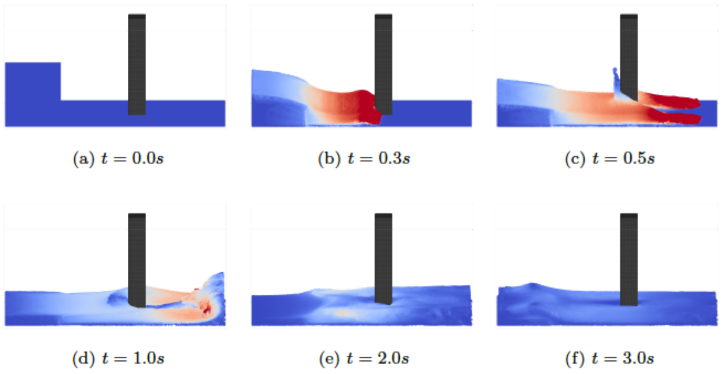

Figure 9: A 3D SPH dambreak simulation (taken from [Pan 2015])

is a serious bottleneck for code efficiency. Among the numerous applications of SPH, we can mention astrophysics [Springel 2010], hydrodynamics [Violeau 2016], geophysics [Libersky 1991, Bui 2008, Douillet-Grellier 2016c, Douillet-Grellier 2016a] and computer graphics [Ihmsen 2014]. Some extensive reviews have been published [Monaghan 2012, Price 2012, Shadloo 2016].

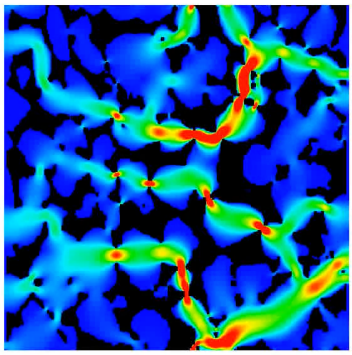

Figure 10: A 2D LBM single flow through porous media simulation (done with Palabos - www.palabos.org)

LBM originates from two distinct approaches: the kinetic gas theory with discrete velocities and the lattice gas cellular automata method (LGCA or LGA [Frisch 1986a]). In the late 80's, probability density functions were introduced within LGCA, giving birth to LBM. It consists in solving the Boltzmann equation in a discrete velocity space, which has been proven to be equivalent to solving the Navier-Stokes equations in the limit of low Mach and Knudsen numbers (as can be shown by a multiscale Chapman-Enskog expansion [Viggen 2009]). In practice, LBM distinguishes itself from other methods for several reasons. First, the LBM operates on an uniform lattice (mostly square or hexagonal lattices). Then, LBM offers a local algorithm involving simple arithmetic operations with no differential terms, which makes it short, fast and particularly well suited for parallel execution [Harting 2005]. Finally, traditional CFD methods are based on the calculation of macroscopic variables (velocity, pressure, density) whereas LBM tracks the evolution of probability distribution functions of the presence of particles at a given location, speed and time [Benzi 1992]. LBM has been used for decades for flow simulations in complex geometries, especially in porous media [Cancelliere 1990, Ferreol 1995, Ahrenholz 2006, Guo 2002a].

Apart from generic validation cases, we had to choose a target application case which is relevant regarding Total's interests and possible to simulate with both methods. Initially, we thought about

porous media flows but the literature was already abundant on that topic and SPH appeared less competitive for this kind of problems compared to LBM. In the end, we have decided to focus on the simulation of slug flows in pipes (also known as plug flow). This flow regime is characterized by the emergence of large bubbles that can fill most of or all the pipe which are separated by pure or almost pure liquid phases as shown on Fig. 11. Theses bubbles can measure up to tens of meters. Therefore, it is a regime that is naturally intermittent. Slug flows can be encountered in numerous industrial and scientific applications [Hewitt 2010] such as chemical and heat transfer systems or solvent extraction equipment but also in meteorology. One of the main examples is the transportation of oil and gas (or oil and water) from reservoirs to refinery facilities through pipelines in the petroleum industry. In that case, these patterns are highly undesirable [Sausen 2012] because they are known to damage facilities (separators flooding, compressors starving, water hammer phenomenon) and to reduce flow efficiency.

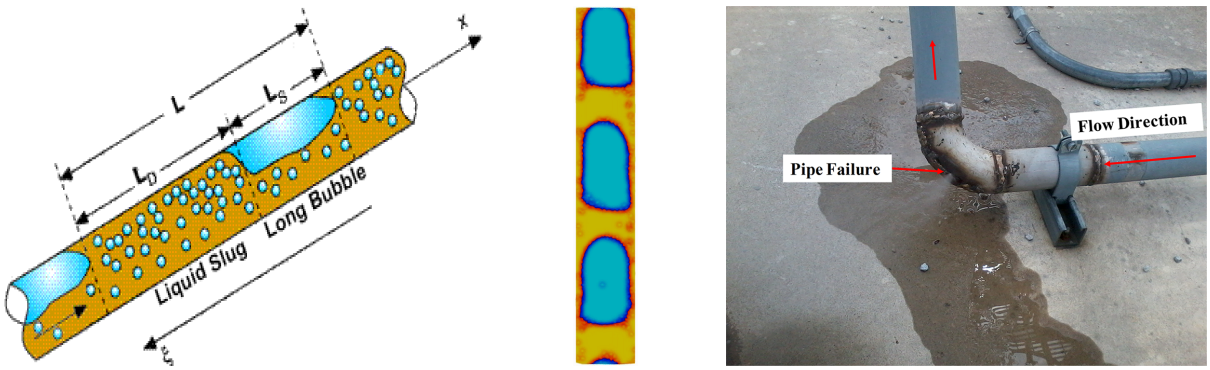

(a) (b) (c)

Figure 11: Examples of slug flows. (a) Schematic fo a slug flow in an oblique pipe. (b) 2D SPH simulation of a slug flow in a vertical pipe. (c) Example of a damaged pipe because of slug flow regime.

The mechanisms of generation of slug flows are well known. On one hand, in the case of horizontal pipes, "hydrodynamic" slugs are induced by the Kelvin-Helmholtz instability. Under certain velocity and geometry conditions, liquid waves can grow in the flow causing a local increase of the gas velocity and a local decrease of the pressure. Consequently, a suction force starts to move the interface higher until reaching the top of the pipe and forming a slug. A common way to avoid the appearance of hydrodynamic slugs is to use flow regime maps such as the one shown on Fig. 12 to operate with flow conditions that are unlikely to generate them.

On the other hand, intermittent flows can be caused by the combined effects of gravity and terrain geometry on which the pipe lies [Sánchez-Silva 2013]. The path of the pipe can have low spots, like elbows, in which the liquid is trapped. It accumulates until reaching the top of the pipe and it is then carried away by the flow forming a slug. Alternatively, severe slugging can occur in risers. In a nutshell, a liquid slug begins to form at the riser base blocking the incoming gas. Moved by the increasing gas pressure, the liquid fills up the riser forming a slug that flood the separator at the end of the riser. Additionally, slugging can be generated by a flow rate change or by pigging. The main question when studying slugging is to know whether or not it will occur and eventually to find the criterion that triggers its formation [Zhang 2017]. If it does, the quantities of interest are the size of slugs and their transit time and frequency. The understanding of the formation of intermittent flow patterns has been a lively research area for years. In this context, Computational Fluid Dynamics (CFD) softwares [Lu 2015, Pedersen 2017] emerged as a useful tool to predict the appearance of a slug flow regime in the oil and gas industry.

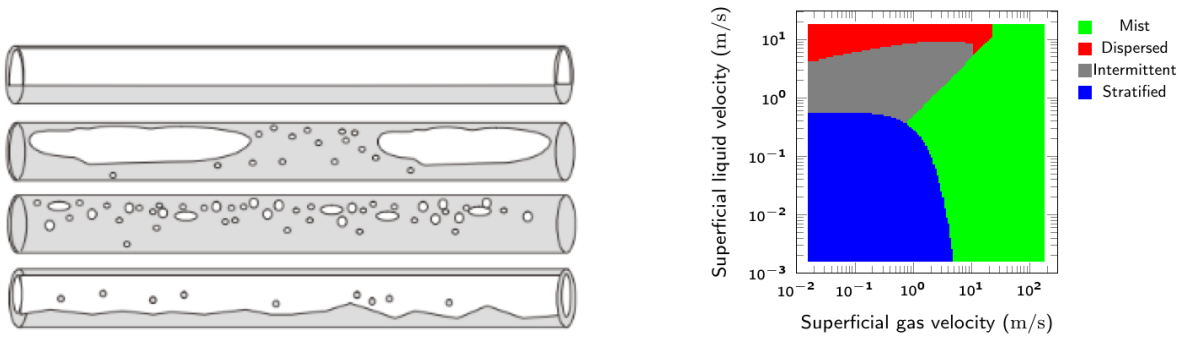

(a) (b)

Figure 12: (a) From top to bottom : stratified flow, intermittent flow, dispersed flow and mist flow. (b) Example of a flow regime map adapted from [Taitel 1976].

At the industrial level, the first simulations [Taitel 1980, Viggiani 1988, Sarica 1991] were done in the mid 80's. Nowadays, in the oil and gas industry, two commercial software products are competing for slugging simulation : OLGA developed by SPT group [Bendiksen 1991] and LedaFlow, proposed by Kongsberg [Kongsberg 2014]. A detailed comparison of both codes [Belt 2011] concludes that although performing equally well on simple cases, they have trouble to simulate complex cases with a dominant gas phase. From an academic perspective, different models and methods have been used for slug flow modeling, for example volume-of-fluid [Taha 2004, Al-Hashimy 2016], level-set [Fukagata 2007, Lizarraga-García 2016], lattice Boltzmann method (LBM) [Yu 2007], smoothed particle hydrodynamics (SPH) [Minier 2016] or phase field [He 2008, Xie 2017], but these are applied on microfluidic problems for the most part. It appeared to be of interest within this doctoral work to explore the contributions and limitations of SPH and LBM for the simulation of slug flows in pipes.

Objectives

The general framework has been described, we can now detail the 3 main goals of this thesis.

1. Recall the mathematical foundations of SPH and LBM and place them in the landscape of particle-based methods.

2. Compare the multiphase formulations of SPH and LBM on reference cases as well as on slug flows cases.

3. Choose the most adapted method and extend the study to applied and experimental cases.

Manuscript outline

This Ph.D manuscript will be composed of 5 chapters :

Chapter 1 will be the opportunity to present an overview of particle-based methods. Indeed, the designation "particle-based" or "particle" can cover a large number of cases (Lagrangian/Eulerian, mesh-based/meshless, discrete/continous, general/specific). It is necessary to provide a clear definition of what

we mean by particle methods. We will therefore recall the main principles of meshless particle methods and non-standard particle methods. Finally, we will propose a classification which will include SPH and LBM.

Chapter 2 will be exclusively devoted to the state of the art of the SPH method. We will present in details the derivation of the SPH interpolation and the SPH approximation of the Navier-Stokes equations. Along the way, we will notably describe the stabilization procedures inherent with SPH, the boundary conditions and the time integration scheme. This chapter will end on a review of the available multiphase SPH formulations with a particular focus on the CSF (*Continuum Surface Force*) approach proposed in [Hu 2006] that will be used later in this work

Chapter 3 will present the state of the art of the LBM. We will focus in particular on the Chapman-Enskog expansion which will lead to the full derivation of the LBM equations starting from Boltzmann equation. We will also review the main boundary conditions and LBM variants available in the literature. As in the previous chapter, we will conclude with a comparative review of the multiphase LBM formulations especially detailing the color gradient model [Reis 2007] which will be used in the rest of the document.

Chapter 4 will get to the heart of the matter proposing a comparison of the two chosen multiphase formulations : the color gradient method for LBM and the CSF method for SPH. To begin, we will work on a collection of various test cases : lid-driven cavity, capillary rise, static bubbles, Rayleigh-Taylor instability. Then, we will continue our study on periodic slug flows cases and finally on slug flows cases generated using inlet/outlet boundary conditions.

Chapter 5 will concern exclusively SPH and will let us explore more precisely the potential of SPH to simulate different flow regimes and flow regimes transitions but also intermittent flows cases with high density and viscosity ratios and more realistic geometry. We will then carry on a parametric study on the influence of a spurious interface corrective term on the previously presented SPH results. Finally, we will conclude with a comparison with experimental data.

Contributions

We summarize the contributions of this doctoral work hereafter. We remind that this is an industry-sponsored thesis so that the contributions are more practical and applied than theoretical.

1. Building of a multiphase SPH/LBM code For the needs of this work, we had to write two codes : one for SPH and one for LBM. It was decided to develop these codes using the Fortran language accelerated with OpenMP. These codes are hosted on the Total development platform located in Houston and are therefore formatted and built according to the company standards. They use some utility functions contained in the Total seismic imaging library. The pre-processor is the same for both codes, it is the open-source program called *pyck* (`https://github.com/brucedjones/pyck`) that was developed by myself and a colleague in Python/C++ (via *swig*) during a previous Total-sponsored project. Post-processing is performed using Paraview for visualization and MATLAB to generate the different plots presented in this work. Input and output files use the VTK format (ASCII and binary are supported). Both codes share the same data structure that consists of two derived types. One holds all the arrays required for the calculations (density, velocity, ...) and the other one holds all the parameters of the simulation. Then, a time loop will perform the required algorithmic operations of SPH and LBM

(macroscopic variables calculation, rate terms computation, boundary conditions, time integration) on the derived types. This time loop generates an output VTK file at regular instants that is used for post-processing. However, there are several differences between the codes. First, SPH uses a decomposition domain in order to achieve a faster nearest neighbor search that is needed for every particle at each time step. This technique allows to only search for neighboring particles of a given particle in the adjacent cells of the cell containing the current particle and not in the whole domain. In addition, to optimize data access, we also regularly sort the arrays so that particles that are close in space are close in memory. the LBM algorithm being local by nature, we made use of vectorization wherever possible in order to quicken the calculations. We have preferred to work directly on the whole arrays in a vectorized operations except when the loop is OpenMP accelerated. Concerning the computational efficiency of both codes, we can say that LBM remains much faster than SPH despite the important progresses made in the SPH community. Indeed, we remind that LBM is based on a lattice so that the connectivity between nodes is known a priori whereas SPH being purely Lagrangian, a nearest neighbor search is needed for every particle at every time step. For information, our LBM code is roughly 4 times faster than our SPH code ($1.03.10^{-6}$s/node for LBM versus $3.85.10^{-6}$s/particle for SPH) on a laptop equipped with an Intel Core i7 processor of 2.9 GHz with 4 cores and 16 Gb of RAM. These numbers are indicative and should be taken with caution since the codes are not optimized and therefore are not representative of the HPC potential of LBM and SPH.

2. Multiphase inlet/outlet boundary conditions During our investigations, we rapidly realized that we would need to implement inlet/outlet boundary conditions. Indeed, periodic boundary conditions are not enough to simulate all the possible cases because they are complicated to setup experimentally. It is much more natural to work with inlet/outlet boundary conditions. In our case, the goal is to inject two phases simultaneously at the inlet with different superficial velocities and to impose a constant pressure at the outlet. In addition, at the inlet, we know the flow profile a priori whereas at the outlet it is not the case, we can have bubbles or pure phases. For SPH, after looking at the existing literature, we have decided to use the ideas developed in [Tafuni 2018, Alvarado-Rodríguez 2017] for the single phase case and extend them to the multiphase context. Our contribution is the interface treatment, see Sect. 4.2 for more details. This approach is based on the use of buffer areas at the inlet and the outlet of the domain to hold entering and leaving particles. For LBM, we have chosen to extend Zou-He boundary conditions [Zou 1997] with a specific treatment for the color field, see Sect. 4.1 for more precision. The main idea is to work with the total distribution function of the color gradient model and to apply them the original Zou-He algorithm. Then, we need to redistribute these quantities among the phases using the color field value. Moreover, because we used a special equilibrium distribution function, we had to re-derive the Zou-He method with that particular function which led to an additional corrective term. These SPH and LBM multiphase boundary conditions are not optimal but they deliver what we expect with a reasonable accuracy and more importantly are stable for a broad range of Reynolds numbers and density and viscosity ratios. On top of that, they are quite simple to implement.

3. Validation and comparison of formulations Once written the codes, we needed to validate them on a collection of reference single phase and multiphase test cases : static bubbles, Rayleigh-Taylor instability, lid-driven cavity and capillary rise. We led that validation campaign in parallel for SPH and LBM in order to compare the results of both methods. Then, we extended the comparison on periodic slug flows cases, as shown for example on Fig. 13, as well as with inlet/outlet boundary conditions. To the best of our knowledge, such a comparison, presented in Chap. 4, was not available in the current literature. We stress that the SPH and LBM formulations adopted for this work could certainly be improved using more elaborate techniques available in the literature. The main conclusion of this work is

that, according to our results, LBM is more accurate and possesses a better order of convergence than SPH but is limited by its quite narrow area of stability. More clearly, when the stability conditions of LBM are met, it is more efficient than SPH. However, these stability conditions strongly reduce the field of application of the method in terms of Reynolds numbers or density/viscosity ratios. Our goal is to extend our analysis further and to simulate more realistic cases which are outside of LBM stability area. In consequence, we have decided to pursue this work with SPH only.

4. Study of SPH applicability to more realistic cases. In Chap. 5, we have chosen to keep working

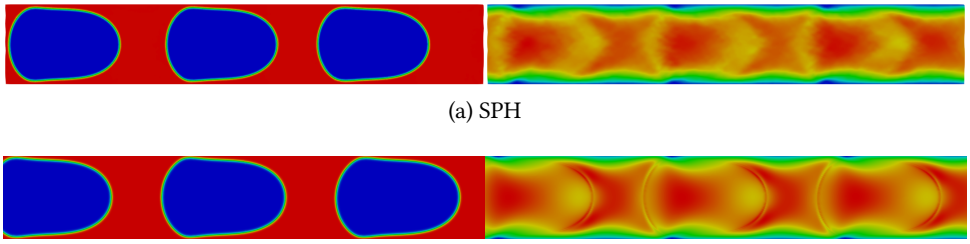

(a) SPH

(b) LBM

Figure 13: Phases distribution (left) and normalized velocity fields (right) at (periodic) steady state for $Re = 50$.

only with SPH and to extend our study to more realistic cases. More precisely, we mean cases with higher inlet velocities, close-to-reality geometries and oil/gas-like density and viscosity ratios. First, we explored in details the flow map of Fig. 12 by simulating multiple cases, different flow regimes (stratified, mist, dispersed) and the transitions between these regimes as shown for example on Fig. 14. Second, we worked on hydrodynamic and terrain slugging cases with realistic proportions. Finally, we conclude this chapter with the comparison between SPH simulations and experimental data. Once again, to the best of our knowledge, this was not available before in the literature.

5. Parametric study of a corrective term for multiphase SPH When using the multiphase SPH

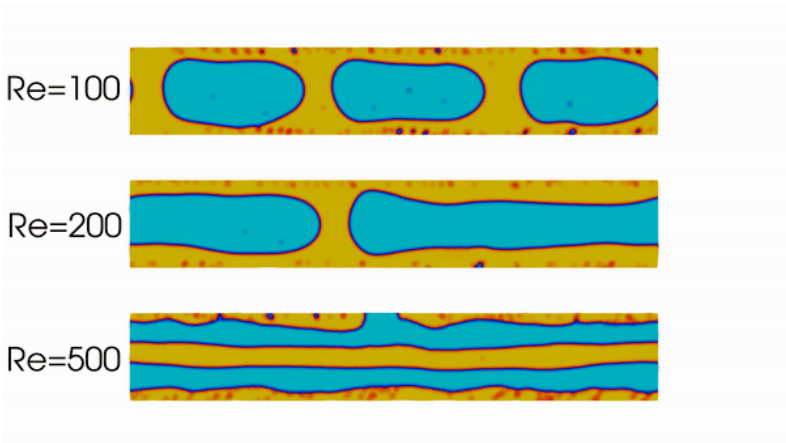

Figure 14: Phases distribution for different flow regimes simulated with SPH with air/water-like density and viscosity ratios.

formulation proposed in [Hu 2006], we were quickly forced, as suggested in the literature, to use a

corrective term defined by $\boldsymbol{F}_a^{corr} = \varepsilon \sum_{b \in \Lambda_a, b \notin \Omega_a} \left(\frac{1}{\Theta_a^2} + \frac{1}{\Theta_b^2} \right) \nabla_a w_{ab}$ to avoid a spurious interface fragmentation. This term is controlled by a free parameter ε. The link between this parameter and physical values is not clear [Szewc 2016]. In Sect. 5.4, we have looked at the impact of this corrective force on the previously presented SPH simulations for different values of ε. In particular, we have noted that this force can act on the intermittent character of the flow regime and must be used with caution.

6. Exploration of entropic considerations of LBM During this doctoral work, we got interested in LBM for 1D advection-diffusion equations with the BGK operator. It is only an early work that is presented in Appendix C. In particular, we are able to obtain an $\mathcal{H}$ theorem from entropic considerations. It allows us to derive fine estimation of the entropy dissipation that we confront with numerical experiments and also to propose a reinterpretation of the BGK collision operator as the gradient of specific Lagrangian functional associated with a minimization problem. It would be interesting to push the analysis further, in 2D especially, but we did not got the time to go that far.

Limitations

HPC aspects In this Ph.D dissertation, we will not discuss the computational efficiency of both methods. Indeed, we have implemented SPH and LBM so that they execute as fast as possible but we did not have the time to take into account the latest progresses on the subject, nor to add an MPI (*Message Passing Interface*) layer for multimachine parallelization, nor to port the code to GPU (*Graphics Processing Unit*). In consequence, we cannot venture a justified opinion on this matter.

2D simulations For practical reasons (computation time, simplicity), all our simulations are done in 2D. Switching to 3D simulations is not a major obstacle, it only requires a heavier implementation, a particular attention for certain geometrical issues and a new validation campaign. We did not have the time to go this far.

Turbulence We did not take into account turbulent phenomena in the models we have used. It is possible to add turbulence models in SPH and LBM and it would be interesting to push the analysis further integrating those models. It would be of particular interest for the few high Reynolds cases presented later in this document because we believe that the turbulent viscosity would help to stabilize the SPH pressure fields.

Publications

This research work has resulted in 4 publications (2 journals, 2 conferences)

- **Douillet-Grellier, T.**, De Vuyst, F., Calandra, H., & Ricoux, P. (2018). Simulations of intermittent two-phase flows in pipes using smoothed particle hydrodynamics. Computers & Fluids.
- **Douillet-Grellier, T.**, De Vuyst, F., Calandra, H., & Ricoux, P. (2018). Influence of the spurious interface fragmentation correction on the simulation of flow regimes. In Proceedings of the International 13th SPHERIC Workshop, June 26-28, Galway, Ireland.
- De Vuyst, F. & **Douillet-Grellier, T.** (2018). Entropic considerations on the LBGK model for advection-diffusion. In Proceedings of 39th Ibero-Latin American Congress on Computational Methods in Engineering (CILAMCE), November 11-14, Paris, France.
- **Douillet-Grellier, T.**, Leclaire, S., Vidal, S., Bertrand F. & De Vuyst, F. (2019). Comparison of multiphase SPH and LBM approaches for the simulation of intermittent flows. Computational

Particle Mechanics.

Moreover, 2 extra publications (2 conferences) related to an SPH project started before the thesis also took place during this doctoral work :

- Pramanik, R., Pan, K., Jones, B. D., Albaiz, A., Williams, J. R., **Douillet-Grellier, T.**, & Pourpak, H. (2017). Numerical Simulation of Fracture Propagation in Layered Rock. In Proceedings of 51st US Rock Mechanics/Geomechanics Symposium, June 25-28, San Francisco, California, USA.
- Raymond, S. J., Jones, B. D., Pramanik, R., Pan, K., **Douillet-Grellier, T.** & Williams, J. R. (2017). On the efficacy of augmenting SPH simulations of mixed-mode failure with the Material Point Method. In Proceedings of the SPHERIC Beijing International Workshop, October 17-20, Beijing, China.

Chapter 1

An overview of particle methods

Contents

1.1 Meshless particle methods **22**

1.1.1 Some reminders and definitions 23

1.1.2 Meshless particle methods based on a partition of unity 29

1.1.3 Non-standard meshless particle methods 32

1.1.4 Related issues 33

1.2 Other particle methods **34**

1.2.1 Molecular Dynamics 34

1.2.2 Vortex method 35

1.2.3 Peridynamics method 35

1.2.4 Lattice Boltzmann Methods 36

1.3 Classification of particle methods **36**

In this chapter, we will give a general overview of particle methods. Note that we consider the term *particle* in a very broad sense : methods based on a particle description of the continuum or involving a numerical representation of physical particles or leaning on material points that are described as particles will be considered. At this point, it is necessary to distinguish two categories of particle methods : meshbased particle methods and meshfree particle methods. Indeed, particle methods are not always meshfree, the most notorious example is the Lattice Boltzmann Method (LBM). Most of the particle methods being meshless, a large part of this chapter will be devoted to this topic.

It is difficult to provide a clean classification of particle methods. Several criteria can be considered : the type of formulations of the partial differential equations (PDE) (strong/weak, local/global), the physical principles (deterministic, probabilistic), the type of approximation functions and decomposition basis (intrinsic/extrinsic basis, type of test/trial functions) and so on. Many methods could fit in one or several categories or in none of them.

First, a review of the theory of meshless particle methods will be presented. Then, a brief summary of other particle methods will follow. Finally, an attempt to classify these methods will conclude this chapter. Note that the content of this chapter has been inspired from [Fries 2004, Nguyen 2008].

1.1 Meshless particle methods

Traditional methods like the finite element method have been introduced in the 1950's and have become the most popular and commonly used tool in engineering simulations. These methods are based on a mesh that is a division of space into non-overlapping discrete elements. The element connectivity is known in advance and does not change throughout the simulation. The interpolation functions needed to approximate the solution are subsequently built upon this mesh. The accuracy and the stability of these methods is directly connected with the quality of the mesh (element type, regularity, distorsion, etc).

As a consequence, these meshbased approaches require a very fine mesh in order to capture certain problems involving very local dynamics, abrupt variations or even discontinuities such as the simulation of fragmentation, cracks initiation and propagation, impacts, multiphase flows or fluid-structure interactions. Moreover, in the case of large deformations, the deterioration of the mesh leads to instabilities and errors. These difficulties have been overcome by using finer meshes or by using remeshing procedures, both being computationally expensive. Indeed, remeshing is a very challenging topic especially in 3D and it requires the projection of variables between successive meshes leading to numerical errors.

The emergence of meshless methods originated from these mesh-related issues. The idea that it could be more advantageous to discretize a continuum by only a set of points (particles) led to the appearance of the first meshless methods [Gingold 1977]. Meshless methods have been applied to a large variety of fields (and scales) of science : from chemistry to earth sciences through astrophysics and hydrodynamics. In general, meshless methods will feature the following properties [Liu 2009] :

1. The node connectivity is computed at every iteration. This is the main reason why meshless methods can easily handle large deformations and moving discontinuities. No mesh or remeshing of any kind is needed. However, meshless methods are in general considerably more expensive than meshbased methods and often rely on a good Nearest Neighbor Search (NNS) algorithm to increase the computational efficiency.
2. The meshfree discretization is simpler than to generate a mesh and can accurately represent complex geometries. This is a major plus when it comes to interact with CAD (Computer Aided Design) softwares and during the pre-processing phase.

3. In general, The adaptivity (h-adaptivity) of meshless methods is easy to address, since it only consists in adding more particles in the model.
4. Most meshless methods do not satisfy the Kronecker delta property which causes difficulties to impose boundary conditions compared to meshbased methods.

1.1.1 Some reminders and definitions

1.1.1.1 Trial and test functions

Definition 1.1.1 (Strong form of a PDE). *Let's consider a Partial Differential Equation (PDE) on $\Omega \subset \mathbb{R}^d$ (d is the dimension) with a boundary Γ defined by the differential operator $\mathcal{L}$ and a linear form f.*

$$\begin{aligned} \mathcal{L}u(\boldsymbol{x}) &= f(\boldsymbol{x}) \ , \forall \boldsymbol{x} \in \Omega, \\ u(\boldsymbol{x}) &= \bar{u}(\boldsymbol{x}) \ , \forall \boldsymbol{x} \in \Gamma. \end{aligned} \tag{1.1.1}$$

Eq. (1.1.1) is the strong form of the PDE.

Definition 1.1.2 (Trial functions). *If we have a set of N nodes i located at position $\boldsymbol{x}_i$, let's assume that u can be expressed as follows :*

$$\boxed{u(\boldsymbol{x}) \approx u^h(\boldsymbol{x}) = \sum_{i=1}^{N} \Phi_i(\boldsymbol{x}) u_i,} \tag{1.1.2}$$

where $\Phi_i \ : \Omega \mapsto \mathbb{R}$ are the trial functions (also called shape functions), $u_i = u(\boldsymbol{x}_i)$ are the nodal values at node i. Note that trial functions are also called shape functions.

Definition 1.1.3 (Residual error). *Replacing u with u^h in the PDE yields :*

$$\varepsilon^h(\boldsymbol{x}) = \mathcal{L}u^h(\boldsymbol{x}) - f(\boldsymbol{x}). \tag{1.1.3}$$

ε^h is the residual error. This residual is non zero due to the approximation.

Definition 1.1.4 (Weak form of a PDE). *Multiplying Eq. (1.1.1) by arbitrary functions $\boldsymbol{\Psi}$ and integrating over Ω, it gives :*

$$\int_\Omega \boldsymbol{\Psi} \mathcal{L}u^h(\boldsymbol{x}) d\Omega = \int_\Omega \boldsymbol{\Psi} f(\boldsymbol{x}) d\Omega \ , \forall \boldsymbol{\Psi}. \tag{1.1.4}$$

The weak form is obtained by applying an integration by parts (depends on $\mathcal{L}$, a boundary integral on Γ appears).

Definition 1.1.5 (Test functions). *Arbitrary functions $\boldsymbol{\Psi}$ used to obtain the weak form of the PDE are called the test functions. The test functions are usually projected on a basis of arbitrary nodal coefficients δu_i as follows :*

$$\boldsymbol{\Psi}(\boldsymbol{x}) = \sum_{i=1}^{N} \Psi_i(\boldsymbol{x}) \delta u_i. \tag{1.1.5}$$

Definition 1.1.6 (Weighted residuals). *A system of equations is built by setting ε^h orthogonal (in the sense of $\langle u, v \rangle = \int_\Omega uv d\Omega$) to the set of test functions $\boldsymbol{\Psi}$.*

$$\int_\Omega \boldsymbol{\Psi} \varepsilon^h d\Omega = 0 \text{ then } \int_\Omega \boldsymbol{\Psi} \left(\mathcal{L}u^h(\boldsymbol{x}) - f(\boldsymbol{x}) \right) d\Omega, \tag{1.1.6}$$

$$\int_\Omega \boldsymbol{\Psi} \left[\mathcal{L} \left(\sum_{i=1}^{N} \Phi_i(x) u_i \right) - f(\boldsymbol{x}) \right] d\Omega = 0. \tag{1.1.7}$$

In order for all the integrals of Eq. (1.1.6) and (1.1.7) to be defined, restrictions have to be applied to $\boldsymbol{\Psi}$ and $\boldsymbol{\Phi}$. They have to be C^{n-1} where n is the order of derivatives in $\mathcal{L}$.

The choice of trial functions Φ and test functions Ψ will engender a family of meshless and meshbased numerical methods.

1.1.1.2 Partition of unity and consistency

Definition 1.1.7 (Polynomial basis). *A polynomial basis of order n in dimension d is defined as :*

$$\boldsymbol{p}(\boldsymbol{x}) = \left\{\boldsymbol{x}^{\boldsymbol{a}}, |\boldsymbol{a}| \leq n\right\}, \tag{1.1.8}$$

with $\boldsymbol{a}^T = (a_1, \ldots, a_d)$ and $\boldsymbol{x}^{\boldsymbol{a}}(x_1^{a_1} \ldots x_d^{a_d}$. For example, if $d = 1$ and $n = 2$, then $\boldsymbol{p}^T = (1, x, x^2)$ and if $d = 2$ and $n = 2$, then $\boldsymbol{p}^T = (1, x, y, x^2, xy, y^2)$

Definition 1.1.8 (Consistency). *The consistency of an approximation refers to the highest polynomial order which can be represented exactly with a given numerical method. Given an approximation of the form of Eq. (1.1.2), it is consistent of order n if the following condition is satisfied :*

$$\sum_{i=1}^{N} \Phi_i(\boldsymbol{x})\boldsymbol{p}(\boldsymbol{x}_i) = \boldsymbol{p}(\boldsymbol{x}) \,, \forall \boldsymbol{x} \in \Omega, \tag{1.1.9}$$

with $\boldsymbol{p}$ the polynomial basis of order n defined in Eq. (1.1.8).

Definition 1.1.9 (Partition of Unity). *The set of trial functions Φ satisfying Eq. (1.1.9) is then called a Partition of Unity (PU) of order n. As an example, the partition of unity of order 0 satisfies $\sum_i \Phi_i(\boldsymbol{x}) = 1$ (hence the name partition of unity). This property is also called completeness (or reproducibility). It is the ability for an approximation to exactly reproduce a polynomial at a certain order.*

Definition 1.1.10 (Kronecker delta property). *Let's consider a set of N nodes i located at position $\boldsymbol{x}_i$, the shape (or trial) functions $\Phi_i(\boldsymbol{x})$ satisfy the Kronecker delta property if :*

$$\Phi_i(\boldsymbol{x}_j) = \delta_{ij}. \tag{1.1.10}$$

1.1.1.3 Kernel functions

Definition 1.1.11 (Kernel functions). *In the rest of the document, it will be often referred to kernel functions (also called weight functions or window functions depending on the context). They are defined as*

$$w \; : \mathbb{R}^d \times \mathbb{R}^+ \mapsto \mathbb{R}^+.$$

These functions need to fulfill the following requirements :

1. *Normalization*

$$\int_\Omega w(\boldsymbol{x}, h) d\Omega = 1. \tag{1.1.11}$$

2. *Compact support of size h*

   h is the dilatation parameter or smoothing length[1]. This size is critical to establish the accuracy and the stability of the solution (like the mesh resolution in FEM).

$$w(\boldsymbol{x}, h) = 0 \quad \textit{for} \quad |\boldsymbol{x}| > \kappa h, \tag{1.1.12}$$

   where κ is a fixed number that controls the size of the compact support.

[1] It has been recently pointed out in [Dehnen 2012, Violeau 2014] that the parameter h is not a good measure of the kernel support, the authors suggest the use of the kernel standard deviation instead, $\sigma^2 = \frac{1}{D}\int_\Omega |\boldsymbol{x}|^2 w(\boldsymbol{x}, h) d\Omega$. This gives a finite value even for the Gaussian kernel and is good estimator of the number of particles within the support.

3. *Positive on its support*

$$w(\boldsymbol{x}, h) \geq 0 \quad \textit{for} \quad |\boldsymbol{x}| \leq \kappa h. \tag{1.1.13}$$

4. *Monotonic decrease*
5. *Dirac delta function condition as $h \longrightarrow 0$*

$$\lim_{h \to 0} w(\boldsymbol{x}, h) = \delta(\boldsymbol{x}). \tag{1.1.14}$$

6. *Even (symmetric) function (thus the derivative is odd)*

$$w(\boldsymbol{x}, h) = w(\boldsymbol{y} - \boldsymbol{x}, h), \tag{1.1.15}$$

$$\nabla w(\boldsymbol{x}, h) = -\nabla w(\boldsymbol{y} - \boldsymbol{x}, h). \tag{1.1.16}$$

7. *Sufficiently smooth (C^1 at least for most methods).*

While these requirements seem quite restrictive, there is actually an infinity of functions satisfying them. The most simple one being the Gaussian function, but splines functions or the so-called Wendland functions also satisfy those properties. These functions will be detailed in the discussion on SPH in Chap. 2.

In most methods, Eulerian kernels are used. It means that the support shape does not change with the deformation and that it is required to look for particles within the support at each time step for each particle (NNS). On the other hand, one could consider Lagrangian kernels which support would deform as the material deforms but for which the neighbors within the support domain stay the same throughout the simulation as shown on Fig. 1.1. In general, Lagrangian kernels are more stable than Eulerian kernels (reduced tensile instability) but they are limited to small deformation because of the distortion of the support domain.

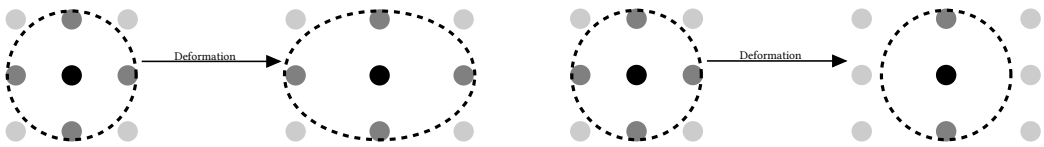

(a) Lagrangian kernel keeps the same neighborhood with deformation

(b) Eulerian kernel keeps the same shape under deformation

Figure 1.1: Lagrangian kernels (a) and Eulerian kernels (b)

Following the presentation order used in [Fries 2004, Nguyen 2008], the commonly used shape functions will be introduced first. Then, according to the values of the trial and test functions, the main meshless particle methods based on a PU will be reviewed. Finally, particle methods that are based on another formalism will be presented.

1.1.1.4 Commonly used shape functions

For comparison purposes, the building of a PU for meshbased is briefly reminded hereafter.

Definition 1.1.12 (Meshbased shape functions)**.** *Let's consider a domain Ω divided into non-overlapping finite elements forming a mesh composed of N located at position $\boldsymbol{x}_i$. Let's impose that the shape functions*

are polynomials $\Phi_i(\boldsymbol{x}) = \boldsymbol{p}^T(\boldsymbol{x})\boldsymbol{a}_i$ *where* $\boldsymbol{p}$ *is the polynomial basis of order* n *defined in Eq.* (1.1.8) *and* $\boldsymbol{a}_i$ *are unknown coefficient vectors. Under these conditions,* $\Phi_i(\boldsymbol{x})$ *are expressed as follows :*

$$\Phi_i(\boldsymbol{x}) = \boldsymbol{p}^T(\boldsymbol{x})\boldsymbol{a}_i \text{ with } \begin{pmatrix} \boldsymbol{a}_1 \\ \vdots \\ \boldsymbol{a}_n \end{pmatrix} = \begin{pmatrix} \boldsymbol{p}^T(\boldsymbol{x}_1) \\ \vdots \\ \boldsymbol{p}^T(\boldsymbol{x}_N) \end{pmatrix}^{-1}. \tag{1.1.17}$$

Proof. In order to compute the unknown coefficients, the Kronecker delta property is imposed for each shape function. $\forall i, j = 1 \dots N$, it yields :

$$\begin{aligned} &\Phi_i(\boldsymbol{x}_j) = \delta_{ij}, \\ &\boldsymbol{p}^T(\boldsymbol{x}_j)\boldsymbol{a}_i = \delta_{ij}, \\ &\begin{pmatrix} \boldsymbol{p}^T(\boldsymbol{x}_1) \\ \vdots \\ \boldsymbol{p}^T(\boldsymbol{x}_N) \end{pmatrix} \begin{pmatrix} \boldsymbol{a}_1 \\ \vdots \\ \boldsymbol{a}_N \end{pmatrix} = \boldsymbol{I}, \\ &\begin{pmatrix} \boldsymbol{a}_1 \\ \vdots \\ \boldsymbol{a}_N \end{pmatrix} = \begin{pmatrix} \boldsymbol{p}^T(\boldsymbol{x}_1) \\ \vdots \\ \boldsymbol{p}^T(\boldsymbol{x}_N) \end{pmatrix}^{-1}. \end{aligned}$$

□

Note that the PU consistency at order n is not imposed directly but is automatically satisfied by the shape functions.

The Moving Least Squares (MLS) method was introduced in [Lancaster 1979] for interpolating scattered data. This method helps to generate smooth approximations to fit a cloud of points and was extended to surface generation.

Definition 1.1.13 (MLS shape functions)**.** *Let's consider a set of* N *nodes* i *located at position* $\boldsymbol{x}_i$*. The MLS shape functions* $\Phi_i(\boldsymbol{x})$ *are expressed are follows :*

$$\Phi_i(\boldsymbol{x}) = \boldsymbol{p}^T(\boldsymbol{x}) \left[\sum_{i=1}^{N} w(\boldsymbol{x} - \boldsymbol{x}_i)\boldsymbol{p}(\boldsymbol{x}_i)\boldsymbol{p}^T(\boldsymbol{x}_i) \right]^{-1} \sum_{i=1}^{N} w(\boldsymbol{x} - \boldsymbol{x}_i)\boldsymbol{p}(\boldsymbol{x}_i), \tag{1.1.18}$$

where w *is a weight function as described in Sec .1.1.1.3.*

Proof. There are at least three different ways to obtain the MLS shape functions :

1. <u>by minimization of a weighted least squares functional</u>
   Let's define $u^{loc}(\boldsymbol{x}, \boldsymbol{x}_0)$ the local approximation of u around $\boldsymbol{x}_0 \in \Omega$. In other words, one can write $u^{loc}(\boldsymbol{x}, \boldsymbol{x}_0) = \begin{cases} u(\boldsymbol{x}) & \forall \boldsymbol{x} \in \Omega, |\boldsymbol{x} - \boldsymbol{x}_0| < \rho \\ 0 & \text{otherwise} \end{cases}$. Assuming that u^{loc} can be decomposed on a polynomial basis such that $u^{loc} \approx \boldsymbol{p}^T(\boldsymbol{x})\boldsymbol{a}(\boldsymbol{x}_0)$, the goal is to compute the unknown vector $\boldsymbol{a}(\boldsymbol{x}_0)$ by minimizing a weighted discrete L_2 error norm $J_{\boldsymbol{x}_0}(\boldsymbol{a}) = \sum_{i=1}^{N} w(\boldsymbol{x} - \boldsymbol{x}_i) \left[\boldsymbol{p}^T(\boldsymbol{x})\boldsymbol{a}(\boldsymbol{x}_0) - u_i\right]^2$.
2. <u>by using a Taylor series expansion</u>
   The function u is equal for $\boldsymbol{x} = \boldsymbol{x}_i$ to $u(\boldsymbol{x}_i) = \sum_{|\boldsymbol{a}|=0}^{+\infty} \frac{(\boldsymbol{x}_i - \boldsymbol{x})^{\boldsymbol{a}}}{|\boldsymbol{a}|} D^{\boldsymbol{a}} u$. Assuming that the shape functions are expressed as $\Phi_i(\boldsymbol{x}) = \boldsymbol{p}^T(\boldsymbol{x})\boldsymbol{a}(\boldsymbol{x})w(\boldsymbol{x} - \boldsymbol{x}_i)$, one can obtain a solvable system of equations for $\boldsymbol{a}(\boldsymbol{x})$.
3. <u>by direct imposition of the PU consistency conditions</u>
   Assuming $\Phi_i(\boldsymbol{x}) = \boldsymbol{p}^T(\boldsymbol{x})\boldsymbol{a}(\boldsymbol{x})w(\boldsymbol{x} - \boldsymbol{x}_i)$ and imposing $\sum_i \Phi_i(\boldsymbol{x})\boldsymbol{p}(\boldsymbol{x}_i) = \boldsymbol{p}(\boldsymbol{x})$ also leads to a solvable system of equations for $\boldsymbol{a}(\boldsymbol{x})$.

Whatever the method used, the result is always the same and the MLS approximation[2] is expressed as :

$$\boxed{u^h(\boldsymbol{x}) = \boldsymbol{p}^T(\boldsymbol{x}) \left[\sum_{i=1}^{N} w(\boldsymbol{x} - \boldsymbol{x}_i) \boldsymbol{p}(\boldsymbol{x}_i) \boldsymbol{p}^T(\boldsymbol{x}_i) \right]^{-1} \sum_{i=1}^{N} w(\boldsymbol{x} - \boldsymbol{x}_i) \boldsymbol{p}(\boldsymbol{x}_i) u_i.} \tag{1.1.19}$$

□

A matrix must be inverted wherever the MLS shape functions are to be evaluated. This is clearly a drawback of MLS because of the computational cost and the possibility that this matrix may be singular. MLS shape functions are a partition of unity but they do not satisfy the Kronecker delta property. At every node, there is more than one shape function $\neq 0$ as shown on Fig. 1.2. Computed values of a meshfree approximation are not nodal values. To have the real values of the approximated function at a point, all influences of shape functions which are non-zero here have to be added up. This aspect makes imposition of boundary conditions difficult.

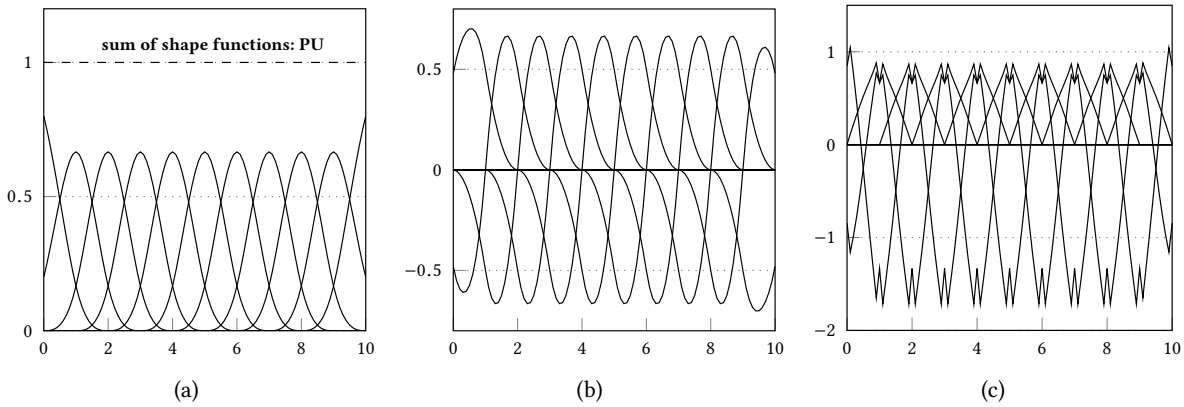

Figure 1.2: MLS shape functions (a) and their 1st (b) and 2nd (c) derivatives

Shape functions are smooth and are polynomial-like, but the derivatives have a more and more non-polynomial character as seen on Fig. 1.2. This causes problems when integrating the integral expressions of the weak form. In addition, the first derivative of the shape functions equals 0 at its corresponding node which leads to numerical instabilities. The derivatives of the shape functions form a partition of nullity.

The Reproducing Kernel Particle Method (RKPM) comes from the theory of wavelets, where functions are represented as a combination of dilatation and translation of a single wavelet and was introduced in the mid 90's [Liu 1995]. The basic idea is to reproduce a function through integration over the domain.

Definition 1.1.14 (RKPM shape functions)**.** *Let's consider a set of N nodes i located at position $\boldsymbol{x}_i$. The RKPM shape functions $\Phi_i(\boldsymbol{x})$ are expressed are follows :*

$$\Phi_i(\boldsymbol{x}) = \boldsymbol{p}^T(\boldsymbol{x}) \left[\sum_{i=1}^{N} \boldsymbol{p}(\boldsymbol{x}_i) \boldsymbol{p}^T(\boldsymbol{x}_i) w(\boldsymbol{x} - \boldsymbol{x}_i) \Delta V_i \right]^{-1} \sum_{i=1}^{N} \boldsymbol{p}(\boldsymbol{x}_i) w(\boldsymbol{x} - \boldsymbol{x}_i) \Delta V_i, \tag{1.1.20}$$

where w is a weight function as described in Sec .1.1.1.3.

[2] If $p(x) = 1$ then $\Phi_i(\boldsymbol{x}) = \frac{w(\boldsymbol{x}-\boldsymbol{x}_i)}{\sum_i^n w(\boldsymbol{x}-\boldsymbol{x}_i)}$ is the Shepard function (Shepard filter). Hence, the so-called Shepard's method is a subcase of MLS.

Proof. The RKPM approximation is defined as :

$$u^h(\boldsymbol{x}) = \int_{\Omega_y} K(\boldsymbol{x}, \boldsymbol{y}) u(\boldsymbol{y}) d\Omega_y. \tag{1.1.21}$$

One can observe that if $K(\boldsymbol{x}, \boldsymbol{y})$ is the Dirac function $\delta(\boldsymbol{x} - \boldsymbol{y})$ then u is exactly reproduced. Contrary to MLS, RKPM is built on a continuous approximation. The kernel function K which acts as a continuous shape functions must satisfy the consistency of PU at order n. One can notice that if $K(\boldsymbol{x}, \boldsymbol{y}) = w(\boldsymbol{x}-\boldsymbol{y})$ (w is a weight function (also called window function)) then the approximation fails to reproduce constant functions, this is why a correction fonction C is added so that $K(\boldsymbol{x}, \boldsymbol{y}) = C(\boldsymbol{x}, \boldsymbol{y}) w(\boldsymbol{x} - \boldsymbol{y})$[3]. It yields :

$$u^h(\boldsymbol{x}) = \int_{\Omega_y} C(\boldsymbol{x}, \boldsymbol{y}) w(\boldsymbol{x} - \boldsymbol{y}) u(\boldsymbol{y}) d\Omega_y. \tag{1.1.22}$$

Similarly to MLS, there are three different ways to compute $C(\boldsymbol{x}, \boldsymbol{y})$:

1. by a direct calculation
   Assuming $u(x)$ can be expressed as polynomial function of order n, $u(\boldsymbol{x}) = \boldsymbol{p}^T(\boldsymbol{x})\boldsymbol{a}$. Hence, it follows :

$$\boldsymbol{p}(\boldsymbol{x}) u(\boldsymbol{x}) = \boldsymbol{p}(\boldsymbol{x}) \boldsymbol{p}^T(\boldsymbol{x}) \boldsymbol{a}, \tag{1.1.23}$$

$$\int_{\Omega_y} \boldsymbol{p}(\boldsymbol{y}) w(\boldsymbol{x} - \boldsymbol{y}) u(\boldsymbol{y}) d\Omega_y = \int_{\Omega_y} \boldsymbol{p}(\boldsymbol{y}) \boldsymbol{p}^T(\boldsymbol{y}) w(\boldsymbol{x} - \boldsymbol{y}) d\Omega_y . \boldsymbol{a}. \tag{1.1.24}$$

   The approximation $u^h(\boldsymbol{x}) = \boldsymbol{p}^T(\boldsymbol{x})\boldsymbol{a}$ can then be substituted in the system of equations for $\boldsymbol{a}$.
2. by minimization of a weighted least squares functional (see MLS in Def. 1.1.13)
3. by using a Taylor series expansion (see MLS in Def. 1.1.13)

In all cases, the following approximation is obtained :

$$u^h(x) = \boldsymbol{p}^T(\boldsymbol{x}) \left[\int_{\Omega_y} \boldsymbol{p}(\boldsymbol{y}) \boldsymbol{p}^T(\boldsymbol{y}) w(\boldsymbol{x} - \boldsymbol{y}) d\Omega_y \right]^{-1} \int_{\Omega_y} \boldsymbol{p}(\boldsymbol{y}) w(\boldsymbol{x} - \boldsymbol{y}) u(\boldsymbol{y}) d\Omega_y. \tag{1.1.25}$$

To evaluate this continuous expression, numerical integration must be employed. This step leads to the discrete version[4] :

$$\boxed{u^h(\boldsymbol{x}) = \boldsymbol{p}^T(\boldsymbol{x}) \left[\sum_{i=1}^{N} \boldsymbol{p}(\boldsymbol{x}_i) \boldsymbol{p}^T(\boldsymbol{x}_i) w(\boldsymbol{x} - \boldsymbol{x}_i) \Delta V_i \right]^{-1} \sum_{i=1}^{N} \boldsymbol{p}(\boldsymbol{x}_i) w(\boldsymbol{x} - \boldsymbol{x}_i) u(\boldsymbol{x}_i) \Delta V_i.} \tag{1.1.26}$$

□

Just like MLS, a matrix must be inverted wherever the RKPM shape functions are used which adds an important computational cost. In general, this matrix (and this is also true for MLS) is symmetric and positive definite and is inverted using a LU, QR or SVD decomposition algorithm. The invertibility (and the condition number) of the matrix is connected to the regularity of the particle distribution [Fries 2004].

[3] Setting $C(\boldsymbol{x}, \boldsymbol{y}) = 1$ leads to the SPH formulation.

[4] As highlighted in [Belytschko 1996, Li 2002, Fries 2004, Nguyen 2008], if $\Delta V_I = 1$ then RKPM is the same as MLS. Although $\Delta V_I = 1$ is a pretty bad approximation for an integral, it is an interesting result since it connects methods from different origins.

1.1.2 Meshless particle methods based on a partition of unity

The shape functions are calculated through a partition of unity (RKPM, MLS) as described previously. In Eq. (1.1.2), the solution $u(\boldsymbol{x})$ is approximated on a basis of nodal values u_i. This is called an intrinsic basis. It is possible to decompose the solution on another basis or to enrich this intrinsic basis. In that case, the basis is called extrinsic. In addition to choosing an intrinsic or an extrinsic basis, one also has to pick a set of test functions $\boldsymbol{\Psi}$ to solve the weak form of the PDE. Setting $\boldsymbol{\Psi}$ as Dirac functions leads to a class of methods called point collocation methods and the weak form reduces to the strong form of the PDE. Using any other functions for $\boldsymbol{\Psi}$ leads to Galerkin methods (Bubnov-Galerkin if $\boldsymbol{\Phi} = \boldsymbol{\Psi}$, Petrov-Galerkin otherwise).

1.1.2.1 Intrinsic Basis

In the case of an intrinsic basis, it is recalled that the approximation of u is $u^h = \sum_{i=1}^{N} \Phi_i u_i$ where u_i are the nodal values and Φ_i the shape functions.

Collocation Methods In the case of a collocation method, the test functions are chosen equal to the Dirac functions $\Psi_i(\boldsymbol{x}) = \delta(\boldsymbol{x} - \boldsymbol{x}_i)$. In that particular case, the weak form of the PDE (Eq. (1.1.7)) reduces to the strong form of the PDE (Eq. (1.1.1)):

$$\begin{aligned} \mathcal{L}u^h(\boldsymbol{x}_i) &= f(\boldsymbol{x}_i) \text{ with } \boldsymbol{x}_i \in \Omega, \\ u(\boldsymbol{x}_i) &= \bar{u}(\boldsymbol{x}_i) \text{ with } \boldsymbol{x}_i \in \Gamma. \end{aligned} \tag{1.1.27}$$

Collocation methods are convenient because no integration is needed to build the system of equations[5]. This removes an error source in the computation. In addition, shape functions are only evaluated at particles position. However, they require the computation of high-order derivatives of the shape functions which can be costly. As a consequence, the shape functions generally needs to be C^k continuous where k is the highest derivative order in $\mathcal{L}$. Moreover, accuracy and robustness are generally lower than other methods and, as stated before, the imposition of boundary conditions is also less natural than in meshbased methods.

The most famous meshless collocation method is certainly the SPH method [Gingold 1977] and its (numerous) variants (to name two of them : Corrected SPH (CSPH) [Bonet 2000], Moving Least Squares SPH (MLSPH) [Dilts 1999, Dilts 2000]). The SPH method will be fully presented in Sect. 2. Other meshfree collocation methods include the Finite Point Method (FPM) [Oñate 1996] and a special case of the Meshfree Local Petrov Galerkin method [Atluri 2005]. More recently, the Moving Particle Semi-Implicit (MPS) method which is closely related to SPH has been introduced in [Gotoh 2005].

Galerkin Methods If different functions are used for the test and trial functions, then a Petrov-Galerkin method is obtained, if not a Bubnov-Galerkin method is obtained.

Diffuse Element Method The oldest Bubnov-Galerkin method is the so-called Diffuse Element Method (DEM, not to be mistaken with the Discrete Element Method) [Nayroles 1992]. it was originally presented as a generalization of the FEM. The fundamental idea is to replace the FEM element-wise approximation by a weighted least squares fitting on a neighborhood of points surrounding the evaluated location (hence, DEM uses the MLS shape functions). In other words, the DEM uses "finite elements" made of a unique integration point, a variable number of nodes and a diffuse domain of influence. From

[5] Let's consider a simple differential equation of the form $a\ddot{u} + b\dot{u} + cu + d = 0$. Using a collocation method for this problem leads to the following discretized equation $\left[a \sum_i \ddot{\Phi}_i + b \sum_i \ddot{\Phi}_i + c \sum_i \Phi_i\right] u_i + d = 0$ which is equivalent to a system $Ku = f$.

this viewpoint, FEM is just a special case of DEM where the weight function is constant over the subdomain. However, DEM has some major issues. First of all, the solution is projected on a polynomial basis assuming spatially constant coefficients which leads to an incorrect evaluation of the derivatives (and not integrable). Then, they used a low-quality quadrature to compute the integrals introducing numerical errors. Finally, the boundary conditions are not properly enforced. Due to these problems, the classic DEM does not pass the patch test and a specific variant called the Petrov-Galerkin DEM (PGDEM) was introduced [Krongauz 1997] to overcome these difficulties. DEM has been mainly applied to fluid problems.

Element Free Galerkin The Element-Free Galerkin (EFG) method was introduced in [Belytschko 1994]. It uses MLS shape functions to build its approximation. Unlike DEM, EFG presents the following features :

1. A correct derivation of the shape functions
2. A better evaluation of the integrals by using more integration points arranged in a cell structure
3. A correct enforcement of boundary conditions by using Lagrange multipliers

The underlying cell structure is of primary importance in the EFG method since it helps to know which points are contributing to the quadrature and also it provides a support for this quadrature. It should be pointed out that a variant of EFG replaces the matrix inversion by a Gram-Schmidt orthogonalization [Lu 1994] which is not faster nor slower but more accurate. EFG has been mostly applied to solid mechanics involving moving discontinuities, in particular fracture growth problems. Compared to EFG, FEM is in general faster (up to some orders of magnitude) but FEM can't properly solve the type of problems EFG is applied to. Another Bubnov-Galerkin method that is worth mentioning is the Method of Finite Spheres (MFS) [De 2000] which, once again, can be seen a special case of the Meshfree Local Petrov Galerkin (MLPG) method.

Meshless Local Petrov Galerkin The Meshfree Local Petrov Galerkin (MLPG) [Atluri 2005] is more a concept than a method in itself. It is based on a local weak form on the PDE. A local weak form is similar to global weak form except that it is built over local subdomains Ω_i with local boundaries Γ_i. For MLPG, the local subdomains Ω_i are assumed to be the compact supports of the weight functions w_i. This is a major difference with previous methods based on weak forms which used a background mesh or a cell structure for their integration. MLPG can be considered a "truly meshless" method. The MLPG method is very versatile as it can make use of any type of shape functions and test functions, giving birth to a family of derived methods.

1. $\Psi_i(\boldsymbol{x}) = \delta(\boldsymbol{x} - \boldsymbol{x}_i)$: This is a collocation method. The local weak forms reduce to the strong form of the PDE.
2. $\Psi_i(\boldsymbol{x}) = \chi_{\Omega_i}$: Using characteristic functions for the test functions leads to the so-called subdomain collocation (similar to the Finite Volume method in the meshbased world).
3. $\Psi_i(\boldsymbol{x}) = \Phi_i(\boldsymbol{x})$: Trial and test functions being the same, it boils down to a Bubnov-Galerkin method similar to DEM or EFG but built on a local weak form instead of global weak form.
4. $\Psi_i(\boldsymbol{x}) = \varepsilon_i(\boldsymbol{x})$: The test functions is equal to the local residual error in the sense of the discrete least squares. This leads to the so-called Least Squares Meshfree Method (LSMM) [Park 2001].
5. $\Psi_i(\boldsymbol{x})$ = fundamental solution of the PDE : Using the fundamental solution of the PDE as a test function (i.e the solution of $\mathcal{L}u(\boldsymbol{x}) = \delta(\boldsymbol{x})$) leads to the Local Boundary Integral Equation method (LBIE) [Zhu 1998]. This last method is a local and meshless equivalent of the well known Boundary Element Method [Katsikadelis 2002]. These methods, although efficient, are limited to problems where a fundamental solution is available.

6. $\Psi_i(\boldsymbol{x}) = w_i(\boldsymbol{x} - \boldsymbol{x}_i)$: Using the weight functions as test functions is convenient because it allows to simplify the local weak form as the weight functions vanish on the local boundaries.

1.1.2.2 Extrinsic basis

It is recalled that the use of an extrinsic basis consists in decomposing the solution on basis that is not (or not only) a basis of nodal values. In other words, the approximation of the solution u is $u^h = \sum_{i=1}^{N} \Phi_i U_i$ where Φ_i are the shape functions and U_i are functions whose choice depends on the problem solved.

Partition of Unity Method The Partition of Unity Method (PUM) [Babuska 1996] and all its variants (Partition of Unity FEM (PUFEM)[Melenk 1996], Generalized FEM (GFEM) [Strouboulis 2001], Extended FEM (XFEM) [Belytschko 2001]) can be both meshbased (hence the name FEM in their names) or meshfree and are all based on the use of extrinsic basis. The basic approximation is the following:

$$u^h(\boldsymbol{x}) = \sum_{i=1}^{N} \Phi_i(\boldsymbol{x}) \sum_{j=1}^{L} p_j(\boldsymbol{x}) v_{ij}, \tag{1.1.28}$$

where L is the number of nodes/particles of the extrinsic basis, $\Phi_i(\boldsymbol{x})$ shape functions based on the MLS or the RKPM approach, v_{ij} are unknowns nodal coefficients and $p_j(\boldsymbol{x})$ the extrinsic basis. It could be made of monomials, Taylor or Lagrange polynomials or any convenient functions.

It should be emphasize that special enhancement functions to treat a specific case like a singularity for example are easily incorporated through the extrinsic basis. This technique requires a priori knowledge of the solution. For example, if one knows that locally the solution has a sinusoidal behavior, it is possible to add a $\sin(\boldsymbol{x})$ to the basis to capture it. In addition, this can be used to properly enforce boundary conditions by incorporating well-chosen functions to the basis. The use of an extrinsic basis is also a way to facilitate p-adaptivity (regions with different orders of consistency). However, it introduces more unknowns in the problem. An exhaustive theoretical description of the PUM is developed in [Babuška 2003].

***hp*-clouds** The hp-clouds method has been introduced in [Duarte 1996b, Duarte 1996a]. The main idea behind the conception of this method is to consider the h-adaptivity and the p-adaptivity directly in the approximation of the solution. It is written as :

$$u^h(\boldsymbol{x}) = \sum_{i=1}^{N} \Phi_i(\boldsymbol{x}) \left(u_i + \sum_{j=1}^{L} p_j(\boldsymbol{x}) v_{ij} \right), \tag{1.1.29}$$

with $p_j(\boldsymbol{x})$ the extrinsic basis, formed of polynomials and/or enhancement functions. These functions are introduced to capture special properties such as discontinuities, singularities, boundary layers or others. The freedom of choice of the extrinsic basis is what facilitates the p-adaptivity. Indeed, one can keep the same number of particles (or clouds in this case if one considers the node and its neighbors in the compact support of the kernel function) while increasing the order of consistency of the PU by adjusting the extrinsic basis. This is done without introducing discontinuities contrary to classic shape functions. Similarly, for h-adaptivity (inherent to meshless methods) is also simple. One can just add more particles in the region of interest with smaller compact supports (smaller clouds) while keeping the same shape functions. It should be pointed out that an hybrid meshfree/meshbased variant of hp-clouds has been developed in [Oden 1998].

1.1.3 Non-standard meshless particle methods

1.1.3.1 Sibsonian/Non-Sibsonian shape functions

The natural interpolation is based on the well-known Voronoi cells and was introduced in [Sibson 1980] for data analysis. A Voronoi cell is defined as follows :

$$V_i = \{\boldsymbol{x} \in \Omega, |\boldsymbol{x} - \boldsymbol{x}_i| < |\boldsymbol{x} - \boldsymbol{x}_j|, \forall i \neq j\}. \tag{1.1.30}$$

The shape functions are defined as :

$$\Phi_i(\boldsymbol{x}) = \frac{A_i(\boldsymbol{x})}{A(\boldsymbol{x})}, \tag{1.1.31}$$

where $A_i(\boldsymbol{x})$ is the area of the intersection of V_i and $V_{\boldsymbol{x}}$ and $A(\boldsymbol{x})$ is the area of the Voronoi cell $V_{\boldsymbol{x}}$ of $\boldsymbol{x}$. The support of those shape functions is complex but can be computed. They are used as both test and trial functions in the weak form of the PDE (so they can be classified in the Bubnov-Galerkin type of method) leading to the Natural Element Method (NEM) [Sukumar 1998]. It is also possible to use non-Sibsonian functions (faster to compute) as shown in [Belikov 1997]. At this point, the Meshless Finite Element Method (MFEM) that also uses non-Sibsonian interpolation should be mention although the meshfree concepts are only used to build the shape functions [Idelsohn 2003].

1.1.3.2 Coupled meshbased/meshless approaches

The Reproducing Kernel Element Method (RKEM) was introduced in [Liu 2004, Li 2004, Lu 2004]. The idea is to mix the best features of meshbased and meshless methods. To achieve that, smooth finite element shape functions are introduced to obtain a higher continuity of the interpolation. The basic approximation in RKEM is the following :

$$u^h(\boldsymbol{x}) = \sum_{e=1}^{N_{elements}} \left[\int_{\Omega_e} K(\boldsymbol{x} - \boldsymbol{y}) d\Omega_e \left(\sum_{i=1}^{N_{nodes}} N^*_{e,i}(\boldsymbol{x}) u(\boldsymbol{x}_{e,i}) \right) \right], \tag{1.1.32}$$

where $N^*_{e,i}$ are global partition polynomials of the FEM approximation that are C^∞ on the domain (in contrast with $N_{e,i} = N^*_{e,i}\chi_e$, classic C^0 shape functions). $K(\boldsymbol{x}-\boldsymbol{y})$ is computed like in the RKPM method. The shape functions that obtained are, in general, way more complex than FEM shape functions, thus more costly to compute. The Moving Particle Finite Element Method (MPFEM) is based on the same idea [Hao 2002].

Another good example of trying to mix the properties of meshless and meshbased method is the Material Point Method (MPM) [Sulsky 1994]. It is based on the Fluid Implicit Particle method (FLIP) [Brackbill 1986] (based itself on the Particle In Cell (PIC) method [Harlow 1955]). MPM uses a background mesh and a set of particles. The equations of motion are solved on the mesh while all the other computations (constitutive equations, integration scheme) are performed on the particles. The communication between the mesh and the particles is achieved through interpolation. At the end of each time step the grid is reset to its original position.

1.1.3.3 Specific approaches

Some methods were explicitly designed to solve certain class of problems. Among them are the Finite Volume particle Method (FVPM) [Hietel 2000] which is built for solving conservation laws. In a nutshell, instead of using characteristic functions for the test functions as in the classic Finite Volume Method (FVM), Shepard functions are used. Another example of meshless methods developed to solve the conservation laws is the Finite Mass Method (FMM) [Gauger 2000] which is based on a discretization of mass instead of space.

1.1.3.4 Generalizations

A good example of a method that generalizes an existing one is the Generalized Finite Difference Method (GFDM) which derives from the classic Finite Difference Method (FDM) but that allows the nodes to placed arbitrary in the domain. It enables the possibility to deal with unstructured meshes and irregular grids and offers a better discretization. The weight functions are computed through the Least Squares approach (MLS) or by using Radial Basis Functions (RBF). It is also worth mentioning the Radial Basis Function (RBF) method is based on the interpolation of the same name [Buhmann 2003]. It yields an approximation of the form $u^h(\boldsymbol{x}) = \sum_{i=0}^{N} a_i w_i(\boldsymbol{x} - \boldsymbol{x}_i)$ where a_i are appropriate weight coefficients and w_i is a set of radial basis functions (i.e. a real function that verifies $w_i(\boldsymbol{x}) = w_i(|\boldsymbol{x}|)$). It appears that RBF is a generalization of collocation methods such as SPH. Finally, the Local Regression Estimator method (LRE) has been introduced in [Dilts 2003] and is a generalization of the MLS method.

1.1.4 Related issues

1.1.4.1 Integration

One major drawback of meshfree Galerkin methods is the numerical integration of the weak form. It is due to the non-polynomial form of most meshless shape functions. Consequently, exact integration is difficult or impossible for most meshless methods. Several techniques exist :

1. Direct nodal integration
   Integrals are evaluated at the nodes that also serve as integration points :
   $$\int_{\Omega} f(\boldsymbol{x}) d\Omega = \sum_{i=1}^{N} f(\boldsymbol{x}_i) \Delta V_i. \tag{1.1.33}$$
   In general the quadrature weights ΔV_j are volumes associated with the node X_i. Nodal integration methods are very similar to collocation methods. Some stabilization techniques exist (least squares stabilization, stress points). In general, methods based on nodal and stress point integration are employed in dynamic problems and where large deformations are expected.
2. Support-based integration
   The integration is performed on the support domain or on the intersection of overlapping supports. It is a natural choice for MLPG methods since they are based on local weak forms.
3. Background mesh or cell structure
   The domain is divided into integration cells over which a Gaussian quadrature is performed. This is a convenient and well known method but it results in the loss of the pure meshfree character of the method.

1.1.4.2 Boundary conditions

The main issue for imposing boundary conditions in meshless methods is the lack of Kronecker delta property. Several generic techniques have been proposed to overcome that issue :

1. Introduction of Lagrange multipliers
   This well known method is very efficient but an extra system has to be solved to find the values of the multipliers resulting in an increased computational cost.
2. Penalty approach or Nitsche's method
   It consists in the introduction of an extra boundary integral in the weak form to satisfy the boundary conditions (or several extra integrals in the case of the Nitsche's method).
3. Coupling with FEM or another meshbased method
   Meshbased method can handle boundary conditions very easily, so coupling with these methods

to treat the boundary is a natural option as shown on Fig. 1.3. There are several commonly used coupling techniques such as ramp functions, imposed reproducing conditions, bridging scales or again Lagrange multipliers for example.

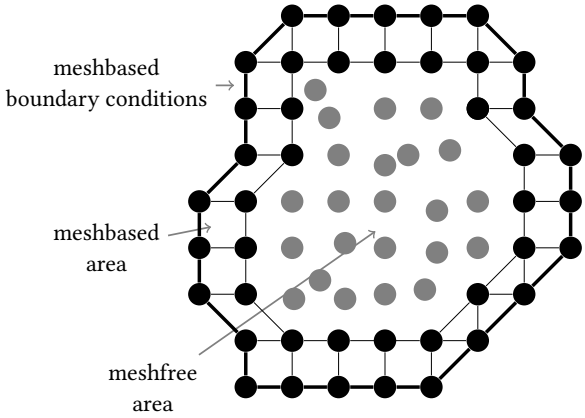

Figure 1.3: Meshbased/meshfree coupling for imposing boundary conditions

4. Transformation method
   This method consists in an arbitrary imposition of the boundary conditions directly on the approximation u^h but it requires the inversion of an $N \times N$ matrix each time a shape function is evaluated.
5. Enrichment of the basis
   As pointed out in the extrinsic basis section, the addition of well chosen function can help to recover the Kronecker delta property and thus facilitate the imposition of boundary conditions.
6. Boundary collocation
   This method is the simplest, it consists in taking the boundary imposition equation $u^h(\boldsymbol{x}_{bc}) = \sum_{i=1}^{N} \Phi_i(\boldsymbol{x}_{bc}) u_i$ as an equation of the total system of equations. This is directly taken from the FEM approach, although the lack of Kronecker delta property involves an important computational cost.
7. D'Alembert principle
   This technique consists in introducing generalized variables and a Jacobian matrix to project the residual of the PDE into the admissible solution space.
8. *(for internal boundaries like cracks)* Modification of the weight functions
   The main approaches are the visibility method, the diffraction method and the transparency method. See [Fries 2004] for details.

1.2 Other particle methods

There are still a number of particle methods that haven't been treated in this section because they do not emerge from a partition of unity. The methods discussed hereafter are from very different origins but can all be classified as particle methods.

1.2.1 Molecular Dynamics

The Molecular Dynamics method (MD) is one of the most used particle method in the scientific community. It has been applied to a wide variety of problems such as mechanical engineering, aerospace

engineering, electrical engineering and others. The concept behind MD is based on scale. It states that the mechanical behaviors observed at a given scale are governed by the mechanical behaviors at a lower scale and so that if it is possible to simulate a system at, let's say, nanoscale, all the observable behaviors at macroscale will naturally emerge. This approach is also called Direct Numerical Simulation (DNS) and has become more and more attractive with the development of High Performance Computing (HPC). The idea is then to take into account the four main forces of the universe (strong interaction, Coulomb force, weak interaction and gravity) and only those ones and to simulate a set of atoms. Currently, simulations up to several billions atoms can be achieved which is far from being enough to replace all the other existing numerical methods.

One famous conceptually derived method from MD is the Discrete Element Method (DEM). It is very similar to MD but include rotational degrees of freedoms and contact laws between particles. Generally applied to solids or granular flows, DEM is governed by Newton's motion laws. Plasticity and fracture models are included through specific interaction and contact laws between the particles.

In order to address problems that are beyond the current capabilities of MD in terms of spatial and temporal scales, the Dissipative Particle Dynamics (DPD) method was introduced by simplifying the interaction forces between particles. It has then been enriched with SPH concepts to become Smoothed Dissipative Particle Dynamics (SDPD) [Español 2003].

1.2.2 Vortex method

The Vortex Method (VM) is based on the vorticity velocity formulation of the Lagrangian Navier-Stokes equations (in contract with the widely used pressure velocity formulation). The vorticity is defined as $\boldsymbol{\omega} = \nabla \times \boldsymbol{u}$. The fundamental idea of this method is to discretize this vorticity-based Navier-Stokes system by a finite set of particles. A comparison between VM and SPH has been done in [Colagrossi 2016].

1.2.3 Peridynamics method

The Peridynamics method comes from a simple assessment : when a material has a discontinuity, typically a crack, the use of partial differential equations is not relevant since partial derivatives do not exist on singularities. Hence, the classic theory of continuum mechanics cannot be applied. This is the reason why Peridynamics is based on an integral theory of continuum mechanics which is defined even in the presence of singularities. Peridynamics is a non local extension of solids mechanics that enables the inclusion of discontinuities. As an example, the equation of motion in this theory is :

$$\rho \ddot{\boldsymbol{u}} = \int_H f(\boldsymbol{u}' - \boldsymbol{u}, \boldsymbol{x}' - \boldsymbol{x}) dV' + \boldsymbol{b}(\boldsymbol{x}, t), \tag{1.2.1}$$

where $\boldsymbol{x}$ is the position vector in the reference configuration, ρ is density, $\boldsymbol{u}$ is displacement, and $\boldsymbol{b}$ is a prescribed body force density. H is a neighborhood of $\boldsymbol{x}$ with radius h, where h is the horizon (cut-off distance). The prime superscript denotes the transformed configuration and f are the pairwise forces that defines the constitutive equations of the material. Thus, Peridynamics is a state-based theory where operators act on quantities in the reference configuration to transform then into quantities in the deformed configuration. It has been shown in [Ganzenmuller 2015] that CSPH in its total Lagrangian formulation (Lagrangian kernel) is a special case of Peridynamics. SPH can be seen as the simplest meshless discretization (nodal integration) of Peridynamics. This is a very interesting result since it connects methods from different backgrounds. Both are meshless Lagrangian methods based on integral formulations but SPH relies on curve fitting to approximate derivatives whereas Peridynamics uses pair interactions instead of PDEs.

1.2.4 Lattice Boltzmann Methods

This class of methods will be fully described later in this document in Chap. 3.

1.3 Classification of particle methods

(next page)

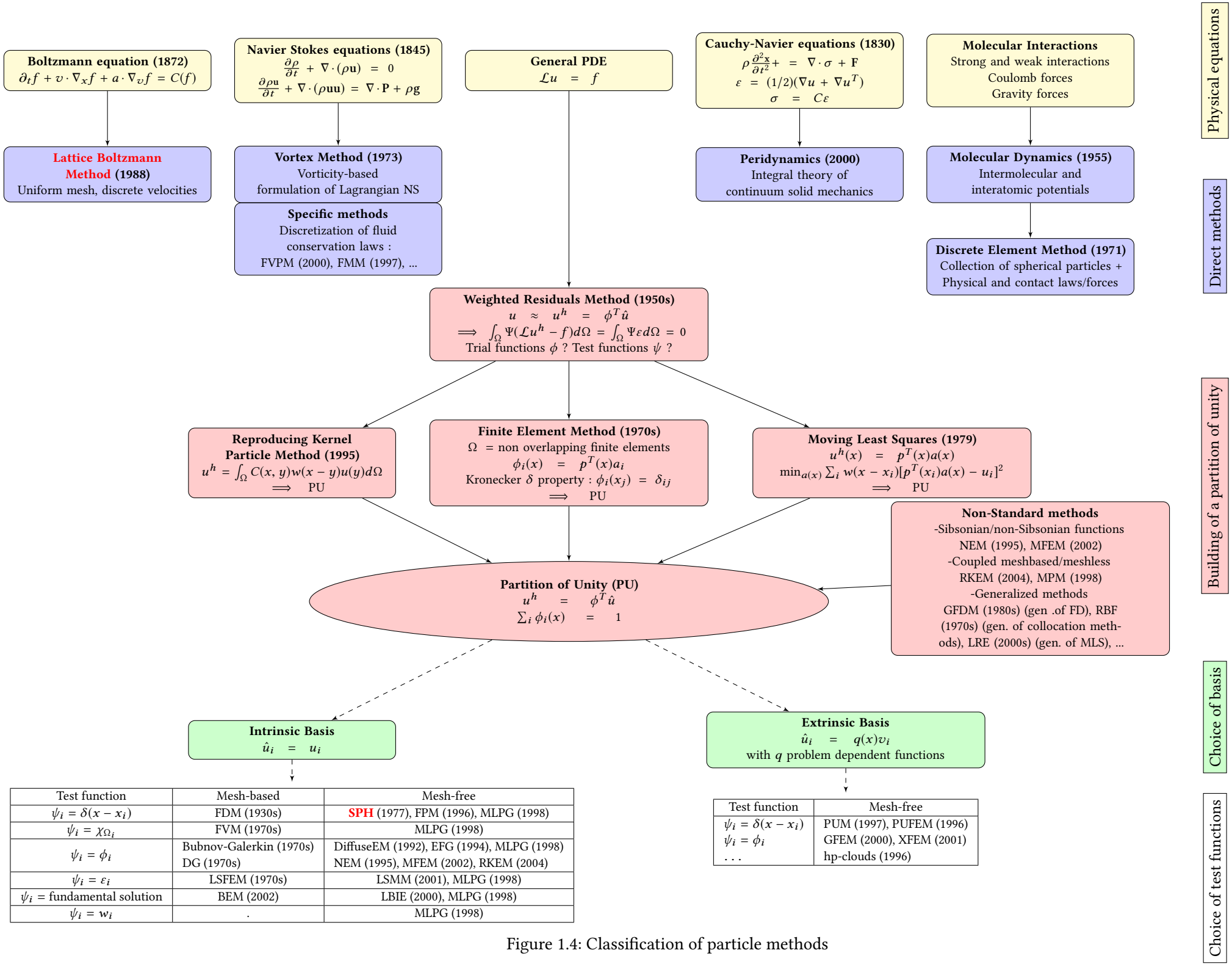

Test function	Mesh-based	Mesh-free
$\psi_i = \delta(x - x_i)$	FDM (1930s)	SPH (1977), FPM (1996), MLPG (1998)
$\psi_i = \chi_{\Omega_i}$	FVM (1970s)	MLPG (1998)
$\psi_i = \phi_i$	Bubnov-Galerkin (1970s) DG (1970s)	DiffuseEM (1992), EFG (1994), MLPG (1998) NEM (1995), MFEM (2002), RKEM (2004)
$\psi_i = \varepsilon_i$	LSFEM (1970s)	LSMM (2001), MLPG (1998)
ψ_i = fundamental solution	BEM (2002)	LBIE (2000), MLPG (1998)
$\psi_i = w_i$	.	MLPG (1998)

Test function	Mesh-free
$\psi_i = \delta(x - x_i)$	PUM (1997), PUFEM (1996)
$\psi_i = \phi_i$	GFEM (2000), XFEM (2001)
...	hp-clouds (1996)

Figure 1.4: Classification of particle methods

Chapter 2

Smoothed particle hydrodynamics

Contents

2.1 Derivation of the SPH interpolation **40**
- 2.1.1 Continuous interpolation 40
- 2.1.2 Kernel functions 43
- 2.1.3 Discrete interpolation 44
- 2.1.4 Numerical aspects 50

2.2 SPH approximation of Euler equations **54**
- 2.2.1 Continuity Equation 54
- 2.2.2 Momentum and Energy Equations 56
- 2.2.3 Alternative Lagrangian derivation of the SPH approximation 57

2.3 Key features **60**

2.4 Stabilization procedures **61**
- 2.4.1 Artificial viscosity 61
- 2.4.2 Physical viscosity 62
- 2.4.3 Tensile instability 63
- 2.4.4 Pairing Instability 64
- 2.4.5 Alternative formulations 64

2.5 Boundary conditions **66**
- 2.5.1 Wall boundary conditions 67
- 2.5.2 Other boundary conditions 68

2.6 Time integration **69**

2.7 Multiphase SPH **69**
- 2.7.1 Main formulations 70
- 2.7.2 Surface tension models 71
- 2.7.3 Corrective terms 73
- 2.7.4 Summary 75

The Smoothed Particle Hydrodynamics (SPH) method was introduced in 1977 in [Lucy 1977, Gingold 1977] and is one of the oldest meshless methods. Among the numerous applications of SPH, one can find astrophysics [Springel 2010], hydrodynamics, geophysics [Libersky 1991, Bui 2008, Douillet-Grellier 2016c, Douillet-Grellier 2016a] and computer graphics [Ihmsen 2014]. Some excellent reviews have been published [Monaghan 2012, Price 2012, Violeau 2016, Shadloo 2016].

Let's consider an arbitrary distribution of point mass particles. The main question SPH tries to answer is : how does one compute the local density of this set of points ? There are several approaches to this question leading to different numerical methods. SPH uses a weighted summation over the nearby particles given by :

$$\rho(\boldsymbol{x}) = \sum_{b=1}^{N} m_b w(\boldsymbol{x} - \boldsymbol{x}_b, h), \tag{2.0.1}$$

where w is a weight function (specified later in this document) whose dimension is the inverse of a volume and h the parameter that measures the rate of fall-off of w. This formula is the fundamental idea behind SPH and is illustrated on Fig. 2.1. Detailed concepts and descriptions of this method can be

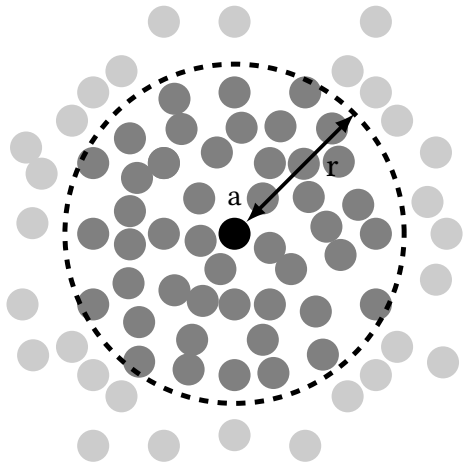

Figure 2.1: In SPH, density is computed using data from neighboring particles within a certain radius r. The number of neighboring particles is under-estimated compared to a real SPH application.

found by Monaghan [Monaghan 1992], Liu and Liu [Liu 2003a] and Violeau [Violeau 2012].

2.1 Derivation of the SPH interpolation

2.1.1 Continuous interpolation

The SPH is based on the following simple identity[1]:

$$\boldsymbol{A}(\boldsymbol{x}) = \int_{\Omega} \boldsymbol{A}(\boldsymbol{y})\delta(\boldsymbol{x} - \boldsymbol{y})d\Omega\,, \qquad \forall\, \boldsymbol{x} \in \Omega \subset \mathbb{R}^D, \tag{2.1.2}$$

[1]This is in fact the definition of the neutral element of the convolution operation. Indeed, if we introduce the convolution operation $(*)$ of two functions f and g as :

$$(f * g)(\boldsymbol{x}) = \int_{\Omega} f(\boldsymbol{y})g(\boldsymbol{x} - \boldsymbol{y})d\Omega = (g * f)(\boldsymbol{x}). \tag{2.1.1}$$

Therefore, the Dirac function is introduced as $(f * \delta) = f$

where $\boldsymbol{A}$ is a vector function of the position vector $\boldsymbol{x}$, Ω is the volume of the integral containing the point $\boldsymbol{x}$, and $\delta(\boldsymbol{x}-\boldsymbol{x}', h)$ is the Dirac function. A Dirac function is not continuous, thus for practical considerations we will approximate it with an interpolation kernel, denoted $w(\boldsymbol{x}-\boldsymbol{y}, h)$. This kernel is a regular function that has a compact or infinite support (condition (1.1.12)). The size of the support, when finite, is measured by the length parameter h called the smoothing length[2]. Moreover, we have $\lim_{h\to 0} w(\boldsymbol{x}-\boldsymbol{y}, h) = \delta(\boldsymbol{x}-\boldsymbol{y})$ (condition (1.1.14)). It is then possible to approximate the Dirac function by the smoothing kernel. It yields

$$\boxed{\tilde{\boldsymbol{A}}(\boldsymbol{x}) = \int_\Omega \boldsymbol{A}(\boldsymbol{y}) w(\boldsymbol{x}-\boldsymbol{y}, h) d\Omega\,, \qquad \forall\, \boldsymbol{x} \in \Omega \subset \mathbb{R}^D.} \tag{2.1.3}$$

The accuracy of this expression can be evaluated by performing a Taylor series expansion around $\boldsymbol{x}$:

$$\boldsymbol{A}(\boldsymbol{y}) = \boldsymbol{A}(\boldsymbol{x}) - (\boldsymbol{y}-\boldsymbol{x})\cdot\nabla\boldsymbol{A} + \frac{1}{2}(\boldsymbol{y}-\boldsymbol{x})\otimes(\boldsymbol{y}-\boldsymbol{x})\cdot\nabla^2\boldsymbol{A} + O(|\boldsymbol{y}-\boldsymbol{x}|^3). \tag{2.1.4}$$

Using the approximation defined in (2.1.3), the Taylor expansion becomes:

$$\begin{aligned}\tilde{\boldsymbol{A}}(\boldsymbol{x}) = \boldsymbol{A}(\boldsymbol{x})\int_\Omega w(\boldsymbol{y}-\boldsymbol{x}, h)d\Omega - \nabla\boldsymbol{A}\cdot\int_\Omega(\boldsymbol{y}-\boldsymbol{x})w(\boldsymbol{y}-\boldsymbol{x}, h)d\Omega \\ + \frac{1}{2}\nabla^2\boldsymbol{A}\cdot\int_\Omega(\boldsymbol{y}-\boldsymbol{x})\otimes(\boldsymbol{y}-\boldsymbol{x})w(\boldsymbol{y}-\boldsymbol{x}, h)d\Omega + \int_\Omega O(|\boldsymbol{y}-\boldsymbol{x}|^3)w(\boldsymbol{y}-\boldsymbol{x}, h)d\Omega.\end{aligned} \tag{2.1.5}$$

In order to be first order accurate, it is needed that :

$$\int_\Omega w(\boldsymbol{y}-\boldsymbol{x}, h)d\Omega = 1, \tag{2.1.6}$$

$$\int_\Omega(\boldsymbol{y}-\boldsymbol{x})w(\boldsymbol{y}-\boldsymbol{x}, h)d\Omega = 0. \tag{2.1.7}$$

The first condition corresponds to condition (1.1.11). The second condition is more difficult to satisfy unless we impose that the kernel is central symmetric (or isotropic) on Ω :

$$w(\boldsymbol{y}-\boldsymbol{x}, h) = w(|\boldsymbol{y}-\boldsymbol{x}|, h). \tag{2.1.8}$$

In that case, the integrand is anti-symmetric and therefore the integral vanishes[3]. This corresponds to condition (1.1.15) (and as a consequence (1.1.16)).

[2]Note that unless otherwise mentioned, the smoothing length will be considered constant.

[3]A simple variable change $\boldsymbol{y}-\boldsymbol{x} = \boldsymbol{x}-\boldsymbol{y}$ leads to :

$$\int_\Omega(\boldsymbol{y}-\boldsymbol{x})w(\boldsymbol{y}-\boldsymbol{x}, h)d\Omega = \int_\Omega(-(\boldsymbol{y}-\boldsymbol{x}))w(-(\boldsymbol{y}-\boldsymbol{x}), h)d\Omega = -\int_\Omega(\boldsymbol{y}-\boldsymbol{x})w(\boldsymbol{y}-\boldsymbol{x}, h)d\Omega. \tag{2.1.9}$$

In a more general way, we do have :

$$\begin{aligned}\int_\Omega \boldsymbol{A}(\boldsymbol{y}-\boldsymbol{x})\underbrace{((\boldsymbol{y}-\boldsymbol{x})\otimes\ldots\otimes(\boldsymbol{y}-\boldsymbol{x}))}_{2n+1\text{ times}}w(\boldsymbol{y}-\boldsymbol{x}, h)d\Omega = 0, \\ \int_\Omega \boldsymbol{A}(\boldsymbol{y}-\boldsymbol{x})\underbrace{((\boldsymbol{y}-\boldsymbol{x})\otimes\ldots\otimes(\boldsymbol{y}-\boldsymbol{x}))}_{2n\text{ times}}\nabla w(\boldsymbol{y}-\boldsymbol{x}, h)d\Omega = 0.\end{aligned} \tag{2.1.10}$$

The fourth term[4] in Eq. (2.1.5) is a $O(h^4)$. The third term[5] is $O((\boldsymbol{y}-\boldsymbol{x})^2)$. It yields :

$$\begin{aligned}\tilde{\boldsymbol{A}}(\boldsymbol{x}) &= \boldsymbol{A}(\boldsymbol{x}) + \frac{1}{2}\nabla^2\boldsymbol{A}\cdot\int_\Omega(\boldsymbol{y}-\boldsymbol{x})\otimes(\boldsymbol{y}-\boldsymbol{x})w(\boldsymbol{y}-\boldsymbol{x},h)d\Omega + O(h^4),\\ \tilde{\boldsymbol{A}}(\boldsymbol{x}) &= \boldsymbol{A}(\boldsymbol{x}) + O(h^2).\end{aligned} \tag{2.1.12}$$

The gradient of the function $\boldsymbol{A}$ at the position of particle a is evaluated as follows starting from Eq. (2.1.2) :

$$\begin{aligned}\nabla\tilde{\boldsymbol{A}}(\boldsymbol{x}) &= \int_\Omega \nabla\boldsymbol{A}(\boldsymbol{y})w(\boldsymbol{x}-\boldsymbol{y},h)d\Omega,\\ &= \int_\Omega \nabla(\boldsymbol{A}(\boldsymbol{y})w(\boldsymbol{x}-\boldsymbol{y},h))d\Omega - \int_\Omega \boldsymbol{A}(\boldsymbol{y})\nabla w(\boldsymbol{x}-\boldsymbol{y},h)d\Omega,\\ &= \cancel{\oint_{\partial\Omega}\boldsymbol{A}(\boldsymbol{y})w(\boldsymbol{x}-\boldsymbol{y},h)\boldsymbol{n}d\Gamma} + \int_\Omega \boldsymbol{A}(\boldsymbol{y})\nabla w(\boldsymbol{x}-\boldsymbol{y},h)d\Omega,\\ &= \int_\Omega \boldsymbol{A}(\boldsymbol{y})\nabla w(\boldsymbol{x}-\boldsymbol{y},h)d\Omega,\end{aligned} \tag{2.1.13}$$

where $\partial\Omega$ is a the boundary of ω and $\boldsymbol{n}$ is the normal directed towards the exterior. Several comments have to be made here. First, the Gauss theorem and the fact that $\nabla w(\boldsymbol{x}-\boldsymbol{y},h)$ is an odd function (Eq. (1.1.16)) have been used in the calculations. Second, in order to eliminate the boundary integral, it is assumed that the point $\boldsymbol{x}$ is far enough from $\partial\Omega$ so that $w(\boldsymbol{x}-\boldsymbol{y},h)$ vanishes due to its compact support. This is the root cause of the difficulties to impose boundary conditions in SPH. On Fig. 2.4, one can observe how the quality of the interpolation is compromised at the boundaries of the domain. Applying the gradient operator to Eq. (2.1.12), we immediately obtain :

$$\nabla\tilde{\boldsymbol{A}}(\boldsymbol{x}) = \nabla\boldsymbol{A}(\boldsymbol{x}) + O(h^2). \tag{2.1.14}$$

In a similar way, the divergence operator is defined as :

$$\nabla\cdot\tilde{\boldsymbol{A}}(\boldsymbol{x}) = \int_\Omega \boldsymbol{A}(\boldsymbol{x})\cdot\nabla w(\boldsymbol{y}-\boldsymbol{x},h)d\Omega. \tag{2.1.15}$$

and is 1st order accurate :

$$\nabla\cdot\tilde{\boldsymbol{A}}(\boldsymbol{x}) = \nabla\cdot\boldsymbol{A}(\boldsymbol{x}) + O(h^2). \tag{2.1.16}$$

We now define the scalar product between two continuous vector functions $\boldsymbol{A}$ and $\boldsymbol{B}$ as follows :

$$\langle \boldsymbol{A}\,,\,\boldsymbol{B}\rangle = \int_\Omega \boldsymbol{A}(\boldsymbol{y})\cdot\boldsymbol{B}(\boldsymbol{y})d\Omega \tag{2.1.17}$$

[4]Indeed, we have $w(\boldsymbol{y}-\boldsymbol{x},h) = O(1)$, therefore $\int_\Omega O(|\boldsymbol{y}-\boldsymbol{x}|^3)w(\boldsymbol{y}-\boldsymbol{x},h)d\Omega = \int_\Omega O(|\boldsymbol{y}-\boldsymbol{x}|^3)d\Omega = O(|\boldsymbol{y}-\boldsymbol{x}|^4)$. In addition, $|\boldsymbol{y}-\boldsymbol{x}|$ is always less then h so it is correct to say that the approximation is in fact up to $O(h^2)$.

[5]$\int_\Omega(\boldsymbol{y}-\boldsymbol{x})\otimes(\boldsymbol{y}-\boldsymbol{x})w(\boldsymbol{y}-\boldsymbol{x},h)d\Omega$ is an isotropic tensor of order 2. Indeed, $(\boldsymbol{y}-\boldsymbol{x})\otimes(\boldsymbol{y}-\boldsymbol{x})$ is symmetric and $w(\boldsymbol{y}-\boldsymbol{x},h)$ is isotropic because of Eq. (2.1.8). In consequence, all the non diagonal terms are zero (anti-symmetric integrands). Moreover, $\int_\Omega|\boldsymbol{y}-\boldsymbol{x}|^2w(\boldsymbol{y}-\boldsymbol{x},h)d\Omega = D\int_\Omega(\boldsymbol{y}-\boldsymbol{x})_i^2|^2w(\boldsymbol{y}-\boldsymbol{x},h)d\Omega$. We can write :

$$\int_\Omega(\boldsymbol{y}-\boldsymbol{x})\otimes(\boldsymbol{y}-\boldsymbol{x})w(\boldsymbol{y}-\boldsymbol{x},h)d\Omega = \frac{\boldsymbol{I}}{D}\int_\Omega|\boldsymbol{y}-\boldsymbol{x}|^2w(\boldsymbol{y}-\boldsymbol{x},h)d\Omega. \tag{2.1.11}$$

In the case of a Gaussian kernel (see Sect. 2.1.2), it yields :

$$\int_\Omega(\boldsymbol{y}-\boldsymbol{x})\otimes(\boldsymbol{y}-\boldsymbol{x})w(\boldsymbol{y}-\boldsymbol{x},h)d\Omega = \frac{\boldsymbol{I}}{D}\alpha(D)\frac{\pi^{D/2}h^{D+2}D}{2} = \frac{h^2}{2}.$$

Recently, the smoothing error has been exactly evaluated in [Violeau 2019].

Moreover, the interpolated operators still verify some usual properties of gradients and divergences such as linearity and skew-adjointness i.e. :

$$\langle \tilde{\boldsymbol{A}}\,,\ (\nabla \cdot \tilde{\boldsymbol{B}})\rangle = -\langle (\nabla \tilde{\boldsymbol{A}})\,,\ \tilde{\boldsymbol{B}}\rangle. \tag{2.1.18}$$

However, the interpolated operators do not comply with the common laws of differential calculus. For example, if $\boldsymbol{A}$ is a matrix and $\boldsymbol{B}$ a vector, $\widetilde{\nabla \cdot (\boldsymbol{A}^T \boldsymbol{B})} \neq \left(\widetilde{\nabla \cdot \boldsymbol{A}}\right) \cdot \boldsymbol{B} + \boldsymbol{A} : \widetilde{\nabla \boldsymbol{B}}$. In consequence, the Gauss theorem is not satisfied neither, which is an important fact to understand SPH consistency issues.

Finally, it is obvious that the approximation and the operator commutes i.e. $\nabla \tilde{\boldsymbol{A}} = \widetilde{\nabla \boldsymbol{A}}$ and $\nabla \cdot \tilde{\boldsymbol{A}} = \widetilde{\nabla \cdot \boldsymbol{A}}$. The main SPH interpolants are gathered in Tab. 2.1.

Operator	Continuous SPH Operator	Accuracy
Vector $\boldsymbol{A}(\boldsymbol{x})$	$\tilde{\boldsymbol{A}}(\boldsymbol{x}) = \int_\Omega \boldsymbol{A}(\boldsymbol{y}) w(\boldsymbol{x}-\boldsymbol{y}, h) d\Omega$	$O(h^2)$
Gradient $\nabla \boldsymbol{A}(\boldsymbol{x})$	$\nabla \tilde{\boldsymbol{A}}(\boldsymbol{x}) = \int_\Omega \boldsymbol{A}(\boldsymbol{y}) \nabla w(\boldsymbol{x}-\boldsymbol{y}, h) d\Omega$	$O(h^2)$
Divergence $\nabla \cdot \boldsymbol{A}(\boldsymbol{x})$	$\nabla \cdot \tilde{\boldsymbol{A}}(\boldsymbol{x}) = \int_\Omega \boldsymbol{A}(\boldsymbol{x}) \cdot \nabla w(\boldsymbol{y}-\boldsymbol{x}, h) d\Omega$	$O(h^2)$

Table 2.1: Continuous SPH Interpolants

2.1.2 Kernel functions

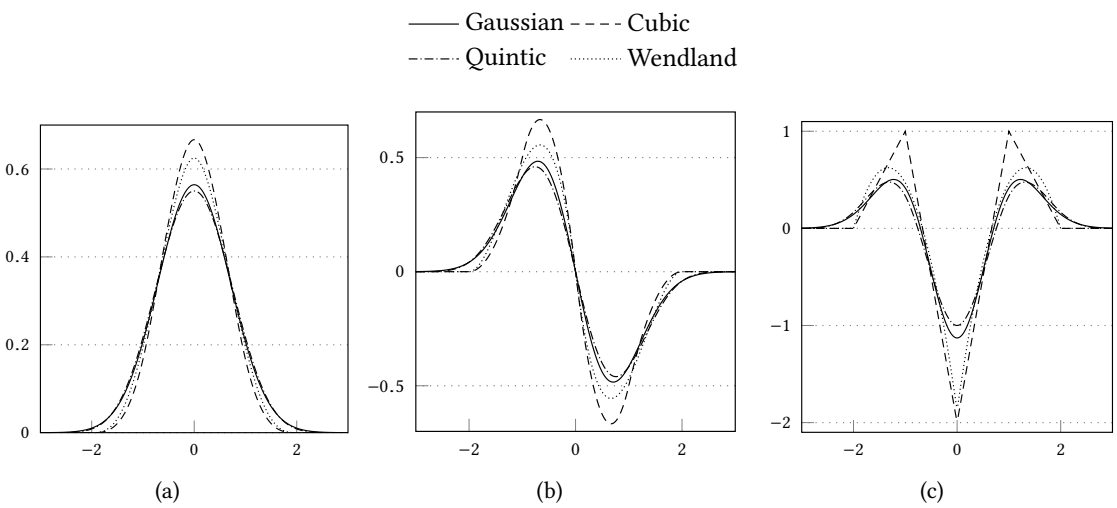

Figure 2.2: Several SPH kernels (a) and their 1st (b) and 2nd (c) derivatives

A smoothing function must satisfy the conditions presented in Sect. 1.1.1.3. The easiest way to ensure that the kernel is symmetric (condition (1.1.15)), is to impose $w(\boldsymbol{y}-\boldsymbol{x}, h) = w(|\boldsymbol{y}-\boldsymbol{x}|, h)$ which is the case for all kernels used in SPH simulations. In addition, the normalization condition (1.1.11) leads to the introduction of normalization factors that depend on the number of dimensions. Different smoothing functions have been tested in the SPH method. Traditional SPH studies all employ either a cubic or a quintic polynomial as the kernel function w. Both polynomial functions mimic a Gaussian distribution function but have the advantage that the compact space is bounded. The maximum value of $R = |\boldsymbol{x}-\boldsymbol{y}|/h$ for which w is not zero will be denoted κ. From now on, $w(\boldsymbol{x}-\boldsymbol{y}, h)$ will always be

Kernel	$w(\boldsymbol{x}-\boldsymbol{y},h)$	$\alpha(D)$
Gaussian ($\kappa=\infty$)	$\alpha(D)\exp(-R^2/2)$	$\frac{1}{h^D}\begin{cases}1/\sqrt{2\pi} & \text{if } D=1\\ 1/(2\pi) & \text{if } D=2\\ 1/(2\pi)^{3/2} & \text{if } D=3\end{cases}$
Cubic ($\kappa=2$)	$\alpha(D)\begin{cases}\frac{1}{4}(2-R)^3-(1-R)^3 & \text{if } 0\leq R\leq 1\\ \frac{1}{4}(2-R)^3 & \text{if } 1\leq R\leq 2\\ 0 & \text{if } 2\leq R\end{cases}$	$\frac{1}{h^D}\begin{cases}2/3 & \text{if } D=1\\ 10/(7\pi) & \text{if } D=2\\ 1/\pi & \text{if } D=3\end{cases}$
Quintic ($\kappa=3$)	$\alpha(D)\begin{cases}(3-R)^5-6(2-R)^5+15(1-R)^5 & \text{if } 0\leq R\leq 1\\ (3-R)^5-6(2-R)^5 & \text{if } 1\leq R\leq 2\\ (3-R)^5 & \text{if } 2\leq R\leq 3\\ 0 & \text{if } 3\leq R\end{cases}$	$\frac{1}{h^D}\begin{cases}1/120 & \text{if } D=1\\ 7/(478\pi) & \text{if } D=2\\ 1/(120\pi) & \text{if } D=3\end{cases}$
Quintic Wendland ($\kappa=2$)	$\alpha(D)\begin{cases}\left(1-\frac{R}{2}\right)^4(1+2R) & \text{if } 0\leq R\leq 2\\ 0 & \text{if } 2\leq R\end{cases}$	$\frac{1}{h^D}\begin{cases}3/4 & \text{if } D=1\\ 7/(4\pi) & \text{if } D=2\\ 21/(16\pi) & \text{if } D=3\end{cases}$

Table 2.2: Examples of kernel functions with $R=|\boldsymbol{x}-\boldsymbol{y}|/h$ and D the dimension

denoted $w(|\boldsymbol{x}-\boldsymbol{y}|,h)$ to ensure condition (2.1.8). Four examples of kernel functions are presented in Tab. 2.2 and shown on Fig. 2.2 along with their 1st and 2nd derivatives.

All these kernels have their first derivatives equal to zero and their second derivatives strictly negative when $R=0$. In consequence, as shown on Fig. 2.2, they are bell-shaped. A straightforward consequence of the symmetry properties of the kernel (Eqs. (1.1.15),(1.1.16) and (2.1.10)) is that the kernel support is rotationally invariant which implies that the support of the kernel is a D-sphere. Recently, it has been shown that pairing instability in SPH simulations is due to the positivity of the Fourier transform of the kernels [Robinson 2009, Dehnen 2012]. In consequence, it is recommended to use the Wendland kernels whose Fourier transforms are positive [Wendland 1995]. For a detailed analysis on how to build smoothing functions for SPH, see [Liu 2003b].

2.1.3 Discrete interpolation

In SPH, a continuum domain is modeled as a collection of particles. However unlike other particle methods such as DEM, these particles are not physical particles such as dust, powder, sand or water droplets, they are material points[6] bearing kinematic and thermodynamic quantities and evolving with time. We consider particles with a **constant** mass. We can write for any particle a :

$$V_a=\frac{m_a}{\rho_a}. \tag{2.1.19}$$

Although this volume is not necessarily constant since most SPH simulations are applied for weakly compressible flows, this volume will barely vary. Hence it is possible to introduce the mean diameter d_a defined as :

$$d_a=\sqrt[D]{V_a}. \tag{2.1.20}$$

At $t=0$, the particles are in general arranged as a lattice so d_a can be identified as the initial particle separation Δp (the equivalent of the grid size in mesh-based method). In general, the ratio between the

[6]By material point, it is referred to any (possibly macroscopic) body that can be described at the geometrical level by a set of three independent coordinates that are coinciding with the coordinates of its center of inertia. They are not point-sized and possess a volume and a mass [Violeau 2012]

smoothing length h and the inter-particular distance Δp lies between 1 and 2 :

$$\frac{h}{\Delta p} \in [1, 2]. \tag{2.1.21}$$

However, note that there is no golden rule in that regard and it is perfectly viable to set $\frac{h}{\Delta p}$ to a value superior to 2. As stated before, this is due to the fact that h is not a good measure of the kernel support, the standard deviation σ should be used instead (hence, the large variation of the number of neighbors in Tab. 2.3 which lacks meaning). All quantities related to a particle do not explicitly depend on space. They only depend on time and on their particle label (which refers to the particle initial position). They are governed by the evolution of their Lagrangian derivatives :

$$\dot{\boldsymbol{A}}_a = \frac{D\boldsymbol{A}_a(t)}{Dt}. \tag{2.1.22}$$

In particular, the velocity is $\boldsymbol{u}_a = \frac{D\boldsymbol{x}_a(t)}{Dt}$. Let's consider a finite set of N particles. The integral can be discretized by replacing it with a summation over the particles (approximation by a Riemann sum).

$$\begin{aligned} \tilde{\boldsymbol{A}}(\boldsymbol{x}) &= \int_\Omega \boldsymbol{A}(\boldsymbol{y}) w(|\boldsymbol{x}-\boldsymbol{y}|, h) d\Omega, \\ &\approx \sum_{b=1}^{N} \boldsymbol{A}(\boldsymbol{y}) w(|\boldsymbol{x}-\boldsymbol{x}_b|, h) V_b \quad = \sum_{b=1}^{N} \frac{m_b}{\rho_b} \boldsymbol{A}(\boldsymbol{y}) w(|\boldsymbol{x}-\boldsymbol{x}_b|, h) = \hat{\boldsymbol{A}}(\boldsymbol{x}). \end{aligned} \tag{2.1.23}$$

From Eq. (2.1.23), if one sets $\boldsymbol{A} = \rho$, Eq. (2.0.1) is obtained. Smoothing kernels have a compact support (see (1.1.12)), then by denoting Λ the set of particles within the compact support of the kernel function centered on $\boldsymbol{x}$[7], the summation is reduced to :

$$\boxed{\hat{\boldsymbol{A}}(\boldsymbol{x}) = \sum_{b \in \Lambda} \boldsymbol{A}(\boldsymbol{x}_b) \frac{m_b}{\rho_b} w(|\boldsymbol{x}-\boldsymbol{x}_b|, h).} \tag{2.1.24}$$

It is possible to estimate the number of particles within Λ. The cardinal number of Λ is :

$$\text{card}(\Lambda) = \frac{V_{\text{compact support}}}{V_{\text{particle}}} = \frac{V_{D\text{-sphere}} \kappa h^D}{\Delta p^D} = \left(\frac{\kappa h}{\Delta p}\right)^D \frac{2\pi^{D/2}}{n\Gamma(D/2)}. \tag{2.1.25}$$

These values can be calculated using Eq. (2.1.21) and are presented in Tab. 2.3. These values that quantify

Kernel	$D = 1$	$D = 2$	$D = 3$
Gaussian		∞	
Cubic/Wendland	[4,8]	[12,50]	[33,269]
Quintic	[6,12]	[28,114]	[114,905]

Table 2.3: Estimation of the number of neighbors in an SPH simulation for $\frac{h}{\Delta p} = [1, 2]$.

the number of interactions with neighboring nodes/particles are higher in SPH than in traditional mesh-based methods which is a clear disadvantage of SPH (and in general of particle mesh-less methods). Moreover, the particles in Λ moves with time and both the cardinal number and the elements in Λ are changing with time. Thus, SPH requires advanced neighbor searching algorithms in order to identify the particles in Λ. The length κh should be chosen such that a reasonably large number of neighbor

[7] Similarly, we will later denote Λ_a the set of particles within the compact support of the kernel function centered on $\boldsymbol{x}_a$.

particles exist, so that a sufficient number of particles are taken into account in the summations. Thus, the parameter κ is not a completely free parameter, but should be chosen high enough such that each particle has a sufficiently high number of surrounding neighbors. On the other hand, κ should be as small as reasonably possible in order to minimize computational time. Applying the discretization technique used to obtain Eq. (2.1.24), it is possible to deduce the discretized gradient and divergence operators.

$$\nabla \hat{\boldsymbol{A}}(\boldsymbol{x}) = \sum_{b\in\Lambda} \boldsymbol{A}_b \frac{m_b}{\rho_b} \nabla w(|\boldsymbol{x}-\boldsymbol{x}_b|, h), \tag{2.1.26}$$

$$\nabla \cdot \hat{\boldsymbol{A}}(\boldsymbol{x}) = \sum_{b\in\Lambda} \boldsymbol{A}_b \frac{m_b}{\rho_b} \cdot \nabla w(|\boldsymbol{x}-\boldsymbol{x}_b|, h). \tag{2.1.27}$$

Finally, once again, the approximation and the discrete operator commutes i.e. $\nabla \hat{\boldsymbol{A}} = \widehat{\nabla \boldsymbol{A}}$ and $\nabla \cdot \hat{\boldsymbol{A}} = \widehat{\nabla \cdot \boldsymbol{A}}$.

Now that we have defined discrete SPH interpolants, one might be tempted to provide an estimation of the error induced by the discretization. However, it depends on the particle position. Thus it is much more complicated to evaluate than the error induced by the continuous SPH interpolants. When the particle distribution is assumed to be evenly distributed, it is reasonably simple to provide an estimation of the error and we will do so hereafter. This will give us a lower bound of the desired error estimation. When the particles are disordered, the discrete interpolation error can be evaluated by a Monte Carlo statistical calculation assuming a random distribution. Nevertheless, this approach will only lead to an upper bound of the desired error since the particles, although disordered, are far from being randomly distributed. Moreover, particles distribution is governed by the fluids equations and therefore is not constant in space time and so is the error. This complicates the estimation of the discrete interpolation error that remains an open question until now. This error estimation is strongly inspired from [Violeau 2012]. In the case of a Cartesian distribution of the particles, the error is :

$$e(F(.)) = \sum_{b\in\Lambda} F(\boldsymbol{x}_b) V_b - \int_\Omega F(\boldsymbol{y}) d\Omega. \tag{2.1.28}$$

Particles are arranged in a Cartesian grid, so their volume and their separation are constant : $V_a = V_p$ and $d_a = \Delta p$. In addition, all the coordinates $\boldsymbol{x}_b$ are multiple of Δp. It is possible to apply the multi-dimensional Poisson formula[8] to F as follows :

$$\begin{aligned}
\sum_{m_i\in\mathbb{Z}^D} F(m_1\Delta p, \ldots, m_D\Delta p) &= \frac{1}{\Delta p^D} \sum_{k_i\in\mathbb{Z}^D} \widehat{f}\left(k_1\frac{2\pi}{\Delta p}, \ldots, k_D\frac{2\pi}{\Delta p}\right), \\
\sum_{m_i\in\mathbb{Z}^D} F(m_1\Delta p, \ldots, m_D\Delta p) &= \frac{1}{\Delta p^D} \sum_{k_i\in\mathbb{Z}^D} \widehat{f}\left(k_1 K, \ldots, k_D K\right), \\
V_p \sum_{b\in\Lambda} F(\boldsymbol{x}_b) &= \frac{1}{\Delta p^D} \sum_{k_i\in\mathbb{Z}^D} \widehat{f}\left(k_1 K, \ldots, k_D K\right),
\end{aligned} \tag{2.1.30}$$

with $K = \frac{2\pi}{\Delta p}$ the wave number and $\widehat{F}(\boldsymbol{w}) = \int_{-\infty}^{\infty} f(\boldsymbol{t}) \exp(-i\boldsymbol{w}\cdot\boldsymbol{t}) d\boldsymbol{t}$. We immediately notice that $\widehat{F}(0) =$

[8] We remind here the more common Poisson formula in 1D. For a continuous function $f(t)$ going to 0 for $t \to \pm\infty$, we have:

$$\sum_{m\in\mathbb{Z}} f(mT) = \frac{1}{T} \sum_{k\in\mathbb{Z}} \widehat{f}\left(k\frac{2\pi}{T}\right), \tag{2.1.29}$$

where $\widehat{f}(w) = \int_{-\infty}^{\infty} f(t) \exp(-iwt) dt$ is the traditional Fourier transform of f. It has been preferred here to use the traditional *hat* notation for the Fourier transform but it should not be confused with the SPH discretization used above.

$\int_\Omega F(\boldsymbol{y})d\Omega$. So we can write :

$$e(F(.)) = \sum_{k_i \in \mathbb{Z}^D \setminus \{0\}} \widehat{f}\left(k_1 K, \ldots, k_D K\right). \tag{2.1.31}$$

Replacing $F(.)$ by $A(.)w(|\boldsymbol{x} - .|, h)$, we obtain $e(A(.)w(|\boldsymbol{x} - .|, h))$ which is equal to $e(A(\boldsymbol{x} - .)w(|.|, h))$ by a simple variable translation. Using Eq. (2.1.4) at first order:

$$\boldsymbol{A}(\boldsymbol{x} - .) = \boldsymbol{A}(.) - (.) \cdot \nabla \boldsymbol{A} + O(|.|^2). \tag{2.1.32}$$

The error can then be expressed:

$$e(A(.)w(|\boldsymbol{x} - .|, h)) = e(A(\boldsymbol{x} - .)w(|.|, h)) = \boldsymbol{A}(\boldsymbol{x})e(w(|.|, h)) - e(w(|.|, h)(.))\nabla \boldsymbol{A} + e(O(|.|^2)w(|.|, h)). \tag{2.1.33}$$

Using Eq. (2.1.31), we can compute some terms of the above equations :

$$\begin{cases} e(w(|.|, h)) & = \sum_{k_i \in \mathbb{Z}^D \setminus \{0\}} \widehat{w}\left(|k_1 K, \ldots, k_D K|\right) = \sum_{k_i \in \mathbb{Z}^D \setminus \{0\}} \widehat{w}\left(\bar{k}K\right), \\ e(w(|.|, h)(.)) & = 0, \end{cases} \tag{2.1.34}$$

with $\boldsymbol{e}_k = \frac{1}{\bar{k}}(k_1, \ldots, k_D)$ and $\bar{k} = \sqrt{\sum_i k_i^2}$. The second error term is zero because $w(|\boldsymbol{x}|, h)\boldsymbol{x}$ is a real odd function and therefore its Fourier transform's real part is zero and also its integral is zero. Furthermore, the last term $e(O(|.|^2)w(|.|, h))$ is $O(h^2)$ in the worst case scenario. We now have :

$$e(A(\boldsymbol{x} - .)w(|.|, h)) = \boldsymbol{A}(\boldsymbol{x}) \sum_{k_i \in \mathbb{Z}^D \setminus \{0\}} \widehat{w}\left(\bar{k}K\right) + O(h^2). \tag{2.1.35}$$

The Fourier transform of the kernels are strongly decreasing towards zero. As an example, we provide the Fourier transforms of the 1D nondimensionalized Gaussian, Cubic, Quintic and Wendland kernels (denoted W where $W = w/\alpha(D)$, see Tab.2.2) in Tab. 2.4[9].

Kernel	$\widehat{W}(q)$
Gaussian	$\sqrt{\pi}\exp\left(-\frac{h^2q^2}{4}\right)$
Cubic	$\frac{3}{2}\left(\frac{2}{hq}\sin\left(\frac{hq}{2}\right)\right)^4$
Quintic	$120\left(\frac{2}{hq}\sin\left(\frac{hq}{2}\right)\right)^6$
Wendland	$\frac{30}{h^6q^6}\left(h^2q^2 + \frac{1}{2}hq\sin(2hq) - 2\sin(hq)^2\right)$

Table 2.4: Fourier transforms of the nondimensionalized kernels in 1D. Note that $\widehat{W}(0) = \int_\Omega w(\boldsymbol{y}, h)\alpha(D)d\Omega = 1\alpha(D)$ for all kernels by construction (see Eq. (1.1.11)).

In fact, we can reasonably state that when $\hat{k}K > \frac{10}{h}$, $\widehat{w}(\hat{k}K) < 0.01$. Using Eq. (2.1.21), this condition on $\bar{k}$ becomes :

$$\bar{k} < \frac{10\Delta p}{2\pi h} \approx 1. \tag{2.1.36}$$

[9]One may remark that only the Gaussian and Wendland kernels have a fully decreasing Fourier transforms.

Therefore, it yields :

$$e(A(\boldsymbol{x}-.)w(|.|,h)) = \boldsymbol{A}(\boldsymbol{x})D\widehat{w}\,(K) + O(h^2), \tag{2.1.37}$$

$$e(A(\boldsymbol{x}-.)w(|.|,h)) = \boldsymbol{A}(\boldsymbol{x})D\widehat{w}\left(\frac{10}{h}\right) + O(h^2), \tag{2.1.38}$$

$$\frac{e(A(\boldsymbol{x}-.)w(|.|,h))}{\boldsymbol{A}(\boldsymbol{x})} \approx 0.01D + O(h^2). \tag{2.1.39}$$

$$\tag{2.1.40}$$

We now can see the ambiguous role of the smoothing length in the error estimation. The higher h, the lower Fourier transform of the kernel (if the Fourier transform of the kernel is fully decreasing which is only the case for the Gaussian and Wendland kernels) and the lower the error because more neighbors are used which reduces the statistical error. But in the meantime, the higher h, the higher $O(h^2)$ and therefore the higher the error because the approximation of the Dirac functions with a Gaussian-type kernel is becoming more and more erroneous. There is an optimum value for h that depends on the particle distribution and on the interpolated quantity $\boldsymbol{A}$. When no particles is on the edge of the domain and still in the case of the Cartesian grid, it is possible to use the second Euler-Maclaurin formula to obtain a better estimation of the error [Violeau 2012] :

$$e(A(.)w(|\boldsymbol{x}-.|,h)) = O\left(\left(\frac{\Delta p}{h}\right)^N\right), \tag{2.1.41}$$

where N is a kernel dependent value[10]. All in all, the global error of the SPH approximation is the following :

$$\boxed{\hat{\boldsymbol{A}}(\boldsymbol{x}) = \boldsymbol{A}(\boldsymbol{x}) + O(h^2) + O\left(\left(\frac{\Delta p}{h}\right)^N\right).} \tag{2.1.42}$$

It is possible to extend this result to an arbitrary particle distribution [Quinlan 2006]. Clearly, this ambiguous role of the smoothing length in the SPH formulation is a major drawback of the method.

We will now introduce the usual notations within the SPH community. Let's consider that the SPH operators are computed at the location of particle a i.e. $\boldsymbol{x} = \boldsymbol{x}_a$. Moreover, we will denote $w_{ab} = w(|\boldsymbol{x}_a - \boldsymbol{x}_b|, h)$ and $\boldsymbol{A}_a = \boldsymbol{A}(\boldsymbol{x}_a)$. Exactly like in the continuous case, the interpolated discrete operators verify some usual properties of gradients and divergences. In particular, the divergence operator and the gradient operator are skew adjoint i.e. :

$$\langle \hat{\boldsymbol{A}}_a\,,\ (\nabla\cdot\hat{\boldsymbol{B}}_a)\rangle = -\langle(\nabla\hat{\boldsymbol{A}}_a)\,,\ \hat{\boldsymbol{B}}_a\rangle. \tag{2.1.43}$$

where, following Eq. (2.1.17), the scalar product between two discrete vector fields $\boldsymbol{A}$ and $\boldsymbol{B}$ is defined by :

$$\langle \boldsymbol{A}_a\,,\ \boldsymbol{B}_a\rangle = \sum_{b\in\Lambda_a} \frac{m_b}{\rho_b}\boldsymbol{A}_b\cdot\boldsymbol{B}_b \tag{2.1.44}$$

The main discretized SPH interpolants are presented in Tab. 2.5.

In practice, it is possible to obtain alternative versions of the gradient and divergence SPH operators by using simple identities such as :

$$\forall k\in\mathbb{N},\ \begin{cases} \nabla\boldsymbol{A} &= \rho^k\nabla\left(\frac{\boldsymbol{A}}{\rho^k}\right) + \frac{\boldsymbol{A}}{\rho^k}\cdot\nabla(\rho^k) = \frac{1}{\rho^k}\nabla\left(\boldsymbol{A}\rho^k\right) - \frac{\boldsymbol{A}}{\rho^k}\cdot\nabla(\rho^k), \\ \nabla\cdot\boldsymbol{A} &= \rho^k\nabla\cdot\left(\frac{\boldsymbol{A}}{\rho^k}\right) + \frac{\boldsymbol{A}}{\rho^k}\cdot\nabla(\rho^k) = \frac{1}{\rho^k}\nabla\cdot\left(\boldsymbol{A}\rho^k\right) - \frac{\boldsymbol{A}}{\rho^k}\cdot\nabla(\rho^k). \end{cases} \tag{2.1.45}$$

Operator	Discrete SPH Operator	Accuracy
Vector $\boldsymbol{A}(\boldsymbol{x}_a)$	$\hat{\boldsymbol{A}}(\boldsymbol{x}_a) = \sum_{b\in\Lambda_a} \boldsymbol{A}_b \frac{m_b}{\rho_b} w_{ab}$	$O(h^2) + O\left(\left(\frac{\Delta p}{h}\right)^N\right)$
Gradient $\nabla \boldsymbol{A}(\boldsymbol{x}_a)$	$\nabla\hat{\boldsymbol{A}}(\boldsymbol{x}_a) = \sum_{b\in\Lambda_a} \boldsymbol{A}_b \frac{m_b}{\rho_b} \nabla_a w_{ab}$	$O(h^2) + O\left(\left(\frac{\Delta p}{h}\right)^N\right)$
Divergence $\nabla\cdot \boldsymbol{A}(\boldsymbol{x}_a)$	$\nabla\cdot\hat{\boldsymbol{A}}(\boldsymbol{x}_a) = \sum_{b\in\Lambda_a} \boldsymbol{A}_b \frac{m_b}{\rho_b} \cdot \nabla_a w_{ab}$	$O(h^2) + O\left(\left(\frac{\Delta p}{h}\right)^N\right)$

Table 2.5: Discrete SPH Interpolants

Standard SPH Operator	Identity Used ($k \in \mathbb{N}$)	Alternative SPH Operator ($k \in \mathbb{N}$)
$\nabla\hat{\boldsymbol{A}}(\boldsymbol{x}_a) = \sum_{b\in\Lambda_a} \boldsymbol{A}_b \frac{m_b}{\rho_b} \nabla_a w_{ab}$	$\rho^k \nabla\left(\frac{\boldsymbol{A}}{\rho^k}\right) + \frac{\boldsymbol{A}}{\rho^k}\cdot\nabla(\rho^k)$	$\nabla_k^+\hat{\boldsymbol{A}}(\boldsymbol{x}_a) = \sum_{b\in\Lambda_a} \frac{m_b}{\rho_b} \frac{\rho_b^{2k}\boldsymbol{A}_a + \rho_a^{2k}\boldsymbol{A}_b}{(\rho_a\rho_b)^k} \nabla_a w_{ab}$
	$\frac{1}{\rho^k}\nabla\left(\boldsymbol{A}\rho^k\right) - \frac{\boldsymbol{A}}{\rho^k}\cdot\nabla(\rho^k)$	$\nabla_k^-\hat{\boldsymbol{A}}(\boldsymbol{x}_a) = -\frac{1}{\rho_a^{2k}} \sum_{b\in\Lambda_a} \frac{m_b}{\rho_b} (\rho_a\rho_b)^k (\boldsymbol{A}_a - \boldsymbol{A}_b) \nabla_a w_{ab}$
$\nabla\cdot\hat{\boldsymbol{A}}(\boldsymbol{x}_a) = \sum_{b\in\Lambda_a} \boldsymbol{A}_b \frac{m_b}{\rho_b} \cdot \nabla_a w_{ab}$	$\rho^k \nabla\cdot\left(\frac{\boldsymbol{A}}{\rho^k}\right) + \frac{\boldsymbol{A}}{\rho^k}\cdot\nabla(\rho^k)$	$\nabla_k^+\cdot\hat{\boldsymbol{A}}(\boldsymbol{x}_a) = \sum_{b\in\Lambda_a} \frac{m_b}{\rho_b} \frac{\rho_b^{2k}\boldsymbol{A}_a + \rho_a^{2k}\boldsymbol{A}_b}{(\rho_a\rho_b)^k} \cdot \nabla_a w_{ab}$
	$\frac{1}{\rho^k}\nabla\cdot\left(\boldsymbol{A}\rho^k\right) - \frac{\boldsymbol{A}}{\rho^k}\cdot\nabla(\rho^k)$	$\nabla_k^-\cdot\hat{\boldsymbol{A}}(\boldsymbol{x}_a) = -\frac{1}{\rho_a^{2k}} \sum_{b\in\Lambda_a} \frac{m_b}{\rho_b} (\rho_a\rho_b)^k (\boldsymbol{A}_a - \boldsymbol{A}_b) \cdot \nabla_a w_{ab}$

Table 2.6: Alternative SPH Interpolants

These alternatives SPH interpolants are shown in Tab. 2.6. The alternative operators have different properties and the choice to use one or the other depend on the problem. "∇_k^+" operators are anti-symmetric with respect to a and b. In particular, the following approximations are often used :

$$\nabla_1^+\hat{\boldsymbol{A}}(\boldsymbol{x}_a) = \rho_a \sum_{b\in\Lambda_a} m_b \frac{\boldsymbol{A}_a}{\rho_a^2} + \frac{\boldsymbol{A}_b}{\rho_b^2} \nabla_a w_{ab}, \tag{2.1.46}$$

$$\nabla_1^+\cdot\hat{\boldsymbol{A}}(\boldsymbol{x}_a) = \rho_a \sum_{b\in\Lambda_a} m_b \frac{\boldsymbol{A}_a}{\rho_a^2} + \frac{\boldsymbol{A}_b}{\rho_b^2} \cdot \nabla_a w_{ab}. \tag{2.1.47}$$

Indeed, their anti-symmetric properties ensure exact conservation of the momentum. In addition, it is the natural SPH operator obtained during the derivation SPH from variational principles [Vila 1999, Bonet 2004]. On the other hand, the following operators are also used :

$$\nabla_1^-\hat{\boldsymbol{A}}(\boldsymbol{x}_a) = -\frac{1}{\rho_a} \sum_{b\in\Lambda_a} m_b (\boldsymbol{A}_a - \boldsymbol{A}_b) \nabla_a w_{ab}, \tag{2.1.48}$$

$$\nabla_1^-\cdot\hat{\boldsymbol{A}}(\boldsymbol{x}_a) = -\frac{1}{\rho_a} \sum_{b\in\Lambda_a} m_b (\boldsymbol{A}_a - \boldsymbol{A}_b) \cdot \nabla_a w_{ab}. \tag{2.1.49}$$

"∇_k^-" operators are symmetric and the term $(\boldsymbol{A}_a - \boldsymbol{A}_b)$ ensures that they are exact for constant functions (in contrast with Eq. (2.1.26)). Moreover, it is worthwhile adding that $\nabla_1^+\hat{\boldsymbol{A}}(\boldsymbol{x}_a)$ and $\nabla_k^+\hat{\boldsymbol{A}}(\boldsymbol{x}_a)$ and $\nabla_k^-\cdot\hat{\boldsymbol{A}}(\boldsymbol{x}_a)$ are skew adjoint i.e.

$$\langle \hat{\boldsymbol{A}}_a \,,\, (\nabla_k^-\cdot\hat{\boldsymbol{B}}_a)\rangle = -\langle (\nabla_k^+\hat{\boldsymbol{A}}_a) \,,\, \hat{\boldsymbol{B}}_a\rangle. \tag{2.1.50}$$

[10]For the cubic spline kernel, $N = 4$. For the quintic spline kernel, $N = 6$. For the Wendland kernel, $N = 6$.

Other operators like the curl operator or the Laplacian operator can derived the same way and can be found in the literature ;

$$\nabla \times \boldsymbol{A}(\boldsymbol{x}_a) = \sum_{b\in\Lambda_a} A_b \frac{m_b}{\rho_b} \times \nabla_a w_{ab},$$
$$\nabla^2 \boldsymbol{A}(\boldsymbol{x}_a) = -2 \sum_{b\in\Lambda_a} \frac{m_b}{\rho_b}(A_a - A_b)\frac{\boldsymbol{x}_{ab}}{|\boldsymbol{x}_{ab}|^2}\nabla_a w_{ab},$$
$$\nabla(\nabla\cdot\boldsymbol{A}(\boldsymbol{x}_a)) = 2\sum_{b\in\Lambda_a}\frac{m_b}{\rho_b}\left[((D+2)A_{ab}\cdot\boldsymbol{x}_{ab})\frac{\nabla_a w_{ab}}{|\boldsymbol{x}_{ab}|^2} - (\boldsymbol{x}_{ab}\cdot\nabla_a w_{ab})(A_a - A_b)\right],$$

with D the spatial dimension and $\boldsymbol{x}_{ab} = \boldsymbol{x}_a - \boldsymbol{x}_b$. We will not go into details about second-order SPH operators (and Laplacian operators in particular) as they will not be used in the rest of the document. We recommend the reading of Sect. 6.2.1 of [Violeau 2012] on that aspect. However, we stress that the properties of auto-adjointness of Laplacian SPH operators guarantee the verification of the 2nd principle of thermodynamics which is fundamental to address problems involving wall and interface frictions such as the ones presented later in this work.

2.1.4 Numerical aspects

2.1.4.1 Consistency

The basic SPH formulation suffers from consistency issues. A simple way to highlight this problem is to insert the Taylor expansion of Eq. (2.1.4) truncated at order 2 into the discrete approximation defined in (2.1.24) :

$$\boldsymbol{A}(\boldsymbol{x}_a) = \boldsymbol{A}_a \sum_{b\in\Lambda_a}\frac{m_b}{\rho_b}w_{ab} + \nabla\boldsymbol{A}_a\cdot\sum_{b\in\Lambda_a}(\boldsymbol{x}_a - \boldsymbol{x}_b)\frac{m_b}{\rho_b}w_{ab} + O(|\boldsymbol{x}_a - \boldsymbol{x}_b|^2). \tag{2.1.51}$$

The above expression is fundamental to understand the consistency issues in SPH. The normalization conditions (2.1.6) we have imposed on the kernel function are under a continuous form and are not exactly satisfied in its discrete form :

$$\sum_{b\in\Lambda_a}\frac{m_b}{\rho_b}w_{ab} \neq 1,$$
$$\sum_{b\in\Lambda_a}(\boldsymbol{x}_a - \boldsymbol{x}_b)\frac{m_b}{\rho_b}w_{ab} \neq 0.$$

One can immediately notice that the basic SPH interpolation cannot even reproduce a constant function exactly (see Fig. 2.4). Indeed, in general SPH is not a partition of unity. This is clearly shown on Fig. 2.3. This is due to the negligence of certain boundary integrals (see Eq. (2.1.13)) and the approximation of the integrals by Riemann sums. It is a disadvantage of standard SPH that can be overcome using specific re-normalization techniques (see Sect. 2.4.5).

2.1.4.2 h-adaptivity

There are two distinct cases where one could need to use an adaptive resolution in an SPH simmulation. First, in presence of strongly variable density fields (which are common in astrophysics), it is mandatory to dynamically adjust the smoothing length in compact and rarefied areas to avoid having too many or too few particles in the support. Second, in the case of simulations with incompressible and/or weakly compressible flows, it is a way to redirect the computational effort towards areas of interest saving

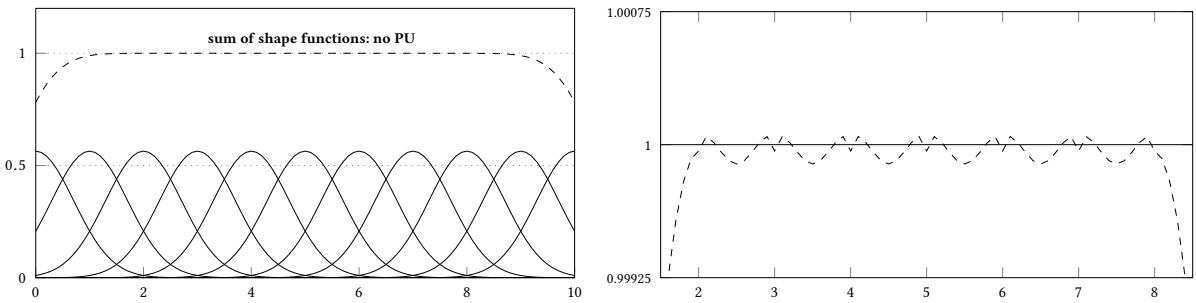

(a) SPH kernel functions (b) SPH kernel functions (zoom)

Figure 2.3: SPH is not an exact partition of unity. (Cubic Spline kernel, $\Delta p = 1$, $h = 1$)

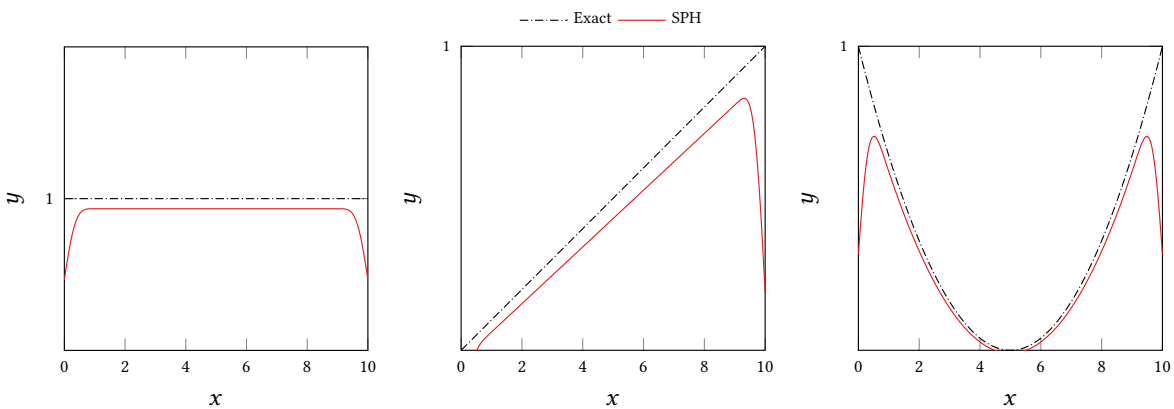

(a) Constant function (b) Linear function (c) Quadratic function

Figure 2.4: Basic SPH Consistency. (Cubic Spline kernel, $\Delta p = 0.01$, $h = 10$)

computation time. As with all numerical simulation methods, an optimum needs to be found between accuracy and computational speed. On one hand, the particles need to be small enough so that result is accurate, but on the other hand, the number of particles in a simulation should be limited for storage and calculation reasons. Note that, in the SPH method, the adaptivity can be understood in two ways ways. Indeed, it is possible to work with variable smoothing lengths h or variable masses m. In general, a constant mass is imposed for the particles to ensure that mass is conserved throughout the simulation (although some authors have investigated the case of a variable mass [Vila 1999]) so that the problem is actually about a variable h. In principle, the initial separation of particles in an SPH calculation may vary, so that more particles are placed where a higher resolution is needed. However, it is necessary to ensure a correct number of neighbors for each particle. This can partly be alleviated by using a different smoothing length h for each different particle (h-adaptivity) but this in turn makes the discretization much more complex and gives potential difficulties at boundaries and free surfaces. In addition, it is not known in advance where particles move to during the simulation: particles may start off in a not-so-eventful region but move into regions where a higher grid resolution would be desirable. Hence, the introduction of two alternative approaches : fixed refinement or dynamic refinement. In other words, in the case of fixed refinement, if the area of interest in known in advance, it is possible to impose spatial conditions to enable the refinement. On the contrary, if the area of interest is not known in advance, one has to define dynamic criterion to enable the refinement. Still, non-uniform particle distribution are rarely seen in practical applications. However, developments have been done on this matter and several formulations exist to treat a variable h within the SPH framework [Price 2008, Cossins 2010, Chiron 2017] and even industrial applications start to emerge [Sarangi 2016].

2.1.4.3 Initial particle packing

Quantities related to a given particle are calculated as a linear combination of the contributions from all neighboring particles. Hence, it is essential to start with initial conditions whose interpolation properties are as accurate as possible. In addition, the initial particle setup should be as close as possible to a configuration that would arise by itself in an SPH simulation. A method for generating initial SPH particle configurations should fulfill the following key requirements:

1. Isotropy : The initial particle configuration should be isotropic. No particular preferred direction at any location should be imposed.
2. High Interpolation Accuracy : The initial packing should be locally uniform to minimize noise in the SPH interpolation.
3. Versatility : The packing algorithm should be able to reproduce any spatial configuration and should not impose any requirement for symmetry.

Due to their well-known interpolation properties and ease of construction, the simplest setup schemes often arrange particles on a lattice or a grid. While there are many lattice configurations that could in principle be used to produce SPH initial conditions, three popular configurations have arisen within the SPH community : simple cubic lattice, cubic close-packed lattice and hexagonal close-packed lattice. The simplest arrangement (and one of the most popular) is the cubic lattice configuration, which has been shown to be an unstable equilibrium configuration and has strong preferred directions [Morris 1995]. Cubic close-packed and hexagonal close-packed lattices represent the two optimal and most efficient ways to pack spheres of equal sizes; they are stable against random perturbation and thus much preferred to a simple cubic lattice [Monaghan 1992]. Other packing configurations have emerged like the Weighted Voronoi Tesselations (WVT) [Diehl 2012] (see Fig. 2.5) or bubble packing algorithms [Colagrossi 2012].

As shown on Fig. 2.6[11], the initial particle packing can have a strong influence on the physical results.

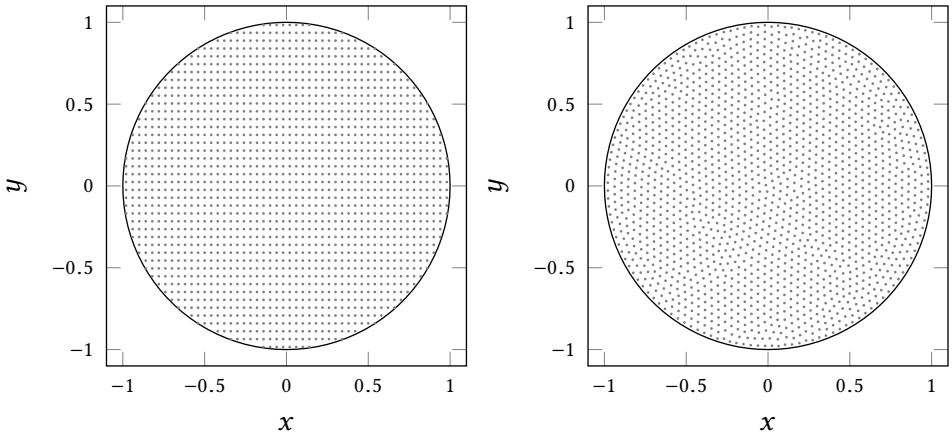

(a) (b)

Figure 2.5: Cartesian (a) and WVT (b) packings of a circle

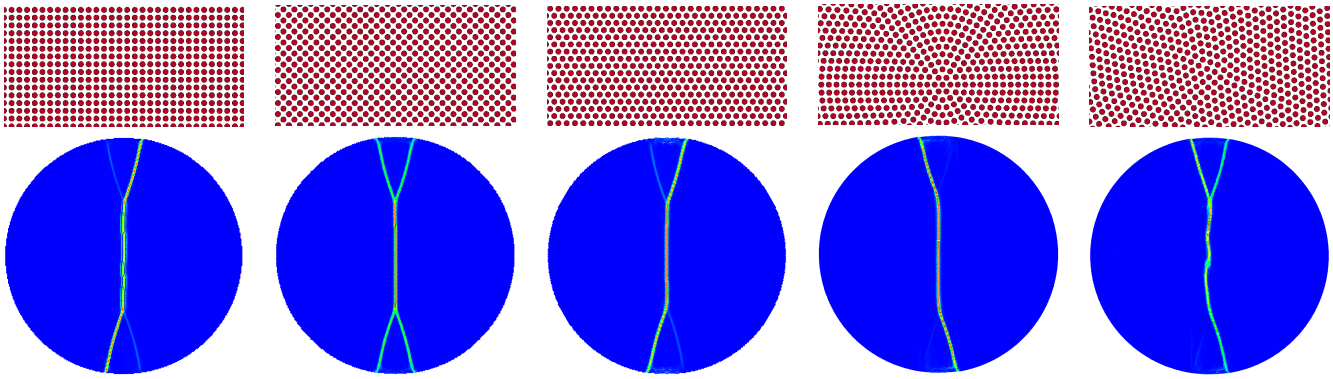

(a) Body-centered cubic (b) Face-centered cubic (c) Hexagonal close-packed (d) Circular (e) Random

Figure 2.6: Impact of the initial particle packing on the fracture pattern in the case of a 2D Brazilian test simulated with SPH. This figure shows unpublished simulation results obtained before this doctoral work during a previous Total-sponsored project and closely related to [Douillet-Grellier 2016a, Das 2016].

[11]This figure shows unpublished simulations done before this doctoral work during a previous Total-sponsored project and closely related with [Douillet-Grellier 2016a, Das 2016].

2.2 SPH approximation of Euler equations

This document will focus on the discretization of the Euler equations which are given by :

$$\frac{D\rho}{Dt} = -\rho\nabla\cdot\boldsymbol{u}, \tag{2.2.1}$$

$$\frac{D\boldsymbol{u}}{Dt} = -\frac{1}{\rho}\nabla p + \boldsymbol{g}, \tag{2.2.2}$$

$$\frac{De}{Dt} = -\frac{p}{\rho}\nabla\cdot\boldsymbol{u}, \tag{2.2.3}$$

where ρ is the density, $\boldsymbol{u}$ is the velocity, p is the pressure tensor, $\boldsymbol{g}$ is the external body force per unit mass, e is the internal energy and $D/Dt = \partial/\partial t + \boldsymbol{u}\cdot$ denotes the material derivative following the motion. To close the system of equations formed by equations (2.2.1)–(2.2.2), a constitutive relation for the evaluation of the pressure must be given. Alternatively, the energy equation (2.2.3) can be also used to close the system. However, the most common method to calculate the pressure in SPH methods for fluids is by using an equation of state that relates the pressure to the density :

$$p = p(\rho). \tag{2.2.4}$$

The most used equation of state is the following :

$$p = \frac{c^2\rho^0}{\gamma}\left[\left(\frac{\rho}{\rho^0}\right)^\gamma - 1\right], \tag{2.2.5}$$

where γ is a constant exponent, c is the speed of sound in the medium and ρ^0 is the initial density. The value c in Eq. (2.2.5) can be chosen equal to the real speed of sound, but it is often convenient to choose c in a numerical simulation much lower than the physical value. This allows for larger time steps to be used in the numerical simulation, without affecting the result. This approach is known as the Weakly Compressible SPH formulation (WCSPH). It is not a truly incompressible approach since the density is allowed to vary because of the Lagrangian nature of the algorithm. This artificial compressibility has to be as weak as possible and is controlled by the speed of sound c. Universal guidelines to set a good value for c are not available. It is common to set a value and adjust it on a case by case basis. In this work, given a reference length L_{ref} and a reference speed U_{ref}, the following formula, adapted from [Morris 2000], was used :

$$c = \max\left(\frac{U_{\text{ref}}}{\sqrt{\Delta\rho}}, \sqrt{\frac{|\boldsymbol{g}|L_{\text{ref}}}{\Delta\rho}}, \sqrt{\frac{\mu U_{\text{ref}}}{\rho^0 L_{\text{ref}}\Delta\rho}}\right), \tag{2.2.6}$$

with $\Delta\rho = 0.01$ to enforce (not strictly) a maximum variation of 1% of the density field. Typically, choosing $\gamma = 7$ gives a fairly accurate physical model for the properties of water at a constant temperature. Note that setting $\gamma = 1$ reduces Eq. (2.2.5) to

$$p = c^2(\rho - \rho^0), \tag{2.2.7}$$

which is a well-known equation of state used in SPH.

2.2.1 Continuity Equation

The basis of any Lagrangian method for fluid dynamics calculations, such as SPH, is the solution of the equations of motion of a fluid particle along its trajectory. The time evolution of the density of a

particle a with density ρ_a, along its trajectory through a velocity field $\boldsymbol{u}_a$, follows from the conservation of mass described in Eq. (2.2.1) :

$$\frac{D\rho_a}{Dt} = -\rho_a \nabla \cdot \boldsymbol{u}_a. \tag{2.2.8}$$

There are two alternative approaches regarding the density calculation :

- Summation approach by using Eq. (2.0.1):

$$\rho_a = \sum_{b \in \Lambda_a} m_b w_{ab}. \tag{2.2.9}$$

- Evolution equation based on discretization of Eq. (2.1.48) :

$$\boxed{\frac{D\rho_a}{Dt} = \sum_{b \in \Lambda_a} m_b (\boldsymbol{u}_a - \boldsymbol{u}_b) \cdot \nabla_a w_{ab}.} \tag{2.2.10}$$

Eq. (2.2.10) does not require any time integration to know the density leading to more accurate estimations. This is a remarkable feature of SPH to propose an exact, time independent solution of the continuity equation. However, the advantage of using Eq. (2.2.10) is that it is an evolution equation that can be solved together with the equations of motion of each particle. Therefore, it is computationally more efficient than solving Eq. (2.2.9), for which an additional nearest-neighbor search is required. More importantly, Eq. (2.2.9) if used "as is" gives incorrect results for the density close to free surfaces (where only a limited number of neighboring particles are present). Recently, a time integrated version of Eq. (2.2.9) has been proposed in [Ferrand 2012] to remediate this issue so that it can be used to solve free surface problems. In consequence, Eq. (2.2.10) or the aforementioned variant of Eq. (2.2.9) are widely used to evaluate the density for the simulation of free surface flows [Monaghan 1994].

Note than any of the operators shown in Tab. 2.6 could also be used with its associated pros and cons. Similarly, applying equation (2.1.24) to the quantity ρ^k with $k \in \mathbb{N}$, we get a generalized version of equation (2.2.9):

$$\rho_a = \sum_{b \in \Lambda_a} m_b \left(\frac{\rho_b}{\rho_a}\right)^{k-1} w_{ab}. \tag{2.2.11}$$

Let us now show how fluxes considerations will lead to a condition on the kernel function. If we consider the continuity equation with volumes instead than densities[12] : $\frac{DV_a}{Dt} = V_a \nabla \cdot \boldsymbol{u}$, we can introduce the volume flux q^V_{ba} from particle b to particle a. Indeed, we can write:

$$\frac{DV_a}{Dt} = \sum_{b \in \Lambda_a} \underbrace{\frac{-m_b}{\rho_a^2} (\boldsymbol{u}_a - \boldsymbol{u}_b) \cdot \nabla_a w_{ab}}_{=q^V_{ba}}. \tag{2.2.12}$$

Let's consider the case where two aligned particles a and b are moving towards the same direction with $|\boldsymbol{u}_a| < |\boldsymbol{u}_b|$. Therefore, intuitively particle a will gain volume from particle b i.e. $q^V_{ba} > 0$ which implies :

$$q^V_{ba} = \frac{-m_b}{\rho_a^2} (\boldsymbol{u}_a - \boldsymbol{u}_b) \cdot \nabla_a w_{ab} = \underbrace{\frac{-m_b}{\rho_a^2} (\boldsymbol{u}_a - \boldsymbol{u}_b) \cdot \frac{\boldsymbol{x}_{ab}}{|\boldsymbol{x}_{ab}|}}_{<0} w'_{ab} > 0. \tag{2.2.13}$$

The above is true if $w'_{ab} < 0$ which corresponds to the monotonic decrease condition on the kernel function imposed in Sect. 1.1.1.3.

[12] We remind that because ρ is > 0 by definition, we have : $\frac{DV_a}{V_a} = -\frac{D\rho_a}{\rho_a}$.

2.2.2 Momentum and Energy Equations

The momentum conservation equation describes the acceleration of a fluid particle on the left-hand-side of Eq. (2.2.2) and the forces acting on the particle contained in the right-hand-side. The terms on the right hand side denote the pressure gradient and the acceleration of gravity. For a particle a, Eq. (2.2.2) becomes :

$$\frac{D\boldsymbol{u}_a}{Dt} = -\frac{1}{\rho_a}\nabla p_a + \boldsymbol{g}_a. \tag{2.2.14}$$

Using Eq. (2.1.46) to discretize the pressure gradient in Eq. (2.2.2), the following equation is obtained:

$$-\frac{\nabla p_a}{\rho_a} = \sum_{b\in\Lambda_a} \underbrace{-m_b\left(\frac{p_a}{\rho_a^2} + \frac{p_b}{\rho_b^2}\right)\nabla_a w_{ab}}_{=\boldsymbol{F}_{ab}/m_a}, \tag{2.2.15}$$

where $\boldsymbol{F}_{ab}$ is the internal force from particle b to particle a. The reason of the use of the alternate operators of type "∇_k^+" to discretize this equation is now observable. Indeed, thanks to the odd nature the kernel gradient:

$$\boldsymbol{F}_{ab} = -m_a m_b\left(\frac{p_a}{\rho_a^2} + \frac{p_b}{\rho_b^2}\right)\nabla_a w_{ab} = -\boldsymbol{F}_{ba}. \tag{2.2.16}$$

This is Newton's third law which ensures conservation of the total momentum of an isolated system. The form of Eq. (2.2.15) can be disturbing for two reasons. First, one might have expected a pressure difference between p_a and p_b to calculate a pressure gradient, but instead one finds an addition of p_a and p_b. Second, the right-hand side of Eq. (2.2.15) can be non-zero even if the pressure is uniform throughout the domain (this is sometimes called the E_0 error). To make this happen, it is sufficient that there are fluctuations in the density: if there is a gradient in the density, then the contribution of a particle b is not compensated by another particle and there will be a resulting net force on the particle a. This is often called a "spurious force", because it is not rooted in any physical pressure gradient but rather in a non-uniform distribution of particles in the SPH simulation. It is precisely the "spurious force" that induces a redistribution of particles. This eventually leads to a more uniform particle distribution as it tends to smear out gradients in the particle density. One of the implications of this "intrinsic remeshing" is that not all initial conditions represent stable configurations for the particles. Eq. (2.2.15) has the property that it provides perfect linear and angular momentum conservation in a simulation in the absence of any dissipation forces.

In the end, the discretized momentum equation for a particle a is obtained by adding the gravity term $\boldsymbol{g}_a = -g\boldsymbol{e}_z$[13] to Eq. (2.2.15) :

$$\boxed{\frac{D\boldsymbol{u}_a}{Dt} = -\sum_{b\in\Lambda_a} m_b\left(\frac{p_a}{\rho_a^2} + \frac{p_b}{\rho_b^2}\right)\nabla_a w_{ab} + \boldsymbol{g}.} \tag{2.2.17}$$

The energy equation (2.2.3) for a particle a is :

$$\frac{De_a}{Dt} = -\frac{p_a}{\rho_a}\nabla\cdot\boldsymbol{u}_a. \tag{2.2.18}$$

We remind that this equation can replace the equation of state to close the system (2.2.1)–(2.2.2). Concerning the discretization of the above equation, it follows the exact same procedure as for the momen-

[13] This can be naturally extended to add any kind of body force to the simulation

tum equation. We get :

$$\boxed{\frac{De_a}{Dt} = -p_a \sum_{b\in\Lambda_a} m_b \left(\frac{\boldsymbol{u}_a}{\rho_a^2} + \frac{\boldsymbol{u}_b}{\rho_b^2}\right) \cdot \nabla_a w_{ab}.} \tag{2.2.19}$$

A common alternative form with convenient symmetry properties can be found through some algebra [Violeau 2012] :

$$\frac{De_a}{Dt} = \frac{1}{2} \sum_{b\in\Lambda_a} m_b \frac{p_a + p_b}{\rho_a \rho_b} (\boldsymbol{u}_a - \boldsymbol{u}_b) \cdot \nabla_a w_{ab}.$$

2.2.3 Alternative Lagrangian derivation of the SPH approximation

It is possible to obtain the discretized SPH fluid equations of the previous section using variationnal principles based on the Lagrangian of a system of particles without going through the continuous Euler equations. This approach was introduced in [Bonet 1999a, Bonet 2004, Oger 2007]. This document does not intend to re-introduce the Lagrangian and Hamiltonian equations so that the basic formulations will be admitted. One can find an extensive presentation of these concepts in the context of fluids mechanics in [Violeau 2012]. Let's just remind that the Lagrangian and the Hamiltonian directly derive from the least action principle and that one can obtain the laws of mechanics from Lagrangian and/or Hamiltonian considerations. The Lagrangian L of a particle system is the difference between the kinetic energy of the system and the potential energy of the system and is given by :

$$L = \sum_b \frac{1}{2} m_b \boldsymbol{u}_b^2 - \sum_b m_b e_b - \sum_b m_b g z_b. \tag{2.2.20}$$

The Hamiltonian H of a particle system is the sum between the kinetic energy of the system and the potential energy of the system and is given by :

$$H = \sum_b \frac{1}{2} m_b \boldsymbol{u}_b^2 + \sum_b m_b e_b + \sum_b m_b g z_b. \tag{2.2.21}$$

All the following calculations will be based on the Lagrangian but it is possible to reach the same conclusion with the Hamiltonian, see [Bonet 2005] for more details. The discrete equations of motion of each particle are provided by the Lagrange equations :

$$\frac{D}{Dt}\frac{\partial L}{\partial \boldsymbol{u}_a} = \frac{\partial L}{\partial \boldsymbol{x}_a}. \tag{2.2.22}$$

The potential energy does not depend on $\boldsymbol{u}_a$ so that we have :

$$\frac{\partial L}{\partial \boldsymbol{u}_a} = m_a \boldsymbol{u}_a. \tag{2.2.23}$$

The right hand side of equation (2.2.22) can also be evaluated :

$$\begin{aligned}
\frac{\partial L}{\partial \boldsymbol{x}_a} &= -\sum_b m_b \frac{\partial e_b}{\partial \boldsymbol{x}_a} - \sum_b m_b g \frac{\partial z_b}{\partial \boldsymbol{x}_a}, \\
&= -\sum_b m_b \underbrace{\frac{\partial e_b}{\partial \rho_b}}_{=\frac{p_b}{\rho_b^2} \text{ combining Eqs. (2.2.8) and (2.2.18)}} \frac{\partial \rho_b}{\partial \boldsymbol{x}_a} - \sum_b m_b g \delta_{ab} \boldsymbol{e}_z, \\
&= -\sum_b m_b \frac{p_b}{\rho_b^2} \frac{\partial \rho_b}{\partial \boldsymbol{x}_a} - m_a \boldsymbol{g}.
\end{aligned} \tag{2.2.24}$$

Using Eq. (2.2.11), we can compute the partial derivative of the density with respect to the position :

$$\frac{\partial \rho_b}{\partial \boldsymbol{x}_a} = m_a \left(\frac{\rho_a}{\rho_b}\right)^{k-1} \nabla_a w_{ab} + \delta_{ab} \sum_c m_c \left(\frac{\rho_c}{\rho_a}\right)^{k-1} \nabla_a w_{ac}. \tag{2.2.25}$$

Inserting Eq. (2.2.25) into Eq. (2.2.24), we obtain :

$$\frac{\partial L}{\partial \boldsymbol{x}_a} = -\sum_b m_a m_b \frac{\rho_a^{k-1} p_b}{\rho_b^{k-1}} \nabla_a w_{ab} - \underbrace{\sum_{b,c} m_b m_c \frac{p_b}{\rho_b^2} \left(\frac{\rho_c}{\rho_a}\right)^{k-1} \delta_{ab} \nabla_a w_{ac}}_{=\sum_b m_a m_b \frac{\rho_b^{k-1} p_a}{\rho_a^{k-1}}} \nabla_a w_{ab} + m_a \boldsymbol{g}. \tag{2.2.26}$$

Finally, the Lagrange equations (2.2.22) become:

$$\boxed{\frac{D\boldsymbol{u}_a}{Dt} = -\sum_{b \in \Lambda_a} m_b \frac{\rho_b^{2k} p_a + \rho_a^{2k} p_b}{(\rho_a \rho_b)^{k+1}} \nabla_a w_{ab} + \boldsymbol{g}.} \tag{2.2.27}$$

If we set $k = 1$, Eq. (2.2.11) becomes Eq. (2.2.9) and the above equation is equivalent to Eq. (2.2.17). Moreover, deriving (2.2.11) with respect to time and using $\frac{De_a}{Dt} = \frac{p_b}{\rho_b^2}\frac{D\rho_a}{Dt}$, we can recover the discretized energy equation. Thus, we have obtained the discretized SPH Euler equations from Lagrangian considerations using operator defined in (2.2.9) for the density and (2.2.17).

Instead of considering (2.2.9) to evaluate the density, let's use the "$\nabla_k^+ \cdot \rho_a$" operator from Tab. 2.6 to discretize the continuity equation. It gives:

$$\frac{D\rho_b}{Dt} = \frac{1}{\rho_b^{2k-2}} \sum_c m_c (\rho_b \rho_c)^{k-1} (\boldsymbol{u}_b - \boldsymbol{u}_c) \cdot \nabla_b w_{bc}, \tag{2.2.28}$$

$$D\rho_b = \frac{1}{\rho_b^{2k-2}} \sum_c m_c (\rho_b \rho_c)^{k-1} (\boldsymbol{u}_b - \boldsymbol{u}_c) Dt \cdot \nabla_b w_{bc}, \tag{2.2.29}$$

$$D\rho_b = \frac{1}{\rho_b^{2k-2}} \sum_c m_c (\rho_b \rho_c)^{k-1} (D\boldsymbol{x}_b - D\boldsymbol{x}_c) \cdot \nabla_b w_{bc}, \tag{2.2.30}$$

$$D\rho_b = \sum_a \frac{1}{\rho_b^{2k-2}} \sum_c m_c (\rho_b \rho_c)^{k-1} (\delta_{ab} - \delta_{ac}) \nabla_b w_{bc} \cdot D\boldsymbol{x}_a. \tag{2.2.31}$$

On the other hand, by definition of the differential, we do have : $D\rho_b = \sum_a \frac{\partial \rho_b}{\partial \boldsymbol{x}_a} \cdot D\boldsymbol{x}_a$. Thus, a term-wise association leads to :

$$\frac{\partial \rho_b}{\partial \boldsymbol{x}_a} = \frac{1}{\rho_b^{2k-2}} \sum_c m_c (\rho_b \rho_c)^{k-1} (\delta_{ab} - \delta_{ac}) \nabla_b w_{bc}. \tag{2.2.32}$$

Inserting Eq. (2.2.32) into Eq. (2.2.24), we obtain :

$$\frac{\partial L}{\partial \boldsymbol{x}_a} = -\sum_{b,c} m_b m_c \frac{p_b}{\rho_b^{2k}} (\rho_b \rho_c)^{k-1} (\delta_{ab} - \delta_{ac}) \nabla_b w_{bc} - m_a \boldsymbol{g}, \tag{2.2.33}$$

$$= \sum_b m_a m_b \frac{p_b}{\rho_b^{2k}} (\rho_a \rho_b)^{k-1} \nabla_b w_{ba} - \sum_c m_a m_c \frac{p_a}{\rho_a^{2k}} (\rho_a \rho_c)^{k-1} \nabla_a w_{ac}, \tag{2.2.34}$$

$$= -\sum_b m_a m_b \frac{p_b}{\rho_b^{2k}} (\rho_a \rho_b)^{k-1} \nabla_b w_{ab} - \sum_b m_a m_b \frac{p_a}{\rho_a^{2k}} (\rho_a \rho_b)^{k-1} \nabla_a w_{ab}, \tag{2.2.35}$$

$$= -\sum_b m_a m_b \frac{p_a \rho_b^{2k} + p_b \rho_a^{2k}}{(\rho_a \rho_c)^{k+1}} \nabla_b w_{ab}. \tag{2.2.36}$$

If we insert the above equation into Eq. (2.2.22), we get Eq. (2.2.27) again. If we set $k = 1$, Eq. (2.2.28) becomes Eq. (2.2.10) and the above equation is equivalent to Eq. (2.2.17).

Another way to obtain the same result while highlighting the important of the skew-adjointness of the gradient and divergence operators is presented hereafter. The continuity equation can be discretized as follows :

$$\frac{D\rho_a}{Dt} = -\rho_a \nabla_k^- \cdot \boldsymbol{u}_a. \tag{2.2.37}$$

Multiplying by Dt on both sides, we get:

$$D\rho_b = -\rho_b \nabla_k^- \cdot D\boldsymbol{x}_b. \tag{2.2.38}$$

In the case of an isolated system of particle, total energy is conserved i.e. $DE_{tot} = DE_{int} + \boldsymbol{F}_{int} \cdot D\boldsymbol{x} = 0$. Expanding the terms into summations over particles, we get :

$$\sum_{a,b} m_b \frac{\partial e_b}{\partial \boldsymbol{x}_a} \cdot D\boldsymbol{x}_a + \sum_a F_{a,int} \cdot D\boldsymbol{x}_a = 0. \tag{2.2.39}$$

Once again combining Eqs. (2.2.8) and (2.2.18), we can write :

$$\begin{aligned}
\sum_a F_{a,int} \cdot D\boldsymbol{x}_a &= -\sum_{a,b} m_b \frac{p_b}{\rho_b^2} \frac{\partial \rho_b}{\partial \boldsymbol{x}_a} \cdot D\boldsymbol{x}_a, && (2.2.40)\\
&= -\sum_b \frac{m_b}{\rho_b} \frac{p_b}{\rho_b} D\rho_b, && (2.2.41)\\
&= \sum_b \frac{m_b}{\rho_b} p_b \nabla_k^- \cdot D\boldsymbol{x}_b, && (2.2.42)\\
&\underset{\text{(discrete scalar product (2.1.44))}}{=} \langle \hat{p}_a \cdot (\nabla_k^- \,,\, D\boldsymbol{x}_a) \rangle, && (2.2.43)\\
&\underset{\text{(Eq. (2.1.50))}}{=} -\langle (\nabla_k^+ \hat{p}_a) \,,\, D\boldsymbol{x}_a \rangle. && (2.2.44)
\end{aligned}$$

All in all, we have $\forall D\boldsymbol{x}_a$ (using the discrete scalar product definition on the left hand side of the above equation) :

$$\langle (\frac{\rho_a}{m_a} F_{a,int}) \,,\, D\boldsymbol{x}_a \rangle = -\langle (\nabla_k^+ \hat{p}_a) \,,\, D\boldsymbol{x}_a \rangle. \tag{2.2.45}$$

Therefore, we can write :

$$\underbrace{\frac{F_{a,int}}{m_a}}_{=\frac{D\boldsymbol{u}_a}{Dt}} = -\frac{\nabla_k^+ \hat{p}_a}{\rho_a}. \tag{2.2.46}$$

We recover Eq. (2.2.27). As suggested in [Violeau 2012], the skew-adjointness property ensures that operators are "compatible" in the SPH sense.

To conclude, the fact that SPH equations of motion directly derive from the Lagrangian and therefore from the least action principle **enforces** the conservation of the total momentum of an isolated system. This property has been verified in theory by several authors. Moreover, because the Lagrangian is isotropic and time-invariant, linear momentum, angular momentum and energy are also conserved (moreover, the formal calculations to verify the energy conservation uses once again the skew-adjointness property of the "compatible" operators). These conservation properties are only guaranteed if the SPH operators are "compatible" in the SPH sense and if time is considered continuous. The time discretization scheme has to chosen carefully to maintain these conservation properties.

2.3 Key features

The basic SPH formulation of the Euler equations for a given particle a is the combination of equations (2.0.1), (2.2.17) and (2.2.7) :

$$\begin{cases} \rho_a = \sum_{b \in \Lambda_a} m_b w_{ab}, \\ \dfrac{D\boldsymbol{u}_a}{Dt} = \sum_{b \in \Lambda_a} m_b \left(\dfrac{p_a}{\rho_a^2} + \dfrac{p_b}{\rho_b^2} \right) \nabla_a w_{ab} + \boldsymbol{g}, \\ p_a = c^2(\rho_a - \rho_0). \end{cases} \tag{2.3.1}$$

This set of equations is generally referred as the Weakly-Compressible SPH. Note that we have dropped the energy Eq. (2.2.3) since it is not coupled with the two others. This discretization contains the main properties of SPH [Price 2011]. These are :

1. Exact, time-independent, solution of the continuity equation (unless Eq. (2.2.10) is used)
2. Advection is computed exactly, thanks to the Lagrangian formulation of SPH. The advection term is difficult to compute for Eulerian grid-based methods, so this a major plus for SPH.
3. Zero intrinsic numerical dissipation : Unless explicit dissipation terms are added, the method will not dissipate or diffuse energy artificially (this is actually a direct consequence of point 2.). However, for some problems, dissipation terms are needed (shock problems). The user has full control on the amount of dissipation added to the method.
4. Exact conservation of mass, momentum, angular momentum, energy and entropy : Thanks to the nature of SPH (Lagrangian based, invariance to translations and rotations, Hamiltonian system), these quantities are exactly conserved. Compared to Eulerian meshbased methods where for example angular momentum conservation depends on the mesh, this is an important advantage.
5. Guaranteed minimum energy state for the particles : The minimum energy state in SPH can be demonstrated from its Hamiltonian formulation. A simple example of that is the natural relaxation of randomly placed SPH particles. In other words, SPH has an intrinsic automatic remeshing feature. This is the reason why SPH maintains a reasonably ordered particle distribution through the simulation. Some alternative particle methods prefer to focus on exact derivative evaluation rather than quantity conservation and therefore generate disordered particle distribution (requiring expensive reordering procedures). It is not the case in SPH.
6. Resolution that follows mass : In SPH, the resolution is automatically adjusted to be higher where the mass is. This is due to the fixed mass discretization. Computational effort is naturally focused in dense areas.

On the other hand, the main drawbacks of SPH can be summarized as follows :

1. Non-local algorithm : SPH suffers from a non-local algorithm which rests on a NNS at every timestep. This makes the method slow and possibly cumbersome to implement.
2. Boundary Conditions : Because of the nature of the SPH method (meshless, Lagrangian), it not as easy and natural as in other methods (meshbased in particularity) to impose boundary conditions of any kind. It is partly due to the lack of a Kronecker delta property and also to the neglect of the boundary integral in Eq. (2.1.13).
3. Order of convergence : The theoretical analysis of SPH consistency and error behavior is complex [Mas-Gallic 1987, Moussa 2000, Lanson 2001, Fatehi 2011] and still under investigation [Zisis 2016, Sigalotti 2016, Franz 2018] but in practical applications, the observed order of convergence is ≈ 1.
4. Weak AMR abilities : Adaptative Mesh Refinement (AMR) is commonly used in meshbased methods to reduce the computational cost by concentrating resources on the areas of interest. Several

attempts have been proposed for SPH in the literature but it remains a complex issue that is still under investigation.

5. Explicit : SPH is an explicit method based on the CFL condition. It implies small timesteps so it is not recommended for long runs. For more information on the time integration in SPH, see Sect. sec:integration
6. Stabilization needed : SPH is a method that needs stabilization to be able to simulate real test cases. Therefore using one of the existing stabilization techniques (see Sect. 2.4) causes the end of the energy conservation.

In a nutshell, SPH is a method suitable for problems involving free surfaces, complex interfaces, fluid structure interaction and multi-physics. To conclude this section, the simplest SPH algorithm is shown in Algorithm 1.

Algorithm 1 The Smoothed Particle Hydrodynamics algorithm

```
for t ← t + Δt do
    for all particles a do
        ρ_a ← 0
        for all particles b do
            if |x_a − y_b| < κh then                    ▷ Nearest neighbor search
                ρ_a ← ρ_a + m_b w_ab                    ▷ Eq. (2.0.1)
            end if
        end for
    end for
    for all particles a do
        du_a/dt ← 0
        p_a = c_s^2(ρ_a − ρ_0)                          ▷ Eq. (2.2.7)
        for all particles b do
            if |x_a − y_b| < κh then                    ▷ Nearest neighbor search
                du_a/dt ← du_a/dt + m_b (p_a/ρ_a^2 + p_b/ρ_b^2) ∇_a w_ab   ▷ Eq. (2.2.17)
            end if
        end for
    end for
    for all particles a do                              ▷ Time integration
        u_a^{t+Δt} = u_a^t + Δt du_a/dt
        x_a^{t+Δt} = x_a^t + Δt u_a^t
    end for
end for
```

2.4 Stabilization procedures

2.4.1 Artificial viscosity

It is very common to add a numerical dissipation term in a numerical method. It is useful to treat shock problems or to make the simulated fluid viscous. This artificial viscosity term can be used as a way to stabilize simulations since it removes the nonphysical phenomenon of particle penetration and due to its dissipative nature it can be used to improve the numerical stability of the simulation. The artificial viscosity term [Monaghan 1992, Monaghan 1997] consists of a linear term proportional

to a dimensionless parameter $\alpha_{\Pi ab}$ to treat discontinuities [Monaghan 1985] and a quadratic term proportional to the dimensionless parameter $\beta_{\Pi ab}$ to prevent particle inter penetration [Lattanzio 1986]. We denote the term here by $\boldsymbol{f}_{a,\text{artificial}}$, which can act as the SPH discretization of the viscosity term in order to stabilize the SPH simulation:

$$\boldsymbol{f}_{a,\text{artificial}} = \sum_{b\in\Lambda_a} m_b \Pi_{ab} \nabla_a w_{ab}, \tag{2.4.1}$$

where Π_{ab} is given by

$$\Pi_{ab} = \begin{cases} \frac{-\alpha_{\Pi ab}\mu_{ab}\bar{c}_{ab}+\beta_{\Pi ab}\mu_{ab}^2}{\bar{\rho}_{ab}} & \boldsymbol{u}_{ab}\cdot\boldsymbol{x}_{ab} < 0, \\ 0 & \boldsymbol{u}_{ab}\cdot\boldsymbol{x}_{ab} \geq 0, \end{cases} \tag{2.4.2}$$

where

$$\mu_{ab} = \frac{h\boldsymbol{u}_{ab}\cdot\boldsymbol{x}_{ab}}{|\boldsymbol{x}_{ab}|^2 + 0.01h^2}, \tag{2.4.3}$$

and $\bar{c}_{ab} = \frac{1}{2}(c_a + c_b)$, $\bar{\rho}_{ab} = \frac{1}{2}(\rho_a + \rho_b)$, $\boldsymbol{u}_{ab} = \boldsymbol{u}_a - \boldsymbol{u}_b$, $\boldsymbol{x}_{ab} = \boldsymbol{x}_a - \boldsymbol{x}_b$, $\alpha_{\Pi ab} = \frac{1}{2}(\alpha_{\Pi a} + \alpha_{\Pi b})$ and $\beta_{\Pi ab} = \frac{1}{2}(\beta_{\Pi a} + \beta_{\Pi b})$. c_a denotes the speed of sound at particle a.

Unlike in Eulerian methods, SPH does not have any kind of numerical dissipation or diffusion so the artificial viscosity term can be related to their physical meaning . $\alpha_{\Pi ab}$ and $\beta_{\Pi ab}$ can be linked with the bulk and shear viscosity of the Navier-Stokes equations [Murray 1996, Lodato 2010]. In conclusion, $\alpha_{\Pi ab}$ and $\beta_{\Pi ab}$ are not empirical parameters to discover but are set by the choice of fluid. For information, the shear viscosity is $\nu = \frac{1}{10}\alpha_{\Pi ab}c_s h$ and the bulk viscosity is $\mu = \frac{5}{3}\nu$.

If one wants to add just the right amount of dissipation at shocks or discontinuities while removing the impact of the extra term elsewhere, it is recommended to use a switch. The most famous ones are the so-called Balsara switch [Balsara 1995], the Morris & Monaghan switch [Morris 1997b] and the more recent Cullen & Dehnen switch [Cullen 2010].

The full momentum equation with artificial viscosity is given by :

$$\frac{D\boldsymbol{u}_a}{Dt} = -\sum_{b\in\Lambda_a} m_b \left(\frac{p_a}{\rho_a^2} + \frac{p_b}{\rho_b^2} + \Pi_{ab}\right) \nabla_a w_{ab} + \boldsymbol{g}. \tag{2.4.4}$$

It has to be mentioned that other viscosity models exist within the SPH community. The two main approaches were developed respectively in [Monaghan 2006] and in [Morris 1997a]. The first one relies on the local compression and expansion of the particle field whereas the second one is based on a two-particles shear force. These two models were introduced after the original artificial viscosity model and are derived from it. Other approaches to add dissipation in the SPH method also include Gudonov-SPH schemes (exact Riemann solvers) or Riemann-SPH schemes (approximate Riemann solvers) which are theoretically better for accuracy and viscosity control but that add a significant computational overhead [Inutsuka 2002].

To conclude, recent studies [Agertz 2007, Price 2008] have proven that if one works with non isothermal flows (and therefore includes an energy or temperature equation in the governing equations), an artificial thermal conductivity term is needed to properly capture the behavior of the flow (especially with contact discontinuities).

2.4.2 Physical viscosity

If the considered fluid problem involves a viscosity term $\frac{1}{\rho}\nabla\cdot\boldsymbol{\tau}$ in Eq. (2.2.2) (with $\boldsymbol{\tau}$ viscous stress tensor), it is possible to discretize it in the SPH framework and to make it contribute to the stabilization

of the SPH model by physically dissipating energy. Since, the viscosity term involves a second order derivative, one could be tempted to use second order SPH interpolants mentioned in Footnote [??] but this leads to errors especially at low resolution. Instead, it is more common to use the approach suggested in [Morris 1997a]. Note that, in the case of an incompressible fluid with a constant viscosity, the viscous term reduces to $\frac{1}{\rho}\nabla\cdot\boldsymbol{\tau} = \frac{\mu}{\rho}\nabla^2\boldsymbol{u} = \nu\nabla^2\boldsymbol{u}$ with μ the fluid viscosity and $\nu = \frac{\mu}{\rho}$ the kinematic viscosity. It reads :

$$\nu_a\nabla^2\boldsymbol{u}_a = \sum_{b\in\Lambda_a}\frac{m_b(\mu_a+\mu_b)}{\rho_a\rho_b}\frac{\boldsymbol{x}_{ab}\cdot\nabla_a w_{ab}}{|\boldsymbol{x}_{ab}|^2+\eta^2}\boldsymbol{u}_{ab}, \tag{2.4.5}$$

where $\eta = 0.01h$ is a safety factor to avoid a division by zero. If adding a physical viscosity is relevant, this term can be enough to stabilize the SPH simulation depending on the context.

2.4.3 Tensile instability

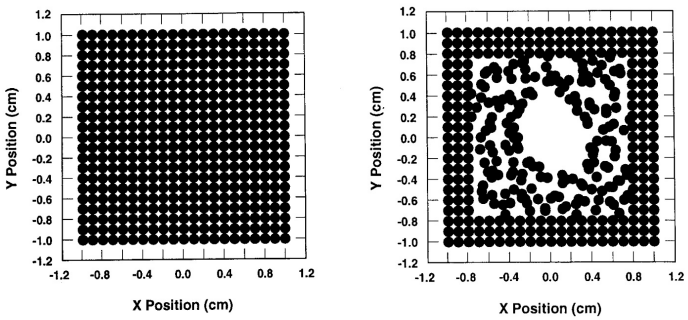

(a) Initial particle positions (b) Particle positions at $100\mu s$

Figure 2.7: The tensile instability phenomena after a velocity perturbation generating tensile stresses in the medium (from [Swegle 1995])

The tensile instability phenomena in the SPH method is an inherent instability of the original SPH method. It causes particles to clump together in a way that could resemble cracks or fracture but that is in fact a numerical artifact. Tensile instability was a limitation of the SPH method when it was introduced. Since then, it has been heavily studied in the literature, most notably in [Swegle 1995], see Fig. 2.7. It shows that this instability only happens under tension. In the case of fluids, it is due to negative pressures generated in the flow. This induces clumping of particles that leads to an nonphysical cavitation with generation of voids. It is connected to the "intrinsic remeshing" property of SPH. Indeed, it is a disadvantage of using a pressure term to regularize the particle distribution. There are several major corrections used to remove this instability.

1. introduce a background pressure p_0 in Eq. (2.2.4) : $p = p(\rho)+p_0$ [Phillips 1985]. p_0 is chosen as the minimum value to obtain non-negative pressure all over the domain. Inspired from [Morris 2000], we recommend the following value

$$p_0 = C\frac{c^2\rho_0}{\gamma}, \tag{2.4.6}$$

where $C \in [0,1]$ is a constant that has to be adjusted on a case by case basis. Some authors recommend $C = 0.1$ but we were not able to obtain stable simulations with such low values for all the cases considered in this work. The background pressure helps stabilizing the simulations but can lead to pressure noises if set too high [Violeau 2014]. In this work, we have not done

an exhaustive sensitivity study and used the expression given in (2.4.6). It might be possible to adjust more carefully the background pressure for each case to attenuate pressure oscillations.

2. use a more accurate but non-conservative gradient estimate [Morris 1996].
3. introduce an artificial repulsive force to prevent the clumping, this approach is generally used for solids and described in [Monaghan 2000]. In a nutshell, it consists of adding a term $(\boldsymbol{R}_{\varepsilon a}+\boldsymbol{R}_{\varepsilon b})f_{ab}^{n}$ in the momentum equation where $\boldsymbol{R}_{\varepsilon a} = -\varepsilon\frac{|p_a|}{\rho_a}$ if $p_a < 0$ (0 otherwise) and $f_{ab} = \frac{w_{ab}}{w(\Delta d,h)}$ (with $n = 4$ and $\varepsilon = 0.2$ for example).
4. subtract the nonphysical source term [Borve 2001].

There is another corrective term that can be added to reduce the impact of the tensile instability and to smooth the particle distribution. It is the so-called XSPH correction. However, it tends to be less and less used as its relevance is questioned. It forces particles to experience an averaged velocity. A detailed analysis of the impact of the variation of these parameters on the quality of the results in SPH for solids is given in [Das 2015].

2.4.4 Pairing Instability

During SPH simulations, it appears that even in the absence of tensile instability, particles tend to pair together in an non physical way. The pairing instability (sometimes called particle clumping) is often mixed with the tensile instability although they have different origins. In the literature, it was originally claimed that it is due to a change of sign in the the first and second derivatives of the kernel. However, recent investigations tend to show that the pairing instability is solely due to the sign of the kernel Fourier transform [Robinson 2009, Dehnen 2012]. Thus, the use of Wendland kernel functions whose Fourier transforms do not change sign is a natural way to fix the issue.

2.4.5 Alternative formulations

Many researchers have developed their own SPH scheme with more or less success. It is impossible to do a full review of all this alternative techniques and corrective terms. Among all of them, some have reached a certain impact in the SPH community, especially the ones that aim to smooth the pressure fields. We will only mention the most commonly used approaches hereafter :

1. Restoring the consistency up to a certain order
   SPH cannot even reproduce constant functions exactly. Therefore many authors proposed to modify the kernel in order to restore consistency up to a given order. It is sometimes called Corrected SPH (CSPH). For example, to restore 0th order consistency, one should use a Shepard filter where the density estimator is modified as :

$$\rho_a = \sum_{b\in\Lambda_a} m_b \hat{w}_{ab}, \tag{2.4.7}$$

   with $\hat{w}_{ab} = w_{ab}/\sum_{b\in\Lambda_a}\frac{m_b}{\rho_b}w_{ab}$. An example of restored consistency of order 0 in SPH using Shepard filters is presented on Fig. 2.8. For higher orders, one need to use a Moving Least Squares interpolation (MLSPH) but it is more computational expensive as it involves a matrix inversion [Bonet 1999b, Colagrossi 2001]. For order 1 and for a given particle a, it reads

$$\widetilde{\nabla w}_{ab} = \boldsymbol{L}_a \nabla w_{ab}, \tag{2.4.8}$$

   where $\boldsymbol{L}_a = \left(\sum_{b\in\Lambda_a}\frac{m_a}{\rho_a}\nabla w_{ab}\otimes(\boldsymbol{x}_b-\boldsymbol{x}_a)\right)^{-1}$. Examples of restored consistency of order 1 and 2 are shown on Fig. 2.9.

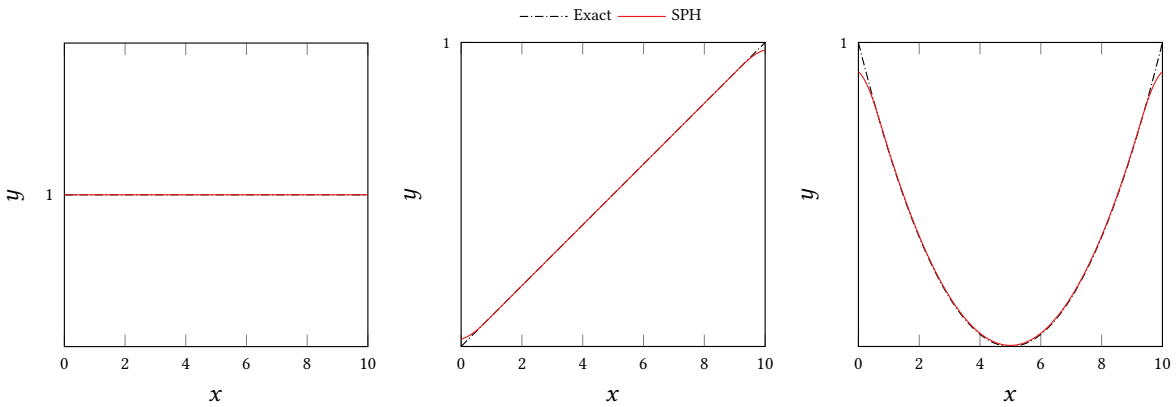

(a) Constant function (b) Linear function (c) Quadratic function

Figure 2.8: Restoring SPH Consistency to order 0. (CSPH, Shepard filter, Cubic Spline kernel, $\Delta p = 0.01$, $h = 10$)

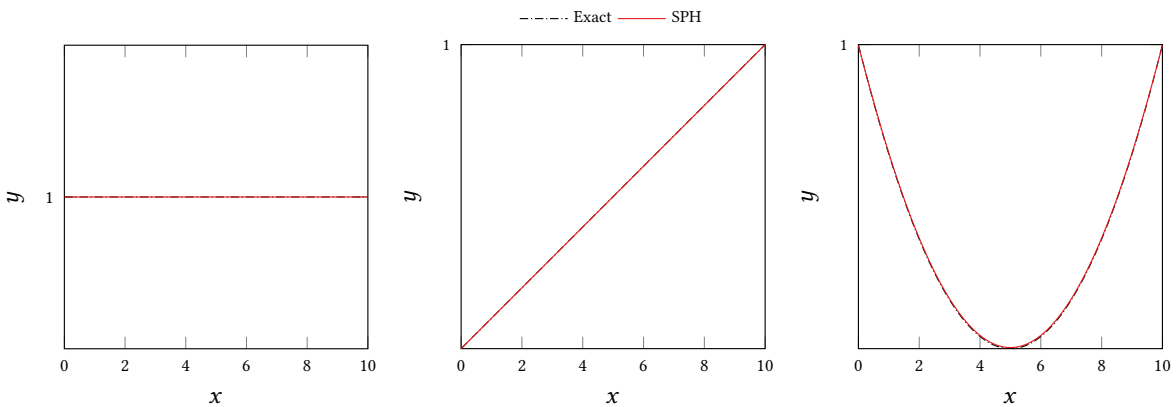

(a) Constant function (Order 1) (b) Linear function (Order 1) (c) Quadratic function (Order 1)

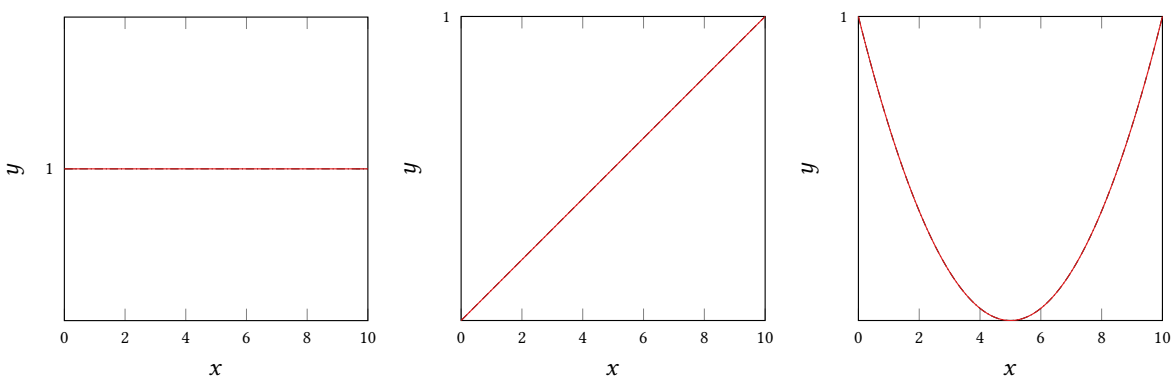

(d) Constant function (Order 2) (e) Linear function (Order 2) (f) Quadratic function (Order 2)

Figure 2.9: Restoring SPH Consistency to order 1 (top) and 2 (bottom) (MLSPH, Cubic Spline kernel, $\Delta p = 0.01$, $h = 10$)

2. Particle shifting
   Introduced in [Xu 2009, Lind 2012, Mokos 2016], this method is used to maintain a good particles distribution. At the end of every timestep, all particles are shifted by a well-chosen distance from their original position to reduce the particles anisotropy. The most advanced version of shifting (within the δ-SPH framework) has been proposed in [Sun 2019]. See Sect. 2.7.3 for more details.
3. Adding a density diffusion term in the continuity equation (δ-SPH)
   This technique is called δ-SPH [Molteni 2009, Marrone 2011, Antuono 2012] and it consists in adding a carefully designed density diffusion terms in the continuity and momentum equations in order to smooth the density variation and therefore the pressure field. This diffusion terms, that we will denote Δ^1_{SPH} and Δ^2_{SPH}, are added to Eq. (2.2.10) and Eq. (2.2.17) respectively and are defined as follows :
   $$\Delta^1_{SPH} = \delta hc \sum_{b\in\Lambda_a} \frac{m_b}{\rho_b} \psi_{ab} \cdot \nabla w_{ab} \tag{2.4.9}$$
   $$\Delta^2_{SPH} = \alpha hc\rho_0 \sum_{b\in\Lambda_a} \frac{m_b}{\rho_b} \pi_{ab} \nabla w_{ab} \tag{2.4.10}$$
   with δ a free parameter that gives this approach its name and that is always set to 0.1, α a free parameter generally set to 0.02 and :
   $$\psi_{ab} = 2(\rho_b - \rho_a)\frac{\boldsymbol{x}_{ab}}{|\boldsymbol{x}_{ab}|^2} - \left(\Delta^L\rho_a + \Delta^L\rho_b\right) \tag{2.4.11}$$
   $$\pi_{ab} = \frac{\boldsymbol{u}_{ab} \cdot \boldsymbol{x}_{ab}}{|\boldsymbol{x}_{ab}|^2} \tag{2.4.12}$$
   where $\Delta^L\rho_a = \sum_{b\in\Lambda_a} \frac{m_b}{\rho_b}(\rho_b - \rho_a)\boldsymbol{L}_a \nabla w_{ab}$ and $\boldsymbol{L}_a = \left(\sum_{b\in\Lambda_a} \frac{m_a}{\rho_a} \nabla w_{ab} \otimes (\boldsymbol{x}_b - \boldsymbol{x}_a)\right)^{-1}$.
   This technique had a lot of success in the SPH community thanks to its simplicity and efficiency and is about to become a standard for single phase flow simulations. For multiphase flows, it is still under investigation but recent progresses have been made [Hammani 2018].
4. Using Riemann solvers (eventually coupled with an ALE framework)
   This approach has been developed in [Vila 1999]. It consists in replacing the classic particle interactions with individual Riemann problems between each pair. In the same paper [Vila 1999], the use of an Arbitrary Lagrangian Eulerian formulation (SPH-ALE) has also been suggested and has been used for some applications [Marongiu 2010, Renaut 2015, Oger 2016, Hermange 2017] with success.
5. Development of an incompressible SPH method (ISPH)
   Originally proposed in [Cummins 1999], this method has been followed and extended by many researchers [Hu 2007, Lind 2012]. It is based on a projection method to ensure the incompressiblity. Please refer to [Violeau 2012] for more details.

Other extensions of SPH include turbulence models [Violeau 2007a, Violeau 2012], total Lagrangian formulation for large deformations [Vidal 2007] and multiphase SPH which is the topic of the next section. Beyond fluid mechanics, SPH formulations are available for other systems of PDEs (magnetohydrodynamics, shallow water equations or solid mechanics to name a few).

2.5 Boundary conditions

Because SPH is a collocation method, the treatment of boundary conditions is far from being trivial and is an active area of research within the community. The SPH European Research Interest Community (SPHERIC) even made this topic one of its Grand Challenges for the development of the SPH method (`http://spheric-sph.org`).

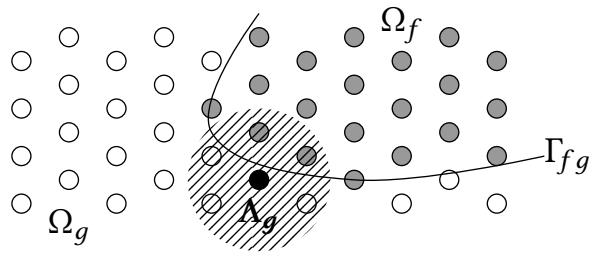

Figure 2.10: Schematic of a ghost particle g (in black) and its associated support domain Λ_g (hatched area) intersecting with the fluid domain Ω_f (gray particles) and the ghost domain Ω_g (white particles) separated by Γ_{fg}.

Originally, in order to impose wall Boundary Conditions (BC), repulsive forces based on the Lennard-Jones potential were used [Monaghan 2005]. However, it was shown in [Ferrand 2012] that it induces strong spurious behaviors near the boundaries. Today, most models are imposing wall BC through the use of ghost particles or mirror particles [Morris 1997a, Colagrossi 2003, Oger 2006, Yildiz 2009]. Recently, a new approach using semi-analytical BC was introduced in [Ferrand 2012, Leroy 2014, Ferrand 2017, Chiron 2017] for both wall and inlet/outlet BC. However, this semi-analytical approach is significantly more complex and time consuming, we preferred to present simpler approaches in view of the simple test cases that we consider in this work.

2.5.1 Wall boundary conditions

The wall boundary conditions are modeled by introducing additional *ghost* SPH particles on the position of the boundary. These particles are regularly distributed on the boundaries (to satisfy the impermeability condition) and have a zero velocity to impose the no-slip condition. To prevent the inconsistency between the density of inner particles and that of the wall, additional layers of dummy particles are placed outside the domain so that the compact support of any fluid particle approaching the wall is full.

No slip In order to apply a no slip condition on the wall, a given ghost particle g carries prescribed values for the pressure p^w, density ρ^w and velocity $\boldsymbol{u}^w$ that are defined as :

$$p_g^w = \frac{1}{V_{ga}} \sum_{a \in \Omega_f \cap \Lambda_g} p_a \frac{m_a}{\rho_a} w_{ga}, \tag{2.5.1}$$

$$\rho_g^w = \frac{1}{V_{ga}} \sum_{a \in \Omega_f \cap \Lambda_g} \rho_a \frac{m_a}{\rho_a} w_{ga}, \tag{2.5.2}$$

$$\boldsymbol{u}_g^w = \frac{-1}{V_{ga}} \sum_{a \in \Omega_f \cap \Lambda_g} \boldsymbol{u}_a \frac{m_a}{\rho_a} w_{ga}, \tag{2.5.3}$$

with $V_{ga} = \sum_{a \in \Omega_f \cap \Lambda_g} \frac{m_a}{\rho_a} w_{ga}$, Ω_f the set of fluid particles and Λ_g the set of neighboring particles of ghost particle g. A schematic drawn on Fig. 2.10 helps to visualize what is the intersection $\Omega_f \cap \Lambda_g$. Note that the velocity of the ghost particle $\boldsymbol{u}_g^w$ is obtained as opposite (negative) of the extrapolated velocity of interior regular particles in order to prevent penetration of regular particles to the described boundary while the pressure and density is simply extrapolated from the interior regular particles.

Free slip Concerning free slip condition on the wall, it is needed to distinguish the tangential prescribed velocity $\boldsymbol{u}_g^{w,t}$ and the normal prescribed velocity $\boldsymbol{u}_g^{w,n}$. It reads :

$$p_g^w = \frac{1}{V_{ga}} \sum_{a \in \Omega_f \cap \Lambda_g} p_a \frac{m_a}{\rho_a} w_{ga}, \tag{2.5.4}$$

$$\rho_g^w = \frac{1}{V_{ga}} \sum_{a \in \Omega_f \cap \Lambda_g} \rho_a \frac{m_a}{\rho_a} w_{ga}, \tag{2.5.5}$$

$$\boldsymbol{u}_g^{w,t} = \frac{1}{V_{ga}} \sum_{a \in \Omega_f \cap \Lambda_g} \boldsymbol{u}_a \frac{m_a}{\rho_a} w_{ga}, \tag{2.5.6}$$

$$\boldsymbol{u}_g^{w,n} = \frac{-1}{V_{ga}} \sum_{a \in \Omega_f \cap \Lambda_g} \boldsymbol{u}_a \frac{m_a}{\rho_a} w_{ga}. \tag{2.5.7}$$

Moving wall If one wants to prescribe a given velocity $\boldsymbol{u}^p$ to apply a so-called moving wall condition, the prescribed values are defined as :

$$p_g^w = \frac{1}{V_{ga}} \sum_{a \in \Omega_f \cap \Lambda_g} p_a \frac{m_a}{\rho_a} w_{ga}, \tag{2.5.8}$$

$$\rho_g^w = \frac{1}{V_{ga}} \sum_{a \in \Omega_f \cap \Lambda_g} \rho_a \frac{m_a}{\rho_a} w_{ga}, \tag{2.5.9}$$

$$\boldsymbol{u}_g^w = 2\boldsymbol{u}^p - \frac{1}{V_{ga}} \sum_{a \in \Omega_f \cap \Lambda_g} \boldsymbol{u}_a \frac{m_a}{\rho_a} w_{ga}. \tag{2.5.10}$$

2.5.2 Other boundary conditions

Inlet/Outlet boundary conditions The inlet/outlet boundary condition is a very useful set of boundary conditions for the study of a large variety of fluid problems. Numerous inlet/outlet SPH formulations are currently available in the literature [Federico 2012, Ferrand 2012, Dong 2014, Khorasanizade 2016, Kunz 2016, Tafuni 2018]. The main issue being with inlet/outlet boundary condition is that it results in spurious reflected waves of significant amplitude that can affect negatively the simulation. Some treatments can remedy at least partially to this issue such as non reflecting boundary conditions but they require a more complex implementation [Lastiwka 2009, Marrone 2013].

Periodic boundary conditions Periodic boundary conditions are useful to reduce the size of the computational domain. In the case of SPH, the only modification need to introduce this kind of boundary conditions is to allow the particles from one side of the domain to interact with particles of the other side of the domain. This ensures that the quantities will be transmitted from one side to the other. Moreover, when a particle crosses the domain periodic frontier; it has to be copied and reintroduced "as is" from the other periodic frontier. When the domain is not continuously packed with particles across the periodic boundary, no extra treatment is need. Otherwise, in order to avoid incomplete kernels, one must ensure the consistency of the packing across the periodic boundary. Indeed, if the packing is not consistent across the periodic boundary, voids can appear within the packing which could lead to incorrect results.

Rigid bodies and floating objects If the floating object or rigid body moves under the influence of the solid/fluid, its wall-bounded particles have to move with it. Their positions are not updated using

classic SPH equations, but rather their equation of motion is given by the actual motion of the structure. In order to solve the equations of motion of the structure one needs to know its total mass, its center of mass and its moments of inertia around the three axes passing through the center of mass. For more details, see for example [Pan 2015].

2.6 Time integration

As with other numerical methods, any time integration scheme could be used. However, it is in generally advised to use a symplectic integrator in SPH. Indeed, the conservative nature of symplectic integrators give them a strong advantage as opposed to non-symplectic schemes even with higher orders. Non-symplectic schemes might be more accurate for the first iterations but the error can increase afterwards if not chosen carefully. SPH numerical stability generally imposes very small timesteps, thus, it is fundamental to ensure the conservation of quantities over a run. In practice, it is also possible to use a non-symplectic integrator but with very low dissipation over time, 4th order Runge-Kutta schemes are a good choice for example [Grenier 2009b, Chiron 2017]. Regarding symplectic integrators, both the Velocity Verlet and Predictor-Corrector leapfrog schemes have proven popular. In this work, the Predictor-Corrector leapfrog scheme was adopted. The algorithm is described hereafter. For every particle a,

1. Predictor Step
$$\boldsymbol{u}^n = \begin{cases} \boldsymbol{u}^0 & \text{if } t = 0, \\ \boldsymbol{u}^{n-\frac{1}{2}} + \frac{\Delta t}{2}\frac{D\boldsymbol{u}}{Dt}^{n-1} & \text{if } t > 0. \end{cases} \tag{2.6.1}$$
2. Compute ρ_a^n and p_a^n using the corresponding expressions in equation (4.2.6).
3. Evaluate $\frac{D\boldsymbol{u}}{Dt}^n$ using the momentum equation in (4.2.6).
4. Corrector Step
$$\boldsymbol{u}^{n+\frac{1}{2}} = \begin{cases} \boldsymbol{u}^n + \frac{\Delta t}{2}\frac{D\boldsymbol{u}}{Dt}^n & \text{if } t = 0, \\ \boldsymbol{u}^{n-\frac{1}{2}} + \Delta t\frac{D\boldsymbol{u}}{Dt}^n & \text{if } t > 0, \end{cases} \tag{2.6.2}$$
$$\boldsymbol{x}^{n+1} = \boldsymbol{x}^n + \Delta t \boldsymbol{u}^{n+\frac{1}{2}}. \tag{2.6.3}$$

The time step Δt has to respect the Courant-Friedrichs-Lewy (CFL) criteria to ensure a stable evolution of the system e.g.

$$\Delta t = \min\left(\Delta t_{\text{visc}}, \Delta t_{\text{grav}}, \Delta t_{\text{speed}}\right), \tag{2.6.4}$$

where, following [Morris 2000], we have

$$\begin{cases} \Delta t_{\text{visc}} & = 0.125\,\frac{h^2\rho^0}{\mu}, \\ \Delta t_{\text{grav}} & = 0.25\sqrt{\frac{h}{|\boldsymbol{g}|}}, \\ \Delta t_{\text{speed}} & = 0.25\,\frac{h}{c}. \end{cases} \tag{2.6.5}$$

A recent article [Violeau 2014] investigated in detail what is the maximum admissible timestep in the WCSPH context.

2.7 Multiphase SPH

There are two steps to extend SPH to multiphase flows. First, the SPH approximation has to be adapted to be able to handle density and viscosity discontinuities. Second, a surface tension force has to be added to the model. Numerous attempts to develop specific multiphase methods for SPH have been

done over the years (recent examples for bed sedimentation can be found in [Fourtakas 2014], for oil spills [Violeau 2007b] or for the Kevin-Helmotz instability [Price 2008]). An exhaustive review of SPH formulations for multiphase flows is given in [Tartakovsky 2015]. Moreover, the key challenges for future developments of multiphase SPH are discussed in the last section of [Violeau 2016]. Note that we will only mention immiscible multiphase SPH models in this section, other approaches such as mixture models (for example [Fonty 2019b, Fonty 2019a]) will not be described here.

2.7.1 Main formulations

Thanks to its success in modeling single phase flows, SPH has quickly been extended to be applied to multiphase flows simulations [Monaghan 1995]. Indeed, the Lagrangian nature makes the capture of the interface dynamics easier than Eulerian meshbased methods. However, the basic SPH model of Eq. (2.3.1) is not suited for large density ratios. It has been reported [Colagrossi 2003, Hu 2006, Violeau 2016, Grenier 2009a, Tofighi 2013] that, because of the squared density term in the denominator, nonphysical voids appear at the interface. Moreover, using Eq. (2.2.10) leads to a smoothing of the density at the interface which is undesirable. Three main approaches have been proposed to remedy these issues.

1. [Colagrossi 2003] suggests to use the SPH interpolants $\nabla_k^+ \hat{\boldsymbol{A}}$ with $k = 0$. It leads to the following set of interpolants :

$$\nabla_0^+ \hat{\boldsymbol{A}}(\boldsymbol{x}_a) = \sum_{b \in \Lambda_a} \frac{m_b}{\rho_b} (\boldsymbol{A}_a + \boldsymbol{A}_b) \nabla_a w_{ab}, \tag{2.7.1}$$

$$\nabla_0^+ \cdot \hat{\boldsymbol{A}}(\boldsymbol{x}_a) = \sum_{b \in \Lambda_a} \frac{m_b}{\rho_b} (\boldsymbol{A}_b - \boldsymbol{A}_a) \nabla_a \cdot w_{ab}. \tag{2.7.2}$$

   However, this approach is not adapted to high density ratio (typically air/water) since the density is still computed through the continuity equation which leads to conservation errors and it also suffers from inconsistencies between the velocity and the density fields.

2. Derived from variational principles, [Hu 2006] proposes to use a slightly different version of Eq. (2.2.9) (borrowed from [Español 2003]) :

$$\rho_a = m_a \sum_{b \in \Lambda_a} w_{ab}. \tag{2.7.3}$$

   The difference is that the density evaluation for a given particle a does not take into account the masses of neighboring particles which allows the treatment of density discontinuities. The corresponding discretized gradient and divergence operators in this formalism are given by :

$$\nabla \boldsymbol{A}(\boldsymbol{x}_a) = \sum_{b \in \Lambda_a} \left(\frac{\boldsymbol{A}_a}{\Theta_a^2} + \frac{\boldsymbol{A}_b}{\Theta_b^2} \right) \Theta_a \nabla_a w_{ab}, \tag{2.7.4}$$

$$\nabla \cdot \boldsymbol{A}(\boldsymbol{x}_a) = \sum_{b \in \Lambda_a} \left(\frac{\boldsymbol{A}_a}{\Theta_a^2} + \frac{\boldsymbol{A}_b}{\Theta_b^2} \right) \Theta_a \nabla_a \cdot w_{ab}, \tag{2.7.5}$$

   where $\Theta_a = \frac{\rho_a}{m_a}$. This approach allows to circumvent the issue of density smoothing at the interface since a direct summation is used[14]. Moreover, they also proposed a modified version of the viscosity term of Eq. (2.4.5) based on the inter-particle averaged shear stress [Flekkoy 2000]

[14] However, it cannot be used "as is" for free surface flows, one needs to use a time integrated version of Eq. (2.7.3) [Ferrand 2012, Ghaitanellis 2017].

and given by :

$$\nu_a \nabla^2 \boldsymbol{u}_a = \frac{1}{m_a} \sum_{b \in \Lambda_a} \frac{2\nu_a \nu_b}{\nu_a + \nu_b} \left(\frac{1}{\Theta_a^2} + \frac{1}{\Theta_b^2} \right) \frac{\boldsymbol{x}_{ab} \cdot \nabla_a w_{ab}}{|\boldsymbol{x}_{ab}|^2 + \eta^2} \boldsymbol{u}_{ab}, \tag{2.7.6}$$

where $\eta = 0.01h$ is a safety factor to avoid a division by zero. This model is quite simple to implement and reasonably efficient and stable to handle large density and viscosity ratios. It is the formulation that will be used in the rest of this work.

3. In [Grenier 2009a], a new volumetric formulation, also based on variational principles, was introduced to handle multiphase flows in SPH. First, the density is computed using the density summation but completed with a Shepard filter. It boils down to Eq. (2.4.7) except that the summation is only done on particles of the same phase. It is written as :

$$\rho_a = \sum_{b \in \Lambda_a \cap \Omega_a} m_b \hat{w}_{ab}, \tag{2.7.7}$$

with $\hat{w}_{ab} = w_{ab}/S_a$, $S_a = \sum_{b \in \Lambda_a} V_b w_{ab}$, V_a the volume of particle a and Ω_a the set of particles belonging to the same phase as particle a. The continuity equation is discretized using the volume-based approach. It gives :

$$\frac{d \log(V/V^0)}{dt} = \frac{1}{S_a} \sum_{b \in \Lambda_a} (\boldsymbol{u}_b - \boldsymbol{u}_a), \tag{2.7.8}$$

where V^0 is the initial volume of the particles. Then it is possible to deduce the discretized gradient operator and the viscous term in this formalism :

$$\nabla \boldsymbol{A}(\boldsymbol{x}_a) = \sum_{b \in \Lambda_a} V_b \left(\frac{\boldsymbol{A}_a}{S_a} + \frac{\boldsymbol{A}_b}{S_b} \right) \nabla_a w_{ab}, \tag{2.7.9}$$

$$\nu_a \nabla^2 \boldsymbol{u}_a = \frac{1}{V_a} \sum_{b \in \Lambda_a} V_b \frac{2\nu_a \nu_b}{\nu_a + \nu_b} \left(\frac{1}{S_a} + \frac{1}{S_b} \right) \frac{\boldsymbol{x}_{ab} \cdot \nabla_a w_{ab}}{|\boldsymbol{x}_{ab}|^2 + \eta^2} \boldsymbol{u}_{ab}. \tag{2.7.10}$$

This formulation returns accurate results with cleaner pressure fields than the other formulations but suffers from inconsistency between the density and the velocity fields just like [Colagrossi 2003]. Moreover, it is limited to low Reynolds number because the viscous term does not suffice to stabilize the scheme.

2.7.2 Surface tension models

In a multiphase problem, one needs to discretize the surface tension force term $\frac{1}{\rho}\boldsymbol{F}^{\text{st}}$ in Eq. (2.2.2). There are two main techniques to include a surface tension model within an SPH formulation, the pair-wise force model and the color gradient approach :

1. the pair-wise force model (PF) [Tartakovsky 2016]
This model is based on the inclusion of a molecular-like pairwise interaction force $\boldsymbol{F}_{ab}^{\text{st}}$ in the discretized momentum equation (inside the summation). It reproduces the cause of the surface tension i.e. attractive forces among particles of the same phase. It reads :

$$\boldsymbol{F}_{ab}^{\text{st}} = \begin{cases} -\sigma^{\alpha\beta} \cos\left(\frac{3\pi}{2h}|\boldsymbol{x}_a - \boldsymbol{x}_b|\right) \frac{\boldsymbol{x}_a - \boldsymbol{x}_b}{|\boldsymbol{x}_a - \boldsymbol{x}_b|}, & \text{if } |\boldsymbol{x}_a - \boldsymbol{x}_b| \leq h, \\ 0, & \text{if } |\boldsymbol{x}_a - \boldsymbol{x}_b| > h, \end{cases} \tag{2.7.11}$$

where $\sigma^{\alpha\beta}$ defines the strength of the interaction between particle a of phase α and particle b of phase β. Then, for a given particle a, one just needs to sum up all the contributions of neighboring particles of the same phase :

$$\boldsymbol{F}_a^{\mathrm{st}} = \sum_{b \in \Lambda_a \cap \Omega_a} \boldsymbol{F}_{ab}^{\mathrm{st}}, \tag{2.7.12}$$

with Ω_a the set of particles belonging to the same phase as particle a. More details about this approach can be found in [Tartakovsky 2015].

2. the color gradient model (or continuum surface force (CSF) [Brackbill 1992, Lafaurie 1994])
This approach aims to simulate the effect of the surface tension i.e. the minimization of the interface area. There are two variants of the CSF model in SPH [Morris 2000, Szewc 2013] : the first one is based on the computation of the curvature of the interface and will be called CSF-κ and the second one depends on the evaluation of the surface stress tensor and will be referred as CSF-Π.
   (a) In the CSF-κ variant, $\boldsymbol{F}^{\mathrm{st}}$ is expressed as :

$$\boldsymbol{F}_a^{\mathrm{st}} = \sigma^{\alpha\beta} \kappa_a^{\alpha\beta} \tilde{\boldsymbol{n}}_a^{\alpha\beta} \delta_a, \tag{2.7.13}$$

   where $\sigma^{\alpha\beta}$ is the surface tension coefficient between phase α and phase β, $\kappa_a = -\nabla \cdot \tilde{\boldsymbol{n}}_a^{\alpha\beta}$ is the curvature between phase α and phase β, $\boldsymbol{n}_a^{\alpha\beta}$ is the normal vector between phase α and phase β and δ_a is a surface delta function set to be equal to $|\boldsymbol{n}_a^{\alpha\beta}|$ and $\tilde{\boldsymbol{n}}_a^{\alpha\beta} = \boldsymbol{n}_a^{\alpha\beta} / |\boldsymbol{n}_a^{\alpha\beta}|$. Then depending on the multiphase formulation chosen, one needs to discretize $\boldsymbol{n}_a^{\alpha\beta}$[15] and κ_a. The CSF-κ technique is highly dependent on the quality of the curvature computation (which is a second order derivative and has to be handled with care [Adami 2010] if not errors occur as shown on Fig. 2.12) and does not include natively a way to deal with contact line (contact angle). A special treatment such as Contact Line Force (CLF) has to be added [Kunz 2015]. Moerover, CSF-κ is known to lack conservation of linear and angular momentum.
   (b) In the CSF-Π variant, $\boldsymbol{F}^{\mathrm{st}}$ is expressed as :

$$\boldsymbol{F}_a^{\mathrm{st}} = -\nabla \cdot \Pi_a, \tag{2.7.16}$$

   with Π the capillary pressure tensor defined by

$$\Pi_a = \sum_{\alpha,\beta | \alpha < \beta} \Pi_a^{\alpha\beta}, \tag{2.7.17}$$

   where $\alpha, \beta \in \{1, \ldots, N_{\mathrm{phases}}\}$ and $\Pi^{\alpha\beta}$ is expressed as

$$\Pi^{\alpha\beta} = -\sigma^{\alpha\beta} \left(\boldsymbol{I} - \tilde{\boldsymbol{n}}^{\alpha\beta} \otimes \tilde{\boldsymbol{n}}^{\alpha\beta} \right) \delta^{\alpha\beta}, \tag{2.7.18}$$

[15] Note that in SPH, the evaluation of normals is performed through the computation of the gradient of a color function χ defined for a given particle a and a given phase α as

$$\chi_a^\alpha = \begin{cases} 1 & \text{if } a \in \text{phase } \alpha, \\ 0 & \text{else.} \end{cases} \tag{2.7.14}$$

The normal vector $\boldsymbol{n}_a^{\alpha\beta}$ of particle a belonging to phase α to the interface $\alpha\beta$ is then computed as $\boldsymbol{n}_a^{\alpha\beta} = \nabla \chi_a^\alpha$. For example, following the formalism of [Hu 2006]. It would lead to :

$$\boldsymbol{n}_a^{\alpha\beta} = \nabla \chi_a^{\alpha\beta} = \sum_{b \in \Lambda_a} \left(\frac{\chi_a^\beta}{\Theta_a^2} + \frac{\chi_b^\beta}{\Theta_b^2} \right) \Theta_a \nabla_a w_{ab}. \tag{2.7.15}$$

with $\tilde{\boldsymbol{n}}^{\alpha\beta}$ the unit normal vector from phase α to phase β, $\sigma^{\alpha\beta}$ the surface tension coefficient between phase α and phase β, $\delta^{\alpha\beta}$ a well-chosen surface delta function set to be equal to $|\boldsymbol{n}_a^{\alpha\beta}|$ and $\boldsymbol{I}$ the identity matrix. Then depending on the multiphase formulation chosen, one needs to discretize $\boldsymbol{n}_a^{\alpha\beta}$. In the case of a three-phase system with a wetting phase s, a non wetting phase n and a solid phase s as described in Figure 2.11, the stress tensor reads $\Pi_a = \Pi_a^{ns} + \Pi_a^{ws} + \Pi_a^{nw}$. The CSF-$\Pi$ approach has the advantage to be able to handle naturally contact line (contact angles) and to be fully conservative. However, in SPH, this approach can lead to instabilities at high resolution. Several treatments are available [Szewc 2013]. In particular, in [Hu 2006], it is recommended to use a modified version of $\Pi^{\alpha\beta}$ given by $\Pi^{\alpha\beta} = -\sigma^{\alpha\beta}\left(\frac{1}{D}\boldsymbol{I} - \tilde{\boldsymbol{n}}^{\alpha\beta} \otimes \tilde{\boldsymbol{n}}^{\alpha\beta}\right)\delta^{\alpha\beta}$ (where D is the dimension). This leads to $\mathrm{Tr}\left(\Pi^{\alpha\beta}\right) = 0$ and therefore, there is no negative spurious pressure contribution. In this work, despite this correction, instabilities were still observed but only after a large number of iterations of a static bubble test.

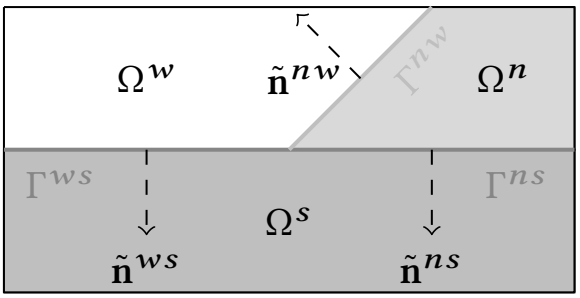

Figure 2.11: A triple point contact line between a non wetting phase Ω_n, a wetting phase Ω_w and a solid phase Ω_s with their associated unit normal vectors $\tilde{\boldsymbol{n}}_{ab}$ and boundary lines Γ_{ab}

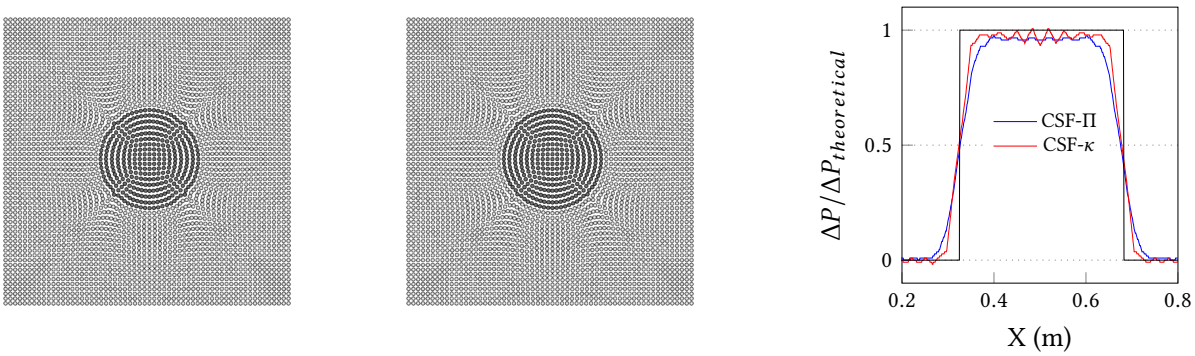

(a) A static bubble simulated with CSF-κ

(b) A static bubble simulated with CSF-Π

(c) Laplace's law verification

Figure 2.12: Comparison of CSF-κ and CSF-Π models for a static bubble test with 3600 particles. Note that in that case, the curvature needed in CSF-κ has been computed without any caution leading to a noisier pressure field.

2.7.3 Corrective terms

Several corrective procedures are available for mulitphase SPH formulation. Hereafter, we briefly describe two of them as they will be used later in this work.

First, the shifting technique for multiphase flows introduced in [Mokos 2016] has also been used to maintain a good particles distribution. At the end of every timestep, all particles are shifted by a distance $\delta \boldsymbol{r}^s$ from their original position. This shifting distance of a particle a is evaluated by doing

$$\delta \boldsymbol{r}_a^s = \begin{cases} -D_a \nabla C_a & \text{if } a \in \text{light phase}, \\ -D_a \left(\frac{\partial C_a}{\partial s} \boldsymbol{s} + \alpha_n \left(\frac{\partial C_a}{\partial n} \boldsymbol{n} - \beta_n \right) \right) & \text{if } a \in \text{heavy phase}, \end{cases} \tag{2.7.19}$$

where $C_a = \sum_{b \in \Lambda_a} \frac{m_a}{\rho_a} w_{ab}$ is the particle concentration, $\nabla C_a = \sum_{b \in \Lambda_a} \frac{m_a}{\rho_a} (C_b - C_a) \nabla w_{ab}$ is the particle concentration gradient, D_a is the diffusion coefficient, $\boldsymbol{s}$ and $\boldsymbol{n}$ are respectively the tangent and normal vectors to the interface light/heavy phase (with $\boldsymbol{n}$ oriented towards the light phase), β_n is a reference concentration gradient (taken equal to its initial value) and α_n is the normal diffusion parameter and is set equal to 0.1. The diffusion coefficient D_a is computed as follows

$$D_a = A_s |\boldsymbol{u}_a| \Delta t, \tag{2.7.20}$$

where A_s is a parameter set to 2, $\boldsymbol{u}_a$ is the velocity of particle a, and Δt is the timestep.

Second, as reported by several authors [Colagrossi 2003, Grenier 2009a, Szewc 2013, Ghaitanellis 2017], multiphase SPH can suffer from sub-kernel micro-mixing phenomena. Around the interface, within a distance corresponding to the range of the kernel smoothing, particles have a tendency to mix. It is due to the fact that there is no mechanism ensuring phases immiscibility in the surface tension's continuum surface stress model. As suggested by the previously mentioned authors, we introduce a small repulsive force between phases as follows

$$\boldsymbol{F}_a^{corr} = \varepsilon \sum_{b \in \Lambda_a, b \notin \Omega_a} \left(\frac{1}{\Theta_a^2} + \frac{1}{\Theta_b^2} \right) \nabla_a w_{ab}, \tag{2.7.21}$$

where $\varepsilon = \frac{L_{\text{ref}}}{h}$ for all simulations as suggested in [Szewc 2016] where L_{ref} is a reference length, typically the diameter for pipes. Note that the alternative formulation given by $\boldsymbol{F}_a^{corr} = \varepsilon \sum_{b \in \Lambda_a, b \notin \Omega_a} \left(\frac{p_a}{\Theta_a^2} + \frac{p_b}{\Theta_b^2} \right) \nabla_a w_{ab}$ with $\varepsilon = 0.1$ produces roughly the same force magnitude at the interface. The impact of this corrective force is shown in Fig. 2.13 and a more exhaustive study can be found in [Douillet-Grellier 2018].

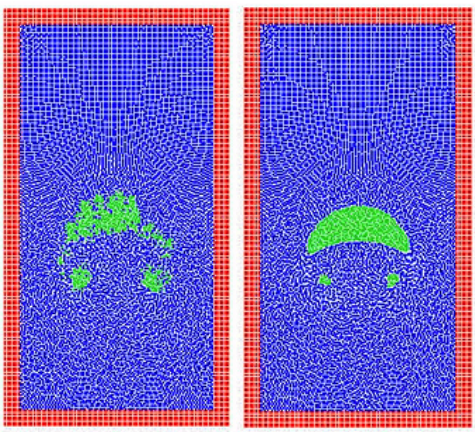

(a) Without $\boldsymbol{F}^{corr}$ (b) With $\boldsymbol{F}^{corr}$

Figure 2.13: Example of the impact of $\boldsymbol{F}^{corr}$ on a circular bubble rising under the influence of gravity.

Models	Advantages	Drawbacks
PF	✓Fast computation ✓Intrinsic contact line dynamics ✓No need for interface correction ✓No normal/curvature computation	×Complex and indirect link between model parameters and macroscopic variables ×Few users
CSF-κ	✓Stable at high resolution	×Normal/Curvature computation ×Extrinsic contact line dynamics ×Need for interface correction ×Not conservative
CSF-Π	✓Intrinsic contact line dynamics ✓Fully conservative ✓No curvature computation	×Instabilities at high resolution ×Need for interface correction

Table 2.7: Summary of the different multiphase SPH approaches

2.7.4 Summary

In this work, we will use the multiphase SPH formulation introduced in [Hu 2006] in association with the CSF-Π approach for the surface tension force. This choice is guided by several reasons. First, concerning the surface tension models, we preferred CSF-Π over CSF-κ because of its conservative nature and the built-in ability to handle contact line dynamics. In addition, it avoids the computation of the curvature. We have done some tests with the PF model but, at that time, there was no clear link between the physical surface tension and the associated numerical parameter (it seems to have been solved at the moment [Tartakovsky 2016]) which was an important drawback. Finally, with respect to the formulations, we chose to use Hu and Adams formulation over Colagrossi's because it was better suited for high density ratios and over Grenier's mostly because it was simpler and less computationally expensive.

Chapter 3

Lattice Boltzmann method

Contents

3.1 Probability distribution functions **78**
3.2 Equilibrium **82**
3.3 Boltzmann Equation **84**
3.4 Chapman-Enskog expansion **86**
3.5 $\mathcal{H}$-Theorem **91**
3.6 Discretization **91**
3.6.1 Velocity space discretization 91
3.6.2 Discrete equilibrium 92
3.6.3 Discrete Chapman-Enskog expansion 96
3.6.4 Time and space discretization 98
3.7 Units **101**
3.8 Key features **102**
3.9 Alternative collision operators **104**
3.9.1 Multiple relaxation time (MRT) operator 104
3.9.2 Regularized operator 105
3.10 Boundary conditions **105**
3.10.1 Periodic boundary conditions 106
3.10.2 Full bounce-back boundary conditions 106
3.10.3 Halfway bounce-back boundary conditions 107
3.10.4 Zou & He boundary conditions 108
3.10.5 Body forces 108
3.11 LBM Variants **109**
3.11.1 LBM for compressible flows 109
3.11.2 LBM for low viscosity flows 109
3.12 Multiphase LBM **110**
3.12.1 Color Gradient Model (CGM) 111
3.12.2 Inter-particular potentials (Shan-Chen's model) 116
3.12.3 Free-Energy Model 118
3.12.4 Mean-Field Model 119
3.12.5 Summary 119

The lattice Boltzmann method has been originated from two distinct approaches : the kinetic gas theory with discrete velocities and the lattice gas cellular automata method (LGCA or LGA). In practice, there are four main differences between the LBM and traditional continuum-based methods. First, the LBM operates on an uniform lattice (square or hexagonal lattices). This avoids some problems related with meshing. However, this comes at some expense. For example, LBM presents a first order accuracy when dealing with curved boundaries (staircase discretization). Second, LBM presents a simple, local, nature of the lattice Boltzmann equation. Indeed, the algorithm consists of a series of simple arithmetic operations involving no differential terms. An LBM code is relatively short when compared to a typical continuum based code, where the LBM algorithm is also particularly well suited to parallel execution [Harting 2005]. Third, traditional CFD methods are based on the calculation of macroscopic variables (velocity, pressure, density) whereas LBM tracks the evolution of Probability Distribution Functions (PDF) and is built on microscopic models and mesoscopic kinetic equations [Benzi 1992, Qian 1992, Boon 2003]. The macroscopic variables are computed through a moment integration of the distribution. Finally, continuum based methods are built on Navier-Stokes equations (macroscale) whereas LBM emerges from the Boltzmann equation (mesoscale). It is possible to derive the full set of Navier-Stokes equations by applying the Chapman-Enskog expansion to the Lattice Boltzmann Method [Viggen 2009, Viggen 2014, Li 2015]. Most of the following is inspired by the first chapter of [Béchereau 2016] and [Viggen 2014].

3.1 Probability distribution functions

Let's consider the mathematical modeling of a **monatomic** gas formed by a collection of n identical interacting particles[1] (where n is a big integer, let's say $10^6 \leq N \leq 10^{23}$) in an euclidean space $\mathbb{R}^N$. Assuming that the position $\boldsymbol{x}$ and the velocity $\boldsymbol{v}$ are enough to describe the state of a particle, the state of the gas can be described by a probability distribution function (PDF) $f_n(\boldsymbol{x}_1, \boldsymbol{v}_1, \ldots, \boldsymbol{x}_n, \boldsymbol{v}_n)$ in the phase space $(\mathbb{R}^N_{\boldsymbol{x}} \times \mathbb{R}^N_{\boldsymbol{v}})^n$. This is a microscopic description.

One can then use Newton's laws and describe the state of the gas and its evolution by forming a huge system of $2n$ differential equations on the position and the velocity of the particles and also with the interaction forces. Historically, particles were considered as hard spheres bouncing on each other like in a pool game.

This model contains way too much information. In general, the model is simplified by using a kinetic approach of the gas. The state of the gas is then described by a distribution $f(\boldsymbol{x}, \boldsymbol{v}, t)$, which measures the probability of finding particles in the phase space $\mathbb{R}^N_{\boldsymbol{x}} \times \mathbb{R}^N_{\boldsymbol{v}}$. This function can be seen as a generalization of density in both physical and velocity space. As an example, $f(\boldsymbol{x}, \boldsymbol{v}, t)d\boldsymbol{v}$ represents the spatial density of particles within the velocity volume $d\boldsymbol{v}$ at $\boldsymbol{v}$ and $f(\boldsymbol{x}, \boldsymbol{v}, t)d\boldsymbol{x}d\boldsymbol{v}$ is the mass of particles within the velocity volume $d\boldsymbol{v}$ at $\boldsymbol{v}$ and the spatial volume $d\boldsymbol{x}$ at $\boldsymbol{x}$. This mesoscopic description leads to the Boltzmann equation.

This definition of distributions is enough to recover the fundamental properties of the fluid (density, momentum, energy). In fact, these properties are computed as moments[2] of the distribution acting as a

[1] Despite using the same word, in this section, the word "particles" will refer to physical particles such as atoms (hard spheres model). This is **different** from SPH particles which are material points bearing kinematic and thermodynamic quantities.

[2] A distribution moment is an integral of the distribution over the velocity space and weighted by a function of $\boldsymbol{v}$.

link between the mesoscopic and the macroscopic scales. These moments are defined as follows :

$$\boxed{\begin{aligned} \rho(\boldsymbol{x},t) &= \int f(\boldsymbol{x},\boldsymbol{v},t)d\boldsymbol{v}, \ (0^{\text{th}} \text{ moment - density}) && (3.1.1)\\ \rho\boldsymbol{u}(\boldsymbol{x},t) &= \int \boldsymbol{v} f(\boldsymbol{x},\boldsymbol{v},t)d\boldsymbol{v}, \ (1^{\text{st}} \text{ moment - momentum}) && (3.1.2)\\ \rho E(\boldsymbol{x},t) &= \frac{1}{2}\int |\boldsymbol{v}|^2 f(\boldsymbol{x},\boldsymbol{v},t)d\boldsymbol{v}, \ (2^{\text{nd}} \text{ moment - energy density}) && (3.1.3)\end{aligned}}$$

with $\boldsymbol{u}$ the macroscopic velocity of the fluid and E the specific energy of the fluid. Note that Eq. (3.1.3) assumes that only the translational velocity contributes to the kinetic energy. This is only true for a monatomic gas as assumed before.

At this point, it is useful to introduce the peculiar velocity $\boldsymbol{\xi}$ which is defined as the difference between the particle velocity $\boldsymbol{v}$ and the fluid (average) velocity $\boldsymbol{u}$ [3] :

$$\boldsymbol{v} = \boldsymbol{u} + \boldsymbol{\xi}. \tag{3.1.4}$$

It is possible to decompose the energy density into two parts : the part induced by the peculiar velocity $\boldsymbol{\xi}$ (also called the internal energy density ρe) and the part induced by the fluid velocity $\boldsymbol{u}$:

$$\rho E = \rho e + \frac{1}{2}\rho|\boldsymbol{u}|^2, \tag{3.1.5}$$

$$\rho e(\boldsymbol{x},t) = \frac{1}{2}\int |\boldsymbol{\xi}|^2 f(\boldsymbol{x},\boldsymbol{v},t)d\boldsymbol{v}. \tag{3.1.6}$$

The macroscopic quantity known as pressure $p(\boldsymbol{x},t)$ is due to particles bouncing off a given surface. Because mass and momentum are conserved through elastic collisions, a particle with a given mass and velocity hitting the surface will bounce keeping the same mass and with an opposite velocity. For example, if the surface is in the $x-y$ plane as shown on Figure 3.1 then the total mass $m_{\boldsymbol{v}}$ of particles hitting the wall with a velocity $\boldsymbol{\xi}$ is :

$$m_{\boldsymbol{\xi}} = f(\boldsymbol{x},\boldsymbol{v},t)d\boldsymbol{x}d\boldsymbol{v}. \tag{3.1.7}$$

The infinitesimal spatial volume $d\boldsymbol{x}$ can be expressed in function of the vertical velocity ξ_z as $d\boldsymbol{x} = dxdy\xi_z dt$ yielding :

$$m_{\boldsymbol{\xi}} = \xi_z f(\boldsymbol{x},\boldsymbol{v},t)d\boldsymbol{v}dxdydt. \tag{3.1.8}$$

The change of momentum $\Delta\boldsymbol{p}_{\boldsymbol{\xi}}$ is then calculated as the total mass $m_{\boldsymbol{\xi}}$ multiplied by the velocity difference before and after collision i.e. $\Delta\xi_z = \xi_z - (-\xi_z) = 2\xi_z$:

$$\Delta\boldsymbol{p}_{\boldsymbol{\xi}} = m_{\boldsymbol{\xi}}\Delta\xi_z = 2\xi_z^2 f(\boldsymbol{x},\boldsymbol{v},t)d\boldsymbol{v}dxdydt. \tag{3.1.9}$$

Among all particles with the above momentum, only those with a v_z that points towards the wall have to be counted. To clarify the idea, if the wall is in the half space $z > 0$, only particles with $v_z > 0$ will contribute to the change of momentum, the others with $v_z > 0$ are moving away from the wall. Assuming that f is symmetric around $\xi = 0$, it yields :

$$\int_{\xi_z<0} \Delta\boldsymbol{p}_{\boldsymbol{\xi}} = \int \Delta\boldsymbol{p}_{\boldsymbol{\xi}} - \int_{\xi_z>0} \Delta\boldsymbol{p}_{\boldsymbol{\xi}}, \tag{3.1.10}$$

$$\int_{\xi_z<0} \Delta\boldsymbol{p}_{\boldsymbol{\xi}} = \frac{1}{2}\int \Delta\boldsymbol{p}_{\boldsymbol{\xi}}. \tag{3.1.11}$$

[3] By definition, the peculiar velocity does not contribute to the momentum : $\int \boldsymbol{\xi} f d\boldsymbol{v} = \int \boldsymbol{v} f d\boldsymbol{v} - \boldsymbol{u}\int f d\boldsymbol{v} = \rho\boldsymbol{u} - \rho\boldsymbol{u} = 0$. We even have $\int \boldsymbol{\xi}^n f d\boldsymbol{v} = 0$ if n is odd (antisymmetric integrand).

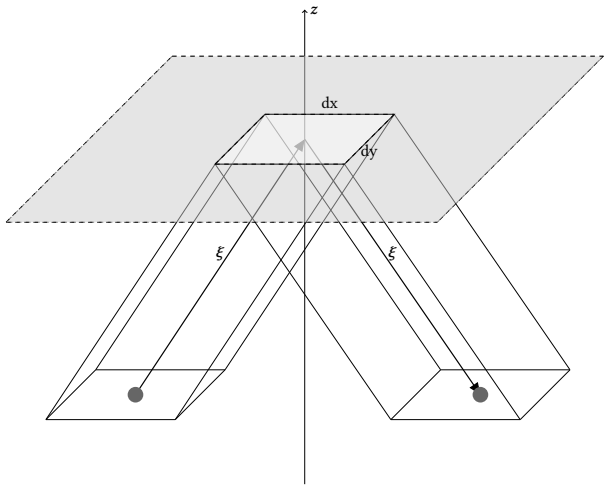

Figure 3.1: Particle hitting the x-y plane

The previous assumption of symmetry around the peculiar velocity is rooted in reality and is equivalent to assume that the gas is in equilibrium. It is based on the observation that a gas at rest evenly distributes the peculiar velocities around $\boldsymbol{u}$ (thermodynamic disorder according to the second law of thermodynamics). As a consequence, the change of momentum due to particles collisions on the wall is then :

$$\int_{v_z<0} \Delta \boldsymbol{p}_{\xi} = dxdydt \int \xi_z^2 f(\boldsymbol{x}, \boldsymbol{v}, t) d\boldsymbol{v}. \tag{3.1.12}$$

To obtain the pressure, one just needs to divide the change of momentum by dt to get the force (Newton's second law) and finally by the area $dxdy$. In the end, we have $p(\boldsymbol{x}, t) = \int \xi_z^2 f(\boldsymbol{x}, \boldsymbol{v}, t) d\boldsymbol{v}$. Applying this reasoning for a wall placed in another plane, we would get the same result with ξ_x or ξ_y inside the integral. Taking the average of those definitions $\frac{1}{3}(\xi_x^2 + \xi_y^2 + \xi_z^2) = \frac{1}{3}|\boldsymbol{\xi}|^2$, the final expression for pressure is obtained :

$$p(\boldsymbol{x}, t) = \frac{1}{3} \int |\boldsymbol{\xi}|^2 f(\boldsymbol{x}, \boldsymbol{v}, t) d\boldsymbol{v}. \tag{3.1.13}$$

Note that combining Eq. (3.1.13), Eq. (3.1.5) and Eq. (3.1.6), it yields :

$$p = \frac{2}{3} \rho e. \tag{3.1.14}$$

The ideal gas equation of state is defined as follows :

$$p = \rho \frac{k_B T}{m}, \tag{3.1.15}$$

with m the mass, $k_B = 1.38 \times 10^{-23} J/K$ the Boltzmann constant and T the temperature. It is also possible to introduce the specific heat capacity at constant volume $c_V = \left(\frac{\partial e}{\partial T}\right)_V$, the specific heat capacity at constant pressure $c_p = c_V + \frac{k_B}{m}$ (for ideal gases only) and their ratio $\gamma = \frac{c_p}{c_V}$:

$$c_V = \left(\frac{\partial e}{\partial T}\right)_V = \frac{3}{2} \frac{k_B}{m}, \tag{3.1.16}$$

$$c_p = \frac{k_B}{m} + c_V = \frac{5}{2} \frac{k_B}{m}, \tag{3.1.17}$$

$$\gamma = \frac{c_p}{c_V} = \frac{5}{3}. \tag{3.1.18}$$

Note that for an arbitrary number D of dimensions, the above expressions are simply :

$$p = \frac{1}{D}\int |\xi|^2 f d\boldsymbol{v} = \rho\frac{k_B T}{m} = \frac{2}{D}\rho e, \tag{3.1.19}$$

$$c_V = \left(\frac{\partial e}{\partial T}\right)_V = \frac{D}{2}\frac{k_B}{m}, \tag{3.1.20}$$

$$c_p = \frac{k_B}{m} + c_V = \frac{D+2}{2}\frac{k_B}{m}, \tag{3.1.21}$$

$$\gamma = \frac{c_p}{c_V} = \frac{D+2}{D}. \tag{3.1.22}$$

For convenience, we will introduce here a notation for some particular moments of f :

$$M_0 = \int f d\boldsymbol{v} = \rho, \tag{3.1.23}$$

$$\boldsymbol{M}_1 = \int \boldsymbol{v} f d\boldsymbol{v} = \rho\boldsymbol{u}, \tag{3.1.24}$$

$$\boldsymbol{M}_2 = \int \boldsymbol{v}\otimes\boldsymbol{v} f d\boldsymbol{v}, \tag{3.1.25}$$

$$\boldsymbol{M}_3 = \int \boldsymbol{v}\otimes\boldsymbol{v}\otimes\boldsymbol{v} f d\boldsymbol{v}, \tag{3.1.26}$$

$$\boldsymbol{M}_3^* = \frac{1}{2}\int \boldsymbol{v}|\boldsymbol{v}|^2 f d\boldsymbol{v}, \tag{3.1.27}$$

$$\boldsymbol{M}_4^* = \int \xi\otimes\xi\otimes\xi\otimes\xi f d\boldsymbol{v}. \tag{3.1.28}$$

In particular, it is interesting to expand $\boldsymbol{M}_2$ using Eq. (3.1.4). Indeed, we have $\boldsymbol{v}\otimes\boldsymbol{v} = (\boldsymbol{u}+\xi)\otimes(\boldsymbol{u}+\xi)$:

$$\begin{aligned}
\boldsymbol{M}_2 &= \int (\boldsymbol{u}\otimes\boldsymbol{u} + \boldsymbol{u}\otimes\xi + \xi\otimes\boldsymbol{u} + \xi\otimes\xi) f d\boldsymbol{v},\\
\boldsymbol{M}_2 &= \rho\boldsymbol{u}\otimes\boldsymbol{u} + \int \xi\otimes\xi f d\boldsymbol{v},\\
\boldsymbol{M}_2 &= \rho\boldsymbol{u}\otimes\boldsymbol{u} - \boldsymbol{\sigma},
\end{aligned} \tag{3.1.29}$$

where we have set $\boldsymbol{\sigma} = -\int \xi\otimes\xi f d\boldsymbol{v}$. In a similar way, M_3^* can be written as follows :

$$\begin{aligned}
\boldsymbol{M}_3^* &= \frac{1}{2}\int \left(\boldsymbol{u}|\boldsymbol{u}|^2 + \boldsymbol{u}|\xi|^2 + 2\xi(\xi.\boldsymbol{u}) + \xi|\xi|^2\right) f d\boldsymbol{v},\\
\boldsymbol{M}_3^* &= \frac{1}{2}\rho\boldsymbol{u}|\boldsymbol{u}|^2 + \rho\boldsymbol{u}e - \boldsymbol{\sigma}.\boldsymbol{u} + \frac{1}{2}\int \xi|\boldsymbol{u}|^2 f d\boldsymbol{v},\\
\boldsymbol{M}_3^* &= \rho\boldsymbol{u}E - \boldsymbol{\sigma}.\boldsymbol{u} + \boldsymbol{q},
\end{aligned} \tag{3.1.30}$$

where we have set $\boldsymbol{q} = \frac{1}{2}\int \xi|\xi|^2 f d\boldsymbol{v}$. It will also be useful later to expand $\boldsymbol{M}_3$ (in index notation as it involves high order tensors) :

$$\begin{aligned}
M_{3abcd} &= \int (u_a u_b u_c + u_a\xi_b\xi_c + u_b\xi_a\xi_c + u_c\xi_a\xi_b) f d\boldsymbol{v},\\
M_{3abcd} &= u_a u_b u_c\left(\int f d\boldsymbol{v}\right) + u_a\left(\int \xi_b\xi_c f d\boldsymbol{v}\right) + u_b\left(\int \xi_a\xi_c f d\boldsymbol{v}\right) + u_c\left(\int \xi_a\xi_b f d\boldsymbol{v}\right),\\
M_{3abcd} &= \rho u_a u_b u_c + u_a\left(\int \xi_b\xi_c f d\boldsymbol{v}\right) + u_b\left(\int \xi_a\xi_c f d\boldsymbol{v}\right) + u_c\left(\int \xi_a\xi_b f d\boldsymbol{v}\right).
\end{aligned} \tag{3.1.31}$$

3.2 Equilibrium

Let us denote f^{eq} the distribution when the gas is in equilibrium. We have seen before that when the gas is at rest, it only depends on $|\boldsymbol{\xi}|$ so that we can write :

$$f^{\text{eq}}(\boldsymbol{x}, \boldsymbol{v}, t) = f^{\text{eq}}(|\boldsymbol{\xi}|). \tag{3.2.1}$$

We can naturally[4] assume that f^{eq} can be expressed under a Gaussian form as :

$$f^{\text{eq}}(|\boldsymbol{\xi}|) = A \exp(-B|\boldsymbol{\xi}|^2), \tag{3.2.2}$$

where A and B are constants to be determined using Eqs. (3.1.1) and, for example, (3.1.13).

$$\begin{aligned}
\rho(\boldsymbol{x}, t) &= \int f^{\text{eq}}(|\boldsymbol{\xi}|) d\boldsymbol{v}, && (3.2.3)\\
&= \int A \exp(-B|\boldsymbol{\xi}|^2) d\boldsymbol{v}, && (3.2.4)\\
&= A \int_{-\infty}^{+\infty} \exp(-B\xi_x^2) d\xi_x \int_{-\infty}^{+\infty} \exp(-B\xi_y^2) d\xi_y \int_{-\infty}^{+\infty} \exp(-B\xi_z^2) d\xi_z, && (3.2.5)\\
&= A \left(\frac{\pi}{B}\right)^{\frac{3}{2}}. && (3.2.6)
\end{aligned}$$

We now have :

$$f^{\text{eq}}(|\boldsymbol{\xi}|) = \rho \left(\frac{B}{\pi}\right)^{\frac{3}{2}} \exp(-B|\boldsymbol{\xi}|^2). \tag{3.2.7}$$

Then, f^{eq} being symmetric around $\boldsymbol{\xi}$, we can replace $d\boldsymbol{v}$ by $\int_0^{2\pi} d\theta \int_0^{\pi} \sin(\phi) d\phi |\boldsymbol{\xi}|^2 d|\boldsymbol{\xi}| = 2\pi 2 |\boldsymbol{\xi}|^2 d|\boldsymbol{\xi}|$ which yields :

$$\begin{aligned}
p &= \frac{1}{3} \int |\boldsymbol{\xi}|^2 f^{\text{eq}}(|\boldsymbol{\xi}|) 4\pi |\boldsymbol{\xi}|^2 d|\boldsymbol{\xi}|, && (3.2.8)\\
&= \frac{4}{3} \rho \pi \left(\frac{B}{\pi}\right)^{\frac{3}{2}} \underbrace{\int_0^{+\infty} |\boldsymbol{\xi}|^4 \exp(-B|\boldsymbol{\xi}|^2) d|\boldsymbol{\xi}|}_{=\frac{3\sqrt{\pi}}{8B^{5/2}}}, && (3.2.9)\\
&= \frac{\rho}{2B}. && (3.2.10)
\end{aligned}$$

So, we have $B = \frac{\rho}{2p}$ which yields the following expression for the equilibrium distribution :

$$f^{\text{eq}}(|\boldsymbol{\xi}|) = \rho \left(\frac{\rho}{2\pi p}\right)^{3/2} \exp\left(-\frac{\rho}{2p}|\boldsymbol{\xi}|^2\right). \tag{3.2.11}$$

This formula is the Maxwell-Boltzmann distribution[5]. As shown on Fig. 3.2, the Maxwell-Boltzmann distribution describes the distribution of velocities among particles in a gas in equilibrium.

Using Eq. (3.1.15), we could obtain a more common form of the Maxwell-Boltzmann distribution :

$$f^{\text{eq}}(|\boldsymbol{\xi}|) = \rho \left(\frac{m}{2\pi k_B T}\right)^{3/2} \exp\left(-\frac{m}{2k_B T}|\boldsymbol{\xi}|^2\right), \tag{3.2.12}$$

$$f^{\text{eq}}(|\boldsymbol{\xi}|) = \rho \left(\frac{3}{4\pi e}\right)^{3/2} \exp\left(-\frac{3}{4e}|\boldsymbol{\xi}|^2\right). \tag{3.2.13}$$

[4] In the sense that it is natural solution of the Boltzmann Eq. (3.3.7) that will be introduced later.

[5] Another way to find this fundamental distribution is to look for the distribution that cancels the original collision operator of Eq. (3.3.2)

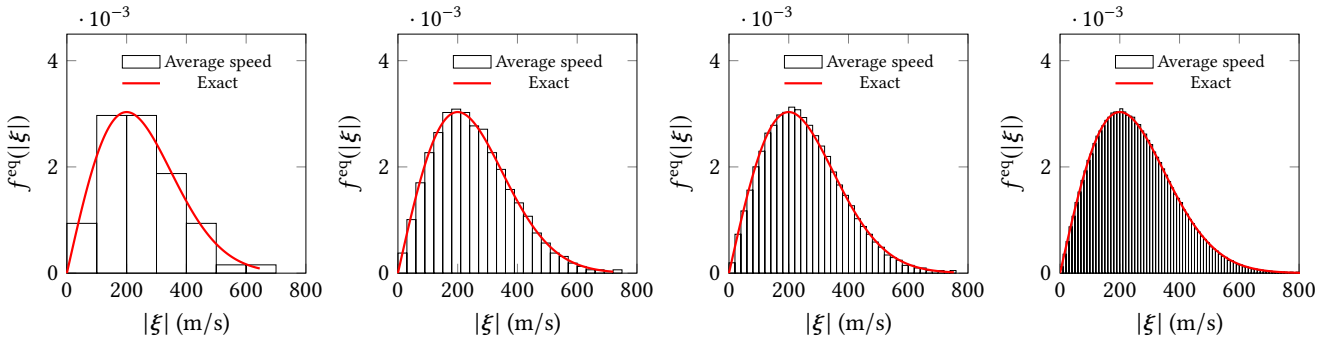

(a) $N = 60$ (b) $N = 500$ (c) $N = 1000$ (d) $N = 5000$

Figure 3.2: Histogram of the average speed distribution over 0.05s for N particles in a 1m × 1m box (random velocity initialization) superposed with the exact value evaluated using Eq. (3.2.11). These plots were obtained during this doctoral work implementing the **SPH-based** approach described in [Simpson 1996].

Note that for an arbitrary number D of dimensions, the above expressions are simply :

$$\boxed{\begin{aligned} f^{\mathrm{eq}}(|\xi|) &= \rho\left(\frac{\rho}{2\pi p}\right)^{D/2}\exp\left(-\frac{\rho}{2p}|\xi|^2\right), && (3.2.14)\\ f^{\mathrm{eq}}(|\xi|) &= \rho\left(\frac{m}{2\pi k_B T}\right)^{D/2}\exp\left(-\frac{m}{2k_B T}|\xi|^2\right), && (3.2.15)\\ f^{\mathrm{eq}}(|\xi|) &= \rho\left(\frac{D}{4\pi e}\right)^{D/2}\exp\left(-\frac{D}{4e}|\xi|^2\right). && (3.2.16)\end{aligned}}$$

In addition, the different moments of the equilibrium distribution are the same as those defined for standard distributions but taken in an equilibrium state. Because we know the expression of f^{eq}, it allows further developments for the equilibrium moments :

$$M_0^{\mathrm{eq}} = \int f^{\mathrm{eq}} d\boldsymbol{v} = \rho, \tag{3.2.17}$$

$$\boldsymbol{M}_1^{\mathrm{eq}} = \int \boldsymbol{v} f^{\mathrm{eq}} d\boldsymbol{v} = \rho\boldsymbol{u}, \tag{3.2.18}$$

$$\boldsymbol{M}_2^{\mathrm{eq}} = \int \boldsymbol{v}\otimes\boldsymbol{v} f^{\mathrm{eq}} d\boldsymbol{v} = \rho\boldsymbol{u}\otimes\boldsymbol{u} - \boldsymbol{\sigma}^{\mathrm{eq}}, \tag{3.2.19}$$

$$\begin{aligned} \boldsymbol{M}_3^{\mathrm{eq}} &= \int \boldsymbol{v}\otimes\boldsymbol{v}\otimes\boldsymbol{v} f^{\mathrm{eq}} d\boldsymbol{v},\\ M_3^{\mathrm{eq}}{}_{abcd} &= \rho u_a u_b u_c + u_a\left(\int \xi_b\xi_c f^{\mathrm{eq}} d\boldsymbol{v}\right) + u_b\left(\int \xi_a\xi_c f^{\mathrm{eq}} d\boldsymbol{v}\right) + u_c\left(\int \xi_a\xi_b f^{\mathrm{eq}} d\boldsymbol{v}\right),\\ M_3^{\mathrm{eq}}{}_{abcd} &= \rho u_a u_b u_c + \rho e\frac{2}{D}(u_a\delta_{bc} + u_b\delta_{ac} + u_c\delta_{ab}), \end{aligned} \tag{3.2.20}$$

$$\boldsymbol{M}_3^{*eq} = \frac{1}{2}\int \boldsymbol{v}|\boldsymbol{v}|^2 f^{\mathrm{eq}} d\boldsymbol{v} = \rho\boldsymbol{u}E - \boldsymbol{\sigma}^{\mathrm{eq}}\cdot\boldsymbol{u} + \boldsymbol{q}^{\mathrm{eq}}, \tag{3.2.21}$$

$$\begin{aligned} \boldsymbol{M}_4^{*eq} &= \int \xi\otimes\xi\otimes\xi\otimes\xi f^{\mathrm{eq}} d\boldsymbol{v},\\ M_4^{*eq}{}_{abcd} &= \rho e^2\frac{4}{D^2}(\delta_{ab}\delta_{cd} + \delta_{ac}\delta_{bd} + \delta_{ad}\delta_{bc}). \end{aligned} \tag{3.2.22}$$

Note that we used technical details about isotropic tensors of order 2 and 4 in the above expressions, see Appendix B.1 for more details.

3.3 Boltzmann Equation

The Boltzmann equation has been introduced by Boltzmann (1844-1906) [Boltzmann 1970] in 1872 and is a fundamental differential equation in gas kinetic theory. It describes the behavior of a gas out of equilibrium following a statistical approach. With $\boldsymbol{x} \in \Omega \subset \mathbb{R}^3$, $\boldsymbol{v} \in \mathbb{R}^3$, $\boldsymbol{a} \in \mathbb{R}^3$ and $\forall t \in \mathbb{R}^+$, it is written as :

$$\boxed{\partial_t f + \boldsymbol{v} \cdot \nabla_{\boldsymbol{x}} f + \boldsymbol{a} \cdot \nabla_{\boldsymbol{v}} f = Q(f, f),} \tag{3.3.1}$$

with Ω a space domain, $\boldsymbol{x}$ the position, $\boldsymbol{v}$ the microscopic velocity and $\boldsymbol{a}$ the acceleration and t the time. f is the particle distribution function (PDF) and is the unknown of the equation.

The fundamental concept brought by this equation is that irreversible macroscopic dynamics (here f is a macroscopic variable because it is collective) can emerge from microscopic reversible dynamics. The acceleration term in the Boltzmann equation corresponds to **the contribution of external forces and will not be considered in the following** i.e. $\boldsymbol{a} = 0$. Nevertheless, it should be taken into account when including gravity effects for example. The velocity term corresponds to the streaming of the particles. The right hand side $Q(f, f)$ of the equation is the collision term.

The original collision operator introduced by Boltzmann was only taking into account binary collisions (one to one collisions) between hard spherical particles. It was also assumed that the collisions were elastic and that the gas was submitted to a molecular chaos (implying that the velocities are not correlated) without external forces. Under these hypothesis, the original collision operator was expressed as a double integral over velocity space :

$$Q(f, f) = \int d\boldsymbol{v} \int B(\Omega)|\boldsymbol{v}_1 - \boldsymbol{v}_2| \left(f(\boldsymbol{v}_1')f(\boldsymbol{v}_2') - f(\boldsymbol{v}_1)f(\boldsymbol{v}_2) \right) d\Omega, \tag{3.3.2}$$

with $d\Omega$ the solid angle where particles are scattered and B the differential cross section of the collision. The prime superscripts denote the quantity after collision (as opposed to before collision without a prime subscript). The subscripts 1 and 2 denote particles 1 and 2 about to collide. We do not go further in explaining this expression that will not be used in the following sections. This formulation was cumbersome and alternatives were sought. A collision operator can have different forms as long as it fulfills certain conditions :

1. It has to conserve mass, momentum and energy (if collisions are elastic which is the case for a monatomic gas).

$$\int Q(f, f) d\boldsymbol{v} = 0, \tag{3.3.3}$$

$$\int \boldsymbol{v} Q(f, f) d\boldsymbol{v} = 0, \tag{3.3.4}$$

$$\int |\boldsymbol{v}|^2 Q(f, f) d\boldsymbol{v} = 0. \tag{3.3.5}$$

2. it has to ensure that the distribution always evolves towards an equilibrium.

In 1954, Bhatnagar, Gross and Krook [Bhatnagar 1954] proposed the BGK collision operator that satisfies the above conditions. It is written as follows :

$$Q(f, f) = -\frac{f(\boldsymbol{x}, \boldsymbol{v}, t) - f^{\mathrm{eq}}(\boldsymbol{x}, \boldsymbol{v}, t)}{\tau}, \tag{3.3.6}$$

with τ the relaxation time for the distribution f to reach its equilibrium f^{eq}. This operator is linear and therefore easy to analyze and implement. It is widely used within the LBM community since its introduction in the field by Qian in 1992 [Qian 1992]. However, this operator imposes that the thermal effects and the viscous effects are of the same magnitude (Prandtl number is one). It is a limitation when it comes to simulate non isothermal flows for example. In the following, we will always consider that the collision operator is the BGK operator, unless otherwise mentioned. Thus, we will work on the following Boltzmann equation :

$$\partial_t f + \boldsymbol{v} \cdot \nabla_{\boldsymbol{x}} f = -\frac{f - f^{\text{eq}}}{\tau}. \tag{3.3.7}$$

We can now use the conditions imposed on $Q(f, f)$ in equations (3.3.3)–(3.3.5) to deduce the conservation of macroscopic quantities. From Eq. (3.3.3), it yields :

$$\int (\partial_t f + \boldsymbol{v} \cdot \nabla_{\boldsymbol{x}} f)\, d\boldsymbol{v} = \int Q(f, f) d\boldsymbol{v} = 0, \tag{3.3.8}$$

$$\partial_t \left(\int f d\boldsymbol{v} \right) + \nabla_{\boldsymbol{x}} \cdot \left(\int \boldsymbol{v} f d\boldsymbol{v} \right) = 0, \tag{3.3.9}$$

$$\partial_t \rho + \nabla_{\boldsymbol{x}} \cdot (\rho \boldsymbol{u}) = 0, \tag{3.3.10}$$

where we have been able to move the derivatives outside the integrals and to commute them with $\boldsymbol{v}$ because t, $\boldsymbol{x}$ and $\boldsymbol{v}$ are independent variables. We recognize the mass conservation equation in Eq. (3.3.10). Similarly for Eq. (3.3.4), we have :

$$\int \boldsymbol{v} (\partial_t f + \boldsymbol{v} \cdot \nabla_{\boldsymbol{x}} f)\, d\boldsymbol{v} = \int \boldsymbol{v} Q(f, f) d\boldsymbol{v} = 0, \tag{3.3.11}$$

$$\partial_t \left(\int \boldsymbol{v} f d\boldsymbol{v} \right) + \nabla_{\boldsymbol{x}} \cdot \left(\int \boldsymbol{v} \otimes \boldsymbol{v} f d\boldsymbol{v} \right) = 0, \tag{3.3.12}$$

$$\partial_t (\rho \boldsymbol{u}) + \nabla_{\boldsymbol{x}} \cdot M_2 = 0, \tag{3.3.13}$$

$$\partial_t (\rho \boldsymbol{u}) + \nabla_{\boldsymbol{x}} \cdot (\rho \boldsymbol{u} \otimes \boldsymbol{u}) = \nabla_{\boldsymbol{x}} \cdot \boldsymbol{\sigma}. \tag{3.3.14}$$

We recognize the momentum conservation equation in Eq. (3.3.14) and it lets us identify $\boldsymbol{\sigma}$ as the Cauchy stress tensor. Finally, using Eq. (3.3.5), we can obtain :

$$\int |\boldsymbol{v}|^2 (\partial_t f + \boldsymbol{v} \cdot \nabla_{\boldsymbol{x}} f)\, d\boldsymbol{v} = \int |\boldsymbol{v}|^2 Q(f, f) d\boldsymbol{v} = 0, \tag{3.3.15}$$

$$\partial_t \left(\int |\boldsymbol{v}|^2 f d\boldsymbol{v} \right) + \nabla_{\boldsymbol{x}} \cdot \left(\int \boldsymbol{v} |\boldsymbol{v}|^2 f d\boldsymbol{v} \right) = 0, \tag{3.3.16}$$

$$\partial_t (\rho E) + \nabla_{\boldsymbol{x}} \cdot \boldsymbol{M}_3^* = 0, \tag{3.3.17}$$

$$\partial_t (\rho E) + \nabla_{\boldsymbol{x}} \cdot (\rho \boldsymbol{u} E) = \nabla_{\boldsymbol{x}} \cdot (\boldsymbol{\sigma} \cdot \boldsymbol{u}) - \nabla_{\boldsymbol{x}} \cdot \boldsymbol{q}. \tag{3.3.18}$$

We recognize the energy conservation equation in Eq. (3.3.18) and it lets us identify $\boldsymbol{q}$ as the heat flux.

From Eqs. (3.3.10)–(3.3.18), it is possible to recover Euler's equations of fluid dynamics by assuming that the distribution is at rest i.e. $f = f^{\text{eq}}$ (where f^{eq} is the Maxwell-Boltzmann distribution of Eq. (3.2.11)). Indeed, the Cauchy stress tensor and the heat flux in an equilibrium state reduce to the following expression :

$$\boldsymbol{\sigma}^{\text{eq}} = -\int \boldsymbol{\xi} \otimes \boldsymbol{\xi} f^{\text{eq}} d\boldsymbol{v} = -p\boldsymbol{I}, \tag{3.3.19}$$

$$\boldsymbol{q}^{\text{eq}} = \frac{1}{2} \int \boldsymbol{\xi} |\boldsymbol{\xi}|^2 f^{\text{eq}} d\boldsymbol{v} = 0. \tag{3.3.20}$$

Therefore, Eqs. (3.3.14) and (3.3.18) become :

$$\partial_t (\rho \boldsymbol{u}) + \nabla_{\boldsymbol{x}} \cdot (\rho \boldsymbol{u} \otimes \boldsymbol{u}) = -\nabla_{\boldsymbol{x}} p, \tag{3.3.21}$$

$$\partial_t (\rho E) + \nabla_{\boldsymbol{x}} \cdot (\rho \boldsymbol{u} E) = -\nabla_{\boldsymbol{x}} \cdot (p \boldsymbol{u}), \tag{3.3.22}$$

which, if combined with Eq. (3.3.10), are Euler's equations.

It will be useful later in this document to gather Euler's equations together and to expand several derivatives :

$$\partial_t \rho + \boldsymbol{u} \cdot \nabla_{\boldsymbol{x}} \rho = -\rho \nabla_{\boldsymbol{x}} \cdot \boldsymbol{u}, \tag{3.3.23}$$

$$\partial_t \boldsymbol{u} + \boldsymbol{u} \cdot \nabla_{\boldsymbol{x}} \boldsymbol{u} = -\frac{\nabla_{\boldsymbol{x}} p}{\rho}, \tag{3.3.24}$$

$$\partial_t e + \boldsymbol{u} \cdot \nabla_{\boldsymbol{x}} e = -\frac{p}{\rho} \nabla_{\boldsymbol{x}} \cdot \boldsymbol{u}. \tag{3.3.25}$$

The last expression seems unusual but is in fact the resultant of the following calculations :

$$\begin{aligned}
\partial_t(\underbrace{\rho E}_{=\rho e + \frac{1}{2}\rho|\boldsymbol{u}|^2 \text{ (3.1.5)}}) + \nabla_{\boldsymbol{x}} \cdot (\underbrace{\rho E}_{=\rho e + \frac{1}{2}\rho|\boldsymbol{u}|^2 \text{ (3.1.5)}} \boldsymbol{u}) &= -\nabla_{\boldsymbol{x}} \cdot (p\boldsymbol{u}), \\
\partial_t \left(\rho e + \frac{1}{2}\rho|\boldsymbol{u}|^2\right) + \nabla_{\boldsymbol{x}} \cdot \left(\boldsymbol{u}\left(\rho e + \frac{1}{2}\rho|\boldsymbol{u}|^2\right)\right) &= -\nabla_{\boldsymbol{x}} \cdot (p\boldsymbol{u}), \\
(\partial_t \rho e + \nabla_{\boldsymbol{x}} \cdot (\rho e \boldsymbol{u})) + \partial_t \left(\frac{1}{2}\rho|\boldsymbol{u}|^2\right) + \nabla_{\boldsymbol{x}} \cdot \left(\frac{1}{2}\rho \boldsymbol{u}|\boldsymbol{u}|^2\right) &= -\nabla_{\boldsymbol{x}} \cdot (p\boldsymbol{u}), \\
(\partial_t \rho e + \nabla_{\boldsymbol{x}} \cdot (\rho e \boldsymbol{u})) + \frac{1}{2}|\boldsymbol{u}|^2 \underbrace{(\partial_t \rho + \nabla_{\boldsymbol{x}} \cdot (\rho \boldsymbol{u}))}_{=0 \text{ (3.3.10)}} + \boldsymbol{u}\, \rho \underbrace{(\partial_t \boldsymbol{u} + \boldsymbol{u} \nabla_{\boldsymbol{x}} \cdot \boldsymbol{u})}_{=-\nabla_{\boldsymbol{x}} p \text{ (3.3.24)}} &= -\nabla_{\boldsymbol{x}} \cdot (p\boldsymbol{u}), \\
(\partial_t \rho e + \nabla_{\boldsymbol{x}} \cdot (\rho e \boldsymbol{u})) - \boldsymbol{u} \nabla_{\boldsymbol{x}} p &= -\nabla_{\boldsymbol{x}} \cdot (p\boldsymbol{u}), \\
\partial_t \rho e + \nabla_{\boldsymbol{x}} \cdot (\rho e \boldsymbol{u}) &= -p \nabla_{\boldsymbol{x}} \cdot \boldsymbol{u}, \\
\partial_t e + \boldsymbol{u} \cdot \nabla_{\boldsymbol{x}} e &= -\frac{p}{\rho} \nabla_{\boldsymbol{x}} \cdot \boldsymbol{u}.
\end{aligned}$$

Let's remark that this last equation can also be interpreted as another way to write a well known thermodynamic identity $dE = -pdV$.

3.4 Chapman-Enskog expansion

In order to find the Euler equations, an equilibrium state has been assumed. However, friction forces (and consequently viscous stresses) are generated by an out-of-equilibrium state. Therefore, an approximate solution of the Boltzmann equation in an out-of-equilibrium state has to be determined to recover the Navier-Stokes equations. In 1916 and 1917, Chapman (1888-1970) [Chapman 1962] and Enskog (1884-1947) [Enskog 1917] proposed a development (well explained in [Viggen 2014]) that allows to derive the Navier-Stokes equations from the Boltzmann equation. It begins by a nondimensionalization of the Boltzmann equation to introduce the Knudsen number K_n. Denoting L_0 the characteristic length, V_0 the characteristic velocity, $T_0 = \frac{L_0}{V_0}$ the characteristic time, L_{mfp} the mean free path between collisions

and $T_{mft} = \frac{L_{mfp}}{V_0}$ the mean free time between collisions, we can write :

$$
\begin{aligned}
t' &= \frac{t}{T_0}, \\
\boldsymbol{x}' &= \frac{\boldsymbol{x}}{L_0}, \\
\boldsymbol{v}' &= \frac{\boldsymbol{v}}{V_0}, \\
\tau' &= \frac{\tau}{T_{mft}}, \\
f' &= \frac{f}{\rho}\left(\frac{k_B T}{m}\right)^{D/2} \quad \text{(from Eq. (3.2.15))}.
\end{aligned}
$$

Inserting these definitions Eq. (3.3.7), it leads to :

$$
\begin{aligned}
\frac{1}{T_0}\rho\cancel{\left(\frac{m}{k_B T}\right)^{D/2}}\partial_{t'} f' + \frac{V_0}{L_0}\rho\cancel{\left(\frac{m}{k_B T}\right)^{D/2}}\boldsymbol{v}' \cdot \nabla_{\boldsymbol{x}'} f' &= -\frac{1}{T_{mft}}\rho\cancel{\left(\frac{m}{k_B T}\right)^{D/2}}\frac{f' - f'^{\text{eq}}}{\tau'}, \\
\frac{\cancel{V_0}}{L_0}\partial_{t'} f' + \frac{\cancel{V_0}}{L_0}\boldsymbol{v}' \cdot \nabla_{\boldsymbol{x}'} f' &= -\frac{\cancel{V_0}}{L_{mft}}\frac{f' - f'^{\text{eq}}}{\tau'}, \\
\frac{L_{mft}}{L_0}\left(\partial_{t'} f' + \boldsymbol{v}' \cdot \nabla_{\boldsymbol{x}'} f'\right) &= -\frac{f' - f'^{\text{eq}}}{\tau'}, \\
K_n\left(\partial_{t'} + \boldsymbol{v}' \cdot \nabla_{\boldsymbol{x}'}\right) f' &= -\frac{f' - f'^{\text{eq}}}{\tau'}.
\end{aligned}
\tag{3.4.1}
$$

K_n is defined as the ratio between the mean free path of a particle and its characteristic length. It is a measure of the continuity of the flow :

- if $K_n \leq 0.01$, the flow is continuous.
- if $0.01 \leq K_n \leq 0.1$, the flow is still continuous but exhibits discontinuities (the so-called Knudsen flow).
- if $K_n \geq 0.1$, the flow is discontinuous (the so-called molecular flow).

For example, the Navier-Stokes equations are based on a continuum hypothesis and are therefore not valid anymore if $K_n > 0.01$. If $K_n \to 0$, the flow goes to equilibrium i.e. $f' \to f'^{\text{eq}}$. Hence, we need to consider the out-of-equilibrium terms to obtain the Navier-Stokes equations. It is then natural to expand the distribution around its equilibrium. It is the Chapman-Enskog expansion. We can write this expansion as follows (dropping the prime superscript as we go back to dimensionalized values) :

$$
\boxed{f = f^{\text{eq}} + f_1 + f_2 + \dots} \tag{3.4.2}
$$

The extra terms f_1, f_2 and so on have an order of magnitude related to the Knudsen number. We do have $f_n = O(K_n^n)$. We consider that all the newly introduced higher order distributions f_1, f_2 and so forth do not contribute to the moments calculation since f and f^{eq} already have the same moments.

Thus, we assume[6] $\forall n \geq 1$:

$$\int f_n d\boldsymbol{v} = 0, \tag{3.4.3}$$

$$\int \boldsymbol{v} f_n d\boldsymbol{v} = 0, \tag{3.4.4}$$

$$\frac{1}{2}\int |\boldsymbol{v}|^2 f_n d\boldsymbol{v} = 0. \tag{3.4.5}$$

To prepare the subsequent calculations, we also need the Cauchy stress tensor and the heat flux expressed under the same form :

$$\boldsymbol{\sigma} = \boldsymbol{\sigma}^{\text{eq}} + \boldsymbol{\sigma}_1 + \boldsymbol{\sigma}_2 + \ldots, \tag{3.4.6}$$

$$\boldsymbol{q} = \boldsymbol{q}^{\text{eq}} + \boldsymbol{q}_1 + \boldsymbol{q}_2 + \ldots, \tag{3.4.7}$$

with $\forall n \geq 1$, $\boldsymbol{\sigma}_n = -\int \boldsymbol{\xi} \otimes \boldsymbol{\xi} f_n d\boldsymbol{v}$ and $\boldsymbol{q}_n = \frac{1}{2}\int \boldsymbol{\xi}|\boldsymbol{\xi}|^2 f_n d\boldsymbol{v}$. The expansion of f is not enough to close the system. To properly do that, it is also needed to expand the time t in function of its relative order of magnitude to K_n as follows :

$$t = t_1 + t_2 + \ldots \tag{3.4.8}$$

$$\partial_t = \partial_{t_1} + \partial_{t_2} + \ldots \tag{3.4.9}$$

We have adopted the same notation for the distribution expansion and for the time expansion. The time expansion is a technique inherited from perturbation theory. Traditionally, t_1 is seen as the time scale related to fast dynamics like advection and t_2 as the time scale related to slow dynamics like diffusion. Note that the subscripts are again related to the order of magnitude of the terms, we still have[7] $t_n = O(K_n^n)$ and $\partial_{t_n} = O(K_n^n)$ for $n \geq 1$. We also need to state that $\nabla_{\boldsymbol{x}} = O(K_n^1)$. Indeed, although fast and slow dynamics occur at different time scale, they occur at the same spatial scale. This will be of **primary importance** when we will need to order the terms in function of their order of magnitude.

Hence, the Boltzmann Eq. (3.3.7) becomes :

$$\left(\partial_{t_1} + \partial_{t_2} + \ldots + \boldsymbol{v}\cdot\nabla_{\boldsymbol{x}}\right)\left(f^{\text{eq}} + f_1 + f_2 + \ldots\right) = -\frac{1}{\tau}\left(f_1 + f_2 + \ldots\right), \tag{3.4.10}$$

We can separate the 1st order terms and the 2nd order terms from Eq. (3.4.10) as follows :

$$1^{\text{st}} \text{ order} : \partial_{t_1} f^{\text{eq}} + \boldsymbol{v}\cdot\nabla_{\boldsymbol{x}} f^{\text{eq}} = -\frac{f_1}{\tau}, \tag{3.4.11}$$

$$2^{\text{nd}} \text{ order} : \partial_{t_2} f^{\text{eq}} + \partial_{t_1} f_1 + \boldsymbol{v}\cdot\nabla_{\boldsymbol{x}} f_1 = -\frac{f_2}{\tau}. \tag{3.4.12}$$

[6]This is a strong assumption as the only natural constraint we have is :

$$\int \Psi(\boldsymbol{v})(f - f^{\text{eq}})d\boldsymbol{v} = 0,$$

$$\int \Psi(\boldsymbol{v})(f_1 + f_2 + \ldots)d\boldsymbol{v} = 0,$$

$$\sum_{n=1}^{\infty}\left[\int \Psi(\boldsymbol{v}) f_n d\boldsymbol{v}\right] = 0,$$

where $\Psi(\boldsymbol{v}) = 1, \boldsymbol{v}, |\boldsymbol{v}|^2$

[7]It makes sense as the term t_0 would vanish because it is an equilibrium term where time does not matter.

Since f_1 does not contribute to the moments of the distribution, one can remark that by taking the 0th moment, 1st moment and 2nd moment of Eq. (3.4.11), we re-obtain Euler's equations (which makes sense since at 0th order, $f = f^{\text{eq}}$) :

$$\partial_{t_1}\rho + \nabla_{\boldsymbol{x}} \cdot (\rho \boldsymbol{u}) = 0, \tag{3.4.13}$$

$$\partial_{t_1}(\rho \boldsymbol{u}) + \nabla_{\boldsymbol{x}} \cdot (\rho \boldsymbol{u} \otimes \boldsymbol{u}) = -\nabla_{\boldsymbol{x}} p, \tag{3.4.14}$$

$$\partial_{t_1}(\rho E) + \nabla_{\boldsymbol{x}} \cdot (\rho \boldsymbol{u} E) = -\nabla_{\boldsymbol{x}} \cdot (p\boldsymbol{u}), \tag{3.4.15}$$

which we can rewrite exactly the same way as equations (3.3.23), (3.3.24) and (3.3.25) :

$$\partial_{t_1}\rho + \boldsymbol{u} \cdot \nabla_{\boldsymbol{x}} \rho = -\rho \nabla_{\boldsymbol{x}} \cdot \boldsymbol{u}, \tag{3.4.16}$$

$$\partial_{t_1}\boldsymbol{u} + \boldsymbol{u} \cdot \nabla_{\boldsymbol{x}} \boldsymbol{u} = -\frac{\nabla_{\boldsymbol{x}} p}{\rho}, \tag{3.4.17}$$

$$\partial_{t_1} e + \boldsymbol{u} \nabla_{\boldsymbol{x}} e = -\frac{p}{\rho} \nabla_{\boldsymbol{x}} \cdot \boldsymbol{u}. \tag{3.4.18}$$

In a similar way, since f_2 does not contribute to the moments of the distribution, by taking the 0th moment, 1st moment and 2nd moment of Eq. (3.4.12), it yields :

$$\partial_{t_2}\rho = 0, \tag{3.4.19}$$

$$\partial_{t_2}(\rho \boldsymbol{u}) = \nabla_{\boldsymbol{x}} \cdot \boldsymbol{\sigma}_1, \tag{3.4.20}$$

$$\partial_{t_2}(\rho E) = \nabla_{\boldsymbol{x}} \cdot (\boldsymbol{\sigma}_1 \cdot \boldsymbol{u}) + \nabla_{\boldsymbol{x}} \cdot \boldsymbol{q}_1. \tag{3.4.21}$$

In order to recover the Navier-Stokes equations from the above equations, we need to compute the first order perturbed moments $\boldsymbol{\sigma}_1$ and $\boldsymbol{q}_1$ and therefore f_1. The only unknown in Eq. (3.4.11) is f_1 and the goal of the following calculations is to evaluate it. Dividing by f^{eq} and using the properties of ln, we get :

$$\begin{aligned} -\frac{\tau}{f^{\text{eq}}}\left(\partial_{t_1} f^{\text{eq}} + \boldsymbol{v} \cdot \nabla_{\boldsymbol{x}} f^{\text{eq}}\right) &= \frac{f_1}{f^{\text{eq}}}, \\ -\tau\left(\partial_{t_1} \ln(f^{\text{eq}}) + \boldsymbol{v} \cdot \nabla_{\boldsymbol{x}} \ln(f^{\text{eq}})\right) &= \frac{f_1}{f^{\text{eq}}}. \end{aligned} \tag{3.4.22}$$

According to Eq. (3.2.16), we have :

$$\ln(f^{\text{eq}}) = \ln(\rho) + \frac{D}{2}\ln\left(\frac{D}{4\pi}\right) - \frac{D}{2}\ln(e) - \frac{D}{4e}|\boldsymbol{\xi}|^2. \tag{3.4.23}$$

We can now compute the time derivative using a chain rule :

$$\begin{aligned} \partial_{t_1} \ln(f^{\text{eq}}) &= \partial_\rho \ln(f^{\text{eq}})\partial_{t_1}\rho + \nabla_{\boldsymbol{u}} \ln(f^{\text{eq}}) \cdot \partial_{t_1}\boldsymbol{u} + \partial_e \ln(f^{\text{eq}})\partial_{t_1} e, \\ &= \frac{1}{\rho}\partial_{t_1}\rho + \frac{D\boldsymbol{\xi}}{2e} \cdot \partial_{t_1}\boldsymbol{u} + \left(-\frac{D}{2e} + \frac{D}{4e^2}|\boldsymbol{\xi}|^2\right)\partial_{t_1} e. \end{aligned} \tag{3.4.24}$$

Th same approach gives us the spatial derivative :

$$\begin{aligned} \nabla_{\boldsymbol{x}} \ln(f^{\text{eq}}) &= \partial_\rho \ln(f^{\text{eq}})\nabla_{\boldsymbol{x}}\rho + \nabla_{\boldsymbol{u}} \ln(f^{\text{eq}}) \cdot \nabla_{\boldsymbol{x}}\boldsymbol{u} + \partial_e \ln(f^{\text{eq}})\nabla_{\boldsymbol{x}} e, \\ &= \frac{1}{\rho}\nabla_{\boldsymbol{x}}\rho + \frac{D\boldsymbol{\xi}}{2e} \cdot \nabla_{\boldsymbol{x}}\boldsymbol{u} + \left(-\frac{D}{2e} + \frac{D}{4e^2}|\boldsymbol{\xi}|^2\right)\nabla_{\boldsymbol{x}} e. \end{aligned} \tag{3.4.25}$$

We can now insert equations (3.4.24) and (3.4.25) into Eq. (3.4.22) leading to :

$$-\frac{f_1}{\tau f^{\text{eq}}} = \frac{D}{2e}(\xi \otimes \xi)\boldsymbol{S} + \frac{\xi}{e}\nabla_{\boldsymbol{x}} e\left(\frac{D|\xi|^2}{4e} - \frac{D}{2} - 1\right),$$

where we have introduced the well known deviatoric strain tensor $\boldsymbol{S} = \frac{1}{2}(\nabla_{\boldsymbol{x}}\boldsymbol{u} + \nabla_{\boldsymbol{x}}\boldsymbol{u}^T) - \frac{1}{D}\operatorname{Tr}(\nabla_{\boldsymbol{x}}\boldsymbol{u})\boldsymbol{I}$. The technical development has been omitted for clarity but can be found in Appendix B.2. Finally, we have :

$$f_1 = -\tau f^{\text{eq}}\left(\frac{D}{2e}(\xi \otimes \xi)\boldsymbol{S} + \frac{\xi}{e}\nabla_{\boldsymbol{x}} e\left(\frac{D|\xi|^2}{4e} - \frac{D}{2} - 1\right)\right). \tag{3.4.26}$$

It is now possible to compute the first order perturbed moments $\boldsymbol{\sigma}_1$ and $\boldsymbol{q}_1$.

$$\begin{aligned}\boldsymbol{\sigma}_1 &= -\int \xi \otimes \xi f_1 d\boldsymbol{v},\\ &= p\tau(\nabla_{\boldsymbol{x}}\boldsymbol{u} + \nabla_{\boldsymbol{x}}\boldsymbol{u}^T - \frac{2}{D}\operatorname{Tr}(\nabla_{\boldsymbol{x}}\boldsymbol{u})\boldsymbol{I}),\\ &= \boldsymbol{\tau}.\end{aligned} \tag{3.4.27}$$

We immediately recognize the deviatoric stress tensor $\boldsymbol{\tau}$ with a shear viscosity $\mu = p\tau = \frac{2}{D}\rho e\tau$ and a bulk viscosity $\mu_B = 0$. In a similar way, for $\boldsymbol{q}_1$, we have :

$$\begin{aligned}\boldsymbol{q}_1 &= \frac{1}{2}\int \xi|\xi|^2 f_1 d\boldsymbol{v},\\ &= -\frac{D+2}{D}\rho e\tau\frac{k_B}{m}\nabla_{\boldsymbol{x}} T,\\ &= -\kappa\nabla_{\boldsymbol{x}} T,\end{aligned} \tag{3.4.28}$$

where we used the ideal gas equation of state (3.1.19) to make the temperature gradient appear which led to the introduction of the thermal conductivity $\kappa = \frac{D+2}{D}\rho e\tau\frac{k_B}{m}$. The mathematical details of the calculation of $\boldsymbol{\sigma}_1$ and $\boldsymbol{q}_1$ have been omitted for clarity but can be found in Appendix B.3 and B.4. Now that we have the values of $\boldsymbol{\sigma}_1 = \boldsymbol{\tau}$ and $\boldsymbol{q}_1 = -\kappa\nabla_{\boldsymbol{x}} T$, we can insert them into Eqs. (3.4.20) and (3.4.21) and perform the following operations :

$$\begin{aligned}&(3.4.16) + (3.4.19),\\ &(3.4.17) + (3.4.20),\\ &(3.4.18) + (3.4.21).\end{aligned}$$

It finally yields the full formulation of the Navier-Stokes equations :

$$\boxed{\begin{aligned}\partial_t\rho + \nabla_{\boldsymbol{x}}\cdot(\rho\boldsymbol{u}) &= 0,\\ \partial_t(\rho\boldsymbol{u}) + \nabla_{\boldsymbol{x}}\cdot(\rho\boldsymbol{u}\otimes\boldsymbol{u}) &= -\nabla_{\boldsymbol{x}} p + \nabla_{\boldsymbol{x}}\cdot\boldsymbol{\tau},\\ \partial_t(\rho E) + \nabla_{\boldsymbol{x}}\cdot(\rho\boldsymbol{u}E) &= \nabla_{\boldsymbol{x}}\cdot(\boldsymbol{\sigma}\cdot\boldsymbol{u}) + \nabla_{\boldsymbol{x}}\cdot(\kappa\nabla_{\boldsymbol{x}} T),\end{aligned}} \tag{3.4.29}$$

where we have set the following parameters : shear viscosity $\mu = \frac{2}{D}\rho e\tau$, bulk viscosity $\mu_B = 0$ and thermal conductivity $\kappa = \frac{D+2}{D}\rho e\tau\frac{k_B}{m}$. It has to be emphasized that the values of these parameters depend on the collision operator (BGK in this case) and on the assumption that the gas is monatomic. A well-known disadvantage of the BGK operator for non-isothermal gases is that it enforces that the Prandtl number Pr is one. Indeed, using Eq. (3.1.21) and the aforementioned expressions for κ and μ, we have :

$$Pr = \frac{c_p\mu}{\kappa} = \frac{\frac{D+2}{2}\cancel{\frac{k_B}{m}}\frac{2}{D}\cancel{\rho e\tau}}{\frac{D+2}{D}\cancel{\rho e\tau}\cancel{\frac{k_B}{m}}} = 1. \tag{3.4.30}$$

This value is inherent with the BGK operator. For example, using the original collision operator of Eq. (3.3.2), $Pr = 2/3$. We have performed the Chapman-Enskog expansion up to $O(K_n^2)$ which is enough to recover the Navier-Stokes equations. However, it is possible to go further to higher orders leading to what are called Burnett models. In practice for low K_n, the difference is negligible. We also have to add that it is possible to recover the Navier-Stokes equations without using a Chapman-Enskog expansion. See for example in [Landau 1990] or in Sect. 3.5.3 of [Violeau 2012].

3.5 $\mathcal{H}$-Theorem

In 1872, Boltzmann [Boltzmann 1970] showed that when a given gas relaxes towards an equilibrium state, a quantity $\mathcal{H}$ decreases monotonically with time. Indeed, if one considers the following quantity :

$$\mathcal{H}(f(\boldsymbol{x}, \boldsymbol{v}, t)) = \int_{\Omega\times\mathbb{R}^3} f(\boldsymbol{x}, \boldsymbol{v}, t) \ln(f(\boldsymbol{x}, \boldsymbol{v}, t)) d^3x d^3v. \tag{3.5.1}$$

The $\mathcal{H}$ theorem claims that :

$$\frac{d\mathcal{H}}{dt} \leq 0. \tag{3.5.2}$$

Assuming that $f > 0$, it is clear that the function $f \mapsto f \ln(f)$ is convex because its second derivative is strictly positive. Hence, $\mathcal{H}(f)$ admits a minimum f^{eq}. This thermodynamic equilibrium is defined by the Maxwell-Boltzmann distribution of Eq. (3.2.14). It was demonstrated in 1973 [Lanford 1975] that the Boltzmann equation yields the $\mathcal{H}$-theorem. The connection of the $\mathcal{H}$-theorem with entropy and the second law of thermodynamics is obvious. Indeed, according to this law, the entropy of an isolated system can only grow with time and is therefore proportional to $-\mathcal{H}$. During this thesis, we have briefly explored some entropic considerations about the BGK operator for advection-diffusion equations. This work is presented in Appendix C.

3.6 Discretization

3.6.1 Velocity space discretization

The direct numerical resolution of the Boltzmann equation is costly. Indeed, in 3D, the equation has 7 dimensions. To overcome that issue and simplify the resolution, the velocity space is reduced to a set of discrete velocities. The number and the direction of these discrete velocities is not free. The goal is still to be able to recover the hydrodynamic behavior of the flow while minimizing the number discrete velocities to facilitate the numerical resolution. The most used networks are composed of 3 velocities in 1D, 9 velocities in 2D and 19 velocities in 3D. They are denoted D1Q3, D2Q9 and D3Q19 and are shown on Figure 3.3. The notation DmQn (m dimensions, n velocities) is standard within the LBM community.

Let $\mathcal{L}$ be the lattice of discrete velocities and n its cardinal. $\forall i \in \{0 \ldots (n-1)\}$, let $\boldsymbol{v}_i \in \mathcal{L}$ be a discrete velocity and $f_i(\boldsymbol{x}, t) = f(\boldsymbol{x}, \boldsymbol{v}_i, t)$ the corresponding discrete distribution. With $\forall x \in \Omega, \forall i \in 0 \ldots (n-1)$ and $\forall t \in \mathbb{R}^+$, the Boltzmann equation then becomes :

$$\partial_t f_i(\boldsymbol{x}, t) + \boldsymbol{v}_i \cdot \nabla \boldsymbol{x} f_i(\boldsymbol{x}, t) = Q(f_i, f_i). \tag{3.6.1}$$

Using the BGK operator, it can be rewritten as :

$$\boxed{\partial_t f_i(\boldsymbol{x}, t) + \boldsymbol{v}_i \cdot \nabla \boldsymbol{x} f_i(\boldsymbol{x}, t) = -\frac{f_i(\boldsymbol{x}, t) - f_i^{\text{eq}}(\boldsymbol{x}, t)}{\tau}.} \tag{3.6.2}$$

This equation is the (velocity) discretized Boltzmann equation. We now need to calculate the discretized equilibrium distribution f_i^{eq}.

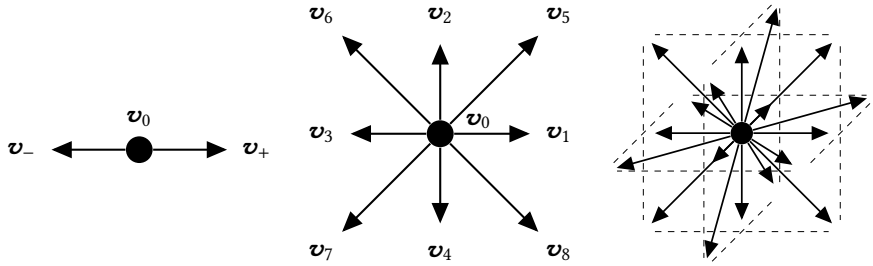

(a) D1Q3 (b) D2Q9 (c) D3Q19 (3×D2Q9)

Figure 3.3: Classic lattices

3.6.2 Discrete equilibrium

The thermodynamic equilibrium distribution f^{eq} is the Maxwell-Boltzmann distribution. However, one needs the discretized version f_i^{eq} in order to develop a numerical scheme.

$$
\begin{aligned}
f^{\mathrm{eq}}(\boldsymbol{x},\boldsymbol{v},t) &= \rho\left(\frac{m}{2\pi k_B T}\right)^{D/2}\exp\left(-\frac{m}{2k_BT}|\boldsymbol{v}-\boldsymbol{u}|^2\right),\\
&= \rho\left(\frac{m}{2\pi k_B T}\right)^{D/2}\exp\left(-\frac{m}{2k_BT}|\boldsymbol{v}|^2\right)\exp\left(\frac{m}{2k_BT}(2\boldsymbol{v}\cdot\boldsymbol{u}-|\boldsymbol{u}|^2)\right),\\
&= \rho\left(\frac{m}{2\pi k_B T}\right)^{D/2}\exp\left(-\frac{m}{2k_BT}|\boldsymbol{v}|^2\right)\left[1+\frac{m(\boldsymbol{v}\cdot\boldsymbol{u})}{k_BT}+\frac{m^2(\boldsymbol{v}\cdot\boldsymbol{u})^2}{2k_B^2T^2}-\frac{m|\boldsymbol{u}|^2}{2k_BT}\right]+O(\boldsymbol{u}^3),\\
&= \rho\left(\frac{1}{2\pi c_s^2}\right)^{D/2}\exp\left(-\frac{1}{2c_s^2}|\boldsymbol{v}|^2\right)\left[1+\frac{(\boldsymbol{v}\cdot\boldsymbol{u})}{c_s^2}+\frac{(\boldsymbol{v}\cdot\boldsymbol{u})^2}{2c_s^4}-\frac{|\boldsymbol{u}|^2}{2c_s^2}\right]+O(\boldsymbol{u}^3),\\
&= \rho w(D)\left[1+\frac{(\boldsymbol{v}\cdot\boldsymbol{u})}{c_s^2}+\frac{(\boldsymbol{v}\cdot\boldsymbol{u})^2}{2c_s^4}-\frac{|\boldsymbol{u}|^2}{2c_s^2}\right]+O(\boldsymbol{u}^3),
\end{aligned}
$$

where the speed of sound c_s has been introduced. In the case of an isothermal, ideal gas, the equation of state is $p=\frac{\rho k_B T}{m}$ (Eq. (3.1.15)) so the speed of sound is given by :

$$
c_s^2=\frac{\partial p}{\partial \rho}=\frac{k_BT}{m}. \tag{3.6.3}
$$

The equation of state becomes $p=\rho c_s^2$. In addition, the weights $w(D)$ are defined as :

$$
w(D)=\exp\left(-\frac{|\boldsymbol{v}|^2}{2c_s^2}\right)/\left(2\pi c_s^2\right)^{D/2}. \tag{3.6.4}
$$

They depend on the choice of lattice $\mathcal{L}$ and their values are given in Tab. 3.1[8]. Truncating at order 2,

i	0	1	2
$\boldsymbol{v}_i$	(0)	(1)	(-1)
w_i	2/3	1/6	1/6

D1Q3 ($c_s = 1/\sqrt{3}$)

i	0	1,2,3,4	5,6,7,8
$\boldsymbol{v}_i$	(0,0)	(0,±1) (±1,0)	(±1,±1)
w_i	4/9	1/9	1/36

D2Q9 ($c_s = 1/\sqrt{3}$)

i	0	1-6	7-18
$\boldsymbol{v}_i$	(0,0,0)	(±1,0,0) (0,±1,0) (0,0,±1)	(0,±1,±1) (±1,0,±1) (±1,±1,0)
w_i	1/3	1/18	1/36

D3Q19 ($c_s = 1/\sqrt{3}$)

Table 3.1: Velocity sets and corresponding weight values for classic lattices

the discretized equilibrium distribution is $\forall i \in \{0 \dots (n-1)\}$:

$$f_i^{\text{eq}} = \rho w_i(D) \left[1 + \frac{(\boldsymbol{v}_i \cdot \boldsymbol{u})}{c_s^2} + \frac{(\boldsymbol{v}_i \cdot \boldsymbol{u})^2}{2c_s^4} - \frac{|\boldsymbol{u}|^2}{2c_s^2} \right]. \tag{3.6.6}$$

The discretized equilibrium distributions f_i^{eq} that we have just calculated in Eq. (3.6.6) also have discretized moments (denoted with a hat $\hat{M}$) that must be equal to the continuous ones in order to recover the hydrodynamics. This is necessary to be able to find the Navier-Stokes equations from the discretized distributions. It yields :

$$\hat{M}_0^{\text{eq}} = \sum_{i=0}^{n-1} f_i^{\text{eq}} = M_0^{\text{eq}} = \rho, \tag{3.6.7}$$

$$\hat{\boldsymbol{M}}_1^{\text{eq}} = \sum_{i=0}^{n-1} \boldsymbol{v}_i f_i^{\text{eq}} = \boldsymbol{M}_1^{\text{eq}} = \rho \boldsymbol{u}, \tag{3.6.8}$$

$$\hat{\boldsymbol{M}}_2^{\text{eq}} = \sum_{i=0}^{n-1} \boldsymbol{v}_i \otimes \boldsymbol{v}_i f_i^{\text{eq}} = \boldsymbol{M}_2^{\text{eq}} = \rho \boldsymbol{u} \otimes \boldsymbol{u} + p\boldsymbol{I} = \rho \boldsymbol{u} \otimes \boldsymbol{u} + \rho c_s^2 \boldsymbol{I}, \tag{3.6.9}$$

$$\hat{\boldsymbol{M}}_3^{\text{eq}} = \sum_{i=0}^{n-1} \boldsymbol{v}_i \otimes \boldsymbol{v}_i \otimes \boldsymbol{v}_i f_i^{\text{eq}} = \boldsymbol{M}_3^{\text{eq}} = \rho u_a u_b u_c + \rho c_s^2 (u_a \delta_{bc} + u_b \delta_{ac} + u_c \delta_{ab}), \tag{3.6.10}$$

where we have use the isothermal equation of state $p = \rho c_s^2$. Note that Eq. (3.6.9) implies $p\boldsymbol{I} = \sum_{i=0}^{n-1} \boldsymbol{\xi}_i \otimes \boldsymbol{\xi}_i f_i^{\text{eq}}$. Inserting Eq. (3.6.6) into Eq. (3.6.7), it yields :

$$\begin{aligned} \sum_{i=0}^{n-1} f_i^{\text{eq}} &= \rho \left(\sum_{i=0}^{n-1} w_i(D) + \frac{\boldsymbol{u}}{c_s^2} \cdot \sum_{i=0}^{n-1} w_i(D) \boldsymbol{v}_i + \frac{\boldsymbol{u} \otimes \boldsymbol{u}}{2c_s^2} : \left(\frac{1}{c_s^2} \sum_{i=0}^{n-1} w_i(D) \boldsymbol{v}_i \otimes \boldsymbol{v}_i - \boldsymbol{I} \sum_{i=0}^{n-1} w_i(D) \right) \right), \\ &= \rho. \end{aligned}$$

[8]There are two ways to compute these values. The first one is to work at the continuous level and to enforce the three distribution moments. Neglecting the 3rd order terms, it yields :

$$\int \psi(\boldsymbol{v}) f^{\text{eq}} d\boldsymbol{v} \approx \rho \int \psi(\boldsymbol{v}) w(D) \left[1 + \frac{(\boldsymbol{v} \cdot \boldsymbol{u})}{c_s^2} + \frac{(\boldsymbol{v} \cdot \boldsymbol{u})^2}{2c_s^4} - \frac{|\boldsymbol{u}|^2}{2c_s^2} \right], \tag{3.6.5}$$

where $\psi(\boldsymbol{v}) = 1, \boldsymbol{v}, \boldsymbol{v} \otimes \boldsymbol{v}, \boldsymbol{v} \otimes \boldsymbol{v} \otimes \boldsymbol{v}$. It leads to pseudo-Gaussian integrals that can be evaluated through a Gauss-Hermite quadrature. On the other hand, it is also possible to enforce the moments on the discretized equilibrium distribution as shown in the document.

The above is only true if the following three conditions are satisfied :

$$\sum_{i=0}^{n-1} w_i(D) = 1, \tag{3.6.11}$$

$$\sum_{i=0}^{n-1} \boldsymbol{v}_i w_i(D) = 0, \tag{3.6.12}$$

$$\sum_{i=0}^{n-1} \boldsymbol{v}_i \otimes \boldsymbol{v}_i w_i(D) = c_s^2 \boldsymbol{I}. \tag{3.6.13}$$

Similarly, Eq. (3.6.8) leads to :

$$\begin{aligned}\sum_{i=0}^{n-1} \boldsymbol{v}_i f_i^{\mathrm{eq}} &= \rho \left(\underbrace{\frac{\boldsymbol{u}}{c_s^2} \cdot \sum_{i=0}^{n-1} w_i(D) \boldsymbol{v}_i \otimes \boldsymbol{v}_i}_{=\boldsymbol{u}} + \left(1 - \frac{|\boldsymbol{u}|^2}{2c_s^2}\right) \underbrace{\sum_{i=0}^{n-1} w_i(D) \boldsymbol{v}_i}_{=0} + \frac{\boldsymbol{u} \otimes \boldsymbol{u}}{2c_s^4} \sum_{i=0}^{n-1} w_i(D) \boldsymbol{v}_i \otimes \boldsymbol{v}_i \otimes \boldsymbol{v}_i \right), \\ &= \rho \boldsymbol{u}.\end{aligned}$$

The above is only true if the following condition is satisfied :

$$\sum_{i=0}^{n-1} w_i(D) \boldsymbol{v}_i \otimes \boldsymbol{v}_i \otimes \boldsymbol{v}_i = 0. \tag{3.6.14}$$

Eq. (3.6.9) leads to :

$$\begin{aligned}\sum_{i=0}^{n-1} \boldsymbol{v}_i \otimes \boldsymbol{v}_i f_i^{\mathrm{eq}} &= \rho \left(\left(1 - \frac{|\boldsymbol{u}|^2}{2c_s^2}\right) \underbrace{\sum_{i=0}^{n-1} \boldsymbol{v}_i \otimes \boldsymbol{v}_i w_i(D)}_{=c_s^2 \boldsymbol{I}} + \frac{\boldsymbol{u}}{c_s^2} \underbrace{\sum_{i=0}^{n-1} w_i(D) \boldsymbol{v}_i \otimes \boldsymbol{v}_i \otimes \boldsymbol{v}_i}_{=0} + \frac{\boldsymbol{u} \otimes \boldsymbol{u}}{2c_s^4} \sum_{i=0}^{n-1} w_i(D) \boldsymbol{v}_i \otimes \boldsymbol{v}_i \otimes \boldsymbol{v}_i \otimes \boldsymbol{v}_i \right), \\ &= \rho \boldsymbol{u} \otimes \boldsymbol{u} + p \boldsymbol{I}.\end{aligned}$$

The above is only true if the following condition is satisfied (expressed using index notation for convenience due to the presence of a 4th order tensor) :

$$\sum_{i=0}^{n-1} \boldsymbol{v}_{ia} \boldsymbol{v}_{ib} \boldsymbol{v}_{ic} \boldsymbol{v}_{id} w_i(D) = c_s^4 (\delta_{ab}\delta_{cd} + \delta_{ac}\delta_{bd} + \delta_{ad}\delta_{bc}). \tag{3.6.15}$$

Eq. (3.6.10) leads to :

$$\begin{aligned}\sum_{i=0}^{n-1} \boldsymbol{v}_i \otimes \boldsymbol{v}_i \otimes \boldsymbol{v}_i f_i^{\mathrm{eq}} &= \rho \Bigg(\left(1 - \frac{|\boldsymbol{u}|^2}{2c_s^2}\right) \underbrace{\sum_{i=0}^{n-1} w_i(D) \boldsymbol{v}_i \otimes \boldsymbol{v}_i \otimes \boldsymbol{v}_i}_{=0} + \frac{\boldsymbol{u}}{c_s^2} \underbrace{\sum_{i=0}^{n-1} w_i(D) \boldsymbol{v}_i \otimes \boldsymbol{v}_i \otimes \boldsymbol{v}_i \otimes \boldsymbol{v}_i}_{=c_s^4(\delta_{ab}\delta_{cd}+\delta_{ac}\delta_{bd}+\delta_{ad}\delta_{bc})}, \\ &\quad + \frac{\boldsymbol{u} \otimes \boldsymbol{u}}{2c_s^4} \sum_{i=0}^{n-1} w_i(D) \boldsymbol{v}_i \otimes \boldsymbol{v}_i \otimes \boldsymbol{v}_i \otimes \boldsymbol{v}_i \otimes \boldsymbol{v}_i \Bigg), \\ &= \frac{\boldsymbol{u} \otimes \boldsymbol{u}}{2c_s^4} \sum_{i=0}^{n-1} w_i(D) \boldsymbol{v}_i \otimes \boldsymbol{v}_i \otimes \boldsymbol{v}_i \otimes \boldsymbol{v}_i \otimes \boldsymbol{v}_i + \rho c_s^2 (u_a \delta_{bc} + u_b \delta_{ac} + u_c \delta_{ab}), \\ &= \rho u_a u_b u_c + \rho c_s^2 (u_a \delta_{bc} + u_b \delta_{ac} + u_c \delta_{ab}).\end{aligned}$$

The above equation is almost true if :

$$\sum_{i=0}^{n-1} w_i(D) \boldsymbol{v}_i \otimes \boldsymbol{v}_i \otimes \boldsymbol{v}_i \otimes \boldsymbol{v}_i \otimes \boldsymbol{v}_i = 0. \tag{3.6.16}$$

Nevertheless, Eq. (3.6.6) does not feature any $\boldsymbol{u}^3$ term because we truncated it at $O(\boldsymbol{u}^3)$, therefore we cannot exactly reproduce $\boldsymbol{M}_3^{\mathrm{eq}}$ (the term $\rho u_a u_b u_c$ will be missing). In consequence, equation (3.6.10) becomes :

$$\hat{\boldsymbol{M}}_3^{\mathrm{eq}} = \sum_{i=0}^{n-1} \boldsymbol{v}_i \otimes \boldsymbol{v}_i \otimes \boldsymbol{v}_i f_i^{\mathrm{eq}} = \rho c_s^2 (u_a \delta_{bc} + u_b \delta_{ac} + u_c \delta_{ab}), \text{ which is } \neq \boldsymbol{M}_3^{\mathrm{eq}}. \tag{3.6.17}$$

The truncation of f_i^{eq} at $O(\boldsymbol{u}^3)$ may seem arbitrary but is in fact a way to limit the number of conditions we obtain. In the end, we have the following constraints on the weights $w_i(D)$:

$$\boxed{\begin{aligned}&\sum_{i=0}^{n-1} w_i(D) = 1, \\ &\sum_{i=0}^{n-1} \boldsymbol{v}_i w_i(D) = 0, \\ &\sum_{i=0}^{n-1} \boldsymbol{v}_i \otimes \boldsymbol{v}_i w_i(D) = c_s^2 \boldsymbol{I}, \\ &\sum_{i=0}^{n-1} w_i(D) \boldsymbol{v}_i \otimes \boldsymbol{v}_i \otimes \boldsymbol{v}_i = 0, \\ &\sum_{i=0}^{n-1} \boldsymbol{v}_{ia} \boldsymbol{v}_{ib} \boldsymbol{v}_{ic} \boldsymbol{v}_{id} w_i(D) = c_s^4 (\delta_{ab}\delta_{cd} + \delta_{ac}\delta_{bd} + \delta_{ad}\delta_{bc}), \\ &\sum_{i=0}^{n-1} w_i(D) \boldsymbol{v}_i \otimes \boldsymbol{v}_i \otimes \boldsymbol{v}_i \otimes \boldsymbol{v}_i \otimes \boldsymbol{v}_i = 0.\end{aligned}} \tag{3.6.18}$$

For example for a D3Q19 lattice shown on Figure 3.3, the discrete velocities are given in Tab. 3.1. For symmetry reasons, we have :

$$\begin{cases} w_1 = w_2 = w_3 = w_4 = w_5 = w_6 (= w_{1-6}), \\ w_7 = w_8 = w_9 = w_{10} = w_{11} = w_{12} = w_{13} = w_{14} = w_{15} = w_{16} = w_{17} = w_{18} (= w_{7-18}). \end{cases} \tag{3.6.19}$$

The symmetry condition can also be found through the zero conditions of Eq. (3.6.18). On the other hand, the non-zero conditions can be expressed as :

$$\begin{cases} w_0 + 6w_{1-6} + 12w_{7-18} = 1, \\ 2w_{1-6} + 8w_{7-18} = c_s^2, \\ 4w_{7-18} = c_s^4, \\ 2w_{1-6} + 8w_{7-18} = 3c_s^4. \end{cases} \tag{3.6.20}$$

The solution[9] of this system of four equations with four unknowns is :

$$\begin{cases} w_0 = 1/3, \\ w_{1-6} = 1/18, \\ w_{7-18} = 1/36, \\ c_s = 1/\sqrt{3}. \end{cases} \tag{3.6.22}$$

3.6.3 Discrete Chapman-Enskog expansion

Looking at Eq. (3.6.2), we now have a (velocity) discretized lattice Boltzmann equation fully clarified since we have just calculated f_i^{eq}. Using the same approach as Sect. 3.4, we still need to verify that we are able to recover the Navier-Stokes equations from Eq. (3.6.2). In addition, because we used the isothermal equation of state to introduce the speed of sound in Eq. (3.6.3), we will place ourselves in the case of an isothermal fluid which implies no energy conservation equation. We recall that we have enforced the values of the discretized equilibrium moments to be the same as the continuous equilibrium moments in order to be able to recover the hydrodynamics in the previous section. Due to the truncation of f_i^{eq} at $O(\boldsymbol{u}^3)$, we were able to exactly reproduce M_0^{eq}, M_1^{eq}, M_2^{eq} but not M_3^{eq}. Thus, we have :

$$\hat{M}_0 = \sum_{i=0}^{n-1} f_i = M_0 = \rho, \tag{3.6.23}$$

$$\hat{\boldsymbol{M}}_1 = \sum_{i=0}^{n-1} \boldsymbol{v}_i f_i = \boldsymbol{M}_1 = \rho \boldsymbol{u}, \tag{3.6.24}$$

$$\hat{\boldsymbol{M}}_2 = \sum_{i=0}^{n-1} \boldsymbol{v}_i \otimes \boldsymbol{v}_i f_i = \boldsymbol{M}_2 = \rho \boldsymbol{u} \otimes \boldsymbol{u} + \hat{\boldsymbol{\sigma}}, \tag{3.6.25}$$

$$\hat{\boldsymbol{M}}_3 = \sum_{i=0}^{n-1} \boldsymbol{v}_i \otimes \boldsymbol{v}_i \otimes \boldsymbol{v}_i f_i = \rho c_s^2 (u_a \delta_{bc} + u_b \delta_{ac} + u_c \delta_{ab}), \tag{3.6.26}$$

$$\tag{3.6.27}$$

[9]Note that, rigorously, we haven't set (yet) $\Delta x = \Delta t = 1$ so that instead of ones, the velocity vectors should be populated with $\frac{\Delta x}{\Delta t}$ leading to the following solution :

$$\begin{cases} w_0 = 1/3, \\ w_{1-6} = 1/18, \\ w_{7-18} = 1/36, \\ c_s = \Delta x / \left(\Delta t \sqrt{3}\right). \end{cases} . \tag{3.6.21}$$

where we have set $\hat{\boldsymbol{\sigma}} = -\sum_{i=0}^{n-1} \boldsymbol{\xi}_i \otimes \boldsymbol{\xi}_i f_i$. The expansion in function of $O(K_n^n)$ is the same as in Sect. 3.4 :

$$\begin{aligned} f_i &= f_i^{\text{eq}} + f_{i1} + f_{i2} + \dots \\ t &= t_1 + t_2 + \dots \\ \partial_t &= \partial_{t_1} + \partial_{t_2} + \dots \\ \hat{\boldsymbol{\sigma}} &= \hat{\boldsymbol{\sigma}}^{\text{eq}} + \hat{\boldsymbol{\sigma}}_1 + \dots \end{aligned} \tag{3.6.28}$$

where we remind that $\hat{\boldsymbol{\sigma}}^{\text{eq}} = p\boldsymbol{I} = \rho c_s^2 \boldsymbol{I} = \sum_{i=0}^{n-1} \boldsymbol{\xi}_i \otimes \boldsymbol{\xi}_i f_i^{\text{eq}}$. In addition, we still have :

$$\begin{aligned} f_n &= O(K_n^n), \forall n \geq 1, \\ t_n &= O(K_n^n), \forall n \geq 1, \\ \partial_{t_n} &= O(K_n^n), \forall n \geq 1, \\ \nabla_{\boldsymbol{x}} &= O(K_n^1). \end{aligned} \tag{3.6.29}$$

Moreover, we have like in the continuous case, $\forall n \geq 1$:

$$\sum_{i=0}^{n-1} f_{in} = 0, \tag{3.6.30}$$

$$\sum_{i=0}^{n-1} \boldsymbol{v} f_{in} = 0. \tag{3.6.31}$$

The discretized Boltzmann Eq. (3.6.2) becomes :

$$\left(\partial_{t_1} + \partial_{t_2} + \dots + \boldsymbol{v} \cdot \nabla_{\boldsymbol{x}}\right) \left(f_i^{\text{eq}} + f_{i1} + f_{i2} + \dots\right) = -\frac{1}{\tau} \left(f_{i1} + f_{i2} + \dots\right). \tag{3.6.32}$$

We can separate the 1st order terms and the 2nd order terms from Eq. (3.6.32) as follows :

$$1^{\text{st}} \text{ order} : \partial_{t_1} f_i^{\text{eq}} + \boldsymbol{v} \cdot \nabla_{\boldsymbol{x}} f_i^{\text{eq}} = -\frac{f_{i1}}{\tau}, \tag{3.6.33}$$

$$2^{\text{nd}} \text{ order} : \partial_{t_2} f_i^{\text{eq}} + \partial_{t_1} f_{i1} + \boldsymbol{v} \cdot \nabla_{\boldsymbol{x}} f_{i1} = -\frac{f_{i2}}{\tau}. \tag{3.6.34}$$

By taking the 0th, 1st and 2nd moments of Eq. (3.6.33), we obtain :

$$\partial_{t_1} \rho + \nabla_{\boldsymbol{x}} \cdot (\rho \boldsymbol{u}) = 0, \tag{3.6.35}$$

$$\partial_{t_1} (\rho \boldsymbol{u}) + \nabla_{\boldsymbol{x}} \cdot (\rho \boldsymbol{u} \otimes \boldsymbol{u}) = -\nabla_{\boldsymbol{x}} p, \tag{3.6.36}$$

$$\partial_{t_1} \left(\rho \boldsymbol{u} \otimes \boldsymbol{u} + \rho c_s^2 \boldsymbol{I}\right) + \nabla_{\boldsymbol{x}} \cdot \left(\rho c_s^2 (u_a \delta_{bc} + u_b \delta_{ac} + u_c \delta_{ab})\right) = -\frac{1}{\tau} \underbrace{\sum_{i=0}^{n-1} \boldsymbol{v}_i \otimes \boldsymbol{v}_i f_{1n}}_{=\hat{\boldsymbol{M}}_{31}} = -\frac{\hat{\boldsymbol{M}}_{31}}{\tau}. \tag{3.6.37}$$

On the other hand, the 0th and 1st moments of Eq. (3.6.34) :

$$\partial_{t_2} \rho = 0, \tag{3.6.38}$$

$$\partial_{t_2} (\rho \boldsymbol{u}) + \nabla_{\boldsymbol{x}} \cdot \hat{\boldsymbol{M}}_{31} = 0. \tag{3.6.39}$$

We can use Eq. (3.6.37) to compute $\hat{M}_{31}$. Before, we need to compute $\partial_{t_1}\left(\rho \boldsymbol{u} \otimes \boldsymbol{u} + \rho c_s^2 \boldsymbol{I}\right)$ and $\nabla_{\boldsymbol{x}} \cdot \left(\rho c_s^2 (u_a \delta_{bc} + u_b \delta_{ac} + u_c \delta_{ab})\right)$:

$$\begin{aligned}
\partial_{t_1}\left(\rho \boldsymbol{u} \otimes \boldsymbol{u} + \rho c_s^2 \boldsymbol{I}\right) &= \partial_{t_1}(\rho \boldsymbol{u} \otimes \boldsymbol{u}) + \partial_{t_1}(\rho c_s^2 \boldsymbol{I}), \\
&= \boldsymbol{u}\partial_{t_1}(\rho \boldsymbol{u}^T) + \boldsymbol{u}^T \partial_{t_1}(\rho \boldsymbol{u}) - \boldsymbol{u} \otimes \boldsymbol{u} \partial_{t_1}\rho + c_s^2 \boldsymbol{I} \partial_{t_1}\rho, \\
&= -\boldsymbol{u}\nabla_{\boldsymbol{x}} \cdot \left(\rho \boldsymbol{u} \otimes \boldsymbol{u} + \rho c_s^2 \boldsymbol{I}\right) - \boldsymbol{u}^T \left(\rho \boldsymbol{u} \otimes \boldsymbol{u} + \rho c_s^2 \boldsymbol{I}\right), \\
&+ (\boldsymbol{u} \otimes \boldsymbol{u})\nabla_{\boldsymbol{x}} \cdot (\rho \boldsymbol{u}) - c_s^2 \boldsymbol{I} \nabla_{\boldsymbol{x}}(\rho \boldsymbol{u}), \\
&= -\nabla_{\boldsymbol{x}} \cdot (\rho \boldsymbol{u} \otimes \boldsymbol{u} \otimes \boldsymbol{u}) - c_s^2(\boldsymbol{u}\nabla_{\boldsymbol{x}}^T \rho + \boldsymbol{u}^T \nabla_{\boldsymbol{x}} \rho) - c_s^2 \boldsymbol{I} \nabla_{\boldsymbol{x}}(\rho \boldsymbol{u}), \quad (3.6.40) \\
\nabla_{\boldsymbol{x}} \cdot \left(\rho c_s^2 (u_a \delta_{bc} + u_b \delta_{ac} + u_c \delta_{ab})\right) &= c_s^2(\nabla_{\boldsymbol{x}} \cdot (\rho \boldsymbol{u}) + \nabla_{\boldsymbol{x}}^T \cdot (\rho \boldsymbol{u})) + c_s^2 \boldsymbol{I} \nabla_{\boldsymbol{x}}(\rho \boldsymbol{u}). \quad (3.6.41)
\end{aligned}$$

Inserting Eqs. (3.6.40) and (3.6.41) into Eq. (3.6.37), we obtain :

$$\hat{\boldsymbol{M}}_{31} = -\rho\tau c_s^2(\nabla_{\boldsymbol{x}}\boldsymbol{u} + \nabla_{\boldsymbol{x}}^T \boldsymbol{u}) + \tau \nabla_{\boldsymbol{x}} \cdot (\rho \boldsymbol{u} \otimes \boldsymbol{u} \otimes \boldsymbol{u}). \quad (3.6.42)$$

The second term should not be here. It is due to the truncation of f_i^{eq} at $O(\boldsymbol{u}^3)$ which led to an error in $\hat{\boldsymbol{M}}_3^{\mathrm{eq}}$ (term $\rho \boldsymbol{u} \otimes \boldsymbol{u} \otimes \boldsymbol{u}$ missing). However, this term is negligible if $\boldsymbol{u}^2 \ll c_s^2$ (which is equivalent to $Ma^2 \ll 1$). Therefore, lattice Boltzmann simulations are only suited for subsonic flows. If we neglect this error term, we have :

$$\begin{aligned}
\hat{\boldsymbol{M}}_{31} &= -\rho\tau c_s^2(\nabla_{\boldsymbol{x}}\boldsymbol{u} + \nabla_{\boldsymbol{x}}^T \boldsymbol{u}), \\
&= -p\tau(\nabla_{\boldsymbol{x}}\boldsymbol{u} + \nabla_{\boldsymbol{x}}^T \boldsymbol{u} - \frac{2}{D}\operatorname{Tr}(\nabla_{\boldsymbol{x}}\boldsymbol{u})\boldsymbol{I} + \frac{2}{D}\operatorname{Tr}(\nabla_{\boldsymbol{x}}\boldsymbol{u})\boldsymbol{I}), \quad (3.6.43) \\
&= -\hat{\boldsymbol{\tau}}.
\end{aligned}$$

We again recognize the deviatoric stress tensor $\hat{\boldsymbol{\tau}}$ with a shear viscosity $\mu = p\tau = \rho c_s^2 \tau$ and a bulk viscosity $\mu_B = \frac{2}{D}\mu$. Finally, we can reassemble the equations :

$$\begin{aligned}
&(3.6.35) + (3.6.38), \\
&(3.6.36) + (3.6.39),
\end{aligned}$$

leading to the Navier-Stokes equations :

$$\boxed{\begin{aligned}
\partial_t \rho + \nabla_{\boldsymbol{x}} \cdot (\rho \boldsymbol{u}) &= 0, \\
\partial_t (\rho \boldsymbol{u}) + \nabla_{\boldsymbol{x}} \cdot (\rho \boldsymbol{u} \otimes \boldsymbol{u}) &= -\nabla_{\boldsymbol{x}} p + \nabla_{\boldsymbol{x}} \cdot \hat{\boldsymbol{\tau}}.
\end{aligned}} \quad (3.6.44)$$

To conclude, the (velocity) discretized Boltzmann Eq. (3.6.2) coupled with conditions of Eq. (3.6.18) are enough to recover the Navier-Stokes equations with a $O(\boldsymbol{u}^3)$ error which is negligible for low Mach numbers.

3.6.4 Time and space discretization

The last step to finalize the derivation of the lattice Boltzmann method is to discretize Eq. (3.6.2) in time and space. Eq. (3.6.2) is an hyperbolic partial differential equation so we can solve it as an initial value problem along characteristics. It is therefore natural to write $f_i = f_i(\boldsymbol{x}(a), t(a))$ with a the position along the characteristic. The total differential of f_i with respect to a :

$$\frac{df_i}{da} = \partial_t f_i \frac{dt}{da} + \nabla_{\boldsymbol{x}} f_i \frac{d\boldsymbol{x}}{da}. \quad (3.6.45)$$

If we impose the following conditions :

$$\begin{cases} \frac{dt}{da} = 1, \\ \frac{d\boldsymbol{x}}{da} = \boldsymbol{v}_i. \end{cases} \tag{3.6.46}$$

Then Eq. (3.6.45) becomes :

$$\frac{df_i}{da} = Q(f, f) = -\frac{f_i - f_i^{\text{eq}}}{\tau}. \tag{3.6.47}$$

If we write f_i as $f_i(\boldsymbol{x} + \boldsymbol{v}_i a, t + a)$, then the first fundamental theorem of calculus gives us $\int_0^{\Delta t} \frac{df_i}{da} = f_i(\boldsymbol{x} + \boldsymbol{v}_i \Delta t, t + \Delta t) - f_i(\boldsymbol{x}, t)$. Therefore, we can write :

$$f_i(\boldsymbol{x} + \boldsymbol{v}_i \Delta t, t + \Delta t) - f_i(\boldsymbol{x}, t) = -\frac{1}{\tau} \int_0^{\Delta t} f_i(\boldsymbol{x} + \boldsymbol{v}_i a, t + a) - f_i^{\text{eq}}(\boldsymbol{x} + \boldsymbol{v}_i a, t + a). \tag{3.6.48}$$

The 1st order discretization of the lattice Boltzmann equation consists in approximating the above integral with a simple rectangle method[10] :

$$f_i(\boldsymbol{x} + \boldsymbol{v}_i \Delta t, t + \Delta t) - f_i(\boldsymbol{x}, t) = -\frac{\Delta t}{\tau} \left(f_i(\boldsymbol{x}, t) - f_i^{\text{eq}}(\boldsymbol{x}, t) \right). \tag{3.6.49}$$

We will expand the distribution $f_i(\boldsymbol{x} + \boldsymbol{v}\Delta t, \boldsymbol{v}, t + \Delta t)$ with Δt the timestep at order 2 (order 2 is enough to recover Navier-Stokes). We have :

$$\begin{aligned}
f_i(\boldsymbol{x} + \boldsymbol{v}_i \Delta t, t + \Delta t) &= f_i(\boldsymbol{x} + \boldsymbol{v}_i \Delta t, t) + \Delta t \partial_t f_i(\boldsymbol{x} + \boldsymbol{v}_i \Delta t, t) + \frac{\Delta t^2}{2} \partial_{t^2} f_i(\boldsymbol{x} + \boldsymbol{v}_i \Delta t, t) + O(\Delta t^3), \\
&= f_i(\boldsymbol{x}, t) + \Delta t \boldsymbol{v}_i \cdot \nabla_{\boldsymbol{x}} f_i(\boldsymbol{x}, t) + \frac{\Delta t^2}{2} \boldsymbol{v}_i^T \cdot \nabla_{\boldsymbol{x}}^2 f_i(\boldsymbol{x}, t) \cdot \boldsymbol{v}_i + \Delta t \partial_t f_i(\boldsymbol{x}, t) + \Delta t^2 \boldsymbol{v}_i \cdot \nabla_{\boldsymbol{x}} \partial_t f_i(\boldsymbol{x}, t), \\
&+ \frac{\Delta t^2}{2} \partial_{t^2} f_i(\boldsymbol{x}, t) + O(\Delta t^3), \\
&= f_i(\boldsymbol{x}, t) + \Delta t \left[\partial_t f_i(\boldsymbol{x}, t) + \boldsymbol{v}_i \cdot \nabla_{\boldsymbol{x}} f_i(\boldsymbol{x}, t) \right] + \frac{\Delta t^2}{2} [\boldsymbol{v}_i^T \cdot \nabla_{\boldsymbol{x}}^2 f_i(\boldsymbol{x}, t) \cdot \boldsymbol{v}_i + 2\boldsymbol{v}_i \cdot \nabla_{\boldsymbol{x}} \partial_t f_i(\boldsymbol{x}, t), \\
&+ \partial t^2 f_i(\boldsymbol{x}, t)] + O(\Delta t^3).
\end{aligned}$$

After truncation and some reordering, we have the following expression :

$$f_i(\boldsymbol{x} + \boldsymbol{v}_i \Delta t, t + \Delta t) - f_i(\boldsymbol{x}, t) = \Delta t \left[\partial_t + \boldsymbol{v}_i \cdot \nabla_{\boldsymbol{x}} \right] f_i(\boldsymbol{x}, t) + \frac{\Delta t^2}{2} \left[\partial_t + \boldsymbol{v}_i \cdot \nabla_{\boldsymbol{x}} \right]^2 f_i(\boldsymbol{x}, t). \tag{3.6.50}$$

We now have to perform one (last) Chapman-Enskog expansion on the following equation (combination of Eqs. (3.6.49) and (3.6.50)) :

$$\Delta t \left[\partial_t + \boldsymbol{v}_i \cdot \nabla_{\boldsymbol{x}} \right] f_i + \frac{\Delta t^2}{2} \left[\partial_t + \boldsymbol{v}_i \cdot \nabla_{\boldsymbol{x}} \right]^2 f_i = -\frac{\Delta t}{\tau} \left(f_i(\boldsymbol{x} + \boldsymbol{v}_i, t) - f_i^{\text{eq}}(\boldsymbol{x} + \boldsymbol{v}_i, t) \right). \tag{3.6.51}$$

We use the usual expansions presented in Eq. (3.6.28). The 1st order terms projection yields :

$$1^{\text{st}} \text{ order} : \partial_{t_1} f_i^{\text{eq}} + \boldsymbol{v} \cdot \nabla_{\boldsymbol{x}} f_i^{\text{eq}} = -\frac{f_{i1}}{\tau}. \tag{3.6.52}$$

[10] Using a trapezoidal method, it is possible to obtain a second order discretization.

Separating the 2nd order terms, we obtain :

$$\partial_{t_2} f_i^{\mathrm{eq}} + \left[\partial_{t_1} + \boldsymbol{v}_i \cdot \nabla_{\boldsymbol{x}}\right] f_{i1} + \frac{\Delta t}{2}\left[\partial_{t_1} + \boldsymbol{v}_i \cdot \nabla_{\boldsymbol{x}}\right]^2 f_i^{\mathrm{eq}} = -\frac{f_{i2}}{\tau},$$

$$\partial_{t_2} f_i^{\mathrm{eq}} + \left[\partial_{t_1} + \boldsymbol{v}_i \cdot \nabla_{\boldsymbol{x}}\right] f_{i1} + \frac{\Delta t}{2}\left[\partial_{t_1} + \boldsymbol{v}_i \cdot \nabla_{\boldsymbol{x}}\right]^2 f_i^{\mathrm{eq}} - \frac{\Delta t}{2}\left[\partial_{t_1} + \boldsymbol{v}_i \cdot \nabla_{\boldsymbol{x}}\right]^2 f_i^{\mathrm{eq}} = -\frac{f_{i2}}{\tau} - \frac{\Delta t}{2}\left[\partial_{t_1} + \boldsymbol{v}_i \cdot \nabla_{\boldsymbol{x}}\right]^2 f_i^{\mathrm{eq}},$$

$$\partial_{t_2} f_i^{\mathrm{eq}} + \left[\partial_{t_1} + \boldsymbol{v}_i \cdot \nabla_{\boldsymbol{x}}\right] f_{i1} = -\frac{f_{i2}}{\tau} - \frac{\Delta t}{2}\left[\partial_{t_1} + \boldsymbol{v}_i \cdot \nabla_{\boldsymbol{x}}\right] \underbrace{\left[\partial_{t_1} + \boldsymbol{v}_i \cdot \nabla_{\boldsymbol{x}}\right] f_i^{\mathrm{eq}}}_{=-\frac{f_{i1}}{\tau}},$$

$$2^{\mathrm{nd}} \text{ order} : \partial_{t_2} f_i^{\mathrm{eq}} + \left(1 - \frac{\Delta t}{2\tau}\right)\left(\partial_{t_1} f_{i1} + \boldsymbol{v} \cdot \nabla_{\boldsymbol{x}} f_{i1}\right) = -\frac{f_{i2}}{\tau}. \tag{3.6.53}$$

Following the same process described in Sect. 3.6.2, we obtain the exact same results with a tiny but crucial modification, the viscosity is now :

$$\boxed{\begin{aligned} \mu &= \rho c_s^2 \left(\tau - \frac{\Delta t}{2}\right), \\ \nu &= c_s^2 \left(\tau - \frac{\Delta t}{2}\right). \end{aligned}} \tag{3.6.54}$$

This equation is linked to the BGK operator. With another operator or with a second order discretization (trapezoidal rule instead of rectangle rule)), the viscosity does not have the same expression. Eq. (3.6.54)

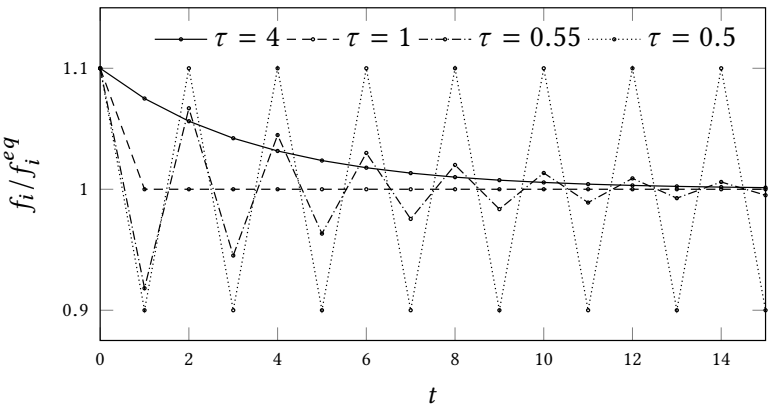

Figure 3.4: Variation of f_i/f_i^{eq} with the BGK operator for different values of τ in the spatially homogeneous case

is unusual. One could wonder why a factor 1/2 suddenly appears. Assuming a spatially homogeneous case, Eq. (3.6.49) can be rewritten as a sequence :

$$X^{t+1} - X^t = -\frac{X^t - 1}{\tau}, \tag{3.6.55}$$

where $X = f_i/f_i^{\mathrm{eq}}$. This sequence can be studied in function of τ. As a consequence, as shown on Figure 3.4, the stability of the BGK operator depends on the value of τ :

- if $\tau > 1$, the distribution is under-relaxed, slowly evolving towards its equilibrium.
- if $\tau = 1$, the distribution is fully relaxed to its equilibrium.
- if $1/2 < \tau < 1$, the distribution is over-relaxed, oscillating around its equilibrium with decaying amplitudes.

- if $\tau = 1/2$, it is the linear stability limit.
- if $\tau < 1/2$, the distribution is over-relaxed, oscillating around its equilibrium with increasing amplitudes (i.e. diverging).

These instabilities have led to the introduction of different collision operators. Among them, the Multiple Relaxation Time (MRT) operator is one of the most famous and is presented in Sect. 3.9.

3.7 Units

When implementing the LBM on a computer, it is convenient to scale time and space so that the lattice space step Δx and lattice time step Δt both equal one. Indeed, in that case, the lattice indexes are equal to the lattice coordinates which greatly simplifies the implementation. This choice leads to the emergence of two different systems of units on the lattice and in reality. The conversion between lattice units and physical units is not a trivial discussion. In this section, the subscripts *la* and *phys* will refer respectively to the lattice units and physical units. Thus, we have seen that, for convenience, $\Delta x_{\text{la}} = 1$ and $\Delta t_{\text{la}} = 1$, so that Eq. (3.6.49) becomes the traditional lattice Boltzmann equation :

$$\boxed{f_i(\boldsymbol{x} + \boldsymbol{v}_i, t+1) - f_i(\boldsymbol{x}, t) = -\frac{f_i(\boldsymbol{x}, t) - f_i^{\text{eq}}(\boldsymbol{x}, t)}{\tau},} \tag{3.7.1}$$

with $\nu = c_{s\text{la}}^2 \left(\tau - \frac{1}{2}\right)$ and $\nu_B = \frac{2}{D}\nu$. We remind that $c_{s\text{la}}$ depends on the lattice choice and is evaluated solving the system formed by Eqs. (3.6.18)[11]. All the main properties and relevant physical quantities of the fluid must be translated from the lattice units to the physical units in order to provide an interpretation of the results.

- Kinematic viscosity :

$$\nu_{\text{la}} = c_{s\text{la}}^2 \left(\tau - \frac{1}{2}\right), \tag{3.7.2}$$

$$\nu_{\text{phys}} = \nu_{\text{la}} \frac{\Delta x_{\text{phys}}^2}{\Delta t_{\text{phys}}}. \tag{3.7.3}$$

- Velocity (and speed of sound) :

$$\boldsymbol{u}_{\text{phys}} = \boldsymbol{u}_{\text{la}} \frac{\Delta x_{\text{phys}}}{\Delta t_{\text{phys}}}, \tag{3.7.4}$$

$$c_{s\text{phys}} = c_{s\text{la}} \frac{\Delta x_{\text{phys}}}{\Delta t_{\text{phys}}}. \tag{3.7.5}$$

The above equations form a system where the only tunable parameter is the relaxation time τ since $c_{s\text{phys}}$ and ν_{phys} and determined by the simulated fluid. Indeed, the physical time and space resolution can be computed as $\Delta x_{\text{phys}} = \frac{c_{s\text{la}}}{c_{s\text{phys}}} \frac{\nu_{\text{phys}}}{\nu_{\text{la}}}$ and $\Delta t_{\text{phys}} = \left(\frac{c_{s\text{la}}}{c_{s\text{phys}}}\right)^2 \frac{\nu_{\text{phys}}}{\nu_{\text{la}}}$[12] A common practice is to relax the constraint of the speed of sound so that a fictitious physical speed of sound is used in the computation. In that case, the system has an extra degree of freedom and both the relaxation time and the space step can be freely chosen by the user. In general to maximize the time and space steps, it is recommended to

[11] Although for classic lattices like D1Q3, D2Q9, D3Q19 or D3Q27, it is simply $c_{s\text{la}} = \frac{1}{\sqrt{3}}$ as shown in Eqs. (3.6.22).

[12] This also gives us the classic version of the lattice Boltzmann kinematic viscosity :

$$\nu = c_{s\text{phys}}^2 \Delta t_{\text{phys}} \left(\tau - \frac{1}{2}\right). \tag{3.7.6}$$

have τ as small as possible. However, in the case of the BGK operator, it leads to instabilities, as shown on Figure 3.4, that can be overcome by using a different collision operator. Concerning the pressure and the density, Δx_{phys} and Δt_{phys} are not sufficient for the conversion. A constant conversion factor C_{phys} for the density is commonly used so that $\rho_{\text{phys}} = C_{\text{phys}}\rho_{\text{la}}$. At rest, if it is assumed that $\rho_{0_{\text{la}}} = 1$ then $C_{\text{phys}} = \rho_{0_{\text{phys}}}$. Hence, it yields :

- Density :

$$\rho_{\text{phys}} = \rho_{0_{\text{phys}}}\rho_{\text{la}}. \tag{3.7.7}$$

- Pressure :

$$p_{\text{phys}} = p_{\text{la}}\frac{\Delta x^2_{\text{phys}}}{\Delta t^2_{\text{phys}}}\rho_{0_{\text{phys}}}. \tag{3.7.8}$$

An exhaustive explanation with numerical examples is given in [Latt 2008a]. We will drop the subscripts *la* and *phys* in the rest of the document (unless necessary for understanding).

3.8 Key features

The Lattice Boltzmann method requires a lattice which is a uniform set of nodes. Each node carries a defined number n of distribution functions $f_i(\boldsymbol{x}, t)$ (with $i = 0 \dots n-1$). These functions f_i represent the density of particles at the position $\boldsymbol{x}$, at time t and with the velocity $\boldsymbol{v}_i$. The velocity vectors have to satisfy a certain number of conditions and therefore have to be chosen carefully if one wants to recover the proper hydrodynamic behavior. Example of the most common lattices for dimension 1, 2 and 3 are shown on Figure 3.3. The macroscopic quantities are computed using the following relationships :

$$\rho(\boldsymbol{x}, t) = \sum_{i=0}^{n-1} f_i(\boldsymbol{x}, t), \tag{3.8.1}$$

$$\boldsymbol{u}(\boldsymbol{x}, t) = \frac{\sum_{i=0}^{n-1} \boldsymbol{v}_i f_i(\boldsymbol{x}, t)}{\sum_{i=0}^{n-1} f_i(\boldsymbol{x}, t)}. \tag{3.8.2}$$

The pressure p is computed using the ideal gas law : $p = \rho c_s^2$. Where the speed of sound c_s depends on the choice of velocity set, although for the most common lattices, it is $c_s = \frac{\Delta x}{\Delta t\sqrt{3}}$. At every timestep, the particles evolve towards a equilibrium state which is defined as follows :

$$f_i^{\text{eq}} = \rho w_i \left[1 + \frac{(\boldsymbol{v}_i \cdot \boldsymbol{u})}{c_s^2} + \frac{(\boldsymbol{v}_i \cdot \boldsymbol{u})^2}{2c_s^4} - \frac{|\boldsymbol{u}|^2}{2c_s^2}\right], \tag{3.8.3}$$

where the weights w_i depend on the choice of lattice. Values for the classic lattices are given in Tab. 3.1. The process at each time step and at each node is the following :

1. a collision step that consists in a relaxation with a characteristic time τ towards the equilibrium distribution f_i^{eq}.

$$f_i(\boldsymbol{x}, t + \Delta t) = f_i(\boldsymbol{x}, t) + Q(f_i). \tag{3.8.4}$$

   In the case of the BGK operator, it gives :

$$f_i(\boldsymbol{x}, t + \Delta t) = f_i(\boldsymbol{x}, t) - \frac{f_i(\boldsymbol{x}, t) - f_i^{\text{eq}}(\boldsymbol{x}, t)}{\tau}. \tag{3.8.5}$$

2. a streaming step to propagate the particles to the adjacent nodes.

$$f_i(\boldsymbol{x} + \boldsymbol{v}_i\Delta t, t + \Delta t) = f_i(\boldsymbol{x}, t + \Delta t). \tag{3.8.6}$$

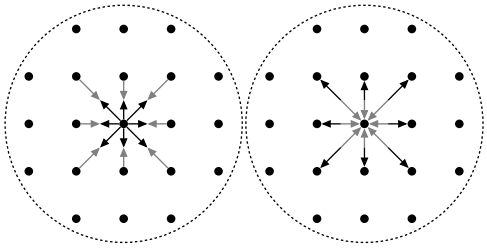

(a) (b)

Figure 3.5: Collision (a) / Streaming (b)

This numerical procedure, illustrated in Figure 3.5, combined with a good choice of lattice is enough to recover the mass and momentum conservation equations. The kinematic shear viscosity is computed using $\nu = \Delta t c_s^2(\tau - \frac{1}{2})$ and the kinematic bulk viscosity is $\nu_B = \frac{2}{D}\nu$. The main advantages of the original LBM approach are summarized hereafter :

1. Simplicity : it is a pseudocompressible method so there is no need to solve a Poisson equation. All in all, the basic LBM algorithm is very simple and can be coded in less than 50 lines of code.
2. Computational efficiency : Its pure local nature makes the LBM algorithm embarrassingly parallel and suited for GPU
3. Boundary conditions : The LBM is build upon a lattice which makes the imposition of boundary conditions efficient and simple.
4. Mass and momentum conservation : Mass and momentum conservation are guaranteed in LBM.
5. Linear and accurate advection : Thanks to the linear nature of the BGK operator, advection is accurately evaluated.
6. No numerical viscosity : In LBM there is no intrinsic dissipation meaning that user has full control on the amount of dissipation included in the model.
7. Multiphase : LBM is particularly adapted for multiphase flows problems and has several well established multiphase formulations available.
8. Mesoscopic-based : LBM emerges from mesoscopic considerations and performs well in the modeling of mesoscopic-based physics such as thermal effects.

On the other hand, there are also drawbacks in LBM, among them one can mention :

1. Stability : LBM is conditionally stable. its stability depends notably on the Mach number Ma and the viscosity ν. Thus, LBM is not recommended "as is" for low viscosity ($\nu = 0$ i.e. $\tau \longrightarrow 1/2$) or fast flows ($Ma = (\frac{|\boldsymbol{u}|}{c_s})^2 \ll 1$).
2. Memory intensive : In general, LBM algorithms are memory bound which could be a bottleneck for large problems.
3. Explicit : LBM is an explicit solver which leads to small timesteps and thus is not really adapted for long runs.
4. Cartesian isotropic grid : LBM being build upon a lattice, it also leads to some disadvantages such as the impossibility to refine a given area of the problem. However, this only true for the basic LBM formulation, other LBM approaches are available to circumvent this issue.

In a nutshell, LBM is a numerical method that is recommended when one needs to discretize complex geometries, subsonic flows and/or multiphase flows. To conclude this section, the simplest algorithm of the method is shown in Algorithm 2.

Algorithm 2 The Lattice Boltzmann Method algorithm

```
for t ← t + Δt do
    for all x nodes do
        ρ ← 0
        u ← 0
        for i = 0 ... (n − 1) do
            ρ ← ρ + f^in_{i,x}                    ▷ Calculate macroscopic variables
            u ← u + v_i f^in_{i,x}
        end for
        u ← u/ρ
        for i = 0 ... (n − 1) do
            f^in_{i,x} = f^in_{i,x} + Q(f^in_{i,x})    ▷ Collision step
            f^out_{i,x+v_iΔt} = f^in_{i,x}             ▷ Streaming step
        end for
    end for
    f^in ← f^out
end for
```

3.9 Alternative collision operators

3.9.1 Multiple relaxation time (MRT) operator

Unlike the BGK operator, the MRT operator offers the possibility to have a distinct relaxation time τ_i for each discrete distribution f_i. It was first introduced by D'Humières in 1992 [d'Humières 2002]. The macroscopic variables are computed as follows :

$$\begin{aligned} \boldsymbol{m} &= \boldsymbol{M}\boldsymbol{f}, \\ \boldsymbol{m}^{\mathrm{eq}} &= \boldsymbol{M}\boldsymbol{f}^{\mathrm{eq}}, \end{aligned} \tag{3.9.1}$$

with $\boldsymbol{m}$ a vector of length n containing the macroscopic variables, $\boldsymbol{f}$ a vector of length n containing the discretized distribution f_i. M is a square matrix whose values are computed through the imposition of constraints on the moments of the distribution. Unlike the classic LBM formulation, because M must be square, the number of moments must be equal to the number of distributions. Some moments are conserved like the density or the momentum (hydrodynamic moments) whereas other are not (kinetic moments). The equilibrium moments vector $\boldsymbol{m}^{\mathrm{eq}}$ can be directly computed without the need to compute f^{eq} first. The expressions of the discrete moment matrices $\boldsymbol{M}^{-1}, \boldsymbol{M}^{-1}$ along with $\boldsymbol{m}^{\mathrm{eq}}$ for the D2Q9 lattice are explicitly given in Appendix A. The lattice Boltzmann equation with an MRT collision operator is :

$$\begin{aligned} f(\boldsymbol{x}+\boldsymbol{v}\Delta t, \boldsymbol{v}, t+\Delta t) - f(\boldsymbol{x}, \boldsymbol{v}, t) &= -\boldsymbol{M}^{-1}\boldsymbol{S}(\boldsymbol{m}(\boldsymbol{x}, \boldsymbol{v}, t) - \boldsymbol{m}^{\mathrm{eq}}(\boldsymbol{x}, \boldsymbol{v}, t), \\ f(\boldsymbol{x}+\boldsymbol{v}\Delta t, \boldsymbol{v}, t+\Delta t) - f(\boldsymbol{x}, \boldsymbol{v}, t) &= -\boldsymbol{M}^{-1}\boldsymbol{S}\boldsymbol{M}(f(\boldsymbol{x}, \boldsymbol{v}, t) - f^{\mathrm{eq}}(\boldsymbol{x}, \boldsymbol{v}, t), \end{aligned} \tag{3.9.2}$$

with $\boldsymbol{S}$ a diagonal matrix such that $S_{ii} = 1/\tau_i$. The challenging part of the MRT approach is to properly set the τ_i. For $D2Q9$, it is established that τ_1, τ_4 and τ_6 do not need to be specified because the corresponding macroscopic variables (i.e. hydrodynamic moments) ρ, ρu_x and ρu_y are recomputed at each timestep due to conservation laws. They can be chosen arbitrarily (and set to 1 in general). The remaining moments are not conserved and are called non-hydrodynamic moments or kinetic moments. They

depend on the hydrodynamic ones. Through a Chapman-Enskog expansion, one can show that :

$$\nu_B = \Delta t \left(\tau_2 - \frac{1}{2}\right) c_s^2, \tag{3.9.3}$$

$$\nu = \Delta t \left(\tau_8 - \frac{1}{2}\right) c_s^2, \tag{3.9.4}$$

$$\tau_8 = \tau_9, \tag{3.9.5}$$

$$\tau_5 = \tau_7. \tag{3.9.6}$$

It follows that one can adjust the kinematic shear viscosity ν and the kinematic bulk viscosity ν_B independently. In the end, the only free parameters are τ_3 and τ_5. A standard choice for the relaxation times is :

$$S = \mathrm{diag}(1.0, 1.4, 1.4, 1.0, 1.2, 1.0, 1.2, \frac{1}{\tau_{BGK}}, \frac{1}{\tau_{BGK}}). \tag{3.9.7}$$

where τ_{BGK} is the value of the relaxation time in the BGK framework. The interest of the MRT approach is the ability to set different relaxation times for the kinetic moments. It is possible to optimize those relaxation times to improve the stability of the method [Lallemand 2000, Ba 2016]. Two main criticisms could be make for this approach. First, the results depend on the choice of relaxation times (no universal results). Second, it is not rooted in kinetic theory and has little physical meaning.

3.9.2 Regularized operator

The regularized operator, introduced in [Latt 2007, Latt 2006], is based on a full reconstruction of the distribution during the collision step :

$$f_i(\boldsymbol{x} + \boldsymbol{v}_i \Delta t, t + \Delta t) = (f_i^{\mathrm{eq}} + f_{i1}^*) - \frac{1}{\tau} f_{i1}^*, \tag{3.9.8}$$

where f_i^{eq} and f_{i1} are the 0th and 1st order terms of the moments-based expansion of Eq. (3.6.28). f_{i1}^* is an approximation of f_{i1} and can be found through the Chapman-Enskog expansion. It is defined as :

$$f_{i1}^* = \frac{w_i(D)}{2c_s^4}(\boldsymbol{v}_i \otimes \boldsymbol{v}_i - c_s^2 \boldsymbol{I}) \sum_{j=0}^{n-1} \boldsymbol{v}_j \otimes \boldsymbol{v}_j (f_j - f_j^{\mathrm{eq}}). \tag{3.9.9}$$

The regularized lattice Boltzmann equation then becomes :

$$f_i(\boldsymbol{x} + \boldsymbol{v}_i \Delta t, t + \Delta t) = f_i^{(0)} + \left(1 - \frac{1}{\tau}\right) f_{i1}^*. \tag{3.9.10}$$

It has been show that under certain assumptions, the regularized operator is equivalent to the MRT operator [Latt 2007].

3.10 Boundary conditions

Within the LBM framework, the main challenge with boundary conditions is to translate a condition on the macroscopic variables to a condition on the distributions. Moreover, due to the nature of the LBM algorithm, on the edges of the domain, some values of the discretized distributions are unknown as show on Figure 3.6. A large variety of boundary conditions have been developed for LBM over the years. To name a few: anti bounceback [Ginzburg 2003], no-slip (Inamuro) [Inamuro 1995] and curved boundaries [Bouzidi 2001]. The bounceback boundary conditions have been extensively analyzed in [Dubois 2015]. A exhaustive presentation of the main boundary conditions in LBM is available in [Walther 2016].

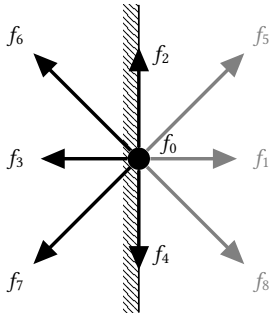

Figure 3.6: A boundary node in a D2Q9 lattice, the gray components are unknown

3.10.1 Periodic boundary conditions

Periodic boundary conditions are a fundamental tool in computational simulations because it allows to reduce the size of the domain while maintaining the accuracy of the results. The concept is well know, the flow that leaves the domain at one end re-enters the domain at the other end. Let's consider a D2Q9 lattice. On node R (on the right of the domain), the flow is leaving the domain while on node L (on the left of the domain), it is entering it. On node R, f_1^R, f_5^R and f_8^R are unknown whereas on node L, f_3^L, f_6^L and f_7^L are unknown. One can impose periodic boundary conditions between node R and node L by setting :

$$\begin{aligned} f_3^L &= \hat{f}_1^R, & f_1^R &= \hat{f}_3^L, \\ f_7^L &= \hat{f}_5^R, & f_5^R &= \hat{f}_7^L, \\ f_6^L &= \hat{f}_8^R, & f_8^R &= \hat{f}_6^L, \end{aligned}$$

with $\hat{f}$ the distribution f after the collision step.

3.10.2 Full bounce-back boundary conditions

It has been observed in Lattice Gas Automata (LGA) that to impose a zero velocity condition (no-slip) on a boundary node, it was enough to reverse the momentum of a particle which collides on a boundary node. This idea has been extended to LBM in a very simple way. At a boundary node, one can just impose the following :

$$f_i = f_{\bar{i}} \tag{3.10.1}$$

where $\bar{i}$ denotes the index of the lattice velocity which is orientated in the direction opposite to the lattice velocity $\boldsymbol{v}_i$[13].

The boundary node on which the distribution are bouncing can be part of the fluid domain (on grid boundary condition or wet boundary, see Figure 3.7) or outside the fluid domain (mid-grid boundary or dry boundary).

[13]For example, for a D2Q9, we have the following :

$$\begin{aligned} i = 0 &\implies \bar{i} = 0, & i = 3 &\implies \bar{i} = 1, & i = 6 &\implies \bar{i} = 8, \\ i = 1 &\implies \bar{i} = 3, & i = 4 &\implies \bar{i} = 2, & i = 7 &\implies \bar{i} = 5, \\ i = 2 &\implies \bar{i} = 4, & i = 5 &\implies \bar{i} = 7, & i = 8 &\implies \bar{i} = 6. \end{aligned}$$

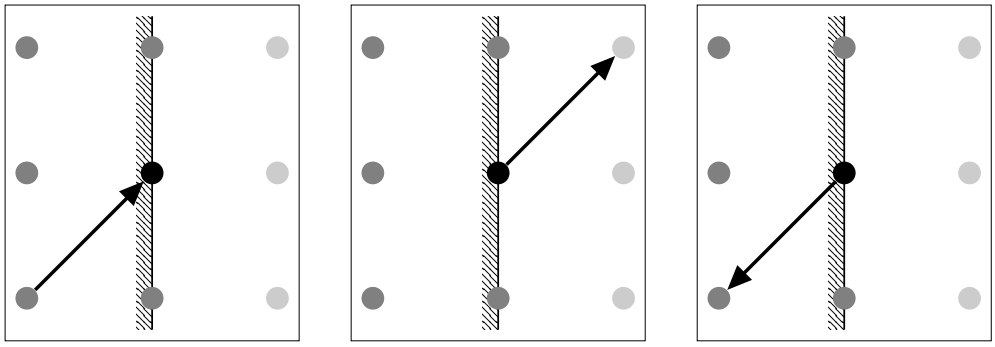

(a) t (b) $t + 1/2$ (c) $t + 1$

Figure 3.7: Full bounceback boundary condition

The bounceback step replaces the collision step for the concerned nodes. This boundary condition is simple and easy to implement, though when used with a BGK operator the bounceback condition is not machine accurate, and exhibits a 1st order error in velocity [He 1997].

3.10.3 Halfway bounce-back boundary conditions

The lack of accuracy of the bounceback boundary condition led the community to introduce another version of the no-slip boundary condition called the halfway bounceback. It is very similar to the full bounceback approach but in this case the distribution has its direction reversed before streaming.

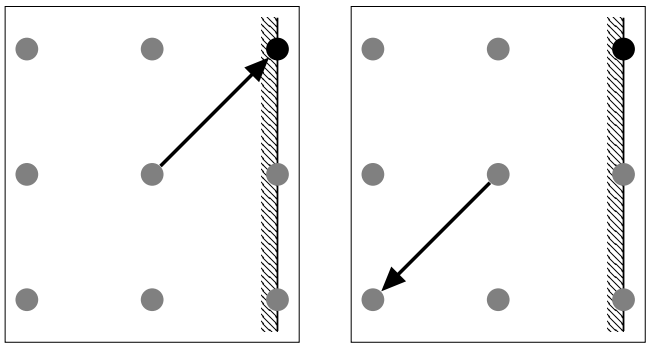

(a) t (b) $t + 1$

Figure 3.8: Halfway bounceback boundary condition

The main difference with full bounceback boundary condition is that the condition is applied during the streaming step and not the collision step. So that, the condition is effective one step earlier than the full bounceback. For straight line boundaries, the half way bounceback is 2nd order accurate in velocity but only 1st order for curved line boundaries [He 1997]. Moreover, one can notice that the halfway bounceback is necessarily applied on a dry boundary and that the physical (wet) boundary of the domain is located halfway between the boundary nodes and its neighbors (hence the name of the method) as shown on Figure 3.8.

3.10.4 Zou & He boundary conditions

In 1997, Zou and He [Zou 1997] introduced a new type of boundary conditions that allows to prescribe a pressure or a velocity on a wall. Let's consider a D2Q9 lattice and assume that one wants to impose a normal velocity u_x and a tangential velocity u_y on the **left** wall. The known distribution are f_0, f_2, f_3, f_4, f_6 and f_7 and the unknown distribution are f_1, f_5 and f_8. Finally, the density ρ is unknown too. Using the density and momentum constraints, it yields :

$$\begin{aligned} f_1 + f_5 + f_8 &= \rho - (f_0 + f_2 + f_4 + f_5 + f_6 + f_7), \\ f_1 + f_5 + f_8 &= \rho u_x + f_3 + f_6 + f_7, \\ f_5 - f_8 &= \rho u_y - f_2 + f_4 - f_6 + f_7. \end{aligned}$$

This is a system of 3 equations with 4 unknowns. We need an extra equation to close the system. The idea of Zou & He is to decompose a given distribution into a equilibrium part and an off-equilibrium part :

$$f_i = f_i^{\textit{off-eq}} + f_i^{\text{eq}}. \tag{3.10.2}$$

Then, it is admitted that the bounceback rule still applies at the boundary for the normal distribution. In the case of a left wall, it yields :

$$\begin{aligned} f_1^{\textit{off-eq}} &= f_3^{\textit{off-eq}}, \\ f_1 - f_1^{\text{eq}} &= f_3 - f_3^{\text{eq}}. \end{aligned}$$

This extra equation closes the system and it can now be solved. The solution is :

$$\begin{aligned} \rho &= \frac{1}{1-u_x}[f_0 + f_2 + f_4 + 2(f_3 + f_6 + f_7)], \\ f_1 &= f_3 + f_1^{\text{eq}} - f_4^{\text{eq}}, \\ f_5 &= f_7 - \frac{1}{2}(f_2 - f_4) + \frac{1}{2}(f_3 - f_1) + \frac{1}{2}(\rho u_x + \rho u_y), \\ f_8 &= f_6 + \frac{1}{2}(f_2 - f_4) + \frac{1}{2}(f_3 - f_1) + \frac{1}{2}(\rho u_x - \rho u_y). \end{aligned}$$

In the case of a prescribed pressure, using the ideal gas law, it is equivalent to impose of prescribed density. The procedure is the same. The prescribed density and one of the velocities are known, the remaining velocity is obtained through the same method. However, one cannot impose both the pressure and the velocity at the same time, the system would be over-constrained. This method is efficient but is hard to generalized to curved line boundaries and is unstable for high Reynolds numbers.

3.10.5 Body forces

The inclusion of body forces such as gravity within the lattice Boltzmann method framework is vital to simulate many flow problems. Apart from gravity, body forces are useful to drive a flow in a periodic domain for example. While other methods exist, the most common one has been introduced by Guo in 2002 [Guo 2002b]. It is based on a modification of the lattice Boltzmann equation:

$$f_i(\boldsymbol{x}, t+1) = f_i(\boldsymbol{x}, t) + Q(f_i) + F_i(\boldsymbol{x}, t). \tag{3.10.3}$$

$F_i(\boldsymbol{x}, t)$ is the nodal body force contribution in the direction given by $\boldsymbol{v}_i$. It is given by :

$$F_i(\boldsymbol{x}, t) = \left(1 - \frac{1}{2\tau}\right)\left(\frac{\boldsymbol{v}_i - \boldsymbol{u}}{c_s^2} + \frac{\boldsymbol{v}_i \cdot \boldsymbol{u}}{c_s^4} \cdot \boldsymbol{v}_i\right) \cdot \boldsymbol{F}(\boldsymbol{x}, t), \tag{3.10.4}$$

where $\boldsymbol{F}(\boldsymbol{x}, t)$ is the body force applied on at node $\boldsymbol{x}$ at time t. Additionally, to compute the macroscopic momentum, one should use :

$$\rho \boldsymbol{u}(\boldsymbol{x}, t) = \sum_{i=0}^{n-1} \boldsymbol{v}_i f_i(\boldsymbol{x}, t) + \frac{\boldsymbol{F}(\boldsymbol{x}, t)}{2}. \tag{3.10.5}$$

It has been shown [Ladd 2001, Guo 2002b] that these modifications allows to recover the Navier-Stokes equations with an external body force through a classic Chapman-Enskog expansion. Guo's approach is the most commonly used technique to incorporate an external force in an LBM scheme. However, other methods exist that can be more accurate. For example, coupling with the Finite Difference method [Wagner 2006], generalizing Guo's term [He 1998] or using the MRT operator [McCracken 2005].

3.11 LBM Variants

A wide range of LBM variants have been introduced over the years to overcome certain limitations inherent with the classic LBM approach or to increase stability and/or accuracy. Here, two of them are presented : the LBM for compressible flows and the entropic LBM.

3.11.1 LBM for compressible flows

Standard LBM is only available for low Mach numbers. Consequently, the flow is always in a weakly compressible regime. To overcome this limitation, a new class of LBM have been introduced in 2008 [Dellar 2008]. The Navier-Stokes-Fourier equations are expressed as follows :

$$\begin{aligned} \partial_t \rho + \nabla \cdot (\rho \boldsymbol{u}) &= 0, \\ \partial_t (\rho \boldsymbol{u}) + \nabla \cdot (\rho \boldsymbol{u} \otimes \boldsymbol{u} + p\boldsymbol{I}) &= \nabla \cdot S(T, \nabla \boldsymbol{u}), \\ \partial_t \left(\rho s(\rho, T)\right) + \nabla \cdot \left(\rho s(\rho, T)\right) \boldsymbol{u} + \nabla \cdot \left(\frac{q(T, \nabla T}{T}\right) &= \sigma, \end{aligned}$$

with T the temperature, s the specific entropy, $\boldsymbol{S}$ the viscous stress tensor, $\boldsymbol{q}$ the heat flux and σ the entropy source rate. The viscous stress tensor verifies :

$$S(T, \nabla \boldsymbol{u}) = \mu(T) \boldsymbol{\tau}(\nabla \boldsymbol{u}) + \mu_B(T) \nabla \cdot (\boldsymbol{u}\boldsymbol{I}), \tag{3.11.1}$$

with $\boldsymbol{\tau}(\nabla \boldsymbol{u}) = \nabla \boldsymbol{u} + (\nabla \boldsymbol{u})^T - \frac{2}{3} \nabla \cdot (\boldsymbol{u}\boldsymbol{I})$. Moreover, the heat flux satisfies the Fourier law :

$$\boldsymbol{q} = -\kappa(T) \nabla T, \tag{3.11.2}$$

with μ is the dynamic viscosity, μ_B the bulk viscosity and κ the thermal conductivity.

These equations are completely describing the evolution of a Newtonian compressible fluid including the thermal effects. The idea is to add an internal energy to the particles and a second set of distributions g_i. The first set of distributions f_i will be used to recover the mass and momentum conservation equations. The second set of distributions will help to recover the energy conservation equations. The two sets of distributions do not have the same lattice nor the same relaxation times. The collision operator is then modified to couple the momentum and the energy which is a necessary step to obtain good thermodynamic properties and a realistic Prandtl number.

3.11.2 LBM for low viscosity flows

Classic LBM techniques are not able to properly simulate low viscosity flows because of the inherent numerical instabilities appearing when τ reaches $1/2$. The main consequence is that simulation of high

Reynolds flows are not possible. In 2000, the so called Entropic LBM (ELBM) was introduced [Ansumali 2000]. The idea was to restore the second law of thermodynamics in LBM via the $\mathcal{H}$-theorem to overcome the previously mentioned limitations. The discretized Boltzmann equation is modified and now reads :

$$f_i(\boldsymbol{x} + \boldsymbol{v}_i \Delta t, \boldsymbol{v}_i, t + \Delta t) = f_i(\boldsymbol{x}, \boldsymbol{v}_i, t) + \alpha\beta(f_i^{\mathrm{eq}}(\boldsymbol{x}, \boldsymbol{v}_i, t) - f_i(\boldsymbol{x}, \boldsymbol{v}_i, t)), \tag{3.11.3}$$

with $\beta = \frac{\Delta t}{2\tau + \Delta t}$. The viscosity is now expressed as a function of β :

$$\nu = c_s^2 \Delta t \left(\frac{1}{2\beta} - \frac{1}{2} \right), \tag{3.11.4}$$

with $\beta \in [0, 1]$. The viscosity vanishes for β equals to 1.

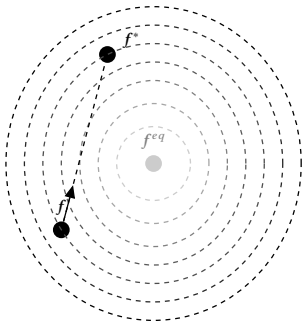

Figure 3.9: Maximum distribution value to satisfy the $\mathcal{H}$-theorem

As seen on Figure 3.9, f^* is the maximal value of f after collision that still satisfies the $\mathcal{H}$-theorem ($\mathcal{H}$ decreasing) and therefore the second law of thermodynamics :

$$f^* = f + \alpha(f^{\mathrm{eq}} - f). \tag{3.11.5}$$

The value of α is computed to ensure that :

$$\mathcal{H}(f^*) = \mathcal{H}(f), \tag{3.11.6}$$

with $\mathcal{H}(f) = \sum_{i=0}^{n-1} f_i \ln\left(\frac{f_i}{w_i}\right)$ (w_i are the weights of the considered lattice). Once both α and f^* are known, the distributions are updated according to :

$$\hat{f} = (1 - \beta)f + \beta f^* = f + \alpha\beta(f^* eq - f). \tag{3.11.7}$$

At this point several remarks can be made. First, one can notice that if $\alpha = 2$, the classic LBM formulation is obtained and the distributions are in equilibrium. Second, it is important to discretize $\mathcal{H}$ first and then to look for its minimum to obtain the ELBM formulation. otherwise, the Maxwell-Boltzmann distribution and the classic LBM are obtained. Thanks to its thermodynamic properties, ELBM is particularly well suited for turbulent flows .

3.12 Multiphase LBM

In LBM multiphase flow simulations, the fluid/fluid interface is not a sharp line but a diffuse interface with a defined thickness. The interface dynamics are controlled by the relative diffusion of each fluid when approaching the contact line. Thanks to this smooth transition between the two phases, there

is no singularity at the interface. On top of that, the no-slip condition is guaranteed. There is no need to track the interface and its evolution naturally emerges from the simulation [Chen 1998]. The use of the lattice Boltzmann method to study multiphase flow can be dated back to the early days of the lattice gas automata (LGA). The first extension of LGA to multiphase was introduced in 1986 in [Frisch 1986b]. Four main multiphase formulations are available for LBM : the pseudo-potential model [Shan 1993], the free energy model [Swift 1995a], the mean field model [He 1999] and the color gradient model [Gunstensen 1991]. We recommend the reading of [Liu 2015, Leclaire 2017] for those looking for a detailed comparison of these techniques.

3.12.1 Color Gradient Model (CGM)

The present LBM approach is the two-phase model introduced in [Reis 2007] and completed with the improvements proposed in [Leclaire 2012, Leclaire 2011] for the recoloring operator and the color gradient. In addition, the contact angle ajustment is based on [Leclaire 2016, Xu 2017] and the corrective procedure to properly recover Navier-Stokes equations is borrowed from [Ba 2016]. We work with 2 sets of distribution functions, one for each fluid. For the sake of clarity, we will place ourselves in the frame of the $D2Q9$ framework. The associated velocity vectors are $\boldsymbol{v}_i$ with $i \in [0, 8]$ are those defined for $D2Q9$ in Tab. 3.1. As traditionally done in LBM, we set the lattice time step Δt and the lattice space step Δx to 1. The distribution functions for a fluid of color k (e.g. $k = r$ for red and $k = b$ for blue) are denoted $f_i^k(\boldsymbol{x}, t)$, while $f_i(\boldsymbol{x}, t) = f_i^r(\boldsymbol{x}, t) + f_i^b(\boldsymbol{x}, t)$ is used for the color-blind distribution function. In the rest of this section, the integer subscript i is varying between $[0, 8]$ while k is referring to the color blue b or red r of the fluid. The lattice Boltzmann equation that describes the evolution of the system is then :

$$f_i^k(\boldsymbol{x} + \boldsymbol{v}_i, t + 1) = f_i^k(\boldsymbol{x}, t) + Q_i^k\big(f_i^k(\boldsymbol{x}, t)\big), \tag{3.12.1}$$

where the collision operator Q_i^k is the result of the combination of three sub operators (as previously done in [Tolke 2002]) :

$$Q_i^k = (Q_i^k)^{(3)} \left[(Q_i^k)^{(1)} + (Q_i^k)^{(2)}\right]. \tag{3.12.2}$$

The Eq. (3.12.1) is solved using four consecutive steps which make use of the following operators :

1. Single phase collision step (see Sect. 3.12.1.1) :

$$f_i^k(\boldsymbol{x}, t_*) = (Q_i^k)^{(1)}\big(f_i^k(\boldsymbol{x}, t)\big). \tag{3.12.3}$$

2. Perturbation step (multiphase collision 1/2) (see Sect. 3.12.1.2) :

$$f_i^k(\boldsymbol{x}, t_{**}) = (Q_i^k)^{(2)}\big(f_i^k(\boldsymbol{x}, t_*)\big). \tag{3.12.4}$$

3. Recoloring step (multiphase collision 2/2) (see Sect. 3.12.1.3) :

$$f_i^k(\boldsymbol{x}, t_{***}) = (Q_i^k)^{(3)}\big(f_i^k(\boldsymbol{x}, t_{**})\big). \tag{3.12.5}$$

4. Streaming step :

$$f_i^k(\boldsymbol{x} + \boldsymbol{v}_i, t + 1) = f_i^k(\boldsymbol{x}, t_{***}). \tag{3.12.6}$$

We will now examine in detail these steps as well as the specific treatments for the imposition of static contact angles and boundary conditions.

3.12.1.1 Single phase collision operators $(Q_i^k)^{(1)}$

BGK operator The first sub operator, $(Q_i^k)^{(1)}$ of Eq. (3.12.3), is the usual BGK operator for single phase LBM. The distribution functions are relaxed towards a local equilibrium as follows :

$$\begin{aligned}(Q_i^k)^{(1)}(f_i^k) &= f_i^k - \tfrac{1}{\tau_{\text{eff}}}\left(f_i^k - f_i^{k,eq}\right),\\ (Q_i^k)^{(1)}(f_i^k) &= f_i^k - \omega_{\text{eff}}\left(f_i^k - f_i^{k,eq}\right),\end{aligned} \tag{3.12.7}$$

where $\omega_{\text{eff}} = \frac{1}{\tau_{\text{eff}}}$ is the effective relaxation rate and τ_{eff} is the effective relaxation time. In practice, we first calculate the fluid densities based on the 0th moment of the distribution functions :

$$\rho_k = \sum_i f_i^k = \sum_i f_i^{k,eq}, \tag{3.12.8}$$

where $f_i^{k,eq}$ are the equilibrium distribution functions. The total fluid density is given by $\rho = \rho_r + \rho_b$, while the total momentum is computed as the 1st moment of the distribution functions :

$$\rho\boldsymbol{u} = \sum_i \sum_k f_i^k \boldsymbol{v}_i = \sum_i \sum_k f_i^{k,eq} \boldsymbol{v}_i, \tag{3.12.9}$$

where $\boldsymbol{u}$ is the density weighted arithmetic average velocity of the fluid. The equilibrium distribution functions $f_i^{k,eq}$ are defined in [Reis 2007] by :

$$f_i^{k,eq}(\rho_k, \boldsymbol{u}, \alpha_k) = \rho_k \left(\phi_i^k + w_i \left[3\boldsymbol{v}_i \cdot \boldsymbol{u} + \frac{9}{2}(\boldsymbol{v}_i \cdot \boldsymbol{u})^2 - \frac{3}{2}(\boldsymbol{u})^2\right]\right). \tag{3.12.10}$$

These equilibrium distribution functions $f_i^{k,eq}$ are chosen to satisfy mass and momentum conservation and are based on the Maxwell-Boltzmann distribution. The weights w_i are those of a standard D2Q9 lattice shown in Tab. 3.1 while the values ϕ_i^k depend on the density ratio. They are expressed as follows :

$$\phi_i^k = \begin{cases} \alpha_k, & i = 0 \\ (1-\alpha_k)/5, & i = 1,3,5,7 \\ (1-\alpha_k)/20, & i = 2,4,6,8 \end{cases}.$$

As introduced in [Grunau 1993] for two-phase flows, the density ratio between red and blue fluids is γ, and must be computed as follows to obtain a stable interface :

$$\gamma = \frac{\rho_r^0}{\rho_b^0} = \frac{1-\alpha_r}{1-\alpha_b}, \tag{3.12.11}$$

where the superscript 0 refers to the initial value of the density. Besides, the pressure of the fluid of color k is :

$$p^k = \frac{3\rho_k(1-\alpha_k)}{5} = \rho_k (c_s^k)^2. \tag{3.12.12}$$

In Eq. (3.12.11), one of the α_k is actually a free parameter. In practice, if we assume that the least dense fluid is the blue one, we set a positive value for $\alpha_b > 0$ (0.2 in this paper) and so we are certain that $0 < \alpha_b \leq \alpha_r < 1$ using Eq. (3.12.11). These parameters define the value of the sound speed c_s^k in each fluid of color k [Reis 2007].

The effective relaxation parameter ω_{eff} is chosen so that the evolution Eq. (3.12.1) allows to recover the macroscopic Navier-Stokes equations for a single-phase flow in the single-phase areas. This parameter depends on the fluid kinematic viscosity ν_k through the following formula: $\omega_k = 1/\left(3\nu_k + \frac{1}{2}\right)$.

However, when the viscosities of the fluids are different, the relaxation parameters are also different and an interpolation procedure is needed to define an effective relaxation parameter ω_{eff} at the interface. It is common to use a quadratic interpolation [Reis 2007, Grunau 1993]. In order to detect in which area we are located (pure red fluid, pure blue fluid or interface), it is necessary to introduce a color field :

$$\psi = \left(\frac{\rho_r}{\rho_r^0} - \frac{\rho_b}{\rho_b^0}\right) \Big/ \left(\frac{\rho_r}{\rho_r^0} + \frac{\rho_b}{\rho_b^0}\right). \tag{3.12.13}$$

The color field ψ lies between -1 and $+1$. Within an interface, the color field is strictly between -1 and $+1$ whereas it is equal to -1 or $+1$ when located in an area that contains respectively only red fluid or blue fluid. The relaxation factor ω_{eff} in Eq. (3.12.1) is then evaluated as follows :

$$\omega_{\text{eff}} = \begin{cases} \omega_r, & \psi > \delta \\ f_r(\psi), & \delta \geq \psi > 0 \\ f_b(\psi), & 0 \geq \psi \geq -\delta \\ \omega_b, & \psi < -\delta \end{cases}, \tag{3.12.14}$$

in which δ is a free parameter and

$$\begin{aligned} f_r(\psi) &= \chi + \eta\psi + \kappa\psi^2, \\ f_b(\psi) &= \chi + \lambda\psi + \nu\psi^2, \end{aligned} \tag{3.12.15}$$

with :

$$\begin{aligned} \chi &= (2\omega_r\omega_b)/(\omega_r + \omega_b), \\ \eta &= (2(\omega_r - \chi))/\delta, \\ \kappa &= -\eta/(2\delta), \\ \lambda &= (2(\chi - \omega_b))/\delta, \\ \nu &= \lambda/(2\delta). \end{aligned} \tag{3.12.16}$$

The parameter δ influences the thickness of the interface when the fluid viscosities are different. The larger δ, the thicker the fluid interface. There is a trade off to find between robustness and interface sharpness. It is set to 0.1 for all simulations in this paper. If the fluid viscosities are identical, δ is ineffective, because $\omega_{\text{eff}} = \omega_r = \omega_b$. Note that χ, η, κ, λ and ν are simply coefficients and should not be mistaken with thermal conductivity or kinematic viscosity for example despite the common symbols.

MRT operator Alternatively, for the first sub operator, $(Q_i^k)^{(1)}$, one can use the MRT operator instead of the BGK operator. This alternative operator is described in Sect. 3.9.1. In the CGM model, it reads as follows :

$$(Q_i^k)^{(1)}(f_i^k) = f_i^k - \boldsymbol{M}^{-1}\boldsymbol{S}\boldsymbol{M}\left(f_i^k - f_i^{k,eq}\right), \tag{3.12.17}$$

where $\boldsymbol{S}$ is a diagonal matrix with $S_{ii} = s_i$. Following [Leclaire 2014], $\forall i \in [0 \ldots 6], s_i = \lambda\omega_{\text{eff}}$ while $s_7 = s_8 = \omega_{\text{eff}}$. As in [Leclaire 2014], we choose $\lambda = 4/5$.

Proper recovery of Navier-Stokes equations It has been emphasized in several papers [Liu 2012, Huang 2013, Leclaire 2013b] that the color gradient model does not fully recover the Navier-Stokes equations. An unwanted error term arises in the momentum equations when the density ratio is not one. Different techniques have been proposed to attenuate this issue [Leclaire 2013b, Holdych 1998, Huang 2013, Ba 2016]. In the present work, we use the correction introduced in [Ba 2016] for the MRT

approach. It consists in two additions. First, a modified equilibrium distribution functions based on the 3rd order Hermite expansion of the Maxwellian distribution [Shan 2006, Li 2012] is used instead of Eq. (3.12.10). It is expressed as follows :

$$f_i^{k,eq}(\rho_k, \boldsymbol{u}, \alpha_k) = \rho_k \phi_i^k + \\ \rho_k w_i \left(\left[3\boldsymbol{v}_i \cdot \boldsymbol{u} \left[1 + \frac{1}{2}\left(3(c_s^k)^2 - 1\right)(3\boldsymbol{v}_i - 4) \right] + \frac{9}{2}(\boldsymbol{v}_i \cdot \boldsymbol{u})^2 - \frac{3}{2}(\boldsymbol{u})^2 \right] \right). \tag{3.12.18}$$

Second, a source term $\boldsymbol{U}^k$ is added in Eq. (3.12.17). It reads :

$$\boldsymbol{U}^k = \boldsymbol{M}^{-1}\boldsymbol{C}^k, \tag{3.12.19}$$

where $\boldsymbol{C}^k = \left[0, C_1^k, 0, 0, 0, 0, 0, C_7^k, 0\right]^T$. The components C_1^k and C_7^k are computed as follows :

$$\begin{aligned} C_1^k &= 3(1 - s_1/2)(\partial_x Q_x^k + \partial_y Q_y^k), \\ C_7^k &= 3(1 - \omega_{\text{eff}}/2)(\partial_x Q_x^k + \partial_y Q_y^k), \end{aligned} \quad \text{with} \quad \begin{aligned} Q_x^k &= (1.8\alpha^k - 0.8)\rho^k u_x, \\ Q_y^k &= (1.8\alpha^k - 0.8)\rho^k u_y. \end{aligned} \tag{3.12.20}$$

In particular, the derivatives are evaluated using a 9-point isotropic finite difference approximation described shortly afterwards in Eq. (3.12.22).

3.12.1.2 Perturbation operator $(Q_i^k)^{(2)}$

In the color gradient model, surface tension forces are introduced by means of a perturbation operator shown in Eq. (3.12.4) [Halliday 1998, Reis 2007, Gunstensen 1991]. To begin, it is needed to introduce the color gradient $\boldsymbol{F}$ of the color field ψ (see Eq. (3.12.13)) that approximates the fluid-fluid interface normal. It is written as :

$$\boldsymbol{F} = \boldsymbol{\nabla}\psi. \tag{3.12.21}$$

In this work, a bi-dimensional S2I4 (spatial order $S = 2$, isotropic order $I = 4$) discrete gradient operator is used [Leclaire 2013a]. As shown in [Leclaire 2011], this kind of gradient operator enhances the accuracy of the color-gradient model significantly while having the advantage to only rest on the nearest neighboring nodes. It takes the following form :

$$\boldsymbol{\nabla} g(\boldsymbol{x}) \approx \sum_i \xi_i \boldsymbol{v}_i g(\boldsymbol{x} + \boldsymbol{v}_i), \text{ with } \xi_i = \begin{cases} 0, & i = 0 \\ 1/3, & i = 1, 3, 5, 7 \\ 1/12, & i = 2, 4, 6, 8 \end{cases}. \tag{3.12.22}$$

The perturbation operator, for the fluid k, is defined by :

$$(Q_i^k)^{(2)}(f_i^k) = f_i^k + \sum_{\substack{l \\ l \neq k}} \frac{A}{2}|\boldsymbol{F}_{kl}| \left[w_i \frac{(\boldsymbol{F} \cdot \boldsymbol{v}_i)^2}{|\boldsymbol{F}|^2} - B_i \right], \tag{3.12.23}$$

where :

$$B_i = \begin{cases} -4/27, & i = 0 \\ 2/27, & i = 1, 3, 5, 7 \\ 5/108, & i = 2, 4, 6, 8 \end{cases}. \tag{3.12.24}$$

The parameter A which can vary in space and time handles the coupling between both fluids and is therefore linked with the surface tension coefficient σ. It is possible to predict the surface tension σ between the two fluids using only the basic parameters of the model. As explained in [Leclaire 2012],

knowing the form of the expression describing the surface tension and performing simulations on planar interfaces, one can derive an expression that links the surface tension across an interface to the model parameters. For isotropic color gradients defined as in Eq. (3.12.22), the surface tension is set as follows :

$$\sigma = \frac{4}{9}\frac{A}{\omega_{\text{eff}}}. \tag{3.12.25}$$

If σ and ω_{eff} are fixed, one can obtain the value of A. Note that Eq. (3.12.25) is not universal and is susceptible to change if one uses a different color gradient or a different gradient operator. It has been shown in [Reis 2007] that the perturbation operator allows to recover, within the macroscopic limit, the capillary stress tensor responsible for the surface tension forces in the macroscopic two-phase flow equations.

3.12.1.3 Recoloring operator $(Q_i^k)^{(3)}$

The recoloring operator $(Q_i^k)^{(3)}$ of Eq. (3.12.5) is used to maximize the amount of fluid k at the interface that is sent to the k fluid region. It guarantees the fluid's immiscibility. It respects the principles of mass and momentum conservation. The form of recoloring used in this paper is a combination of ideas taken from [Latva-Kokko 2005] and [Halliday 2007] and fully developed in [Leclaire 2012]. It reads :

$$\begin{aligned}(Q_i^r)^{(3)}(f_i^r) &= \tfrac{\rho_r}{\rho} f_i + \beta \tfrac{\rho_r \rho_b}{\rho^2} \cos(\varphi_i) \textstyle\sum_k f_i^{k,eq}(\rho_k, \mathbf{0}, \alpha_k),\\ (Q_i^b)^{(3)}(f_i^b) &= \tfrac{\rho_b}{\rho} f_i - \beta \tfrac{\rho_r \rho_b}{\rho^2} \cos(\varphi_i) \textstyle\sum_k f_i^{k,eq}(\rho_k, \mathbf{0}, \alpha_k),\end{aligned} \tag{3.12.26}$$

where $\beta \in [0 \ldots 1]$ is a parameter controlling the interface thickness [Latva-Kokko 2005] that will be set to 0.99 unless otherwise stated. $\cos(\varphi_i) = (\boldsymbol{v}_i \cdot \boldsymbol{F})/(|\boldsymbol{v}_i||\boldsymbol{F}|)$ is the cosine of the angle between the color gradient $\boldsymbol{F}$ and the lattice direction vector $\boldsymbol{v}_i$. Note that for $i = 0$ or $|\boldsymbol{F}| = 0$, there is a division by 0. In such a case, we set the whole term equal to 0 to respect mass conservation.

3.12.1.4 Adjustment of the color gradient for static contact angles

Based on [Leclaire 2016], the imposition of a contact angle is performed using the method described in [Xu 2017]. In order to properly describe the wetting boundary conditions, we divide the lattice nodes in two categories C_{f} and C_{s}, each category being also subdivided in two subcategories C_{fs}, C_{ff}, C_{sf} and C_{ss}.

- C_{f} : the set of fluid lattice nodes
  - C_{fs} : fluid lattice nodes in contact with at least one solid lattice node
  - C_{ff} : fluid lattice nodes not in contact with any solid lattice node
- C_{s} : the set of solid lattice nodes
  - C_{sf} : solid lattice nodes in contact with at least one fluid lattice node
  - C_{ss} : solid lattice nodes not in contact with any fluid lattice node

When computing the color gradient in the fluid (i.e. for lattice nodes $\in C_{\text{f}}$), the knowledge of the color field at the boundary is required (i.e. for lattice nodes $\in C_{\text{sf}}$) because Eq. (3.12.22) involves the neighboring lattice nodes. Therefore, we need to extrapolate the color field to the boundary nodes, we do so using the following expression :

$$\forall \boldsymbol{x} \in C_{\text{sf}}, \quad \phi(\boldsymbol{x}) = \sum_{\substack{i \\ \boldsymbol{x}+\boldsymbol{v}_i \in C_{\text{fs}}}} w_i \phi(\boldsymbol{x} + \boldsymbol{v}_i) c_{i\alpha} \Bigg/ \sum_{\substack{i \\ \boldsymbol{x}+\boldsymbol{v}_i \in C_{\text{fs}}}} w_i. \tag{3.12.27}$$

It is now possible to evaluate the orientation of the color gradient in the fluid using the expression hereafter :

$$\boldsymbol{n}^* = \frac{\nabla\phi(\boldsymbol{x})}{|\nabla\phi(\boldsymbol{x})|}. \tag{3.12.28}$$

Note that the exact same approach based on a color field is used in SPH, see Eq. (2.7.14).

In [Xu 2017], they use an 8th order isotropic stencil to compute the surface normal $\boldsymbol{n}^s$. In the subsequent simulations, boundary surfaces are flat and normals are known so we directly input the exact value. The correct color gradient orientation $\boldsymbol{n}$ depends on the prescribed contact angle θ and is evaluated as follows :

$$\boldsymbol{n} = \begin{cases} \boldsymbol{n}^1, & \text{if } D_1 < D_2 \\ \boldsymbol{n}^2, & \text{if } D_1 > D_2 \\ \boldsymbol{n}^s, & \text{if } D_1 = D_2, \end{cases}, \tag{3.12.29}$$

where D_1 and D_2 are the Euclidean distances between the current unit normal vector $\boldsymbol{n}^*$ and the two possible theoretical unit normal vectors $\boldsymbol{n}^1$ and $\boldsymbol{n}^2$ of the interface at the contact line and are given by :

$$\begin{aligned} D_1 &= |\boldsymbol{n}^* - \boldsymbol{n}^1|, \\ D_2 &= |\boldsymbol{n}^* - \boldsymbol{n}^2|, \end{aligned} \tag{3.12.30}$$

with :

$$\begin{aligned} \boldsymbol{n}^1 &= \left(\boldsymbol{n}^s_x \cos\theta - \boldsymbol{n}^s_y \sin\theta, \boldsymbol{n}^s_y \cos\theta + \boldsymbol{n}^s_x \sin\theta\right), \\ \boldsymbol{n}^2 &= \left(\boldsymbol{n}^s_x \cos\theta + \boldsymbol{n}^s_y \sin\theta, \boldsymbol{n}^s_y \cos\theta - \boldsymbol{n}^s_x \sin\theta\right). \end{aligned} \tag{3.12.31}$$

Finally, once $\boldsymbol{n}$ is known, the corrected color gradient value is computed by taking :

$$\nabla\phi(\boldsymbol{x}) = |\nabla\phi(\boldsymbol{x})|\boldsymbol{n}. \tag{3.12.32}$$

3.12.2 Inter-particular potentials (Shan-Chen's model)

The introduction of inter-particle potentials to model multiphase flows in LBM has been done by Shan and Chen [Shan 1993] based on their work on similar concepts for LGA. They propose to use a nearest-neighbor interaction model to incorporate the effect of the inter-molecular potential. This interaction model can be considered as an approximation of the Lennard-Jones potential. In practice, the Shan-Chen (SC) force $\mathbf{F}^{f-f}$ for a Single-Component Multi-Phase (SCMP) system was originally written as :

$$\mathbf{F}^{f-f}(\mathbf{x}, t) = -\mathcal{G}\psi(\mathbf{x}, t)\sum_i w_i\psi(\mathbf{x} + \mathbf{v}_i, t)\mathbf{v}_i, \tag{3.12.33}$$

with $\mathcal{G}$ a constant that controls the strength of the interaction force and ψ the effective mass (which can take several forms, for example $\psi = \rho_0(1 - \exp(-\rho/\rho_0))$). This force can be implemented into the classic LBM algorithm using a forcing term such as Guo's approach described in Sect. 3.10.5. The "magic" of the SC force is that a surface tension term emerges from the Taylor expansion of $\mathbf{F}^{f-f}$. Indeed, it gives :

$$\mathbf{F}^{f-f} = -\mathcal{G}(c_s^2\psi\nabla\psi + \frac{c_s^4}{2}\psi\nabla(\Delta\psi) + \ldots). \tag{3.12.34}$$

This 1st term leads to a modified EOS $p = \rho c_s^2 + \frac{\mathcal{G}}{2}c_s^2\psi^2$ (compared with Eq. (3.1.15)). The 2nd term generates a surface tension. One can directly see a major drawback of the SC model : the coupling

between $\mathcal{G}$, ψ, the EOS and the surface tension. This coupling controls which densities can coexist for a given $\mathcal{G}$ as shown on Figs. 3.10a[14] and 3.10b.

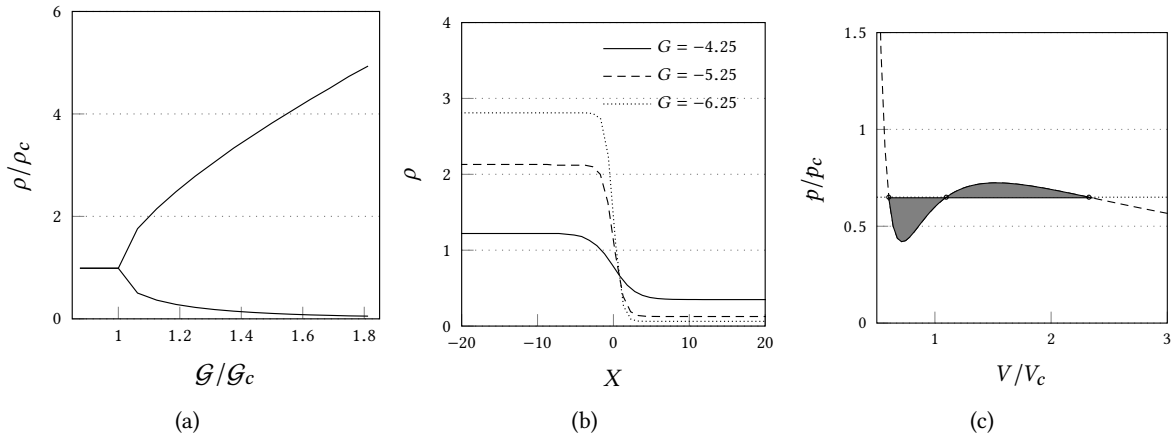

Figure 3.10: (a) Coexisting densities in function of $\mathcal{G}$. (b) Density distribution accross the interface for different $\mathcal{G}$.

It is possible to know in advance the coexisting densities for a given value of $\mathcal{G}$ using the Maxwell reconstruction rule. This rule states the phase segregation happens only for a pressure p_ss where the integral equals to zero which gives the equilibrium values of light and heavy densities

$$\int_{V_h}^{V_l} p dV = p_s(V_l - V_h), \tag{3.12.37}$$

where V_h, V_l are the volumes of the light and heavy phase. Graphically, when adjusting the horizontal pressure level, the two gray areas on Fig. 3.10c have to be equal. Using this setup and carrying out static bubble tests, it is possible to deduce the surface tension coefficient σ via the Laplace's law as shown on Fig. 3.11a. Note that by including another force $\mathbf{F}^{f-s}$ to handle the interaction between the fluids and the solid boundary it is possible to impose a prescribed contact angle by adjusting $\mathcal{G}_s$ as shown on Fig. 3.11b :

$$\mathbf{F}^{f-s}(\mathbf{x}, t) = -\mathcal{G}_s \psi(\mathbf{x}, t) \sum_i w_i s(\mathbf{x} + \mathbf{v}_i, t) \mathbf{v}_i. \tag{3.12.38}$$

The main advantage of this model is that it has a better physical meaning because the phase separation is governed by an inter-particle potential (instead of maximizing the color density gradient). Moreover, computation is more efficient and easily parallelizable since the algorithm involves local interactions, and the interface is automatically computed which is also numerically more efficient. Nevertheless, the major drawback of this approach is the coupling between the parameters as explained

[14] ρ_c and $\mathcal{G}_c$ are the critical values. They are obtained by solving the following system :

$$\begin{aligned} \partial_\rho p &= 0, \\ \partial_\rho^2 p &= 0. \end{aligned} \tag{3.12.35}$$

It yields :

$$\begin{aligned} \rho_c &= \rho_0 \ln(2), \\ \mathcal{G}_c &= -\frac{4}{\rho_0}. \end{aligned} \tag{3.12.36}$$

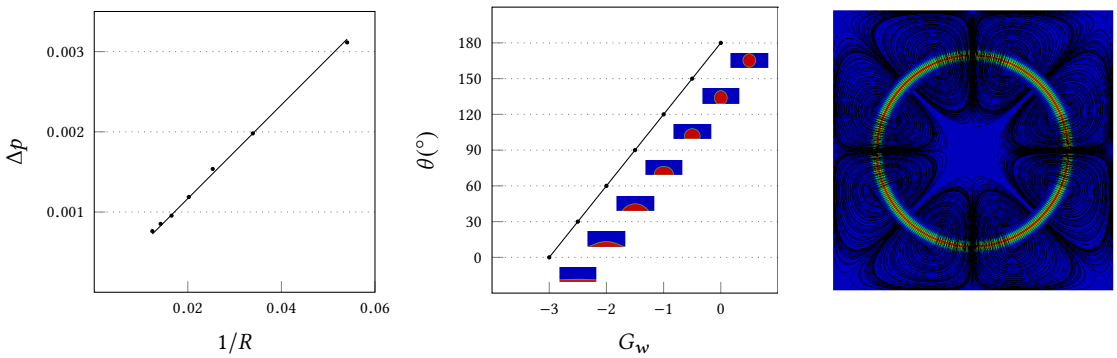

(a) (b) (c)

Figure 3.11: (a) Laplace's law verification for $G = -5$. From linear regression, $\sigma = 0.05839 l.u.$. (b) Contact angle in function of the value of $\mathcal{G}_s$. (c) Example of spurious currents in the SC model for a static bubble test.

before. This makes the SC model not "engineer-friendly" since one cannot set a given two-phase problem as simply as in classic methods. Moreover, as many other multiphase approaches, SC suffers from spurious currents as shown on Figure 3.11c.

3.12.3 Free-Energy Model

As shown in [Swift 1995a], it is important for a multiphase model to be consistent with thermodynamics. In other words, the equation of state, pressure tensor, chemical potential, etc. must be derivable from the free energy. The free-energy model was proposed in [Swift 1995b] and developed to overcome the thermodynamic limitations of the previous multiphase LBM models. The following constraint is imposed :

$$\sum_i f_i^{\mathrm{eq}} \boldsymbol{v}_i \otimes \boldsymbol{v}_i = p\boldsymbol{I} + \rho \boldsymbol{u} \otimes \boldsymbol{u}, \tag{3.12.39}$$

with $p\boldsymbol{I}$ the pressure tensor defined by $p(\boldsymbol{x}) = \rho \frac{\partial \Psi}{\partial \rho}(\boldsymbol{x}) - \Psi(\boldsymbol{x})$ and Ψ the free energy density defined as :

$$\Psi = \int \left(\psi(\rho, T) + \frac{\sigma}{2} |\nabla \rho|^2 \right) \mathrm{d}\boldsymbol{r}, \tag{3.12.40}$$

with σ a parameter that controls the surface tension. The first part of Eq. (3.12.40) represent the free energy of of each fluid while the second term is related to the interface dynamics.

This constraint provides a convenient way to incorporate the free energy in LBM multiphase models. The free energy model is a milestone in LBM because it relates the method to thermodynamics which was an important step to apply it to multiphase flow applications. This model generates a thin interface and allows to simulate fluids with important density or viscosity ratios. Additionally, the surface tension is controlled by an independent parameter. The main drawback of the free energy model is that it is not Galilean invariant but this issue has been solved in [Pooley 2008]. Moreover, this model cannot simulate fluids with simultaneous high density and high viscosity ratios. The use of a free energy to simulate a physical system has been introduced in the so-called phase field theory which has been used to simulate many kind of physical problems. Various models based the phase field theory for multiphase LBM have been proposed over the years, among them, one of the most promising is the stabilized diffuse interface model introduced in [Lee 2010] and that can simulate density ratios up to

1000 without spurious velocities and respecting the thermodynamics (at the cost of computational efficiency).

3.12.4 Mean-Field Model

Based on Enskog's theory for dense fluids and mean-field theory, the mean-field model for multiphase LBM was introduced in [He 1998]. The basic idea for this model is to use the mean-field theory to describe the long-range attraction among particles and the Enskog's theory for dense fluids to model the short range repulsion. This approach allows the user to recover the mass, momentum and energy equations and also the thermodynamics. The lattice Boltzmann mean field equation is written as :

$$f_i(\boldsymbol{x} + \boldsymbol{v}_i \Delta t, t + \Delta t) - f_i(\boldsymbol{x}, t) = -\chi \frac{f_i - f_i^{\mathrm{eq}}}{\tau^* + 1/2} + \frac{\tau^*}{\tau^* + 1/2} Q_i f_i^{\mathrm{eq}} \Delta t, \tag{3.12.41}$$

with :

- χ the density-dependent collision probability determined by an equation of state. For example the Van Der Waals EOS, $\chi = \frac{1}{1-b\rho}$ where $b = 2\pi d^3/3m$ with d the diameter and m the molecular mass.
- $\tau^* = \tau/\Delta t$ with τ the relaxation parameter.
- Q_i the collision operator

$$Q_i = \frac{(\boldsymbol{v}_i - \boldsymbol{u}) \cdot \boldsymbol{F}}{RT}.$$

- f_i^{eq} the equilibrium distribution

$$f_i^{\mathrm{eq}} = w_i \left[1 + \frac{\boldsymbol{v}_i \cdot \boldsymbol{u}}{RT} + \frac{(\boldsymbol{v}_i \cdot \boldsymbol{u})^2}{2(RT)^2} - \frac{\boldsymbol{u}^2}{2RT} \right].$$

- the macroscopic variables computed using

$$\rho = \sum_i f_i, \qquad \rho \boldsymbol{u} = \sum_i f_i \boldsymbol{v}_i + \frac{\boldsymbol{F} \rho \Delta t}{2}, \qquad \frac{3\rho RT}{2} = \sum_i f_i \frac{(\boldsymbol{v}_i - \boldsymbol{u})^2}{2}.$$

Note that a time integration scheme of at least 2nd-order is necessary for these LBM multiphase models [He 1998], otherwise, nonphysical properties such as spurious currents arise in simulations. The mean-field LBM multiphase model is derived from kinetic theory with the inter-molecular potential incorporated intrinsically. From this perspective, it inherits the fundamental feature of the inter-particle potential model. At the same time, the mean field theory guarantees thermodynamic consistency. The drawback of the mean field LBM multiphase model is that it cannot simulate multiphase flows with high density ratio. This drawback is likely due to the assumption that the density field across an interface must be smooth. How to improve these mean-field LBM multiphase models to simulate high density ratios flows is still under investigation.

3.12.5 Summary

In this work, we choose to work with the Color Gradient Model described in Sect. 3.12.1 because among the diffuse interface approaches, it is the one with a thin interface compared to the pseudo potential approach for example. In addition, the pseudo-potential model is cumbersome to use and to parameterize because there is coupling between the basic parameters [Leclaire 2017]. The free energy model requires solving a Poisson equation at every time step which is time consuming and the mean field approach is limited to small density ratios [Prosperetti 2009]. Moreover, the color gradient model benefits from the large body of verification and validation cases available in the literature [Leclaire 2011, Leclaire 2012, Leclaire 2013b, Leclaire 2014, Leclaire 2015, Leclaire 2016, Leclaire 2017].

Models	Advantages	Drawbacks
CGM	✓Thin interface ✓Independent surface tension ✓Local conservation of mass and momentum ✓Widely used	×Interface tracking at each time step ×Small density ratios ×Anisotropic surface tension ×Spurious velocities
SC	✓Automatic interface tracking ✓Widely used ✓Easily parallelizable	×Small density ratios ×Thick interface ×Surface tension/EOS coupling ×Spurious velocities ×Thermodynamics inconsistent
Free-Energy	✓Thermodynamically consistent ✓Liquid/liquid interface ✓Independent surface tension ✓Thin interface	×No Galilean invariant ×Small density ratios ×Small viscosity ratios ×Spurious velocities
Mean-Field	✓Thermodynamically consistent ✓Local conservation of mass and momentum	×Small density ratios ×Spurious velocities

Table 3.2: Summary of the different multiphase LBM approaches

Chapter 4

Comparison of multiphase formulations of SPH and LBM

Contents

4.1 Multiphase LBM model **122**

4.2 Multiphase SPH model **126**

4.3 Validation test cases **131**

4.3.1 Lid-driven cavity flow 131

4.3.2 Rayleigh-Taylor Instability 140

4.3.3 Static bubble tests 142

4.3.4 Capillary Rise 147

4.4 Intermittent two-phase flows in pipes **148**

4.4.1 Periodic case 148

4.4.2 Inlet/outlet case 153

4.5 Conclusion **159**

Our goal in this chapter is to propose a comparison of the multiphase SPH formulation presented in [Hu 2006] and the color-gradient multiphase LBM formulation introduced in [Reis 2007], on a collection of standard 2D test cases and on the simulation of slug flow regimes with periodic and inlet/outlet boundary conditions. To the best of our knowledge, this is the first time such a comparison is presented. We first detail the multiphase LBM and SPH formulations used in this work including surface tension models and boundary conditions in Sects. 4.1 and 4.2. Then, we compare both approaches on a set of validation cases : lid-driven cavity flow, Rayleigh-Taylor instability, capillary rise and static bubble tests with different density and viscosity ratios. Finally, we extend the comparison to two cases of slug flows, one induced by gravity with periodic boundary conditions and the other one based on inlet/outlet boundary conditions. This chapter is mainly adapted from [Douillet-Grellier 2019].

4.1 Multiphase LBM model

We stress that the LBM model described in this section will be the one used throughout this entire manuscript. A summary of the model and its main features is shown on Tab. 4.1

Feature	Choice	Section/Reference
Multiphase model	CGM	Sect. 3.12.1 [Reis 2007, Leclaire 2012]
Collision operator	MRT - Eq. (3.12.17)	Sect. 3.9.1 and 3.12.1 [Leclaire 2014]
Surface tension	CGM perturbation operator	Sect. 3.12.1.2 [Leclaire 2011, Leclaire 2012]
Contact line	Eqs. (3.12.27) to (3.12.32)	Sect. 3.12.1.4 [Leclaire 2016, Xu 2017]
Galilean invariance recovery	Eqs. (3.12.18) to (3.12.20)	Sect. 3.12.1 [Ba 2016]
Wall boundary conditions	Full bounce back	Sect. 3.10.2
Inlet/outlet boundary conditions	Zou-He	Sect. 3.10.4 and 4.1 [Zou 1997]

Table 4.1: Summary of the LBM model considered in this manuscript

LBM formulation In this work, the immiscible multiphase LBM model based on a color gradient approach and fully detailed in Sect. 3.12.1 has been used.

Multiphase inlet/outlet boundary conditions For multiphase LBM, the case of inlet/outlet boundary conditions is particularly difficult because specific treatments are needed to handle the interface when the fluids are entering and/or leaving the domain. Being able to have efficient inlet/outlet boundary conditions is attractive because it extends the range of two-phase flow simulations that could be explored [Lou 2013, Li 2017, Huang 2017, Hou 2018, Tarksalooyeh 2018] and is mandatory for open channels. Here, inlet/outlet boundary conditions are achieved using a modified version of Zou-He boundary conditions [Zou 1997]. The approach detailed in this chapter is very similar to what is described for two-phase pressure boundary conditions in [Huang 2017]. First, we will describe how we inject two phase flows with two different velocities $\boldsymbol{u}^b_{\text{inlet}}$ and $\boldsymbol{u}^r_{\text{inlet}}$ from the north wall. The prescribed velocity fields $\boldsymbol{v}^{b,\text{in}}$ and $\boldsymbol{v}^{r,\text{in}}$ are designed so that $\boldsymbol{v}^{b,\text{in}} = \boldsymbol{u}^b_{\text{inlet}}$ on blue boundary lattice nodes and $\boldsymbol{v}^{b,\text{in}} = 0$ on red boundary lattice nodes. Similarly, $\boldsymbol{v}^{r,\text{in}} = \boldsymbol{u}^r_{\text{inlet}}$ on red boundary lattice nodes and $\boldsymbol{v}^{r,\text{in}} = 0$ on blue boundary lattice nodes. It is then possible to generate a color-blind prescribed velocity field $\boldsymbol{v}^{\text{in}} = \boldsymbol{v}^{b,\text{in}} + \boldsymbol{v}^{r,\text{in}}$. Following the classic Zou-He procedure described in [Zou 1997], we can then

compute the modified density and distribution functions. It reads :

$$\begin{aligned}
\rho^{\text{in}} &= \tfrac{1}{1+\boldsymbol{v}_y^{\text{in}}}\left(f_0+f_1+f_3+2\left(f_2+f_5+f_6\right)\right),\\
f_4 &= f_2-\tfrac{2}{3}\rho^{\text{in}}\boldsymbol{v}_y^{\text{in}}+H^{\text{in}},\\
f_7 &= f_5+\tfrac{1}{2}\left(f_1-f_3\right)-\tfrac{1}{2}\rho^{\text{in}}\boldsymbol{v}_x^{\text{in}}-\tfrac{1}{6}\rho^{\text{in}}\boldsymbol{v}_y^{\text{in}}-\tfrac{1}{2}H^{\text{in}},\\
f_8 &= f_6+\tfrac{1}{2}\left(f_3-f_1\right)+\tfrac{1}{2}\rho^{\text{in}}\boldsymbol{v}_x^{\text{in}}-\tfrac{1}{6}\rho^{\text{in}}\boldsymbol{v}_y^{\text{in}}-\tfrac{1}{2}H^{\text{in}},
\end{aligned} \tag{4.1.1}$$

where H^{in} is a corrective term that depends if we use Eq. (3.12.10) or Eq. (3.12.18) for the equilibrium. In practice, to derive Zou-He boundary conditions, one has to solve a linear system where one term comes from the equilibrium distribution function as shown in Sect. 3.10.4. If we use Eq. (3.12.18), we obtain extra terms compared to the classical Zou-He approach due to the Hermite expansion. It is computed as follows :

$$H^{\text{in}} = \begin{cases} 0 \quad \text{if we use Eq. (3.12.10)},\\ \left[\tfrac{\phi+1}{2}3\rho^{\text{in}}(c_s^b)^2+\left(1-\tfrac{\phi+1}{2}\right)3\rho^{\text{in}}(c_s^r)^2-\rho^{\text{in}}\right]\tfrac{1}{3}\boldsymbol{v}_y^{\text{in}} \quad \text{if we use Eq. (3.12.18)}. \end{cases} \tag{4.1.2}$$

It is then needed to redistribute these quantities in function of the color field value :

$$\begin{aligned}
\rho^b &= \tfrac{\phi+1}{2}\rho^{\text{in}}, & \rho^r &= \left(1-\tfrac{\phi+1}{2}\right)\rho^{\text{in}},\\
f_4^b &= \tfrac{\phi+1}{2}f_4, & f_4^r &= \left(1-\tfrac{\phi+1}{2}\right)f_4,\\
f_7^b &= \tfrac{\phi+1}{2}f_7, & f_7^r &= \left(1-\tfrac{\phi+1}{2}\right)f_7,\\
f_8^b &= \tfrac{\phi+1}{2}f_8, & f_8^r &= \left(1-\tfrac{\phi+1}{2}\right)f_8.
\end{aligned} \tag{4.1.3}$$

Second, we will describe how we impose a constant pressure p^{out} at the outlet located on the south wall. The corresponding prescribed densities are $\rho^{b,out} = p^{\text{out}}/(c_s^b)^2$ and $\rho^{r,out} = p^{\text{out}}/(c_s^r)^2$. The color-blind prescribed density is then $\rho^{\text{out}} = \rho^{b,out}+\rho^{r,out}$. In addition, we also have :

$$\begin{aligned}
v_x^{\text{out}} &= 0\\
v_y^{\text{out}} &= \tfrac{1}{\rho^{\text{out}}}\left(f_0+f_1+f_3+2\left(f_4+f_7+f_8\right)\right),\\
f_2 &= f_4+\tfrac{2}{3}\rho^{\text{out}}v_y^{\text{out}}+H^{\text{out}},\\
f_5 &= f_7-\tfrac{1}{2}\left(f_1-f_3\right)-\tfrac{1}{2}\rho^{\text{out}}v_x^{\text{out}}+\tfrac{1}{6}\rho^{\text{out}}v_y^{\text{out}}-\tfrac{1}{2}H^{\text{out}},\\
f_6 &= f_8-\tfrac{1}{2}\left(f_3-f_1\right)+\tfrac{1}{2}\rho^{\text{out}}v_x^{\text{out}}+\tfrac{1}{6}\rho^{\text{out}}v_y^{\text{out}}-\tfrac{1}{2}H^{\text{out}},
\end{aligned} \tag{4.1.4}$$

where H^{out} is evaluated as follows :

$$H^{\text{out}} = \begin{cases} 0 \quad \text{if we use Eq. (3.12.10)},\\ -\left[\tfrac{\phi+1}{2}3\rho^{\text{out}}(c_s^b)^2+\left(1-\tfrac{\phi+1}{2}\right)3\rho^{\text{out}}(c_s^r)^2-\rho^{\text{out}}\right]\tfrac{1}{3}\boldsymbol{v}_y^{\text{out}} \quad \text{if we use Eq. (3.12.18)}. \end{cases} \tag{4.1.5}$$

We can then redistribute these quantities similarly with what was done in Eq. (4.1.3) :

$$\begin{aligned}
\rho^b &= \tfrac{\phi+1}{2}\rho^{\text{out}}, & \rho^r &= \left(1-\tfrac{\phi+1}{2}\right)\rho^{\text{out}},\\
f_2^b &= \tfrac{\phi+1}{2}f_2, & f_2^r &= \left(1-\tfrac{\phi+1}{2}\right)f_2,\\
f_5^b &= \tfrac{\phi+1}{2}f_5, & f_5^r &= \left(1-\tfrac{\phi+1}{2}\right)f_5,\\
f_6^b &= \tfrac{\phi+1}{2}f_6, & f_6^r &= \left(1-\tfrac{\phi+1}{2}\right)f_6.
\end{aligned} \tag{4.1.6}$$

A test case has been setup to check the performance of these boundary conditions. Initial configuration can be found in Fig. 4.1a and the simulation parameters are displayed on Tab. 4.2. The steady-state

phases distribution is shown on Fig. 4.1b. One can observe a deformation after the inlet that is due to the fact that we inject the heavy fluid 6 times faster that the light fluid and that velocity injection profiles are constant by phase. In Fig. 4.2 is shown the evolution of the inlet velocities and outlet pressure with the number of iterations. Note that quantities have been averaged along the height of the pipe. We can see that we are recovering the prescribed velocities $v^{\text{in}}_{\text{light}}$ and $v^{\text{in}}_{\text{heavy}}$ at the inlet after a transient period with a maximum discrepancy $\leq 4\%$ for the light phase and $\leq 0.5\%$ for the heavy phase with respect the prescribed quantities. Similarly, at the outlet, we recover the prescribed pressure p^{out} after a transient period with a maximum discrepancy $\ll 0.001\%$ with respect to the prescribed value. In Fig. 4.3, we see the distribution of the color field, the inlet velocity and the outlet pressure along the height of the pipe. It is possible to observe a velocity peak and a pressure peak located at the interface. In addition, we provide the steady-state normalized pressure field p/p^{out} after 50000 iterations on Fig 4.1c and we can observe that there are moderate discrepancies at the interface at the inlet and the outlet. These discrepancies are likely due to the fact that fluids are mixed at the interface resulting in governing equations not being properly solved at this location. Moreover, slight discrepancies can be seen at the walls due to boundary conditions. In addition, we can also add that there are pressure reflections between the inlet and the outlet for about 10000 iterations at the beginning of the simulation. Overall, the previously described boundary conditions are giving satisfactory results and will be used later in the chapter. However, we must state that although they are reasonably functioning, they can certainly be improved using another approach.

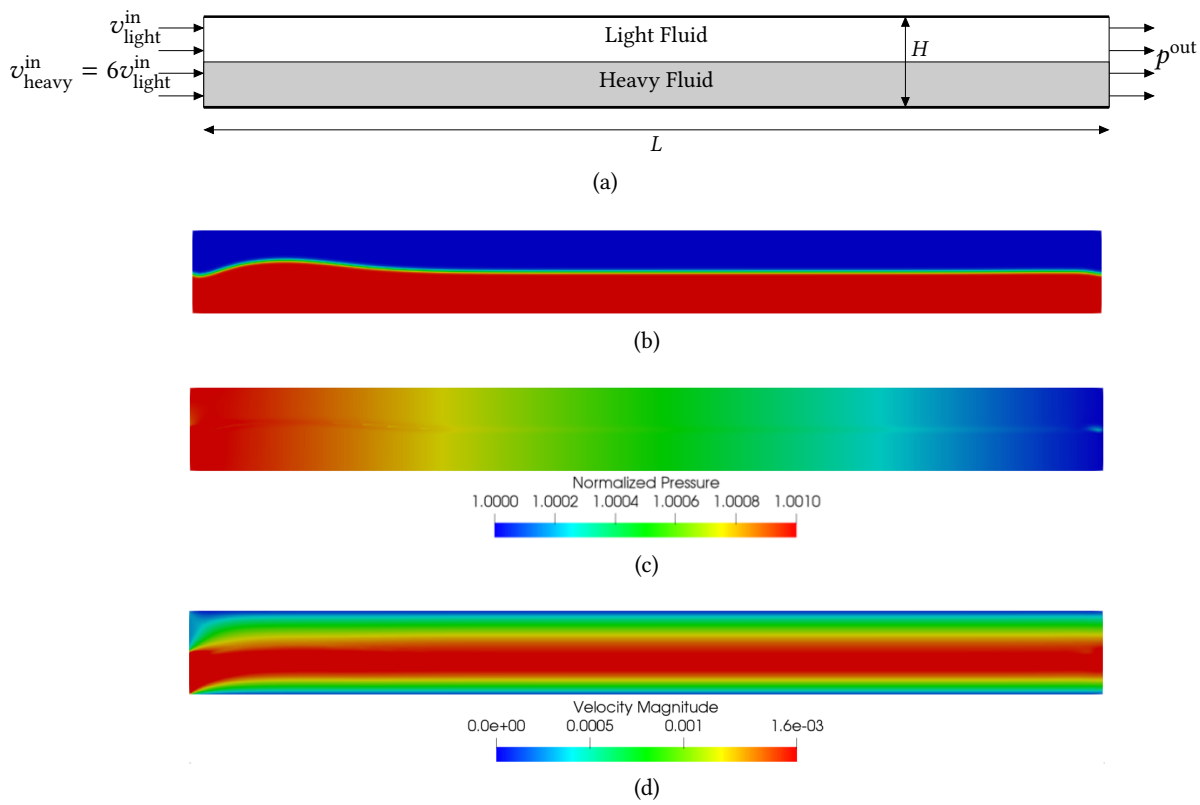

Figure 4.1: (a) Initial configuration sketch. (b) Phases distribution at steady-state after 50000 iterations. (c) Normalized pressure field p/p^{out} at steady-state after 50000 iterations. (d) Velocity field at steady-state after 50000 iterations.

Property	Light Phase	Heavy Phase	Units
Density (ρ)	1.0	5.0	$l.u.$
Relaxation time (τ)	1.0	0.7	$l.u.$
Viscosity (μ)	1.67×10^{-1}	3.34×10^{-1}	$l.u.$
Sound speed (c_s)	0.5773503		$l.u.$
Surface tension (σ^{nw})	2.2×10^{-4}		$l.u.$
Contact angle (θ_c)	90		$^\circ$
Gravity (g_z)	0		$l.u.$
Space step (Δx)	2.0×10^{-2}		$l.u.$
Time step (Δt)	1.33×10^{-3}		$l.u.$
Domain size ($L_x \times L_y$)	500×50		$l.u.$
Inlet velocity (v^{in})	2.67×10^{-4}	1.6×10^{-3}	$l.u.$
Outlet pressure (p^{out})	0.48		$l.u.$

Table 4.2: Simulation parameters for the case shown on Fig. 4.1a ($l.u.$ stands for lattice units).

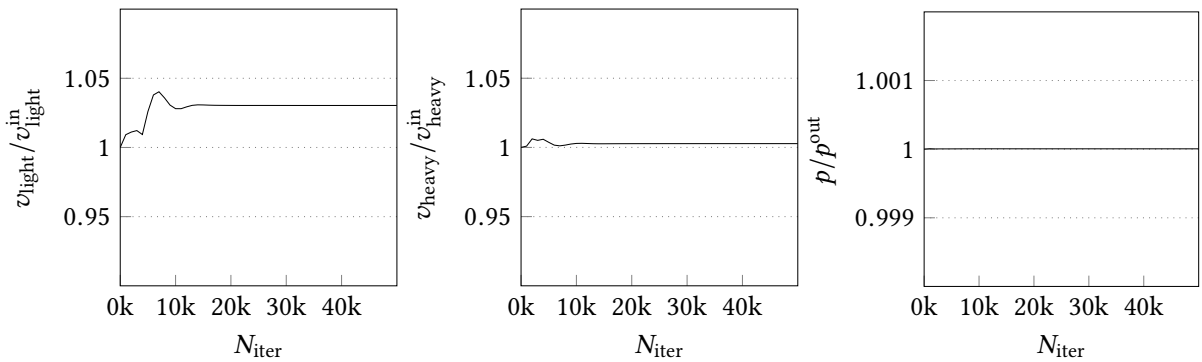

(a) Inlet light phase velocity (b) Inlet heavy phase velocity (c) Outlet pressure

Figure 4.2: Evolution of selected quantities with the number of iterations

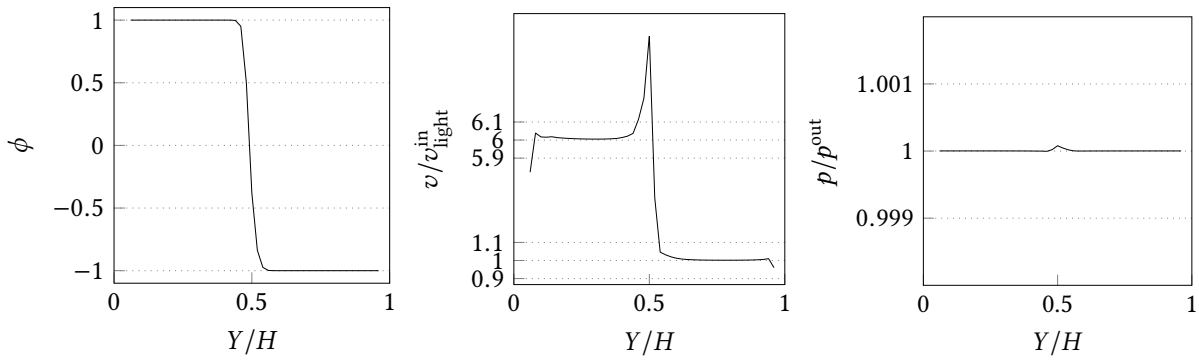

(a) Color field (b) Inlet velocity (c) Outlet pressure

Figure 4.3: Variation of selected quantities along the height of the pipe at steady state

4.2 Multiphase SPH model

We stress that the SPH model described in this section will be the one used throughout this entire manuscript. A summary of the model and its main features is shown on Tab. 4.3

Feature	Choice	Section/Reference
Continuity equation	$\rho_a = m_a \sum_{b\in\Lambda_a} W_{ab}$	Sect. 2.7.1 [Hu 2006]
Momentum Equation	$\frac{D\boldsymbol{u}}{Dt} = -\frac{1}{m_a}\sum_{b\in\Lambda_a}\left(\frac{p_a I+\Pi_a}{\Theta_a^2}+\frac{p_b I+\Pi_b}{\Theta_b^2}\right)\nabla_a W_{ab}$ $+\frac{1}{m_a}\sum_{b\in\Lambda_a}\frac{2\mu_a\mu_b}{\mu_a+\mu_b}\left(\frac{1}{\Theta_a^2}+\frac{1}{\Theta_b^2}\right)\frac{\boldsymbol{x}_{ab}\cdot\nabla_a W_{ab}}{\lvert\boldsymbol{x}_{ab}\rvert^2+\eta^2}\boldsymbol{u}_{ab}$ $+\boldsymbol{g}$	Sect. 2.7.1 [Hu 2006]
Surface tension/Contact line	CSF-Π	Sect. 2.7.2 [Lafaurie 1994, Szewc 2013]
Equation of state	Tait : $p_a = \frac{c_a^2\rho_{0a}}{\gamma_a}\left[\left(\frac{\rho_a}{\rho_{0a}}\right)^{\gamma_a}-1\right]+p_0$	Sect. 2.2 [Monaghan 1994, Colagrossi 2003]
Kernel	Quintic Wendland in Tab. 2.2	Sect. 2.1.2 [Wendland 1995, Dehnen 2012]
Smoothing length	$h/\Delta p = 1.5$ or 2 (will be precised for each case)	Eq. (2.1.21)
Background Pressure	Eq. (2.4.6) and Eq. (4.2.2)	Sect. 2.4.3 and 4.2 [Phillips 1985, Morris 2000]
Speed of sound	Eq. (2.2.6) and Eqs. (4.2.2)-(4.2.3)	Sect. 2.2 and 4.2 [Morris 2000, Zhang 2015]
Consistency	1st order restoration with Eqs. (2.4.7)-(2.4.8)	Sect. 2.4.5 [Bonet 1999b, Colagrossi 2001]
Shifting	Eqs. (2.7.19)-(2.7.20)	Sect. 2.7.3 [Mokos 2016]
Interface correction	Eq. (2.7.21)	Sect. 2.7.3 [Szewc 2013, Szewc 2016]
Time integration	Predictor-Corrector Leapfrog	Sect. 2.6 and 4.2
Wall boundary conditions	Fixed ghost particles	Sect. 2.5.1
Inlet/outlet boundary conditions	Buffer-based	Sect. 4.2 [Tafuni 2018]

Table 4.3: Summary of the SPH model considered in this manuscript

Governing equations The governing equations of the problem for a single incompressible fluid phase consist of mass and momentum conservation equations in a Lagrangian system previously recalled in Eqs. (2.3.1) associated two extra terms in the momentum equation, a viscosity term detailed in Sect. 2.4.2 and the surface tension term explained in Sect. 2.7.2. In the end, the full set of governing equations is given as

$$\begin{cases} \frac{D\rho}{Dt} &= -\rho\nabla\cdot\boldsymbol{u}, \\ \frac{D\boldsymbol{u}}{Dt} &= -\frac{\nabla p}{\rho}+\nu\nabla^2\boldsymbol{u}+\frac{F^{st}}{\rho}+\boldsymbol{g}, \\ p &= \frac{c^2\rho_0}{\gamma}\left[\left(\frac{\rho}{\rho_0}\right)^{\gamma}-1\right]+p_0, \end{cases} \tag{4.2.1}$$

with $\boldsymbol{u}$ fluid velocity, ρ fluid density, ν the fluid kinematic viscosity, p fluid pressure, μ fluid dynamic viscosity, $\boldsymbol{g}$ gravity, c fluid speed of sound (here constant), γ fluid adiabatic index, ρ_0 fluid initial density and p_0 background pressure and D/Dt denotes the material derivative following the motion.

In the case of single phase problem, c and p_0 are set using Eqs. (2.2.6) and (2.4.6). However, in the multiphase context, these definitions are slightly modified. Given a reference length L_{ref} and a reference speed U_{ref}, the following formulas, taken from [Morris 2000], were used

$$\begin{cases} c_\alpha &= \max\left(\frac{U_{\text{ref}}}{\sqrt{\Delta\rho}}, \sqrt{\frac{\lvert\boldsymbol{g}\rvert L_{\text{ref}}}{\Delta\rho}}, \sqrt{\frac{\sigma^{\alpha\beta}}{\rho_{0\alpha}L_{\text{ref}}}}, \sqrt{\frac{\mu_\alpha U_{\text{ref}}}{\rho_{0\alpha}L_{\text{ref}}\Delta\rho}}\right), \quad \forall\alpha\in\{1,\dots,N_{\text{phases}}\}, \\ p_0 &= \max_{\alpha\in\{1,\dots,N_{\text{phases}}\}}\frac{c_\alpha^2\rho_{0\alpha}}{\gamma_\alpha}, \end{cases} \tag{4.2.2}$$

with $\Delta\rho = 0.01$ to enforce (not strictly) a maximum variation of 1% of the density field and $\sigma^{\alpha\beta}$ the surface tension coefficient between phase α and β. N_{phases} is the number of different phases. In practice, in the case of a two-phase simulation with a light phase and a heavy phase, we first compute the speed

of sound of the heavy phase c_{heavy} using Eq. (4.2.2) and we then compute the speed of sound of the light phase c_{light} doing :

$$c_{\text{light}} = c_{\text{heavy}}\sqrt{\frac{{c_{\text{heavy}}}^2 \gamma_{\text{light}} \rho_{0\text{heavy}}}{\gamma_{\text{heavy}} \rho_{0\text{light}}}} \tag{4.2.3}$$

This approach is taken from [Colagrossi 2003, Zhang 2015] and ensures that the pressure is continuous at the interface. It leads $c_{\text{light}} >> c_{\text{heavy}}$ when the density ratio is important, which makes the time step smaller and the simulation longer.

SPH Formulation In this work, we use the formalism introduced in [Hu 2006] and described in Sect. 2.7.1. Within this framework, we briefly remind that :
- the continuity equation is directly solved using Eq. (2.7.3)
- the discretized pressure term $-\frac{\nabla p_a}{\rho_a}$ for a particle a is given by

$$-\frac{\nabla p_a}{\rho_a} = -\frac{1}{m_a}\sum_{b\in\Lambda_a}\left(\frac{p_a}{\Theta_a^2} + \frac{p_b}{\Theta_b^2}\right)\nabla_a W_{ab}, \tag{4.2.4}$$

  where the pressures p_a and p_b are computed using the equation of state (2.2.5)
- the discretized viscous term $\nu_a \nabla^2 \boldsymbol{u}_a$ for a particle a is obtained using Eq. (2.7.6)
- the discretized surface tension term $\frac{\boldsymbol{F}_a^{st}}{\rho_a}$ for a particle a is given by

$$\frac{\boldsymbol{F}_a^{st}}{\rho_a} = -\frac{1}{m_a}\sum_{b\in\Lambda_a}\left(\frac{\Pi_a}{\Theta_a^2} + \frac{\Pi_b}{\Theta_b^2}\right)\nabla_a W_{ab}, \tag{4.2.5}$$

  where the stress tensors Π_a and Π_b are computed using equations (2.7.17)-(2.7.18).

Finally, the set of Eqs. (4.2.1) becomes :

$$\begin{cases} \rho_a & = m_a \sum_{b\in\Lambda_a} W_{ab}, \\ \frac{D\boldsymbol{u}}{Dt} & = -\frac{1}{m_a}\sum_{b\in\Lambda_a}\left(\frac{p_a \boldsymbol{I} + \Pi_a}{\Theta_a^2} + \frac{p_b I + \Pi_b}{\Theta_b^2}\right)\nabla_a W_{ab} \\ & \quad + \frac{1}{m_a}\sum_{b\in\Lambda_a}\frac{2\mu_a\mu_b}{\mu_a+\mu_b}\left(\frac{1}{\Theta_a^2} + \frac{1}{\Theta_b^2}\right)\frac{\boldsymbol{x}_{ab}\cdot\nabla_a W_{ab}}{|\boldsymbol{x}_{ab}|^2+\eta^2}\boldsymbol{u}_{ab} \\ & \quad + \boldsymbol{g}, \\ p_a & = \frac{c_a^2 \rho_{0a}}{\gamma_a}\left[\left(\frac{\rho_a}{\rho_{0a}}\right)^{\gamma_a} - 1\right] + p_0, \\ \frac{D\boldsymbol{x}_a}{Dt} & = \boldsymbol{u}_a. \end{cases} \tag{4.2.6}$$

Corrective terms In this chapter, three SPH correction procedures have been used for all subsequent simulations[1] :
- the kernel gradient correction to restore consistency up to order 1 using Eqs. (2.4.7) and (2.4.8)
- the particle shifting algorithm for multiphase flows detailed in Sect. 2.7.3
- the interface correction procedure described in Sect. 2.7.3

Time Integration The time integration scheme chosen for the rest of the manuscript is the Predictor-Corrector Leapgrog scheme described in Sect. 2.6. However, in the multiphase context, one needs to add an extra constraint on the timestep that depends on the surface tension coefficients. It reads :

$$\Delta t = \min\left(\Delta t_{\text{visc}}, \Delta t_{\text{grav}}, \Delta t_{\text{speed}}, \Delta t_{\text{st}}\right), \tag{4.2.7}$$

where Δt_{visc}, Δt_{grav} and Δt_{speed} are defined in Eq. (2.6.5) and $\Delta t_{\text{st}} = 0.25\ \min_{\alpha,\beta\in\{1,\ldots,N_{\text{phases}}\}}\sqrt{\frac{h^3\rho_\alpha^0}{2\pi\sigma^{\alpha\beta}}}$

[1]Except for the single phase simulations of Sect. 4.3.1 where no shifting or interface correction were used.

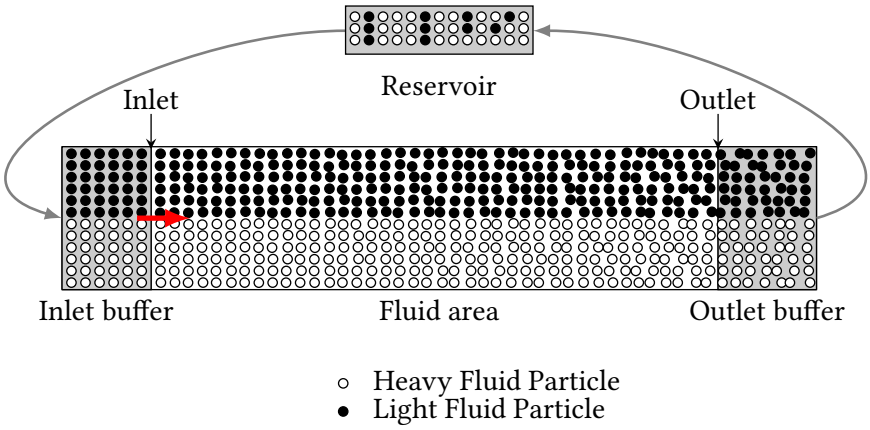

Figure 4.4: Schematic of the inlet/outlet implementation based on buffers.

Multiphase Inlet/Outlet Boundary Conditions Inlet/outlet BC have also been subject to many investigations among SPH researchers. The main issue being that the naive way to implement those inlet/outlet BC results in spurious reflected waves [Lastiwka 2009, Dong 2014, Khorasanizade 2016, Kunz 2016, Alvarado-Rodríguez 2017]. However, to the best of our knowledge, none of them addresses the issue of inlet/outlet BC for multiphase flows. The only known discussion on that matter is proposed in [Fonty 2019a] but it uses a mixture multiphase SPH model which is not our case here. In this work, it has been decided to use the idea presented in [Tafuni 2018] and adapt it to multiphase SPH. To this end, the inlet and outlet boundaries are extended with a buffer layer of size κh to ensure a full kernel support as shown on Fig. 4.4. At the inlet, the goal is to inject the particles with a prescribed velocity profile. On the contrary, at the outlet, the particles need to leave the domain smoothly while imposing a prescribed pressure profile (or density since they are connected through Eq. (2.2.5)). On one hand, a particle i in the inlet buffer is moving with a prescribed velocity profile $\boldsymbol{u}^p$ and it carries the following values of pressure p^{in}, density ρ^{in} and velocity $\boldsymbol{u}^{in}$

$$p_i^{in} = \frac{1}{V_{ia}} \sum_{a \in \Omega_f \cap \Lambda_i} p_a \frac{m_a}{\rho_a} W_{ia}, \tag{4.2.8}$$

$$\rho_i^{in} = \frac{1}{V_{ia}} \sum_{a \in \Omega_f \cap \Lambda_i} \rho_a \frac{m_a}{\rho_a} W_{ia}, \tag{4.2.9}$$

$$\boldsymbol{u}_i^{in} = 2\boldsymbol{u}^p - \frac{1}{V_{ia}} \sum_{a \in \Omega_f \cap \Lambda_i} \boldsymbol{u}_a \frac{m_a}{\rho_a} W_{ia}. \tag{4.2.10}$$

with $V_{ia} = \sum_{a \in \Omega_f \cap \Lambda_i} \frac{m_a}{\rho_a} W_{ia}$ and Λ_i the set of neighboring particles of inlet particle i. We remind that all the different set of particles are explicited in Fig. 2.10.

On the other hand, at the outlet, a particle o in the buffer is moved according to a smoothed convective velocity $\boldsymbol{u}^{conv}$. This idea is taken from [Alvarado-Rodríguez 2017]. For example, if the outlet boundary is vertical and the flow leaves along the x direction, it reads

$$\boldsymbol{u}_o^{out,conv} = \frac{1}{V'_{oa}} \sum_{a \in \Lambda_o} \boldsymbol{u}_a \frac{m_a}{\rho_a} W_{oa}, \tag{4.2.11}$$

with $V'_{oa} = \sum_{a \in \Lambda_o} \frac{m_a}{\rho_a} W_{oa}$ the set of neighboring particles of outlet particle o. Note that in Eq. (4.2.11), the summation is over the full kernel support Λ_o including fluid and outlet particles and not only over

the intersection $\Omega_f \cap \Lambda_o$. Besides, particle o also carries the following values of pressure p^{out}, density ρ^{out} and velocity $\boldsymbol{u}^{out}$

$$p_o^{out} = 2p^p - \frac{1}{V_{oa}} \sum_{a \in \Omega_f \cap \Lambda_o} p_a \frac{m_a}{\rho_a} W_{oa}, \tag{4.2.12}$$

$$\rho_o^{out} = 2\rho^p - \frac{1}{V_{oa}} \sum_{a \in \Omega_f \cap \Lambda_o} \rho_a \frac{m_a}{\rho_a} W_{oa}, \tag{4.2.13}$$

$$v_{o,x}^{out} = \frac{1}{V_{oa}} \sum_{a \in \Omega_f \cap \Lambda_o} v_{a,x} \frac{m_a}{\rho_a} W_{oa}, \tag{4.2.14}$$

$$v_{o,y}^{out} = \frac{-1}{V_{oa}} \sum_{a \in \Omega_f \cap \Lambda_o} v_{a,y} \frac{m_a}{\rho_a} W_{oa}, \tag{4.2.15}$$

with $V_{oa} = \sum_{a \in \Omega_f \cap \Lambda_o} \frac{m_a}{\rho_a} W_{oa}$, p^p and ρ^p the prescribed pressure and density. Concerning the velocity, note that null cross velocities (here v_y) are enforced to ensure a divergence free velocity field at the outlet.

One last but important point is the treatment of the interface stress Π_a introduced in equations (2.7.17)-(2.7.18). After experimenting with different approaches, we concluded that the best option is to explicitly calculate the interface stress even within the buffer areas (no extrapolation) to guarantee a clean interface, especially at the outlet where the interface position is not known a priori. Similarly, we found that it was more stable to extrapolate certain physical parameters (mass m_a, speed of sound c_a, viscosity ν_a, initial density ρ_{0a}) from the fluid area to the inlet/outlet buffer areas.

In order to illustrate how this boundary condition implementation performs, a test case was simulated where a stratified flow (50% light upper phase and 50% heavy lower phase) is injected with the following prescribed velocities : $u_g = 1.4$ m/s and $u_l = 0.12$ m/s. At the outlet, the prescribed pressure is equal to the background pressure. The density ratio is 5 and the viscosity ratio is 2. Simulations are done with the following resolutions $L/\Delta r = 312$, 444 and 704 which corresponds approximately to 10000, 20000 and 50000 particles. Several indicators are presented on Figures 4.5 to 4.7. By 'Normalized Average Pressure/Velocity', we mean that the pressure/velocity is averaged among all particles over a distance of κh inside the fluid flow and over 10 timesteps. Finally, it is divided by the prescribed value.

On Figures 4.5b, 4.6b and 4.7b, we note that the number of particles within the fluid flow is maintained throughout the simulation. The prescribed velocity at the inlet is reasonably well reproduced with an error that stays within ±5% for the light phase and ±15% for the heavy phase as shown on Figures 4.5d, 4.6d and 4.7d. The difference between the two phases is likely due to the relatively low number of particles (especially in the y direction) and to the case geometry where the heavy phase has to push against the light phase causing more disturbances in the velocity field for the heavy phase. On the other hand, at the outlet, the prescribed pressure is very well recovered with an maximum error of ±1% as presented on Figures 4.5c, 4.6c and 4.7c. Besides, we observe that the errors are decreasing when the number of particles increases. These boundary conditions are not optimal but they perform reasonably well and are very easy to implement. One may notice that phases are distributed differently at the outlet between SPH (Fig. 4.5a) and LBM (Fig. 4.1b). In fact, at the outlet, the difference is that in LBM we impose a pure pressure condition whereas in SPH it is mix of pressure and convective boundary conditions.

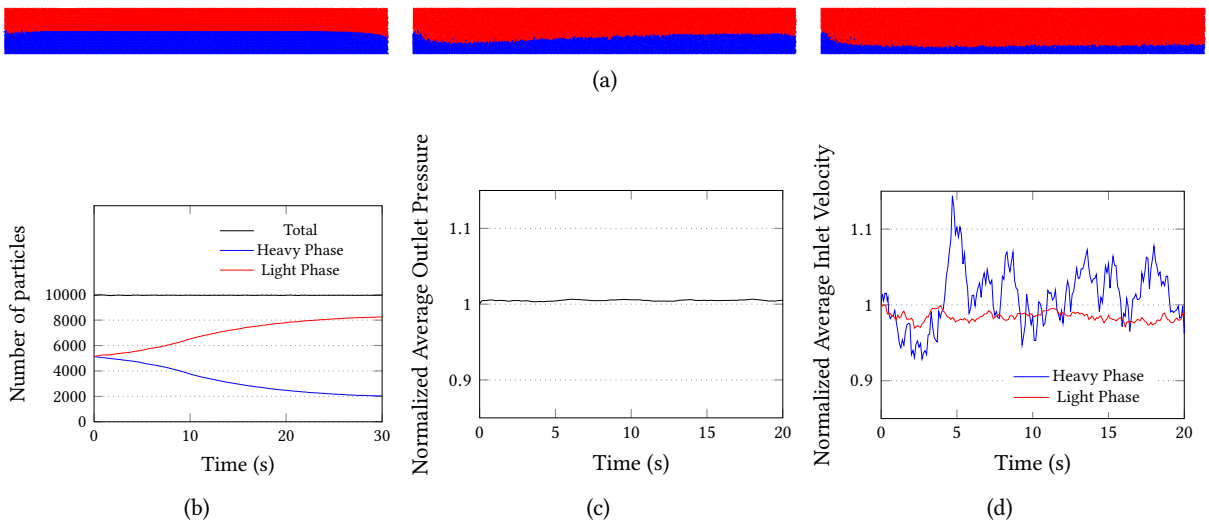

Figure 4.5: Case $L/\Delta r = 312$ (10000 particles). (a) Evolution of the phases distribution at $t = 1$ s, $t = 10$ s and $t = 30$ s (not at scale). (b) Evolution of the number of particles with time. (c) Evolution of the outlet pressure with time. (d) Evolution of the inlet velocities with time.

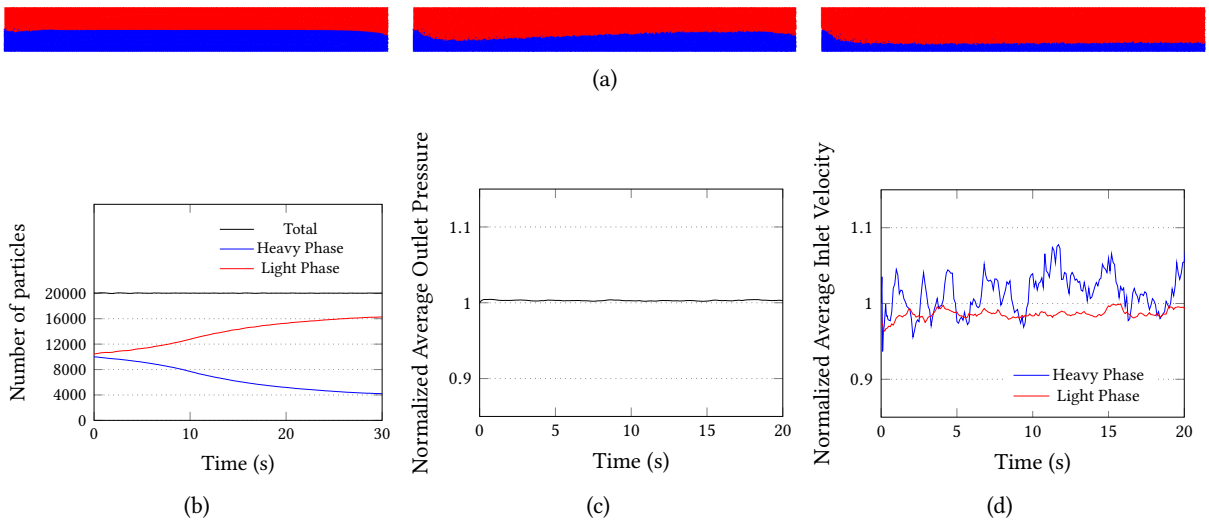

Figure 4.6: Case $L/\Delta r = 444$ (20000 particles). (a) Evolution of the phases distribution at $t = 1$ s, $t = 10$ s and $t = 30$ s (not at scale). (b) Evolution of the number of particles with time. (c) Evolution of the outlet pressure with time. (d) Evolution of the inlet velocities with time.

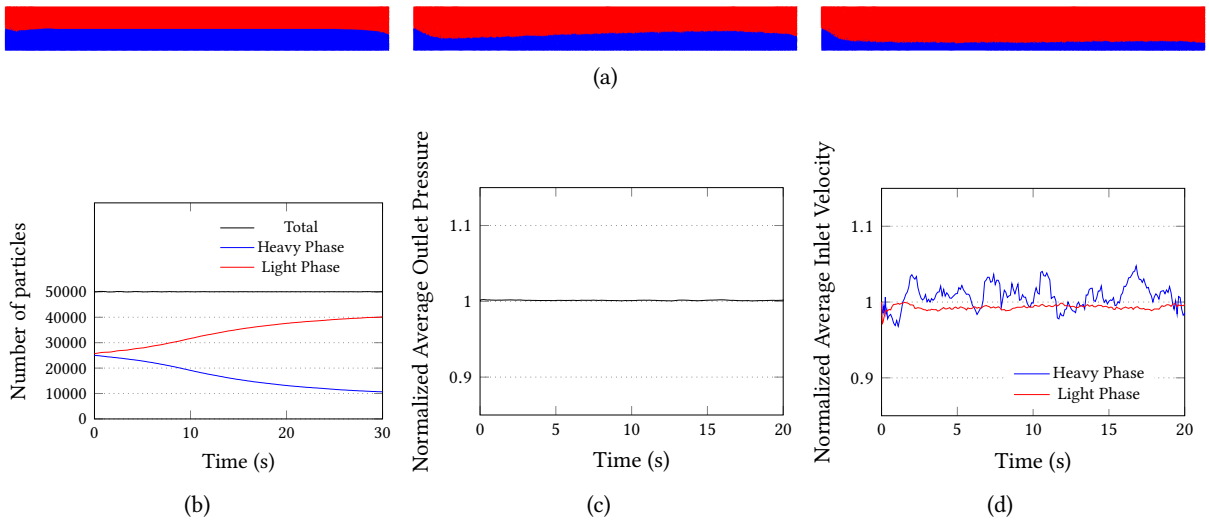

Figure 4.7: Case $L/\Delta r = 704$ (50000 particles). (a) Evolution of the phases distribution at $t = 1$ s, $t = 10$ s and $t = 30$ s (not at scale). (b) Evolution of the number of particles with time. (c) Evolution of the outlet pressure with time. (d) Evolution of the inlet velocities with time.

4.3 Validation test cases

4.3.1 Lid-driven cavity flow

The goal of this section is to validate the implementation of SPH and LBM for the single phase Navier-Stokes case. The test case chosen for this purpose is the well-known 2D lid-driven cavity flow problem shown in Fig. 4.8. This is a common problem in the fluid mechanics community and numerous reference solutions performed with different numerical methods are available in the literature. In this case, we use Ghia et al. solution as a reference [Ghia 1982]. Note that Ghia's solution is also numerical. We must add that this 2D flow is fictitious [Erturk 2009].

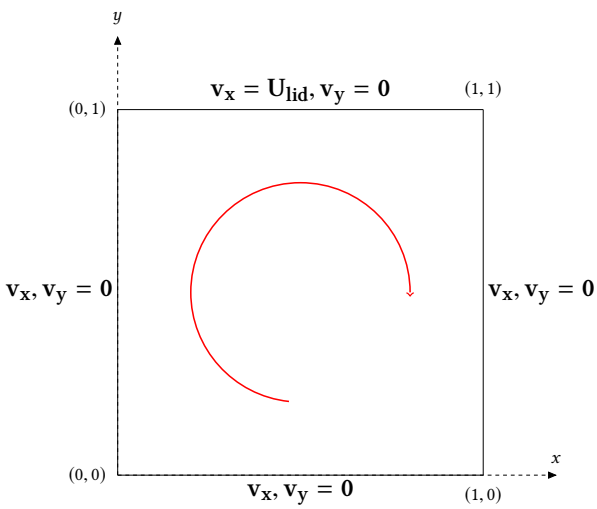

Figure 4.8: The 2D lid-driven cavity flow problem

The Reynolds number for this problem is defined as follows $Re = \frac{U_{\text{lid}} L}{\nu}$ where U_{lid} is the lid velocity imposed at the top boundary, ν is the kinematic viscosity and L is the characteristic length of the

problem. The simulations were performed for $Re = 100$, 400, 1000 and 10000 and for $50 \times 50 = 2500$, $100 \times 100 = 10000$ and $200 \times 200 = 40000$ particles or nodes (respectively for SPH and LBM). $h/\Delta p$ is set to 2 for this case. The density is set to 1000 kg/m^3, the velocity of the lid is $U_{\text{lid}} = 0.1\ l.u.$ for LBM and 1 m/s for SPH, the domain is $L_x \times L_y = 1\text{ m} \times 1\text{ m}$ and the viscosity ν is adjusted to reach the desired Reynolds number.

For LBM, due to stability issues, the MRT collision operator was used. The standard set of relaxation times $\boldsymbol{S}$ defined in Eq. (3.9.7). In order to have stable results for at least one lattice size for every Reynolds number, a specific setup was used where indicated (referred as $LBM*$). The relaxation times are the following :

$$\boldsymbol{S}^* = \text{diag}(1.0, 1.0, 1.0, 1.0, 1.0, 1.0, 1.0, \omega_{\text{eff}}, \omega_{\text{eff}}) \tag{4.3.1}$$

and the lid velocity is increased $U^*_{\text{lid}} = 0.4 l.u.$.

The velocity boundary condition at the top boundary has been applied using the procedure described in Sect. 4.2 for SPH and in Sect. 4.1 for LBM. For the other boundaries, a no-slip boundary conditions has been applied. The simulations are terminated when a steady state is reached (i.e. $\sqrt{\sum_a \frac{|\rho_a^{n+1} - \rho_a^n|}{\rho_a^n}} < 1e^{-2}$ or after 60 s of real simulated time).

4.3.1.1 $Re = 100$

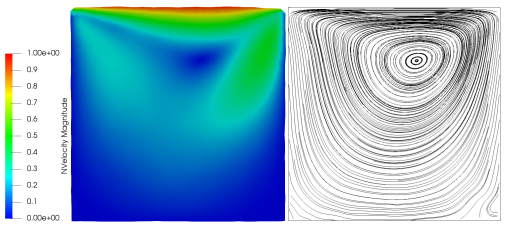

50 × 50 - Velocity (left) - Streamlines (right)

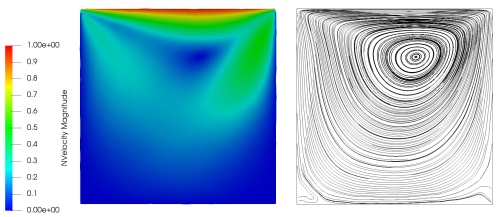

100 × 100 - Velocity (left) - Streamlines (right)

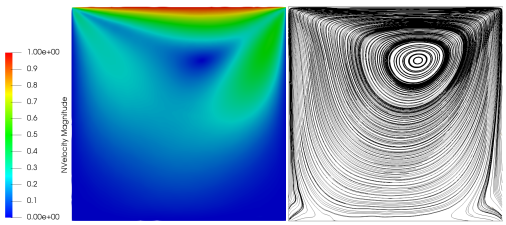

200 × 200 - Velocity (left) - Streamlines (right)

Figure 4.9: SPH results for $Re = 100$

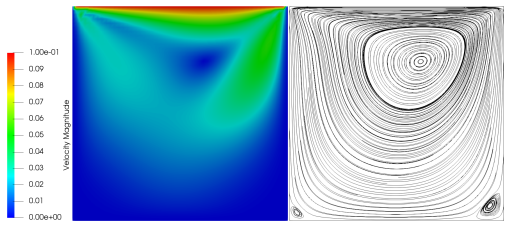

50 × 50 - Velocity (left) - Streamlines (right)

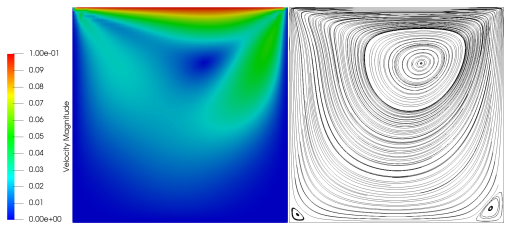

100 × 100 - Velocity (left) - Streamlines (right)

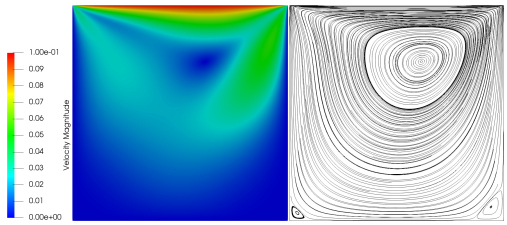

200 × 200 - Velocity (left) - Streamlines (right)

Figure 4.10: LBM results for $Re = 100$

When $Re = 100$, the MRT operator for LBM with the standard relaxation times $\boldsymbol{S}$ is able to simulate the test case for all grid resolutions that were considered. As shown in Fig. 4.13, both LBM and SPH are able to reproduce the velocity field more and more accurately as the lattice/particles resolution is increased. However, LBM always present a higher order of convergence ($\approx$ 2 times faster). Moreover,

LBM is the method that offers the best accuracy compared with Ghia et al.'s solution with an L_2 discrepancy of ≤ 0.025 for the 200×200 lattice resolution. On the other hand, the SPH method shows a higher L_2 discrepancy (at the boundaries in particular) with a maximum discrepancy of $\lesssim 0.06$ for the 200×200 particles resolution.

Concerning the spatial distribution of the flow shown in Figs. 4.10 and 4.9, LBM shows the appearance of two vortices at the two bottom corners of the domain which is in accordance with the theory. On the contrary, SPH is not able to reproduce those two vertexes but instead has flow perturbations in the concerned areas.

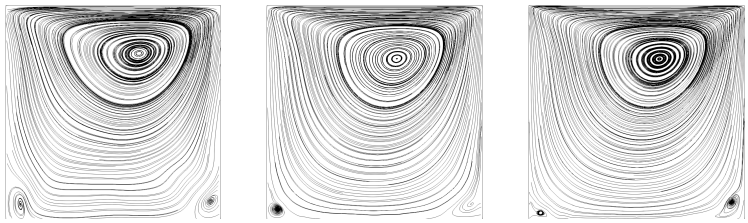

50×50 - $t = 2.48$s 100×100 - $t = 46.66$s 200×200 - $t = 54.31$s

Figure 4.11: SPH streamlines for $Re = 100$ at selected timesteps

In Fig. 4.11, one can note that the two expected vertexes at the corners are in fact appearing during the SPH simulations but they are highly unstable. They keep forming (together or independently) and vanishing as the simulation progresses. It indicates that SPH captures an instability in the correct areas but fails to reach a steady state thus the formation of spurious perturbations. Those vertexes being of small intensity, their formation is probably affected by the boundary conditions.

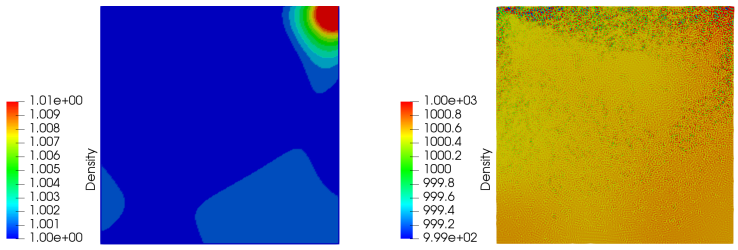

LBM - 200×200 SPH - 200×200

Figure 4.12: Density fields for $Re = 100$

The density fields of the two methods for $Re = 100$ in Fig. 4.12 show that LBM has a smoother density field compared with SPH. As expected, due to the choice to use the weakly compressible approach, SPH presents a noisy density field. It is expected that specific SPH density treatments available in the literature would improve the quality of the density (and thus pressure) field. We can mention *delta*-SPH models [Marrone 2011], SPH-ALE schemes (with Riemann solvers) [Inutsuka 2002, Oger 2016], turbulence models or the incompressible SPH approach (ISPH - with a Poisson solver) [Hu 2007, Lind 2012]. These observations are valid for all four Reynolds numbers studied in this section.

4.3.1.2 $Re = 400$

For $Re = 400$, the MRT operator for LBM with the standard relaxation times S is able to simulate the test case for all grid resolutions that were considered.

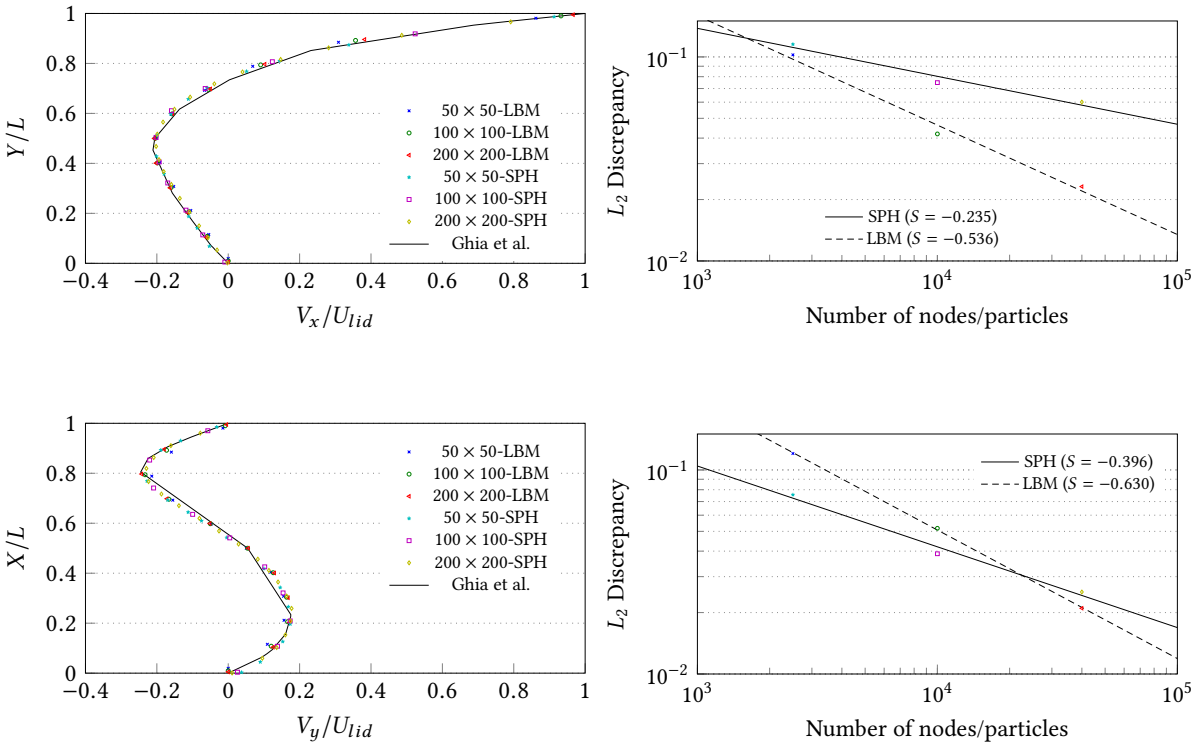

Figure 4.13: $Re = 100$

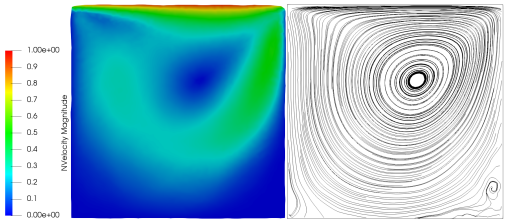

50 × 50 - Velocity (left) - Streamlines (right)

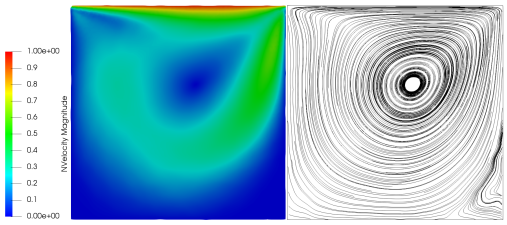

100 × 100 - Velocity (left) - Streamlines (right)

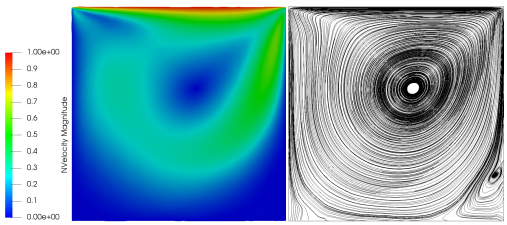

200 × 200 - Velocity (left) - Streamlines (right)

Figure 4.14: SPH results for $Re = 400$

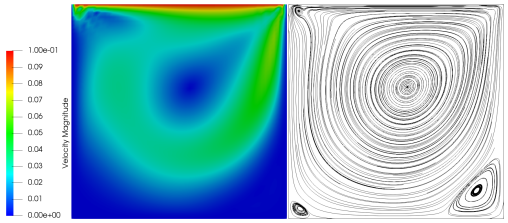

50 × 50 - Velocity (left) - Streamlines (right)

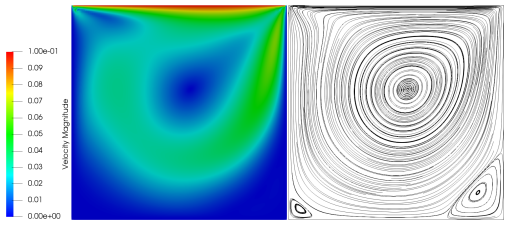

100 × 100 - Velocity (left) - Streamlines (right)

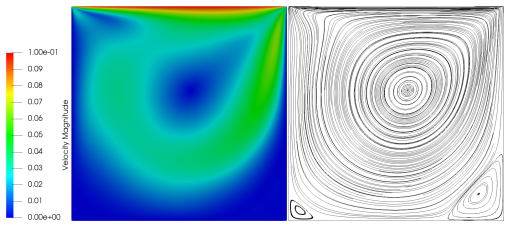

200 × 200 - Velocity (left) - Streamlines (right)

Figure 4.15: LBM results for $Re = 400$

The superiority of LBM in terms of accuracy is magnified in that case. The LBM method shows more accurate results that SPH for all resolutions considered as shown in Fig. 4.17. The maximum discrepancy is always located at the domain's boundaries. As an example, for the 200×200 resolution, both LBM and SPH have a maximum difference with Ghia's reference $\geq 8\%$ at the right boundary whereas it is $\leq 2\%$ and $\leq 5\%$ inside the domain for LBM and SPH respectively.

Once again, LBM shows a better global accuracy for the same resolution and a higher order of convergence than SPH as shown in Fig. 4.17. In particular, for the 200×200 resolution, the LBM L_2 discrepancy on V_x along the vertical centerline is more than 3 times lower than the SPH one. For V_y along the horizontal centerline, both methods have a comparable discrepancy.

The streamlines plots of Figs. 4.15 and 4.14 are showing that LBM correctly reproduces the existence of two vertexes at the bottom corners of the domain. For the 50×50 case, a spurious vertex appears at the top left corner of the domain and is likely due to the combination of boundary conditions (bounceback + Zou-He) at this location as it is smoothed out when the resolution increases.

On the other hand, the SPH results are not able to simulate an established vertex pattern at the bottom corners. In the bottom right corner where the vertex is the strongest, for the 50×50 and 200×200 cases, a vertex appears to be growing but is either not at the correct location or not with the correct amplitude. In fact, when looking at earlier streamlines plots as shown in Fig. 4.16, one can see that SPH does generate vortices in the correct areas at selected instants during the simulation but they fail to stabilize and are continuously appearing and disappearing.

50×50 - $t = 31.6s$ 100×100 - $t = 58.17s$ 200×200 - $t = 52.6s$

Figure 4.16: SPH streamlines for $Re = 400$ at selected timesteps

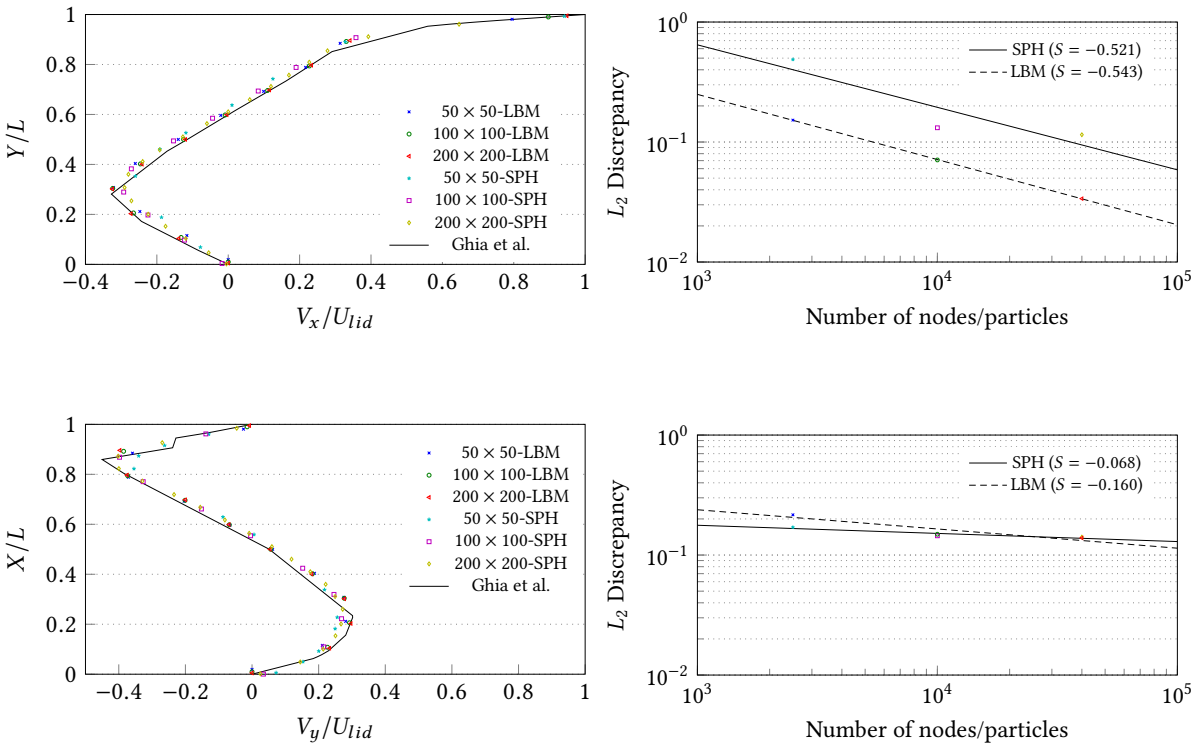

Figure 4.17: $Re = 400$

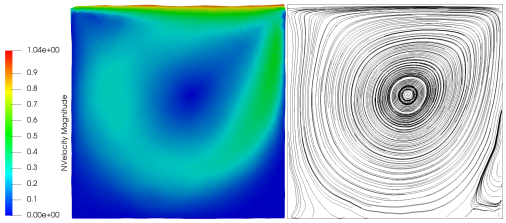

50 × 50 - Velocity (left) - Streamlines (right)

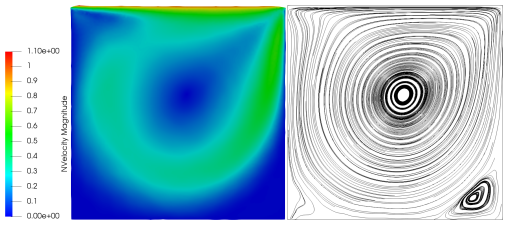

100 × 100 - Velocity (left) - Streamlines (right)

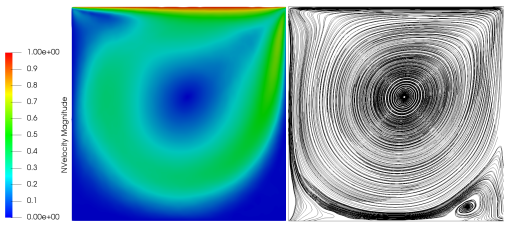

200 × 200 - Velocity (left) - Streamlines (right)

Figure 4.18: SPH results for $Re = 1000$

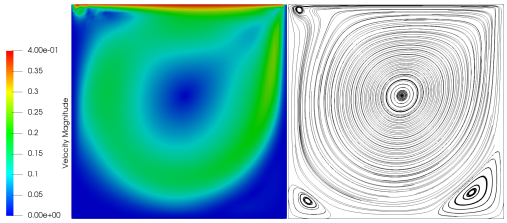

50 × 50 - Velocity (left) - Streamlines (right)

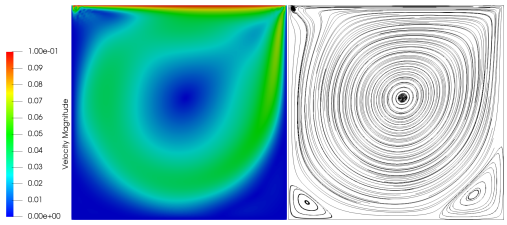

100 × 100 - Velocity (left) - Streamlines (right)

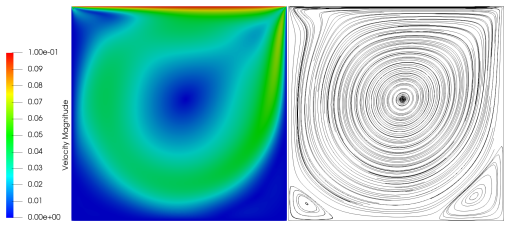

200 × 200 - Velocity (left) - Streamlines (right)

Figure 4.19: LBM results for $Re = 1000$

4.3.1.3 $Re = 1000$

For $Re = 1000$, the MRT operator with the standard relaxation times $\boldsymbol{S}$ fails to give stable results for the 50×50 resolution. However, when using another set of relaxation times $\boldsymbol{S}^*$, one can obtain a stable solution. The impact of empirically adjusting the relaxation times to "make it work" remains to be investigated.

As in the previous cases, one can observe in Fig. 4.21 that LBM exhibits a better accuracy than SPH for almost all resolutions. For the highest resolution, LBM has a maximum L_2 discrepancy of ≈ 0.07. For the same resolution, SPH gives a L_2 discrepancy of ≈ 0.16. Besides, the LBM order of convergence is still up to $2 - 3$ times higher than the SPH one.

For this Reynolds number, it can be seen in Figs. 4.19 and 4.18 that SPH is capable of generating a vertex pattern at the bottom right corner for the two highest resolutions but it is unstable for the smallest resolution. Moderate deviations of the flow indicating a potential growing vortex can be seen at the bottom left corner. When looking at the streamlines of the SPH simulations, we observe that all three resolutions are generating vertexes in the correct spots at selected instants but only the 200×200 case manage to stabilize one at the bottom right corner.

As previously said for the smaller Reynolds numbers, LBM is again showing the appearance of the two vertexes at the correct locations. An instability is growing at the top left corner but disappears at the highest resolution.

For this Reynolds number, it can be seen in Figs. 4.19 and 4.18 that SPH is capable of generating a vertex pattern at the bottom right corner for the two highest resolutions but it is unstable for the smallest resolution. Moderate deviations of the flow indicating a potential growing vortex can be seen at the bottom left corner. When computing the streamlines for selected timesteps of the SPH simulations

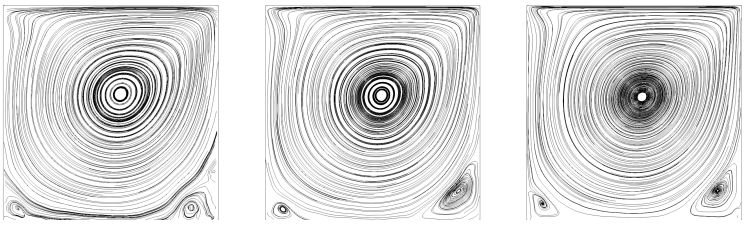

Figure 4.20: SPH streamlines for $Re = 1000$ at selected timesteps

as shown in Fig. 4.20, it is seen that all three resolutions are generating vertexes in the correct spots but only the 200×200 case manage to stabilize one at the bottom right corner.

As previously said for the smaller Reynolds numbers, LBM is again showing the appearance of the two vertexes at the correct locations. An instability is growing at the top left corner but disappears at the highest resolution.

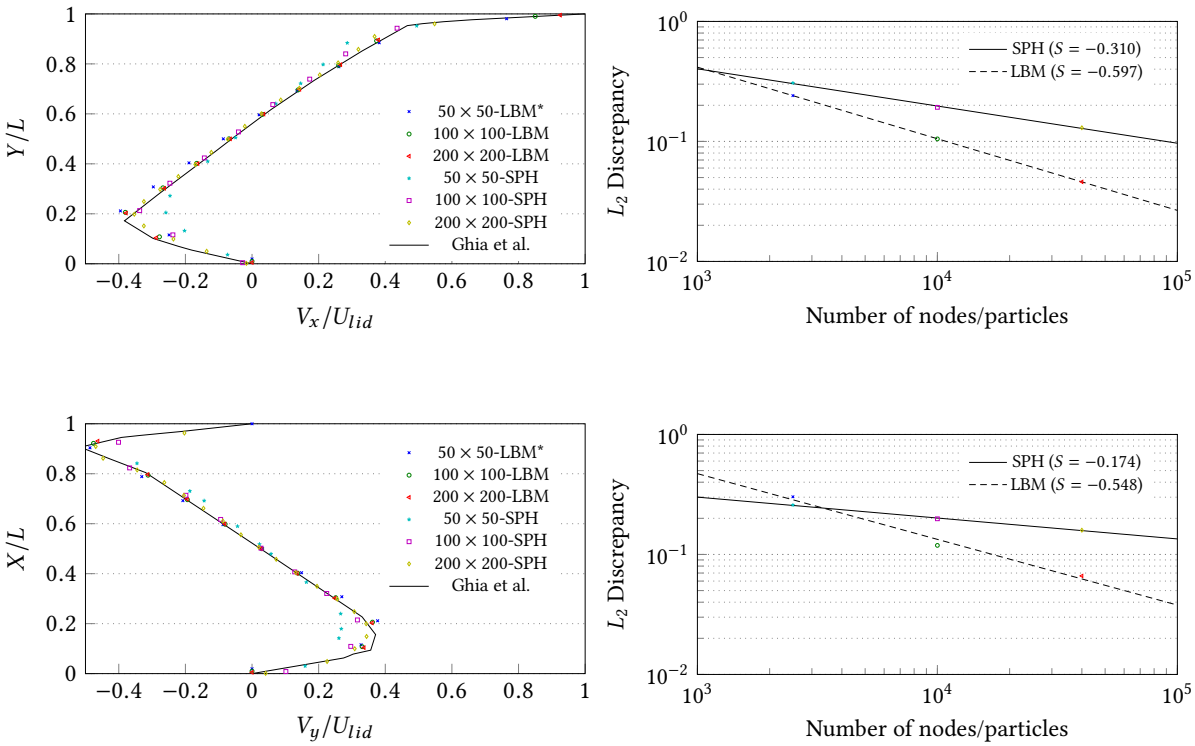

Figure 4.21: $Re = 1000$

4.3.1.4 $Re = 10000$

For $Re = 10000$, the MRT operator despite its superior stability properties compared to BGK is unable to give stable results for none of the considered lattice resolutions. Even using the set of relaxation times S^*, only the highest lattice resolution 200×200 prevents the simulation to blow up. In fact, Zou-he

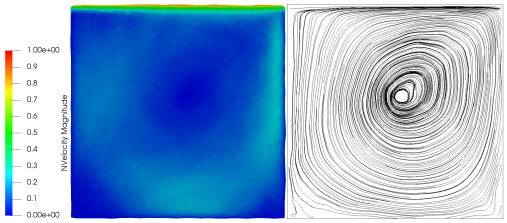

50 × 50 - Velocity (left) - Streamlines (right)

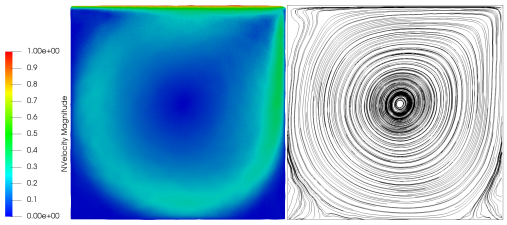

100 × 100 - Velocity (left) - Streamlines (right)

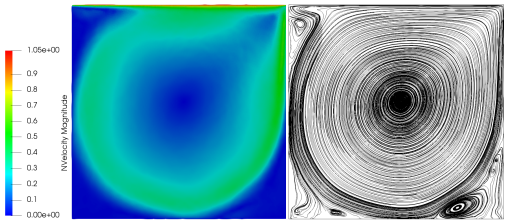

200 × 200 - Velocity (left) - Streamlines (right)

Figure 4.22: SPH results for $Re = 10000$

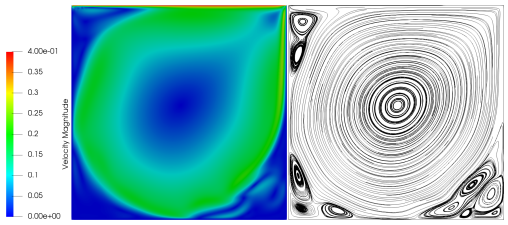

200 × 200 - Velocity (left) - Streamlines (right)

Figure 4.23: LBM results for $Re = 10000$

boundary conditions are known to be unstable at high Re and this is likely to be one the reasons the LBM simulations fail for the lowest resolutions considered. It is possible to enhance the stability of the velocity boundary conditions, see [Latt 2008b] for example.

For high Reynolds numbers, a fluid flow is typically considered turbulent. Although in the case of the lid-driven cavity flow, this assertion is strongly questioned [Erturk 2009]. In addition, the flow is not bi-dimensional anymore. Since no LBM nor SPH models considered in this study include the effect of turbulence and are bi-dimensional, results are to be taken with caution. In consequence, both methods are showing larger errors than in the previous cases where Re was much smaller. Nevertheless, the pattern is the same. As observed in Fig. 4.26, LBM always offers a much better accuracy than SPH for the 200×200 resolution.

In Fig. 4.23, the LBM results are showing a high number of vertexes at the bottom right corner (5 vertexes), the bottom left corner (3 vertexes) and the top left corner (2 vertexes). This is not agreeing with the theory where only 1 vertex is reported at the top left and bottom left corners and 2 vertexes at bottom right corner. These spurious vertexes could be due to the use of the MRT operator with relaxation times tuned based on a trial-and-error approach. The number of vortices is variable during the simulation as shown in Fig. 4.25 where the number of vortices is correct. Extra vortices keep appearing and disappearing throughout the simulation. No steady state is reached by the LBM in this case. The SPH streamlines plots of Fig. 4.22 are not showing any vertex pattern until the highest resolution is reached. For this 200×200 case, one can note the appearance of a vertex at the top left corner, a small growing vertex at the bottom left corner and a growing vertex next to two very small vertexes at the bottom right corner. Those vertexes are stable through the simulation unlike the one at the bottom left corner as suggested by Figs. 4.24. Those figures also show that at a smaller resolution,

none of the expected vertexes are stable.

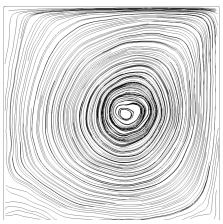

50×50 - $t = 59.5s$

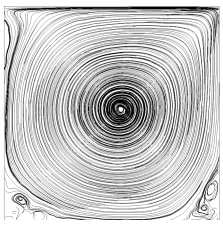

100×100 - $t = 46.56s$

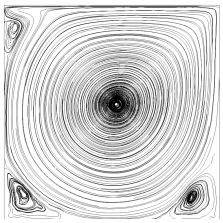

200×200 - $t = 51.05s$

Figure 4.24: SPH streamlines for $Re = 10000$ at selected timesteps

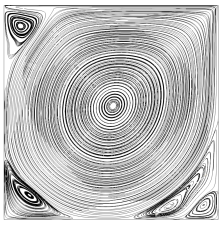

200×200

Figure 4.25: LBM streamlines for $Re = 10000$ at selected timestep

4.3.2 Rayleigh-Taylor Instability

The Rayleigh-Taylor instability is a well-known two-phase problem in which a heavy fluid is placed on top of a light fluid with a given interface shape and submitted to gravity. Several previous works have reproduced this case with SPH or LBM, for example [Grenier 2009a, Szewc 2013, Banari 2012, Ba 2016]. The test case and its parameters are borrowed from [Grenier 2009a]. The computational domain is twice as high as long, $H \times L$ with $H = 2L$ and populated with 40000 nodes/particles. $h/\Delta p$ is set to 1.5 for this case. The density ratio is 1.8 while the viscosity ratio is 1. Gravity is set $g = 9.81$ m/s^{-2} for SPH and $g = 1 \times 10^{-4}$ $l.u.$ and oriented downwards. Therefore, the viscosity ν is adjusted to match the desired Reynolds number $Re = \sqrt{\frac{(H/2)^3 g}{\nu}} = 420$. No surface tension is used. No slip boundary conditions are applied to the walls. The interface is initialized as follows : $y = 1 - \sin(2\pi x)$. Time t is non-dimensionalized by $t_g = 1/\sqrt{g/H}$. The distribution of the two phases is shown at selected timesteps in Fig. 4.27, superposed with results from [Grenier 2009a]. Both methods are able to simulate the instability patterns as expected. Some differences are observable when $t/t_g \geq 3$ in particular when the interface is strongly distorted. LBM grows instabilities slightly faster than SPH and is closer to the behavior of the superposed Level-Set interface. On the other hand, our SPH results are naturally closer to the other SPH interface extracted from [Grenier 2009a]. SPH appears to be more able than LBM (at the same resolution) to capture finer structures such the ones at $t/t_g = 5$ located on both ends of the mushroom-like shapes, but at an higher computational cost.

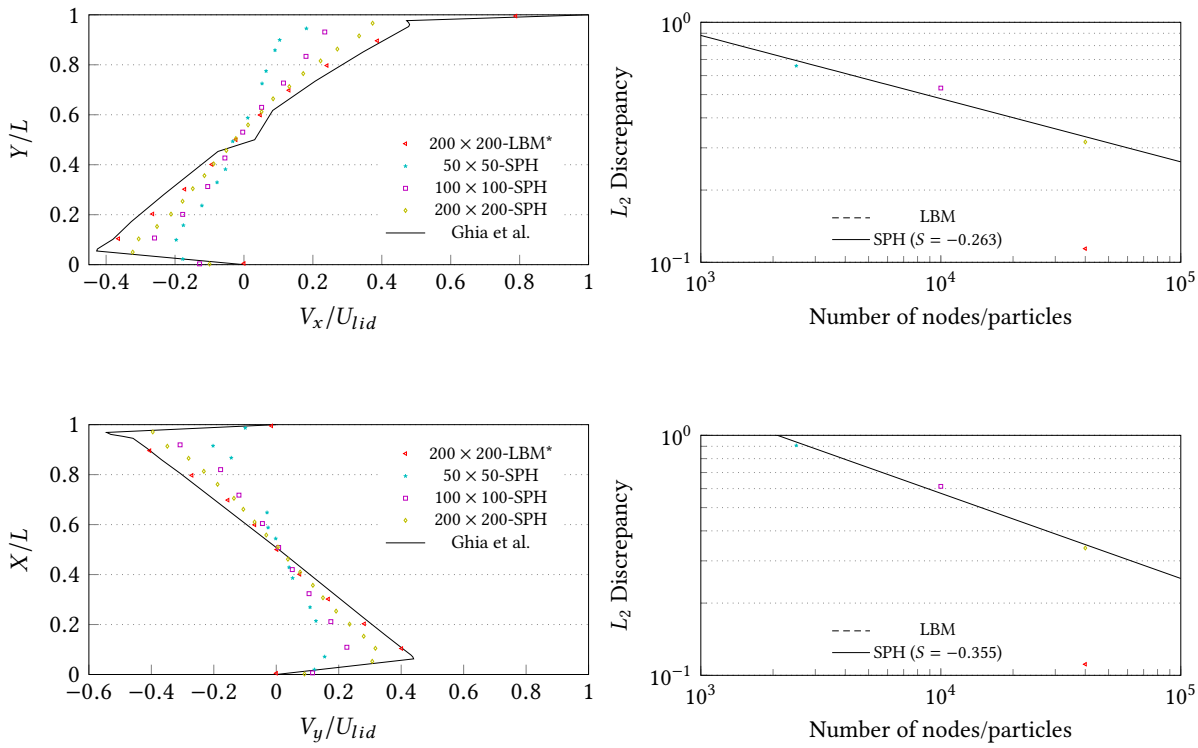

Figure 4.26: $Re = 10000$

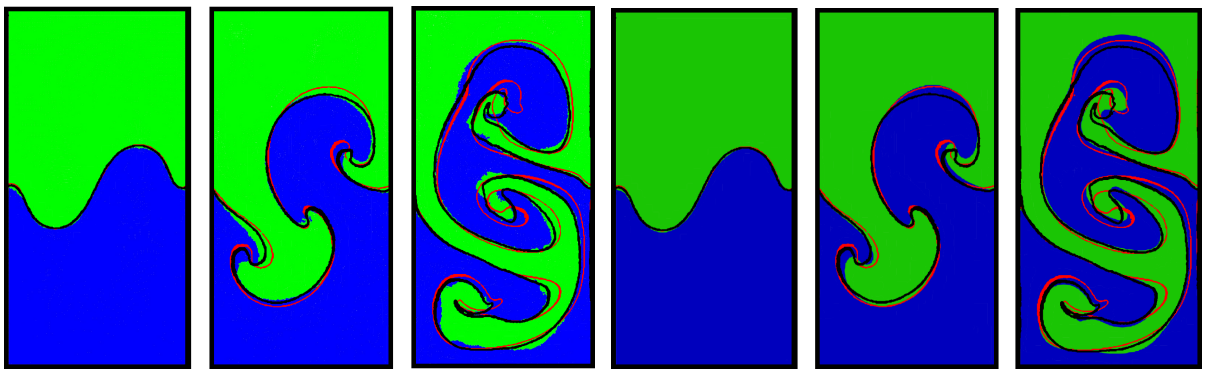

(a) SPH (b) LBM

Figure 4.27: Phase distribution of Rayleigh-Taylor instability at selected timesteps : $t/t_g = 1$, 3 and 5. Superposed with SPH interface (in black) and with Level-Set interface (in red) both extracted from [Grenier 2009a].

4.3.3 Static bubble tests

In this section, the goal is to validate and compare the implementation of LBM and SPH surface tension models respectively described in Sects. 3.12.1.2 and 2.7.2.

Square-to-droplet case The standard square-to-droplet test case is simulated and when a steady state is reached, the pressure difference between the exterior and the interior of the bubble is measured and compared to Laplace's formula :

$$\Delta P = \frac{\sigma}{R} = \frac{\sigma\sqrt{\pi}}{a}, \tag{4.3.2}$$

with ΔP the pressure difference, σ the surface tension coefficient, R the bubble's radius and a the lateral dimension of the initial square bubble. Simulations are performed for three different resolutions : 60×60, 100×100 and 200×200 nodes/particles. $h/\Delta p$ is set to 2 for this case. Four different combinations of density and viscosity ratios were tested : $(\frac{\rho_{\text{heavy}}}{\rho_{\text{light}}}, \frac{\mu_{\text{heavy}}}{\mu_{\text{light}}}) = (1,1)$, $(5,2)$, $(1000,1000)$ and $(1,100)$. The surface tension coefficients and the corresponding Laplace numbers are summarized in Tab. 4.4. The viscosity is then adjusted to match the Laplace number. Note that for each combination $(\frac{\rho_{\text{heavy}}}{\rho_{\text{light}}}, \frac{\mu_{\text{heavy}}}{\mu_{\text{light}}})$, whatever the resolution, the viscosities (and the relaxations times in the case of LBM) are identical. The whole domain is 1 m $\times$ 1 m and the lateral size of the initial square droplet is $a = 0.33$ m. The time is normalized by $t_\sigma = \sqrt{\rho a^3/\sigma}$. Note that, following [Leclaire 2015], parameter β in Eq. 3.12.26 is adjusted when the resolution is increased taking the lowest resolution as a reference i.e. :

$$\beta = \beta_{60\times60}\left(\frac{\Delta x}{\Delta x_{60\times60}}\right)^{5/8}, \tag{4.3.3}$$

with $\beta_{60\times60} = 0.99$.

Case $(\frac{\rho_{\text{heavy}}}{\rho_{\text{light}}}, \frac{\mu_{\text{heavy}}}{\mu_{\text{light}}})$	$La = \frac{\sigma\rho_{\text{heavy}}a}{\mu^2_{\text{heavy}}}$	σ^{SPH} (N/m)	$\sigma^{\text{LBM}}_{60\times60}$ $(l.u.)$	$\sigma^{\text{LBM}}_{100\times100}$ $(l.u.)$	$\sigma^{\text{LBM}}_{200\times200}$ $(l.u.)$
$(1,1)$	15	1.88	2.08×10^{-2}	1.26×10^{-2}	6.22×10^{-3}
$(5,2)$	15	1.88	1.67×10^{-2}	1.01×10^{-2}	4.98×10^{-3}
$(1000,1000)$	0.1	1.25	1.39×10^{-1}	8.41×10^{-2}	4.15×10^{-2}
$(1,100)$	0.0015	1.88	8.33×10^{-6}	5.05×10^{-6}	2.49×10^{-6}

Table 4.4: Laplace numbers and surface tension values for each static bubble case.

Initially, when the density and viscosity ratios are set to one, one can observe in Fig. 4.28 the deformation of an initial square bubble towards a circular bubble under the influence of the surface tension. The Lagrangian/Eulerian difference between SPH and LBM is magnified in Fig. 4.28. We clearly see that, in SPH, particles of each phase move to form a circular bubble over time whereas in LBM, nodes are fixed and they switch phase to form the expect circular bubble. Besides, when the circular bubble is stabilized, both methods present residual velocities around the interface as shown in Fig. 4.29. However, those spurious currents are much more spread into the domain in SPH compared to LBM where they are localized around the interface. Note that, in the LBM color gradient framework, it is possible to significantly reduce the amplitude of spurious currents by choosing a more isotropic gradient operator [Leclaire 2011] but, as it involves second range neighbors, it is more computationally expensive. For SPH, Hu and Adams' formulation [Hu 2006] used in this chapter has been reported to generate stronger spurious currents than other formulations [Kunz 2015].

In Fig. 4.30, the pressure profiles at steady state for the different resolutions and the different density and viscosity ratios considered are shown along with the corresponding L_2 error plots. First, one can

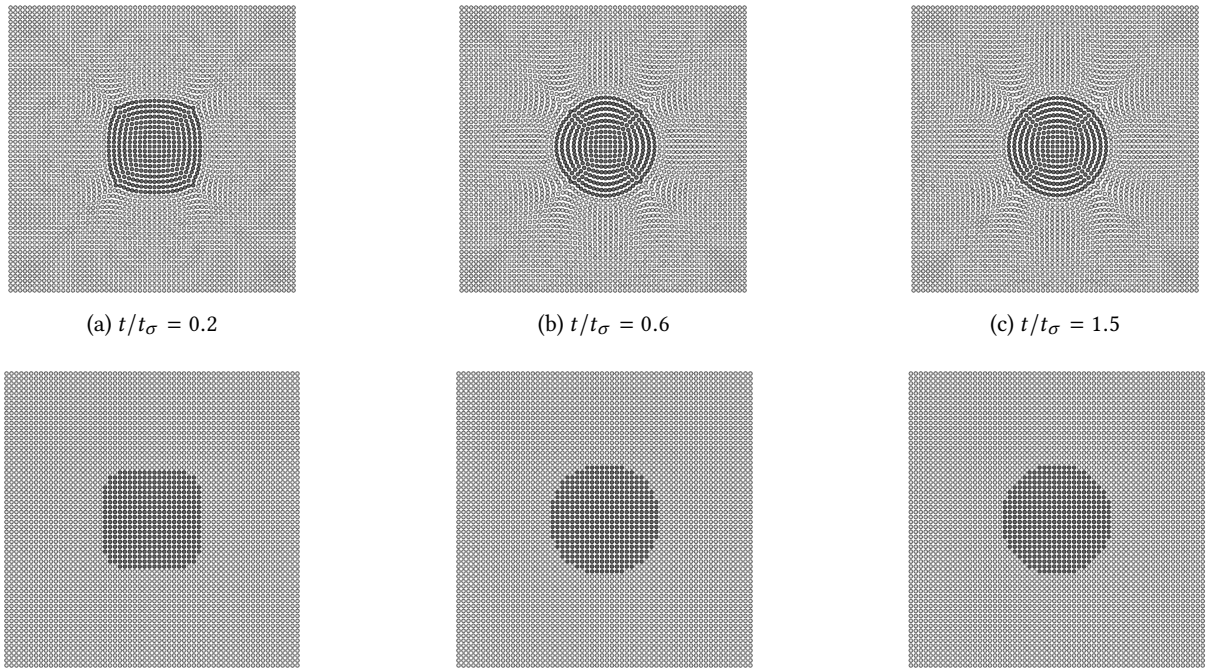

(a) $t/t_\sigma = 0.2$ (b) $t/t_\sigma = 0.6$ (c) $t/t_\sigma = 1.5$

(d) $t/t_\sigma = 0.2$ (e) $t/t_\sigma = 0.6$ (f) $t/t_\sigma = 1.5$

Figure 4.28: Evolution of the initial square bubble at selected timesteps. (a,b,c) SPH. (d,e,f) LBM.

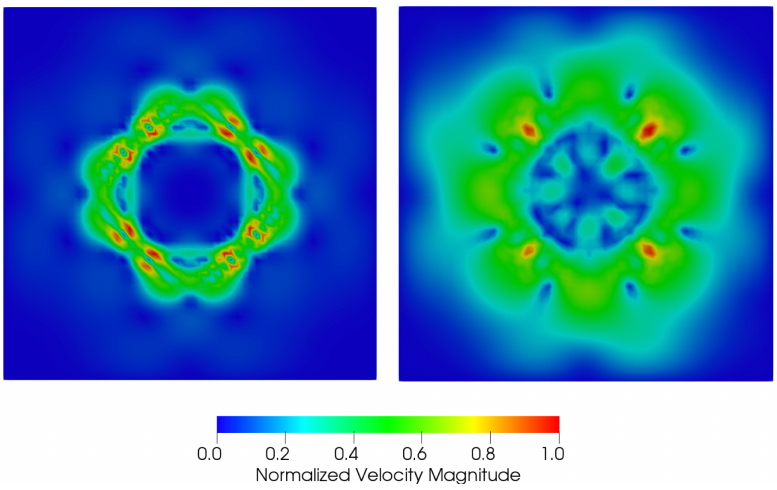

Figure 4.29: Normalized velocity field $\frac{|\boldsymbol{u}|}{|\boldsymbol{u}_{max}|}$ for LBM (left) and SPH (right) at $t/t_\sigma = 1.5$.

clearly see that LBM is returning incorrect pressure values at the interface. Indeed, LBM presents non-physical pressure peaks at the bubble's interface that tend to grow with the number of nodes. In fact, in the LBM color gradient method, the pressure is not well-defined at the interface. The pressure formula of Eq. (3.12.12) does not make sense at the interface where fluids are mixed and there is no mixture pressure defined in the considered framework. Hence, summing the fluid pressures is just an analytical construction that depends on the density profiles and the interface width. Thus, if we look at the LBM L_2 error along the whole horizontal centerline, we do not have mesh convergence since the error is growing at the interface. However, when we restrict the calculation of the L_2 error inside the bubble (i.e. when $0.4\ \mathrm{m} < X < 0.6\ \mathrm{m}$), we do obtain a negative slope indicating mesh convergence.

Next, analyzing the impact of the density and viscosity ratios, for the case where $(\frac{\rho_{\mathrm{heavy}}}{\rho_{\mathrm{light}}}, \frac{\mu_{\mathrm{heavy}}}{\mu_{\mathrm{light}}}) = (1, 1)$ in Figs. 4.30a and 4.30b, we get approximately the same order of convergence for both methods (0.768 and 0.838 for LBM and SPH respectively) and the same error levels ($\leq 1\%$ at the bubble's center) even though SPH always has a slightly higher error level. Next, when the density and viscosity ratios remains moderate (i.e. respectively up to 5 and 2 in Figs. 4.30c and 4.30d), both methods are under 2.5% error compared to the reference solution. Additionally, we see that LBM offers a better order of convergence than SPH. In fact, LBM sees its order of convergence maintained (from 0.768 to 0.792) compared to the previous case unlike SPH where it decreases (from 0.838 to 0.392). Moreover, LBM is less accurate than SPH for the two lowest resolutions 60×60 and 100×100 but performs better for the 200×200 case thanks to its higher order of convergence. Overall, although both methods are returning satisfactory results for this case, we begin to observe a fall in performance whether it is for the order of convergence (for SPH) or for the error levels (for LBM and SPH) because gradients at stake are steeper. Then, for the high density ratio case where $(\frac{\rho_{\mathrm{heavy}}}{\rho_{\mathrm{light}}}, \frac{\mu_{\mathrm{heavy}}}{\mu_{\mathrm{light}}}) = (1000, 1000)$ shown in Figs. 4.30e and 4.30f, we can see that the order of convergence of SPH remains roughly the same compared to the previous case (0.838 vs 0.778). The maximum error level is $\leq 6\%$ i.e. higher than the first case. This tends to indicate that when the density ratio increases, SPH is a quite robust and offers a reasonable accuracy for the same order of convergence. On the other hand, LBM sees its order of convergence not affected by the presence of this density ratio (0.759 vs 0.768) while maintaining approximately the same error level. Finally, we looked at one last case, shown in Figs. 4.30g and 4.30h, where the density ratio is equal to 1 and the viscosity ratio increased up to 100. One can immediately note that, for both methods, the pressure profiles are heavily impacted at the interface (oscillations) in particular for the 60×60 case. However, when looking at the pressure jump at the center of the bubble, LBM appears very robust to the presence of such a strong viscosity ratio. Indeed, we see that the error levels are of the same order than those of the first case and that the order of convergence is even higher (0.768 vs 0.891). It shows that refining the lattice strongly helps to stabilize the pressure field. On the contrary, SPH appears more affected. The error levels are the highest of all four cases considered and the order of convergence is inferior to the first case (0.838 vs 0.658). Moreover, the error does not seem to decrease anymore exponentially with the number of particles although more simulations would be needed to further check that statement.

To sum up, for limited density ratios and viscosity ratios, both methods are able to reproduce the pressure jump predicted by Eq. (4.3.2) with a good accuracy and with steep and clean pressure/density profiles. When the density ratio increases up to 1000, SPH seems to be more resilient than LBM in the sense that its order of convergence is not impacted by the presence of such a strong density ratio. LBM seems less robust in the same situation. On the contrary, when the viscosity ratio goes up to 100, both methods render perturbed pressure profiles. However, it is SPH that appears to have more problem to handle a strong viscosity ratio whereas LBM maintains its performance level.

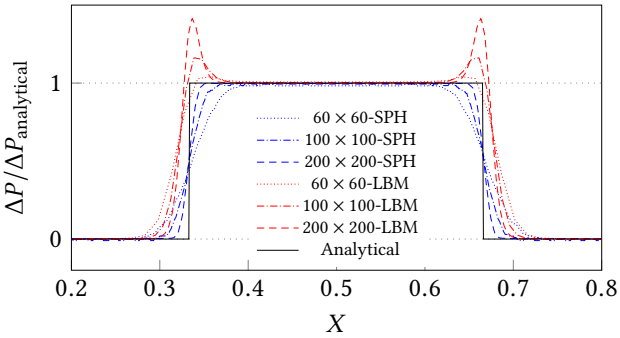

(a) $(\frac{\rho_{\text{heavy}}}{\rho_{\text{light}}}, \frac{\mu_{\text{heavy}}}{\mu_{\text{light}}}) = (1, 1)$

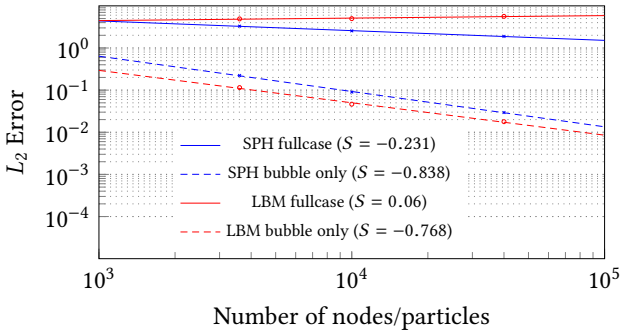

(b) $(\frac{\rho_{\text{heavy}}}{\rho_{\text{light}}}, \frac{\mu_{\text{heavy}}}{\mu_{\text{light}}}) = (1, 1)$

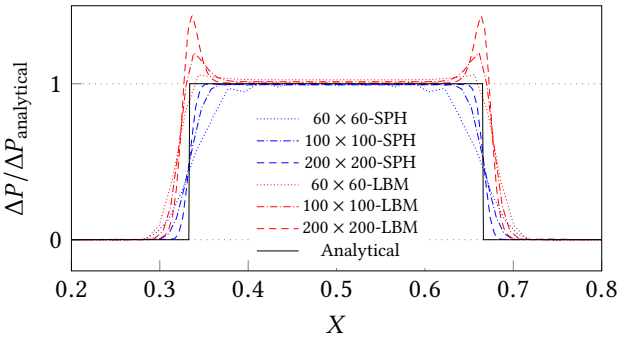

(c) $(\frac{\rho_{\text{heavy}}}{\rho_{\text{light}}}, \frac{\mu_{\text{heavy}}}{\mu_{\text{light}}}) = (5, 2)$

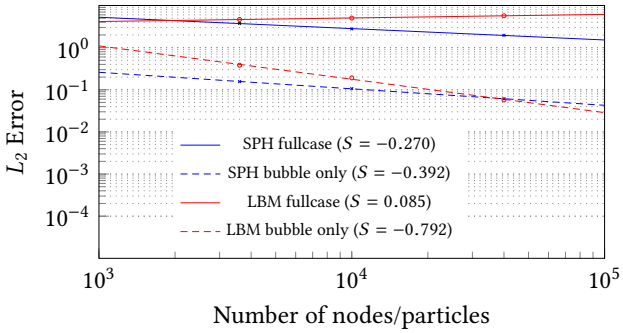

(d) $(\frac{\rho_{\text{heavy}}}{\rho_{\text{light}}}, \frac{\mu_{\text{heavy}}}{\mu_{\text{light}}}) = (5, 2)$

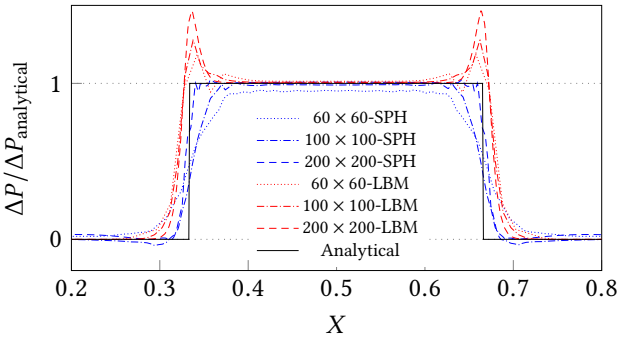

(e) $(\frac{\rho_{\text{heavy}}}{\rho_{\text{light}}}, \frac{\mu_{\text{heavy}}}{\mu_{\text{light}}}) = (1000, 1000)$

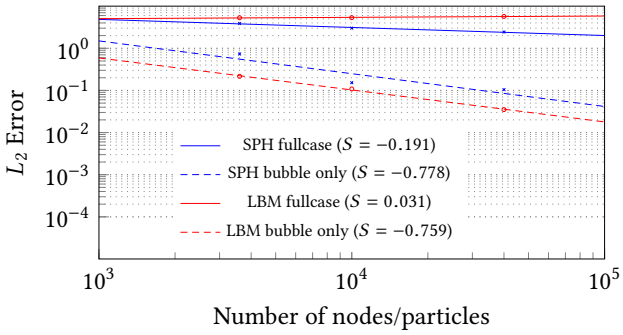

(f) $(\frac{\rho_{\text{heavy}}}{\rho_{\text{light}}}, \frac{\mu_{\text{heavy}}}{\mu_{\text{light}}}) = (1000, 1000)$

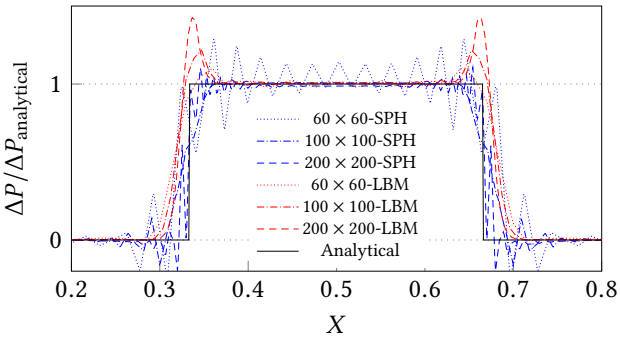

(g) $(\frac{\rho_{\text{heavy}}}{\rho_{\text{light}}}, \frac{\mu_{\text{heavy}}}{\mu_{\text{light}}}) = (1, 100)$

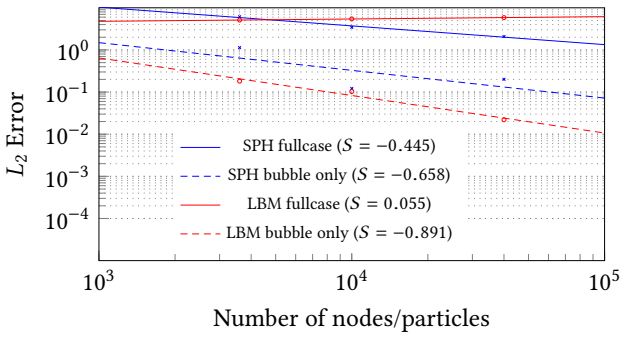

(h) $(\frac{\rho_{\text{heavy}}}{\rho_{\text{light}}}, \frac{\mu_{\text{heavy}}}{\mu_{\text{light}}}) = (1, 100)$

Figure 4.30: (a,c,e,g) Pressure profiles at steady state for different resolutions and different density and viscosity ratios. (b,d,f,h) Log-log L_2 error plots as function of resolution (superposed with linear regressions of slope S).

Contact angle case In addition, we compared the ability of the previously described implementations of SPH and LBM to impose a contact angle in a three phase problem (wetting phase,non-wetting phase,solid phase). We consider a square domain (1 m×1 m) with an initial rectangular droplet (0.33 m× 0.165 m) discretized with 100 × 100 nodes/particles. $h/\Delta p$ is set to 2 for this case. The density ratio and the viscosity ratio between the fluid phases are set to one. For SPH, the surface tension coefficient between the wetting and non-wetting phase, denoted σ^{nw}, and the one between the wetting and the solid phase, denoted σ^{sw}, are both fixed and respectively set to $\sigma^{nw} = 1.88$ N/m and $\sigma^{sw} = 0$ N/m. The surface tension coefficient between the non-wetting and the solid phase, σ^{sn}, is adjusted to match the desired contact angle $\theta_c^{\text{prescribed}}$ using the Young-Laplace equation $\theta_c = \frac{\sigma^{sw}-\sigma^{sn}}{\sigma^{nw}}$. For LBM, we follow the procedure described in Sect. 3.12.1.4. The surface tension coefficient is set to $\sigma = 1.26 \times 10^{-2}$ $l.u.$. Once a steady state is reached, the observed contact angle $\theta_c^{\text{observed}}$ is measured and reported in Fig. 4.31. The coefficient of determination is ≥ 0.99 for both methods confirming that can properly prescribed a contact angle at the triple point. Finally, one can observe the normalized velocity field at steady state for $\theta_c^{\text{prescribed}} = 150°$. The same comments made before are still valid, LBM spurious currents are less spread throughout the domain than in SPH. This is likely due to the Lagrangian nature of SPH where particles have to rearrange to match the simulated physics.

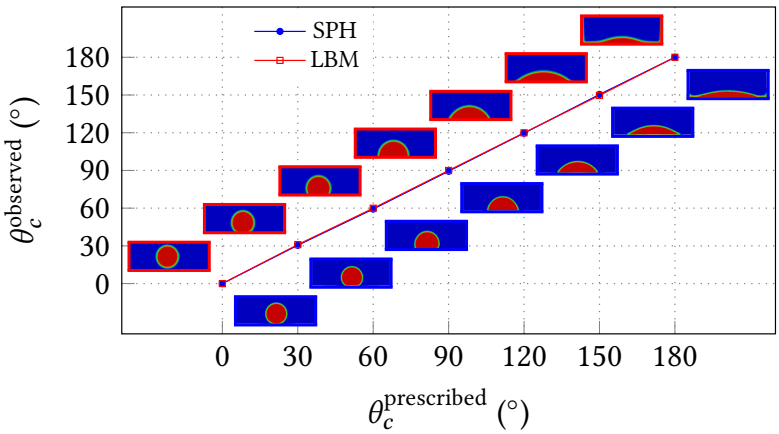

Figure 4.31: Comparison between prescribed and observed contact angles for both SPH and LBM (density and viscosity ratios are both equal to one).

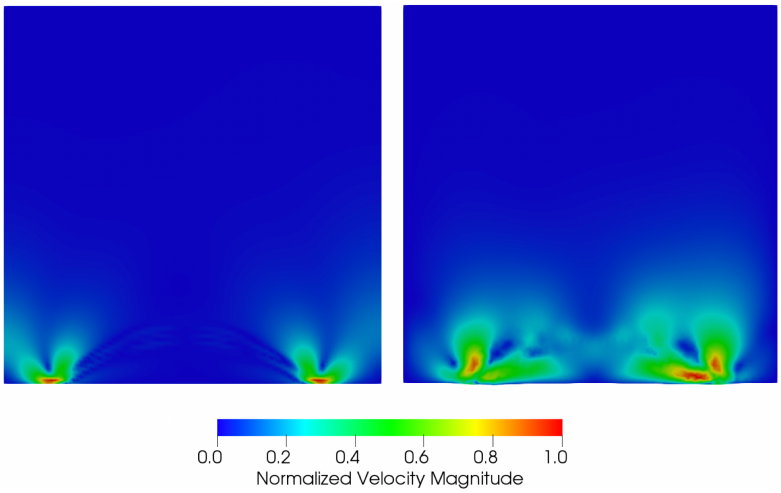

Figure 4.32: Normalized velocity field for LBM (left) and SPH (right) for $\theta_c^{\text{prescribed}} = 150°$.

4.3.4 Capillary Rise

The well-known capillary rise problem is a simple test case to further verify the ability of both models to reproduce contact line dynamics. The problem is described in Figure 4.33. It consists of two fluids, one on top of the other. Two vertical parallel plates are immersed in the fluids. Thanks to the action of surface tension, the lower fluid will rise along the parallel plates forming a meniscus between them. The lower liquid height reached at steady state follows Jurin's law

$$H_{\mathrm{J}} = \frac{2\sigma^{nw}\cos\theta_c}{(\rho_w - \rho_n)gD} \tag{4.3.4}$$

with σ^{nw} the surface tension coefficient between the wetting and the non-wetting phase, θ_c the contact angle, ρ_w and ρ_n the densities of the wetting and non-wetting phase, g the gravity and $D = \frac{4L}{5}$ the horizontal distance between the two plates (with $L = 2.5$cm).

For SPH, simulations were performed with four different resolutions : 100×100, 140×140 and 223×223 particles. The surface tension coefficient is set to 0.25 N/m. $\gamma = 7.0$ for both fluids. For LBM, simulations were performed with four different resolutions : 223×223, 316×316 and 447×447 nodes. $h/\Delta p$ is set to 1.5 for this case. The surface tension coefficient is set to 0.01 $l.u.$. The density and viscosity ratios are both equal to one.

The final height of the lower fluid is then measured and reported in Figure 4.35. On Figure 4.34, one can observe the final particle distributions for different resolutions. The top and bottom boundaries are modeled with non-slip conditions whereas the left and right boundaries are periodic.

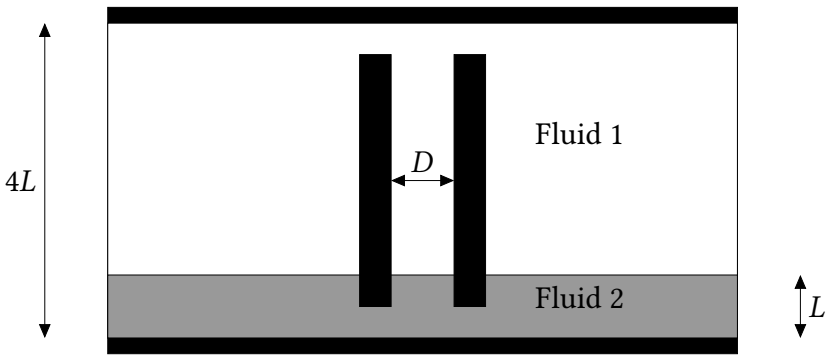

Figure 4.33: The capillary rise problem

It is not completely fair to compare both methods on this case since we do not simulate the exact same Reynolds number and because the geometry is not consistent. For example, the walls in SPH are constituted with the minimum number of particles so that particles on one side do not interact with

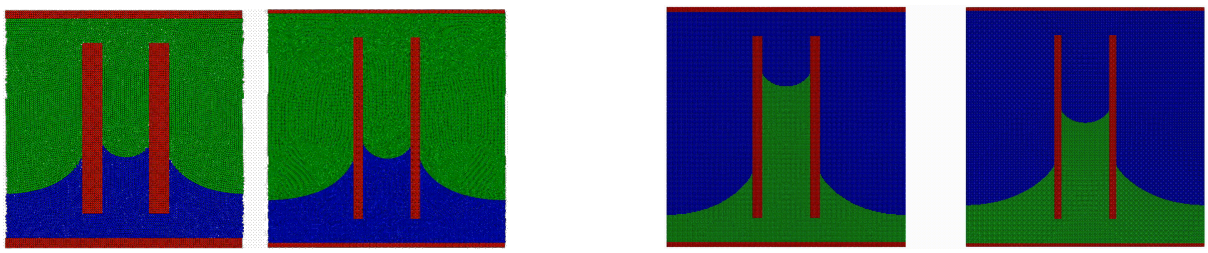

(a) SPH (from left to right 10k and 50k particles)

(b) LBM (from left to right 50k and 100k nodes)

Figure 4.34: Steady state results with for $\theta_c = 30°$

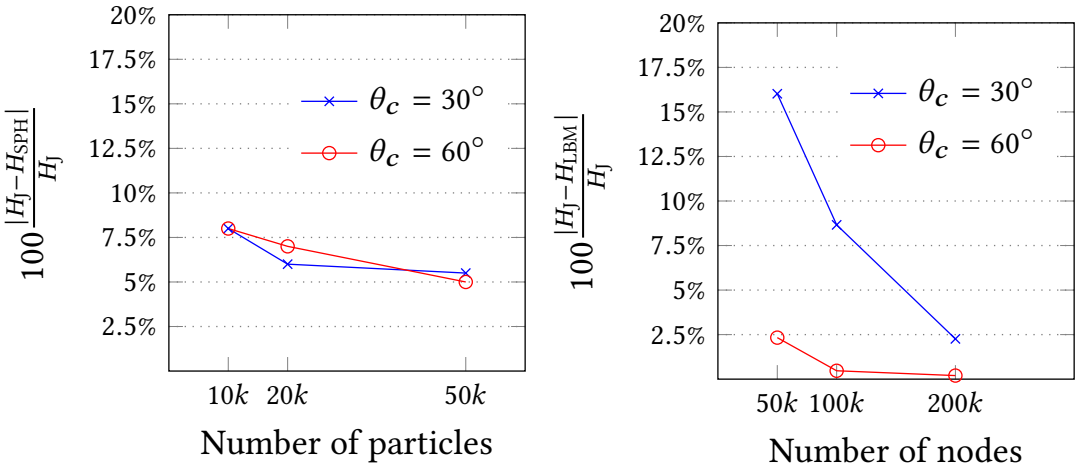

(a) SPH (b) LBM

Figure 4.35: Measured error between the final height of the lower fluid for different resolutions and different contact angles

the particles on the other side which results in a changing geometry. Similarly in LBM, the physical surface tension value changes[2] as we increase the resolution (that is why on Fig. 4.34, the fluid level is different for LBM). In addition, because we have used periodic boundary conditions, we realized later that there are actually two "Jurin's law" in competition whereas Jurin's law is assuming a fluid at rest outside the column which is not the case here. However, regarding the results shown in Fig. 4.35, we see that for both methods the behavior depends on the contact angle value. When the contact angle is smaller, both methods are less efficient in terms of convergence and/or accuracy. Moreover, for the case $50k$ particles/nodes and $\theta_c = 60°$, LBM is much more accurate (2.5% vs 5%) than SPH while SPH appears more resilient in front of low contact angle than SPH.

4.4 Intermittent two-phase flows in pipes

In the following section, we extend our comparative study to two cases of intermittent two-phase flows in pipes for different Reynolds numbers. The first one is periodic and gravity-driven while the second one is generated by a velocity inlet and a pressure boundary condition respectively at the inlet and outlet of the pipe.

4.4.1 Periodic case

In this section, we study the establishment of different periodic two-phase flow patterns under the influence of gravity $\boldsymbol{g}$ starting from a given bubbly flow. Following [Minier 2016], the initial configuration is composed of 27.25% of light phase and 72.75% of heavy phase and is described in Fig. 4.36. All physical properties and simulation properties are in Tab. 4.5. The heavy phase viscosity μ_l is adjusted as function of the Reynolds number $Re = \frac{gH^3}{8\nu_l^2}$. The initial velocity field $\boldsymbol{u}$ is $\boldsymbol{u}(x, y) = \frac{g}{2\nu_l} y(H - y)$. Viscosity values and dimensionless numbers for each case are reported in Tabs. 4.6 and 4.7. No-slip boundary conditions are applied to the walls. The simulations is done with 50000 nodes/particles for $t = 30$ s. $h/\Delta p$ is set to 2 for this case. Four different Reynolds numbers were tested : $Re = 10, 50, 100$

[2]We remind that as described in Sect. 3.7, we can write : $\sigma_{\text{phys}} = \sigma_{\text{la}} \frac{\Delta x_{\text{phys}}^3}{\Delta t_{\text{phys}}^2} \rho_{0\text{phys}}$.

and 500. The phase distributions, pressure fields and velocity fields at final state are shown in Figs. 4.37, 4.39 and 4.40 respectively.

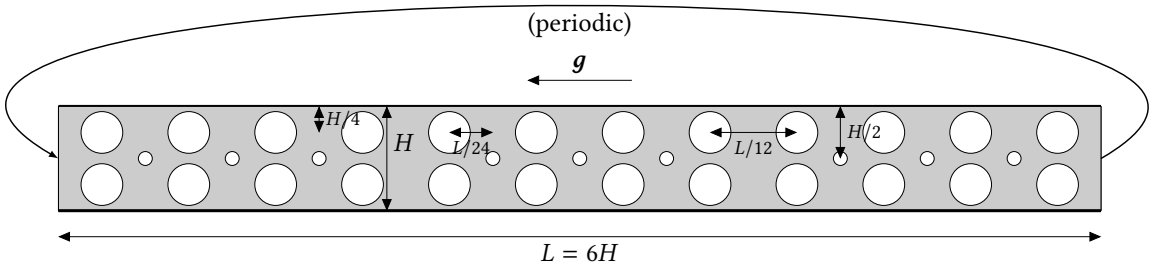

Figure 4.36: Initial configuration sketch. The large bubbles radius is $R = 0.2H$ and the small bubbles' radius is $R_2 = R/3$. The pipe height is $H = 0.1$ m.

Property	Light Phase	Heavy Phase	Units	Light Phase	Heavy Phase	Units
Density (ρ)	1.0	5.0	kg/m^3	1.0	5.0	$l.u.$
Viscosity (μ)	$\mu_g = \mu_l/2$	μ_l	Pa.s	$\mu_g = \mu_l/2$	μ_l	$l.u.$
Contact Angle (θ_c)	0		°	0		°
Surface Tension (σ^{nw})	5.0968×10^{-2}		N/m	2.11×10^{-2}		$l.u.$
Gravity (g_x)	1.0		m/s^2	5.0×10^{-7}		$l.u.$
Space step (Δx)	1.09×10^{-3}		m	1.09×10^{-3}		$l.u.$
Domain size ($L_x \times L_y$)	0.6×0.1		m	551×91		$l.u.$

(a) SPH (b) LBM

Table 4.5: Simulation parameters.

Case	μ_g (Pa.s)	μ_l (Pa.s)	μ_g ($l.u.$)	μ_l ($l.u.$)	τ_g	τ_l
1 ($Re = 10$)	8.84×10^{-3}	1.77×10^{-2}	6.86×10^{-2}	3.43×10^{-1}	1.014	0.706
2 ($Re = 50$)	3.95×10^{-3}	7.91×10^{-3}	7.67×10^{-2}	1.53×10^{-2}	0.730	0.592
3 ($Re = 100$)	2.79×10^{-3}	5.59×10^{-3}	5.42×10^{-2}	1.08×10^{-2}	0.663	0.565
4 ($Re = 500$)	1.25×10^{-2}	2.50×10^{-3}	2.43×10^{-2}	4.85×10^{-2}	0.572	0.529

(a) SPH (b) LBM

Table 4.6: Viscosity values for each case.

In Fig. 4.37, it is possible to see that both methods reproduce the same flow pattern for all four Re numbers considered. For $10 \leq Re \leq 100$, we obtain a bubbly flow composed of three different Taylor bubbles whereas for $Re = 500$, we have an annular flow where the heavy phase is in contact with the pipe and the light phase travels in the middle. For $Re = 10$, we observe that SPH present a bubbly flow where one bubble is clearly smaller than the two others. It is not the case in LBM where all bubbles are identical within each case. Besides, for this case, we have heavy phase droplets than are captured inside light phase bubbles. Note that these small bubbles are to be absorbed by the main flow if the simulation lasted longer because they are moving slower than their environment. For $Re = 50$ and $Re = 100$, we obtain in all cases the same pattern made of three identical Taylor bubbles. Moreover, as shown in Fig. 4.38, the bubbles' shapes between SPH and LBM for $10 \leq Re \leq 100$ are very similar.

Case	$Re = \frac{gL_y^3}{8\nu_l^2}$	$La = \frac{\sigma \rho_l L_y}{\mu_l^2}$	$Bo = \frac{\Delta\rho g L_y^2}{\sigma}$
1	10	82	0.7848
2	50	408	0.7848
3	100	816	0.7848
4	500	4077	0.7848

Table 4.7: Reynolds, Laplace and Bond numbers for each case.

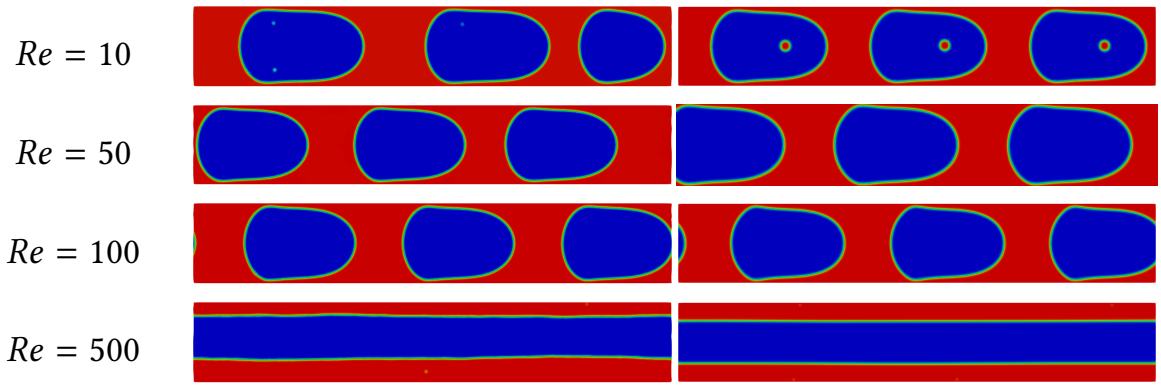

Figure 4.37: Steady state for different Re. SPH and LBM results are on the left and right columns respectively.

Finally, as Re grows, the Taylor bubbles are getting slightly shorter and higher in size. For $Re = 500$, we again see that LBM offers a perfectly symmetric annular pattern. On the contrary, the bottom heavy phase layer in SPH is thicker than the top one. In general, LBM provides more symmetric results than SPH because of its Eulerian nature.

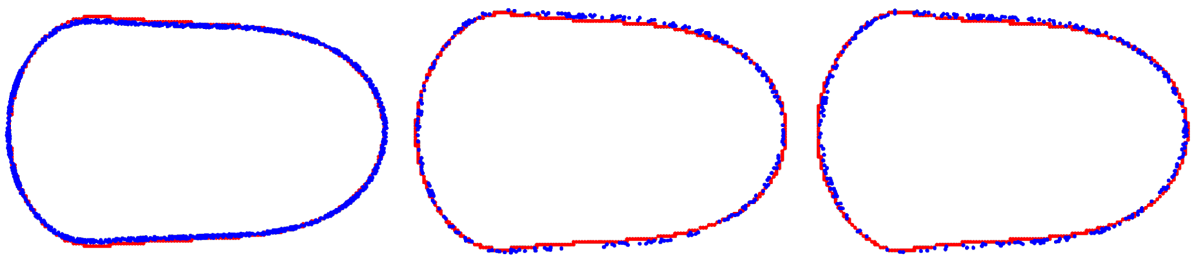

$Re = 10$ $Re = 50$ $Re = 100$

Figure 4.38: Superposition of bubbles' shapes obtained with SPH (blue) and LBM (red) for different Reynolds numbers.

In Fig. 4.39, we can see that for $Re = 10$, the pressure fields is dominated by the captured droplets of heavy phase inside the bubbles. For $Re = 50$ and 100, the pressure field reaches a maximum for SPH inside the bubbles whereas for LBM it is at the interface. Nevertheless, as predicted by Laplace's law, the pressure is higher inside the light phase's bubbles than in the heavy phase bulk. When looking at the velocity fields in Fig. 4.40, we see that they are also very similar. The same patterns surrounding the bubbles can be observed. For the annular case where $Re = 500$, it is possible to see that the no-slip

condition on the walls affects the flow more strongly in LBM than in SPH which results in a flatter velocity profile for the latter.

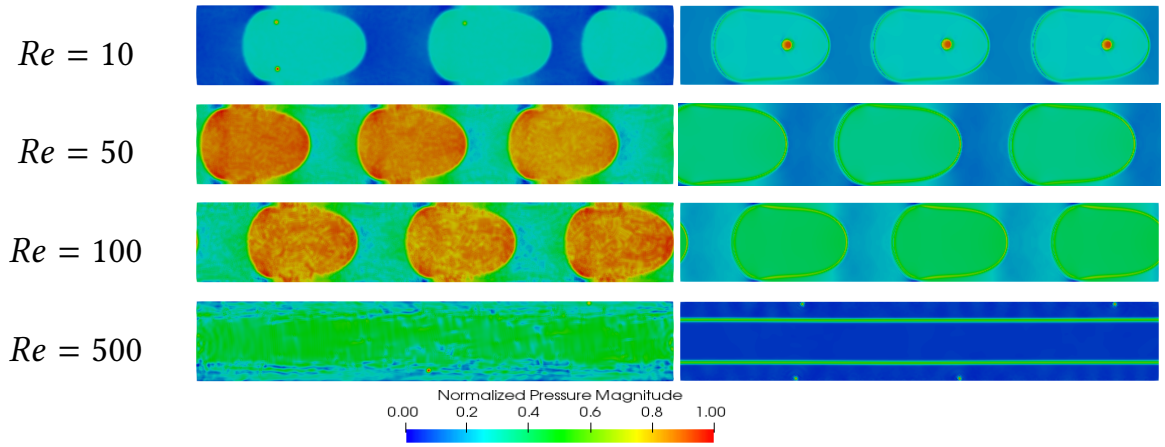

Figure 4.39: Normalized pressure fields at steady state for different Re. SPH and LBM results are on the left and right columns respectively. Pressure is normalized by the maximum pressure inside the bubbles.

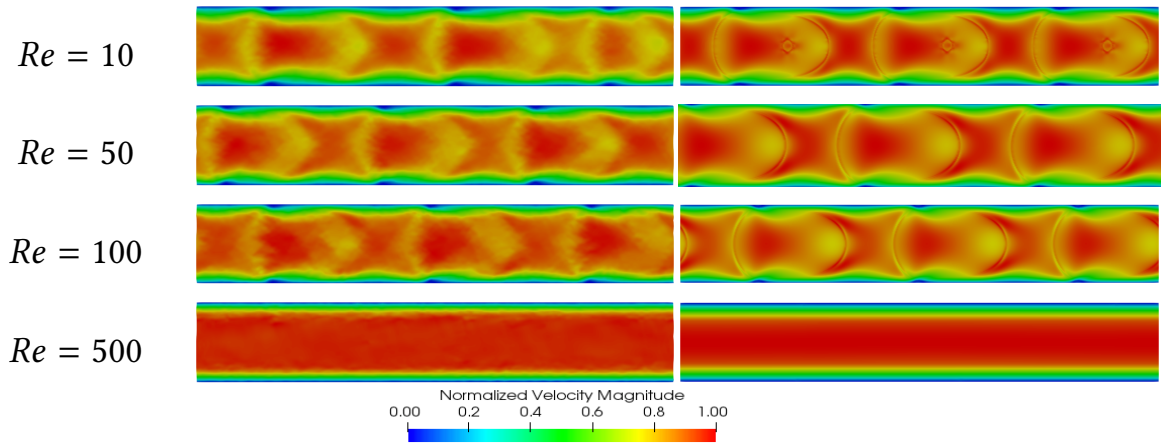

Figure 4.40: Normalized velocity fields at steady state for different Re. SPH and LBM results are on the left and right columns respectively.

For $Re = 50$ and $Re = 100$, where the SPH and LBM patterns are the closest, we compared the density, velocity and pressure fields along the centerline on Figs. 4.41 and 4.42. Note that because the bubbles do not have the exact same position, we have shifted the LBM profiles from a fixed distance to be able to superpose the profiles. On the density plots of Figs. 4.41a and 4.42a, the different density treatment in both methods clearly appears. In LBM, the density is smoothed at the interface whereas in SPH, thanks to its Lagrangian nature, there is no interface smoothing in the density field because a given particle belongs to one phase or not, there is no intermediate state. Concerning the pressure fields shown in Figs. 4.41b and 4.42b, we observe that LBM suffers from the same overshoots at the interface that were described and explained in Sect. 4.3.3. On the other hand, the SPH pressure field is polluted with noise. Despite these discrepancies, both profiles are very close. Finally, in Figs. 4.41c

and 4.42c, we see the velocity profiles in both methods have the same shape. The bubbles are moving at a much higher speed than the surrounding fluid (about 30% faster). At each interface, the velocity reaches a local minimum. The only differences between both profiles is that in certain areas, the SPH velocity peaks have a smaller amplitude than in LBM. For example, the bubble velocity is the same for all three bubbles in LBM for $Re = 50$ whereas for SPH the last bubble travels about 10% faster than the other ones. One last comment is that in LBM at the interface, the velocity field present non-physical oscillations due to the fluids mixing at the interface. It is not the case in SPH because the pressure field does not suffer from pressure overshoots and fluids are not mixed at the interface.

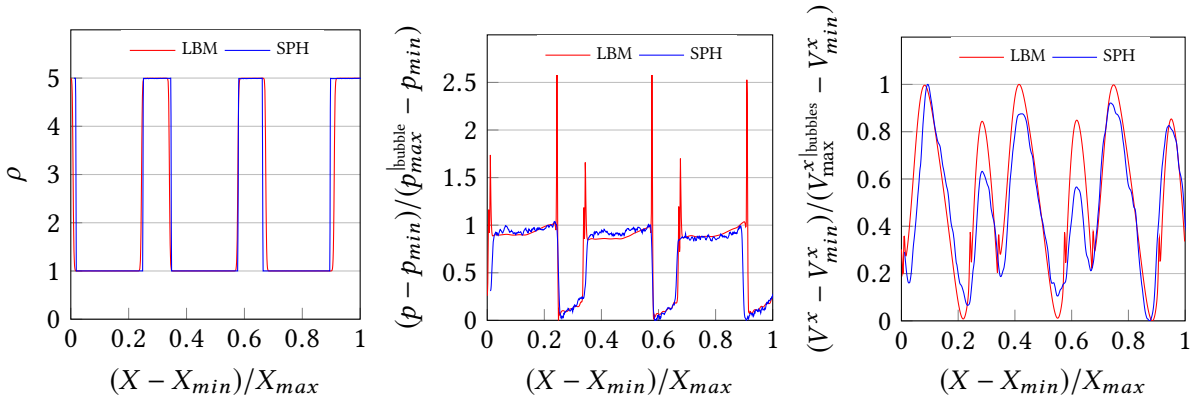

(a) Density (b) Normalized Pressure (c) Normalized Velocity

Figure 4.41: Case $Re = 50$. (a) Superposed densities. (b) Superposed normalized pressures. (c) Superposed normalized velocities.

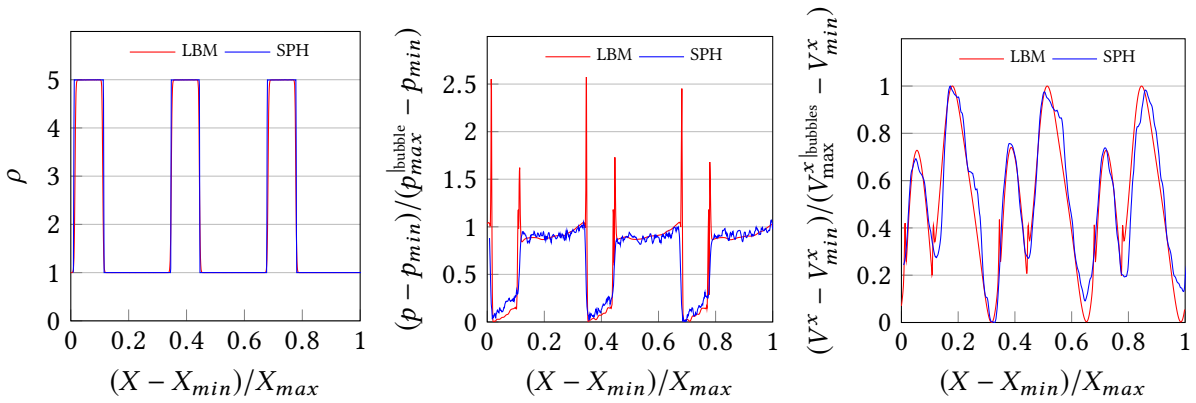

(a) Density (b) Normalized Pressure (c) Normalized Velocity

Figure 4.42: Case $Re = 100$. (a) Superposed densities. (b) Superposed normalized pressures. (c) Superposed normalized velocities.

To conclude, we can add that SPH and LBM are both well capable of simulating the transition from a given bubbly flow to a slug flow composed of Taylor bubbles for $Re \leq 500$. To further assess their relative performance, an extended comparison with other methods or with experimental data would be of great interest. Note that we have limited our study to $Re \leq 500$ because, for higher velocities and/or smaller viscosities, we lie outside LBM stability region whether because the low Mach rule is violated or because the relaxation time is too close from 0.5.

4.4.2 Inlet/outlet case

In this section, we study the ability of both methods to simulate a predicted intermittent flow regime. We consider an horizontal pipe of diameter $D = 1$ m and length $L = 10D$. The light phase and heavy phase are denoted with a g and l subscript respectively. The flow enters from the inlet (left) and is assumed to be stratified with given volume fractions for each phase $\alpha_g = 0.2$ and $\alpha_l = 0.8$. All the physical properties are summarized in Tab. 4.8. Using these properties, it is possible to plot the flow regime map, see Fig. 4.44[3], and to pick an area to be investigated in the intermittent region. In this area, we adjust the viscosity to choose two cases that correspond to $Re = 125$ and $Re = 312.5$. Viscosity values and dimensionless numbers for each case are reported in Tabs. 4.9 and 4.10. Both cases were simulated in 2D with 25000 nodes/particles. $h/\Delta p$ is set to 2 for this case. The simulation time was 30 s. At the inlet, each phase is injected with a constant velocity corresponding to its superficial velocity $u^s_{g,l} = \alpha_{g,l} u_{g,l}$. At the outlet, a constant pressure equal to the initial pressure p_0 is prescribed. Free slip boundary conditions are applied on the top wall and no slip boundary conditions on the bottom wall (we were not able to generate a slug flow in LBM with no-slip boundary conditions on both walls). Since the flow map [Taitel 1976] assumed the light phase is a gas, it is reasonable to impose free slip boundary conditions on the top wall because the gas is not supposed to stick to the wall. The initial setup is presented in Fig. 4.43. The phases distributions for each case are shown in Fig. 4.45 along with the associated plots showing the volume fraction evolution over time, the average pressure drop evolution over time, the heavy/light phase velocity evolution over time respectively in Fig. 4.46, Fig. 4.48 and Fig. 4.49. Note that unlike previous sections in which only the dimensionless numbers such as Re were similar between SPH and LBM, in this section, we simulate the exact same test case in both methods. It means when converting LBM lattice units from Tab. 4.8b to physical units following [Latt 2008a], one can re-obtain the values shown in Tab. 4.8a.

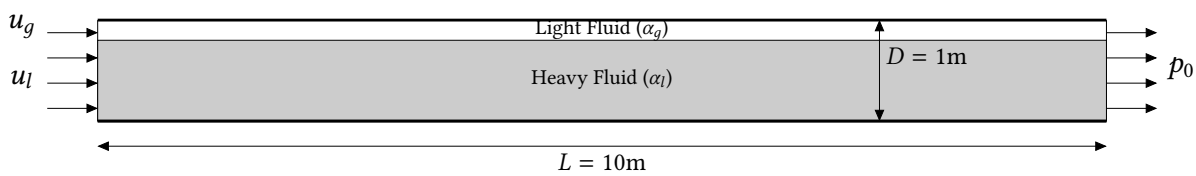

Figure 4.43: Initial configuration sketch.

In Fig. 4.45, one can see snapshots of the phases' distribution for both methods at selected timesteps. It is clear that both methods are able to generate a slug flow as predicted by the flow map of Fig. 4.44. However, LBM produces a much more regular intermittent flow pattern with a lower slug frequency than SPH. This can also be seen in Figs. 4.46 and 4.47. For example, for $Re = 312.5$, the LBM slug frequency at the outlet is approximately 1.52 Hz whereas for SPH it is close to 3.22 Hz. The slug frequency seems to remain roughly stable or to slightly increase (about +1.1 Hz for LBM and about +0.8 Hz for SPH for the highest peak) when Re changes from 125 to 312.5 although it is less obvious in SPH periodograms due to the noise and composition of the signal. It is expected that the slug frequency increases when Re increases but we could not raise Re higher without making LBM simulations unstable ($\tau \longrightarrow 0$ or $Ma \longrightarrow 1$). In addition, SPH periodograms are noisier with 2 to 4 major frequency components unlike LBM where one frequency clearly emerges. It indicates that SPH volume fraction signals are less regular and are composed of signals with different frequencies. Moreover, we can observe in both methods that the point where the first slug appears is in general closer from the pipe entry when Re is smaller. This is expected since when velocities are smaller at the entry, the first slug tends to form earlier in the pipe.

[3]In order to plot the map, one has to compute the Lockhart-Martelli [Lockhart 1949] parameter which depends on n, m, C_g and C_l. In this study, we used $n = m = 2$ and $C_g = C_l = 0.042$

Property	Light Phase	Heavy Phase	Units
Density (ρ)	1.0	5.0	kg/m^3
Viscosity (μ)	$\mu_g = \mu_l/2$	μ_l	Pa.s
Sound speed (c_s)	153.73	68.75	m/s
Surface Tension (σ^{nw})	0.01		N/m
Contact Angle (θ_c)	90		°
Gravity (g_z)	5.556		m/s^2
Space step (Δx)	0.02		m
Time step (Δt)	6.53×10^{-5}		s
Domain size ($L_x \times L_y$)	10×1		m
Inlet velocity (u)	1.0416	6.25	m/s

(a) SPH

Light Phase	Heavy Phase	Units
1.0	5.0	$l.u.$
$\mu_g = \mu_l/2$	μ_l	$l.u.$
0.5773503		$l.u.$
7.2×10^{-5}		$l.u.$
90		°
1.6×10^{-5}		$l.u.$
1.0×10^{-2}		$l.u.$
2.4×10^{-4}		$l.u.$
500×50		$l.u.$
1.25×10^{-2}	7.5×10^{-2}	$l.u.$

(b) LBM

Table 4.8: Simulation parameters.

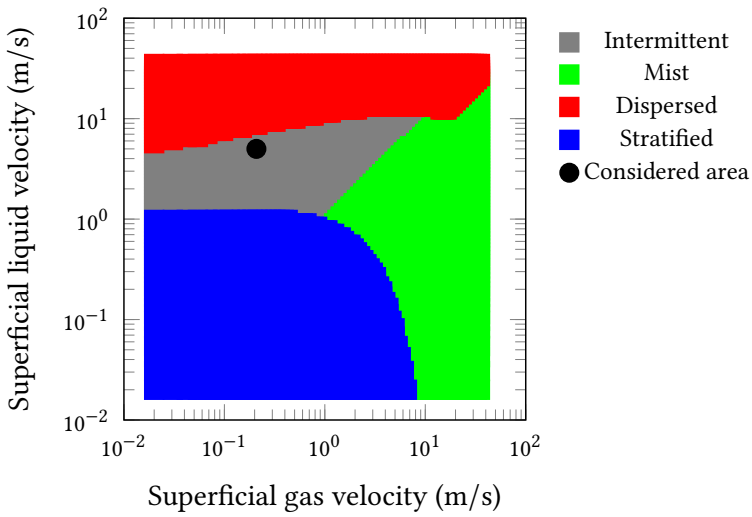

Figure 4.44: Flow regime map

Case	μ_g (Pa.s)	μ_l (Pa.s)
1 ($Re = 125$)	1.25×10^{-1}	2.5×10^{-1}
2 ($Re = 312.5$)	5×10^{-2}	1×10^{-1}

(a) SPH

μ_g ($l.u.$)	μ_l ($l.u.$)	τ_g	τ_l
7.5×10^{-2}	1.5×10^{-1}	0.725	0.59
3.0×10^{-2}	6.0×10^{-2}	0.59	0.536

(b) LBM

Table 4.9: Viscosity values for each case.

Case	$Re = \frac{L_y u_l}{\nu_l}$	$La = \frac{\sigma \rho_l L_y}{\mu_l^2}$	$Bo = \frac{\Delta \rho g L_y^2}{\sigma}$
1	125	0.8	2222
2	312.5	5	2222

Table 4.10: Reynolds, Laplace and Bond numbers for each case.

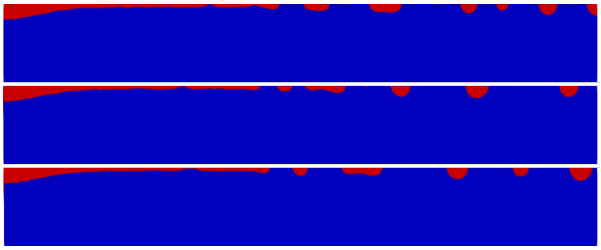

(a) SPH - $Re = 125$

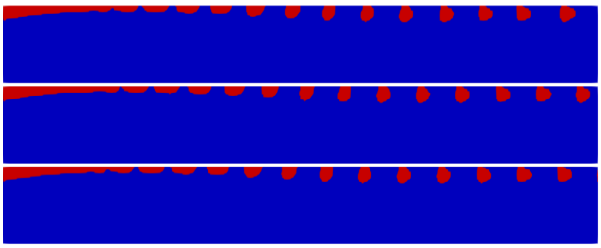

(b) LBM - $Re = 125$

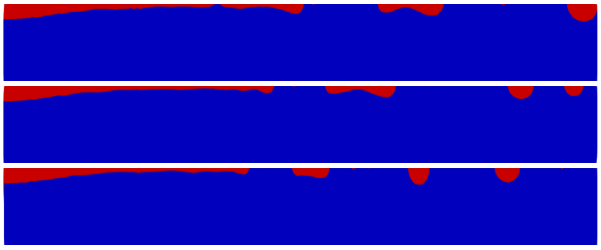

(c) SPH - $Re = 312.5$

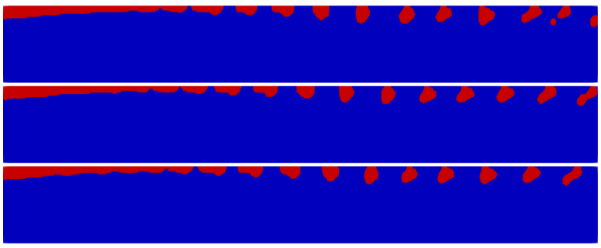

(d) LBM - $Re = 312.5$

Figure 4.45: (a, b) From top to bottom : snapshots at $t = 4.7$ s, 13.5 s, 25 s. (c, d) From top to bottom : snapshots at $t = 4.2$ s, 16.4 s, 25.6 s.

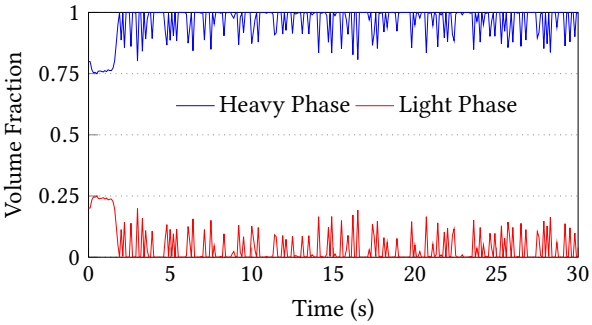

(a) SPH - $Re = 125$

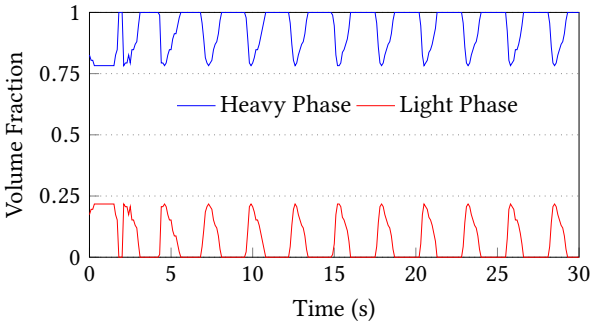

(b) LBM - $Re = 125$

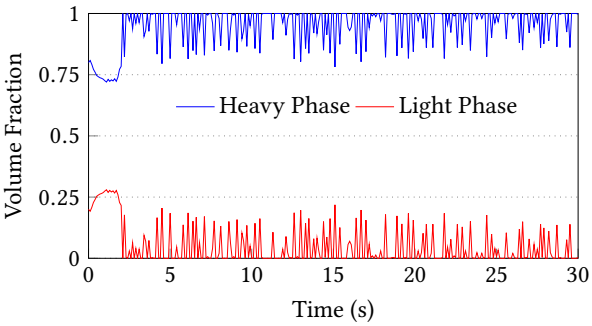

(c) SPH - $Re = 312.5$

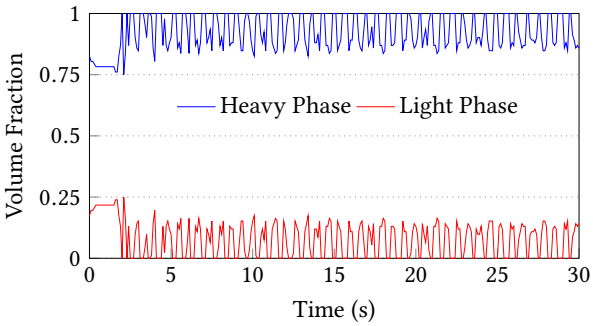

(d) LBM - $Re = 312.5$

Figure 4.46: Evolution of the volume fractions at the outlet over time.

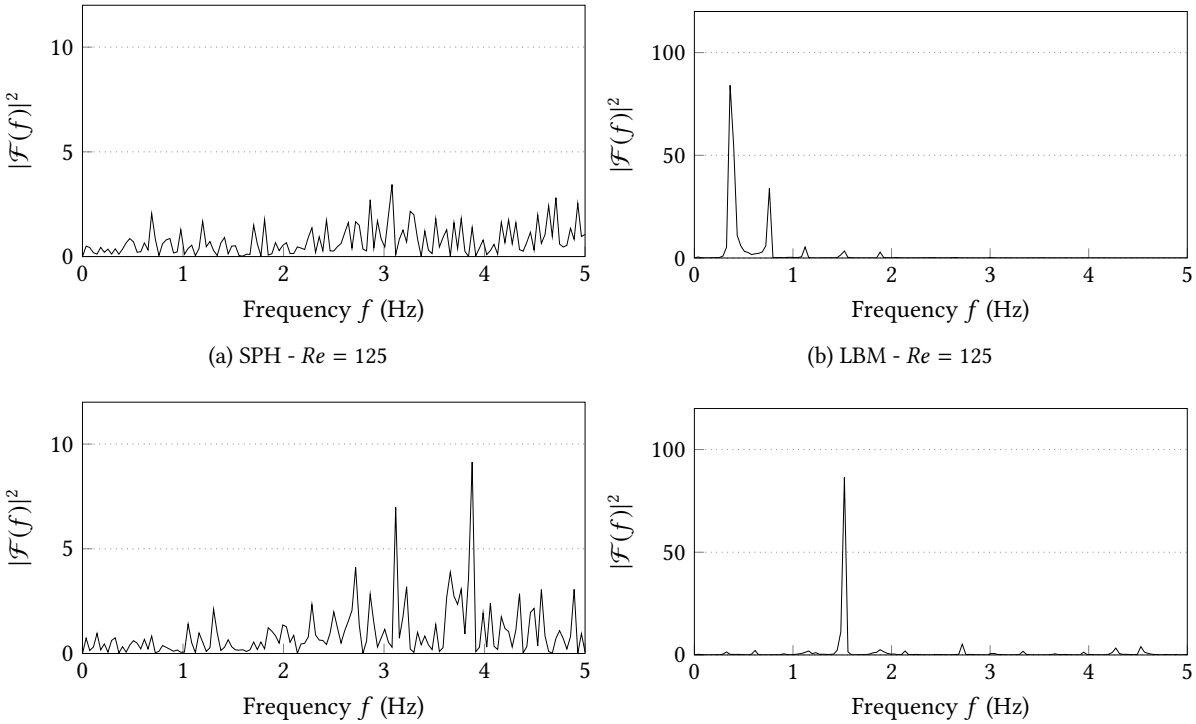

(a) SPH - $Re = 125$

(b) LBM - $Re = 125$

(c) SPH - $Re = 312.5$

(d) LBM - $Re = 312.5$

Figure 4.47: Periodograms of the heavy phase volume fraction time series (in blue in Fig. 4.46). The mean has been removed from the signal before performing the Fourier transform to remove the 0 Hz frequency component.

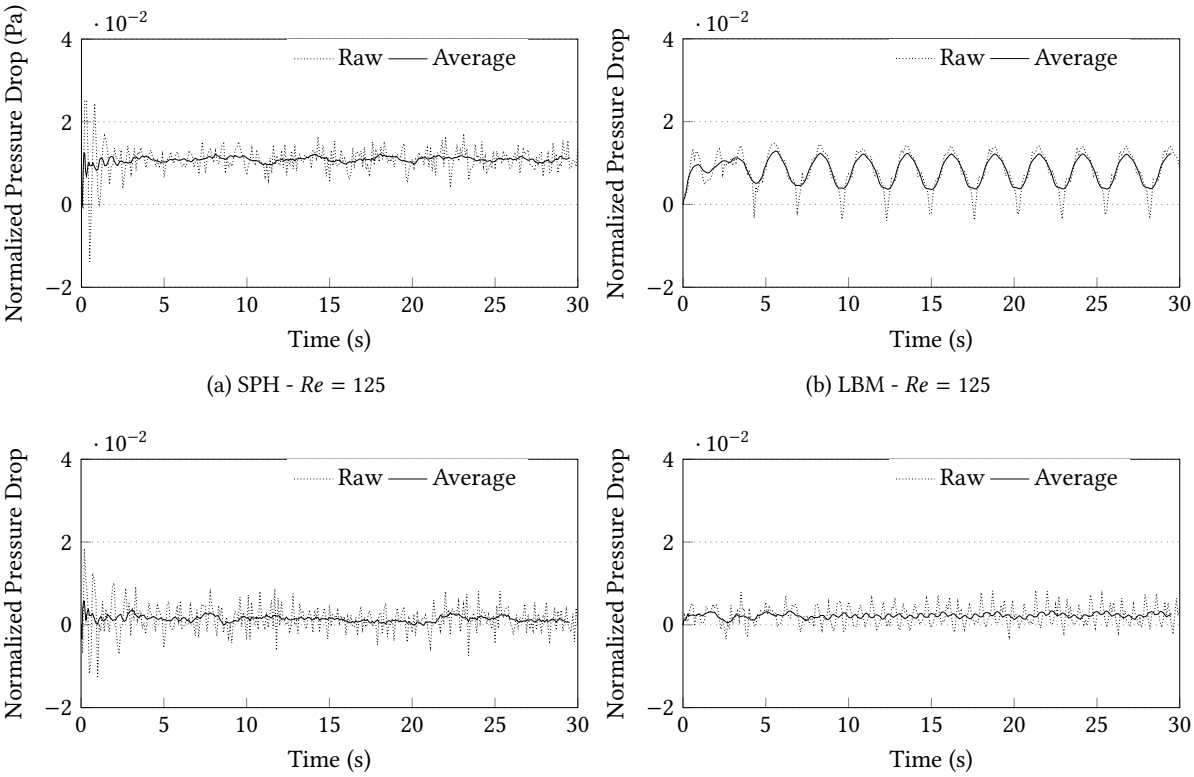

(a) SPH - $Re = 125$

(b) LBM - $Re = 125$

(c) SPH - $Re = 312.5$

(d) LBM - $Re = 312.5$

Figure 4.48: Evolution of the normalized pressure drops over time.

In Fig. 4.48, the raw and average pressure drops evolution over time for all the different cases studied are shown. One can notice that in all cases, the pressure drops are ≥ 0 on average (even though strong oscillations are observed). We observe that both methods are returning the same average pressure drop level around $\approx 0.01p_0$ for $Re = 125$ and $\approx 0.003p_0$ for $Re = 312.5$. However, for both methods the pressure drop level slightly decreases when Re increases which is unlikely. It may be due to several factors : the quality of the boundary conditions, the recirculation areas at the entry that tend to lower the pressure and the averaging area chosen (i.e. 0.1 m (from the inlet) $\times D$). In addition, we see that SPH plots present high frequency oscillations. This is a known issue in weakly compressible SPH where the particles spatial distribution is directly linked to the density/pressure.

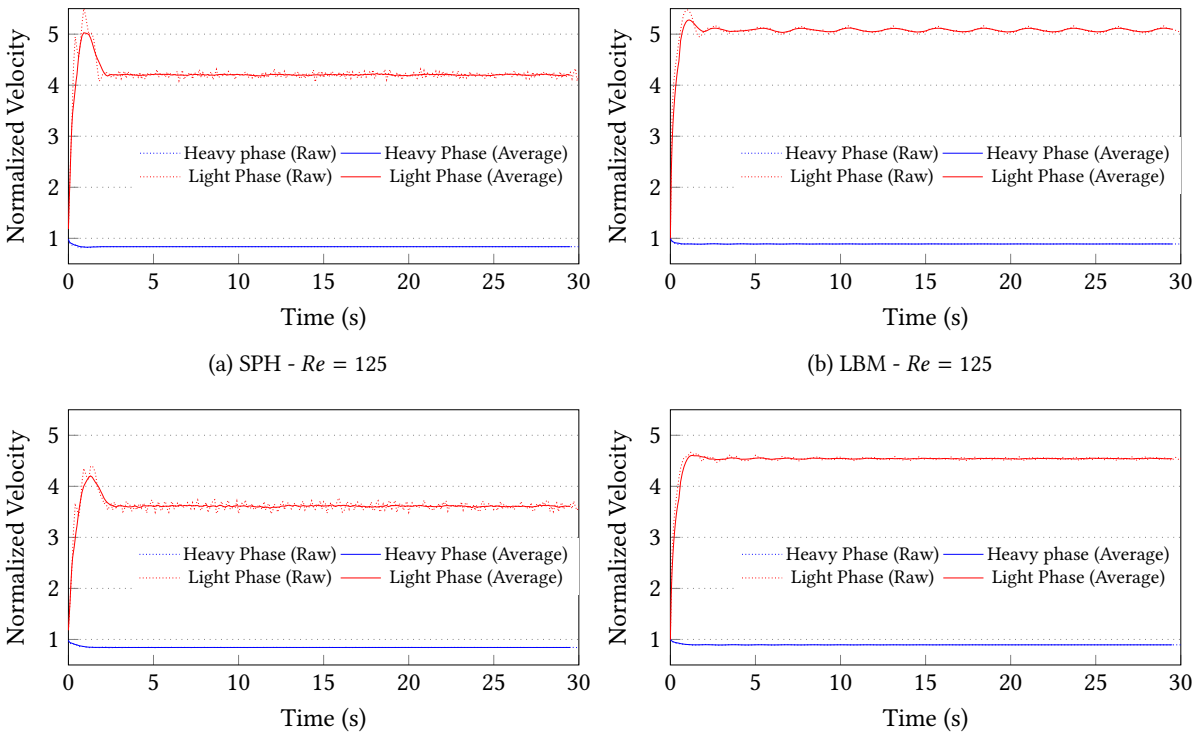

(a) SPH - $Re = 125$

(b) LBM - $Re = 125$

(c) SPH - $Re = 312.5$

(d) LBM - $Re = 312.5$

Figure 4.49: Evolution of the normalized velocities over time.

In Fig. 4.49, the evolution over time of the heavy phase and light phase velocities within the whole pipe are shown for all cases considered. After a transient period of ≈ 4 s, the light and heavy phase velocities stabilize around a fixed value when a periodic state is reached. The main difference between SPH and LBM on this aspect is that the final velocity values are higher in LBM than they are in SPH. Overall, the average velocity field in LBM is $20\% v^{\text{in}}$ higher than in SPH. In our opinion, this is due to the wall boundary conditions that are handled in a very different way in both methods (full bounce back approach in LBM and interpolation-based approach in SPH) and to the wetting boundary conditions that is also handled differently. Those can strongly affect the flow, especially in dynamic cases like the ones considered in this section. From a general point of view, one can add that the oscillations observed in Figs. 4.48 and 4.49 are gaining amplitude when Re increases in SPH whereas it is not the case in LBM for which they tend to reduce. The major slug frequency being higher in SPH than in LBM tends to indicate that the LBM contact angle imposition procedure results in a stickier wall behavior of the bubbles, despite the fact that the global flow velocity is higher in LBM than in SPH.

In a nutshell, as predicted by Taitel and Dukler's flow map, both methods are capable to generate a slug flow pattern starting from the exact same simulation setup. Nevertheless, unlike all previous test cases for which the results were globally similar, we obtain significantly different flow patterns. Indeed, SPH produces bigger bubbles and in a more irregular way compared to LBM. We tend to believe that it is due to boundary conditions. In addition, we could not extend our study to higher *Re* number because LBM was not stable anymore. Although, we tend to think that LBM is entitled to propose the best solution, in particular because of its superior accuracy, its narrow stability range may be a serious drawback to simulate two-phase flows in pipes at realistic *Re* numbers.

4.5 Conclusion

In this chapter, we presented inlet/outlet boundary conditions for multiphase flows for SPH by combining ideas from [Tafuni 2018, Alvarado-Rodríguez 2017] and for LBM by extending LBM Zou-He boundary conditions.

From a general point of view, we have confirmed that LBM offers a better order of convergence and a better accuracy than SPH although it suffers from a more narrow stability range than SPH. In many situations for which the Mach number is too high or the viscosity is too low, LBM will be unstable contrary to SPH which is only controlled by the CFL condition. Note that research on the extension of LBM to high Mach numbers is very active. In addition, SPH tends to generate pressure fields that are noisier than with LBM because of the Lagrangian behavior of particles whose position is directly linked to pressure through the density evaluation. This problem has been the subject of many investigations and several treatments are available (*delta*-SPH [Marrone 2011], SPH-ALE [Oger 2016], turbulence models [Violeau 2007a] or ISPH [Hu 2007]). Moreover, LBM is more computationally efficient than SPH by construction.

On the multiphase aspects, both methods are very capable to simulate a variety of dynamic incompressible multiphase flow problems with good precision in the case of moderate density and viscosity ratios. However, we have noted that, on one hand, SPH appears more robust for high density ratios than LBM and, on the other hand, SPH has more trouble to handle high viscosity ratios than LBM. Another difference is that, at the interface, the fluids are mixed resulting in a diffuse interface whereas with SPH, particles are affected to one phase or the other without any mixing. More specifically, both methods have been able to simulate slug flows where expected but, due to boundary conditions, there might be differences in slug frequency and/or slug sizes.

To conclude, according to the results presented in this chapter, our recommendation would be to use LBM when stability is not an issue and SPH otherwise.

Chapter 5

Multiphase SPH for the simulation of intermittent flows in pipes

Contents

5.1 Flow regimes **162**
5.2 Flow transitions **169**
5.3 Applied cases with high density and viscosity ratios **174**
5.4 Influence of the spurious interface fragmentation correction **176**
5.4.1 Flow Regimes 177
5.4.2 Visual comparison with Xie et al. 178
5.4.3 Flow Transitions 180
5.4.4 High density and viscosity ratios 181
5.5 Comparison with experimental data **186**
5.5.1 Suzanne test case 187
5.5.2 Imperial test case 189
5.6 Conclusion **194**

Our goal with this chapter is to contribute to the ongoing effort to show that SPH can be applied to industrial cases. To this end, we used recent multiphase SPH features available in the literature to simulate a set of close-to-industry test cases. To the best of our knowledge, the only previous SPH study on the topic is available in [Minier 2016] and is focused on the transition from bubbly flow to slug flow using periodic boundary conditions and a gravity-based driving force.

In this chapter, we first verify the ability of our SPH model to recover different flow regimes predicted by Taitel and Dukler's flow map [Taitel 1976] and we study the transition processes between two flow patterns in sections 5.1 and 5.2. Then, in Sect. 5.3, we present two more realistic cases involving high density and viscosity ratios. Next in Sect. 5.4, we come back on selected results of the previous sections but this time studying the influence of the spurious interface correction detailed in Eq. (2.7.21) on these results. Finally in Sect. 5.5, we conclude this chapter with a comparison with experimental data on real cases of stratified and slug flows.

SPH immiscible multiphase model For the following simulations, the immiscible multiphase SPH model previously presented in Sect. 4.2 has been used.

5.1 Flow regimes

We consider an horizontal pipe of diameter $D = 1$m and length $L = 10D$. The light phase and heavy phase are denoted with a g and l subscript respectively. The flow enters from the inlet (left) and is assumed to be stratified with equal volume fraction for each phase $\alpha_g = \alpha_l = 0.5$ (50% of heavy phase and 50% of light phase). We stress that despite the use of volume fractions to describe the problem, the fluids are not initially mixed. All the physical properties are summarized in Tab. 5.1. Using these properties, it is possible to plot the flow regime map, see Fig. 5.2[1], and to pick four cases, one in each region, to be simulated. Those cases and their corresponding parameters are presented in Tab. 5.2 and marked by different symbols on Fig. 5.2. All cases were simulated in 2D with three different resolutions $L/\Delta r = 312$, 444 and 704 which corresponds approximately to 10000, 20000 and 50000 particles. $h/\Delta p$ is set to 2 for this case. The simulation time was 30 s. At the inlet, each phase is injected with a constant velocity corresponding to its superficial velocity $u^s_{g,l} = \alpha_{g,l} u_{g,l}$. At the outlet, a constant pressure equal to the background pressure is prescribed. The initial setup is presented on Fig. 5.1. The final two-flow patterns for the different cases, the evolution of the volume fraction with time at the outlet and the average pressure drop between both ends of the pipe is presented on Figs. 5.3 to 5.7. In addition, the evolution of the velocity magnitude along the pipe's length for each phase for the three particle resolutions considered is shown on Figs. 5.8 and 5.9.

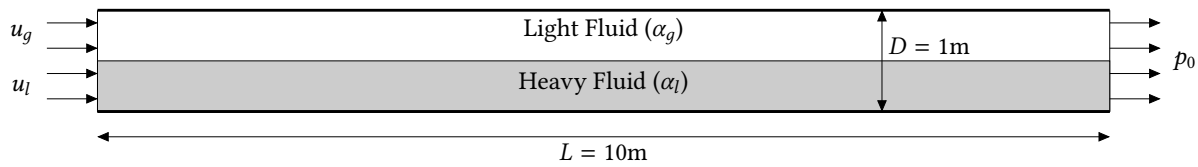

Figure 5.1: The initial configuration for all cases (not at scale).

[1]There exists a large variety of flow regime maps to help characterize two-phase flow regime in pipes. For the particular case of horizontal pipes, one can mention Baker's map [Baker 1953] and Barnea's map [Barnea 1987]. In this work, Taitel and Dukler's map [Taitel 1976] has been used to predict flow regimes. In order to plot the map, one has to compute the Lockhart-Martelli [Lockhart 1949] parameter which depends on n, m, C_g and C_l. In this study, we used $n = m = 2$ and $C_g = C_l = 0.042$

Property	Light Phase	Heavy Phase	Units
Density (ρ)	1	5	kg/m^3
Viscosity (μ)	5×10^{-3}	1×10^{-2}	Pa.s
Adiabatic index (γ)	7	7	-
Surface Tension (σ^{nw})	0.001		N/m
Contact Angle (θ_c)	90		$^\circ$
Gravity (g_z)	-1		m/s^2

Table 5.1: Physical Properties

Property	Case 1	Case 2	Case 3	Case 4	Units
Flow pattern	Mist	Dispersed	Intermittent	Stratified	-
Superficial velocities (u_g^s,u_l^s)	(4.9,0.06)	(0.05,8)	(0.25,2)	(0.7,0.06)	m/s
Reynolds number ($Re = \frac{(u_g^s+u_l^s)D}{\nu_g\alpha_g+\nu_l\alpha_l}$)	1417.14	2300	642.86	217.14	-
Friedel Pressure Drop Prediction ($\Delta p^{\text{Friedel}}$)	20.931	98.513	11.961	4.1	Pa

Table 5.2: Cases properties

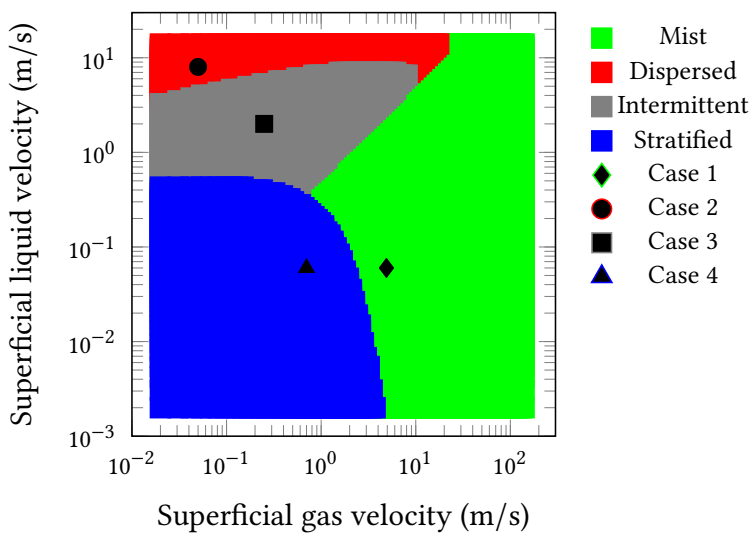

Figure 5.2: Flow regime map adapted from [Taitel 1976]

For information purposes, Friedel correlation [Friedel 1979] has been used to evaluate the expected pressure drops for the four considered cases of Fig. 5.2. These values reported in Tab. 5.2 are to be taken with caution as the Friedel correlation has proven not to be very reliable for rectangular channels, separated flows and/or viscous fluids [Müller-Steinhagen 1986, Wambsganss 1992, Spedding 2006]. Besides, on the same table, we also report the average Reynolds number for the considered geometry and flow conditions. Note that this is an average value. Depending on how it is computed, the Reynolds number could be locally much higher than the given value.

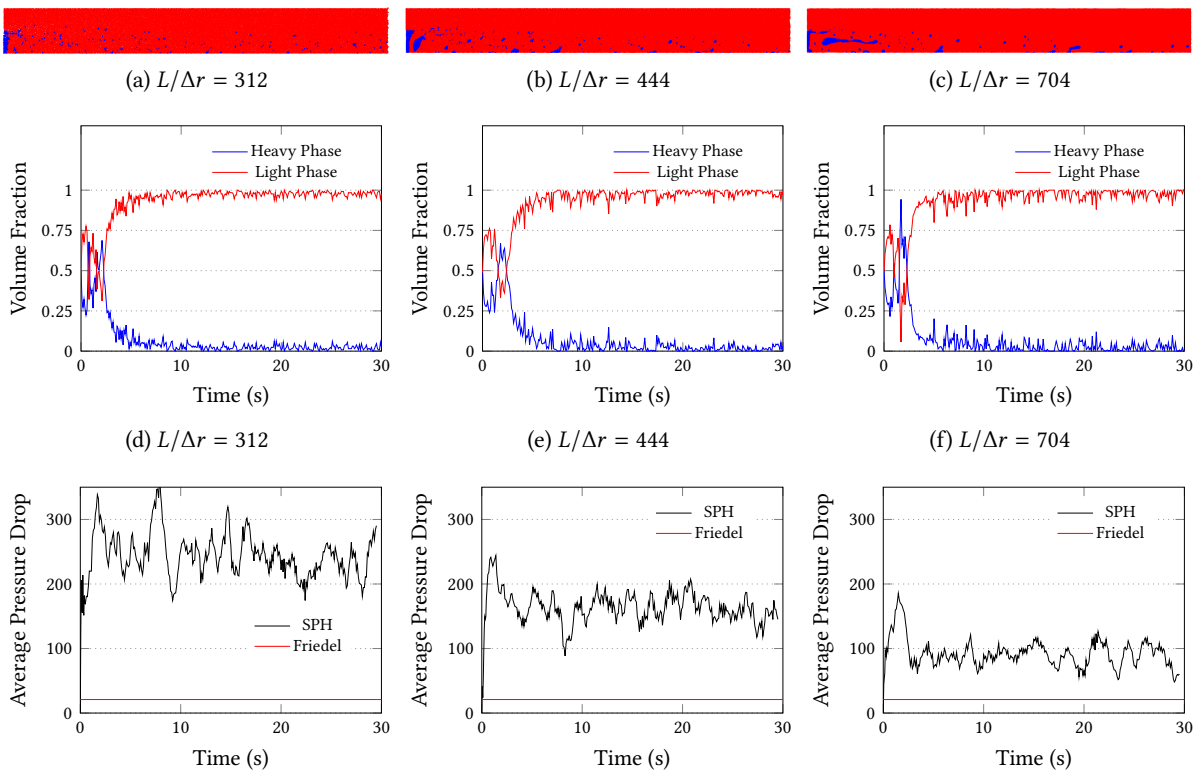

(a) $L/\Delta r = 312$ (b) $L/\Delta r = 444$ (c) $L/\Delta r = 704$

(d) $L/\Delta r = 312$ (e) $L/\Delta r = 444$ (f) $L/\Delta r = 704$

(g) $L/\Delta r = 312$ (h) $L/\Delta r = 444$ (i) $L/\Delta r = 704$

Figure 5.3: Results for case 1 (Mist flow) : (a,b,c) Phases distribution at $t = 30$ s (not at scale). (d,e,f) Evolution of the volume fractions at the outlet with time. (g,h,i) Evolution of the average pressure drop at the outlet with time.

On Figs. 5.3a to 5.3c, one can observe that a mist flow pattern where the heavy phase is scattered by the light phase. It is confirmed by Figs. 5.3d to 5.3f where we see that the light phase outlet volume fraction goes to 1 after a transient period. Note that, in 3D, this mist pattern could be an annular flow under certain conditions. As the number of particles increases, Figs. 5.3g to 5.3i show that the pressure drop level decreases and appears to stabilize around ≈ 100 Pa. This is higher than predicted by Friedel correlation. Note that turbulence is not included in the present model whereas the Reynolds number Re is becoming turbulent and that the turbulent viscosity would contribute to stabilize the pressure field. For turbulence modeling in an SPH context, one can refer to [Shao 2005, Violeau 2007a, Rogers 2008] or [Monaghan 2011].

On Figs. 5.4a to 5.4c, pictures show a typical dispersed bubbly flow pattern where the light phase is spread-out by the heavy phase. Figs. 5.4d to 5.4f support this claim as one can note that the heavy phase outlet volume fraction quickly goes to 1 after a transient period. On Figs. 5.4g to 5.4i, the pressure drop evolution with time presents large oscillations and its average level varies strongly with the particles'

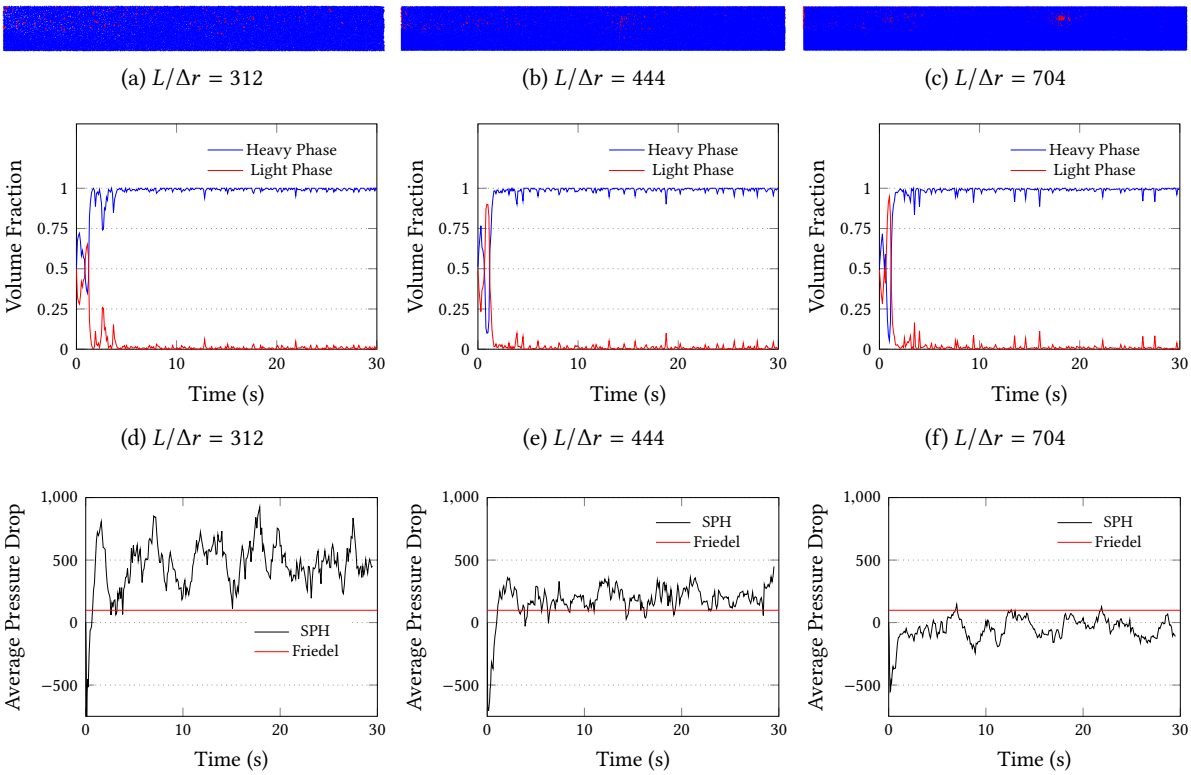

(a) $L/\Delta r = 312$ (b) $L/\Delta r = 444$ (c) $L/\Delta r = 704$

(d) $L/\Delta r = 312$ (e) $L/\Delta r = 444$ (f) $L/\Delta r = 704$

(g) $L/\Delta r = 312$ (h) $L/\Delta r = 444$ (i) $L/\Delta r = 704$

Figure 5.4: Results for case 2 (Dispersed flow) : (a,b,c) Phases distribution at $t = 30$ s (not at scale). (d,e,f) Evolution of the volume fractions at the outlet with time. (g,h,i) Evolution of the average pressure drop at the outlet with time.

resolution (from ≈ 500 Pa to ≈ 0 Pa). It even becomes negative at some instants testifying the occurrence of important recirculation areas near the light phase inlet. It is also higher than what Friedel correlation predicts. However, as stated before, turbulence effects are not taken into account whereas the Reynolds number *Re* is typically turbulent. We believe the turbulent viscosity would help to stabilize the pressure field.

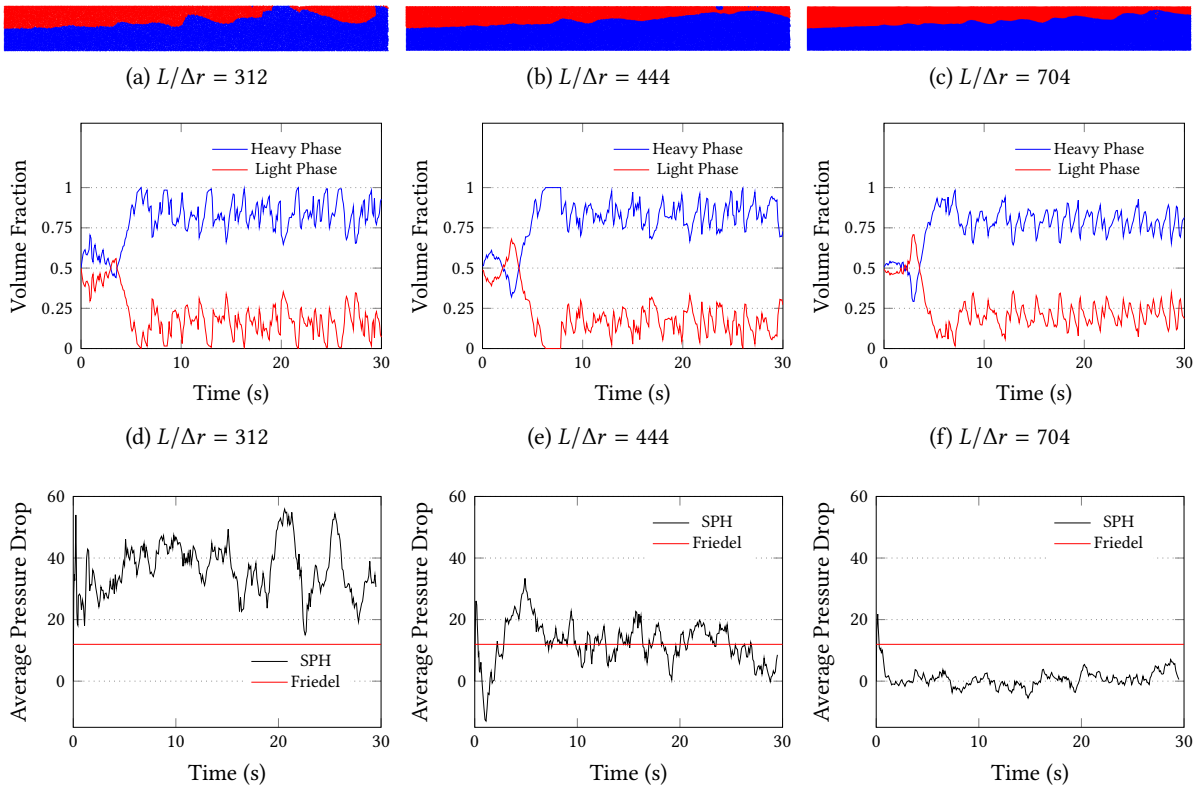

(a) $L/\Delta r = 312$ (b) $L/\Delta r = 444$ (c) $L/\Delta r = 704$

(d) $L/\Delta r = 312$ (e) $L/\Delta r = 444$ (f) $L/\Delta r = 704$

(g) $L/\Delta r = 312$ (h) $L/\Delta r = 444$ (i) $L/\Delta r = 704$

Figure 5.5: Results for case 3 (Intermittent flow) : (a,b,c) Phases distribution at $t = 30$ s (not at scale). (d,e,f) Evolution of the volume fractions at the outlet with time. (g,h,i) Evolution of the average pressure drop at the outlet with time.

On Figs. 5.5a to 5.5c, we can see that an intermittent flow is established as expected. The intermittent character of the flow pattern is later confirmed by the volume fraction time series of Figs. 5.5d to 5.5f where we can see that the light phase volume fraction is strongly oscillating between 0.25 and 0. It means that long bubbles are generated at a given frequency which corresponds to the definition of a slug flow. On Figs. 5.5g to 5.5i, the pressure drop average level decreases when the number of particles increases, varying from ≈ 30 Pa to ≈ 5 Pa. Friedel correlation predicts a pressure drop of ≈ 10 Pa which is of the same order of magnitude. It goes under 0 Pa during brief instants or during the transient phase because of the recirculation areas near the inlet. As shown on Fig. 5.6, the intermittent flow presented in this plots would evolve towards a fully developed slug flow if the pipe was longer.

Finally, on Figs. 5.7a to 5.7c, we observe a fully developed stratified flow. Figs. 5.7d to 5.7f show that the phase distribution is adjusting itself with time to reach a periodic steady state where the light phase volume fraction is ≈ 0.25 and the heavy phase volume fraction is ≈ 0.75. The pressure drop evolution presented on Figs. 5.7g to 5.7i show much smaller oscillations than the other cases because the flow is evolving at a smaller speed. Its average level goes from ≈ 7.5 Pa for the lowest resolution to ≈ 2.5 Pa

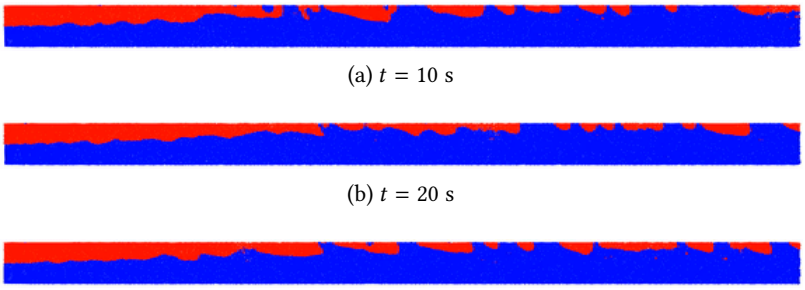

(a) $t = 10$ s

(b) $t = 20$ s

(c) $t = 30$ s

Figure 5.6: Phases distribution at selected instants for case 3 (Intermittent flow) with a pipe of 20 m ($L/\Delta r = 312$, not at scale).

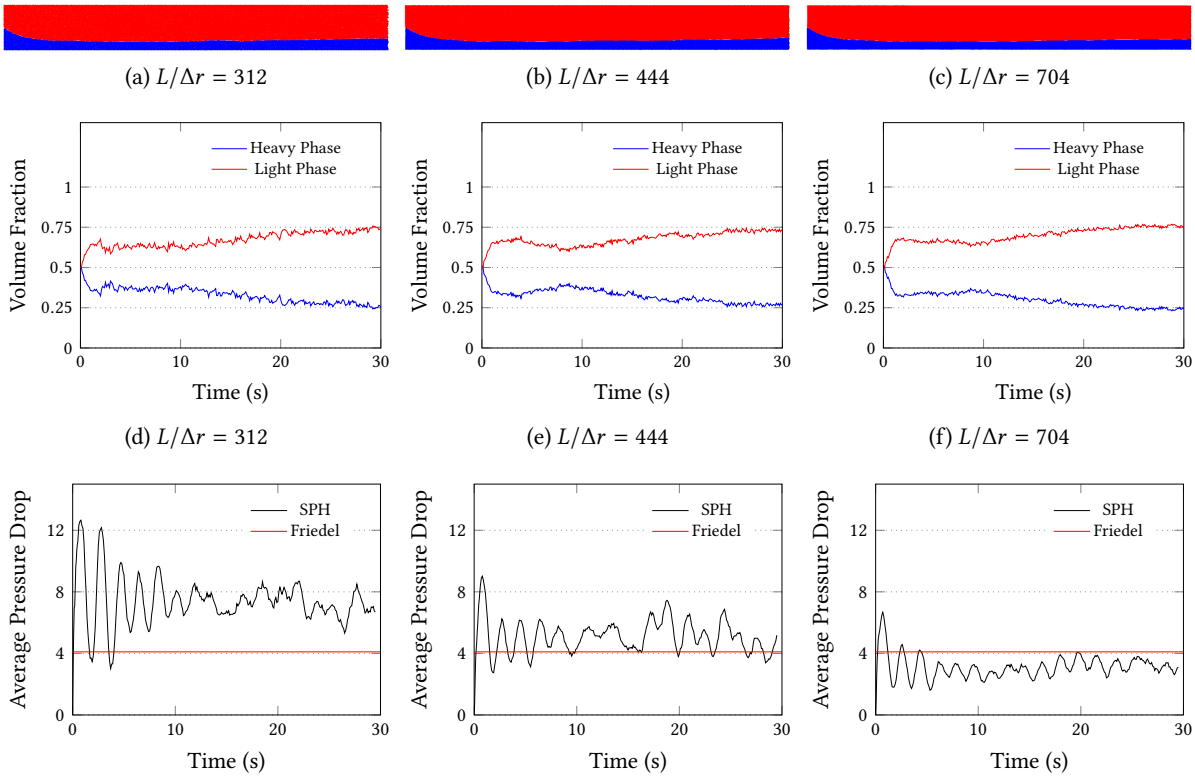

(a) $L/\Delta r = 312$ (b) $L/\Delta r = 444$ (c) $L/\Delta r = 704$

(d) $L/\Delta r = 312$ (e) $L/\Delta r = 444$ (f) $L/\Delta r = 704$

(g) $L/\Delta r = 312$ (h) $L/\Delta r = 444$ (i) $L/\Delta r = 704$

Figure 5.7: Results for case 4 (Stratified flow) : (a,b,c) Phases distribution at $t = 30$ s (not at scale). (d,e,f) Evolution of the volume fractions at the outlet with time. (g,h,i) Evolution of the average pressure drop at the outlet with time.

for the highest resolution. Friedel correlation gives an expected pressure drop of ≈ 4 Pa which is of the same order of magnitude.

To sum up, one can observe that our current implementation of SPH is able to reproduce the two-phase flow patterns predicted by the flow map of Fig. 5.2. Moreover, increasing the number of particles helps to reduce the pressure field oscillations while reproducing the same physics.

Moreover, on Figs. 5.8 and 5.9, we provide plots showing the evolution of the velocity magnitude along the pipe length at $t = 30$ s to verify that we do have a convergence of the velocity field when the number of particles increases. To obtain these plots, the velocity magnitude has been averaged along the pipe's height for each phase. Note that, for the mist case (respectively the dispersed case), we do not show the heavy phase velocity (respectively the light phase velocity) since there are not enough particles of that phase to be considered within the pipe's height. From a general point of view, what we observed is that, as the resolution increases, the velocity field tends to become more stable solution, presenting smaller oscillations and converging towards a steady state. This is particularly clear for the stratified case of Figs. 5.8c and 5.9c. For the intermittent case, the velocity field also depends on the distribution of the bubbles of light phase. For instance, the peak on Fig. 5.8b for the lowest resolution corresponds to the tail of the bubble of Fig. 5.5a. This bubble just got formed and is self-adjusting its shape under the effect of surface tension, hence the peak in velocity. Concerning the mist and dispersed case of Figs. 5.9a and 5.8a, we do not recover the prescribed velocity of the dominant phase at the inlet. It is because we average the velocity along the pipe's height so that we include the recirculation areas at the entry which tends to reduce the magnitude of the velocity field. It is difficult to see a convergence of the pressure drops' evolution when refining the resolution in Figs. 5.3 to 5.7 because of the inherent pressure noise due to the weakly compressible SPH and more importantly because of the pressure waves reflections at the boundaries. However, we can visually observe that convergence in the velocity field especially for the steadier cases such as the stratified case.

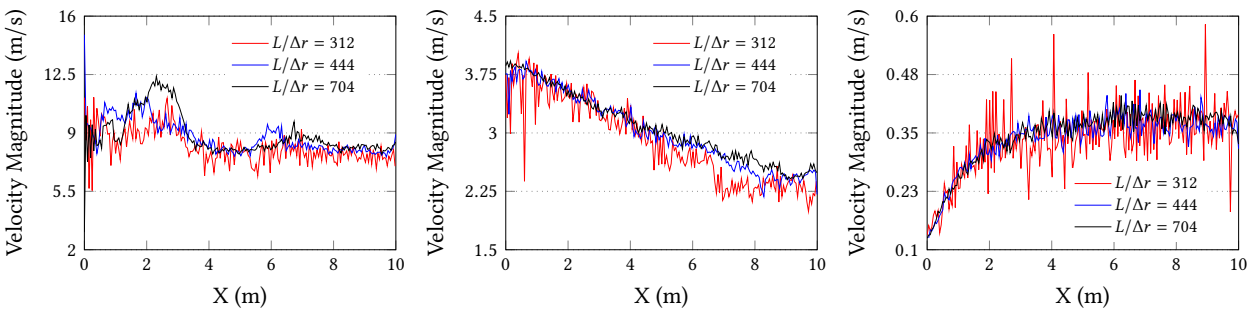

(a) Case 2 (Dispersed flow) (b) Case 3 (Intermittent flow) (c) Case 4 (Stratified flow)

Figure 5.8: Heavy phase velocity magnitude along the pipe length at $t = 30$ s in function of the particle resolution.

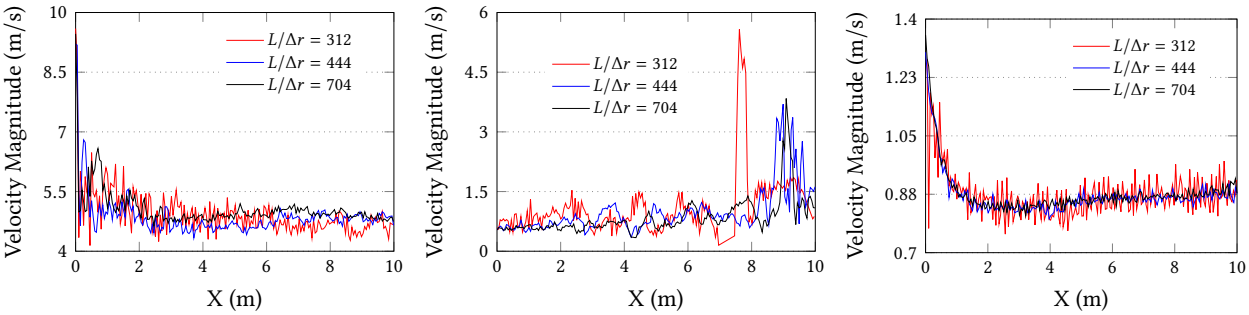

(a) Case 1 (Mist flow) (b) Case 3 (Intermittent flow) (c) Case 4 (Stratified flow))

Figure 5.9: Light phase velocity magnitude along the pipe length at $t = 30$ s as a function of the particle resolution.

5.2 Flow transitions

Using the same geometry, fluid properties and flow map as in the previous section, we picked four different paths from one flow pattern to the other. For each path, we simulated four different cases that are marked with different symbols on Fig. 5.10 and the corresponding parameters are shown on Tab. 5.3. All cases were simulated in 2D with a particle resolution of $L/\Delta r = 312$ which corresponds approximately to 10000 particles. $h/\Delta p$ is set to 2 for this case. The simulation time was 30 s. At the inlet, each phase is injected with a constant velocity corresponding to its superficial velocity $u^s_{g,l} = \alpha_{g,l} u_{g,l}$. At the outlet, a constant pressure equal to the background pressure is prescribed. The final two-flow patterns for the different cases, the evolution of the volume fraction with time at the outlet and the average pressure drop between both ends of the pipe are shown on Figs. 5.11 to 5.14.

Property		Path 1	Path 2	Path 3	Path 4	Units
Flow pattern		Stratified to Mist	Mist to Intermittent	Stratified to Intermittent	Intermittent to Dispersed	-
Superficial velocities	#1 (u^s_g,u^s_l)	(1.0,0.06)	(3.0,0.4)	(0.3,0.15)	(0.22,3.0)	m/s
	#2	(1.5,0.06)	(2.0,0.8)	(0.25,0.25)	(0.15,4.0)	m/s
	#3	(2.5,0.06)	(1.0,1.2)	(0.2,0.6)	(0.1,6.0)	m/s
	#4	(3.5,0.06)	(0.5,1.6)	(0.2,1.0)	(0.07,7.0)	m/s
Reynolds number	#1 ($Re = \frac{(u^s_g+u^s_l)D}{\nu_g\alpha_g+\nu_l\alpha_l}$)	302.86	971.43	128.57	920.00	-
	#2	445.71	800.00	142.86	1185.71	-
	#3	731.43	228.57	642.86	1742.86	-
	#4	1017.14	600.00	342.86	2020.00	-

Table 5.3: Cases properties for the different paths

On Figs. 5.11a to 5.11d, the transition from a stratified to a mist flow (path 1) is shown. As the superficial velocity of the light phase increases from case #1 to case #4, the volume fraction of the light phase is going to ≈ 1 while the volume fraction of the heavy fluid is going to 0. In between, we can see that the heavy fluid layer is divided in pieces until being completely dispersed by the light phase. Volume fractions plots of Figs. 5.11e to 5.11h show that the transition between the two patterns goes through a phase of intermittent flow where the heavy phase layer dislocates forming drops. On Figs. 5.11i to 5.11l, the pressure drop level increases from ≈ 10 Pa to ≈ 150 Pa and present stronger and

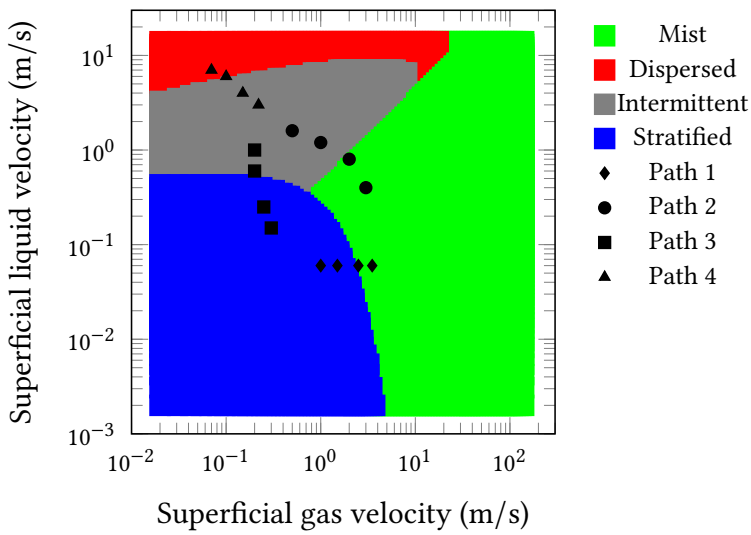

Figure 5.10: Four different paths from one flow pattern to another.

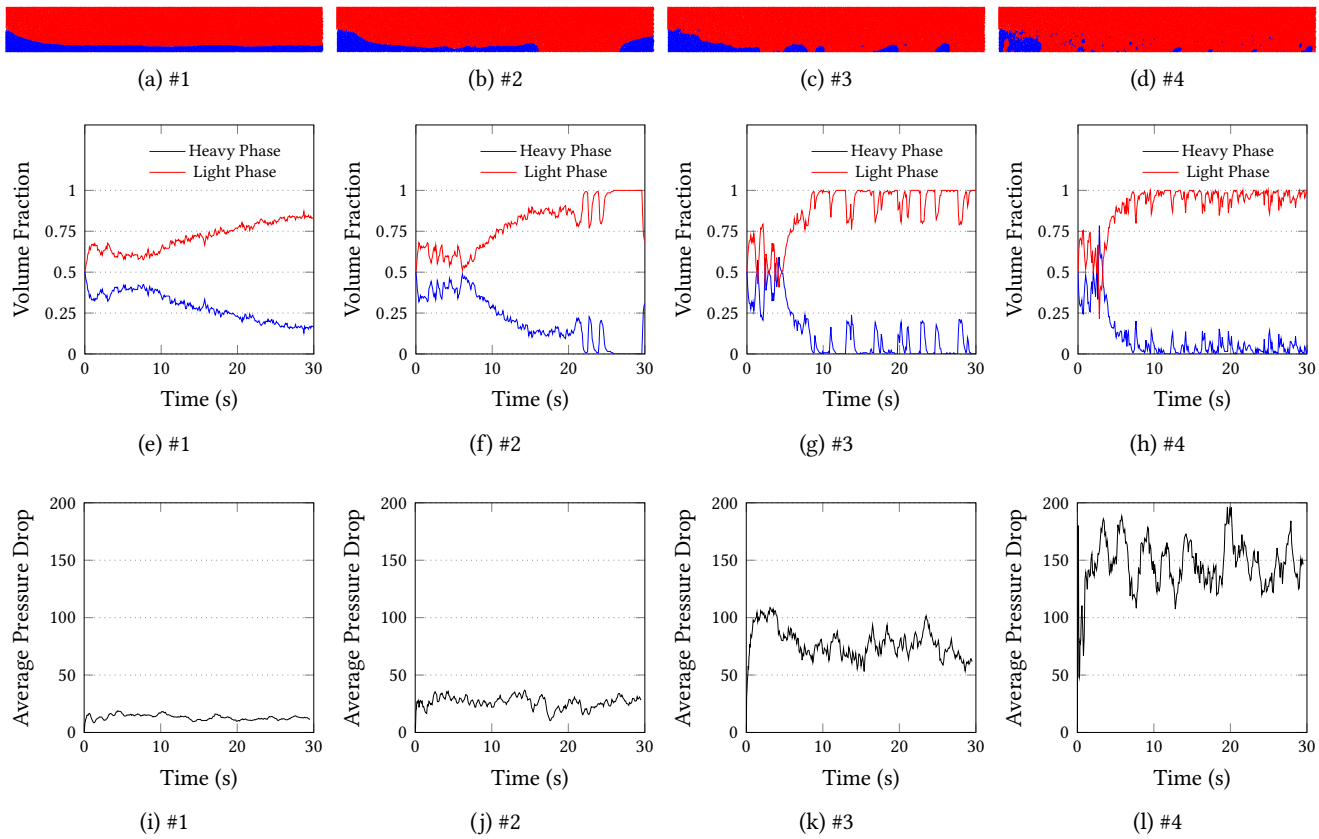

Figure 5.11: Results for path 1 (Stratified to Mist) : (a,b,c,d) Phases distribution at $t = 30$ s (not at scale). (e,f,g,h) Evolution of the volume fractions at the outlet with time. (i,j,k,l) Evolution of the average pressure drop at the outlet with time.

stronger oscillations while transitioning to the mist flow pattern.

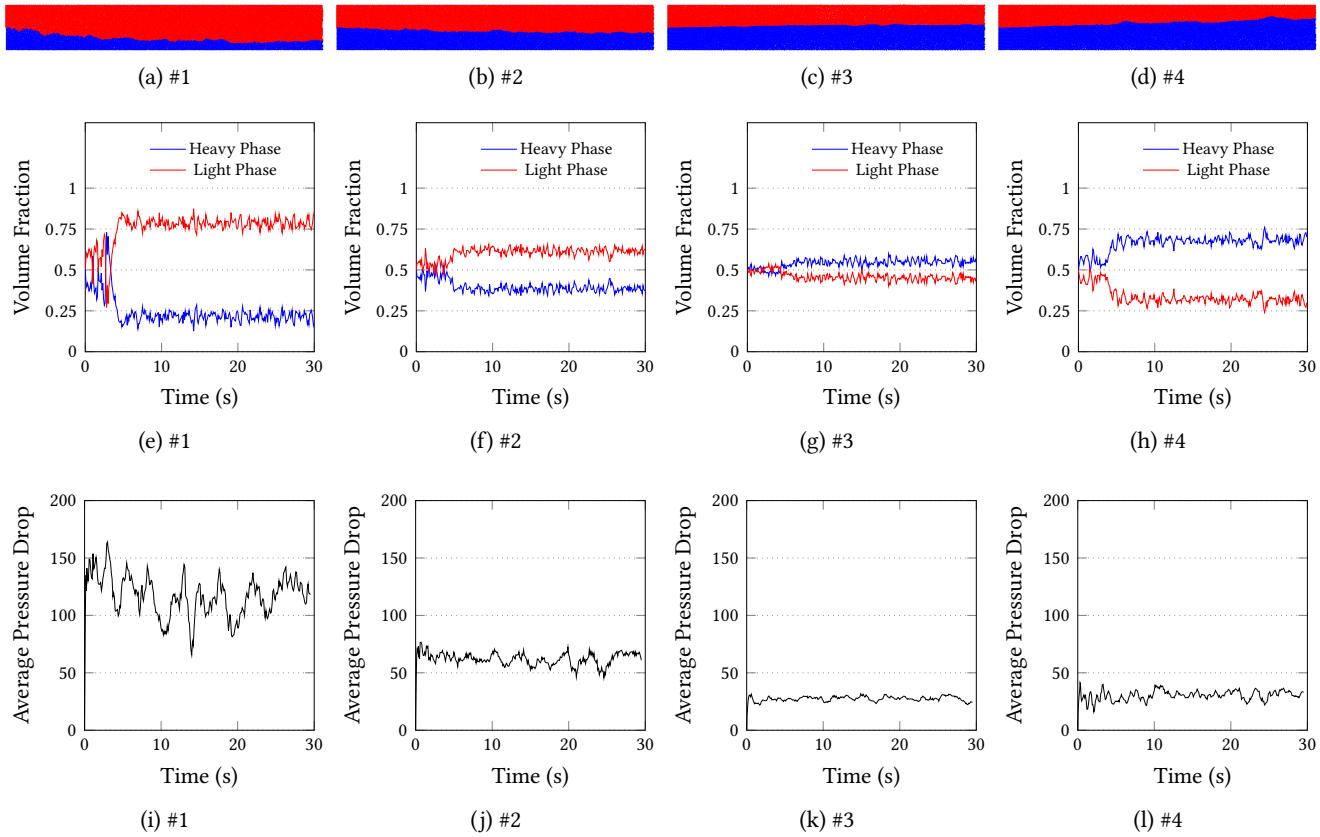

Figure 5.12: Results for path 2 (Mist to Intermittent) : (a,b,c,d) Phases distribution at $t = 30$ s (not at scale). (e,f,g,h) Evolution of the volume fractions at the outlet with time. (i,j,k,l) Evolution of the average pressure drop at the outlet with time.

The transition from mist flow to intermittent flow (path 2) is presented on Figs. 5.12a to 5.12d. From a quasi-mist flow in case #1, we see that, as the heavy phase superficial velocity increases, the fluid becomes wavy and then evolves towards an intermittent flow. This is magnified by the volume fractions evolution plots of Figs. 5.12e to 5.12h where we see that the light phase dominant in case #1 whereas the heavy phase is dominant in case #4. In all four cases, volume fractions are showing significant oscillations so that it is not obvious to qualify where the flow becomes really intermittent. This supports the well-known fact that flow maps are only an indicative tool and that the transition lines are not lines but smooth transitions areas. Concerning the pressure drop evolution of Figs. 5.12i to 5.12l, we can see that the average level drops from $\approx$ 125 Pa to $\approx$ 25 Pa. The case #3 is particular since in that case, superficial velocities and volume fractions are the same, therefore it is a very stable case where the pressure drop oscillations are the smallest.

On Figs. 5.13a to 5.13d, we present the phases distribution for the transition from a stratified flow pattern to an intermittent flow pattern. As the heavy phase velocity increases, the heavy phase becomes dominant and the interface with the light phase is more and more wavy near the outlet which prefigures the emergence of an intermittent flow. Volume fractions plots shown on Figs. 5.13e to 5.13h support that observation as the amplitudes of their oscillations are increasing when we move towards the intermittent flow pattern. On Figs. 5.13i to 5.13l, one can note that the pressure drops evolutions behave similarly and their average level increases from $\approx$ 4 Pa to $\approx$ 8 Pa.

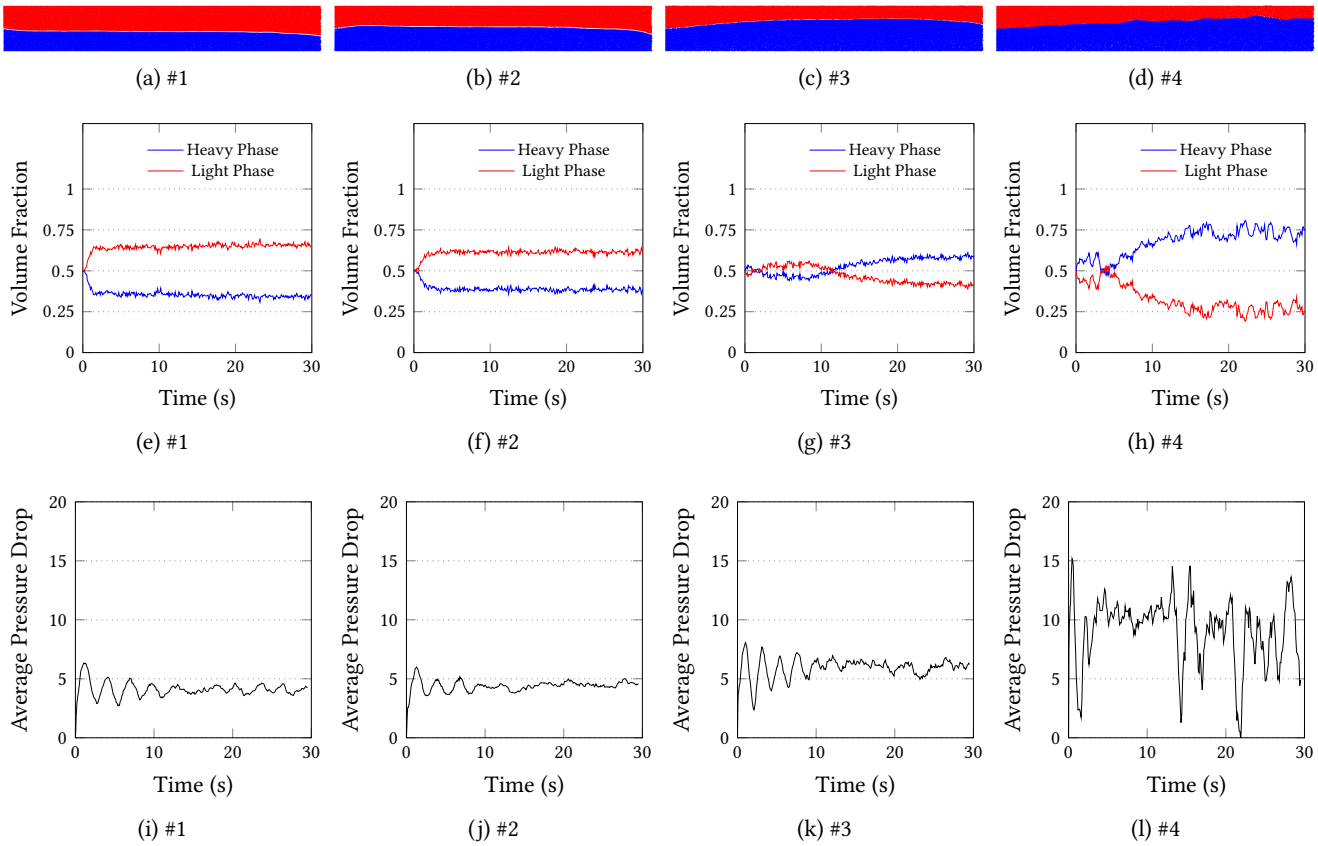

Figure 5.13: Results for path 3 (Stratified to Intermittent) : (a,b,c,d) Phases distribution at $t = 30$ s (not at scale). (e,f,g,h) Evolution of the volume fractions at the outlet with time. (i,j,k,l) Evolution of the average pressure drop at the outlet with time.

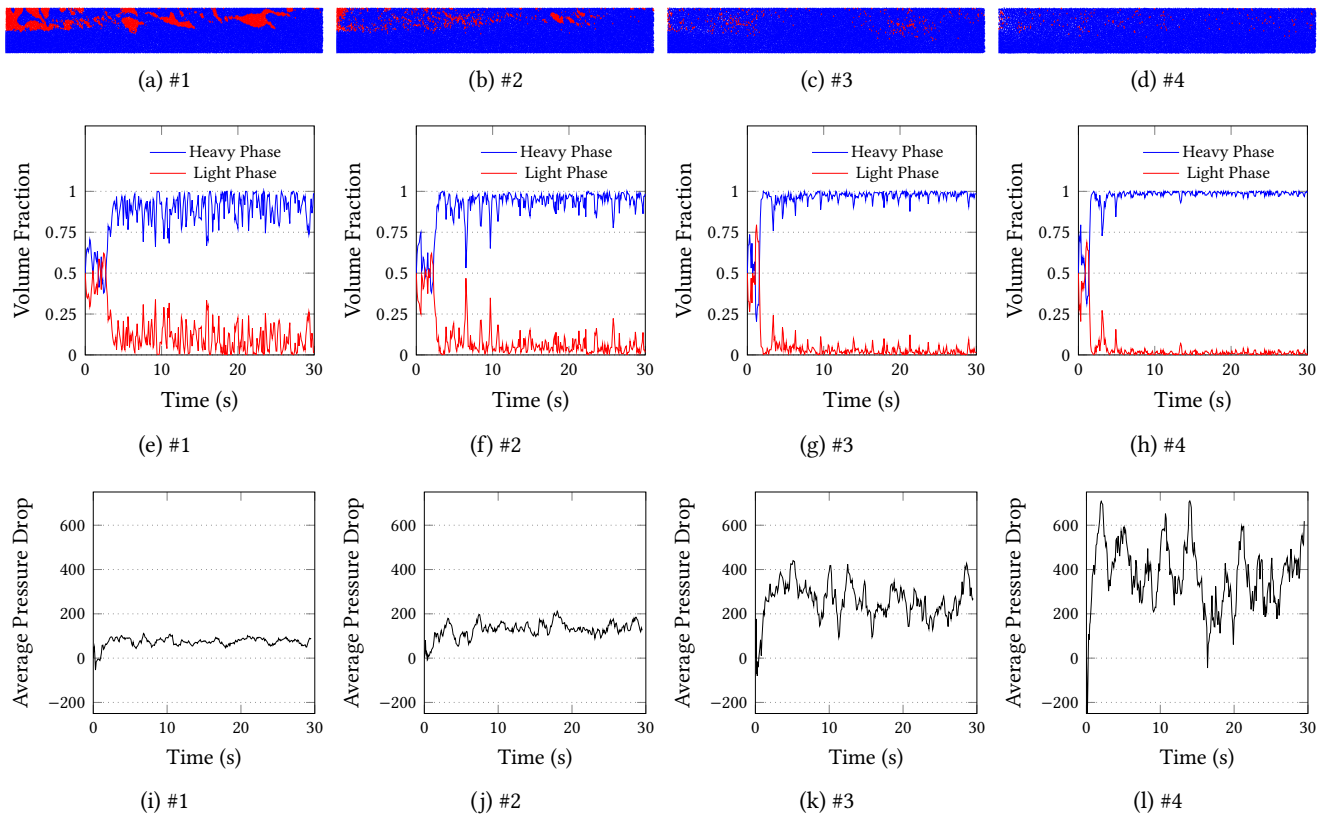

Figure 5.14: Results for path 4 (Intermittent to Dispersed) : (a,b,c,d) Phases distribution at $t = 30$ s (not at scale). (e,f,g,h) Evolution of the volume fractions at the outlet with time. (i,j,k,l) Evolution of the average pressure drop at the outlet with time.

The transition from intermittent flow to dispersed flow is presented on Figs. 5.14a to 5.14d. The flow pattern evolves from a disturbed intermittent flow that we could qualify of plug flow towards a dispersed flow as the heavy phase velocity increases. On Figs. 5.14e to 5.14h, one can observe that volume fractions time series are initially very unstable which is characteristic of an intermittent flow. The light phase and heavy phase volume fractions are going to ≈ 0 and ≈ 1 respectively as the dispersed flow pattern emerges. Concerning the pressure drops of Figs. 5.14i to 5.14l, as expected, it increases from ≈ 75 Pa to ≈ 400 Pa with growing oscillations.

To conclude, we have explored the flow map of Fig. 5.10 by simulating several cases located around the transitions from one pattern to the other. We observed that the transition areas are not lines but in fact smooth bands. Also, it appears that the intermittent flow area gathers different patterns such as wavy flows (in the lower part), slug flows (in the center) and even plug flows (in the upper area). The pressure drop plots are providing useful information on the pressure field but are showing strong variations which are due to the use of the weakly compressible formulation. This approach is known to generate disturbances in the pressure calculations because of density and pressure are linked through an equation of state (2.2.5). A truly incompressible SPH formulation would likely improve this aspect. See [Hu 2007, Kunz 2015] for multiphase incompressible SPH models. Besides, the inlet, outlet and wall boundary conditions that we have used are known to introduce spurious waves in the flow. We believe that implementing more accurate boundary conditions based on analytical considerations [Ferrand 2012] and adapted to inlet/outlet for multiphase flows could also improve the quality of the results. Nevertheless, we think that these results show that SPH could be a complementary tool to study the emergence of intermittent flow patterns in pipes in industrial applications.

5.3 Applied cases with high density and viscosity ratios

In order to further demonstrate the potential of SPH to model intermittent flows, we have simulated two applied cases. The fluids considered for these cases are generic oil and natural gas whose properties are indicated in Tab. 5.4. The two different geometries corresponding to a hydrodynamic slugging case and a terrain slugging case are shown on Fig. 5.15 and are discretized with resolutions $L/\Delta r = 634$ (≈ 10000 particles) and $L/\Delta r = 687$ (≈ 15000 particles) respectively. $h/\Delta p$ is set to 2 for this case. Simulation times are 0.05s and 0.25s respectively. Fluids are injected with superficial velocities and volume fractions given in Tab. 5.5. Note that we have chosen to work with a micro-geometry for computational and time constraints while trying to preserve realistic proportions. Phases distributions for both cases are shown on Figs. 5.16 and 5.17.

Property	**Gas Phase**	**Oil Phase**	**Units**
Density (ρ)	1.6454	702.6926	kg/m^3
Viscosity (μ)	1.27×10^{-5}	4.19×10^{-4}	Pa.s
Adiabatic index (γ)	1.4	7	-
Surface Tension (σ^{nw})	0.02139		N/m
Contact Angle (θ_c)	90		$^\circ$
Gravity (g_z)	-9.81		m/s^2

Table 5.4: Physical Properties

On Fig. 5.16, it is possible to observe the typical formation process of a hydrodynamic slug. First, from $t = 0$ s to $t = 0.025$ s, waves begin to grow. At $t = 0.026$ s, one the waves' crest is high enough to reach the top of pipe : a slug is formed. From $t = 0.0275$ s to $t = 0.03$ s, other waves reach the

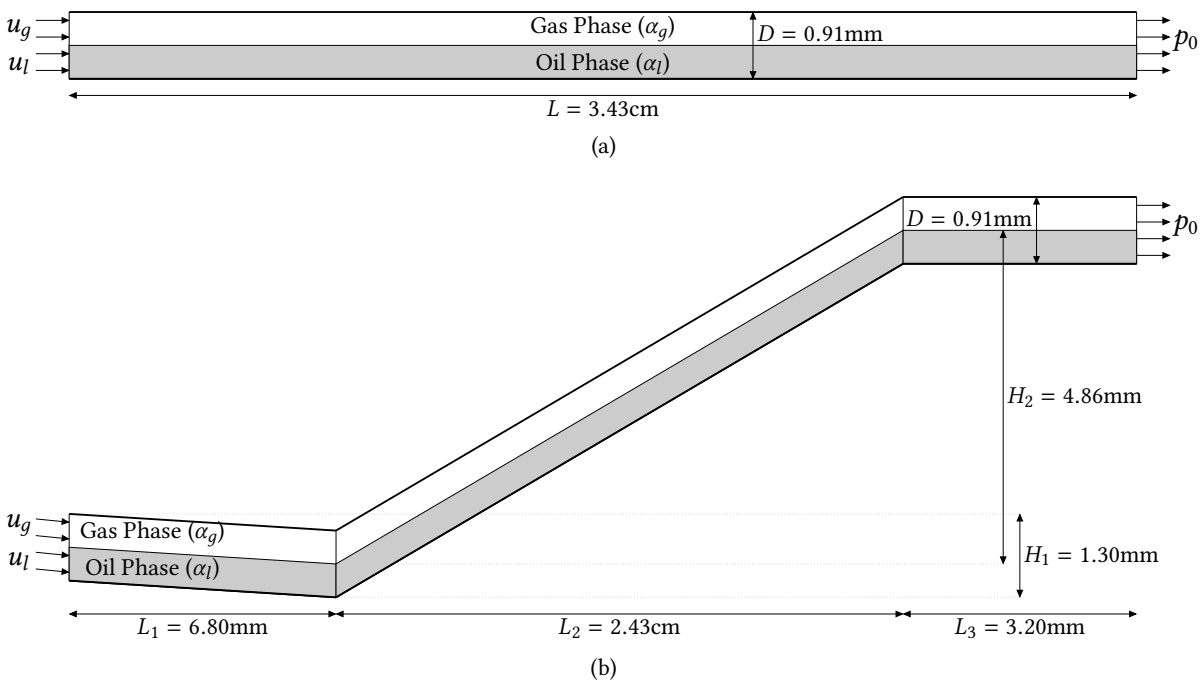

Figure 5.15: Geometrical configurations for the two applied cases (not at scale). (a) Hydrodynamic slugging. (b) Terrain slugging.

Property	**Hydrodynamic slugging**	**Terrain slugging**	**Units**
Volume fractions (α_g,α_l)	(0.25,0.75)	(0.25,0.75)	m/s
Superficial velocities (u_g^s,u_l^s)	(0.35,0.76125)	(0.35,0.76125)	m/s

Table 5.5: Cases Properties

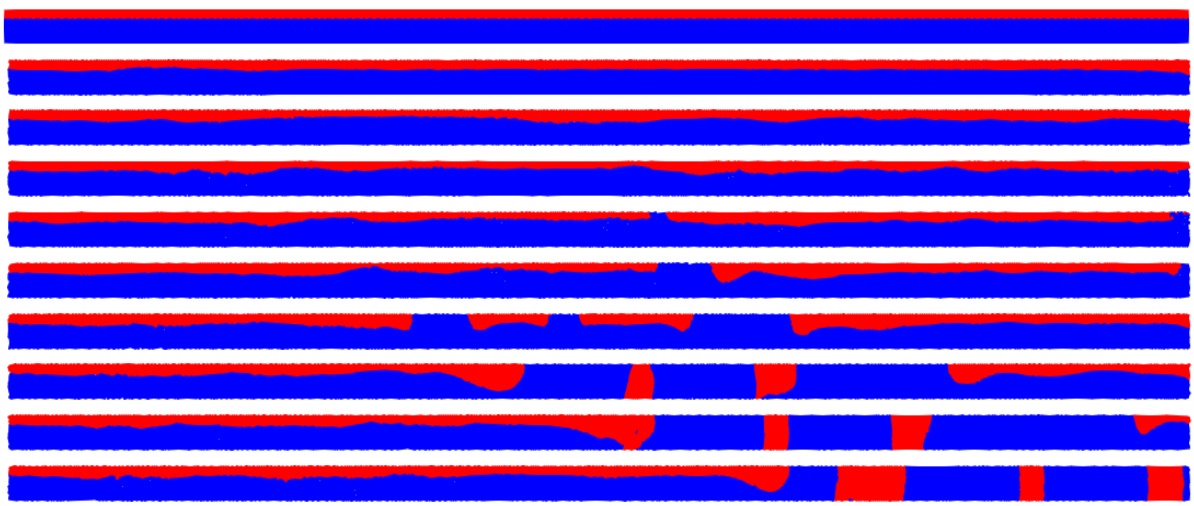

Figure 5.16: Phases distribution for the hydrodynamic slugging case (not at scale). From top to bottom, at t = 0 s, 0.01 s, 0.02 s, 0.025 s, 0.026 s, 0.0275 s, 0.03 s, 0.035 s, 0.04 s and 0.05 s

top of the pipe forming new slugs. After that, one can note that some slugs see their length reduced and their height increased until occupying the whole pipe's height. This example confirms that SPH can reproduce the dynamics of slug flows with high viscosity and density ratios (here ≈ 32 and ≈ 427 respectively).

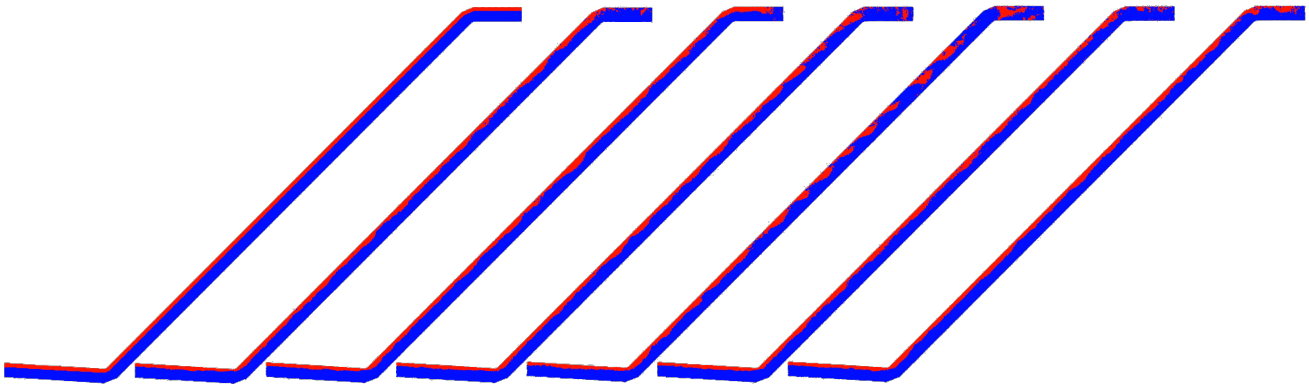

(a)

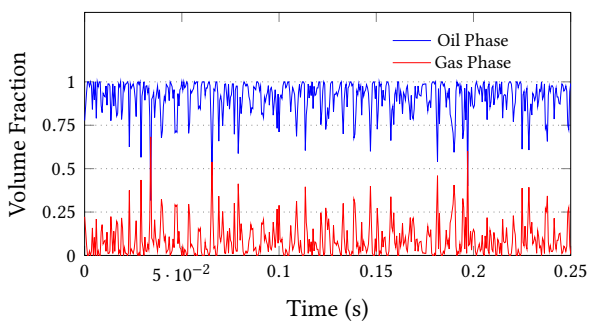

(b)

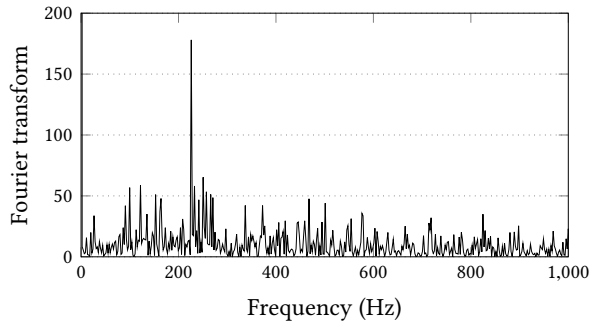

(c)

Figure 5.17: (a) Phases distribution for the terrain slugging case. From left to right, at $t = 0$ s, 0.05 s, 0.1 s, 0.13 s, 0.188 s, 0.2 s and 0.25 s (b) Evolution of the volume fractions at the outlet with time. (c) Fourier transform of the gas phase volume fraction time series (in red on (b))

On Fig. 5.17, we present the results of a "riser-like" case where the oil and gas mixture extracted from the reservoir is lifted from the sea ground to the land. A slug flow does not have the required distance to grow in the initial descending part of the pipe. However, under the effect of gravity, slugging begins to occur in the ascending part of the pipe. The evolution of volume fractions at the outlet of Fig. 5.17b shows strong oscillations as expected in a slug flow. When performing a Fourier transform analysis on the gas phase volume fraction evolution as presented on Fig. 5.17c, one can see that one frequency clearly dominates, thus suggesting that the slug frequency in that particular case geometry would be around 226 Hz.

5.4 Influence of the spurious interface fragmentation correction

In this section, we investigate the influence of the spurious interface correction proposed in [Szewc 2013] on the previously shown SPH simulations. First in Sect. 5.4.1, we check its impact on the flow regimes simulations of Sect. 5.1 and we visually compare to a similar work done with phase field models [Xie 2017]

in Sect. 5.4.2. Then in Sect. 5.4.3, we look at the influence of this interface correction on some dispersed to intermittent and stratified to intermittent flow transitions simulations of Sect. 5.2. Finally in Sect. 5.4.4, we conclude with the effect of the correction on the terrain slugging shown on Fig. 5.17.

5.4.1 Flow Regimes

We consider the same case as before. It consists in an horizontal pipe of length $L = 10$ m and diameter $D = 1$ m. Geometry is detailed on Fig. 5.1. A stratified flow with 50% of heavy phase and 50% of light phase is assumed at the inlet. Fluid properties are shown on Tab. 5.1. All simulations presented in this section are in 2D. The simulation time was 30 s. For clarity purposes, in the rest of the section, Interface Correction will be referred to as IC.

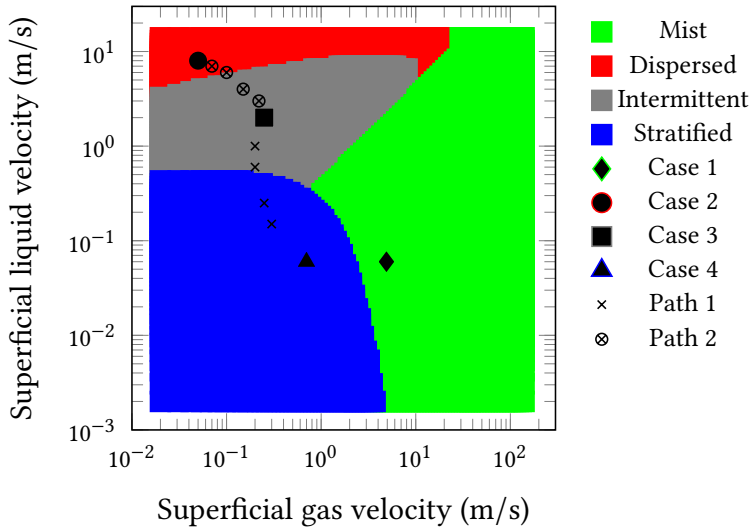

Figure 5.18: Flow regime map adapted from [Taitel 1976]

First, we want to verify that our implementation is able to reproduce different flow regimes and how the interface sharpness correction affects these results. To this end, fluids are injected with superficial velocities corresponding to four different flow regime cases : mist, dispersed, intermittent and stratified as indicated on Fig. 5.18. At the outlet, we impose a constant pressure profile equal to the background pressure. For this subsection, we consider a resolution $L/\Delta r = 704$ (≈ 50000 particles).

A visual comparison of the final flow patterns at $t =$ 30s with and without IC is shown on Fig. 5.19. The evolution of the volume fraction with time at the outlet and the average pressure drop between both ends of the pipe is presented on Fig. 5.20. By 'Average Pressure Drop', we mean that the pressure is averaged among all particles over a distance of κh inside the fluid flow and over 10 timesteps. We then do the subtraction between the inlet value and the outlet value.

On Fig. 5.19, we see that SPH is able to reproduce the flow regimes predicted by Taitel & Dukler's flow map. For the mist case on Fig. 5.19a, the light phase is going much faster than the heavy phase and thus scatters the heavy phase as it progresses along the pipe. IC makes particles of a given phase less miscible with other phase's particles and contributes to the formation of larger droplets. For the dispersed case on Fig. 5.19b, it is the heavy phase that goes faster than the light phase and it disperses the light phase in very small bubbles. Most bubbles are composed of only one particle. This case is the one that involves the highest velocities and we see that the influence of IC is mitigated by these high velocities. One cluster of particles is formed in the last third of the pipe unlike the case without IC. On

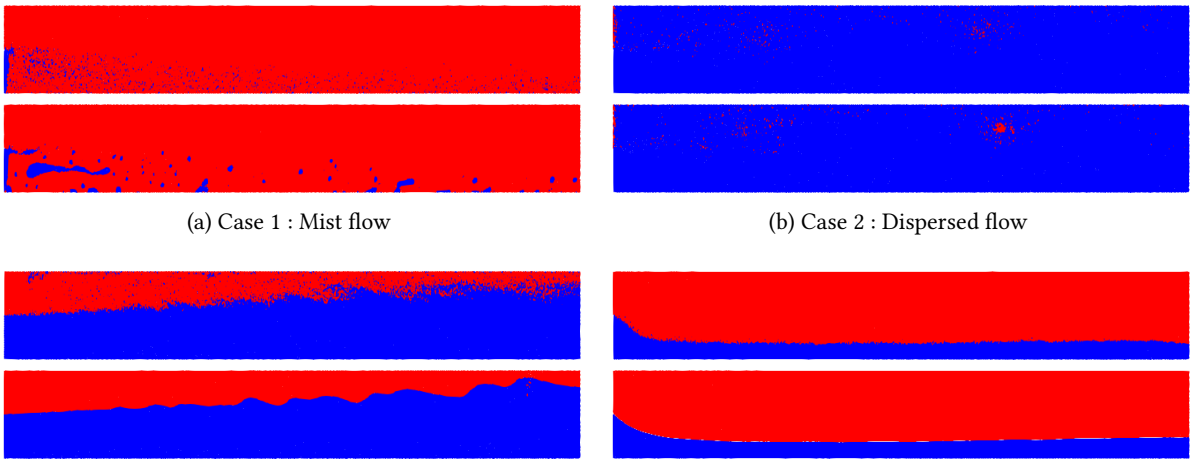

(a) Case 1 : Mist flow

(b) Case 2 : Dispersed flow

(c) Case 3 : Intermittent flow

(d) Case 4 : Stratified flow

Figure 5.19: Phases distribution at $t = 30$ s (not at scale). Top : without IC. Bottom : with IC.

the intermittent flow case of Fig. 5.19c, we observe the emergence of a slug flow pattern where large bubbles are in formation. Note that we only present a snapshot of the simulation at $t = 30$ s but the intermittent behavior of the flow is perhaps more visible on Fig. 5.21b at an earlier simulation time. IC, as shown in [Szewc 2016], attenuates the Kelvin-Helmholtz instability generated at the interface. As a result, the interface is cleaner and phases are well separated. However, it is difficult to say if it is closer to reality or not without more information. Concerning the stratified case on Fig. 5.19d, we recover the expected flow pattern in both cases. The influence of IC is almost invisible for the stratified flow. Indeed, in that case, relative velocities are small so the micro-mixing phenomenon is less prominent.

On Fig. 5.20, it is possible to see the influence of IC on the volume fraction and average pressure drop time series for all four cases considered. The main observation is that IC accentuates the oscillations of the volume fractions series. It is particularly clear on Fig. 5.20e where the intermittent character of the flow is strongly emphasized by IC. On the other hand, IC does not seem to have a significant impact on the pressure drop variations. Those pressure drops are showing strong variations, especially when the superficial velocities are important (case 1 and case 2) and are apparently stabilizing around a given level as time goes by. These plots should be taken with caution as the weakly compressible SPH formulation is known to produce a noisy pressure field. Additionally, the pressure evaluation near the inlet/outlet boundaries is necessarily influenced by the boundary conditions. Moreover, note that turbulence is not included in the present model whereas the Reynolds number Re is typically turbulent for case 1 and case 2 in particular and that the turbulent viscosity would contribute to stabilize the pressure field.

5.4.2 Visual comparison with Xie et al.

In this subsection, we present on Fig. 5.21 a visual comparison with the results obtained with the phase field method in [Xie 2017]. Fluids properties and geometry are the same one as in subsection 5.4.1 and are shown on Tab. 5.1 and Fig. 5.1 respectively. Three different flow patterns were simulated : stratified, intermittent and dispersed with heavy/light fluid volume fractions at the inlet of 20%/80%, 50%/50% and 80%/20% respectively. Superficial velocities are indicated on Fig. 5.2 for the corresponding cases 2, 3 and 4.

On Figs. 5.21a and 5.21c, we see that we obtain stratified and dispersed flow patterns that are very

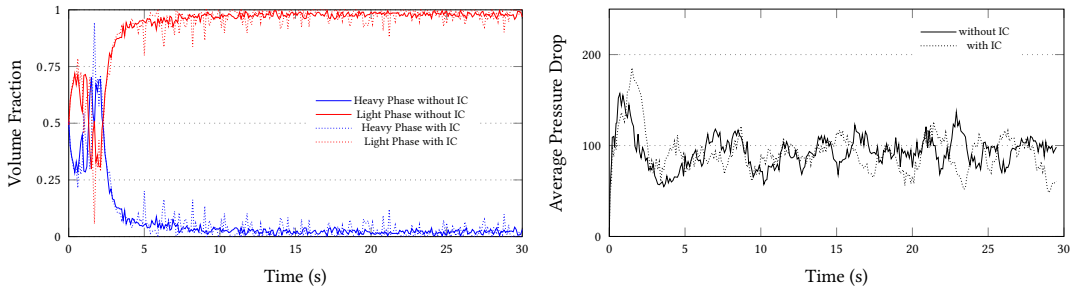

(a) Case 1 : Mist flow

(b) Case 1 : Mist flow

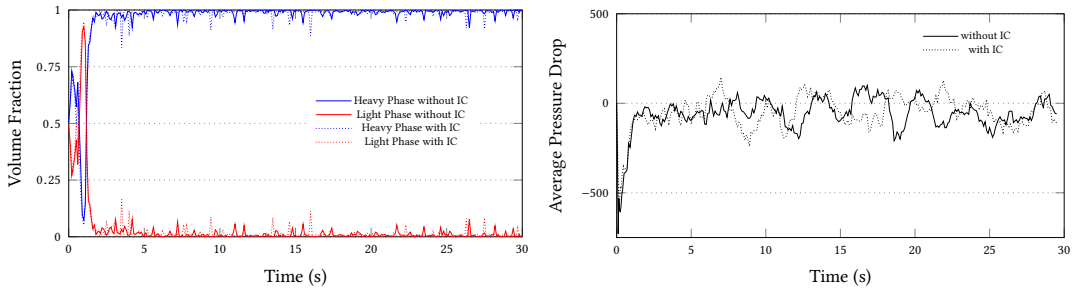

(c) Case 2 : Dispersed flow

(d) Case 2 : Dispersed flow

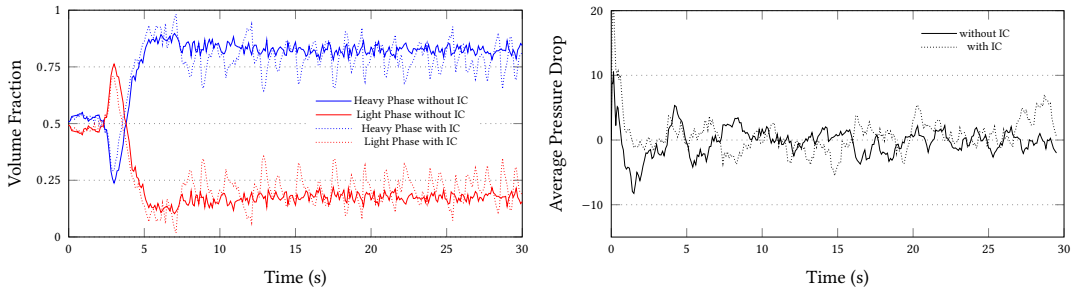

(e) Case 3 : Intermittent flow

(f) Case 3 : Intermittent flow

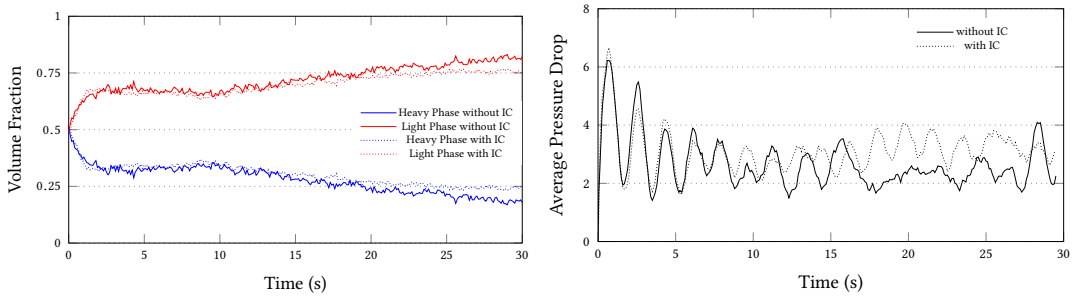

(g) Case 4 : Stratified flow

(h) Case 4 : Stratified flow

Figure 5.20: (a,c,e,g) Evolution of the volume fractions at the outlet with time. (b,d,f,h) Evolution of the average pressure drop at the outlet with time.

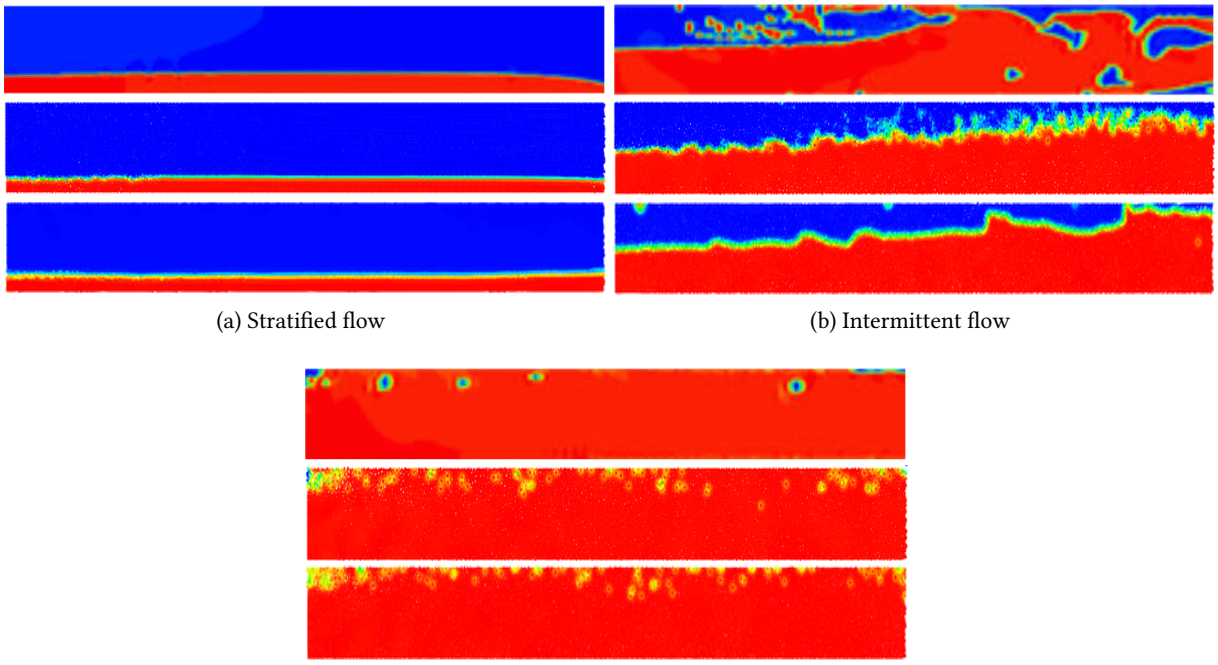

(a) Stratified flow

(b) Intermittent flow

(c) Dispersed flow

Figure 5.21: Visual comparison with Xie et al. [Xie 2017]. Top : Adapted from Fig. 4 of Xie et al. [Xie 2017] (reproduced here with permission). Middle : without IC. Bottom : with IC.

similar to the ones obtained in [Xie 2017]. Concerning the slug flow case of Fig. 5.21b, we obtain a quite different flow pattern with or without IC than [Xie 2017]. However, we note that the phase field simulation does not suffer from interface fragmentation and present a clear phase separation. This tends to advocate in favor of the fact that the surface tension model (continuum surface force or stress) as it is implemented today in SPH lacks a procedure that would ensure immiscibility. It explains why some authors needed to introduce an IC force to impose it.

5.4.3 Flow Transitions

Hereafter, we look at how we transition from one flow pattern to the other. Geometry and fluid properties are identical to the ones considered in Subsect. 5.4.1 and are shown on Fig. 5.1 and Tab. 5.1. We focused on two specific paths, path 1 and path 2, that are indicated on Fig. 5.2. Path 1 corresponds to the transition from stratified flow to intermittent flow and path 2 corresponds to dispersed flow to intermittent flow.

At the inlet, fluid phases are injected with heavy/light fluid volume fractions of 50%/50% and with superficial velocities indicated on Fig. 5.2. At the outlet, a constant pressure profile equal to the background pressure is imposed. For this subsection, we considered a resolution $L/\Delta r = 312$ (≈ 10000 particles) in order to accelerate the calculations.

On Fig. 5.22, we see the evolution of the phases distribution in the pipe as we move from a stratified flow pattern to an intermittent flow pattern. As the fluid velocities are increasing from Fig. 5.22a to 5.22d, the heavy fluid occupies more and more space in the pipe and progressively imposes an intermittent flow pattern. Since the velocities considered here are reasonably low, the influence of IC is limited to ensuring a clean interface.

On Fig. 5.23, we see the influence of IC is more prominent as we move towards the intermittent

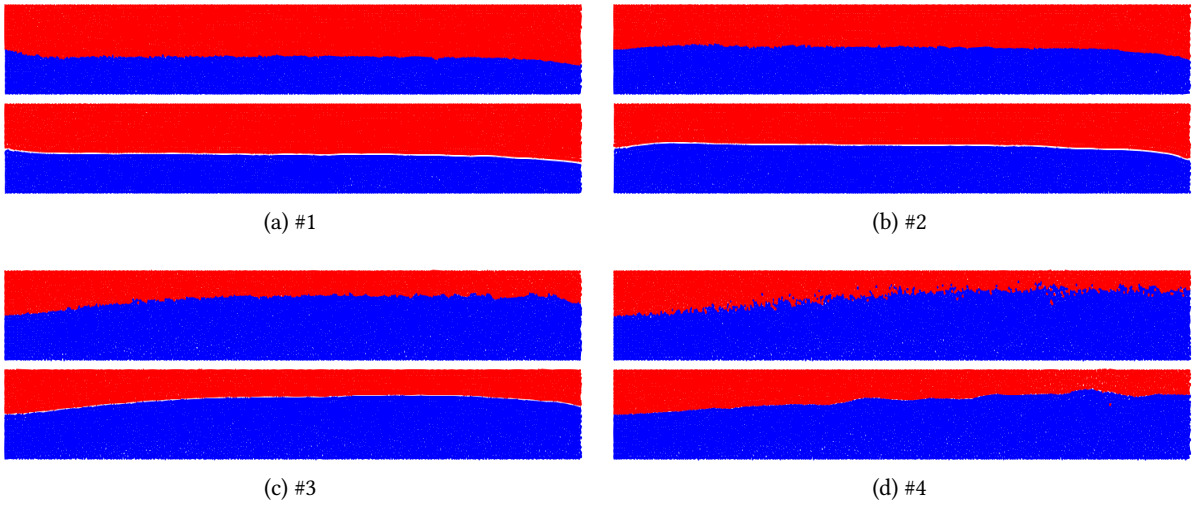

Figure 5.22: Results for path 1 (Stratified to Intermittent). Phases distribution at $t = 30$ s (not at scale). Top : without IC. Bottom : with IC.

flow pattern. Initially, both volume fractions time series are almost identical and the pressure drop is smoother and slightly higher with IC than without IC. As velocities increase, we see that IC affects the pressure drop variations rather strongly.

On Fig. 5.24, we see the evolution of the phases distribution in the pipe as we move from a dispersed flow pattern to an intermittent flow pattern. When the velocities are getting smaller and smaller, we see that clusters of light phase particles are beginning to appear. IC clearly favors the formation of these clusters. The final pattern with IC could be classified as a slug or plug flow pattern as predicted by the flow map whereas without IC it is more likely to be classified as a dispersed flow pattern.

On Fig. 5.25, on the contrary to path 1 where velocities are lower, we observe that the influence of IC is more visible on the volume fraction time series where oscillations are strongly amplified. However, on the pressure drops plots, we obtain roughly the same levels with and without IC.

5.4.4 High density and viscosity ratios

We will now present a more realistic case of slugging with steeper density and viscosity ratios. The fluids considered for these cases are generic oil and natural gas whose properties are indicated in Tab. 5.4. The oil phase and the gas phase are injected with a superficial velocity of 0.7612 m/s and 0.35 m/s respectively and a volume fraction of 25% and 75% respectively. Geometry is described on Fig. 5.15 and is discretized with a resolution of $L/\Delta r = 780$ (≈ 20000 particles). Note that we have chosen to work with a micro-geometry for computational and time constraints while trying to preserve realistic proportions of a terrain slugging case. Phases distribution for different values of ε are shown on Figs. 5.26.

On Fig. 5.26, we can observe the rather strong impact of IC on the phase distribution. Even during the early timesteps of Figs. 5.26a, 5.26b and 5.26c, we note that the oil waves are not located at the same positions which will result in different slug locations.

After some time, the four simulations present different flow patterns and these differences are amplified when ε increases. Even when $\varepsilon = 0.1\frac{L_{\text{ref}}}{h}$, we see that the flow evolves differently.

We recall that, according to [Szewc 2016], for inviscid fluids (which is not the case here), $\varepsilon \gtrsim \frac{A}{h} + B$ with $A = \frac{\pi \rho_g \rho l (u_g - u_l)^2 L_{\text{ref}}}{2(\rho_g + \rho l)}$ and $B = g\|\rho_g - \rho_l\|$ to suppress the interface instabilities. In this case, it gives $\varepsilon \gtrsim 10$. When ε is above this value, interface stabilities are indeed reduced but at the price of a

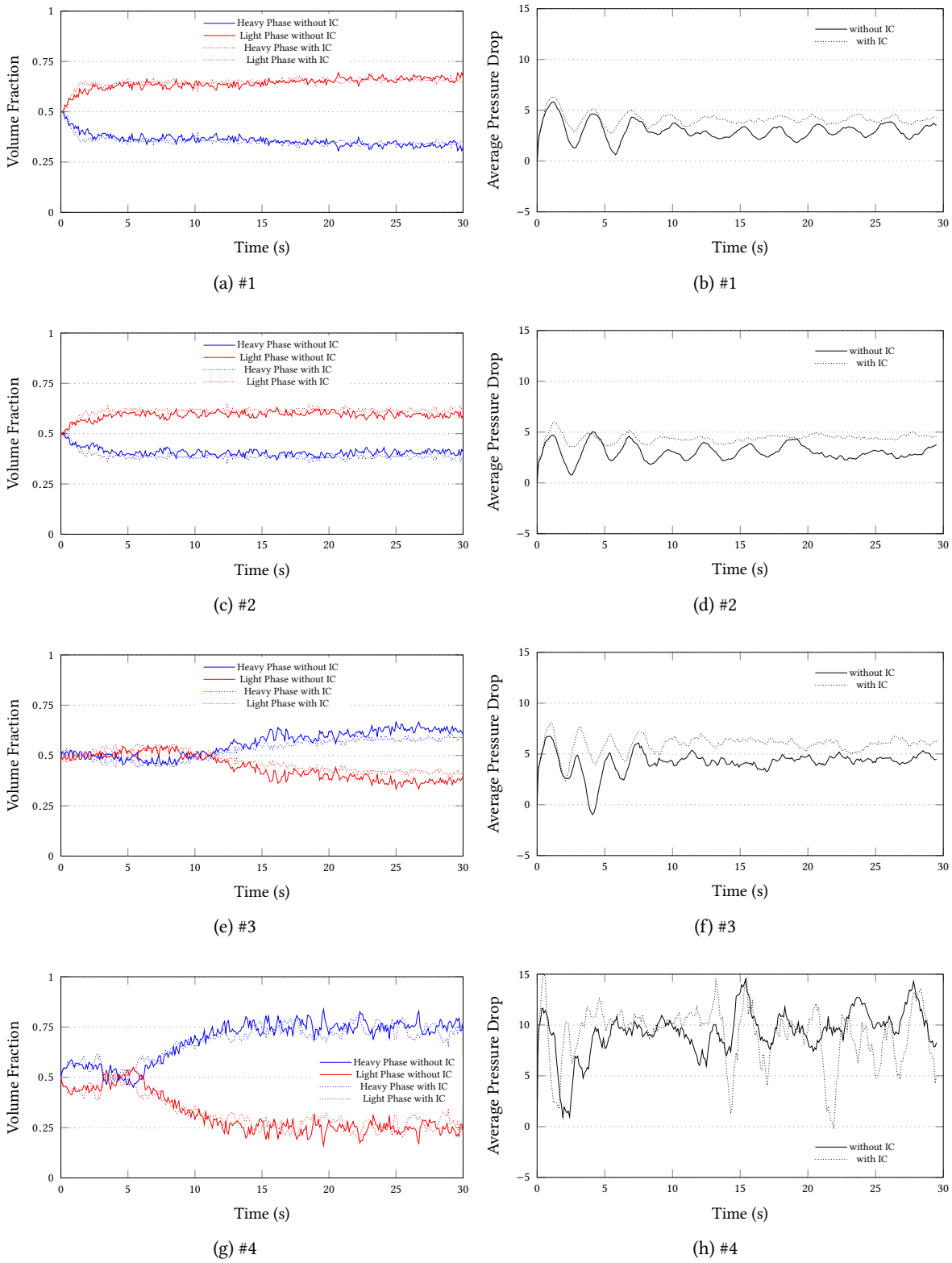

Figure 5.23: Results for path 1 (Stratified to Intermittent). (a,c,e,g) Evolution of the volume fractions at the outlet with time. (b,d,f,h) Evolution of the average pressure drop at the outlet with time.

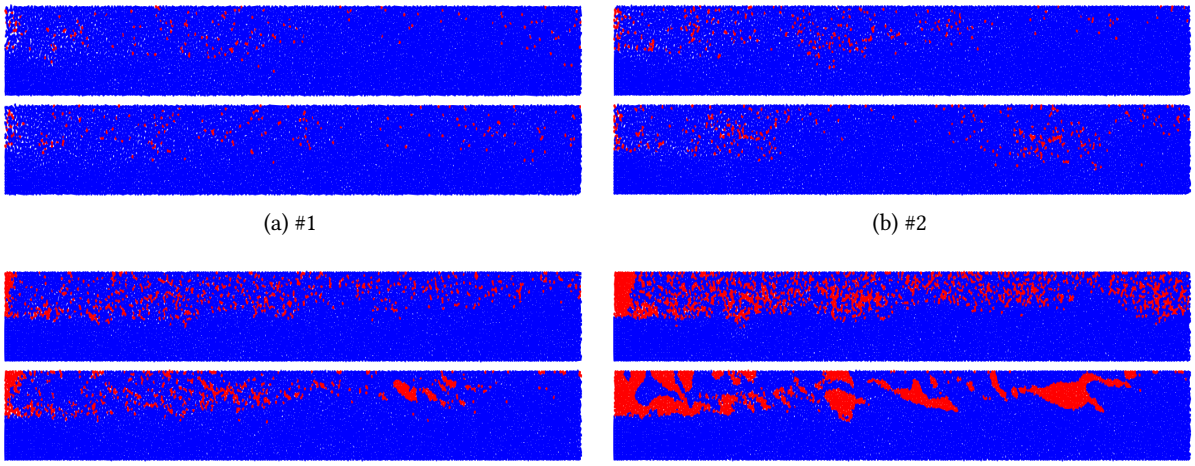

(a) #1 (b) #2

(c) #3 (d) #4

Figure 5.24: Results for path 2 (Dispersed to Intermittent). Phases distribution at $t = 30$ s (not at scale). Top : without IC. Bottom : with IC.

modification of the flow evolution. Additionally, it also appears on these figures that IC's interaction with the outlet boundary conditions importantly affect the flow near the outlet, especially when ε is high (which was not the case previously). Moreover, from a more general point of view, for micro-geometries such as the one used in this example, surface tension is much stronger and seems to be enough to ensure a reasonable immiscibility. Thus, the use of IC in this case can be questioned.

We can confirm observations made by several authors before [Colagrossi 2003, Das 2009, Grenier 2009a, Szewc 2013]. that, even in the presence of surface tension, particles at the interface tend to mix in what appears to be a non-physical way. The reason of this fragmentation remains unclear and is generally attributed to the lack of a procedure that ensures immiscibility in the surface tension model and/or to the Lagrangian manifestation of the numerical diffusion at the interface. However, this interface fragmentation is amplified for low numbers of particles and for important density, viscosity and velocity ratios (and thus linked with the Kelvin-Helmholtz instability). Other numerical methods do not suffer from these issues (or under attenuated form) so that this interface fragmentation problem can potentially reduce the growing use of SPH for multiphase applications. Therefore, it advocates in favor of a search for a solution or a correction to prevent the interface fragmentation.

In the case of simulations of flow regimes, the results show that the presence of the interface correction force can strongly affect the flow pattern. In general, it accentuates the intermittent character of the flow and can lead to an overestimation of the pressure drop.

To conclude, it is clear that the interface correction procedure is to be used with caution. On one hand, it is employed to correct what appears to be a weakness in the multiphase SPH formulation and is sometimes necessary to capture the intermittent character of a typical slug or plug flow in particular for low number of particles. On the other hand, it can strongly affects the flow behavior which questions the accuracy of the reproduced physics.

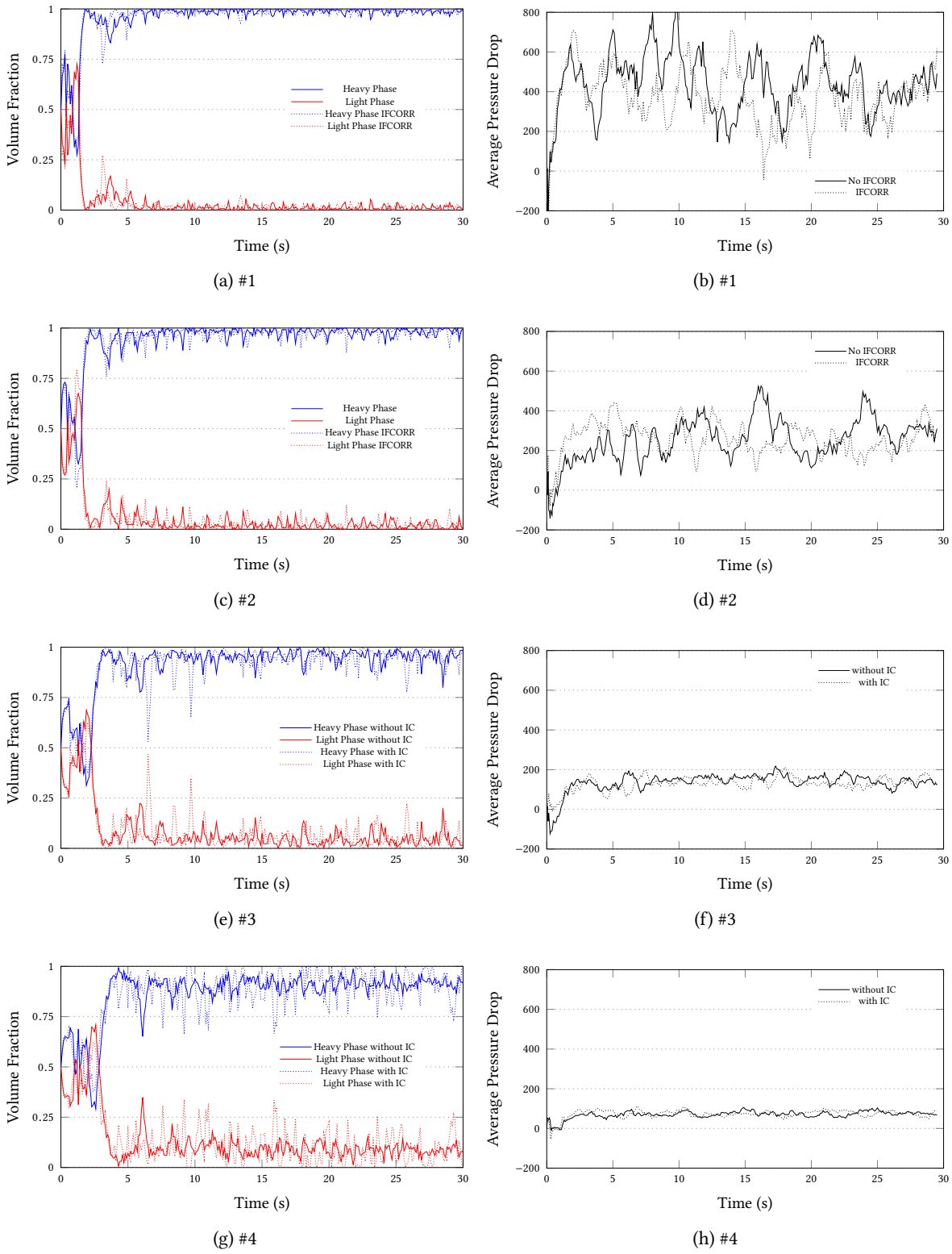

(a) #1 (b) #1

(c) #2 (d) #2

(e) #3 (f) #3

(g) #4 (h) #4

Figure 5.25: Results for path 2 (Dispersed to Intermittent). (a,c,e,g) Evolution of the volume fractions at the outlet with time. (b,d,f,h) Evolution of the average pressure drop at the outlet with time.

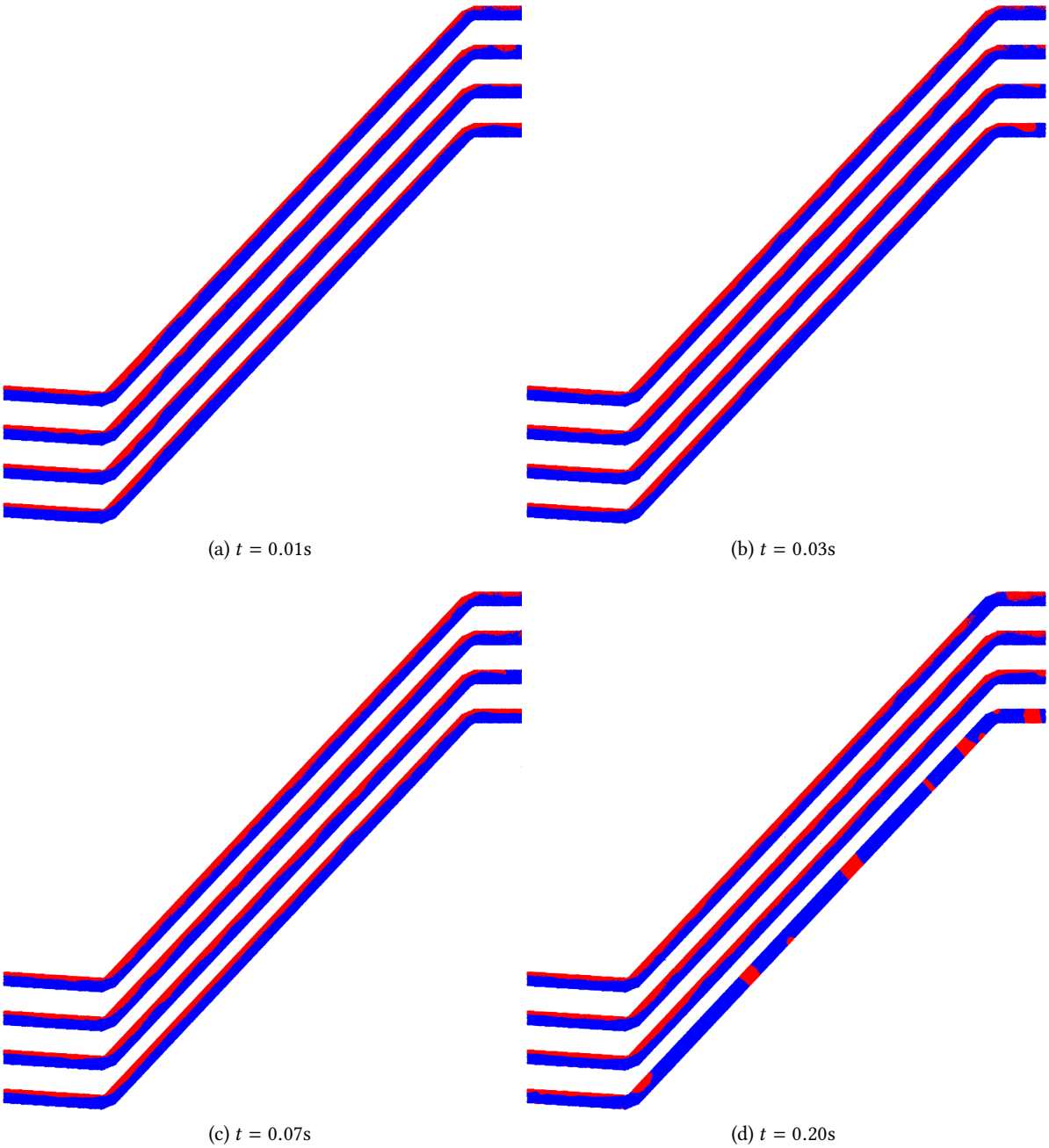

(a) $t = 0.01$s

(b) $t = 0.03$s

(c) $t = 0.07$s

(d) $t = 0.20$s

Figure 5.26: Phases distribution. From left to right : $\varepsilon = 0$, $\varepsilon = 0.1\frac{L_{\text{ref}}}{h} \approx 9$, $\varepsilon = \frac{L_{\text{ref}}}{h} \approx 90$ and $\varepsilon = 10\frac{L_{\text{ref}}}{h} \approx 900$

5.5 Comparison with experimental data

To conclude this chapter, we propose two attempts to compare our SPH code with experimental data. The main difficulty we have encountered is to find usable data to compare ourselves with. Initially, we tried to use the commercial software Ledaflow[2] to reproduce some results presented earlier in this manuscript but we were never able to obtain a slug flow with this program whereas the flow map, SPH and LBM all predicted the appearance of a slug flow regime. We finally managed to obtain utilizable data on two flow regimes experiments : a stratified flow experiment presented in [Suzanne 1985, Fabre 1987] and a slug flow experiment described in [Ujang 2003] (respectively labeled *Suzanne test case* and *Imperial test case* in the rest of this section). The geometrical configurations of the two cases are shown on Fig. 5.27 and the fluid properties on Tab. 5.6. Note that for stability reasons, we had to use an artificial viscosity (with $\alpha = 0.1$ and $\beta = 0$ in Eq. (2.4.2)) because the real viscosity term was not enough to stabilize the simulation. The inlet velocities for the Suzanne test case and the Imperial test case are respectively $(u_g, u_l) = (4.03 \text{ m/s}, 0.39 \text{ m/s})$ and $(u_g, u_l) = (9.28 \text{ m/s}, 1.222 \text{ m/s})$. All subsequent simulations are performed with 100000 particles for 30 s for the Suzanne test case and 15 s for the Imperial test case. $h/\Delta p$ is set to 1.5 for this case.

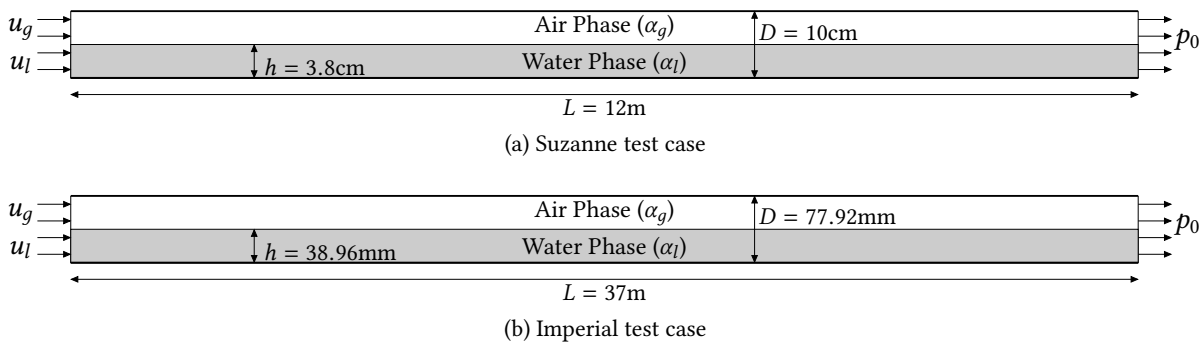

Figure 5.27: Geometrical configurations for the two experimental cases (not at scale).

Property	Air Phase	Water Phase	Units
Density (ρ)	1.18	997.1	kg/m^3
Viscosity (μ)	1.83×10^{-5}	0.98×10^{-3}	Pa.s
Adiabatic index (γ)	1.4	7	-
Surface Tension (σ^{nw})	0.037		N/m
Contact Angle (θ_c)	90		°
Gravity (g_z)	-9.81		m/s^2

Table 5.6: Physical Properties

[2]LedaFlow (`http://www.ledaflow.com`) is developed by SINTEF in collaboration with Total and ConocoPhilips and commercialized by Kongsberg. It is based on the multi-fluid multi-field theory. It consists in solving multiphase hydrodynamic conservation equations in 1D on a mesh [Bonizzi 2009]. The behavior of the fluids is then extrapolated in other dimensions using closure laws derived from laboratory experiments.

5.5.1 Suzanne test case

The Suzanne test case is composed of a pipe of of length 12 m, height 10 cm and width 20 cm. The pipe is supposed to have an upward inclination of 0.1% but it has been neglected in the subsequent simulations because it was too small to be notable with the considered resolution. On Fig. 5.28, we provide snapshots of the simulation at selected time steps and on Figs. 5.29 and 5.30, we show the comparison between the SPH results and the experimental data extracted from [Suzanne 1985, Fabre 1987].

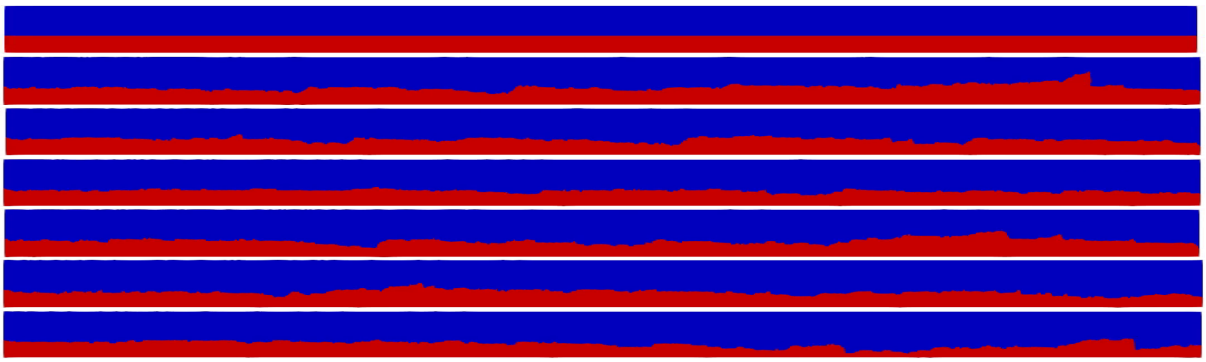

Figure 5.28: Phases distribution for the hydrodynamic slugging case (not at scale). From top to bottom, at $t = 0$ s, 5 s, 10 s, 15 s, 20 s, 25 s and 30 s

On Fig. 5.28, we see that the SPH simulation produces a wavy stratified flow with important variations of the water level towards the end of the pipe. On the other hand, the experiment produces a classic stratified flow. This discrepancy is likely due to the boundary conditions and the neglected effects in SPH compared to the experiment (2D vs 3D, turbulence, friction, ...).

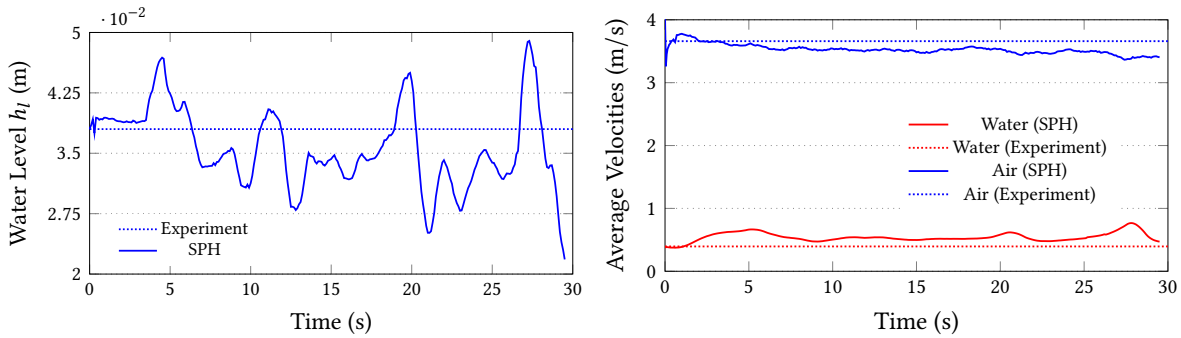

(a) Evolution of the water level h_l at $x = 9.1$ m with time.

(b) Evolution of the average velocities by phase with time.

Figure 5.29: Comparison of SPH results with experimental data extracted from [Suzanne 1985, Fabre 1987] (1/2)

First, on Fig. 5.29a, we can observe that SPH returns a water level at $x = 9.1$ m that varies around the experimental value but the general trend seems to be a slow decrease during the 30 s of the simulation. Second, Fig. 5.29b show the average velocity by phase in function of time compared to the experimental value. There is good agreement between SPH and the experiment in that case although SPH tends to slightly overestimate the water velocity and to underestimate the air velocity. We remind that the experimental value shown on Fig. 5.29 is an average value over the simulated time.

On Fig. 5.30, we present a comparison between SPH and the Suzanne experiment on the kinematic

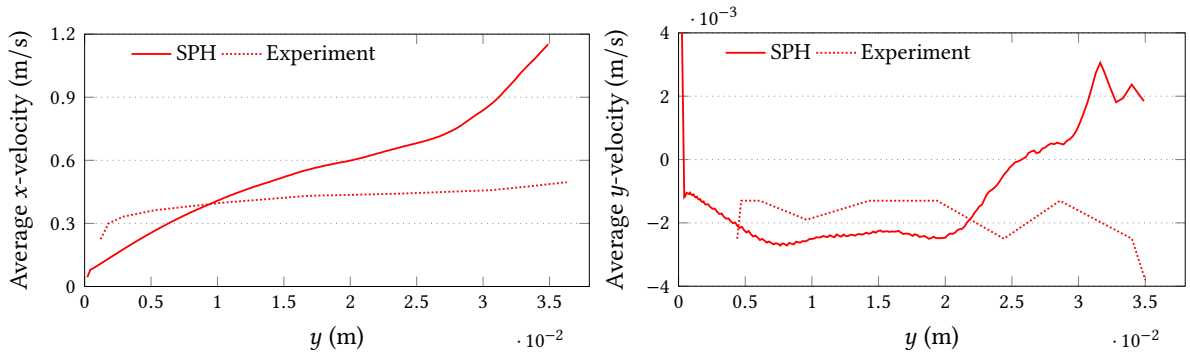

(a) Evolution of the average x-velocity in the **water** phase at $x = 9.1$ m with the height y of the pipe.

(b) Evolution of the average y-velocity in the **water** phase at $x = 9.1$ m with the height y of the pipe.

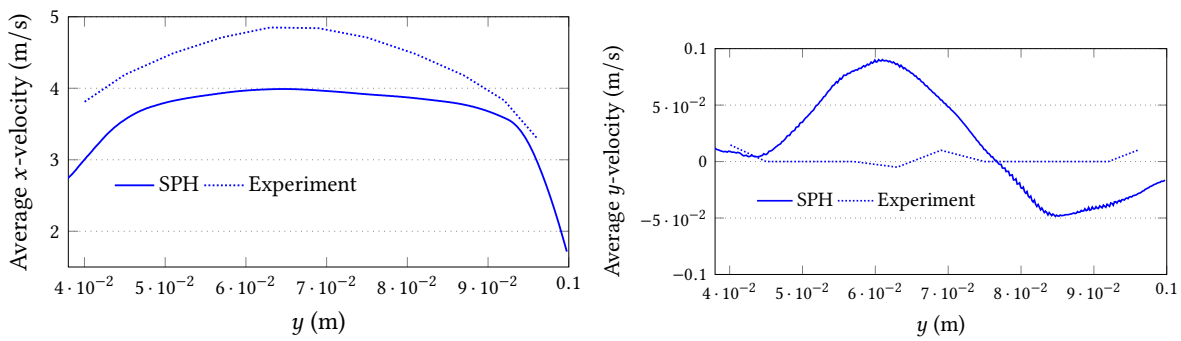

(c) Evolution of the average x-velocity in the **air** phase at $x = 9.1$ m with the height y of the pipe.

(d) Evolution of the average y-velocity in the **air** phase at $x = 9.1$ m with the height y of the pipe.

Figure 5.30: Comparison of SPH results with experimental data extracted from [Suzanne 1985, Fabre 1987] (2/2)

structure of the flow. Indeed, we compare the distribution of the velocity components in the air phase and in the water phase along the height of the pipe. On Fig. 5.30a, we see that both SPH and the experiment show an increase of the longitudinal velocity of water phase from the bottom of the pipe to the interface. Since we impose no-slip boundary conditions on the walls, it is expected that the velocity is close to zero at $y = 0$ m. However, SPH strongly overestimates the velocity and we end up at the interface with a water longitudinal velocity more than two times the one in the experiment. Concerning Fig. 5.30b, we see that the water phase has a very small transversal velocity at that location. SPH is in quite good agreement with the experiment up to $y \leq 2$ cm and then returns different results when $y \geq 2$ cm. As we get closer to the interface, the transversal velocity becomes positive in SPH whereas it remains negative in the experiment. However, the magnitude of this transversal velocity is small compared to the longitudinal one so the impact is moderate. On Fig. 5.30c, the longitudinal velocity of the air phase presents a bell-shaped aspect comparable to the experiment, however the SPH estimation is approximately 20% lower than in the experiment. Concerning the transversal air velocity shown on Fig. 5.30d, it is almost zero in the experiment while in SPH it is not exactly the case. We have a positive y-velocity near the interface and a negative one near the wall. Combined with Fig. 5.30b, it indicates that the interface is rising in average at the considered location. Elsewhere, the transversal velocity is negative, most likely due to the influence of gravity.

In a nutshell, we think that comparison demonstrates that SPH is producing reasonably accurate results with credible physical behaviors. Nevertheless, the flow appears more agitated than in the experiment and that is likely due to the boundary conditions at then entry and exit of the pipe. In addition, it would be interesting to re-run this case with more particles but the current state of the code prevent us to do it in a reasonable amount of time.

5.5.2 Imperial test case

For the Imperial test case, we compare ourselves to the experimental data but also with numerical data obtained with TransAT[3] (taken from a presentation provided by Total, to the best of our knowledge no papers were published following that presentation). In the experiment, the pipe is 37 m long. However, given the computational efficiency of our SPH code, it was not realistic to run such a case in a reasonable amount of time. Therefore, we decided to run two SPH simulations : one with a 8 m pipe and another with a 16 m pipe. In both cases, the number of particles is limited to 100000. Note that, the same approach (reduce the pipe length) was used for the TransAT simulations. On Fig. 5.31, we show snapshots of the simulations at selected time steps. On Figs. 5.32 and 5.33, we present the evolution of the water level h_l (normalized by the diameter D of the pipe) with time at different locations in the pipe. Finally, on Fig. 5.34, we show the evolution of the slug frequency in function of the position from the inlet in the pipe. In [Ujang 2003], it was not clear how they compute the slug frequency. In the sake of fairness, we decided to do the following : each time the normalized water level overcomes a threshold value, we count it a slug. Then, we divide the number of slugs by the simulation/experiment time. Three different threshold values were considered : $1.65\frac{\bar{h}_l}{D}$, $1.75\frac{\bar{h}_l}{D}$ and $1.85\frac{\bar{h}_l}{D}$ where $\bar{h}_l$ is the mean water level during the simulation/experiment at the given location. We label this quantity *slug frequency* for clarity but the term *slug* can clearly be questioned. Note that the same approach (using a threshold value) was also used in the presentation from which we have extracted the TransAT results.

On Fig. 5.31, we see that we obtained very wavy flows in both simulations. Large waves are appearing at different locations in the pipe but none of them actually reach the top of pipe to form a proper

[3]TransAT (`https://www.transat-cfd.com`) is a multi-scale finite volume CFD solver developed by ASCOMP AG Switzerland. It includes an original meshing approach called immersed surface technology and also comes with LES-based models for turbulence modeling and level-set, VOF and phase field approaches for interface tracking [Lakehal 2013].

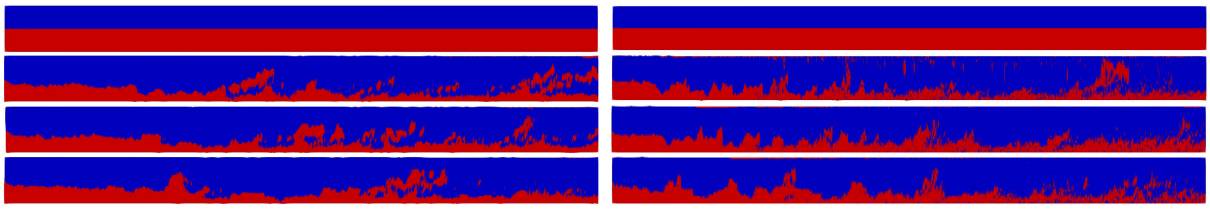

Figure 5.31: Phases distribution for the Imperial test case. From top to bottom, at $t = 0$ s, 5 s, 10 s and 15 s. The left column shows the results for a 8 m pipe and the right column the results for a 16 m pipe (not at scale).

slug. As shown on Figs. 5.32 and 5.33, we see that it is also the case in the TransAT simulations and the experiment, however they do reveal a more intermittent pattern with regular spikes of increasing amplitude as we progress along the pipe. Up until $x \leq 1.46$ m, there is a global agreement among all considered data on the average water level. After that, it is more difficult to draw conclusions since signals are quite different. The main issue appears to be the incapacity of SPH (at the considered resolutions) to reproduce the regular water level spikes. Indeed, the SPH water levels are indeed intermittent and they do present spikes but much smaller in amplitude compared to the experiment and the TransAT simulation. It is much more informative to look at Fig. 5.34. We see that the results depend on the threshold value considered. For the lowest threshold values ($1.65\frac{\bar{h}_l}{D}$ and $1.75\frac{\bar{h}_l}{D}$), we see that the 8 m long SPH simulation provides approximately the correct slug frequencies except the one at $x = 5.01$ m which is overestimated. The 16 m long SPH simulation is strongly underestimating the correct frequencies for $x \leq 8$ m but performs relatively well for $x > 8$ m. For the highest threshold ($1.85\frac{\bar{h}_l}{D}$), the 16 m long SPH simulation performs best. In all cases, the TransAT simulation returns roughly the same value (0.4 Hz for $x > 7$ m) which means that in that case, whatever the threshold value, when the water level overcomes the threshold, it is a spike of high amplitude (i.e. a slug). All in all, we think that those results are encouraging concerning SPH especially given the numerous neglected phenomena between the SPH results and the experiment.

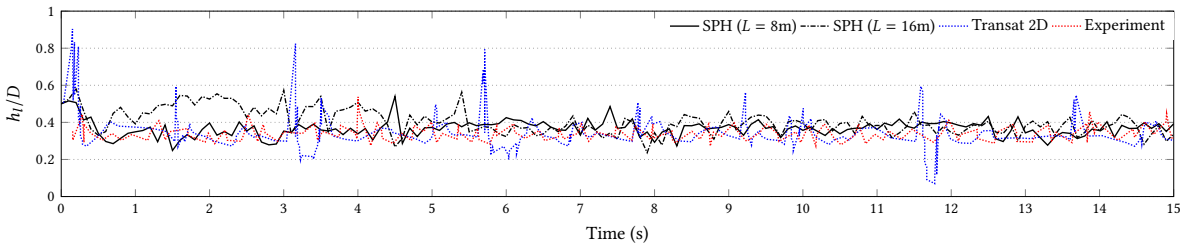

(a) x = 0.76 m

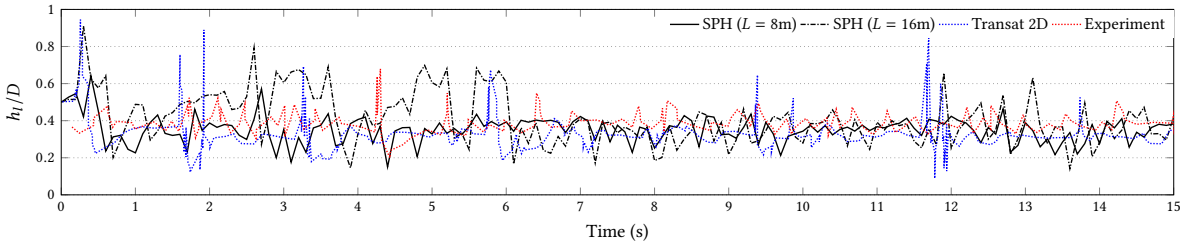

(b) x = 1.46 m

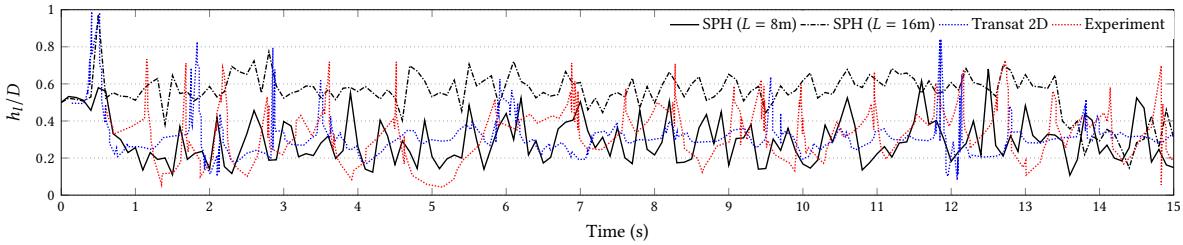

(c) x = 2.86 m

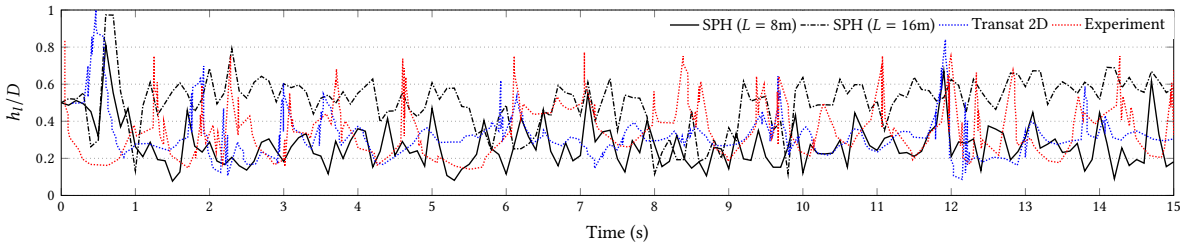

(d) x = 3.56 m

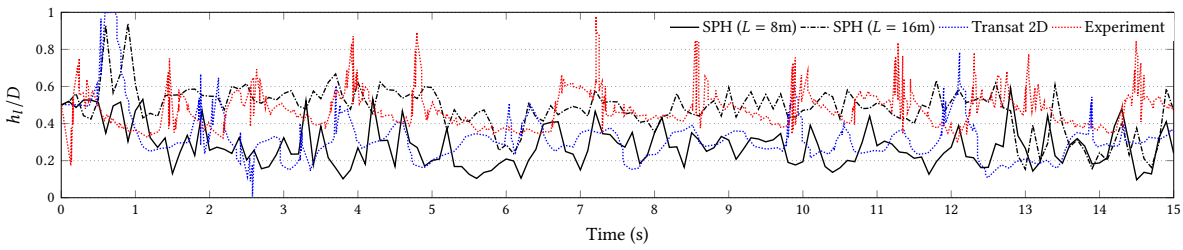

(e) x = 5.01 m

Figure 5.32: Normalized water levels (h_l/D) at different positions x from the inlet in function of time (1/2).

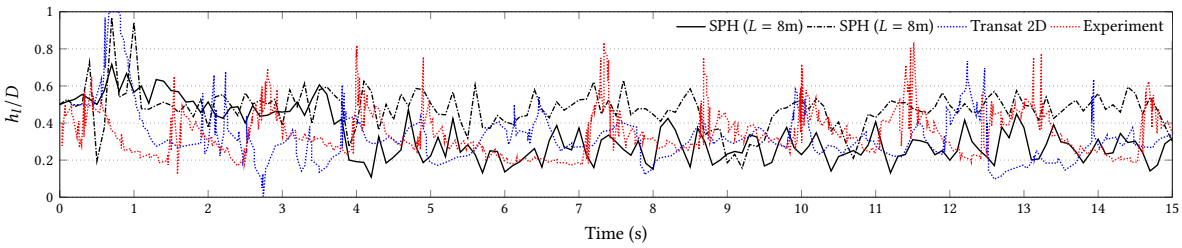

(a) x = 5.695 m

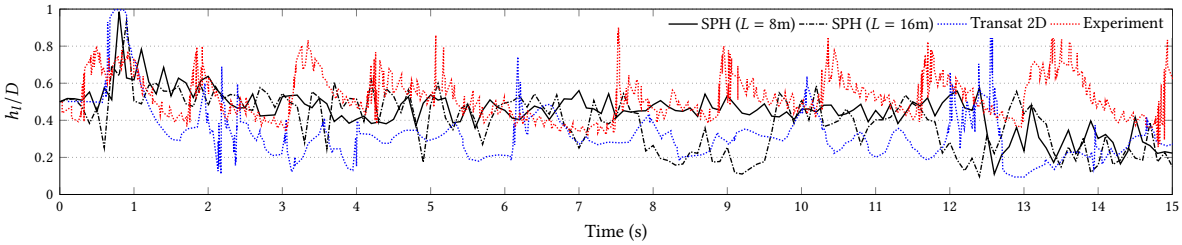

(b) x = 6.995 m

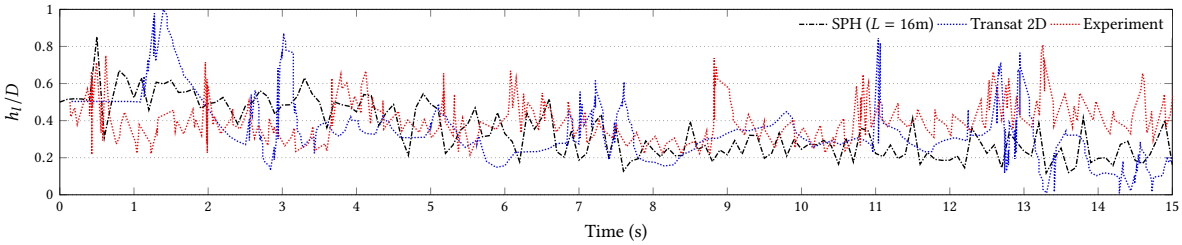

(c) x = 13.319 m

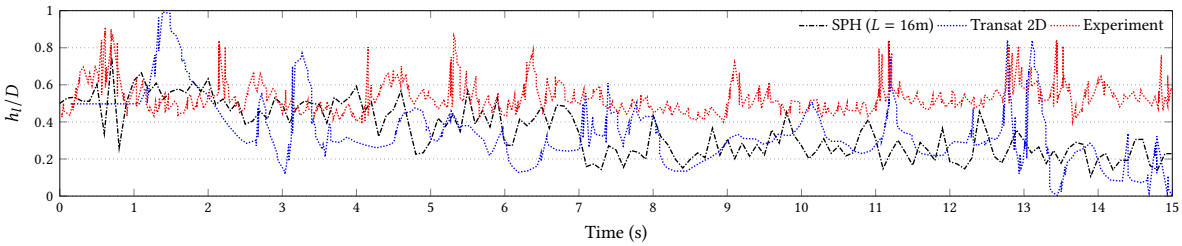

(d) x = 14.392 m

Figure 5.33: Normalized water levels (h_l/D) at different positions x from the inlet in function of time (2/2).

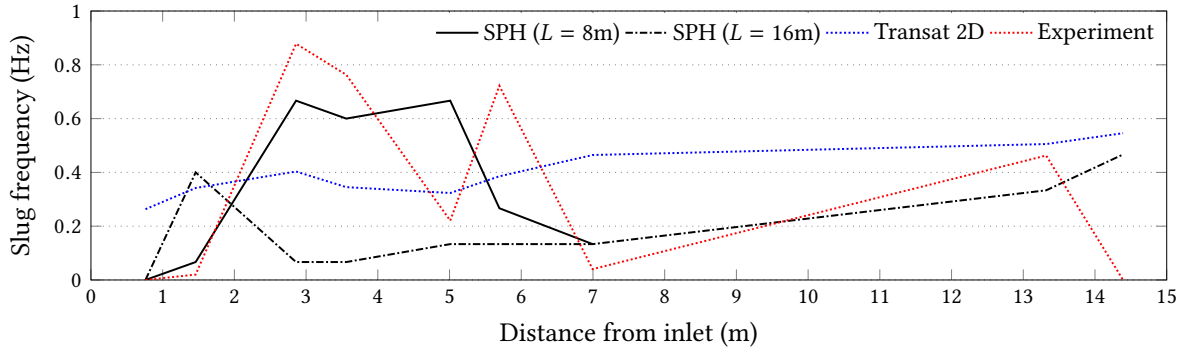

(a) Threshold $1.65\frac{\bar{h}_l}{D}$

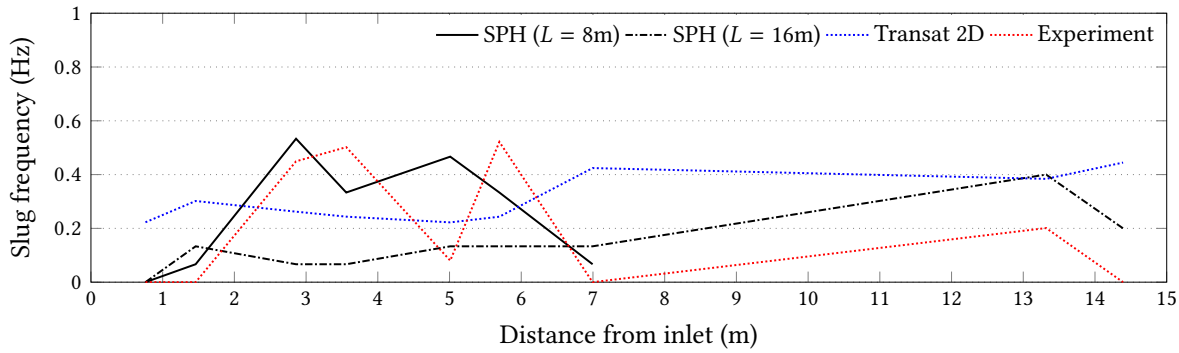

(b) Threshold $1.75\frac{\bar{h}_l}{D}$

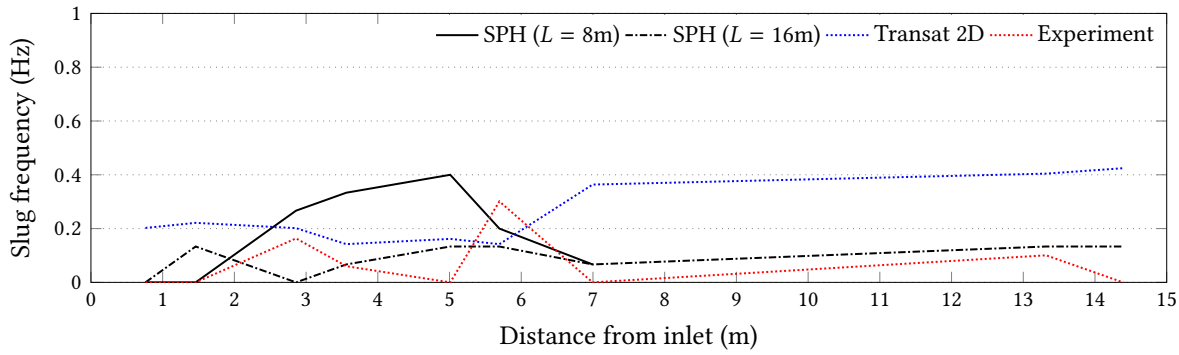

(c) Threshold $1.85\frac{\bar{h}_l}{D}$

Figure 5.34: Evolution of the slug frequency in function of the position from the inlet for different threshold values.

5.6 Conclusion

From theses simulations, we have confirmed that SPH has a strong potential to model two-phase flow in pipes and to understand how one pattern evolves into another one. However, we believe that our boundary conditions, although simple and easy to implement, are not optimal and that a semi-analytic approach [Ferrand 2012] could improve the quality of the results. Similarly, pressure drops of our simulations have reasonable levels that correspond to flow velocities but are also presenting large oscillations due to the weakly compressible approach. A truly incompressible formulation based on a Poisson solver could remediate this issue but the most promising approaches regarding that matter are the aforementioned δ-SPH and SPH-ALE (with Riemann solvers) formulations. Then, we have simulated two cases of hydrodynamic slugging and terrain slugging involving high density and viscosity ratios to demonstrate the applicability of multiphase SPH to more realistic problems. However, we were puzzled by the influence of the spurious interface correction force and decided to explore its influence on the previous results. We showed that although needed to properly capture the interface, it can strongly affect the flow and must be finely tuned. Unfortunately, there is no clear rule to detail how to tune it properly and it must be done by hand on a case to case basis. Finally, we propose a comparison with experimental measurements and numerical results done with TransAT that show reasonable agreement but failed to capture a proper slug flow when expected. New runs with more particles woulds be useful to ensure that it is not a resolution issue but the current state of the code prevents us to test it.

Albeit satisfactory, our results could certainly be improved. To this end, three main tasks can be identified. First, it would be interesting to verify if including the turbulence effects and increasing the number of particles would stabilize the pressure field, especially for high Reynolds cases. For a general point of view, the implementation of a multiphase δ-SPH scheme (like in [Hammani 2018] for example) in our solver appears to be a mandatory task to smooth our density and pressure fields. Then, it could be interesting to clarify the influence of shifting on the results through a parameter study. Finally, more comparisons with results obtained from other numerical methods, from different experimental data or from commercial software would be mandatory to further assess the potential interest of SPH in slugging modeling.

Although in general slower than other numerical methods, this study intended to show that SPH, thanks to its ease of handling interface dynamics, could be used in industrial applications to model intermittent flows and in particular slug and plug flows with reliable results. This work hopes to serve as a basis on which to build more complex SPH models including turbulence effects to capture the flow behavior with more accuracy.

Conclusions and perspectives

Summary This thesis aimed to explore the contributions and limitations of SPH and LBM in the context of intermittent flows in pipes. To this end, we have recalled the mathematical foundations of these two methods while replacing them within the family of particle-based methods in Chaps. 1 to 3. We have explained that SPH can be described from two distinct point of views. On one hand, it is a pure meshless method based on the collocation approach used to discretize partial differential equations (see Sects. 1.1.2.1, 2.1 and 2.2.3). On the other hand, SPH can be seen as a a fluid or solid dynamic problem numerically represented by a system of material points ("particles") using a regularizing function. LBM, for its part, comes from a completely different origin. It is a method devoted to fluid mechanics that consists in solving the Boltzmann equation on a Cartesian grid in a discrete velocity space by tracking the evolution of probability distribution functions. This approach has been proven equivalent to solving the Navier-Stokes equations in the limit of low Mach and Knudsen numbers (as can be shown by a multiscale Chapman-Enskog expansion, see Sect. 3.4). Then, the different formulations for multiphase modeling available for SPH (see Sect. 2.7) were discussed and some of them compared. It was then decided to use an SPH model based the Hu and Adams formulation [Hu 2006] with a stress-based surface tension model (CSF-Π) so that the computation of the curvature is avoided. Nevertheless, this approach requires a specific correction treatment to avoid a spurious interface fragmentation. The same comparison process has been done for LBM (see Sect. 3.12) and we have chosen to work with the CGM model described in [Reis 2007, Leclaire 2012] because it is a versatile multiphase model with a thin interface.

Then, we have carried out a validation campaign in parallel for both methods on several classic fluid mechanics test cases (see Sect. 4.3) : lid-driven cavity flow, capillary rise, Rayleigh-Taylor instability and static bubbles. First, it is a way to verify that our implementations of SPH and LBM are producing independently the correct results with the expected accuracy. Second, it allows us to compare SPH and LBM with an analytical and/or a reference solution. In a nutshell, we have shown that from a general point of view LBM produces more accurate results but at the price of a much more narrow stability range. Indeed, LBM was often the limiting factor. In order to propose a side to side comparison of both methods, we often had to adapt the parameters of the targeted test case (lower velocities, lower density ratios, lower viscosity ratios, lower surface tension values) because LBM was unstable. In that regard, SPH appears much more robust and flexible than LBM which, beyond accuracy, is an important advantage from an engineering point of view. Next, in Sect. 4.4, we extended our comparison to the simulation of intermittent flows with moderate density and viscosity ratios (respectively 5 and 2), first with periodic boundary conditions in a vertical pipe and then with inlet/outlet boundary conditions in an horizontal pipe. The periodic case results shown good agreement between SPH and LBM. Once again, it would have been interested to push the two methods further by increasing the Reynolds number (here limited to 500) but we were limited by the LBM stability issues. Afterwards, we focused on inlet/outlet slug flow cases. To that end, we had to develop inlet velocity boundary conditions and outlet pressure boundary conditions for SPH and LBM that suit our needs (see Sects. 4.1 and 4.2). For SPH, we have combined ideas from [Tafuni 2018, Alvarado-Rodríguez 2017] and adapt them to the multiphase context. For LBM, we have started from single phase Zou-He boundary conditions for velocity and pressure [Zou 1997] and adapt them to the multiphase context following ideas already developed in [Huang 2017]. Whether it is for SPH or LBM, the main challenges when developing these boundary conditions were to treat the interface variables interpolation properly and to limit the spurious pressure oscillations. All in all, we propose multiphase inlet/outlet boundary conditions for SPH and LBM that are reasonably accurate for our needs and more importantly stable for the range of Reynolds numbers we are interested in.

However, we are well aware that the accuracy and consistency of these aforementioned boundary conditions could certainly be improved because they are not entirely satisfactory. There are pressure wave reflections of variable amplitude and spurious behaviors, although limited, are still observable at the interface. In the end, the results of the inlet/outlet horizontal slug flow test cases matched the prediction of Taitel and Dukler's flow map in terms of flow regime type but were significantly different between SPH and LBM. In order to know which method was closer to reality, we wanted to compare to reference results (whether analytical, experimental or from other methods). We looked for such results in the literature without success, it is mainly because almost all results and/or flow maps available were done with air/water-like fluids which we cannot simulate with the LBM approach. We tried to use a commercial software designed for slug flow analysis called Ledaflow, but it did not generate a slug flow when it was predicted by Taitel and Dukler's flow map. Because of these LBM stability issues, we decided for the next chapter to limit our study to SPH only. It would let us simulate more demanding cases with different geometries and higher Reynolds numbers and higher density and viscosity ratios.

Finally, in Chap. 5, we let LBM aside to focus exclusively on SPH. First, we have started by a much more complete exploration of Taitel and Dukler's flow map (see Sects. 5.1 and 5.2). SPH simulations were in good agreement with the flow regimes predicted by the flow map. In those cases, the pressure drop evolution is a key quantity and although the qualitative behavior (increase/decrease) matched the predictions, it presented strong oscillations. In addition, when compared to the Friedel correlation for pressure drops in two phase flows, we observed important discrepancies. Then, in Sect. 5.3, we explored the ability of SPH to generate hydrodynamic and terrain slugging regimes for real fluids such as oil and gas with good results. Next, in Sect. 5.4, we have redone all the previous SPH simulations but this time varying the value of parameter ε which controls the interface correction term described in Sect. 2.7.3. We have shown that this correction force can strongly influence the flow regime in a quantitative and qualitative way and that its use must be done with caution. Finally, in Sect. 5.5, we proposed a comparison between SPH results and experimental data for real cases with moderate but encouraging agreement.

Conclusions This work lets us draw some general conclusions on the different aspects treated all along this thesis manuscript. First, we can state that particle-based methods covers a wide range of very different methods. Therefore, the term is not well suited to describe a clearly defined family of methods, it is too vague. For example, we would recommend "meshless" for SPH and "kinetic-based" for LBM. In spite of its name, SPH does not really involve physical particles but calculation points that happen to carry some material properties and is much better characterized by the absence of a mesh than the so called particles. On the other hand, LBM is a class of methods by itself that looks like no other and it is rather confusing to describe it as particle-based even if it rests on a particulate description of the matter. LBM emerges from kinetic and statistical considerations that involves physical particles but the link ends here. Indeed, despite their (debatable) common particle-based foundations, SPH and LBM formulations (used in this work) have in fact very little in common. The main aspect that draw them closer is probably their ease to handle multiphase flows but this apparent ease comes from very different reasons.

Then, concerning the multiphase formulations of both methods, we can add a few comments. The multiphase SPH formulation adopted for this work has been proven efficient in many situations presented in the available literature and also in this work. It is reasonably accurate, robust and versatile. We stress that being able to simulate in a stable way a large range of Reynolds numbers and density and viscosity ratios does not mean that it achieves a good precision but only that the simulation can run and returns visually credible results. This point can explain why SPH has been quite popular in the computer graphics community which paradoxically was also a deterrent for scientists in the past. In

addition, from an engineering point of view, there is a fistful of non-physical parameters to tune : mainly the background pressure p_0, the shifting parameter A_s and the spurious interface correction parameter ε. Their influence is far from negligible. Although we provide formulas to pre-compute these parameters, one may need to manually tune them in certain situations which is not very handy. Finally, we add the the stress-based approach for the surface tension model suffers from instabilities in long runs when the numbers of particles increases which is a serious drawback. As stated before, the curvature-based approach does not suffer from this problem but is more computationally expensive and cumbersome and requires a specific treatment for contact angle imposition. The multiphase LBM formulation used in this work benefits from a large body of published literature to present its abilities. We confirm that aspect by showing that this formulation can accurately simulate several well-known fluid mechanics problems. However, some limitations have to be highlighted. First (and this is inherent with LBM in general), the fact that LBM uses lattice units that are not the physical ones can be troublesome and can lead to human errors. There is a quite simple conversion procedure between real units and physical units but it requires some arithmetic manipulations that have to be undergone with caution if one wants to simulate the targeted problem. Otherwise, non-dimensionalization of the results is recommended. There are a few free parameters (the interface thickness β, one of the α for surface tension, some MRT relaxation times) but this is less tricky than in SPH since they have less impact on the simulation or have known optimal values. The main issue we have encountered when using the multiphase LBM formulation approach used here, and it has already been mentioned several times in this manuscript, is the stability. From the point of view of a plain user of the method, it restricts strongly the range of applications of the method (limited velocities, limited density/viscosity ratios). On another matter, our experience shows that the implementation of multiphase SPH is harder and longer that the LBM one.

In fact, one of the most challenging parts of this doctoral work was probably to develop, test and validate inlet/outlet boundary conditions for both methods but in particular for SPH. Indeed, for LBM, it was quite natural to start from single-phase Zou-He boundary conditions. Then, adapting them to multiphase context using the color field while taking into account the specific correction linked with the Hermite-based equilibrium functions was reasonably simple and gave quickly functional results. On the other hand, for SPH, it was much more difficult and time consuming. Indeed, once the decision was taken to work with buffers at both ends of the domain, we had to test multiple possibilities to define the quantities of the particles in the buffer. In addition, in Chap. 5, the injection velocities are quite high and so are the Reynolds numbers, so we had to ensure that the boundary conditions were stable under these conditions.

The comparison of SPH and LBM presented in Chap. 4 is divided in two parts : the validation part and the slug flow part. The validation part teaches us information that one who is familiar with both methods could reasonably expect. From a general point of view, whether it is single phase or multiphase, LBM has a better order of convergence than SPH and is more accurate for the same resolution. It is not simple to give reason why this is the case since the two methods are very different but the fact that LBM rests on a lattice with a known node connectivity strongly helps to get a good order of convergence. Obviously, SPH pressure fields depends on the particle spatial arrangement and are much more noisy that in LBM which can also affect the quality of the results. In addition, SPH wall boundary conditions that we have used in this work are based on an extrapolation from fluid particles to boundary particles which is known to affect the order of convergence. In LBM, we used full bounceback which is cleaner. Moreover, both methods present a deterioration of their abilities when simulation cases with more demanding conditions (higher Re, higher density or viscosity ratios) especially at low resolution. In some circumstances, LBM is not even able to run the case at the lowest resolution for the most “extreme” cases because of stability issues. The slug flow comparison part is also rich of teachings. The type of boundary conditions plays a crucial role on the conclusions we can draw from the results. The periodic

slug flow case shows very good quantitative agreement between SPH and LBM. However, it is possible to see differences in the velocity and pressure fields at the boundary and at the interface in particular. On the other hand, the inlet/outlet slug flow cases is more differentiating than the previous case, in particular the flow evolution is not the same between both methods. Clearly, it is due to the difference in the treatment of the boundary conditions which strongly affect the simulations.

The last part of this work which is devoted exclusively to SPH. Being freed of the stability issues inherent with LBM has let us explore much more realistic cases by gradually increasing complexity. We obtained results that were in agreement with the predictions of Taitel and Dukler's flow map. However, the observed pressure drops were in general very noisy and not agreeing with the Friedel's correlation. This makes us think that the present SPH formulation cannot accurately predict the pressure drops of the simulated test cases and therefore raises general doubts on the ability of the method to be used "as is" to model slug flow in a engineering context. Finally, the comparison with experimental and numerical data in the last section of this work gives mitigate results. Although it shows that SPH produces physically credible results, it does not fully agree with the experimental data. Of course, many factors were neglected in the SPH simulations compared to the reality but it appears that boundary conditions play a huge role in these discrepancies and need to be improved.

All in all, we believe that LBM in the formulation presented in this work, is not well suited for slug flow simulations because of its stability issues that prevent it to be applied to realistic cases involving air-water like fluids and $Re > 500$. On the contrary, the present SPH formulation showed promising capabilities in that regard although important problems remains to be overcome. In our opinion, the demonstrated potential of using a tool based on SPH in complement to existing software such as Ledaflow is worth continuing these investigations. It could help engineers have a better description of the flow regime in development in a given pipe and in particular help them improve their prediction of slug flow regimes to avoid the related undesired consequences.

Perspectives As of future perspectives regarding this work, we have identified a few directions of research where it would be of great interest to pursue investigations.

First, we have noticed two multiphase SPH formulations in the literature that would worth testing but it was not done because we lacked time and/or we discovered the corresponding papers too late. First, the formulation described in [Ghaitanellis 2017] which extends the re-normalization process (initially introduced in the USAW framework) to the Hu & Adams formulation in association with corrections for noisy pressure fields looks very efficient. In the end, the implementation appears more complex but exhibits clean pressure fields. In addition, they use USAW (Unified Semi-Analytical Wall) boundary conditions for wall boundary conditions that are much more efficient that the ones used in this work. Moreover, it appears that USAW boundary conditions are extendable to open boundary conditions [Ferrand 2017] so that an extension to multiphase flows is conceivable. Another approach that caught our attention was the one briefly presented in [Hammani 2018]. It is an extension of the δ-SPH approach, briefly described in Sect. 2.4.5 and that is becoming the standard in the SPH community, to multiphase flows in order, once again, to smooth out the pressure fields in WCSPH. Actually, we have implemented this formulation and tried to redo the simulations shown in Sect. 5.1. The pressure field was indeed smoother but it id not fully eliminate the oscillations and the reflections so we dropped the idea. Regarding the smoothing of the density field in WCSPH, we could also try to include Riemann solvers to solve each particles pair interaction and/or to use an SPH-ALE formulation [Oger 2016]. These density smoothing treatments could considerably help to improve the results by removing the spurious pressure fluctuations that were observed in our simulations. In addition, as done in Sect. 2.7.21, it would be interesting to further explore the influence of non-physical treatments such as the shifting procedure on the results. Second, in our opinion, the next phase of this work should be focused on

consolidating the confidence we can have in the formulations by providing comparisons with more reference cases and experimental data. It is not that easy to access usable experimental data so an alternative would be to use an existing software based on another numerical method able to simulate two-phase flow problems such as slug flows. In particular, in Sect. 4.4, it would be of great interest to rely on trusted data to decide which method is more accurate. Similarly, in Chap. 5, having reference solutions would help to determine more precisely the accuracy oh multiphase SPH when simulating slug flows. In the relation with what is aforementioned, it would also help to decide between SPH formulations.

Third, although we do propose a comparison with experimental data in Sect. 5.5, there are a few features that are missing in the codes to carry on a full comparison with real experiments. Obviously, all our simulations are 2D and it is needed to extend our study to 3D to take into account inherent 3D effects that would for example allow us to simulate a real annular flow. Additionally, there are turbulence models available in the literature for SPH and LBM which could be integrated in the codes to properly capture the related effects. As stated before, the turbulent viscosity would have a smoothing effect on the pressure fields that could benefit the SPH simulations. Similarly, improving the model for the boundary walls to take into account physical parameters such as roughness could also be considered. On a purely computational aspect, we were often limited during this doctoral work by the calculation time of SPH simulations. We had to use quite low numbers of particles to remain within acceptable time limits for our runs. Adding an MPI layer to the SPH would help to circumvent this issue while taking advantage of the multi-machines supercomputers available at Total. We believe that these modifications of the code are reasonably easy to implement because already available in the literature but require great care and extensive validation which are very time consuming and explains why we did not do it during this work.

Appendix A

$D2Q9$ MRT matrixes

$$\boldsymbol{M} = \begin{pmatrix} 1 & 1 & 1 & 1 & 1 & 1 & 1 & 1 & 1 \\ -4 & -1 & -1 & -1 & -1 & 2 & 2 & 2 & 2 \\ 4 & -2 & -2 & -2 & -2 & 1 & 1 & 1 & 1 \\ 0 & 1 & 0 & -1 & 0 & 1 & -1 & -1 & 1 \\ 0 & -2 & 0 & 2 & 0 & 1 & -1 & -1 & 1 \\ 0 & 0 & 1 & 0 & -1 & 1 & 1 & -1 & -1 \\ 0 & 0 & -2 & 0 & 2 & 1 & 1 & -1 & -1 \\ 0 & 1 & -1 & 1 & -1 & 0 & 0 & 0 & 0 \\ 0 & 0 & 0 & 0 & 0 & 1 & -1 & 1 & -1 \end{pmatrix}$$

$$\boldsymbol{M}^{-1} = \frac{1}{36} \begin{pmatrix} 4 & -4 & 4 & 0 & 0 & 0 & 0 & 0 & 0 \\ 4 & -1 & -2 & 6 & -6 & 0 & 0 & 9 & 0 \\ 4 & -1 & -2 & 0 & 0 & 6 & -6 & -9 & 0 \\ 4 & -1 & -2 & -6 & 6 & 0 & 0 & 9 & 0 \\ 4 & -1 & -2 & 0 & 0 & -6 & 6 & -9 & 0 \\ 4 & 2 & 1 & 6 & 3 & 6 & 3 & 0 & 9 \\ 4 & 2 & 1 & -6 & -3 & 6 & 3 & 0 & -9 \\ 4 & 2 & 1 & -6 & -3 & -6 & -3 & 0 & 9 \\ 4 & 2 & 1 & 6 & 3 & -6 & -3 & 0 & -9 \end{pmatrix}$$

$$\boldsymbol{m}^{eq} = \begin{pmatrix} \rho \\ e \\ \varepsilon \\ j_x \\ q_x \\ j_y \\ q_y \\ p_{xx} \\ p_{xy} \end{pmatrix} = \begin{pmatrix} \rho \\ -2\rho + 3\rho^2(u_x^2 + u_y^2) \\ \rho - 3\rho^2(u_x^2 + u_y^2) \\ \rho u_x \\ -\rho u_x \\ \rho u_y \\ -\rho u_y \\ \rho^2(u_x^2 - u_y^2) \\ \rho^2 u_x u_y \end{pmatrix} = \begin{pmatrix} \text{density } (0^{th} \text{ order}) \\ \text{energy } (2^{nd} \text{ order}) \\ \text{energy square } (4^{th} \text{ order}) \\ \text{momentum X-direction } (1^{st} \text{ order}) \\ \text{heat flux X-direction } (3^{rd} \text{ order}) \\ \text{momentum Y-direction } (1^{st} \text{ order}) \\ \text{heat flux Y-direction } (3^{rd} \text{ order}) \\ \text{diagonal stress } (2^{nd} \text{ order}) \\ \text{off-diagonal stress } (2^{nd} \text{ order}) \end{pmatrix}$$

Appendix B

Technical details in the Chapman-Enskog expansion

B.1 Isotropic tensors of order 2 and 4

We remind that because f^{eq} is rotationally invariant around $\boldsymbol{\xi} = 0$, the moments integrals of the peculiar velocity $\boldsymbol{\xi}$ must be isotropic. This is a consequence of the fact that anti-symmetric integrand cancels the integrals over the whole domain. Isotropic tensors of order two are scalar multiple of the identity tensor $\boldsymbol{I}$ [Jeffreys 1931], so we can write $\int \xi_a \xi_b f^{eq} d\boldsymbol{v} = A\boldsymbol{I}$. Moreover we also have $\int |\boldsymbol{\xi}|^2 f^{eq} d\boldsymbol{v} = D \int \xi_a^2 f^{eq} d\boldsymbol{v}$ [Wolfram 1986] :

$$\int \boldsymbol{\xi} \otimes \boldsymbol{\xi} f^{eq} d\boldsymbol{v} = \int \xi_a \xi_b f^{eq} d\boldsymbol{v} = \boldsymbol{I} \underbrace{\int \xi_a^2 f^{eq} d\boldsymbol{v}}_{=\frac{1}{D}\int |\boldsymbol{\xi}|^2 f^{eq} d\boldsymbol{v}} = \frac{1}{D}\boldsymbol{I} \underbrace{\int |\boldsymbol{\xi}|^2 f^{eq} d\boldsymbol{v}}_{=Dp=2\rho e}.$$

Isotropic tensors of order four are always under the form ${M_4^*}^{eq}{}_{abcd} = A\delta_{ab}\delta_{cd} + B\delta_{ac}\delta_{bd} + C\delta_{ad}\delta_{bc}$ [Jeffreys 1931]. In addition, the symmetric terms are invariant to index order *i.e.* $\int \xi_a \xi_a \xi_b \xi_b f^{eq} d\boldsymbol{v} = \int \xi_a \xi_b \xi_a \xi_b f^{eq} d\boldsymbol{v} = \int \xi_b \xi_a \xi_b \xi_a f^{eq} d\boldsymbol{v} - \int \xi_b \xi_b \xi_a \xi_a f^{eq} d\boldsymbol{v}$ so $A = B = C$. Therefore, we have ${M_4^*}^{eq}{}_{abcd} = A(\delta_{ab}\delta_{cd} + \delta_{ac}\delta_{bd} + \delta_{ad}\delta_{bc})$. Using the following identity $\int |\boldsymbol{\xi}|^4 f^{eq} d\boldsymbol{v} = D(D+2) \int \xi_a \xi_a \xi_b \xi_b f^{eq} d\boldsymbol{v}$ [Wolfram 1986], we can write :

$$\begin{aligned}\int \boldsymbol{\xi} \otimes \boldsymbol{\xi} \otimes \boldsymbol{\xi} \otimes \boldsymbol{\xi} f^{eq} d\boldsymbol{v} &= \underbrace{\int \xi_a \xi_b \xi_c \xi_d f^{eq} d\boldsymbol{v}}_{=\int \xi_a \xi_a \xi_b \xi_b f^{eq} d\boldsymbol{v} (\delta_{ab}\delta_{cd} + \delta_{ac}\delta_{bd} + \delta_{ad}\delta_{bc})} = (\delta_{ab}\delta_{cd} + \delta_{ac}\delta_{bd} + \delta_{ad}\delta_{bc}) \underbrace{\int \xi_a \xi_a \xi_b \xi_b f^{eq} d\boldsymbol{v}}_{=\frac{1}{D(D+2)}\int |\boldsymbol{\xi}|^4 f^{eq} d\boldsymbol{v}}, \\ &= (\delta_{ab}\delta_{cd} + \delta_{ac}\delta_{bd} + \delta_{ad}\delta_{bc}) \frac{1}{D(D+2)} \underbrace{\int |\boldsymbol{\xi}|^4 f^{eq} d\boldsymbol{v}}_{=4\rho e^2 \frac{D+2}{D}}.\end{aligned}$$

B.2 Calculation of f_1

$$
\begin{aligned}
-\frac{f_1}{\tau f^{eq}} &= \frac{1}{\rho}\left(\partial_{t_1}\rho + \boldsymbol{v}\cdot\nabla_{\boldsymbol{x}}\rho\right) + \frac{D\xi}{2e}\cdot\left(\partial_{t_1}\boldsymbol{u} + \boldsymbol{v}\cdot\nabla_{\boldsymbol{x}}\boldsymbol{u}\right) + \left(-\frac{D}{2e} + \frac{D}{4e^2}|\xi|^2\right)\left(\partial_{t_1}e + \boldsymbol{v}\cdot\nabla_{\boldsymbol{x}}e\right),\\
&= \frac{1}{\rho}\underbrace{\left(\partial_{t_1}\rho + (\boldsymbol{u}+\xi)\cdot\nabla_{\boldsymbol{x}}\rho\right)}_{=\xi\cdot\nabla_{\boldsymbol{x}}\rho-\rho\nabla_{\boldsymbol{x}}\cdot\boldsymbol{u}\ (3.4.16)} + \frac{D\xi}{2e}\cdot\underbrace{\left(\partial_{t_1}\boldsymbol{u} + (\boldsymbol{u}+\xi)\cdot\nabla_{\boldsymbol{x}}\boldsymbol{u}\right)}_{=\xi\cdot\nabla_{\boldsymbol{x}}\boldsymbol{u}-\frac{\nabla_{\boldsymbol{x}}p}{\rho}\ (3.4.17)}\\
&+ \left(-\frac{D}{2e} + \frac{D}{4e^2}|\xi|^2\right)\underbrace{\left(\partial_{t_1}e + (\boldsymbol{u}+\xi)\cdot\nabla_{\boldsymbol{x}}e\right)}_{=\xi\cdot\nabla_{\boldsymbol{x}}e-\frac{p}{\rho}\nabla_{\boldsymbol{x}}\cdot\boldsymbol{u}\ (3.4.18)},\\
&= \frac{1}{\rho}\left(\xi\cdot\nabla_{\boldsymbol{x}}\rho - \rho\nabla_{\boldsymbol{x}}\cdot\boldsymbol{u}\right) + \frac{D\xi}{2e}\cdot\Big(\xi\cdot\nabla_{\boldsymbol{x}}\boldsymbol{u} - \underbrace{\frac{\nabla_{\boldsymbol{x}}p}{\rho}}_{=\frac{2}{D}\nabla_{\boldsymbol{x}}e+\frac{2e}{D\rho}\nabla_{\boldsymbol{x}}\rho\ (3.1.14)}\Big)\\
&+ \left(-\frac{D}{2e} + \frac{D}{4e^2}|\xi|^2\right)\Big(\xi\cdot\nabla_{\boldsymbol{x}}e - \underbrace{\frac{p}{\rho}}_{=\frac{2e}{D}\ (3.1.14)}\nabla_{\boldsymbol{x}}\cdot\boldsymbol{u}\Big),\\
&= \frac{1}{\rho}\left(\cancel{\xi\cdot\nabla_{\boldsymbol{x}}\rho} - \cancel{\rho\nabla_{\boldsymbol{x}}\cdot\boldsymbol{u}}\right) + \frac{D\xi}{2e}\cdot\left(\xi\cdot\nabla_{\boldsymbol{x}}\boldsymbol{u} - \frac{2}{D}\nabla_{\boldsymbol{x}}e - \cancel{\frac{2e}{D\rho}\nabla_{\boldsymbol{x}}\rho}\right)\\
&- \frac{D}{2e}\left(\xi\cdot\nabla_{\boldsymbol{x}}e - \cancel{\frac{2e}{D}\nabla_{\boldsymbol{x}}\cdot\boldsymbol{u}}\right) + \frac{D}{4e^2}|\xi|^2\left(\xi\cdot\nabla_{\boldsymbol{x}}e - \frac{2e}{D}\nabla_{\boldsymbol{x}}\cdot\boldsymbol{u}\right),\\
&= \frac{D}{2e}\left(\underbrace{\xi\cdot(\xi\cdot\nabla_{\boldsymbol{x}}\boldsymbol{u})}_{=(\xi\otimes\xi):\nabla_{\boldsymbol{x}}\boldsymbol{u}} - \underbrace{\frac{|\xi|^2}{D}}_{=\frac{1}{D}(\xi\otimes\xi)\boldsymbol{I}}\underbrace{\nabla_{\boldsymbol{x}}\cdot\boldsymbol{u}}_{=\mathrm{Tr}(\nabla_{\boldsymbol{x}}\boldsymbol{u})}\right) + \frac{\xi}{e}\nabla_{\boldsymbol{x}}e\left(\frac{D|\xi|^2}{4e} - \frac{D}{2} - 1\right),\\
&= \frac{D}{2e}\left(\frac{1}{2}\Big((\xi\otimes\xi):\nabla_{\boldsymbol{x}}\boldsymbol{u} + \underbrace{(\xi\otimes\xi):\nabla_{\boldsymbol{x}}\boldsymbol{u}}_{=(\xi\otimes\xi)^T:\nabla_{\boldsymbol{x}}\boldsymbol{u}^T=(\xi\otimes\xi):\nabla_{\boldsymbol{x}}\boldsymbol{u}^T}\Big) - \frac{1}{D}(\xi\otimes\xi)\boldsymbol{I}\,\mathrm{Tr}(\nabla_{\boldsymbol{x}}\boldsymbol{u})\right)\\
&+ \frac{\xi}{e}\nabla_{\boldsymbol{x}}e\left(\frac{D|\xi|^2}{4e} - \frac{D}{2} - 1\right),\\
&= \frac{D}{2e}(\xi\otimes\xi)\left(\frac{1}{2}(\nabla_{\boldsymbol{x}}\boldsymbol{u} + \nabla_{\boldsymbol{x}}\boldsymbol{u}^T) - \frac{1}{D}\mathrm{Tr}(\nabla_{\boldsymbol{x}}\boldsymbol{u})\boldsymbol{I}\right) + \frac{\xi}{e}\nabla_{\boldsymbol{x}}e\left(\frac{D|\xi|^2}{4e} - \frac{D}{2} - 1\right),\\
&= \frac{D}{2e}(\xi\otimes\xi)\boldsymbol{S} + \frac{\xi}{e}\nabla_{\boldsymbol{x}}e\left(\frac{D|\xi|^2}{4e} - \frac{D}{2} - 1\right),
\end{aligned}
$$

where we have introduced the well known deviatoric strain tensor $\boldsymbol{S} = \frac{1}{2}(\nabla_{\boldsymbol{x}}\boldsymbol{u} + \nabla_{\boldsymbol{x}}\boldsymbol{u}^T) - \frac{1}{D}\mathrm{Tr}(\nabla_{\boldsymbol{x}}\boldsymbol{u})\boldsymbol{I}$.

B.3 Calculation of σ_1

$$
\begin{aligned}
\boldsymbol{\sigma}_1 &= -\int \boldsymbol{\xi} \otimes \boldsymbol{\xi} f_1 d\boldsymbol{v}, \\
&= \tau \left(\frac{DS}{2e} \int (\boldsymbol{\xi} \otimes \boldsymbol{\xi} \otimes \boldsymbol{\xi} \otimes \boldsymbol{\xi}) f^{eq} d\boldsymbol{v} + \frac{\nabla_{\boldsymbol{x}} e}{e} \underbrace{\int \left(\frac{D|\boldsymbol{\xi}|^2}{4e} - \frac{D}{2} - 1 \right) (\boldsymbol{\xi} \otimes \boldsymbol{\xi} \otimes \boldsymbol{\xi}) f^{eq} d\boldsymbol{v}}_{=0 \text{ (antisymmetric integrand)}} \right), \\
&= \frac{\tau DS}{2e} \int (\boldsymbol{\xi} \otimes \boldsymbol{\xi} \otimes \boldsymbol{\xi} \otimes \boldsymbol{\xi}) f^{eq} d\boldsymbol{v}, \\
\sigma_{ab_1} &\underset{\substack{\text{(temporary index} \\ \text{notation for} \\ 4^{th} \text{ order tensor)}}}{=} \frac{\tau DS_{cd}}{2e} \underbrace{\int \xi_a \xi_b \xi_c \xi_d f^{eq} d\boldsymbol{v}}_{=M_4^{*eq}{}_{abcd} = \frac{4}{D^2} \rho e^2 (\delta_{ab}\delta_{cd} + \delta_{ac}\delta_{bd} + \delta_{ad}\delta_{bc}) \text{ (equation (3.2.22))}}, \\
&= \frac{\tau DS_{cd}}{2e} \frac{4}{D^2} \rho e^2 (\delta_{ab}\delta_{cd} + \delta_{ac}\delta_{bd} + \delta_{ad}\delta_{bc}), \\
&= \frac{2\rho e \tau}{D} (\underbrace{\delta_{ab}\delta_{cd}S_{cd}}_{=\delta_{ab}\,\mathrm{Tr}(\boldsymbol{S})=0} + \underbrace{\delta_{ac}\delta_{bd}S_{cd}}_{=S_{ab}} + \underbrace{\delta_{ad}\delta_{bc}S_{cd}}_{S_{ab}}), \\
\boldsymbol{\sigma}_1 &\underset{\substack{\text{(back to} \\ \text{tensor notation)}}}{=} \frac{4\rho e \tau}{D} \boldsymbol{S}, \\
&= p\tau (\nabla_{\boldsymbol{x}} \boldsymbol{u} + \nabla_{\boldsymbol{x}} \boldsymbol{u}^T - \frac{2}{D} \mathrm{Tr}(\nabla_{\boldsymbol{x}} \boldsymbol{u}) \boldsymbol{I}), \\
&= \boldsymbol{\tau}.
\end{aligned}
$$

We immediately recognize the deviatoric stress tensor $\boldsymbol{\tau}$ with a shear viscosity $\mu = p\tau = \frac{2}{D}\rho e \tau$ and a bulk viscosity $\mu_B = 0$.

B.4 Calculation of $\mathbf{q}_1$

$$
\begin{aligned}
\boldsymbol{q}_1 &= \frac{1}{2}\int \xi|\xi|^2 f_1 d\boldsymbol{v}, \\
&= -\frac{\tau}{2}\left(\frac{DS}{2e}\underbrace{\int |\xi|^2(\xi\otimes\xi\otimes\xi)f^{eq}d\boldsymbol{v}}_{=0\text{ (antisymmetric integrand)}} + \frac{\nabla_{\boldsymbol{x}} e}{e}\int\left(\frac{D|\xi|^2}{4e}-\frac{D}{2}-1\right)|\xi|^2(\xi\otimes\xi)f^{eq}d\boldsymbol{v}\right), \\
&= -\frac{\tau\nabla_{\boldsymbol{x}} e}{2e}\left(\left(\frac{D}{4e}\right)\underbrace{\int |\xi|^4(\xi\otimes\xi)f^{eq}d\boldsymbol{v}}_{\substack{\text{antisymmetric integrand}\\ \text{except on the diagonal}}} - \left(\frac{D}{2}+1\right)\underbrace{\int |\xi|^2(\xi\otimes\xi)f^{eq}d\boldsymbol{v}}_{\substack{\text{antisymmetric integrand}\\ \text{except on the diagonal}}}\right), \\
&= -\frac{\tau\nabla_{\boldsymbol{x}} e}{2e}\left(\left(\frac{D}{4e}\right)\frac{\boldsymbol{I}}{D}\int |\xi|^6 f^{eq}d\boldsymbol{v} - \left(\frac{D}{2}+1\right)\frac{\boldsymbol{I}}{D}\int |\xi|^4 f^{eq}d\boldsymbol{v}\right), \\
&= -\frac{\tau\nabla_{\boldsymbol{x}} e}{2e}\left(\frac{1}{4e}\boldsymbol{I}\underbrace{\int |\xi|^6 f^{eq}d\boldsymbol{v}}_{=\rho K_6(D)\frac{64e^3}{D^3}} - \left(\frac{D+2}{2D}\right)\boldsymbol{I}\underbrace{\int |\xi|^4 f^{eq}d\boldsymbol{v}}_{=\rho K_4(D)\frac{16e^2}{D^2}}\right), \\
&= -\frac{8K_6(D)-4(D+2)K_4(D)}{D^3}\rho e\tau\nabla_{\boldsymbol{x}} e, \\
&= -\underbrace{\frac{4K_6(D)-2(D+2)K_4(D)}{D^2}}_{=\frac{D+2}{D}}\rho e\tau\frac{k_B}{m}\nabla_{\boldsymbol{x}} T, \\
&= -\frac{D+2}{D}\rho e\tau\frac{k_B}{m}\nabla_{\boldsymbol{x}} T, \\
&= -\kappa\nabla_{\boldsymbol{x}} T,
\end{aligned}
$$

where we used the ideal gas equation of state (3.1.19) to make the temperature gradient appear which led to the introduction of the thermal conductivity $\kappa = \frac{D+2}{D}\rho e\tau\frac{k_B}{m}$. Moreover, we introduced the coefficients $K_4(D)$ and $K_6(D)$ that depend on the evaluation of a Gaussian-type integral in D dimensions. Their values are shown in Tab. B.1. For information, the evaluation of the integrals can be done by switching to the D-spherical coordinate system and is detailed in Appendix B.5.

D	1	2	3	Formula
$K_4(D)$	3/4	2	15/4	$\frac{D}{4}(D+2)$
$K_6(D)$	15/8	6	105/8	$\frac{D}{8}(D+2)(D+4)$

Table B.1: Values of K_4 and K_6 for $D = 1,2,3$

B.5 Gaussian-type integrals in D dimensions

The evaluation of the integrals can be done by switching to the D-spherical coordinate system. If $\boldsymbol{x} = (x_1, x_2, \ldots, x_D)$ then the D-spherical coordinates are $r = \sqrt{x_1^2 + x_2^2 + \ldots + x_D^2}$ and $D-1$ angles ϕ_i. In addition, we have $d\boldsymbol{x} = dr d\phi_{D-1} \prod_{i=1}^{D-2} \sin(\phi_i)^{D-1-i} d\phi_i$. In the end, we can write :

$$\int_{-\infty}^{\infty} |\boldsymbol{x}|^n \exp(-a|\boldsymbol{x}|^2) d\boldsymbol{x} = 2 \underbrace{\int_0^{\infty} r^n \exp(-ar^2) r^{D-1} dr}_{\text{known Gaussian integral}} \underbrace{\int_0^{\pi} d\phi_{D-1}}_{\pi \text{ (only for} D>1)} \underbrace{\prod_{i=1}^{D-2} \int_0^{\pi} \sin(\phi_i)^{D-1-i} d\phi_i}_{\text{product of known Wallis' integrals (only for} D>1)} ,$$

$$= \frac{\Gamma(\frac{n+D}{2})}{a^{\frac{n+D}{2}}} \underbrace{\pi \prod_{i=1}^{D-2} \frac{\sqrt{\pi}\Gamma(\frac{D-i}{2})}{\Gamma(\frac{D+1-i}{2})}}_{\text{only if } D>1} .$$

If n is even ($n = 2m$) and using the properties of the Γ function, it simplifies:

$$\int_{-\infty}^{\infty} |\boldsymbol{x}|^{2m} \exp(-a|\boldsymbol{x}|^2) d\boldsymbol{x} =$$

$$\begin{cases} \frac{\Gamma(m+\frac{1}{2})}{a^{m+\frac{1}{2}}} = \frac{1}{2^m a^{m+\frac{1}{2}}} \underbrace{\Gamma\left(\frac{1}{2}\right)}_{=\sqrt{\pi}} \prod_{i=0}^{m-1} (D+2i) \text{ if } D = 1, \\ \frac{\Gamma(m+\frac{D}{2})}{a^{m+\frac{D}{2}}} \pi \prod_{i=1}^{D-2} \frac{\sqrt{\pi}\Gamma(\frac{D-i}{2})}{\Gamma(\frac{D+1-i}{2})} = \frac{\pi^{\frac{D}{2}}}{2^m a^{m+\frac{D}{2}}} \prod_{i=0}^{m-1} (D+2i) \times \underbrace{\Gamma\left(\frac{D}{2}\right) \prod_{i=1}^{D-2} \frac{\Gamma(\frac{D-i}{2})}{\Gamma(\frac{D+1-i}{2})}}_{=\Gamma(1)=1 \text{ (terms simplify one by one)}} \quad \text{if } D > 1, \end{cases}$$

$$= \frac{\pi^{\frac{D}{2}}}{2^m a^{m+\frac{D}{2}}} \prod_{i=0}^{m-1} (D+2i) .$$

Appendix C

Entropic considerations on the LBGK model for advection-diffusion

Contents

C.1 LB method for the 1D advection-diffusion equation **210**

C.2 Equilibrium distributions **211**

C.2.1 Entropy functional 211

C.2.2 Entropy minimization problem 211

C.2.3 Reinterpretation of the BGK collision term 212

C.3 Discrete H-Theorem **212**

C.3.1 Semi-discrete form 212

C.3.2 Discrete form 213

C.3.3 Whole discrete entropy inequality 214

C.4 Numerical experiments **214**

C.5 Other entropy functionals **216**

C.5.1 General case 216

C.5.2 Example of the Kullback entropy 216

C.6 Conclusion **217**

In this appendix, we explore intrinsic entropy properties of Lattice Boltzmann methods with a BGK collision model. For the sake of simplicity, we focus on a macroscopic one-dimensional convection-diffusion equation. We show that the lattice BGK methods satisfy an entropy property for a particular entropy functional. The BGK term is seen as the gradient of a Lagrangian functional, sum of the entropy plus a 0th-moment equality constraint. We retrieve the standard numerical stability limit on the numerical Knudsen number to get an entropy decay. We also exhibit the entropy dissipation source terms and the entropy fluxes. Numerical experiments validate the theoretical results. Note that this appendix has been published as a conference paper in the proceedings of XXXIX Ibero-Latin American Congress on Computational Methods in Engineering (CILAMCE) that took place in November 2019 in Paris and is authored by Florian De Vuyst and Thomas Douillet-Grellier [Vuyst 2018].

The kinetic origin of the LB method yields the question of the compatibility of the LB method with the H-theorem. This topic has gained attention [Karlin 1998, Luo 2000] because it is strongly connected to the stability properties of the method. In particular, in order to palliate the fact that classic LB schemes do not verify the H-theorem, new LB formulations have been introduced based on the construction of specific equilibria equipped with an H-theorem [Ansumali 2002] or entropy-controlled schemes [Ansumali 2000, Boghosian 2001].

In the following, we study the entropy properties of the D1Q3 LBGK scheme applied to the 1D advection-diffusion equation. First, we introduce the considered model and its relevant properties. Then, we show how it satisfies a discrete H-theorem for a particular entropy functional. In this process, we reinterpret the BGK operator as a gradient of a Lagrangian functional while exhibiting the entropy dissipation source terms and the entropy fluxes. Our observations are validated through numerical experiments. Moreover, equilibrium distributions are obtained from minimization principles.

C.1 LB method for the 1D advection-diffusion equation

Let's consider the 1D advection-diffusion equation with a constant advection speed $u \in \mathbb{R}$:

$$\partial_t \rho + \partial_x(\rho u) - \nu\, \partial^2_{xx}\rho = 0, \quad x \in \mathbb{R},\ t > 0, \tag{C.1.1}$$

with $\rho = \rho(x,t)$ the density and ν the viscosity. The initial condition is $\forall x \in \mathbb{R}, \rho(x, t = 0) = \rho^0(x)$ where ρ^0 is the initial density distribution. Additionally, we assume $\nu > 0$ and we only consider positive solutions of Eq. (C.1.1) such that $\rho(x,t) \geq 0$.

Let us consider the D1Q3 lattice with its discrete velocities $\boldsymbol{v} = (v_-, v_0, v_+)^T = (-c, 0, c)^T$ and its discrete distribution vector $\boldsymbol{f} = (f_-, f_0, f_+)^T$. The LB equations (LBE) are given hereafter in vector form

$$\partial_t \boldsymbol{f} + \Lambda\, \partial_x \boldsymbol{f} = \boldsymbol{q}(\boldsymbol{f}), \tag{C.1.2}$$

where the source terms $\boldsymbol{q}$ is the collision term and with the diagonal and constant advection matrix Λ defined by $\Lambda = \text{diag}(-c, 0, -c)$ We connect the LBE (C.1.2) with the macroscopic Eq. (C.1.1) by imposing the following constraints

$$\langle \boldsymbol{f}, \boldsymbol{e} \rangle = \rho, \quad \langle \boldsymbol{q}(\boldsymbol{f}), \boldsymbol{e} \rangle = 0, \tag{C.1.3}$$

where $\langle ., . \rangle$ denotes the standard scalar product, and $\boldsymbol{e} = (1,1,1)^T$, $\boldsymbol{q}(\boldsymbol{f}) = (q_i(\boldsymbol{f}))_i$.

The BGK collision model is defined as a relaxation term towards a discrete equilibrium distribution $\boldsymbol{f}^{\text{eq}}$, i.e.

$$\boldsymbol{q}(\boldsymbol{f}) = \frac{\boldsymbol{f}^{\text{eq}} - \boldsymbol{f}}{\tau'}, \tag{C.1.4}$$

with $\tau' > 0$ a relaxation time.

It is also expected that $\boldsymbol{f}^{\mathrm{eq}}$ has the 0th-order moment property but also the 1st-order and 2nd-order moment consistency properties. For a certain constant $\gamma > 0$, We can write

$$\langle \boldsymbol{f}^{\mathrm{eq}}, \boldsymbol{e} \rangle = \rho, \quad \langle \boldsymbol{f}^{\mathrm{eq}}, \boldsymbol{v} \rangle = \rho u, \quad \langle \boldsymbol{f}^{\mathrm{eq}}, \boldsymbol{v}^2 \rangle = \gamma \rho c^2. \tag{C.1.5}$$

C.2 Equilibrium distributions

In this section, we will obtain the equilibrium distributions associated with the entropy functional defined in Eq. (C.2.1) from minimization principles.

C.2.1 Entropy functional

As shown in the previous section, consistency is obtained under the hypothesis of small flow velocities. Thus, it is always assumed that $|u| \ll c$. In particular, the inequality $1 - \frac{3|u|}{2c} < 1$ holds. Therefore, the following functional $H(\boldsymbol{f})$ is clearly strictly convex

$$H(\boldsymbol{f}) = \sum_{i \in \{-,0,+\}} h_i(f_i), \tag{C.2.1}$$

with h_i defined as $h_i(f_i) = \frac{f_i^2}{2} w_i, \quad i \in \{-, 0, +\}$ and $w_- = \dfrac{1}{1 - \frac{3u}{2c}}$, $w_0 = 1$, $w_+ = \dfrac{1}{1 + \frac{3u}{2c}}$.

We call $H(\boldsymbol{f})$ an entropy for $\boldsymbol{f}$. The entropy functional H of Eq. (C.2.1) can be rewritten

$$H(\boldsymbol{f}) = \frac{1}{2} \langle D\boldsymbol{f}, \boldsymbol{f} \rangle = \frac{1}{2} \|\boldsymbol{f}\|_D^2. \tag{C.2.2}$$

where $D = \mathrm{diag}(\frac{1}{1-\frac{3u}{2c}}, 1, \frac{1}{1+\frac{3u}{2c}})$

Remark. *Note that the 1st and 2nd derivatives of H are $\nabla H(f) = D\boldsymbol{f}$ and $\nabla^2 H(\boldsymbol{f}) = D$ respectively.*

C.2.2 Entropy minimization problem

To begin, let us consider the constrained minimization problem

$$\min_{\boldsymbol{f} = (f_-, f_0, f_+)^T} \quad H(\boldsymbol{f}), \tag{C.2.3}$$

subject to

$$\begin{cases} \boldsymbol{f} \geq 0, \\ \langle \boldsymbol{f}, \boldsymbol{e} \rangle = \rho. \end{cases} \tag{C.2.4}$$

The functional H is coercive, strictly convex and the admissible set is non-empty, closed and convex. Therefore, there is a unique solution $\boldsymbol{f}^{\mathrm{eq}}$ to the problem (C.2.3-C.2.4). The functional φ for the equality constraint is linear and defined by

$$\varphi(\boldsymbol{f}) = \langle \boldsymbol{f}, \boldsymbol{e} \rangle - \rho \tag{C.2.5}$$

To this minimization problem, we associate a Lagrange multiplier $\lambda \in \mathbb{R}$ and the Lagrangian functional $\mathscr{L} : \mathbb{R}^3 \times \mathbb{R} \to \mathbb{R}$ expressed as

$$\mathscr{L}(\boldsymbol{f}, \lambda) = H(\boldsymbol{f}) + \lambda\, \varphi(\boldsymbol{f}). \tag{C.2.6}$$

The necessary 1st order optimality conditions are given by the Euler-Lagrange equations

$$\nabla \mathscr{L}(\boldsymbol{f}^{\mathrm{eq}}, \lambda^\star) = \nabla H(\boldsymbol{f}^{\mathrm{eq}}) + \lambda^\star\, \boldsymbol{e} = 0, \tag{C.2.7}$$

where $\lambda^\star$ is the Lagrange multiplier lambda that satisfies the above equation. We can then write

$$D\boldsymbol{f}^{\mathrm{eq}} + \lambda^\star\, \boldsymbol{e} = 0, \tag{C.2.8}$$

and we finally obtain

$$\boldsymbol{f}^{\mathrm{eq}} = -\lambda^\star D^{-1}\boldsymbol{e} = 0. \tag{C.2.9}$$

From the 0th order moment condition $\langle \boldsymbol{f}, \boldsymbol{e}\rangle = \rho$ we get $\lambda^\star = -\rho$, thus leading to the following solution

$$(f_-)^{\mathrm{eq}} = \frac{\rho}{3} - \frac{\rho u}{2c}, \quad (f_0)^{\mathrm{eq}} = \frac{\rho}{3}, \quad (f_+)^{\mathrm{eq}} = \frac{\rho}{3} + \frac{\rho u}{2c}.$$

Remark. *We have a natural consistency with both the convective and the diffusive terms of the advection-diffusion equation, in the sense that*

$$\sum_i v_i (f_i)^{eq} = \rho u, \tag{C.2.10}$$

$$\sum_i (v_i)^2 (f_i)^{eq} = \gamma \rho c^2 \tag{C.2.11}$$

with $\gamma = \frac{2}{3}$.

C.2.3 Reinterpretation of the BGK collision term

We now focus on the collision term of the LBE. Let us choose the collision term as

$$\boldsymbol{q}(\boldsymbol{f}) = -\frac{1}{\tau'} D^{-1} \nabla_f \mathscr{L}(\boldsymbol{f}, \lambda), \tag{C.2.12}$$

with $\tau' > 0$ a characteristic time of collision and $\mathscr{L}(\boldsymbol{f}, \lambda)$ defined in Eq. (C.2.6). We can write

$$\boldsymbol{q}(\boldsymbol{f}) \quad = \quad -\frac{1}{\tau'} D^{-1} \left(\nabla H(\boldsymbol{f}) + \lambda\, \boldsymbol{e}\right) = \frac{\boldsymbol{f}^{\mathrm{eq}} - \boldsymbol{f}}{\tau'}.$$

We retrieve the standard BGK collision term [Bhatnagar 1954].

Remark. *The matrix D^{-1} in (C.2.12) can be viewed as a rescaling operator allowing us to return the standard LBGK relaxation term. Because D is a positive definite matrix, the vector $-D^{-1}\nabla_f \mathscr{L}(\boldsymbol{f}, \lambda)$ is still a local descent direction for the functional $\mathscr{L}(., \lambda)$.*

C.3 Discrete H-Theorem

C.3.1 Semi-discrete form

In this section, we derive a Lyapunov functional decay property similar to the well-known Boltzmann's H-theorem [Boltzmann 1970]. Let us multiply Eq. (C.1.2) on the left by $\nabla H(\boldsymbol{f})^T$. We obtain

$$\partial_t H(\boldsymbol{f}) + \nabla H(\boldsymbol{f})^T \cdot \Lambda\, \partial_x \boldsymbol{f} \quad = \quad \nabla H(\boldsymbol{f})^T \cdot \boldsymbol{q}(\boldsymbol{f}), \tag{C.3.1}$$

$$\partial_t H(\boldsymbol{f}) + \sum_i (D\Lambda)_{ii}\, \partial_x (f_i)^2/2 \quad = \quad \nabla H(\boldsymbol{f})^T \cdot \boldsymbol{q}(\boldsymbol{f}). \tag{C.3.2}$$

Because H is convex and since $\boldsymbol{f}^{\mathrm{eq}}$ realizes the minimum of the optimization problem (C.2.3)-(C.2.4), we get the entropy dissipation balance equation

$$\partial_t H(\boldsymbol{f}) + \sum_i \partial_x [(D\Lambda)_{ii} (f_i)^2/2] \quad \leq \quad \frac{1}{\tau'} \left(H(\boldsymbol{f}^{\mathrm{eq}}) - H(\boldsymbol{f})\right) \leq 0.$$

It is worth mentioning that the entropy dissipation is linked to the amount of nonequilibrium. In the present particular case of quadratic functional, using a Taylor expansion leads to a finer entropy dissipation estimate as

$$\partial_t H(\boldsymbol{f}) + \sum_i \partial_x[(D\Lambda)_{ii}(f_i)^2/2] = \frac{1}{\tau'}\left(H(\boldsymbol{f}^{\mathrm{eq}}) - H(\boldsymbol{f})\right) - \frac{1}{2\tau'}\|\boldsymbol{f} - \boldsymbol{f}^{\mathrm{eq}}\|_D^2. \tag{C.3.3}$$

C.3.2 Discrete form

The time partial derivative is now discretized by the Euler explicit scheme. The lattice relaxation time is chosen as $\tau = \dfrac{\tau'}{\Delta t}$.

C.3.2.1 Collision step

We first study the entropy property of the collision step. To simplify notations, we omit the dependency in x position, and denote $\boldsymbol{f}$ at discrete time $t^n = n\Delta t$ by $\boldsymbol{f}^n$. The collision step on a time step Δt reads

$$\hat{\boldsymbol{f}}^n = \boldsymbol{f}^n + \frac{1}{\tau}\left(\boldsymbol{f}^{eq,n} - \boldsymbol{f}^n\right). \tag{C.3.4}$$

By multiplying on the left by $\frac{1}{2}(D(\hat{\boldsymbol{f}}^n + \boldsymbol{f}^n))$, we get

$$\begin{aligned}
\frac{1}{2}(D(\hat{\boldsymbol{f}}^n + \boldsymbol{f}^n))\cdot(\hat{\boldsymbol{f}}^n - \boldsymbol{f}^n) &= \frac{1}{2}\|\hat{\boldsymbol{f}}^n\|_D^2 - \frac{1}{2}\|\boldsymbol{f}^n\|_D^2, \\
&= H(\hat{\boldsymbol{f}}^n) - H(\boldsymbol{f}^n), \\
&= \frac{1}{2\tau}(D(\hat{\boldsymbol{f}}^n + \boldsymbol{f}^n))\cdot\left(\boldsymbol{f}^{eq,n} - \boldsymbol{f}^n\right).
\end{aligned} \tag{C.3.5}$$

From (C.3.4) we can write

$$\frac{\hat{\boldsymbol{f}}^n + \boldsymbol{f}^n}{2} = \boldsymbol{f}^n + \frac{1}{2\tau}\left(\boldsymbol{f}^{eq,n} - \boldsymbol{f}^n\right), \tag{C.3.6}$$

so that

$$H(\hat{\boldsymbol{f}}^n) - H(\boldsymbol{f}^n) = \frac{1}{\tau}\langle D\boldsymbol{f}^n, \boldsymbol{f}^{eq,n} - \boldsymbol{f}^n\rangle + \frac{1}{2\tau^2}\|\boldsymbol{f}^{eq,n} - \boldsymbol{f}^n\|_D^2. \tag{C.3.7}$$

The second term of the right hand side is anti-dissipative (nonnegative). This is due to the explicit Euler discretization of the collision term. Regarding the right hand side, let us remark that

$$\begin{aligned}
\langle D\boldsymbol{f}^n, \boldsymbol{f}^{eq,n} - \boldsymbol{f}^n\rangle &= \langle D(\boldsymbol{f}^n - \boldsymbol{f}^{eq,n} + \boldsymbol{f}^{eq,n}), \boldsymbol{f}^{eq,n} - \boldsymbol{f}^n\rangle, \\
&= -\|\boldsymbol{f}^{eq,n} - \boldsymbol{f}^n\|_D^2 + \langle D\boldsymbol{f}^{eq,n}, \boldsymbol{f}^{eq,n} - \boldsymbol{f}^n\rangle.
\end{aligned} \tag{C.3.8}$$

We recall that $D\boldsymbol{f}^{eq,n} = \nabla H(\boldsymbol{f}^{eq,n}) = -\lambda^\star \boldsymbol{e}$ (see Eq. (C.2.7)). Since $\langle \boldsymbol{e}, \boldsymbol{f}^{eq,n}\rangle = \langle \boldsymbol{e}, \boldsymbol{f}^n\rangle = \rho$, we have $\langle D\boldsymbol{f}^{eq,n}, \boldsymbol{f}^{eq,n} - \boldsymbol{f}^n\rangle = 0$. Therefore, we obtain

$$\langle D\boldsymbol{f}^n, \boldsymbol{f}^{eq,n} - \boldsymbol{f}^n\rangle = -\|\boldsymbol{f}^{eq,n} - \boldsymbol{f}^n\|_D^2 \tag{C.3.9}$$

and finally

$$H(\hat{\boldsymbol{f}}^n) - H(\boldsymbol{f}^n) = -\frac{1}{\tau^2}(\tau - \frac{1}{2})\,\|\boldsymbol{f}^{eq,n} - \boldsymbol{f}^n\|_D^2. \tag{C.3.10}$$

We then get a local entropy dissipation proportional to $\|\boldsymbol{f}^{eq,n} - \boldsymbol{f}^n\|^2$, as soon as $\tau > \frac{1}{2}$. We notice that the numerical stability limit, $\tau > 1/2$, is naturally recovered through entropic considerations.

Furthermore, the following identity is verified $H(\boldsymbol{f}^n) = H(\boldsymbol{f}^{eq,n}) + \frac{1}{2}\|\boldsymbol{f}^n - \boldsymbol{f}^{eq,n}\|_D^2$. Then, we also have the equivalent entropy balance

$$H(\hat{\boldsymbol{f}}^n) - H(\boldsymbol{f}^n) = -\frac{1}{2\tau^2}(\tau - \frac{1}{2})\ (H(\boldsymbol{f}^n) - H(\boldsymbol{f}^{eq,n})) \tag{C.3.11}$$

which is negative if $\tau > 1/2$.

C.3.2.2 Transport step

Let us now consider the transport step. At a lattice node x and at instant t^{n+1}, this reads

$$f_i^{n+1}(x) = \hat{f}_i^n(x - v_i\Delta t). \tag{C.3.12}$$

In a flux difference splitting script, it can be written in the equivalent form

$$f_i^{n+1}(x) = \hat{f}_i^n(x) - \left[\hat{f}_i^n(x) - \hat{f}_i^n(x - v_i\Delta t)\right], \tag{C.3.13}$$

leading to $f_0^{n+1}(x) = \hat{f}_0^n(x)$ and

$$f_\pm^{n+1}(x) = \hat{f}_\pm^n(x) - \frac{\Delta t}{h}\left[c\hat{f}_\pm^n(x) - c\hat{f}_\pm^n(x \mp c\Delta t)\right]. \tag{C.3.14}$$

Let us now consider the transport of entropy quantities. From (C.3.12), we get the conservation scheme

$$H(\boldsymbol{f}^{n+1}(x)) = H(\hat{\boldsymbol{f}}^n(x)) - \frac{\Delta t}{h}\left[\phi^n(x + h/2) - \phi^n(x - h/2)\right]. \tag{C.3.15}$$

where the numerical entropy flux $\phi^n(x + h/2) = \phi^n(\hat{\boldsymbol{f}}(x), \hat{\boldsymbol{f}}(x + h))$ is given by

$$\phi^n(x + h/2) = c\, h_+(\hat{f}_+(x)) - c\, h_-(\hat{f}_-(x + h)). \tag{C.3.16}$$

C.3.3 Whole discrete entropy inequality

By combining entropy balances for both collision (C.3.10) and transport (C.3.15) steps, we get a discrete entropy balance for the LBGK scheme:

$$H(\boldsymbol{f}^{n+1}(x)) - H(\boldsymbol{f}^n(x)) + \frac{\Delta t}{h}\left[\phi^n(x + h/2) - \phi^n(x - h/2)\right] = -\frac{1}{\tau^2}(\tau - \frac{1}{2})\,\|\boldsymbol{f}^{eq,n} - \boldsymbol{f}^n\|_D^2 \leq 0. \tag{C.3.17}$$

C.4 Numerical experiments

As a numerical illustration of the behavior of Eq. (C.3.17), a couple of numerical experiments have been undergone. The spatial domain is $\Omega = [0, 1]$ (in meters for example) and is closed with periodic boundary conditions. Ω is discretized with 4000 lattice points, so that the space step $h = 2.5 \times 10^{-4}$ m. Regarding the physical parameters, we have set the advection speed $u = 0.1$m/s and the speed of sound $c = 2$ m/s. Consequently, the time step is $dt = h/c = 2.5 \times 10^{-4}$ s. The initial density profile to be advected is chosen as piece-wise constant $\rho^0(x) = 1_{x\in[1/3,2/3]}(x)$. Fig. C.1 shows the density profile at $t = 10$ s and the corresponding entropy dissipation for two different values of τ.

It is observed on both figures that the entropy dissipation is strictly negative up to machine precision as predicted by Eq. (C.3.17). Note that we have tested to compute the entropy dissipation as $H(\boldsymbol{f}^{n+1}(x)) - H(\boldsymbol{f}^n(x)) + \frac{\Delta t}{h}\left[\phi^n(x + h/2) - \phi^n(x - h/2)\right]$ or as $-\frac{1}{\tau^2}(\tau - \frac{1}{2})\,\|\boldsymbol{f}^{eq,n} - \boldsymbol{f}^n\|_D^2$ and that it gives exactly the same results. The entropy dissipation is a good indicator of density changes and could eventually been used as a tool to track discontinuities in a multi-fluid context.

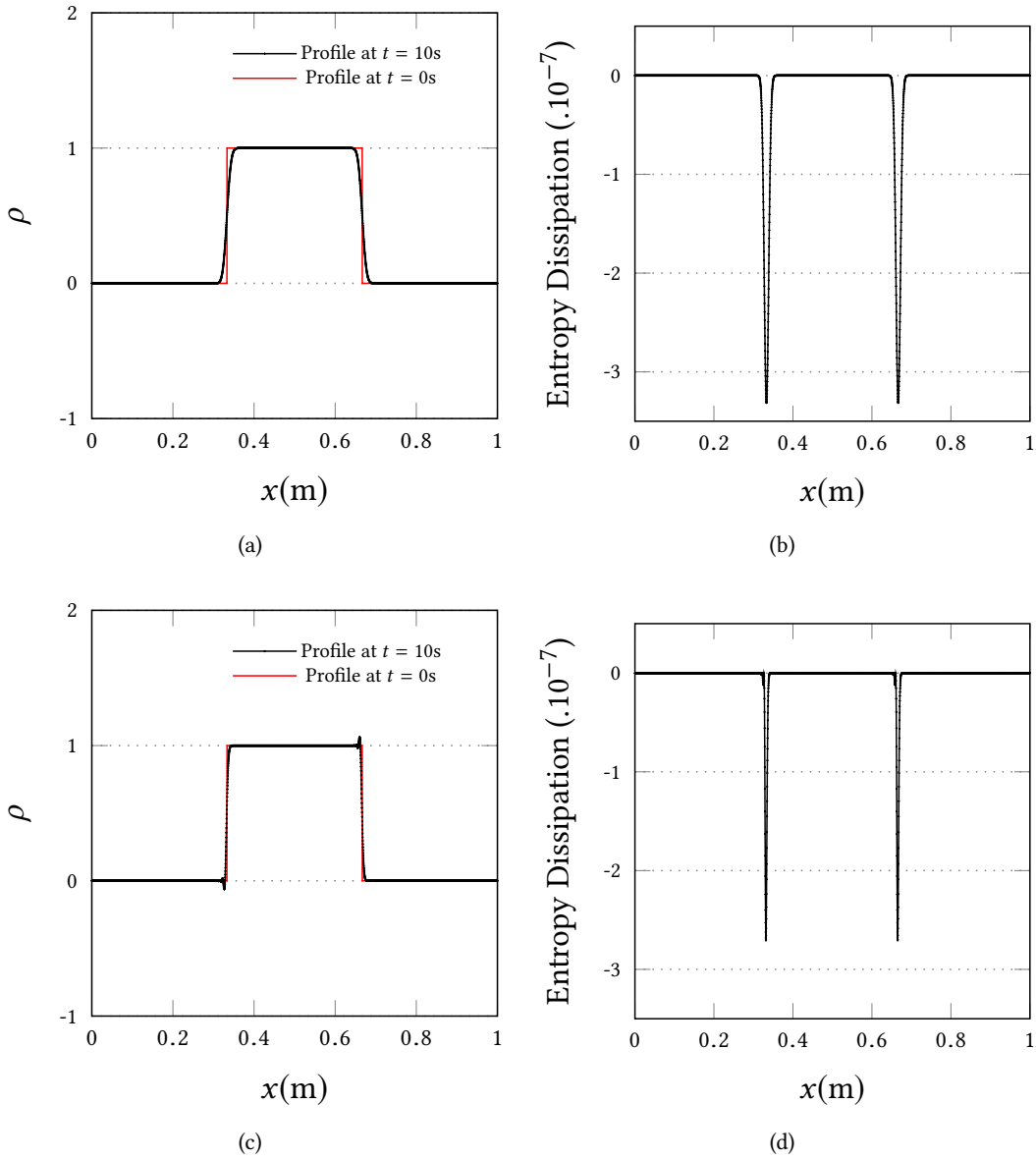

Figure C.1: Advection of a rectangular profile for 10s and its associated entropy dissipation for $\tau = 0.51$ (a,b) and $\tau = 0.501$ (c,d)

C.5 Other entropy functionals

In this section, we will consider the case of other forms of entropy functionals with a particular focus on the Kullback entropy.

C.5.1 General case

Let's consider a convex function $H : \mathbb{R}^3 \to \mathbb{R}$ with $H \in \mathscr{C}^2$. Let's call $\boldsymbol{f}^{\mathrm{eq}}$ the unique solution of the minimization problem (C.2.3-C.2.4). One can write

$$\nabla H(\boldsymbol{f}) \quad = \quad \nabla H(\boldsymbol{f}^{\mathrm{eq}}) + (\boldsymbol{f} - \boldsymbol{f}^{\mathrm{eq}})\,\bar{S}(\boldsymbol{f}). \tag{C.5.1}$$

with $\bar{S}(\boldsymbol{f}) = \int_0^1 \nabla^2 H(\boldsymbol{f}^{\mathrm{eq}} + t(\boldsymbol{f} - \boldsymbol{f}^{\mathrm{eq}}))$ symmetric and positive-definite matrix.

Similarly to what was done in section C.2.3, we can define the collision term $\boldsymbol{q}(\boldsymbol{f})$ as follows

$$\boldsymbol{q}(\boldsymbol{f}) = -\frac{1}{\tau'}\,[\bar{S}(\boldsymbol{f})]^{-1}\nabla_f \mathscr{L}(\boldsymbol{f}, \lambda). \tag{C.5.2}$$

where $\mathscr{L}$ is the same as in Eq. (C.2.6). This is equivalent to replace the rescaling operator D^{-1} in Eq. (C.2.12) by $[S(\boldsymbol{f})]^{-1}$. Therefore, using Eq. (C.5.1), we can expand Eq. (C.5.2).

$$\boldsymbol{q}(\boldsymbol{f}) \quad = \quad -\frac{1}{\tau'}[\bar{S}(\boldsymbol{f})]^{-1}\,(\nabla H(\boldsymbol{f}) + \lambda \boldsymbol{e}) = -\frac{1}{\tau'}(\boldsymbol{f} - \boldsymbol{f}^{\mathrm{eq}})$$

We retrieve once again the standard BGK relaxation collision term. Moreover, by convexity of H and because $\boldsymbol{f}^{\mathrm{eq}}$ is the minimum of H, we have the following inequality

$$\langle \nabla H(\boldsymbol{f}), \boldsymbol{q}(\boldsymbol{f})\rangle \leq \frac{1}{\tau'}\,(H(\boldsymbol{f}^{\mathrm{eq}}) - H(\boldsymbol{f})) \leq 0, \tag{C.5.3}$$

which leads to an entropy inequality similar to Eq. (C.3.3).

C.5.2 Example of the Kullback entropy

Let's consider the so called Kullback entropy function given by

$$h(f) = f \ln f - f. \tag{C.5.4}$$

The convex kinetic entropy functional (analog to Eq. (C.2.1)) can then be introduced as follows

$$H(\boldsymbol{f}) = \frac{h(f_-)}{1 - \frac{3u}{2c}} + h(f_0) + \frac{h(f_-)}{1 + \frac{3u}{2c}}. \tag{C.5.5}$$

Under the low Mach number hypothesis $\mathrm{Ma} = \frac{|u|}{c} \ll 1$, it leads to the set of equilibrium distributions given hereafter

$$f_-^{\mathrm{eq}} \approx e^{-\lambda}(1 - \frac{3u}{2c}), \quad f_0^{\mathrm{eq}} \approx e^{-\lambda}, \quad f_+^{\mathrm{eq}} \approx e^{-\lambda}(1 + \frac{3u}{2c}).$$

The constraint $\langle \boldsymbol{f}^{\mathrm{eq}}, \boldsymbol{e}\rangle = \rho$ gives $\sum_i f_i^{\mathrm{eq}} = \rho = 3e^{-\lambda} + \mathscr{O}(\mathrm{Ma}^2)$, then $e^{-\lambda} = \frac{\rho}{3} + \mathscr{O}(\mathrm{Ma}^2)$.

If we substitute $e^{-\lambda}$ by $\frac{\rho}{3}$ in Eq. (C.5.6) leads to the same equilibrium distributions of Eq. (C.2.10). This suggests that whatever the convex kinetic entropy functional considered, we always approximately end up on the same equilibrium distribution under the low Mach number hypothesis.

C.6 Conclusion

In this appendix, we have shown that by considering a particular entropy functional, it is possible to derive a discrete H-theorem for the LBGK scheme applied to the 1D advection-diffusion equation in a non-standard way. A fine evaluation of the entropy dissipation is presented where the dissipation source terms due to the collision step and the entropy fluxes associated with the transport step are exhibited. The quantification of entropy dissipation is verified by numerical experiments that confirm the theoretical results.

Through the exploration of the intrinsic entropic properties of this LBGK scheme, we have obtained the equilibrium distribution by solving an entropic minimization problem and proposed a reinterpretation of the BGK collision term as the gradient of the Lagrangian functional associated with this minimization problem.

Finally, using the example of the Kullback entropy, we have obtained equilibrium distributions that are approximately equal to the one obtained with a quadratic functional under the low Mach hypothesis.

Future work will be focused on extending our approach to more general entropy functionals, to 2D, to different collision operators and to non-periodic domains. We aim to improve the understanding of the numerical stability conditions of the LBGK scheme using these entropic considerations.

Bibliography

[Adami 2010] S. Adami, X. Hu and N. Adams. *A new surface-tension formulation for multi-phase SPH using a reproducing divergence approximation.* Journal of Computational Physics, vol. 229, no. 13, pages 5011–5021, jul 2010. (Cited on page 72.)

[Agertz 2007] O. Agertz, B. Moore, J. Stadel, D. Potter, F. Miniati, J. Read, L. Mayer, A. Gawryszczak, A. Kravtsov, Å. Nordlund, F. Pearce, V. Quilis, D. Rudd, V. Springel, J. Stone, E. Tasker, R. Teyssier, J. Wadsley and R. Walder. *Fundamental differences between SPH and grid methods.* Monthly Notices of the Royal Astronomical Society, vol. 380, no. 3, page 963, 2007. (Cited on page 62.)

[Ahrenholz 2006] B. Ahrenholz, J. Tilke and M. Krafczyk. *Lattice-Boltzmann simulations in reconstructed parametrized porous media.* International Journal of Computational Fluid Dynamics, vol. 20, no. 6, pages 369–377, 2006. (Cited on pages 3 and 12.)

[Al-Hashimy 2016] Z. I. Al-Hashimy, H. H. Al-Kayiem, R. W. Time and Z. K. Kadhim. *Numerical Characterisation Of Slug Flow In Horizontal Air/water Pipe Flow.* International Journal of Computational Methods and Experimental Measurements, vol. 4, no. 2, pages 114–130, 2016. (Cited on pages 4 and 14.)

[Alvarado-Rodríguez 2017] C. E. Alvarado-Rodríguez, J. Klapp, L. D. G. Sigalotti, J. M. Domínguez and E. de la Cruz Sánchez. *Nonreflecting outlet boundary conditions for incompressible flows using SPH.* Computers & Fluids, vol. 159, pages 177 – 188, 2017. (Cited on pages 7, 16, 128, 159 and 195.)

[Ansumali 2000] S. Ansumali and I. V. Karlin. *Stabilization of the lattice Boltzmann method by the $\mathcal{H}$-theorem: A numerical test.* Phys. Rev. E, vol. 62, pages 7999–8003, Dec 2000. (Cited on pages 110 and 210.)

[Ansumali 2002] S. Ansumali and I. V. Karlin. *Entropy function approach to the lattice Boltzmann method.* Journal of Statistical Physics, vol. 107, no. 1-2, pages 291–308, 2002. (Cited on page 210.)

[Antuono 2012] M. Antuono, A. Colagrossi and S. Marrone. *Numerical diffusive terms in weakly-compressible SPH schemes.* Computer Physics Communications, vol. 183, no. 12, pages 2570–2580, dec 2012. (Cited on page 66.)

[Atluri 2005] S. N. Atluri and S. Shen. *The basis of meshless domain discretization: the meshless local Petrov–Galerkin (MLPG) method.* Advances in Computational Mathematics, vol. 23, no. 1, pages 73–93, 2005. (Cited on pages 29 and 30.)

[Ba 2016] Y. Ba, H. Liu, Q. Li, Q. Kang and J. Sun. *Multiple-relaxation-time color-gradient lattice Boltzmann model for simulating two-phase flows with high density ratio.* Phys. Rev. E, vol. 94, page 023310, Aug 2016. (Cited on pages 105, 111, 113, 122 and 140.)

[Babuska 1996] I. Babuska and J. M. Melenk. *The Partition of Unity Method.* International Journal of Numerical Methods in Engineering, vol. 40, pages 727–758, 1996. (Cited on page 31.)

[Babuška 2003] I. Babuška, U. Banerjee and J. E. Osborn. *Survey of meshless and generalized finite element methods: a unified approach.* Acta Numerica, vol. 12, pages 1–125, 2003. (Cited on page 31.)

[Baker 1953] O. Baker. *Design of Pipelines for the Simultaneous Flow of Oil and Gas.* In Fall Meeting of the Petroleum Branch of AIME. Society of Petroleum Engineers, 1953. (Cited on page 162.)

[Balsara 1995] D. S. Balsara. *Von Neumann stability analysis of smoothed particle hydrodynamics: suggestions for optimal algorithms.* Journal of Computational Physics, vol. 121, no. 2, pages 357 – 372, 1995. (Cited on page 62.)

[Banari 2012] A. Banari, C. F. Janssen and S. T. Grilli. *An improved two-phase Lattice Boltzmann model for high density ratios : application to wave breaking.* 2012. (Cited on page 140.)

[Barnea 1987] D. Barnea. *A unified model for predicting flow-pattern transitions for the whole range of pipe inclinations.* International Journal of Multiphase Flow, vol. 13, no. 1, pages 1–12, jan 1987. (Cited on page 162.)

[Béchereau 2016] M. Béchereau. *Élaboration de méthodes Lattice Boltzmann pour les écoulements bifluides à ratio de densité arbitraire.* PhD thesis, ENS Paris-Saclay, 2016. (Cited on page 78.)

[Belikov 1997] V. Belikov, V. Ivanov, V. Kontorovich, S. Korytnik and A. Y. Semenov. *The non-Sibsonian interpolation: A new method of interpolation of the values of a function on an arbitrary set of points.* Computational mathematics and mathematical physics, vol. 37, no. 1, pages 9–15, 1997. (Cited on page 32.)

[Belt 2011] R. Belt, E. Duret, D. Larrey, B. Djoric and S. Kalali. *Comparison of Commercial Multiphase Flow Simulators with Experimental and Field Databases.* In 15th International Conference on Multiphase Production Technology, Cannes, France, 2011. BHR Group. (Cited on pages 4 and 14.)

[Belytschko 1994] T. Belytschko, Y. Y. Lu and L. Gu. *Element-free Galerkin methods.* International Journal for Numerical Methods in Engineering, vol. 37, no. 2, pages 229–256, 1994. (Cited on page 30.)

[Belytschko 1996] T. Belytschko, Y. Krongauz, D. Organ, M. Fleming and P. Krysl. *Meshless methods: An overview and recent developments.* Computer Methods in Applied Mechanics and Engineering, vol. 139, no. 1-4, pages 3 – 47, 1996. (Cited on page 28.)

[Belytschko 2001] T. Belytschko, N. Moes, S. Usui and C. Parimi. *Arbitrary discontinuities in finite elements.* International Journal for Numerical Methods in Engineering, vol. 50, no. 4, pages 993–1013, 2001. (Cited on page 31.)

[Bendiksen 1991] K. H. Bendiksen, D. Maines, R. Moe and S. Nuland. *The Dynamic Two-Fluid Model OLGA: Theory and Application.* SPE, 1991. (Cited on pages 4 and 14.)

[Benzi 1992] R. Benzi, S. Succi and M. Vergassola. *The lattice Boltzmann equation: theory and applications.* Physics Reports, vol. 222, no. 3, pages 145 – 197, 1992. (Cited on pages 3, 12 and 78.)

[Bhatnagar 1954] P. L. Bhatnagar, E. P. Gross and M. Krook. *A Model for Collision Processes in Gases. I. Small Amplitude Processes in Charged and Neutral One-Component Systems.* Phys. Rev., vol. 94, pages 511–525, May 1954. (Cited on pages 84 and 212.)

[Boghosian 2001] B. M. Boghosian, J. Yepez, P. V. Coveney and A. Wager. *Entropic lattice Boltzmann methods.* Proceedings of the Royal Society of London A: Mathematical, Physical and Engineering Sciences, vol. 457, no. 2007, pages 717–766, 2001. (Cited on page 210.)

[Boltzmann 1970] L. Boltzmann. Weitere studien über das wärmegleichgewicht unter gasmolekülen, pages 115–225. Vieweg+Teubner Verlag, Wiesbaden, 1970. (Cited on pages 84, 91 and 212.)

[Bonet 1999a] J. Bonet and T.-S. Lok. *Variational and momentum preservation aspects of Smooth Particle Hydrodynamic formulations.* Computer Methods in Applied Mechanics and Engineering, vol. 180, no. 1?2, pages 97 – 115, 1999. (Cited on page 57.)

[Bonet 1999b] J. Bonet and T.-S. Lok. *Variational and momentum preservation aspects of Smooth Particle Hydrodynamic formulations.* Computer Methods in Applied Mechanics and Engineering, vol. 180, no. 1, pages 97 – 115, 1999. (Cited on pages 64 and 126.)

[Bonet 2000] J. Bonet and S. Kulasegaram. *Correction and stabilization of smooth particle hydrodynamics methods with applications in metal forming simulations.* International Journal for Numerical Methods in Engineering, vol. 47, no. 6, pages 1189–1214, 2000. (Cited on page 29.)

[Bonet 2004] J. Bonet, S. Kulasegaram, M. X. Rodriguez-Paz and M. Profit. *Variational formulation for the smooth particle hydrodynamics (SPH) simulation of fluid and solid problems.* Computer Methods in Applied Mechanics and Engineering, vol. 193, no. 12-14, pages 1245–1256, 2004. (Cited on pages 49 and 57.)

[Bonet 2005] J. Bonet and M. X. RodrÃguez-Paz. *Hamiltonian formulation of the variable-h SPH equations.* Journal of Computational Physics, vol. 209, no. 2, pages 541 – 558, 2005. (Cited on page 57.)

[Bonizzi 2009] M. Bonizzi, P. Andreussi and S. Banerjee. *Flow regime independent, high resolution multi-field modelling of near-horizontal gas–liquid flows in pipelines.* International Journal of Multiphase Flow, vol. 35, no. 1, pages 34–46, January 2009. (Cited on page 186.)

[Boon 2003] J. P. Boon. *The Lattice Boltzmann Equation for Fluid Dynamics and Beyond.* European Journal of Mechanics - B/Fluids, vol. 22, no. 1, page 101, jan 2003. (Cited on page 78.)

[Borve 2001] S. Borve, M. Omang and J. Trulsen. *Regularized Smoothed Particle Hydrodynamics: A New Approach to Simulating Magnetohydrodynamic Shocks.* The Astrophysical Journal, vol. 561, no. 1, page 82, 2001. (Cited on page 64.)

[Bouzidi 2001] M. Bouzidi, M. Firdaouss and P. Lallemand. *Momentum transfer of a Boltzmann-lattice fluid with boundaries.* Physics of Fluids, vol. 13, no. 11, pages 3452–3459, 2001. (Cited on page 105.)

[Brackbill 1986] J. Brackbill and H. Ruppel. *FLIP: A method for adaptively zoned, Particle-In-Cell calculations of fluid flows in two dimensions.* Journal of Computational Physics, vol. 65, no. 2, pages 314–343, 1986. (Cited on page 32.)

[Brackbill 1992] J. Brackbill, D. Kothe and C. Zemach. *A continuum method for modeling surface tension.* Journal of Computational Physics, vol. 100, no. 2, pages 335 – 354, 1992. (Cited on page 72.)

[Buhmann 2003] M. D. Buhmann. *Radial basis functions: theory and implementations.* Cambridge Monographs on Applied and Computational Mathematics, vol. 12, pages 147–165, 2003. (Cited on page 33.)

[Bui 2008] H. Bui, R. Fukagawa, K. Sako and S. Ohno. *Lagrangian meshfree particles method (SPH) for large deformation and failure flows of geomaterial using elastic–plastic soil constitutive model.* International Journal for Numerical and Analytical Methods in Geomechanics, vol. 32, no. 12, pages 1537–1570, 2008. (Cited on pages 2, 12 and 40.)

[Cancelliere 1990] A. Cancelliere, C. Chang, E. Foti, D. H. Rothman and S. Succi. *The permeability of a random medium: Comparison of simulation with theory.* Physics of Fluids A, vol. 2, no. 12, pages 2085–2088, 1990. (Cited on pages 3 and 12.)

[Chapman 1962] S. Chapman and T. G. Cowling. *The Mathematical Theory of Non-Uniform Gases.* American Journal of Physics, vol. 30, no. 5, pages 389–389, 1962. (Cited on page 86.)

[Chen 1998] S. Chen and G. D. Doolen. *Lattice Boltzmann Method for fluid flows.* Annual Review of Fluid Mechanics, vol. 30, no. 1, pages 329–364, jan 1998. (Cited on page 111.)

[Chiron 2017] L. Chiron. *Couplage et améliorations de la méthode SPH pour traiter des écoulements à multi-échelles temporelles et spatiales.* PhD thesis, Ecole Centrale de Nantes (ECN), 2017. (Cited on pages 52, 67 and 69.)

[Colagrossi 2001] A. Colagrossi, M. Landrini and M. Tulin. *A Lagrangian meshless method for free-surface flows.* In Proceedings of the 4th Numerical Towing Tank Symposium, Hamburg, 2001. (Cited on pages 64 and 126.)

[Colagrossi 2003] A. Colagrossi and M. Landrini. *Numerical simulation of interfacial flows by smoothed particle hydrodynamics.* Journal of Computational Physics, vol. 191, no. 2, pages 448 – 475, 2003. (Cited on pages 67, 70, 71, 74, 126, 127 and 183.)

[Colagrossi 2012] A. Colagrossi, B. Bouscasse, M. Antuono and S. Marrone. *Particle packing algorithm for SPH schemes.* Computer Physics Communications, vol. 183, no. 8, pages 1641–1653, 2012. (Cited on page 52.)

[Colagrossi 2016] A. Colagrossi, E. Rossi, S. Marrone and D. Le Touzé. *Particle Methods for Viscous Flows: Analogies and Differences Between the SPH and DVH Methods.* Communications in Computational Physics, vol. 20, no. 03, pages 660–688, 2016. (Cited on page 35.)

[Cossins 2010] P. J. Cossins. *Smoothed Particle Hydrodynamics*, 2010. (Cited on page 52.)

[Cullen 2010] L. Cullen and W. Dehnen. *Inviscid smoothed particle hydrodynamics.* Monthly Notices of the Royal Astronomical Society, vol. 408, no. 2, pages 669–683, jul 2010. (Cited on page 62.)

[Cummins 1999] S. J. Cummins and M. Rudman. *An SPH Projection Method.* Journal of Computational Physics, vol. 152, no. 2, pages 584–607, jul 1999. (Cited on page 66.)

[Das 2009] A. Das and P. Das. *Bubble evolution through submerged orifice using smoothed particle hydrodynamics: Basic formulation and model validation.* Chemical Engineering Science, vol. 64, no. 10, pages 2281–2290, may 2009. (Cited on page 183.)

[Das 2015] R. Das and P. W. Cleary. *Evaluation of Accuracy and Stability of the Classical SPH Method Under Uniaxial Compression.* Journal of Scientific Computing, vol. 64, no. 3, pages 858–897, 2015. (Cited on page 64.)

[Das 2016] S. Das, R. Pramanik, T. Douillet-Grellier, D. Deb, K. Pan, B. Jones and J. R. Williams. *Numerical Study of Rock Failure Process in Indirect Tension.* ARMA 50th US Rock Mechanics/Geomechanics Symposium, 26-29 June, Houston, Texas, USA, 2016. (Cited on pages 1, 11 and 53.)

[De 2000] S. De and K. Bathe. *The method of finite spheres.* Computational Mechanics, vol. 25, no. 4, pages 329–345, 2000. (Cited on page 30.)

[Dehnen 2012] W. Dehnen and H. Aly. *Improving convergence in smoothed particle hydrodynamics simulations without pairing instability.* Monthly Notices of the Royal Astronomical Society, vol. 425, no. 2, pages 1068–1082, 2012. (Cited on pages 24, 44, 64 and 126.)

[Dellar 2008] P. J. Dellar. *Two routes from the Boltzmann equation to compressible flow of polyatomic gases.* Progress in Computational Fluid Dynamics, an International Journal, vol. 8, no. 1-4, pages 84–96, 2008. (Cited on page 109.)

[d'Humières 2002] D. d'Humières. *Multiple–relaxation–time lattice Boltzmann models in three dimensions.* Philosophical Transactions of the Royal Society of London A: Mathematical, Physical and Engineering Sciences, vol. 360, no. 1792, pages 437–451, 2002. (Cited on page 104.)

[Diehl 2012] S. Diehl, G. Rockefeller, C. L. Fryer, D. Riethmiller and T. S. Statler. *Generating Optimal Initial Conditions for Smoothed Particle Hydrodynamics Simulations.* ArXiv e-prints, November 2012. (Cited on page 52.)

[Dilts 1999] G. A. Dilts. *Moving-least-squares-particle hydrodynamics. Consistency and stability.* International Journal for Numerical Methods in Engineering, vol. 44, no. 8, pages 1115–1155, 1999. (Cited on page 29.)

[Dilts 2000] G. A. Dilts. *Moving least-squares particle hydrodynamics II: conservation and boundaries.* International Journal for Numerical Methods in Engineering, vol. 48, no. 10, pages 1503–1524, 2000. (Cited on page 29.)

[Dilts 2003] G. A. Dilts, A. Haque and J. Wallin. *Tuned Local Regression Estimators for the Numerical Solution of Differential Equations.* In Meshfree Methods for Partial Differential Equations, pages 87–104. Springer, 2003. (Cited on page 33.)

[Dong 2014] S. Dong, G. Karniadakis and C. Chryssostomidis. *A robust and accurate outflow boundary condition for incompressible flow simulations on severely-truncated unbounded domains.* Journal of Computational Physics, vol. 261, pages 83 – 105, 2014. (Cited on pages 68 and 128.)

[Douillet-Grellier 2016a] T. Douillet-Grellier, B. D. Jones, R. Pramanik, K. Pan, A. Albaiz and J. R. Williams. *Mixed-mode fracture modeling with smoothed particle hydrodynamics.* Computers and Geotechnics, vol. 79, pages 73–85, oct 2016. (Cited on pages 1, 2, 11, 12, 40 and 53.)

[Douillet-Grellier 2016b] T. Douillet-Grellier, R. Pramanik, K. Pan, A. Albaiz, B. D. Jones and J. R. Williams. *Development of stress boundary conditions in smoothed particle hydrodynamics (SPH)*

for the modeling of solids deformation. Computational Particle Mechanics, vol. 4, no. 4, pages 451–471, October 2016. (Cited on pages 1 and 11.)

[Douillet-Grellier 2016c] T. Douillet-Grellier, R. Pramanik, K. Pan, A. Albaiz, B. D. Jones, H. Pourpak and J. R. Williams. *Mesh-Free Numerical Simulation of Pressure-Driven Fractures in Brittle Rocks.* SPE Hydraulic Fracturing Technology Conference, 2016. (Cited on pages 1, 2, 11, 12 and 40.)

[Douillet-Grellier 2018] T. Douillet-Grellier, F. D. Vuyst, H. Calandra and P. Ricoux. *Influence of the spurious interface fragmentation correction on the simulation of flow regimes.* In Proceedings of the International 13th SPHERIC Workshop, June 26-28, Galway, Ireland, 2018. (Cited on page 74.)

[Douillet-Grellier 2019] T. Douillet-Grellier, S. Leclaire, D. Vidal, F. Bertrand and F. D. Vuyst. *Comparison of multiphase SPH and LBM approaches for the simulation of intermittent flows.* Computational Particle Mechanics, June 2019. (Cited on page 122.)

[Duarte 1996a] C. A. Duarte and J. T. Oden. *h-p clouds: an h-p meshless method.* Numerical Methods for Partial Differential Equations, vol. 12, no. 6, pages 673–705, 1996. (Cited on page 31.)

[Duarte 1996b] C. Duarte and J. Oden. *An h-p adaptive method using clouds.* Computer Methods in Applied Mechanics and Engineering, vol. 139, no. 1-4, pages 237 – 262, 1996. (Cited on page 31.)

[Dubois 2015] F. Dubois, P. Lallemand and M. M. Tekitek. *Taylor expansion method for analyzing bounce-back boundary conditions for lattice Boltzmann method.* ESAIM: Proc., vol. 52, pages 25–46, 2015. (Cited on page 105.)

[Enskog 1917] D. Enskog. Kinetische theorie der vorgänge in mässig verdünnten gasen ... Kinetische Theorie der Vorgänge in mässig verdünnten Gasen. Almquist & Wiksell, 1917. (Cited on page 86.)

[Erturk 2009] E. Erturk. *Discussions on driven cavity flow.* International Journal for Numerical Methods in Fluids, vol. 60, no. 3, pages 275–294, May 2009. (Cited on pages 131 and 139.)

[Español 2003] P. Español and M. Revenga. *Smoothed dissipative particle dynamics.* Physical Review E, vol. 67, no. 2, February 2003. (Cited on pages 35 and 70.)

[Fabre 1987] J. Fabre, C. Suzanne and L. Masbernat. *Experimental Data Set no. 7: Stratified Flow, Part I: Local Structure.* Multiphase Science and Technology, vol. 3, no. 1-4, pages 285–301, 1987. (Cited on pages 186, 187 and 188.)

[Fatehi 2011] R. Fatehi and M. Manzari. *Error estimation in smoothed particle hydrodynamics and a new scheme for second derivatives.* Computers & Mathematics with Applications, vol. 61, no. 2, pages 482–498, January 2011. (Cited on page 60.)

[Federico 2012] I. Federico, S. Marrone, A. Colagrossi, F. Aristodemo and M. Antuono. *Simulating 2D open-channel flows through an SPH model.* European Journal of Mechanics - B/Fluids, vol. 34, pages 35 – 46, 2012. (Cited on page 68.)

[Ferrand 2012] M. Ferrand, D. R. Laurence, B. D. Rogers, D. Violeau and C. Kassiotis. *Unified semi-analytical wall boundary conditions for inviscid, laminar or turbulent flows in the meshless SPH method.* International Journal for Numerical Methods in Fluids, vol. 71, no. 4, pages 446–472, mar 2012. (Cited on pages 55, 67, 68, 70, 174 and 194.)

[Ferrand 2017] M. Ferrand, A. Joly, C. Kassiotis, D. Violeau, A. Leroy, F.-X. Morel and B. D. Rogers. *Unsteady open boundaries for SPH using semi-analytical conditions and Riemann solver in 2D.* Computer Physics Communications, vol. 210, pages 29 – 44, 2017. (Cited on pages 67 and 198.)

[Ferreol 1995] B. Ferreol and D. H. Rothman. *Lattice-Boltzmann simulations of flow through Fontainebleau sandstone.* Transport in Porous Media, vol. 20, no. 1, pages 3–20, 1995. (Cited on pages 3 and 12.)

[Flekkoy 2000] E. G. Flekkoy, P. V. Coveney and G. De Fabritiis. *Foundations of dissipative particle dynamics.* Phys. Rev. E, vol. 62, pages 2140–2157, Aug 2000. (Cited on page 70.)

[Fonty 2019a] T. Fonty, M. Ferrand, A. Leroy and D. Violeau. *A first air entrainment SPH model using a two-phase mixture formulation.* In Proceedings of the International 14th SPHERIC Workshop, June 25-27, Exeter, United Kingdom, 2019. (Cited on pages 70 and 128.)

[Fonty 2019b] T. Fonty, M. Ferrand, A. Leroy, A. Joly and D. Violeau. *Mixture model for two-phase flows with high density ratios: A conservative and realizable SPH formulation.* International Journal of Multiphase Flow, vol. 111, pages 158–174, feb 2019. (Cited on page 70.)

[Fourtakas 2014] G. Fourtakas. *Modelling multi-phase flows in Nuclear Decommissioning using SPH.* PhD thesis, The University of Manchester, 2014. (Cited on page 70.)

[Franz 2018] T. Franz and H. Wendland. *Convergence of the Smoothed Particle Hydrodynamics Method for a Specific Barotropic Fluid Flow: Constructive Kernel Theory.* SIAM Journal on Mathematical Analysis, vol. 50, no. 5, pages 4752–4784, January 2018. (Cited on page 60.)

[Friedel 1979] L. Friedel. *Improved friction pressure drop correlations for horizontal and vertical two-phase pipe flow.* In European Two-Phase Flow Group Meeting, Ispra, Italy. European Two-Phase Flow Group, 1979. (Cited on page 164.)

[Fries 2004] T.-P. Fries and H.-g. Matthias. *Classification and overview of meshfree methods.* Department of Mathematics and Computer Science, Technical Univ. of Braunschweig, page 64, 2004. (Cited on pages 22, 25, 28 and 34.)

[Frisch 1986a] U. Frisch, B. Hasslacher and Y. Pomeau. *Lattice-Gas Automata for the Navier-Stokes Equation.* Phys. Rev. Lett., vol. 56, pages 1505–1508, Apr 1986. (Cited on pages 2 and 12.)

[Frisch 1986b] U. Frisch, B. Hasslacher and Y. Pomeau. *Lattice-Gas Automata for the Navier-Stokes Equation.* Phys. Rev. Lett., vol. 56, pages 1505–1508, Apr 1986. (Cited on page 111.)

[Fukagata 2007] K. Fukagata, N. Kasagi, P. Ua-arayaporn and T. Himeno. *Numerical simulation of gas–liquid two-phase flow and convective heat transfer in a micro tube.* International Journal of Heat and Fluid Flow, vol. 28, no. 1, pages 72–82, feb 2007. (Cited on pages 4 and 14.)

[Ganzenmuller 2015] G. C. Ganzenmuller, S. Hiermaier and M. May. *On the similarity of meshless discretizations of Peridynamics and Smooth-Particle Hydrodynamics.* Computers and Structures, vol. 150, pages 71–78, 2015. (Cited on page 35.)

[Gauger 2000] C. Gauger, P. Leinen and H. Yserentant. *The Finite Mass Method.* SIAM Journal on Numerical Analysis, vol. 37, no. 6, pages 1768–1799, 2000. (Cited on page 32.)

[Ghaitanellis 2017] A. Ghaitanellis. *Modélisation du charriage sédimentaire par une approche granulaire avec SPH.* PhD thesis, Université Paris-Est, 2017. Thèse de doctorat dirigée par Violeau, Damien Mécanique des fluides Paris Est 2017. (Cited on pages 70, 74 and 198.)

[Ghia 1982] U. Ghia, K. Ghia and C. Shin. *High-Re solutions for incompressible flow using the Navier-Stokes equations and a multigrid method.* Journal of Computational Physics, vol. 48, no. 3, pages 387 – 411, 1982. (Cited on page 131.)

[Gingold 1977] R. Gingold and J. Monaghan. *Smoothed particle hydrodynamics-theory and application to non-spherical stars.* Monthly Notices of the Royal Astronomical Society, vol. 181, pages 375–389, 1977. (Cited on pages 1, 11, 22, 29 and 40.)

[Ginzburg 2003] I. Ginzburg and D. d'Humières. *Multireflection boundary conditions for lattice Boltzmann models.* Phys. Rev. E, vol. 68, page 066614, Dec 2003. (Cited on page 105.)

[Gotoh 2005] H. Gotoh, H. Ikari, T. Memita and T. Sakai. *Lagrangian Particle Method for Simulation of Wave Overtopping on a Vertical Seawall.* Coastal Engineering Journal, vol. 47, no. 02n03, pages 157–181, 2005. (Cited on page 29.)

[Grenier 2009a] N. Grenier, M. Antuono, A. Colagrossi, D. L. Touzé and B. Alessandrini. *An Hamiltonian interface SPH formulation for multi-fluid and free surface flows.* Journal of Computational Physics, vol. 228, no. 22, pages 8380 – 8393, 2009. (Cited on pages 70, 71, 74, 140, 141 and 183.)

[Grenier 2009b] N. Grenier. *Modélisation numérique par la méthode SPH de la séparation eau-huile dans les séparateurs gravitaires.* PhD thesis, Ecole Centrale de Nantes (ECN), 2009. (Cited on page 69.)

[Grunau 1993] D. Grunau, S. Chen and K. Eggert. *A lattice Boltzmann model for multiphase fluid flows.* Physics of Fluids A: Fluid Dynamics, vol. 5, no. 10, pages 2557–2562, oct 1993. (Cited on pages 112 and 113.)

[Gunstensen 1991] A. K. Gunstensen, D. H. Rothman, S. Zaleski and G. Zanetti. *Lattice Boltzmann model of immiscible fluids.* Phys. Rev. A, vol. 43, pages 4320–4327, Apr 1991. (Cited on pages 111 and 114.)

[Guo 2002a] Z. Guo and T. S. Zhao. *Lattice Boltzmann model for incompressible flows through porous media.* Phys. Rev. E, vol. 66, page 036304, Sep 2002. (Cited on pages 3 and 12.)

[Guo 2002b] Z. Guo, C. Zheng and B. Shi. *Discrete lattice effects on the forcing term in the lattice Boltzmann method.* Phys. Rev. E, vol. 65, page 046308, Apr 2002. (Cited on pages 108 and 109.)

[Halliday 1998] I. Halliday, S. P. Thompson and C. M. Care. *Macroscopic surface tension in a lattice Bhatnagar-Gross-Krook model of two immiscible fluids.* Physical Review E, vol. 57, no. 1, pages 514–523, jan 1998. (Cited on page 114.)

[Halliday 2007] I. Halliday, A. P. Hollis and C. M. Care. *Lattice Boltzmann algorithm for continuum multicomponent flow.* Physical Review E, vol. 76, no. 2, aug 2007. (Cited on page 115.)

[Hammani 2018] I. Hammani, G. Oger, D. L. Touzé, A. Colagrossi and S. Marrone. *How to derive the multi-fluid delta-SPH model.* In Proceedings of the International 13th SPHERIC Workshop, June 26-28, Galway, Ireland, 2018. (Cited on pages 66, 194 and 198.)

[Hao 2002] S. Hao, H. S. Park and W. K. Liu. *Moving particle finite element method.* International Journal for Numerical Methods in Engineering, vol. 53, no. 8, pages 1937–1958, 2002. (Cited on page 32.)

[Harlow 1955] F. H. Harlow and M. Evans. *A machine calculation method for hydrodynamic problems.* LAMS-1956, 1955. (Cited on page 32.)

[Harting 2005] J. Harting, J. Chin, M. Venturoli and P. V. Coveney. *Large-scale lattice Boltzmann simulations of complex fluids: advances through the advent of computational Grids.* Philosophical Transactions of the Royal Society of London A: Mathematical, Physical and Engineering Sciences, vol. 363, no. 1833, pages 1895–1915, 2005. (Cited on pages 2, 12 and 78.)

[He 1997] X. He, Q. Zou, L.-S. Luo and M. Dembo. *Analytic solutions of simple flows and analysis of nonslip boundary conditions for the lattice Boltzmann BGK model.* Journal of Statistical Physics, vol. 87, no. 1, pages 115–136, 1997. (Cited on page 107.)

[He 1998] X. He, X. Shan and G. D. Doolen. *Discrete Boltzmann equation model for nonideal gases.* Phys. Rev. E, vol. 57, pages R13–R16, Jan 1998. (Cited on pages 109 and 119.)

[He 1999] X. He, S. Chen and R. Zhang. *A Lattice Boltzmann Scheme for Incompressible Multiphase Flow and Its Application in Simulation of Rayleigh-Taylor Instability.* Journal of Computational Physics, vol. 152, no. 2, pages 642 – 663, 1999. (Cited on page 111.)

[He 2008] Q. He and N. Kasagi. *Phase-Field simulation of small capillary-number two-phase flow in a microtube.* Fluid Dynamics Research, vol. 40, no. 7-8, pages 497–509, jul 2008. (Cited on pages 4 and 14.)

[Hermange 2017] C. Hermange. *Numerical simulation of the fluid-structure interactions inside the aquaplaning problem.* Theses, École centrale de Nantes, June 2017. (Cited on page 66.)

[Hewitt 2010] G. F. Hewitt. *Two-Phase Flows.* In A-to-Z Guide to Thermodynamics, Heat and Mass Transfer, and Fluids Engineering. Begellhouse, 2010. (Cited on pages 3 and 13.)

[Hietel 2000] D. Hietel, K. Steiner and J. Struckmeier. *A Finite Volume Particle Method for Compressible Flows.* Mathematical Models and Methods in Applied Sciences, vol. 10, no. 09, pages 1363–1382, 2000. (Cited on page 32.)

[Holdych 1998] D. J. Holdych, D. Rovas, J. G. Georgiadis and R. O. Buckius. *An Improved Hydrodynamics Formulation for Multiphase Flow Lattice-Boltzmann Models.* International Journal of Modern Physics C, vol. 09, no. 08, pages 1393–1404, dec 1998. (Cited on page 113.)

[Hou 2018] Y. Hou, H. Deng, Q. Du and K. Jiao. *Multi-component multi-phase lattice Boltzmann modeling of droplet coalescence in flow channel of fuel cell.* Journal of Power Sources, vol. 393, pages 83–91, jul 2018. (Cited on page 122.)

[Hu 2006] X. Hu and N. Adams. *A multi-phase SPH method for macroscopic and mesoscopic flows.* Journal of Computational Physics, vol. 213, no. 2, pages 844 – 861, 2006. (Cited on pages 5, 8, 15, 17, 70, 72, 73, 75, 122, 126, 127, 142 and 195.)

[Hu 2007] X. Hu and N. Adams. *An incompressible multi-phase SPH method.* Journal of Computational Physics, vol. 227, no. 1, pages 264 – 278, 2007. (Cited on pages 66, 133, 159 and 174.)

[Huang 2013] H. Huang, J.-J. Huang, X.-Y. LU and M. C. Sukop. *On simulations of high-density ratio flows using color-gradient multiphase lattice Boltzmann models.* International Journal of Modern Physics C, vol. 24, no. 04, page 1350021, apr 2013. (Cited on page 113.)

[Huang 2015] H. Huang, M. C. Sukop and X.-Y. Lu. Multiphase lattice boltzmann methods: Theory and application. John Wiley & Sons, Ltd, jul 2015. (Cited on pages 1 and 11.)

[Huang 2017] J. Huang, F. Xiao and X. Yin. *Lattice Boltzmann simulation of pressure-driven two-phase flows in capillary tube and porous medium.* Computers & Fluids, vol. 155, pages 134–145, sep 2017. (Cited on pages 122 and 195.)

[Idelsohn 2003] S. R. Idelsohn, E. Oñate, N. Calvo and F. Del Pin. *The meshless finite element method.* International Journal for Numerical Methods in Engineering, vol. 58, no. 6, pages 893–912, 2003. (Cited on page 32.)

[Ihmsen 2014] M. Ihmsen, J. Orthmann, B. Solenthaler, A. Kolb and M. Teschner. *SPH fluids in computer graphics.* The Eurographics Association, 2014. (Cited on pages 2, 12 and 40.)

[Inamuro 1995] T. Inamuro, M. Yoshino and F. Ogino. *A non-slip boundary condition for lattice Boltzmann simulations.* Physics of Fluids, vol. 7, no. 12, pages 2928–2930, 1995. (Cited on page 105.)

[Inutsuka 2002] S. Inutsuka. *Reformulation of Smoothed Particle Hydrodynamics with Riemann Solver.* Journal of Computational Physics, vol. 179, no. 1, pages 238 – 267, 2002. (Cited on pages 62 and 133.)

[Jeffreys 1931] H. Jeffreys. *Cartesian tensors.* 1931. (Cited on page 203.)

[Karlin 1998] I. V. Karlin, A. N. Gorban, S. Succi and V. Boffi. *Maximum entropy principle for lattice kinetic equations.* Physical Review Letters, vol. 81, no. 1, page 6, 1998. (Cited on page 210.)

[Katsikadelis 2002] J. T. Katsikadelis. Boundary elements: theory and applications. Elsevier, 2002. (Cited on page 30.)

[Khorasanizade 2016] S. Khorasanizade and J. M. M. Sousa. *An innovative open boundary treatment for incompressible SPH.* International Journal for Numerical Methods in Fluids, vol. 80, no. 3, pages 161–180, 2016. FLD-14-0455.R2. (Cited on pages 68 and 128.)

[Kongsberg 2014] Kongsberg. Ledaflow - the new multiphase simulator: User guide. Kongsberg, 2014. (Cited on pages 4 and 14.)

[Krongauz 1997] Y. Krongauz and T. Belytschko. *A Petrov-Galerkin Diffuse Element Method (PG DEM) and its comparison to EFG.* Computational Mechanics, vol. 19, no. 4, pages 327–333, 1997. (Cited on page 30.)

[Kunz 2015] P. Kunz, I. M. Zarikos, N. K. Karadimitriou, M. Huber, U. Nieken and S. M. Hassanizadeh. *Study of Multi-phase Flow in Porous Media: Comparison of SPH Simulations with Micro-model Experiments.* Transport in Porous Media, vol. 114, no. 2, pages 581–600, nov 2015. (Cited on pages 72, 142 and 174.)

[Kunz 2016] P. Kunz, M. Hirschler, M. Huber and U. Nieken. *Inflow/outflow with Dirichlet boundary conditions for pressure in ISPH.* Journal of Computational Physics, vol. 326, pages 171 – 187, 2016. (Cited on pages 68 and 128.)

[Ladd 2001] A. J. C. Ladd and R. Verberg. *Lattice-Boltzmann Simulations of Particle-Fluid Suspensions.* Journal of Statistical Physics, vol. 104, no. 5, pages 1191–1251, 2001. (Cited on page 109.)

[Lafaurie 1994] B. Lafaurie, C. Nardone, R. Scardovelli, S. Zaleski and G. Zanetti. *Modelling Merging and Fragmentation in Multiphase Flows with SURFER.* Journal of Computational Physics, vol. 113, no. 1, pages 134 – 147, 1994. (Cited on pages 72 and 126.)

[Lakehal 2013] D. Lakehal, C. Narayanan, D. Caviezel, J. von Rickenbach and S. Reboux. *Progress in computational microfluidics using TransAT.* Microfluidics and Nanofluidics, vol. 15, no. 3, pages 415–429, March 2013. (Cited on page 189.)

[Lallemand 2000] P. Lallemand and L.-S. Luo. *Theory of the lattice Boltzmann method: Dispersion, dissipation, isotropy, Galilean invariance, and stability.* Phys. Rev. E, vol. 61, pages 6546–6562, Jun 2000. (Cited on page 105.)

[Lancaster 1979] P. Lancaster and K. Sakauskas. Surfaces generated by moving least squares methods. Research paper. University of Calgary, Department of Mathematics and Statistics, 1979. (Cited on page 26.)

[Landau 1990] L. Landau, E. Lifchitz and L. Pitaevskii. Cine'tique physique, volume 10. Ed. Mir, The address, 1990. (Cited on page 91.)

[Lanford 1975] O. E. Lanford. Time evolution of large classical systems, pages 1–111. Springer Berlin Heidelberg, Berlin, Heidelberg, 1975. (Cited on page 91.)

[Lanson 2001] N. Lanson and J. Vila. *Meshless methods for conservation laws.* Mathematics and Computers in Simulation, vol. 55, no. 4-6, pages 493–501, March 2001. (Cited on page 60.)

[Lastiwka 2009] M. Lastiwka, M. Basa and N. J. Quinlan. *Permeable and non-reflecting boundary conditions in SPH.* International Journal for Numerical Methods in Fluids, vol. 61, no. 7, pages 709–724, 2009. (Cited on pages 68 and 128.)

[Latt 2006] J. Latt and B. Chopard. *Lattice Boltzmann Method with regularized non-equilibrium distribution functions.* Math. Comp. Sim., vol. 72, pages 165–168, 2006. (Cited on page 105.)

[Latt 2007] J. Latt. *Hydrodynamic limit of lattice Boltzmann equations*, 03/09 2007. (Cited on page 105.)

[Latt 2008a] J. Latt. *Choice of units in lattice Boltzmann simulations.* 2008. (Cited on pages 102 and 153.)

[Latt 2008b] J. Latt, B. Chopard, O. Malaspinas, M. Deville and A. Michler. *Straight velocity boundaries in the lattice Boltzmann method.* Physical Review E, vol. 77, no. 5, may 2008. (Cited on page 139.)

[Lattanzio 1986] J. C. Lattanzio, J. J. Monaghan, H. Pongracic and M. P. Schwarz. *Controlling Penetration.* SIAM Journal on Scientific and Statistical Computing, vol. 7, no. 2, pages 591–598, 1986. (Cited on page 62.)

[Latva-Kokko 2005] M. Latva-Kokko and D. H. Rothman. *Diffusion properties of gradient-based lattice Boltzmann models of immiscible fluids.* Physical Review E, vol. 71, no. 5, may 2005. (Cited on page 115.)

[Leclaire 2011] S. Leclaire, M. Reggio and J.-Y. Trépanier. *Isotropic color gradient for simulating very high-density ratios with a two-phase flow lattice Boltzmann model.* Computers & Fluids, vol. 48, no. 1, pages 98–112, sep 2011. (Cited on pages 111, 114, 119, 122 and 142.)

[Leclaire 2012] S. Leclaire, M. Reggio and J.-Y. Trépanier. *Numerical evaluation of two recoloring operators for an immiscible two-phase flow lattice Boltzmann model.* Applied Mathematical Modelling, vol. 36, no. 5, pages 2237–2252, may 2012. (Cited on pages 111, 114, 115, 119, 122 and 195.)

[Leclaire 2013a] S. Leclaire, M. El-Hachem, J.-Y. Trépanier and M. Reggio. *High Order Spatial Generalization of 2D and 3D Isotropic Discrete Gradient Operators with Fast Evaluation on GPUs.* Journal of Scientific Computing, vol. 59, no. 3, pages 545–573, sep 2013. (Cited on page 114.)

[Leclaire 2013b] S. Leclaire, N. Pellerin, M. Reggio and J.-Y. Trépanier. *Enhanced equilibrium distribution functions for simulating immiscible multiphase flows with variable density ratios in a class of lattice Boltzmann models.* International Journal of Multiphase Flow, vol. 57, pages 159–168, dec 2013. (Cited on pages 113 and 119.)

[Leclaire 2014] S. Leclaire, N. Pellerin, M. Reggio and J.-Y. Trépanier. *Unsteady immiscible multiphase flow validation of a multiple-relaxation-time lattice Boltzmann method.* Journal of Physics A: Mathematical and Theoretical, vol. 47, no. 10, page 105501, feb 2014. (Cited on pages 113, 119 and 122.)

[Leclaire 2015] S. Leclaire, N. Pellerin, M. Reggio and J.-Y. Trépanier. *An approach to control the spurious currents in a multiphase lattice Boltzmann method and to improve the implementation of initial condition.* International Journal for Numerical Methods in Fluids, vol. 77, no. 12, pages 732–746, jan 2015. (Cited on pages 119 and 142.)

[Leclaire 2016] S. Leclaire, K. Abahri, R. Belarbi and R. Bennacer. *Modeling of static contact angles with curved boundaries using a multiphase lattice Boltzmann method with variable density and viscosity ratios.* International Journal for Numerical Methods in Fluids, vol. 82, no. 8, pages 451–470, oct 2016. (Cited on pages 111, 115, 119 and 122.)

[Leclaire 2017] S. Leclaire, A. Parmigiani, B. Chopard and J. Latt. *Three-dimensional lattice Boltzmann method benchmarks between color-gradient and pseudo-potential immiscible multi-component models.* International Journal of Modern Physics C, vol. 28, no. 07, page 1750085, jul 2017. (Cited on pages 111 and 119.)

[Lee 2010] T. Lee and L. Liu. *Lattice Boltzmann simulations of micron-scale drop impact on dry surfaces.* Journal of Computational Physics, vol. 229, no. 20, pages 8045 – 8063, 2010. (Cited on page 118.)

[Leroy 2014] A. Leroy, D. Violeau, M. Ferrand and C. Kassiotis. *Unified semi-analytical wall boundary conditions applied to 2-D incompressible SPH.* Journal of Computational Physics, vol. 261, pages 106–129, mar 2014. (Cited on page 67.)

[Li 2002] S. Li, B. Ca and W. K. Liu. *Meshfree and particle methods and their applications.* Applied Mechanics Reviews, vol. 55, no. 1, page 1, 2002. (Cited on page 28.)

[Li 2004] S. Li, H. Lu, W. Han, W. K. Liu and D. C. Simkins. *Reproducing kernel element method Part II: Globally conforming Im/Cn hierarchies.* Computer Methods in Applied Mechanics and Engineering, vol. 193, no. 12-14, pages 953 – 987, 2004. Meshfree Methods: Recent Advances and New Applications. (Cited on page 32.)

[Li 2012] Q. Li, K. H. Luo, Y. L. He, Y. J. Gao and W. Q. Tao. *Coupling lattice Boltzmann model for simulation of thermal flows on standard lattices.* Phys. Rev. E, vol. 85, page 016710, Jan 2012. (Cited on page 114.)

[Li 2015] J. Li. *Appendix: Chapman-Enskog Expansion in the Lattice Boltzmann Method*, 2015. (Cited on page 78.)

[Li 2016] Q. Li, K. Luo, Q. Kang, Y. He, Q. Chen and Q. Liu. *Lattice Boltzmann methods for multiphase flow and phase-change heat transfer.* Progress in Energy and Combustion Science, vol. 52, pages 62–105, feb 2016. (Cited on pages 1 and 11.)

[Li 2017] L. Li, X. Jia and Y. Liu. *Modified Outlet Boundary Condition Schemes for Large Density Ratio Lattice Boltzmann Models.* Journal of Heat Transfer, vol. 139, no. 5, page 052003, mar 2017. (Cited on page 122.)

[Libersky 1991] L. D. Libersky and A. G. Petschek. *Advances in the Free-Lagrange Method Including Contributions on Adaptive Gridding and the Smooth Particle Hydrodynamics Method: Proceedings of the Next Free-Lagrange Conference Held at Jackson Lake Lodge, Moran, WY, USA 3–7 June 1990.* pages 248–257, Berlin, Heidelberg, 1991. Springer Berlin Heidelberg. (Cited on pages 2, 12 and 40.)

[Lind 2012] S. Lind, R. Xu, P. Stansby and B. Rogers. *Incompressible smoothed particle hydrodynamics for free-surface flows: A generalised diffusion-based algorithm for stability and validations for impulsive flows and propagating waves.* Journal of Computational Physics, vol. 231, no. 4, pages 1499–1523, feb 2012. (Cited on pages 66 and 133.)

[Liu 1995] W. K. Liu, S. Jun, S. Li, J. Adee and T. Belytschko. *Reproducing kernel particle methods for structural dynamics.* International Journal for Numerical Methods in Engineering, vol. 38, no. 10, pages 1655–1679, 1995. (Cited on page 27.)

[Liu 2003a] G.-R. Liu and M. B. Liu. Smoothed particle hydrodynamics: a meshfree particle method. World Scientific, 2003. (Cited on page 40.)

[Liu 2003b] M. Liu, G. Liu and K. Lam. *Constructing smoothing functions in smoothed particle hydrodynamics with applications.* Journal of Computational and Applied Mathematics, vol. 155, no. 2, pages 263 – 284, 2003. (Cited on page 44.)

[Liu 2004] W. K. Liu, W. Han, H. Lu, S. Li and J. Cao. *Reproducing kernel element method. Part I: Theoretical formulation.* Computer Methods in Applied Mechanics and Engineering, vol. 193, no. 12-14, pages 933 – 951, 2004. Meshfree Methods: Recent Advances and New Applications. (Cited on page 32.)

[Liu 2009] G.-R. Liu. Meshfree methods: moving beyond the finite element method. Taylor & Francis, 2009. (Cited on page 22.)

[Liu 2012] H. Liu, A. J. Valocchi and Q. Kang. *Three-dimensional lattice Boltzmann model for immiscible two-phase flow simulations.* Phys. Rev. E, vol. 85, page 046309, Apr 2012. (Cited on page 113.)

[Liu 2015] H. Liu, Q. Kang, C. R. Leonardi, S. Schmieschek, A. Narváez, B. D. Jones, J. R. Williams, A. J. Valocchi and J. Harting. *Multiphase lattice Boltzmann simulations for porous media applications.* Computational Geosciences, vol. 20, no. 4, pages 777–805, dec 2015. (Cited on page 111.)

[Lizarraga-García 2016] E. Lizarraga-García. *A study of Taylor bubbles in vertical and inclined slug flow using multiphase CFD with level set.* PhD thesis, Massachusetts Institute of Technology, 2016. (Cited on pages 4 and 14.)

[Lockhart 1949] R. W. Lockhart and R. C. Martinelli. *Proposed correlation of data for isothermal two-phase, two-component flow in pipes.* Chemical Engineering Progress, vol. 45, no. 1, pages 39–48, 1949. (Cited on pages 153 and 162.)

[Lodato 2010] G. Lodato and D. J. Price. *On the diffusive propagation of warps in thin accretion discs.* Monthly Notices of the Royal Astronomical Society, vol. 405, no. 2, pages 1212–1226, 2010. (Cited on page 62.)

[Lou 2013] Q. Lou, Z. Guo and B. Shi. *Evaluation of outflow boundary conditions for two-phase lattice Boltzmann equation.* Physical Review E, vol. 87, no. 6, jun 2013. (Cited on page 122.)

[Lu 1994] Y. Lu, T. Belytschko and L. Gu. *A new implementation of the element free Galerkin method.* Computer Methods in Applied Mechanics and Engineering, vol. 113, no. 3-4, pages 397 – 414, 1994. (Cited on page 30.)

[Lu 2004] H. Lu, S. Li, D. C. S. Jr., W. K. Liu and J. Cao. *Reproducing kernel element method Part III: Generalized enrichment and applications.* Computer Methods in Applied Mechanics and Engineering, vol. 193, no. 12-14, pages 989 – 1011, 2004. Meshfree Methods: Recent Advances and New Applications. (Cited on page 32.)

[Lu 2015] M. Lu. *Experimental and computational study of two-phase slug flow.* PhD thesis, Imperial College London, 2015. (Cited on pages 4 and 13.)

[Lucy 1977] L. B. Lucy. *A numerical approach to the testing of the fission hypothesis.* The astronomical journal, vol. 82, pages 1013–1024, 1977. (Cited on pages 1, 11 and 40.)

[Luo 2000] L.-S. Luo. *Some recent results on discrete velocity models and ramifications for lattice Boltzmann equation.* Computer Physics Communications, vol. 129, no. 1, pages 63 – 74, 2000. (Cited on page 210.)

[Marongiu 2010] J.-C. Marongiu, F. Leboeuf, J. Caro and E. Parkinson. *Free surface flows simulations in Pelton turbines using an hybrid SPH-ALE method.* Journal of Hydraulic Research, vol. 48, no. sup1, pages 40–49, 2010. (Cited on page 66.)

[Marrone 2011] S. Marrone, M. Antuono, A. Colagrossi, G. Colicchio, D. L. Touzé and G. Graziani. *δ-SPH model for simulating violent impact flows.* Computer Methods in Applied Mechanics and Engineering, vol. 200, no. 13-16, pages 1526–1542, March 2011. (Cited on pages 66, 133 and 159.)

[Marrone 2013] S. Marrone, A. Colagrossi, M. Antuono, G. Colicchio and G. Graziani. *An accurate SPH modeling of viscous flows around bodies at low and moderate Reynolds numbers.* Journal of Computational Physics, vol. 245, pages 456 – 475, 2013. (Cited on page 68.)

[Mas-Gallic 1987] S. Mas-Gallic and P. A. Raviart. *A particle method for first-order symmetric systems.* Numerische Mathematik, vol. 51, no. 3, pages 323–352, May 1987. (Cited on page 60.)

[McCracken 2005] M. E. McCracken and J. Abraham. *Multiple-relaxation-time lattice-Boltzmann model for multiphase flow.* Phys. Rev. E, vol. 71, page 036701, Mar 2005. (Cited on page 109.)

[Melenk 1996] J. Melenk and I. Babuska. *The partition of unity finite element method: Basic theory and applications.* Computer Methods in Applied Mechanics and Engineering, vol. 139, no. 1-4, pages 289 – 314, 1996. (Cited on page 31.)

[Minier 2016] J.-P. Minier. Simulation of two-phase flow patterns with a new approach based on smoothed particle hydrodynamics. NUGENIA Project SPH-2PHASEFLOW Presentation Slides, 2016. (Cited on pages 4, 14, 148 and 162.)

[Mokos 2016] A. Mokos, B. D. Rogers and P. K. Stansby. *A multi-phase particle shifting algorithm for SPH simulations of violent hydrodynamics with a large number of particles.* Journal of Hydraulic Research, vol. 55, no. 2, pages 143–162, sep 2016. (Cited on pages 66, 74 and 126.)

[Molteni 2009] D. Molteni and A. Colagrossi. *A simple procedure to improve the pressure evaluation in hydrodynamic context using the SPH.* Computer Physics Communications, vol. 180, no. 6, pages 861 – 872, 2009. (Cited on page 66.)

[Monaghan 1985] J. Monaghan. *Particle Methods for Hydrodynamics.* Computer Physics Reports, vol. 3, pages 71–124, 1985. (Cited on page 62.)

[Monaghan 1992] J. Monaghan. *Smoothed particle hydrodynamics.* Annu, Rev, Astron. Astrophys., vol. 30, pages 543–74, 1992. (Cited on pages 40, 52 and 61.)

[Monaghan 1994] J. Monaghan. *Simulating free surface flows with SPH.* Journal of Computational Physics, vol. 110, pages 399–399, 1994. (Cited on pages 55 and 126.)

[Monaghan 1995] J. Monaghan and A. Kocharyan. *SPH simulation of multi-phase flow.* Computer Physics Communications, vol. 87, no. 1, pages 225 – 235, 1995. (Cited on page 70.)

[Monaghan 1997] J. Monaghan. *SPH and Riemann Solvers.* Journal of Computational Physics, vol. 136, no. 2, pages 298 – 307, 1997. (Cited on page 61.)

[Monaghan 2000] J. Monaghan. *SPH without a Tensile Instability.* Journal of Computational Physics, vol. 159, no. 2, pages 290–311, apr 2000. (Cited on page 64.)

[Monaghan 2005] J. J. Monaghan. *Smoothed particle hydrodynamics.* Reports on Progress in Physics, vol. 68, no. 8, page 1703, 2005. (Cited on page 67.)

[Monaghan 2006] J. Monaghan. *Smoothed particle hydrodynamic simulations of shear flow.* Monthly Notices of the Royal Astronomical Society, vol. 365, no. 1, pages 199–213, 2006. (Cited on page 62.)

[Monaghan 2011] J. Monaghan. *A turbulence model for Smoothed Particle Hydrodynamics.* European Journal of Mechanics - B/Fluids, vol. 30, no. 4, pages 360–370, jul 2011. (Cited on page 164.)

[Monaghan 2012] J. Monaghan. *Smoothed Particle Hydrodynamics and Its Diverse Applications.* Annual Review of Fluid Mechanics, vol. 44, no. 1, pages 323–346, 2012. (Cited on pages 2, 12 and 40.)

[Morris 1995] J. P. Morris. *A Study of the Stability Properties of SPH.* ArXiv Astrophysics e-prints, April 1995. (Cited on page 52.)

[Morris 1996] J. Morris. *Analysis of smoothed particle hydrodynamics with applications.* PhD thesis, University of Monash, Melbourne, Australia, 1996. (Cited on page 64.)

[Morris 1997a] J. Morris, P. Fox and Y. Zhu. *Modeling low Reynolds number incompressible flows using SPH.* Journal of Computational Physics, vol. 136, no. 1, pages 214–226, 1997. (Cited on pages 62, 63 and 67.)

[Morris 1997b] J. Morris and J. Monaghan. *A switch to reduce SPH viscosity.* Journal of Computational Physics, vol. 136, no. 1, pages 41–50, 1997. (Cited on page 62.)

[Morris 2000] J. P. Morris. *Simulating surface tension with smoothed particle hydrodynamics.* International Journal for Numerical Methods in Fluids, vol. 33, no. 3, pages 333–353, 2000. (Cited on pages 54, 63, 69, 72 and 126.)

[Moussa 2000] B. B. Moussa and J. P. Vila. *Convergence of SPH Method for Scalar Nonlinear Conservation Laws.* SIAM Journal on Numerical Analysis, vol. 37, no. 3, pages 863–887, January 2000. (Cited on page 60.)

[Müller-Steinhagen 1986] H. Müller-Steinhagen and K. Heck. *A simple friction pressure drop correlation for two-phase flow in pipes.* Chemical Engineering and Processing: Process Intensification, vol. 20, no. 6, pages 297–308, nov 1986. (Cited on page 164.)

[Murray 1996] J. R. Murray. *SPH simulations of tidally unstable accretion discs in cataclysmic variables.* Monthly Notices of the Royal Astronomical Society, vol. 279, no. 2, pages 402–414, 1996. (Cited on page 62.)

[Nayroles 1992] B. Nayroles, G. Touzot and P. Villon. *Generalizing the finite element method: Diffuse approximation and diffuse elements.* Computational Mechanics, vol. 10, no. 5, pages 307–318, 1992. (Cited on page 29.)

[Nguyen 2008] V. P. Nguyen, T. Rabczuk, S. Bordas and M. Duflot. *Meshless methods: A review and computer implementation aspects.* Mathematics and Computers in Simulation, vol. 79, no. 3, pages 763 – 813, 2008. (Cited on pages 22, 25 and 28.)

[Oñate 1996] E. Oñate, S. Idelsohn, O. C. Zienkiewicz and R. L. Taylor. *A Finite Point Method In Computational Mechanics. Applications to convective Transport and Fluid Flow.* International Journal for Numerical Methods in Engineering, vol. 39, no. 22, pages 3839–3866, 1996. (Cited on page 29.)

[Oden 1998] J. T. Oden, C. Duarte and O. C. Zienkiewicz. *A new cloud-based hp finite element method.* Computer methods in applied mechanics and engineering, vol. 153, no. 1, pages 117–126, 1998. (Cited on page 31.)

[Oger 2006] G. Oger, M. Doring, B. Alessandrini and P. Ferrant. *Two-dimensional SPH simulations of wedge water entries.* Journal of Computational Physics, vol. 213, no. 2, pages 803 – 822, 2006. (Cited on page 67.)

[Oger 2007] G. Oger, M. Doring, B. Alessandrini and P. Ferrant. *An Improved SPH Method: Towards Higher Order Convergence.* J. Comput. Phys., vol. 225, no. 2, pages 1472–1492, August 2007. (Cited on page 57.)

[Oger 2016] G. Oger, S. Marrone, D. Le Touzé and M. De Leffe. *SPH accuracy improvement through the combination of a quasi-Lagrangian shifting transport velocity and consistent ALE formalisms.* Journal of Computational Physics, vol. 313, pages 76–98, 2016. (Cited on pages 66, 133, 159 and 198.)

[Pan 2015] K. Pan, R. H. A. IJzermans, B. D. Jones, A. Thyagarajan, B. W. H. Beest and J. R. Williams. *Application of the SPH method to solitary wave impact on an offshore platform.* Computational Particle Mechanics, pages 1–12, 2015. (Cited on pages 2, 12 and 69.)

[Pan 2018] K. Pan, R. Pramanik, B. D. Jones, T. Douillet-Grellier, A. Albaiz and J. R. Williams. *Development of fluid-solid coupling for the study of hydraulic fracturing using SPH.* In Proceedings of the International 11th SPHERIC Workshop, June 13-16, Munich, Germany, 2018. (Cited on pages 1 and 11.)

[Park 2001] S.-H. Park and S.-K. Youn. *The least-squares meshfree method.* International Journal for Numerical Methods in Engineering, vol. 52, no. 9, pages 997–1012, 2001. (Cited on page 30.)

[Pedersen 2017] S. Pedersen, P. Durdevic and Z. Yang. *Challenges in slug modeling and control for offshore oil and gas productions: A review study.* International Journal of Multiphase Flow, vol. 88, pages 270 – 284, 2017. (Cited on pages 4 and 13.)

[Phillips 1985] G. Phillips and J. Monaghan. *A numerical method for three-dimensional simulations of collapsing, isothermal, magnetic gas clouds.* Monthly Notices of the Royal Astronomical Society, vol. 216, no. 4, pages 883–895, 1985. (Cited on pages 63 and 126.)

[Pooley 2008] C. M. Pooley, H. Kusumaatmaja and J. M. Yeomans. *Contact line dynamics in binary lattice Boltzmann simulations.* Phys. Rev. E, vol. 78, page 056709, Nov 2008. (Cited on page 118.)

[Pramanik 2016] R. Pramanik, T. Douillet-Grellier, K. Pan, B. Jones, A. Albaiz, H. Pourpak, J. R. Williams, J. Du and D. Deb. *A SPH Approach to the Simulation of Hydraulic Fracture Propagation in Naturally Fractured Rock Medium.* ARMA 50th US Rock Mechanics/Geomechanics Symposium, 26-29 June, Houston, Texas, USA, 2016. (Cited on pages 1 and 11.)

[Price 2008] D. J. Price. *Modelling discontinuities and Kelvin–Helmholtz instabilities in SPH.* Journal of Computational Physics, vol. 227, no. 24, pages 10040–10057, 2008. (Cited on pages 52, 62 and 70.)

[Price 2011] D. J. Price. *Smoothed particle hydrodynamics: things I wish my mother taught me.* arXiv preprint arXiv:1111.1259, 2011. (Cited on page 60.)

[Price 2012] D. J. Price. *Smoothed particle hydrodynamics and magnetohydrodynamics.* Journal of Computational Physics, vol. 231, no. 3, pages 759 – 794, 2012. Special Issue: Computational Plasma PhysicsSpecial Issue: Computational Plasma Physics. (Cited on pages 2, 12 and 40.)

[Prosperetti 2009] A. Prosperetti and G. Tryggvason. Computational methods for multiphase flow. Cambridge University Press, 2009. (Cited on page 119.)

[Qian 1992] Y. H. Qian, D. D'Humières and P. Lallemand. *Lattice BGK Models for Navier-Stokes Equation.* EPL (Europhysics Letters), vol. 17, no. 6, page 479, 1992. (Cited on pages 78 and 85.)

[Quinlan 2006] N. J. Quinlan, M. Basa and M. Lastiwka. *Truncation error in mesh-free particle methods.* International Journal for Numerical Methods in Engineering, vol. 66, no. 13, pages 2064–2085, 2006. (Cited on page 48.)

[Reis 2007] T. Reis and T. N. Phillips. *Lattice Boltzmann model for simulating immiscible two-phase flows.* Journal of Physics A: Mathematical and Theoretical, vol. 40, no. 14, page 4033, 2007. (Cited on pages 5, 15, 111, 112, 113, 114, 115, 122 and 195.)

[Renaut 2015] G.-A. Renaut. *Schémas d'ordre élevé pour la méthode SPH-ALE appliquée à des simulations sur machines hydrauliques.* PhD thesis, Ecole centrale de Lyon, 2015. (Cited on page 66.)

[Robinson 2009] M. Robinson. *Turbulence and viscous mixing using smoothed particle hydrodynamics.* PhD thesis, University of Monash, Melbourne, Australia, 2009. (Cited on pages 44 and 64.)

[Rogers 2008] B. D. Rogers and R. A. Dalrymple. *SPH modeling of tsunami waves.* In Advances in Coastal and Ocean Engineering, pages 75–100. World Scientific, sep 2008. (Cited on page 164.)

[Sánchez-Silva 2013] F. Sánchez-Silva, I. Carvajal-Mariscal, M. Toledo-Velázquez, D. Libreros, M. Toledo-Velázquez and H. Saidani-Scott. *Experiments in a combined up stream downstream slug flow.* EPJ Web of Conferences, vol. 45, page 01082, 2013. (Cited on pages 4 and 13.)

[Sarangi 2016] S. Sarangi, A. Thyagarajan, K. Pan and J. Williams. *Modeling the multiphase flow characteristics in randomly packed bed reactor with complex shapes of catalyst pellets using adaptive SPH.* In Proceedings of the SPHERIC 2016, June 13-16, Munich Germany, 2016. (Cited on page 52.)

[Sarica 1991] C. Sarica and O. Shoham. *A simplified transient model for pipeline-riser systems.* Chemical Engineering Science, vol. 46, no. 9, pages 2167 – 2179, 1991. (Cited on pages 4 and 14.)

[Sausen 2012] A. Sausen, P. Sausen and M. de. *The Slug Flow Problem in Oil Industry and Pi Level Control.* In New Technologies in the Oil and Gas Industry. InTech, oct 2012. (Cited on pages 3 and 13.)

[Shadloo 2016] M. Shadloo, G. Oger and D. Le Touzé. *Smoothed particle hydrodynamics method for fluid flows, towards industrial applications: Motivations, current state, and challenges.* Computers & Fluids, vol. 136, pages 11–34, 2016. (Cited on pages 2, 12 and 40.)

[Shan 1993] X. Shan and H. Chen. *Lattice Boltzmann model for simulating flows with multiple phases and components.* Physical Review E, vol. 47, no. 3, pages 1815–1819, mar 1993. (Cited on pages 111 and 116.)

[Shan 2006] X. Shan, X. Yuan and H. Chen. *Kinetic theory representation of hydrodynamics: A way beyond the Navier-Stokes equation.* Journal of Fluid Mechanics, vol. 550, pages 413–441, 3 2006. (Cited on page 114.)

[Shao 2005] S. Shao and H. Gotoh. *Turbulence particle models for tracking free surfaces.* Journal of Hydraulic Research, vol. 43, no. 3, pages 276–289, may 2005. (Cited on page 164.)

[Sibson 1980] R. Sibson. *A vector identity for the Dirichlet tessellation.* Mathematical Proceedings of the Cambridge Philosophical Society, vol. 87, pages 151–155, 1980. (Cited on page 32.)

[Sigalotti 2016] L. D. G. Sigalotti, J. Klapp, O. Rendón, C. A. Vargas and F. Peña-Polo. *On the kernel and particle consistency in smoothed particle hydrodynamics.* Applied Numerical Mathematics, vol. 108, pages 242–255, oct 2016. (Cited on page 60.)

[Simpson 1996] J. C. Simpson and M. A. Wood. *Classical kinetic theory simulations using smoothed particle hydrodynamics.* Physical Review E, vol. 54, no. 2, pages 2077–2083, aug 1996. (Cited on page 83.)

[Spedding 2006] P. Spedding, E. Benard and G. Donnelly. *Prediction of pressure drop in multiphase horizontal pipe flow.* International Communications in Heat and Mass Transfer, vol. 33, no. 9, pages 1053–1062, nov 2006. (Cited on page 164.)

[Springel 2010] V. Springel. *Smoothed Particle Hydrodynamics in Astrophysics.* Annual Review of Astronomy and Astrophysics, vol. 48, no. 1, pages 391–430, aug 2010. (Cited on pages 2, 12 and 40.)

[Strouboulis 2001] T. Strouboulis, K. Copps and I. Babuska. *The generalized finite element method.* Computer Methods in Applied Mechanics and Engineering, vol. 190, no. 32-33, pages 4081 – 4193, 2001. (Cited on page 31.)

[Sukumar 1998] N. Sukumar, B. Moran and T. Belytschko. *The natural element method in solid mechanics.* International Journal for Numerical Methods in Engineering, vol. 43, no. 5, pages 839–887, 1998. (Cited on page 32.)

[Sulsky 1994] D. Sulsky, Z. Chen and H. Schreyer. *A particle method for history-dependent materials.* Computer Methods in Applied Mechanics and Engineering, vol. 118, no. 1-2, pages 179 – 196, 1994. (Cited on page 32.)

[Sun 2019] P. Sun, A. Colagrossi, S. Marrone, M. Antuono and A.-M. Zhang. *A consistent approach to particle shifting in the δ-Plus-SPH model.* Computer Methods in Applied Mechanics and Engineering, vol. 348, pages 912–934, May 2019. (Cited on page 66.)

[Suzanne 1985] C. Suzanne. *Structure de l'écoulement stratifié de gaz et de liquide en canal rectangulaire.* PhD thesis, Institut National Polytechnique de Toulouse, 1985. (Cited on pages 186, 187 and 188.)

[Swegle 1995] J. Swegle, D. Hicks and S. Attaway. *Smoothed particle hydrodynamics stability analysis.* Journal of Computational Physics, vol. 116, no. 1, pages 123–134, 1995. (Cited on page 63.)

[Swift 1995a] M. R. Swift, W. R. Osborn and J. M. Yeomans. *Lattice Boltzmann Simulation of Nonideal Fluids.* Physical Review Letters, vol. 75, no. 5, pages 830–833, jul 1995. (Cited on pages 111 and 118.)

[Swift 1995b] M. R. Swift, W. R. Osborn and J. M. Yeomans. *Lattice Boltzmann Simulation of Nonideal Fluids.* Phys. Rev. Lett., vol. 75, pages 830–833, Jul 1995. (Cited on page 118.)

[Szewc 2013] K. Szewc. *Développement d'une approche particulaire de type SPH pour la modélisation des écoulements multiphasiques avec interfaces variables.* PhD thesis, Université de Lorraine, jun 2013. (Cited on pages 72, 73, 74, 126, 140, 176 and 183.)

[Szewc 2016] K. Szewc and M. T. Lewandowski. *Further investigation of the spurious interface fragmentation in multiphase Smoothed Particle Hydrodynamics*, 2016. (Cited on pages 8, 18, 74, 126, 178 and 181.)

[Tafuni 2018] A. Tafuni, J. Domínguez, R. Vacondio and A. Crespo. *A versatile algorithm for the treatment of open boundary conditions in Smoothed particle hydrodynamics GPU models.* Computer Methods in Applied Mechanics and Engineering, 2018. (Cited on pages 7, 16, 68, 126, 128, 159 and 195.)

[Taha 2004] T. Taha and Z. Cui. *Hydrodynamics of slug flow inside capillaries.* Chemical Engineering Science, vol. 59, no. 6, pages 1181–1190, mar 2004. (Cited on pages 4 and 14.)

[Taitel 1976] Y. Taitel and A. E. Dukler. *A model for predicting flow regime transitions in horizontal and near horizontal gas-liquid flow.* AIChE Journal, vol. 22, no. 1, pages 47–55, jan 1976. (Cited on pages 4, 14, 153, 162, 163 and 177.)

[Taitel 1980] Y. Taitel, D. Bornea and A. E. Dukler. *Modelling flow pattern transitions for steady upward gas-liquid flow in vertical tubes.* AIChE Journal, vol. 26, no. 3, pages 345–354, 1980. (Cited on pages 4 and 14.)

[Tarksalooyeh 2018] V. W. A. Tarksalooyeh, G. Závodszky, B. J. M. van Rooij and A. G. Hoekstra. *Inflow and outflow boundary conditions for 2D suspension simulations with the immersed boundary lattice Boltzmann method.* Computers & Fluids, vol. 172, pages 312–317, aug 2018. (Cited on page 122.)

[Tartakovsky 2015] A. M. Tartakovsky, N. Trask, K. Pan, B. Jones, W. Pan and J. R. Williams. *Smoothed particle hydrodynamics and its applications for multiphase flow and reactive transport in porous media.* Computational Geosciences, pages 1–28, 2015. (Cited on pages 70 and 72.)

[Tartakovsky 2016] A. M. Tartakovsky and A. Panchenko. *Pairwise Force Smoothed Particle Hydrodynamics model for multiphase flow: Surface tension and contact line dynamics.* Journal of Computational Physics, vol. 305, pages 1119 – 1146, 2016. (Cited on pages 71 and 75.)

[Tofighi 2013] N. Tofighi and M. Yildiz. *Numerical simulation of single droplet dynamics in three-phase flows using ISPH.* Computers & Mathematics with Applications, vol. 66, no. 4, pages 525 – 536, 2013. (Cited on page 70.)

[Tolke 2002] J. Tolke, M. Krafczyk, M. Schulz and E. Rank. *Lattice Boltzmann simulations of binary fluid flow through porous media.* Philosophical Transactions of the Royal Society A: Mathematical, Physical and Engineering Sciences, vol. 360, no. 1792, pages 535–545, mar 2002. (Cited on page 111.)

[Ujang 2003] P. M. Ujang. *Studies of slug initiation and development in two-phase gas-liquid pipeline flow.* PhD thesis, Imperial College London, 2003. (Cited on pages 186 and 189.)

[Vidal 2007] Y. Vidal, J. Bonet and A. Huerta. *Stabilized updated Lagrangian corrected SPH for explicit dynamic problems.* International Journal for Numerical Methods in Engineering, vol. 69, no. 13, pages 2687–2710, 2007. (Cited on page 66.)

[Viggen 2009] E. M. Viggen. *The Lattice Boltzmann Method with Applications in Acoustics.* PhD thesis, Norwegian University of Science and Technology, 2009. (Cited on pages 2, 12 and 78.)

[Viggen 2014] E. M. Viggen. *The lattice Boltzmann method : Fundamentals and acoustics.* PhD thesis, Norwegian University of Science and Technology, 2014. (Cited on pages 78 and 86.)

[Viggiani 1988] M. Viggiani, O. Mariani, V. Battarra, A. Annunziato and U. Bollettini. *A Model to Verify the Onset of Severe Slugging.* In PSIG Annual Meeting, Toronto, Ontario, 1988. Pipeline Simulation Interest Group. (Cited on pages 4 and 14.)

[Vila 1999] J. Vila. *On particle weighted methods and smooth particle hydrodynamics.* Mathematical models and methods in applied sciences, vol. 9, no. 02, pages 161–209, 1999. (Cited on pages 49, 52 and 66.)

[Violeau 2007a] D. Violeau and R. Issa. *Numerical modelling of complex turbulent free-surface flows with the SPH method: an overview.* International Journal for Numerical Methods in Fluids, vol. 53, no. 2, pages 277–304, 2007. (Cited on pages 66, 159 and 164.)

[Violeau 2007b] D. Violeau, C. Buvat, K. Abed-Meraïm and E. De Nanteuil. *Numerical modelling of boom and oil spill with SPH.* Coastal Engineering, vol. 54, no. 12, pages 895–913, 2007. (Cited on page 70.)

[Violeau 2012] D. Violeau. Fluid mechanics and the SPH method theory and applications. Oxford University Press, 2012. (Cited on pages 40, 44, 46, 48, 50, 57, 59, 66 and 91.)

[Violeau 2014] D. Violeau and A. Leroy. *On the maximum time step in weakly compressible SPH.* Journal of Computational Physics, vol. 256, pages 388 – 415, 2014. (Cited on pages 24, 63 and 69.)

[Violeau 2016] D. Violeau and B. D. Rogers. *Smoothed particle hydrodynamics (SPH) for free-surface flows: past, present and future.* Journal of Hydraulic Research, vol. 54, no. 1, pages 1–26, 2016. (Cited on pages 2, 12, 40 and 70.)

[Violeau 2019] D. Violeau and T. Fonty. *Exact calculation of the SPH smoothing error.* In Proceedings of the International 14th SPHERIC Workshop, June 25-27, Exeter, United Kingdom, 2019. (Cited on page 42.)

[Vuyst 2018] F. D. Vuyst and T. Douillet-Grellier. *Entropic considerations on the LBGK model for advection-diffusion.* In Proceedings of XXXIX Ibero-Latin American Congress on Computational Methods in Engineering (CILAMCE). Adnan Ibrahimbegovic and Paulo De Mattos Pimenta, 2018. (Cited on page 210.)

[Wagner 2006] A. J. Wagner. *Thermodynamic consistency of liquid-gas lattice Boltzmann simulations.* Phys. Rev. E, vol. 74, page 056703, Nov 2006. (Cited on page 109.)

[Walther 2016] E. Walther. *Lattice Boltzmann Method applied to Building Physics.* PhD thesis, Université Paris-Saclay, January 2016. (Cited on page 105.)

[Wambsganss 1992] M. Wambsganss, J. Jendrzejczyk and D. France. *Two-phase flow and pressure drop in flow passages of compact heat exchangers.* Technical report, Argonne National Lab., IL (United States), 1992. (Cited on page 164.)

[Wang 2016] Z.-B. Wang, R. Chen, H. Wang, Q. Liao, X. Zhu and S.-Z. Li. *An overview of smoothed particle hydrodynamics for simulating multiphase flow.* Applied Mathematical Modelling, vol. 40, no. 23-24, pages 9625–9655, dec 2016. (Cited on pages 1 and 11.)

[Wendland 1995] H. Wendland. *Piecewise polynomial, positive definite and compactly supported radial functions of minimal degree.* Advances in Computational Mathematics, vol. 4, no. 1, pages 389–396, Dec 1995. (Cited on pages 44 and 126.)

[Wolfram 1986] S. Wolfram. *Cellular automaton fluids 1: Basic theory.* Journal of Statistical Physics, vol. 45, no. 3, pages 471–526, 1986. (Cited on page 203.)

[Xie 2017] F. Xie, X. Zheng, M. S. Triantafyllou, Y. Constantinides, Y. Zheng and G. Em Karniadakis. *Direct numerical simulations of two-phase flow in an inclined pipe.* Journal of Fluid Mechanics, vol. 825, page 189?207, 2017. (Cited on pages 4, 14, 176, 178 and 180.)

[Xu 2009] R. Xu, P. Stansby and D. Laurence. *Accuracy and stability in incompressible SPH (ISPH) based on the projection method and a new approach.* Journal of Computational Physics, vol. 228, no. 18, pages 6703–6725, oct 2009. (Cited on page 66.)

[Xu 2017] Z. Xu, H. Liu and A. J. Valocchi. *Lattice Boltzmann simulation of immiscible two-phase flow with capillary valve effect in porous media.* Water Resources Research, vol. 53, no. 5, pages 3770–3790, 2017. (Cited on pages 111, 115, 116 and 122.)

[Yildiz 2009] M. Yildiz, R. A. Rook and A. Suleman. *SPH with the multiple boundary tangent method.* International Journal for Numerical Methods in Engineering, vol. 77, no. 10, pages 1416–1438, mar 2009. (Cited on page 67.)

[Yu 2007] Z. Yu, O. Hemminger and L.-S. Fan. *Experiment and lattice Boltzmann simulation of two-phase gas–liquid flows in microchannels.* Chemical Engineering Science, vol. 62, no. 24, pages 7172–7183, dec 2007. (Cited on pages 4 and 14.)

[Zhang 2015] A. Zhang, P. Sun and F. Ming. *An SPH modeling of bubble rising and coalescing in three dimensions.* Computer Methods in Applied Mechanics and Engineering, vol. 294, pages 189–209, September 2015. (Cited on pages 126 and 127.)

[Zhang 2017] M. Zhang, L. ming Pan, P. Ju, X. Yang and M. Ishii. *The mechanism of bubbly to slug flow regime transition in air-water two phase flow: A new transition criterion.* International Journal of Heat and Mass Transfer, vol. 108, pages 1579 – 1590, 2017. (Cited on pages 4 and 13.)

[Zhu 1998] T. Zhu, J.-D. Zhang and S. N. Atluri. *A local boundary integral equation (LBIE) method in computational mechanics, and a meshless discretization approach.* Computational Mechanics, vol. 21, no. 3, pages 223–235, 1998. (Cited on page 30.)

[Zisis 2016] I. Zisis, J. H. M. Evers, B. van der Linden and M. H. Duong. *Recent results in the systematic derivation and convergence of SPH*, 2016. (Cited on page 60.)

[Zou 1997] Q. Zou and X. He. *On pressure and velocity boundary conditions for the lattice Boltzmann BGK model.* Physics of Fluids, vol. 9, no. 6, pages 1591–1598, 1997. (Cited on pages 7, 16, 108, 122 and 195.)

Nomenclature

List of Acronyms

ALE	Arbitrary Eulerian Lagrangian
AMR	Adaptative Mesh Refinement
ANRT	Association Nationale de la Recherche et de la Technologie
BC	Boundary Conditions
BEM	Boundary Element Method
BGK	Bhatnagar Gross Krook
CAD	Computer Aided Design
CFD	Computational Fluid Dynamics
CFL	Courant Friedrichs Lewy
CGM	Color Gradient Model
CIFRE	Convention Industrielle de Formation par la REcherche
CLF	Contact Line Force
CSF	Continuum Surface Force
CSPH	Corrected Smoothed Particle Hydrodynamics
DEM	Discrete Element Method or Diffuse Element Method
DG	Discrete Galerkin
DNS	Direct Numerical Simulation
DPD	Dissipative Particle Dynamics
EFG	Element Free Galerkin
EOS	Equation Of State
FDM	Finite Difference Method
FEM	Finite Element Method
FLIP	FLuid Implicit Particle
FMM	Finite Mass Method
FPM	Finite Point Method
FVM	Finite Volume Method

FVPM Finite Volume Particle Method

GFDM Generalized Finite Difference Method

GFEM Generalized Finite Element Method

GPU Graphics Processing Unit

HPC High Performance Computing

IF InterFace

LBIE Local Boundary Integral Equation

LBM Lattice Boltzmann Method

LES Large Eddy Simulation

LGA Lattice Gas Automata

LRE Local Regression Estimator

LSMM Least Squares Meshfree Method

MD Molecular Dynamics

MFEM Meshless Finite Element Method

MFS Method of Finite Soheres

MLPG Meshfree Local Petrov Galerkin

MLS Moving Least Squares

MLSPH Moving Least Squares Smoothed Particle Hydrodynamics

MPFEM Moving Particle Finite Element Method

MPI Message Passing Interface

MPM Material Point Method

MPS Moving Particle Semi-implicit

MRT Multiple Relaxation Time

NEM Natural Element Method

NNS Nearest Neighbor Search

PDE Partial Differential Equation(s)

PF Pairwise Force

PGDEM Petrov-Galerkin Diffuse Element Method

PIC Particle In Cell

PU Partition of Unity

PUFEM Partition of Unity Finite Element Method

PUM Partition of Unity Method

RBF Radial Basis Functions

RKEM Reproducing Kernel Element Method

RKPM Reproducing Kernel Particle Method

SC Shan-Chen

SCMP Single-Component Multi-Phase

SDPD Smoothed Dissipative Particle Dynamics

SPH Smoothed Particle Hydrodynamics

USAW Unified Semi-Analytical Wall

VM Vortex Method

VOF Volume Of Fluid

WCSPH Weakly Compressible SPH

WVT Weighted Voronoi Tesselation

XFEM eXtended Finite Element Method

université PARIS-SACLAY
École doctorale de mathématiques Hadamard (EDMH)

Titre : Étude comparative des méthodes d'origine particulaire SPH et LBM pour la simulation d'écoulements polyphasiques intermittents dans des conduites

Mots clés : SPH, LBM, polyphasique, écoulement à bouchons

Résumé : L'objectif de cette thèse est d'étudier les apports et les limitations de deux méthodes d'origine particulaire, SPH et LBM, dans le cadre de la simulation des écoulements à bouchons dans des conduites. Dans l'industrie pétrolière, ce type d'écoulement, que l'on retrouve par exemple dans les pipelines qui acheminent le pétrole et le gaz jusqu'aux raffineries, est connu pour endommager les installations et pour réduire l'efficacité du transport des fluides. Il est donc important de bien comprendre leur formation. Nous avons donc implémenté ces deux méthodes, ainsi que leurs variantes polyphasiques, et avons mené une campagne de validation et de comparaison afin de sélectionner la méthode la plus adéquate, pour poursuivre ensuite avec des simulations de cas plus appliqués et réalistes. Les contributions présentées se concentrent principalement sur trois axes. Tout d'abord, il a fallu construire les codes de calcul nécéssaires, les valider puis comparer des différentes formulations polyphasiques disponibles pour SPH et LBM. Ensuite, nous avons développé des conditions aux limites d'entrée/sortie adaptées au contexte polyphasique pour être en mesure d'injecter les fluides avec des vitesses imposées et de les évacuer du domaine avec un pression donnée. Enfin, nous avons simulé différents cas d'écoulements à bouchons académiques avec SPH et LBM, puis sur des cas appliqués avec des géométries réalistes et des ratios de densité et de viscosité de type air/eau avec SPH seulement.

Title : Comparative study of particle-based methods SPH and LBM for the simulation of multiphase slug flows in pipes

Keywords : SPH, LBM, multiphase, slug flows

Abstract : The main objective of this thesis is to study the contributions and limitations of two particle-based methods, SPH and LBM, for the simulation of slug flows in pipes. In the petroleum industry, these flow regimes, found for example during the transportation of oil and gas from reservoirs to refinery facilities through pipelines, are highly undesirable because they are known to damage facilities and to reduce flow efficiency. Therefore, it is important to understand its formation. We have implemented both methods, as well as their multiphase variants, and have led a validation and comparison campaign in order to to select the most suited method and to continue with simulations of more applied and realistic cases. The main contributions of this work can summarized in three points. First, we had to write the necessary computation codes, validate them and compare the different multiphase formulations available for SPH and LBM. Then, we have developed inlet/outlet boundary conditions adapted to the multiphase context so that we are able to inject fluids with prescribed velocities and let them exit he domain with a given pressure. Finally, we have simulated different academic test cases of slug flows with SPH and LBM and then on applied cases with realistic geometries and air-water like density and viscosity ratios with SPH only.

Université Paris-Saclay
Espace Technologique / Immeuble Discovery
Route de l'Orme aux Merisiers RD 128 / 91190 Saint-Aubin, France